APPROACHES THAT FOSTER A PRO-REGENERATIVE ENVIRONMENT

EDITED BY: Carl Austin Gregory, Fei Liu, Daniel Alge, Ryang Hwa Lee and Paul Genever

PUBLISHED IN: Frontiers in Bioengineering and Biotechnology

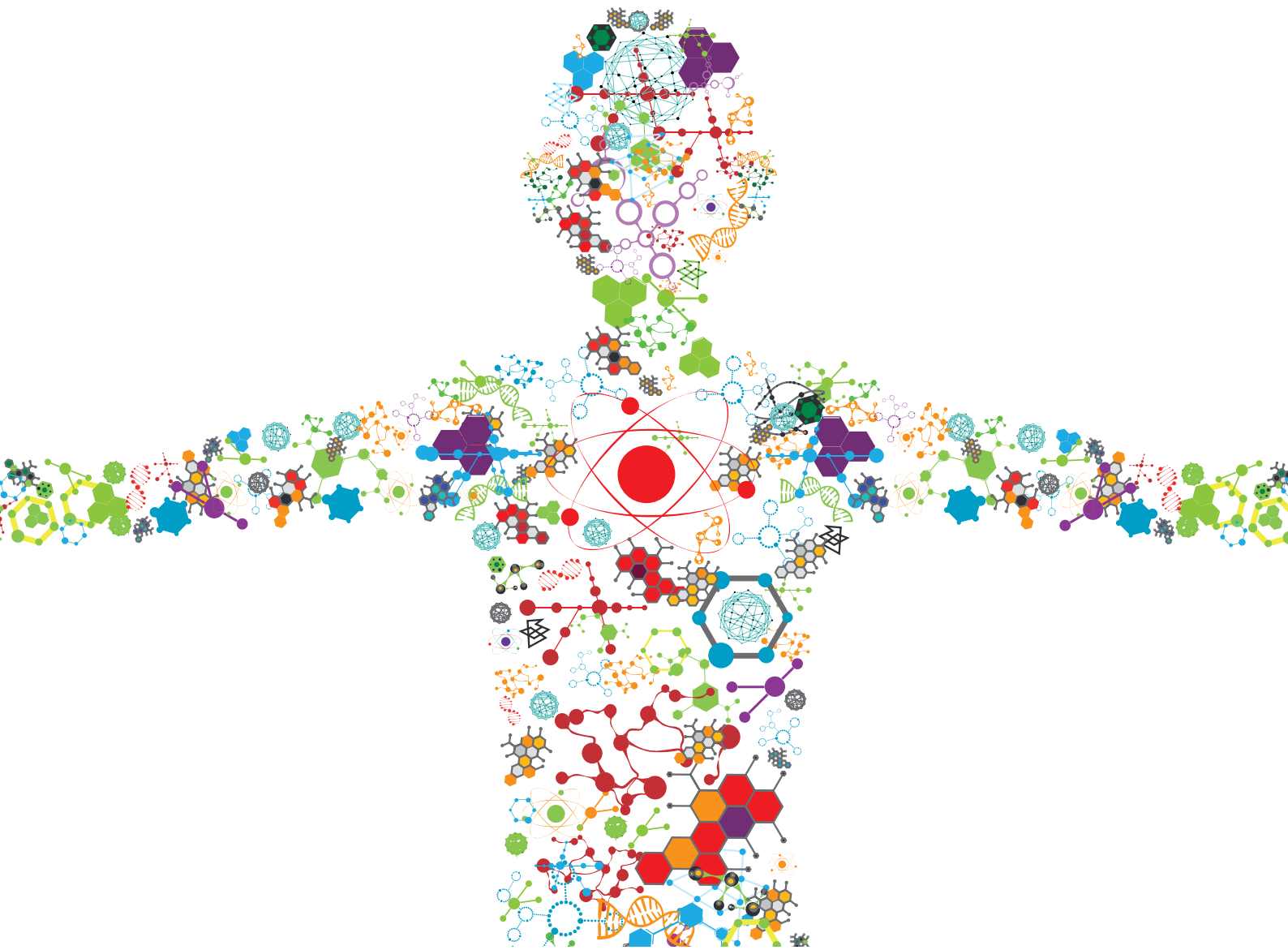

frontiers Research Topics

frontiers

ISSN 1664-8714
ISBN 978-2-88974-804-4
DOI 10.3389/978-2-88974-804-4

About Frontiers

Frontiers is more than just an open-access publisher of scholarly articles: it is a pioneering approach to the world of academia, radically improving the way scholarly research is managed. The grand vision of Frontiers is a world where all people have an equal opportunity to seek, share and generate knowledge. Frontiers provides immediate and permanent online open access to all its publications, but this alone is not enough to realize our grand goals.

Frontiers Journal Series

The Frontiers Journal Series is a multi-tier and interdisciplinary set of open-access, online journals, promising a paradigm shift from the current review, selection and dissemination processes in academic publishing. All Frontiers journals are driven by researchers for researchers; therefore, they constitute a service to the scholarly community. At the same time, the Frontiers Journal Series operates on a revolutionary invention, the tiered publishing system, initially addressing specific communities of scholars, and gradually climbing up to broader public understanding, thus serving the interests of the lay society, too.

Dedication to Quality

Each Frontiers article is a landmark of the highest quality, thanks to genuinely collaborative interactions between authors and review editors, who include some of the world's best academicians. Research must be certified by peers before entering a stream of knowledge that may eventually reach the public - and shape society; therefore, Frontiers only applies the most rigorous and unbiased reviews.
Frontiers revolutionizes research publishing by freely delivering the most outstanding research, evaluated with no bias from both the academic and social point of view. By applying the most advanced information technologies, Frontiers is catapulting scholarly publishing into a new generation.

What are Frontiers Research Topics?

Frontiers Research Topics are very popular trademarks of the Frontiers Journals Series: they are collections of at least ten articles, all centered on a particular subject. With their unique mix of varied contributions from Original Research to Review Articles, Frontiers Research Topics unify the most influential researchers, the latest key findings and historical advances in a hot research area! Find out more on how to host your own Frontiers Research Topic or contribute to one as an author by contacting the Frontiers Editorial Office: frontiersin.org/about/contact

APPROACHES THAT FOSTER A PRO-REGENERATIVE ENVIRONMENT

Topic Editors:
Carl Austin Gregory, Texas A&M Health Science Center, United States
Fei Liu, Texas A&M University, United States
Daniel Alge, Texas A&M University, United States
Ryang Hwa Lee, Texas A&M University, United States
Paul Genever, University of York, United Kingdom

Citation: Gregory, C. A., Liu, F., Alge, D., Lee, R. H., Genever, P., eds. (2022). Approaches That Foster a Pro-Regenerative Environment. Lausanne: Frontiers Media SA. doi: 10.3389/978-2-88974-804-4

Table of Contents

frontiers in Bioengineering and Biotechnology

EDITORIAL
published: 09 March 2022
doi: 10.3389/fbioe.2022.873375

Editorial: Approaches That Foster a Pro-Regenerative Environment

Carl A. Gregory[1]*, *Ryang Hwa Lee*[1], *Fei Liu*[1] and *Daniel Alge*[2]

[1]Department of Molecular and Cellular Medicine, Texas A&M University Health Science Center, Bryan, TX, United States, [2]College of Engineering, Texas A&M University, College Station, TX, United States

Keywords: autotherapy, regeneration, stem cells, immunomodulation, therapy

Editorial on the Research Topic

Approaches That Foster a Pro-Regenerative Environment

The term *autotherapy* was originally coined in the early 1900's, referring primarily to the re-administration of crude preparations of biological fluids (e.g., wound exudates, blood) from diseased patients in an attempt to accelerate inherent healing processes. Reports of its successful implementation were numerous and convincing, especially for infectious diseases, but the therapeutic mechanism of such an intervention was unclear, with hypotheses ranging from modulation of immune responses to purely psychosomatic effects (Duncan, 1914; Duncan, 1917; Greval, 1949). In 2018, Lumelsky and others at the National Institute of Dental and Craniofacial Research (NIDCR) revived the definition of autotherapy, applying it specifically to those approaches that stimulate inherent tissue responses, manipulate stem cell niches, and modulate endogenous tissue microenvironments to enhance tissue healing and regeneration (Lumelsky et al., 2018).

Modern autotherapeutic concepts can be crudely divided into i) strategies that modulate the stem cell niche (e.g., stem cells, modulation or recapitulation of the stem cell niche) ii) those that foster a pro-regenerative environment (immune modulation, anti-inflammatory approaches, angiogenesis, metabolism, microbiome) and (iii) direct lineage reprogramming of stem cells or trans-differentiation of differentiated cells (e.g., epigenetic or genetic modification *in situ* with non-viral agents). As it relates to tissue engineering and regenerative medicine, this could be achieved by the transient modulatory effects of cell therapy, administration of stem-cell derived factors such as extracellular vesicles (EVs), secreted ligands or extracellular matrices (ECMs), or from synthetic small molecules, genetic engineering tools, biomaterials or scaffolds. The entire field of autotherapy is extremely broad, but in this collection, we focus on approaches that foster a pro-regenerative environment through stimulation of stem cells and/or modulation of the immune system.

We begin with Dr Lumelsky's opinion article (Lumelsky) stressing the importance of local control in the propagation of a pro-regenerative environment. In particular, Dr Lumelsky emphasizes the contribution of the stem cell niche in this process, stressing that its individual components, stem cells, stromal cells, extracellular matrices and soluble mediators play distinct but equally important roles in maintaining regenerative homeostasis. In addition, the contribution of the immune system is discussed, with emphasis on the need for precise modulation of inflammatory and post-inflammatory processes to support tissue regeneration rather than fibrosis. Within this context, the potential of synthetic biomaterials to control cell adhesion characteristics, biomechanical forces, and soluble factor delivery is discussed. In keeping with the emphasis on biomaterials and their potential for immune modulation, Karkanitza et al. reviews our current understanding of immune reactions to biomaterials, and considers how this knowledge might be employed to drive regeneration and reduce the probability of adverse reactions.

OPEN ACCESS

Edited and reviewed by:
Ranieri Cancedda, Independent Researcher, Genova, Italy

***Correspondence:**
Carl A. Gregory
cgregory@tamu.edu

Specialty section:
This article was submitted to Tissue Engineering and Regenerative Medicine, a section of the journal Frontiers in Bioengineering and Biotechnology

Received: *10 February 2022*
Accepted: *14 February 2022*
Published: *09 March 2022*

Citation:
Gregory CA, Lee RH, Liu F and Alge D (2022) Editorial: Approaches That Foster a Pro-Regenerative Environment. Front. Bioeng. Biotechnol. 10:873375. doi: 10.3389/fbioe.2022.873375

One of the major challenges in the translation of experimental therapies to clinical implementation is the selection of appropriate animal models for preclinical testing. In most cases, and especially for musculoskeletal applications, a large animal model is required, mimicking as closely as possible, the load and weight bearing characteristics of the human body. Although largely overlooked, the canine system is an excellent model for skeletal regeneration, with similar anatomy to humans, well-developed surgical techniques, and the capacity to perform gait analysis. Dobson et al. examine the mechanism of canine mesenchymal stem cells (MSCs) during bone formation. Using canine MSCs in mouse recipients, they describe for the first time that MSCs and sub-therapeutic levels of bone morphogenic proteins synergize to drive bone repair. In these studies, the implanted MSCs were essential for rapid repair, but did not persist at the site of injury suggesting that MSCs, when triggered with very low levels of BMP, stimulate the host's inherent bone repair mechanisms rather than directly differentiate into osteoblasts. This study represents an excellent example of cell-mediated autotherapy and contributes to the rapidly growing number of studies supporting autotherapy as the predominant mechanism of MSC-mediated healing. Han et al. offer an alternative approach for therapeutic enhancement of adipose derived MSCs through *ex vivo* exposure to decellularized adipose tissue ECM. In this work, the authors demonstrate that culturing of MSCs on decellularized adipose tissue ECM enhanced secretion of regenerative and immune-modulatory factors. This process could, in the future, improve the autotherapeutic potential of adult stem cells.

While stem cells have the potential to deliver multiple bioactive factors with the means to adapt to the dynamic healing environment, some autotherapeutic effects can be achieved by simple and direct administration of defined factors. Liebman et al. present an intriguing strategy for the stabilization of labile biological ligands hepatocyte growth factor and fibroblast growth factor 2 by attachment to immunoglobulins. In a porcine model of myocardial ischemia and perfusion, the immunoglobulin-sequestered factors were stable and promoted repair of cardiac tissue. Sankar et al. describe the broad autotherapeutic applications of RAD16, a synthetic peptide with hemostatic properties that also serves as an ECM analog for cell attachment and migration. To address the issue of radiation-induced salivary gland damage during treatment of head and neck cancer, Gilman et al. employed the non-steroidal anti-inflammatory drug indomethacin to inhibit prostaglandin E2-mediated inflammatory processes and promote regeneration of the gland. In a related study, Nam et al. employ hydrogels to deliver Laminin-1 peptides for enhanced autotherapy of salivary glands through stimulation of the salivary stem cell niche and by modulation of macrophages to adopt a pro-regenerative phenotype. Xu et al. demonstrate that simple, naturally occurring substances can be employed as autotherapeutic tools. In their study, a simple preparation of platelet rich plasma stimulated regenerative characteristics of human dental pulp cells, providing some credence to the reports of autotherapy in the early 1900's.

Fetz et al. and Hymel et al. represent excellent examples of the utilization of synthetic materials to regulate local release of therapeutic factors into the regenerative microenvironment. Fetz et al. employed electrospun polydioxanone to slowly release chloroquine which in turn caused neutrophils to downregulate inflammatory factors and adopt a more resolving, putatively regenerative phenotype. Using a similar approach, Hymel et al. utilized nanofibers to release bioactive lipid into the myogenic microenvironment to enhance myofiber growth and promote regenerative immunological processes.

We hope this diverse collection of studies showcases many aspects of the autotherapy concept and recent efforts in developing innovative approaches to enhance our inherent capacity for tissue healing and regeneration.

AUTHOR CONTRIBUTIONS

CG wrote the editorial RL edited the article FL edited the article DA edited the article.

REFERENCES

Duncan, C. H. (1917). Autotherapy. *Ind. Med. Gaz.* 52 (5), 179–180.

Duncan, C. H. (1914). Autotherapy in the Prevention and Cure of Purulent Infections. 1914. *Practitioner* 258 (2581774), 34.

Greval, S. D. (1949). Autotherapy. *Ind. Med. Gaz.* 83 (12), 549–551.

Lumelsky, N., O'Hayre, M., Chander, P., Shum, L., and Somerman, M. J. (2018). Autotherapies: Enhancing Endogenous Healing and Regeneration. *Trends Mol. Med.* 24 (11), 919–930. doi:10.1016/j.molmed.2018.08.004

Conflict of Interest: The authors declare that the research was conducted in the absence of any commercial or financial relationships that could be construed as a potential conflict of interest.

frontiers in Bioengineering and Biotechnology

ORIGINAL RESEARCH
published: 18 March 2021
doi: 10.3389/fbioe.2021.642465

Preconditioning Human Adipose-Derived Stromal Cells on Decellularized Adipose Tissue Scaffolds Within a Perfusion Bioreactor Modulates Cell Phenotype and Promotes a Pro-regenerative Host Response

*Tim Tian Y. Han[1], John T. Walker[1], Aaron Grant[2], Gregory A. Dekaban[3,4] and Lauren E. Flynn[1,5,6]**

[1] Department of Anatomy & Cell Biology, Schulich School of Medicine & Dentistry, The University of Western Ontario, London, ON, Canada, [2] Division of Plastic and Reconstructive Surgery, Schulich School of Medicine & Dentistry, The University of Western Ontario, London, ON, Canada, [3] Molecular Medicine Research Laboratories, Robarts Research Institute, The University of Western Ontario, London, ON, Canada, [4] Department of Microbiology & Immunology, Schulich School of Medicine & Dentistry, The University of Western Ontario, London, ON, Canada, [5] Department of Chemical and Biochemical Engineering, Faculty of Engineering, The University of Western Ontario, London, ON, Canada, [6] Bone and Joint Institute, The University of Western Ontario, London, ON, Canada

Cell-based therapies involving the delivery of adipose-derived stromal cells (ASCs) on decellularized adipose tissue (DAT) scaffolds are a promising approach for soft tissue augmentation and reconstruction. Our lab has recently shown that culturing human ASCs on DAT scaffolds within a perfusion bioreactor prior to implantation can enhance their capacity to stimulate *in vivo* adipose tissue regeneration. Building from this previous work, the current study investigated the effects of bioreactor preconditioning on the ASC phenotype and secretory profile *in vitro*, as well as host cell recruitment following implantation in an athymic nude mouse model. Immunohistochemical analyses indicated that culturing within the bioreactor increased the percentage of ASCs co-expressing inducible nitric oxide synthase (iNOS) and arginase-1 (Arg-1), as well as tumor necrosis factor-alpha (TNF-α) and interleukin-10 (IL-10), within the peripheral regions of the DAT relative to statically cultured controls. In addition, bioreactor culture altered the expression levels of a range of immunomodulatory factors in the ASC-seeded DAT. *In vivo* testing revealed that culturing the ASCs on the DAT within the perfusion bioreactor prior to implantation enhanced the infiltration of host $CD31^+$ endothelial cells and $CD26^+$ cells into the DAT implants, but did not alter $CD45^+F4/80^+CD68^+$ macrophage recruitment. However, a higher fraction of the $CD45^+$ cell population

OPEN ACCESS

Edited by:
Carl Austin Gregory, Texas A&M Health Science Center, United States

Reviewed by:
Bruce Alan Bunnell, University of North Texas Health Science Center, United States
Dietmar W. Werner Hutmacher, Queensland University of Technology, Australia

***Correspondence:**
Lauren E. Flynn
lauren.flynn@uwo.ca

Specialty section:
This article was submitted to Tissue Engineering and Regenerative Medicine, a section of the journal Frontiers in Bioengineering and Biotechnology

Received: *16 December 2020*
Accepted: *05 February 2021*
Published: *18 March 2021*

Citation:
Han TTY, Walker JT, Grant A, Dekaban GA and Flynn LE (2021) Preconditioning Human Adipose-Derived Stromal Cells on Decellularized Adipose Tissue Scaffolds Within a Perfusion Bioreactor Modulates Cell Phenotype and Promotes a Pro-regenerative Host Response. Front. Bioeng. Biotechnol. 9:642465. doi: 10.3389/fbioe.2021.642465

expressed the pro-regenerative macrophage marker CD163 in the bioreactor group, which may have contributed to enhanced remodeling of the scaffolds into host-derived adipose tissue. Overall, the findings support that bioreactor preconditioning can augment the capacity of human ASCs to stimulate regeneration through paracrine-mediated mechanisms.

Keywords: bioreactors, decellularized adipose tissue, preconditioning, angiogenesis, immunomodulation, macrophage, adipose-derived stromal cell

INTRODUCTION

Tissue-engineering strategies represent a promising approach for the long-term augmentation and regeneration of damaged or deficient subcutaneous adipose tissue for applications in plastic and reconstructive surgery. Recent advancements in the field have focused on using a combined approach involving cell-seeded scaffolds as a means to provide both immediate volumetric augmentation and promote the stable regeneration of host-derived soft tissues (Choi et al., 2009; Brett et al., 2017). In particular, decellularized adipose tissue (DAT) has emerged as a promising pro-adipogenic platform for this application (Flynn, 2010; Mohiuddin et al., 2019). DAT scaffolds can be fabricated from human adipose tissue that is abundantly discarded as surgical waste, and have been shown to retain biochemical and biophysical properties that mimic the native tissue source, which may be favorable for adipose tissue regeneration (Haddad et al., 2016; Kuljanin et al., 2017).

While applying DAT as an off-the-shelf scaffold is appealing, studies have suggested that the rate and extent of adipose tissue regeneration can be enhanced by seeding the scaffolds with pro-regenerative progenitor cells (Young et al., 2014; Wang et al., 2013). This strategy may be critical for the larger volume augmentation that is required for many reconstructive applications in the clinic, as a lack of angiogenesis and host cell infiltration can result in implant failure. Previous work from our lab supports that seeding the DAT with adipose-derived stromal cells (ASCs) can enhance *in vivo* angiogenesis and host adipogenesis in immunocompetent mouse and rat models (Han et al., 2015; Robb et al., 2020). ASCs are a logical cell source for this application given their relative abundance and accessibility (Bourin et al., 2013), their high tolerance of ischemic conditions such as those immediately following implantation (Suga et al., 2010), as well as their enhanced adipogenic potential compared to other mesenchymal stromal cell (MSC) sources (Pizzute et al., 2015). Most clinical plastic surgery studies to date have focused on using the stromal vascular fraction (SVF) of adipose tissue to avoid the translational hurdles associated with the use of cultured ASC populations. However, through careful consideration of the cell culture microenvironment, it may be possible to design systems for cell expansion and preconditioning that would augment the capacity of the ASCs to stimulate regeneration, resulting in a more robust and predictable response that would justify the additional costs and regulatory hurdles involved.

In our previous work, the static seeding methods used resulted in a sparse and heterogeneous spatial distribution of ASCs on the DAT scaffolds, which may have restricted their capacity to stimulate regeneration. To address this limitation, we recently investigated the effects of culturing human ASCs on the 3-D DAT scaffolds used for cell delivery within a scaffold-based perfusion bioreactor system (Han and Flynn, 2020). Our findings demonstrated that dynamic culture under 2% O_2 promoted human ASC expansion in the peripheral regions of the DAT. Further, culturing within the bioreactor under 2% O_2 for 14 days prior to implantation significantly augmented blood vessel infiltration and host-derived adipose tissue formation within the DAT scaffolds in a subcutaneous implant model in athymic nude (*nu/nu*) mice in comparison to scaffolds cultured within the bioreactor under 20% O_2, as well as statically cultured, freshly seeded, and unseeded controls (Han and Flynn, 2020). While the restrictions on the implant size and differences in the structure of the skin make it challenging to translate the findings of mouse models to predict future outcomes in humans, *in vivo* studies in immunocompromised mice remain a valuable tool for characterizing the effects of human ASCs in a complex physiological environment and for comparing the efficacy of varying ASC culture strategies or delivery platforms.

Although the delivery of a higher density of ASCs within the DAT scaffolds likely contributed to the enhanced adipose tissue regeneration observed in the 2% O_2 bioreactor group, the dynamic culture conditions may have also preconditioned the ASCs to have a more pro-regenerative phenotype. A growing body of evidence supports that ASCs delivered within scaffolds primarily stimulate regeneration through transient paracrine-mediated effects, rather than through long-term engraftment and differentiation (Chazenbalk et al., 2011; Suga et al., 2014; Kang et al., 2014). More specifically, ASCs can secrete a diverse range of growth factors and cytokines that can promote the recruitment and/or modulate the response of host cells, including endothelial cells, adipogenic progenitors, and immune cell populations that can contribute to implant remodeling and *de novo* adipose tissue formation (Kapur and Katz, 2013). While the stimulatory effects of hypoxia on pro-angiogenic factor and cytokine secretion are well documented (Thangarajah et al., 2009; Hsiao et al., 2013), the effects of dynamic culture on MSC paracrine factor expression remain largely unexplored, with most bioreactor studies to date focused on characterizing the effects on proliferation and/or differentiation (Zhao and Ma, 2005; Alvarez-Barreto et al., 2011; Dos Santos et al., 2014; Yu et al., 2017).

Recognizing that dynamic culture may enhance the pro-regenerative capacity of the ASCs, we hypothesized that culturing the ASCs on the DAT scaffolds within the perfusion bioreactor would modulate their phenotype and paracrine function. Building from our previous work, human ASCs were cultured on

DAT scaffolds under 2% O_2 either within the perfusion bioreactor or statically within the culture inserts for 14 days. *In vitro* analyses were first performed to assess the effects of dynamic culturing on ASC phenotype and paracrine factor expression. Subsequently, the impact of bioreactor preconditioning on the pro-regenerative paracrine functionality of the ASC-seeded DAT scaffolds was explored by characterizing host cell recruitment at 1-, 4-, and 8-weeks post-implantation in the athymic nude mouse model.

MATERIALS AND METHODS

Materials

Unless otherwise stated, all reagents were purchased from Sigma Aldrich Canada Ltd., and used as received (Oakville, Canada).

Human Adipose Tissue Collection and Processing

Surgically discarded subcutaneous adipose tissue was collected with informed consent from female donors undergoing elective lipo-reduction surgeries at the University Hospital or St. Joseph's Hospital in London, ON, Canada. Human Research Ethics Board approval for this study was obtained from Western University (HSREB# 105426). The fresh tissues were transported to the lab in sterile phosphate buffered saline (PBS) supplemented with 2% bovine serum albumin (BSA) on ice. Within 2 h of collection, the adipose tissue was processed for either ASC isolation or decellularization following established protocols (Flynn, 2010). The human ASCs were cultured on T75 flasks (Corning, Fisher Scientific, Ottawa, Canada) in proliferation medium (DMEM:Ham F12 (Wisent, St. Bruno, Canada) supplemented with 10% fetal bovine serum (FBS; Wisent, St. Bruno, Canada) and 100 U/mL penicillin and 0.1 mg/mL streptomycin (1% pen-strep; Thermo Fisher Scientific, Waltham, MA, United States).

To prepare the DAT scaffolds for cell culture, DAT samples were lyophilized and cut into individual scaffolds having a mass of 8 ± 1 mg, sized to fit within the cylindrical culture inserts used for both groups in this study (height 11 mm, inner diameter 5 mm) (Han and Flynn, 2020). The scaffolds were rehydrated in deionized water, decontaminated through repeated rinsing in 70% ethanol, and washed in sterile PBS. Prior to seeding, the scaffolds were equilibrated in fresh proliferation medium for 24 h.

Scaffold Seeding and Culture

Adipose-derived stromal cells were seeded at passage 3 at a density of 1×10^6 cells/scaffold as previously described (Han and Flynn, 2020), transferred into the culture inserts, and cultured in proliferation medium for 14 days either statically in 15 mL vented-cap conical tubes or dynamically within a customized perfusion bioreactor system (Tissue Growth Technologies, Instron) under a flow rate of 0.5 mL/min (Han and Flynn, 2020). Both the dynamic and static control samples were cultured within the cylindrical inserts (Han and Flynn, 2020) to ensure that the scaffold geometry and the surface area that was in direct contact with the media prior to perfusion were consistent between the groups. Hypoxic conditions (2% O_2/93% N_2/5% CO_2, 37°C) were maintained for all cultures using a tri-gas incubator (ThermoFisher Forma Series II 3110).

Immunohistochemical Assessment of the Effects of Bioreactor Culture on the DAT on Phenotypic Markers

Immunohistochemical analyses were performed to assess the expression of inducible nitric oxide synthase (iNOS), a marker associated with the immunomodulatory function of murine MSCs (Ren et al., 2008; Li et al., 2012; Maria et al., 2018), as well as arginase-1 (Arg-1), in the ASCs within the peripheral (<200 μm from the scaffold edge) or central (>200 μm from the scaffold edge) regions of the DAT scaffolds cultured either dynamically or statically for 14 days. In addition, triple staining was performed for Arg-1 with the immunomodulatory cytokines interleukin-10 (IL-10) and tumor necrosis factor-α (TNFα). The primary and secondary antibodies and dilutions are summarized in **Table 1**.

For both analyses, scaffolds were fixed in 4% paraformaldehyde for 24 h at 4°C before being embedded in paraffin and sectioned (7 μm sections). The sections were de-paraffinized in an ethanol series and heat-mediated antigen retrieval was performed by incubating in Tris-EDTA buffer (10 mM tris base, 1 mM EDTA, 0.05% Tween-20, pH 9.0) at 95°C on a hot plate for 25 min. The sections were cooled for 25 min and then blocked with 5% BSA in PBS-T (0.1% Tween 20) for 1 h at room temperature before being incubated with the primary antibodies for iNOS in combination with Arg-1 or Arg-1 in combination with TNF-α and IL-10 at 4°C overnight. Next, the sections were washed with PBS and incubated with the secondary antibodies for 1 h at room temperature. Mouse spleen and liver were used as tissue positive controls, and no primary antibody controls were included in all trials.

Stained cross-sections were mounted in Fluoroshield Mounting Medium with DAPI (Abcam, Cambridge, MA, United States) and visualized with an EVOS® FL Cell Imaging System (Thermo Fisher Scientific). Positively stained cells from five non-overlapping fields of view from both the central and peripheral regions were quantified manually in a blinded fashion using ImageJ Software in three non-adjacent cross-sections taken at least 100 μm apart from each scaffold. For the analyses, grayscale images for each color channel were used, and a brightness threshold of 50–255 was applied with a particle size >50 used to quantify $DAPI^+$ cells. A total of 3 trials were performed with ASCs from different donors ($N = 3$).

Quantitative Analysis of the Effects of Perfusion Bioreactor Culture on Immunomodulatory Factor Expression in Human ASCs Cultured on the DAT

A Human Magnetic Luminex® Assay was performed to compare the protein expression levels of a range of pro-angiogenic and immunomodulatory factors between the static and dynamic groups at 14 days. TNF-α and IL-10 were selected based on their well-recognized counterbalancing roles in regulating the inflammatory response, as well as to compare with the IHC findings. Hepatocyte growth factor (HGF) was chosen as a

TABLE 1 | Primary and secondary antibodies and dilutions used for immunostaining in the *in vitro* studies.

Primary antibody	Primary Dilution	Secondary antibody	Secondary Dilution
Arg-1 (Millipore ABS535)	1:100	Goat anti-chicken Alexa® 488 (Abcam ab150169)	1:200
iNOS (Abcam ab15323)	1:100	Goat anti-rabbit Alexa® 594 (Abcam ab150080)	1:200
TNF-α (Abcam ab6671)	1:200	Goat anti-rabbit Alexa® 594 (Abcam ab150080)	1:400
IL-10 (R&D AF519)	1:50	Donkey anti-goat Alexa® 680 (ThermoFisher A-21084)	1:100

pleiotropic factor that is highly expressed by ASCs, which can have both pro-angiogenic and anti-inflammatory effects (Cai et al., 2007; Ceccarelli et al., 2020). Chemokine C-X-C motif 10 (CXCL-10) was selected as a marker associated with inflammation in adipose tissue (Kochumon et al., 2020), as well as macrophage recruitment in other tissues (Petrovic-Djergovic et al., 2015). Finally, C-X-C motif ligand 2 (CXCL-2) was chosen as a pro-inflammatory chemokine that has been shown to be upregulated during adipogenic differentiation (Kusuyama et al., 2016; Siebert et al., 2016), and interleukin-6 (IL-6) was included as an additional pro-inflammatory adipokine that can modulate both lipid metabolism and macrophage polarization within adipose tissue (Trujillo et al., 2004; Braune et al., 2017).

For this assay, three replicate scaffolds from each group ($n = 3$) were analyzed per ASC donor, and a total of five trials were performed with different ASC donors ($N = 5$). In preparation for the Luminex® assay, the individual scaffolds were frozen in liquid nitrogen, crushed with a mortar and pestle, and resuspended in a lysis buffer (50 mM Tris-HCl, 100 mM NaCl, 10% glycerol, 1% Triton X-100, pH 7.4). The samples were then briefly sonicated with an ultrasonic dismembrator (ThermoFisher Model 100) and centrifuged at 13,000 × *g* for 10 min at 4°C. The supernatant from each sample was then analyzed with a Human Magnetic Luminex® Assay (R&D Systems) using a MAGPIX® System (Millipore), in accordance with the manufacturer's protocols. Protein concentrations were determined based on comparison to standard curves and normalized to the double stranded DNA (dsDNA) content measured in each sample using a PicoGreen® dsDNA Assay (Han and Flynn, 2020), following the manufacturer's instructions.

Subcutaneous Implantation Surgeries

In vivo studies were performed to compare the effects of culturing the ASCs on the DAT scaffolds for 14 days under static or dynamic conditions on the host cell response. All animal studies followed Canadian Council on Animal Care (CCAC) guidelines and the protocols were reviewed and approved by the Western University Animal Care Committee (Protocol #2015-049). Female athymic nude mice (Nu-*Foxn1*^{nu}) (Charles River Laboratories, Sherbrooke, Canada) of 10–13 weeks of age were used for this study ($N = 6$ mice per scaffold group/timepoint). Subcutaneous implantation surgeries were performed following established protocols (Han and Flynn, 2020). At 1, 4, and 8 weeks, the mice were sacrificed by CO_2 overdose and the scaffolds were excised within their surrounding tissues. The samples were fixed in 4% paraformaldehyde at 4°C overnight before being embedded in paraffin and sectioned (7 μm) for immunohistochemical analyses.

Immunohistochemical Analysis of Host Cell Recruitment

Immunostaining was performed to assess host cell infiltration into the scaffolds at 1, 4, and 8 weeks. More specifically, CD31 staining was performed to examine host endothelial cell recruitment. In addition, co-staining was performed for CD26, a marker that has been associated with highly proliferative multipotent progenitors that give rise to preadipocytes in murine subcutaneous adipose tissue (Merrick et al., 2019), along with the human cell marker Ku80 (Allard et al., 2014), to distinguish the host-derived CD26^{+} population. Finally, host immune cell recruitment was characterized through triple staining for the pan-leukocyte marker CD45, the murine macrophage marker F4/80, and the phagocytic macrophage marker CD68. The phenotype of the infiltrating macrophages was also probed by co-staining for CD45 in combination with the pro-regenerative macrophage marker CD163. For each explanted scaffold that was analyzed ($N = 6$ for CD31, CD26 and CD163 analyses, $N = 4$ for macrophage recruitment), three non-adjacent cross-sections at least 100 μm apart were assessed. Immunohistochemical staining and imaging were performed following the methods described above and using the antibodies summarized in **Table 2**. Quantification was performed within 10 randomly selected and non-overlapping, non-adjacent fields of view in each section as previously described.

Statistical Methods

Statistical analyses were performed using linear mixed effects models and multiple comparisons were corrected as described by Hothorn et al. (2008). Statistical analyses were performed with R statistics software (R Core Team, 2017) using the "lme4" package for linear and non-linear mixed effects models (Bates et al., 2015), and the "multcomp" package for simultaneous inference in general parametric models (Hothorn et al., 2008). For *in vitro* immunofluorescence studies, sample location (peripheral/central) and treatment (static/dynamic) were included as fixed effects, and ASC donor was included as a random effect. For the Luminex® assay, treatment was included as a fixed effect and ASC donor was included as a random effect. For analyses of *in vivo* samples, treatment and time were included

TABLE 2 | Primary and secondary antibodies and dilutions used for immunostaining in the *in vivo* study.

Primary antibody	Primary Dilution	Secondary antibody	Secondary Dilution
CD31 (Abcam ab28364)	1:100	Goat anti-rabbit Alexa® 594 (Abcam ab150080)	1:200
Ku80 (Cell Signaling 2180)	1:200	Goat anti-rabbit Alexa® 594 (Abcam ab150080)	1:400
CD26 (R&D AF954)	1:50	Donkey anti-goat Alexa® 680 (ThermoFisher A-21084)	1:100
CD45 (R&D AF114)	1:100	Donkey anti-goat Alexa® 680 (ThermoFisher A-21084)	1:200
CD68 (BioRad MCA1957)	1:100	Goat anti-rat Alexa® 488 (ThermoFisher A-11006)	1:200
F4/80 (Abcam ab111101)	1:50	Goat anti-rabbit Alexa® 594 (Abcam ab150080)	1:100
CD163 (Abcam ab182422)	1:200	Goat anti-rabbit Alexa® 594 (Abcam ab150080)	1:400

as fixed effects, and ASC donor and mouse were included as random effects. Corrected p-values <0.05 were considered to be statistically significant. Graphs were produced using GraphPad Prism version 6 (GraphPad, La Jolla, CA, United States). Error bars represent the standard deviation.

RESULTS

Dynamic Culture Increased the Percentage of ASCs Expressing iNOS Within the Peripheral Regions of the DAT Scaffolds

Immunostaining was performed to assess the expression of iNOS and Arg-1 in the ASCs that were cultured statically or dynamically on the DAT scaffolds for 14 days. A high density of $iNOS^+$ cells was visualized along the peripheral edges of the scaffolds in the dynamic group, while Arg-1^+ cells were distributed throughout the scaffolds in both groups (**Figure 1A**). Consistent with our previous findings that dynamic culture within the bioreactor under 2% O_2 promoted ASC expansion within the periphery of the DAT (Han and Flynn, 2020), DAPI quantification confirmed that the ASC density was significantly higher in the peripheral region (<200 μm from scaffold edge) of the dynamic group (562 ± 116 cells/mm^2), as compared to the central region (>200 μm from scaffold edge) of the dynamic group (213 ± 54 cells/mm^2) and the peripheral region of the static group (284 ± 80 cells/mm^2) (**Supplementary Figure 1**).

Quantification of $iNOS^+$Arg-1^+DAPI^+ cells in the peripheral and central regions of the scaffolds was performed. A significantly higher density of $iNOS^+$Arg 1^+DAPI^+ cells was observed in the peripheral region of the dynamic group (114 ± 5 cells/mm^2) as compared to the peripheral region of the static group (18 ± 13 cells/mm^2) and the central region of the dynamic group (27 ± 10 cells/mm^2) (**Figure 1B**). The data was also analyzed as a percentage to account for differences in the total cell density in the two regions for each of the groups, and assess whether there was significant upregulation in the relative levels of positive cells with media perfusion. Analysis of the $iNOS^+$Arg-1^+DAPI^+ cell population relative to the total $DAPI^+$ cell population confirmed that a significantly higher percentage of the ASCs co-expressed iNOS and Arg-1 within the peripheral region in the dynamic group ($30.9 \pm 7.3\%$) as compared to the peripheral region of the static group ($13.6 \pm 6.8\%$) and the central region of the dynamic group ($14.0 \pm 1.6\%$) (**Figure 1C**), suggesting that culturing within the perfusion bioreactor altered the phenotype of the ASCs within the scaffold periphery.

Further probing the numbers of cells expressing the individual markers, the density of $iNOS^+DAPI^+$ cells was significantly higher in the peripheral region of the dynamic group (122 ± 2 cells/mm^2) as compared to the peripheral region of the static group (22 ± 16 cells/mm^2) and the central region of the dynamic group (32 ± 8 cells/mm^2) (**Supplementary Figure 2A**). When assessed relative to the total $DAPI^+$ cell population, the percentage of $iNOS^+DAPI^+$ cells was highest in the peripheral region of the dynamic group ($33.2 \pm 7.5\%$), and significantly greater than both the central region of the dynamic group ($16.6 \pm 0.8\%$) and the peripheral region of the static group ($14.5 \pm 7.4\%$) (**Supplementary Figure 2B**). A significantly higher density of Arg-1^+DAPI^+ cells was also observed in the peripheral region of the dynamic group (306 ± 68 cells/mm^2) as compared to the peripheral region of the static group (117 ± 38 cells/mm^2) and the central region of the dynamic group (146 ± 51 cells/mm^2) (**Supplementary Figure 2C**). However, when evaluated relative to the total $DAPI^+$ population, there were no significant differences between the regions or groups, with a high percentage ($>70\%$) of the ASCs expressing Arg-1 under all conditions (**Supplementary Figure 2D**).

Dynamic Culture Increased the Density of ASCs Expressing TNF-α and IL-10 in the DAT Scaffolds at 14 Days

Immunostaining was performed for Arg-1 in combination with TNF-α and IL-10 to determine whether dynamic culture modulated the abundance and distribution of ASCs expressing these cytokines. High densities of Arg-1^+, TNF-α^+, and IL-10^+ cells were observed within the peripheral regions of the DAT scaffolds in the dynamic group (**Figure 2A**). Quantification of the

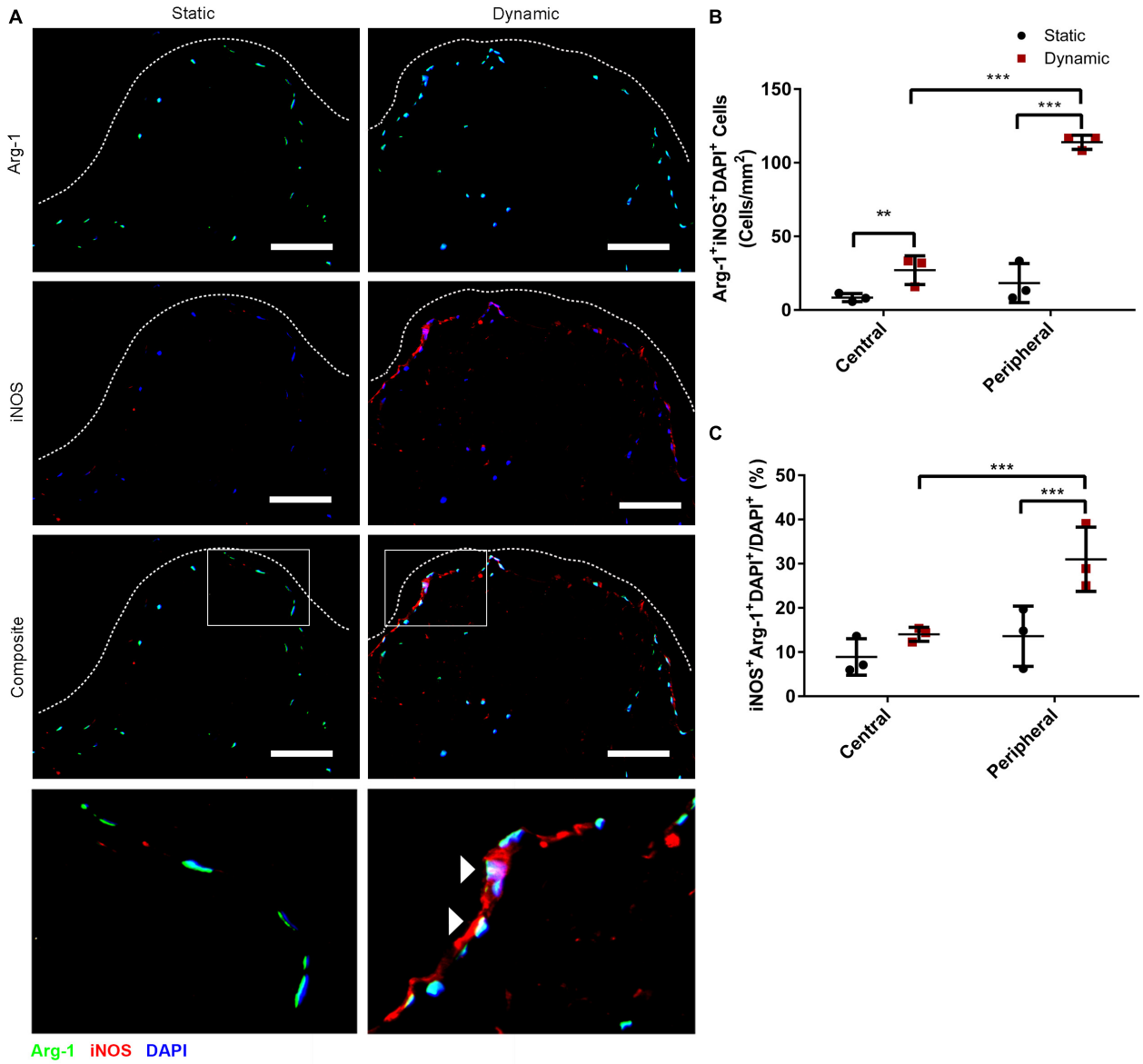

FIGURE 1 | Dynamic culture within the perfusion bioreactor for 14 days increased the percentage of human ASCs co-expressing iNOS and Arg-1 within the peripheral region of the DAT scaffolds. **(A)** Representative immunostaining for Arg-1 (green) and iNOS (red) with DAPI (blue) for the static and dynamic groups at 14 days. Dashed lines indicate the edge of the DAT scaffolds. Scale bars represent 100 μm. Boxed regions in the composite images are shown at higher magnification below. White arrowheads highlight Arg-1$^+$iNOS$^+$DAPI$^+$ cells. **(B)** The density of iNOS$^+$Arg-1$^+$DAPI$^+$ cells and **(C)** the percentage of iNOS$^+$Arg-1$^+$DAPI$^+$ cells relative to the total DAPI$^+$ cell population in the central (>200 μm from scaffold edge) and peripheral (<200 μm from scaffold edge) regions of the DAT scaffolds cultured statically or dynamically. $^{**}p < 0.01$, $^{***}p < 0.001$.

TNF-α$^+$DAPI$^+$ cells in the peripheral (<200 μm from scaffold edge) and central (>200 μm from scaffold edge) scaffold regions revealed a significantly greater density of positive cells in the peripheral region of the dynamic group (154 ± 23 cells/mm^2) as compared to the peripheral region of the static group (46 ± 11 cells/mm^2) and the central region of the dynamic group (72 ± 12 cells/mm^2) (**Figure 2B**). In addition, the TNF-α$^+$DAPI$^+$ cell density was significantly greater in the central region of the dynamic group as compared to the central region of the static group (17 ± 1 cells/mm^2). When expressed as a percentage of the total DAPI$^+$ cell population, a significantly higher percentage of cells were TNF-α$^+$ in the peripheral region of the dynamic group (46.6 ± 10.9%) as compared to the static group (25.7 ± 7.9%) (**Figure 2C**).

Similarly, there were significantly more IL-10$^+$ cells in the peripheral region of the dynamic group (121 ± 20 cells/mm^2) as compared to the peripheral region of the static group (39 ± 12 cells/mm^2) and the central region of the dynamic

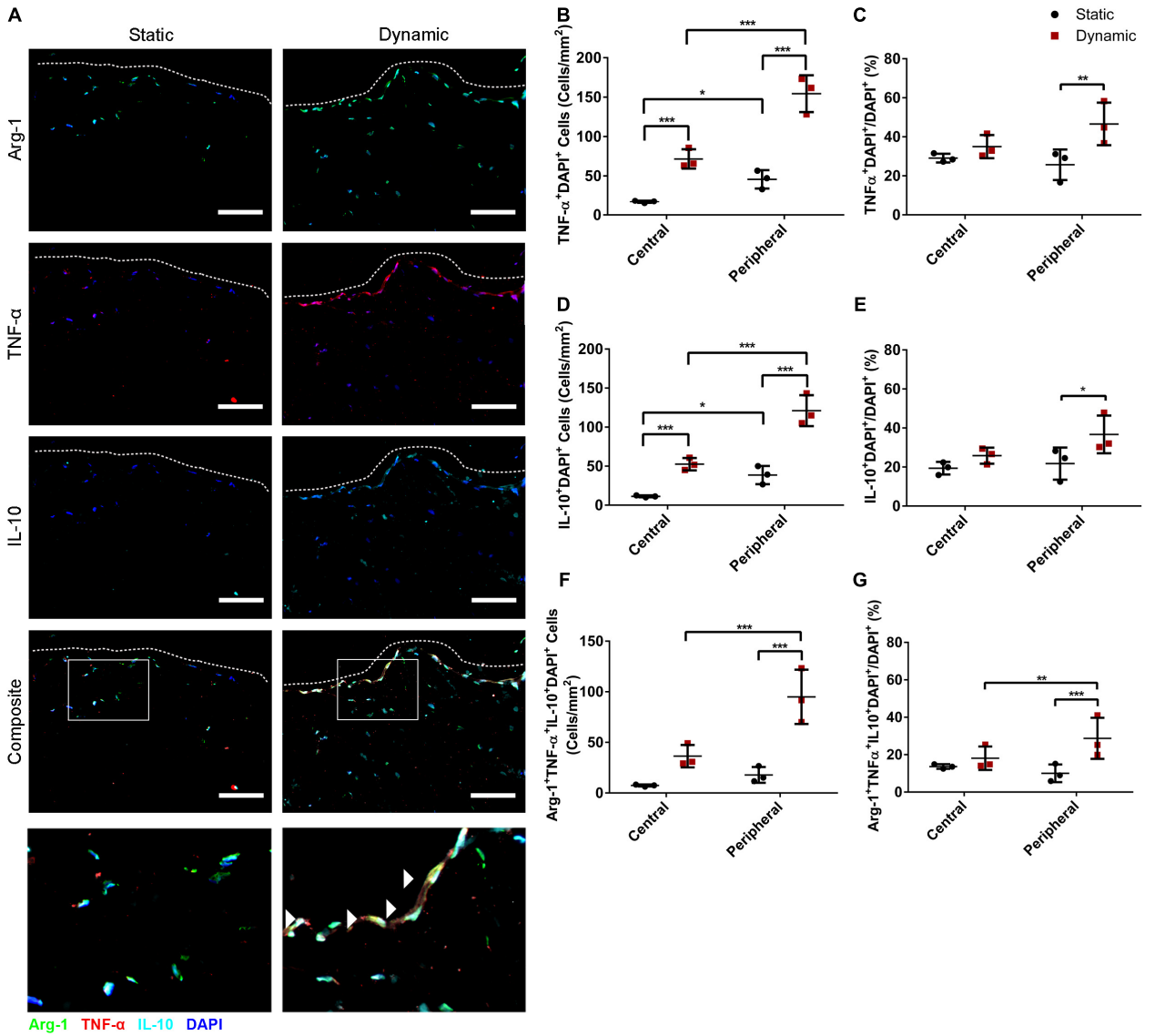

FIGURE 2 | Dynamic culture within the perfusion bioreactor for 14 days increased the percentage of human ASCs expressing TNF-α^+ and IL-10^+ in the peripheral region of the DAT scaffolds. **(A)** Representative immunostaining showing Arg-1 (green), TNF-α (red), and IL-10 (cyan) expression with DAPI counterstaining (blue) for the static and dynamic groups. Dashed lines indicate the edge of the DAT scaffolds. Scale bars represent 100 μm. Boxed regions in the composite images are shown at higher magnification below. White arrowheads highlight Arg-1^+TNF-α^+ IL-10^+DAPI$^+$ cells. In the central (>200 μm from scaffold edge) and peripheral (<200 μm from scaffold edge) regions of the DAT scaffolds in the static and dynamic groups: **(B)** The TNF-α^+DAPI$^+$ cell density and **(C)** Percentage of cells expressing TNF-α. **(D)** The IL-10^+DAPI$^+$ cell density and **(E)** Percentage of cells expressing IL-10. **(F)** The Arg-1^+TNF-α^+IL-10^+DAPI$^+$ cell density and **(G)** Percentage of cells co-expressing Arg-1, TNF-α and IL-10. *$p < 0.05$, **$p < 0.01$, ***$p < 0.001$.

group (52 ± 8 cells/mm^2), which was significantly greater than the central region of the static group (11 ± 1 cells/mm^2) (**Figure 2D**). When analyzed as a percentage, a significantly higher percentage of cells in the peripheral region were IL-10^+ in the dynamic group (36.7 ± 9.7%) as compared to the static group (21.8 ± 8.2%) (**Figure 2E**).

Quantification also indicated that the Arg-1^+TNF-α^+IL-10^+DAPI$^+$ cell density was significantly higher in the peripheral region of the dynamic group (95 ± 27 cells/mm^2) as compared to the peripheral region of the static group (18 ± 8 cells/mm^2) and the central region of the dynamic group (36 ± 11 cells/mm^2) (**Figure 2F**). Furthermore, a significantly higher percentage of the DAPI$^+$ cells were TNF-α^+IL-10^+ (29.8 ± 11.3%) (**Supplementary Figure 3**) and Arg-1^+TNF-α^+IL-10^+ (28.7 ± 10.9%) (**Figure 2G**) in the peripheral regions of the DAT scaffolds in the dynamic group as compared to the static group (11.2 ± 6.1% and 10.0 ± 4.7%, respectively). Taken together, these findings suggest that culturing in the perfusion bioreactor increased the fraction of ASCs that were expressing both TNF-α and IL-10 in the

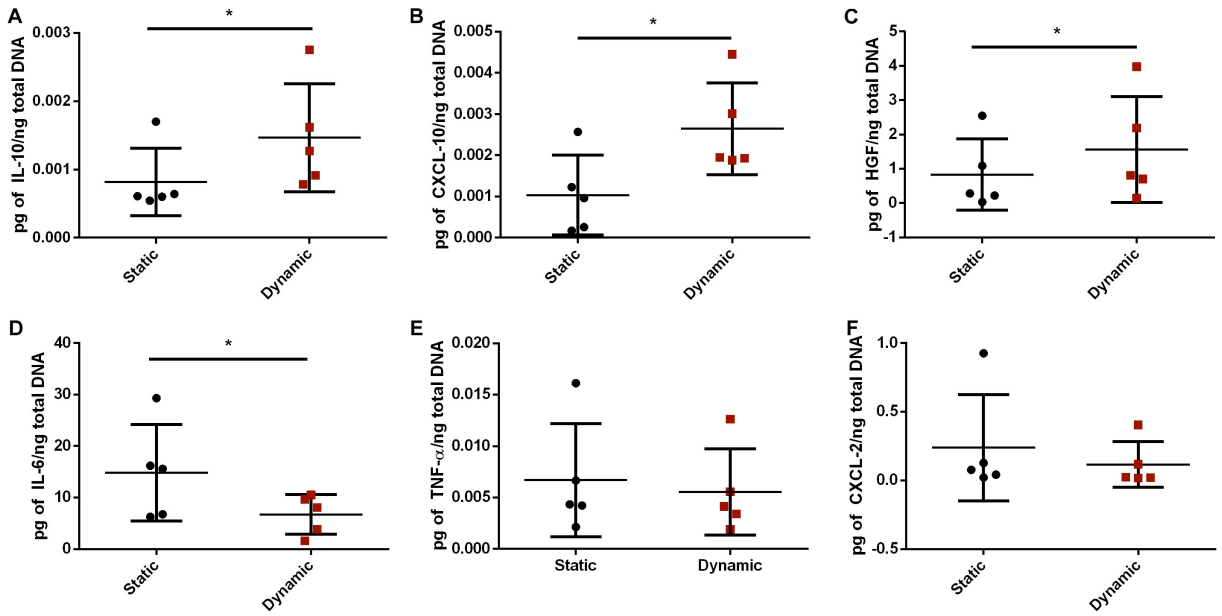

FIGURE 3 | Dynamic culture within the perfusion bioreactor altered the paracrine factor expression profile of the human ASCs cultured on the DAT scaffolds for 14 days. Expression of **(A)** IL-10, **(B)** CXCL-10, **(C)** HGF, **(D)** IL-6, **(E)** TNF-α, and **(F)** CXCL-2 as measured by Human Magnetic Luminex® Assay normalized to total dsDNA content. *$p < 0.05$.

periphery of the DAT, and that the majority of these cells were also Arg-1$^+$.

Dynamic Culture Altered the Paracrine Factor Expression Profile of the ASCs in the DAT Scaffolds

To further probe whether bioreactor preconditioning altered the expression levels of some key immunomodulatory factors expressed within adipose tissue, a custom Luminex® assay was performed. Protein expression levels of IL-10, CXCL-10, HGF, IL-6, TNF-α, and CXCL-2 were assessed in lysates prepared from the ASC-seeded DAT in the static and dynamic groups after 14 days of culture. After normalizing to total dsDNA content, the protein expression levels of IL-10, CXCL-10, and HGF were significantly higher, and IL-6 expression was significantly lower, in the dynamic group as compared to the static group (**Figure 3**). No significant differences were observed between the groups in the protein expression levels of TNF-α or CXCL-2.

Dynamic Culture of ASCs on the DAT Enhanced CD31$^+$ Endothelial Cell Recruitment Into the Scaffolds Following Implantation in the *nu/nu* Mouse Model

Following *in vitro* characterization, *in vivo* studies were performed to probe how bioreactor preconditioning modulated the capacity of the ASC-seeded DAT to stimulate the recruitment of a range of host cell populations at 1-, 4-, and 8-weeks post-implantation, which may have contributed to the markedly enhanced adipose tissue regeneration previously reported in this group (**Supplementary Figure 4**; Han and Flynn, 2020). Given the importance of angiogenesis in adipose tissue regeneration (Laschke et al., 2006), the initial characterization focused on assessing the presence and distribution of CD31$^+$ endothelial cells within the implants (**Figure 4A**). Quantification of the staining confirmed that the CD31$^+$ cell density was significantly greater in the dynamic group as compared to the static group at 1- (46 ± 9 cells/mm^2 versus 10 ± 9 cells/mm^2), 4- (67 ± 23 cells/mm^2 versus 30 ± 15 cells/mm^2), and 8-weeks (63 ± 16 cells/mm^2 versus 20 ± 6 cells/mm^2) post-implantation (**Figure 4B**), supporting that bioreactor preconditioning enhanced angiogenesis within the implants.

Dynamic Culture of ASCs on the DAT Scaffolds Enhanced the Recruitment of CD26$^+$ Host Cells at 1-Week Post-implantation in the *nu/nu* Mouse Model

Co-staining was performed for CD26 and for human-specific Ku80 (**Figure 5A** and **Supplementary Figure 5**) to probe host CD26$^+$ cell infiltration into the implants at 1, 4, and 8 weeks post-implantation, as a potential marker of multipotent progenitor cells that can give rise to preadipocytes and adipocytes (Merrick et al., 2019). Quantification of the CD26$^+$Ku80$^-$DAPI$^+$ cell population indicated that there was a significantly higher density of CD26$^+$ host cells in the DAT implants within the dynamic group at 1-week post-implantation (142 ± 81 cells/mm^2) as compared to the static group (53 ± 49 cells/mm^2), as well as the dynamic group at both 4- (56 ± 30 cells/mm^2) and 8-weeks (35 ± 15 cells/mm^2) post-implantation (**Figure 5B**).

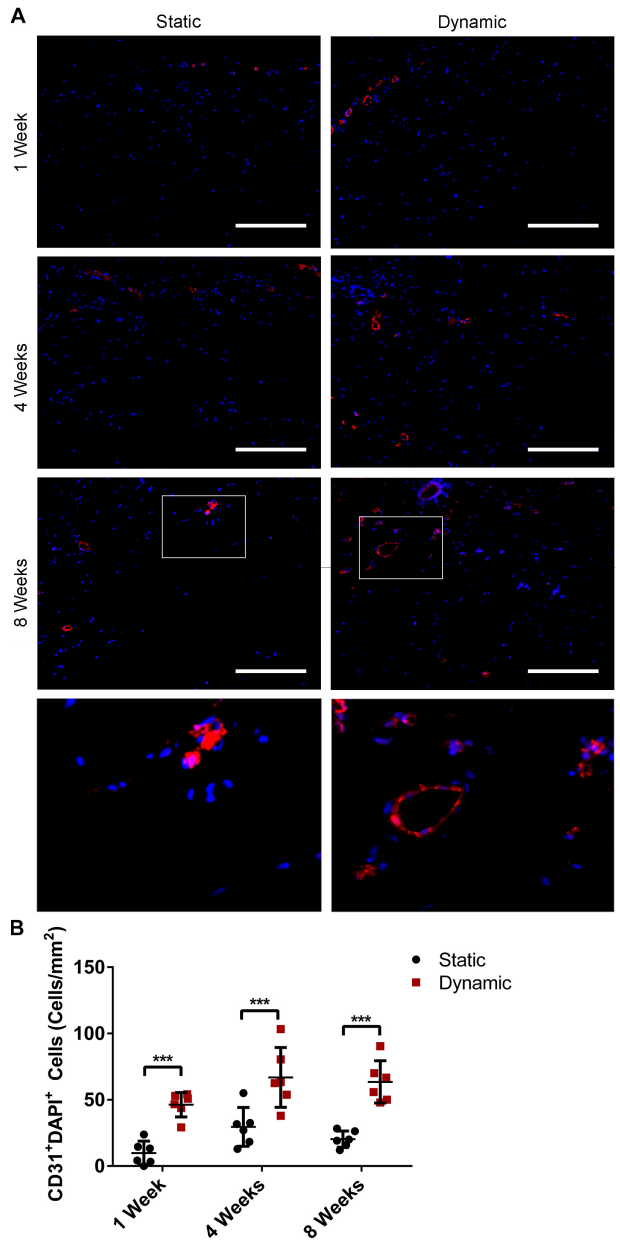

FIGURE 4 | Dynamic culture of ASCs on the DAT scaffolds enhanced $CD31^+$ cell recruitment following implantation in the *nu/nu* mouse model. **(A)** Representative immunostaining showing CD31 (red) with DAPI counterstaining (blue) within the DAT implants for both the static and dynamic groups at 1-, 4- and 8-weeks post-implantation. Scale bars represent 100 μm. Boxed regions in the 8-week images are shown at higher magnification below. **(B)** $CD31^+DAPI^+$ endothelial cell density in the implants. ***$p < 0.001$.

Quantification of the $Ku80^+DAPI^+$ human ASC population was also performed. The $Ku80^+DAPI^+$ cell density was significantly higher in the dynamic group relative to the static group at 1-week post-implantation (196 ± 44 cells/mm^2 versus 69 ± 18 cells/mm^2), as well as the dynamic group at both 4- (81 ± 43 cells/mm^2) and 8-weeks (62 ± 76 cells/mm^2) post-implantation (**Supplementary Figure 6**). No significant differences were observed in the $Ku80^+DAPI^+$ cell density between the static and dynamic groups at 4 or 8 weeks. However, there was substantial variability in the dynamic group at 8 weeks, with fewer human cells present in the implants that had undergone more substantial remodeling into adipose tissue.

Dynamic Culture of ASCs on the DAT Scaffolds Did Not Alter Host Macrophage Recruitment Following Implantation in the *nu/nu* Mouse Model

To probe host macrophage infiltration into the DAT implants over time, immunostaining was performed for mouse CD45 as a pan-leukocyte marker in combination with F4/80 as a marker of mature mouse macrophages, and CD68 as a marker of phagocytic macrophages. Qualitatively, high densities of $CD45^+$, $F4/80^+$ and $CD68^+$ cells were observed within the DAT implants in both groups at 1- (**Figure 6A**), 4- (**Supplementary Figure 7**), and 8-weeks (**Supplementary Figure 8**) post-implantation. Quantification of the $CD45^+F4/80^+CD68^+DAPI^+$ cells indicated there was a significantly higher density in the dynamic group at 1-week post-implantation (596 ± 187 cells/mm^2) as compared to both 4- (310 ± 97 cells/mm^2) and 8-weeks (249 ± 86 cells/mm^2) (**Figure 6B**). However, no significant differences were observed between the dynamic and static groups at any of the timepoints.

Analysis of the percentage of $CD45^+$ cells that co-expressed both F4/80 and CD68 within the total $CD45^+DAPI^+$ cell population in the DAT implants indicated that the majority (∼95%) of the $CD45^+$ cells were $F4/80^+CD68^+$ at 1 and 4 weeks, but a significant decline in this subpopulation was observed within both groups at 8 weeks, with (80.8 ± 6.1%) and (81.3 ± 3.5%) of the $CD45^+$ population co-expressing $F4/80^+CD68^+$ in the dynamic and static groups respectively (**Figure 6C**). Individual analysis of the $CD45^+F4/80^+DAPI^+$ (**Supplementary Figure 9A**) and $CD45^+CD68^+DAPI^+$ (**Supplementary Figure 9B**) populations as a percentage of the total $CD45^+DAPI^+$ population within the implants confirmed that a high percentage (>90%) of the $CD45^+$ population expressed these macrophage markers at 1 and 4 weeks. However, a similar significant decline in the relative expression levels of both individual markers was observed at 8 weeks.

Dynamic Culture of the Human ASCs on the DAT Scaffolds Prior to Implantation Modulated Macrophage Phenotype Within the Implants in the *nu/nu* Mouse Model

To probe the macrophage phenotype within the implants, co-staining was performed for the pan-leukocyte marker CD45 with the pro-regenerative macrophage marker CD163 (**Figure 7A**). Interestingly, while $CD45^+$ cells were observed infiltrating the implants at 1, 4, and 8 weeks, a relatively small number of $CD45^+CD163^+$ cells were visualized within the scaffolds, with the exception of the dynamic group at

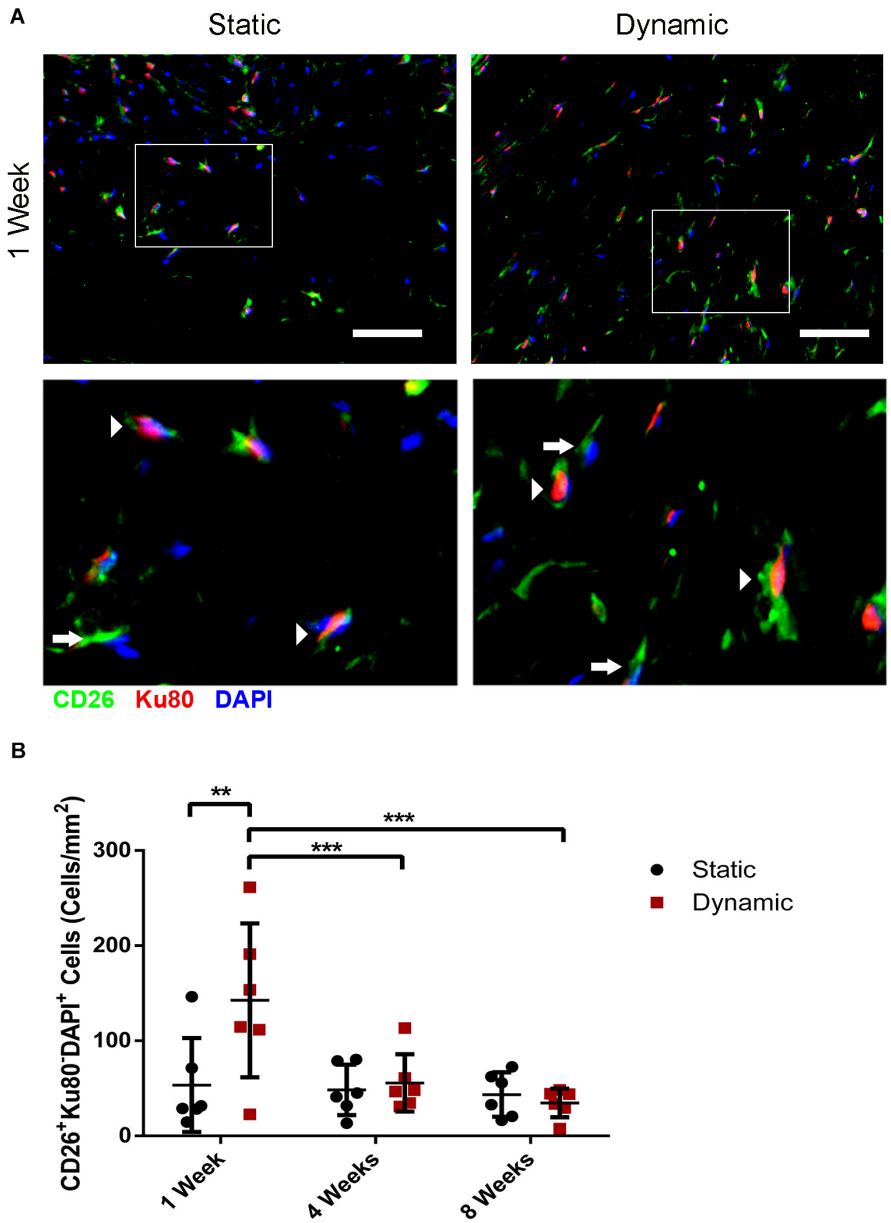

FIGURE 5 | Dynamic culture of human ASCs on the DAT scaffolds enhanced the recruitment of $CD26^+$ host cells at 1-week post-implantation in the *nu/nu* mouse model. **(A)** Representative immunostaining of CD26 (green) in combination with human-specific Ku80 (red), with DAPI counterstaining (blue) at 1-week post-implantation. Scale bars represent 50 μm. Boxed regions are shown at higher magnification below. Arrows indicate $CD26^+Ku80^-DAPI^+$ mouse cells and arrowheads highlight $CD26^+Ku80^+DAPI^+$ human cells. **(B)** $CD26^+$ host cell ($CD26^+Ku80^-DAPI^+$) density within the DAT implants at 1, 4, and 8 weeks. $^{**}p < 0.01$, $^{***}p < 0.001$.

8 weeks. The density of $CD45^+CD163^+DAPI^+$ cells was quantified within the implanted scaffolds, excluding the fibrous capsule. The analysis confirmed that there were significantly more $CD45^+CD163^+DAPI^+$ cells within the DAT implants in the dynamic group at 8 weeks (131 ± 31 cells/mm^2) relative to the static group at 8 weeks (45 ± 12 cells/mm^2), as well as the dynamic group at 1 (35 ± 11 cells/mm^2) and 4 (63 ± 18 cells/mm^2) weeks post-implantation (**Figure 7B**). When expressed as a percentage of the total $CD45^+DAPI^+$ cell population, a significantly higher fraction of the $CD45^+$ cells were $CD163^+$ in the dynamic group as compared to the static group at 1 (17.8 ± 3.8% versus 8.9 ± 1.8%), 4 (27.9 ± 7.3% versus 21.8 ± 5.3%) and 8 (47.3 ± 6.5% versus 22.2 ± 7.4%) weeks, with significantly higher levels observed for the dynamic group at 8-weeks post-implantation as compared to both earlier timepoints (**Figure 7C**), supporting that bioreactor preconditioning promoted a more pro-regenerative macrophage phenotype within the implants over time.

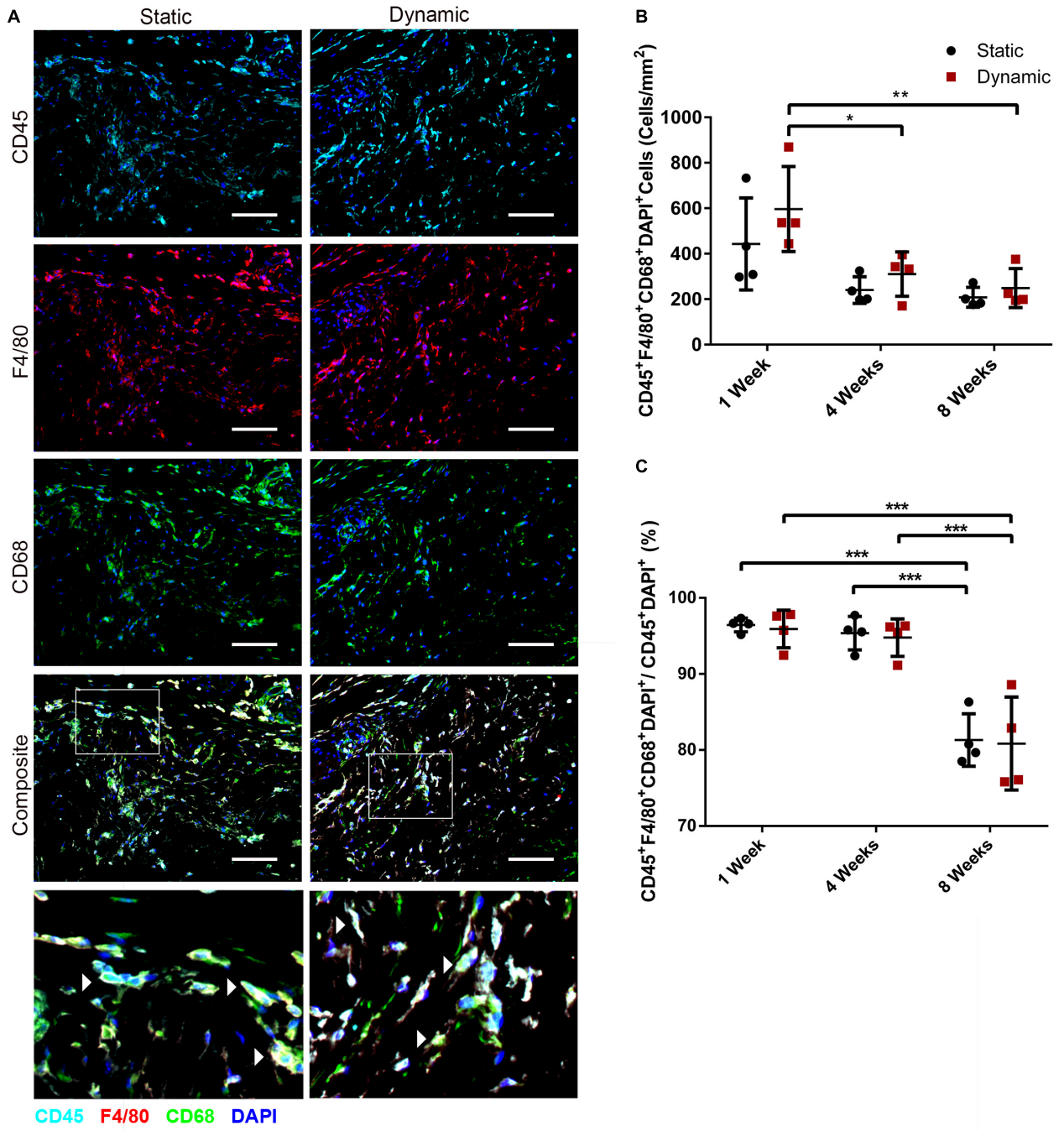

FIGURE 6 | The recruitment of $CD45^+F4/80^+CD68^+$ macrophages was similar in the ASC-seeded DAT scaffolds that were cultured dynamically and statically for 14 days prior to implantation in the *nu/nu* mouse model. **(A)** Representative images showing CD45 (cyan), F4/80 (red), and CD68 (green) expression with DAPI counterstaining (blue) at 1-week post-implantation. Scale bars represent 100 μm. Boxed regions in the composite images are shown at higher magnification below. White arrowheads highlight $CD45^+F4/80^+CD68^+DAPI^+$ cells. **(B)** $CD45^+F4/80^+CD68^+DAPI^+$ cell density in the static and dynamic groups. **(C)** The percentage of $CD45^+F4/80^+CD68^+DAPI^+$ cells relative to the total $CD45^+DAPI^+$ cell population at 1, 4, and 8 weeks. $^*p < 0.05$, $^{**}p < 0.01$, $^{***}p < 0.001$.

DISCUSSION

Culturing human ASCs on DAT scaffolds within the perfusion bioreactor under 2% O_2 over 14 days was previously shown to promote cell expansion and markedly enhance angiogenesis and host adipogenesis following subcutaneous implantation in the *nu/nu* mouse model (Han and Flynn, 2020). The *in vivo* effects were likely attributed in part to the delivery of a significantly

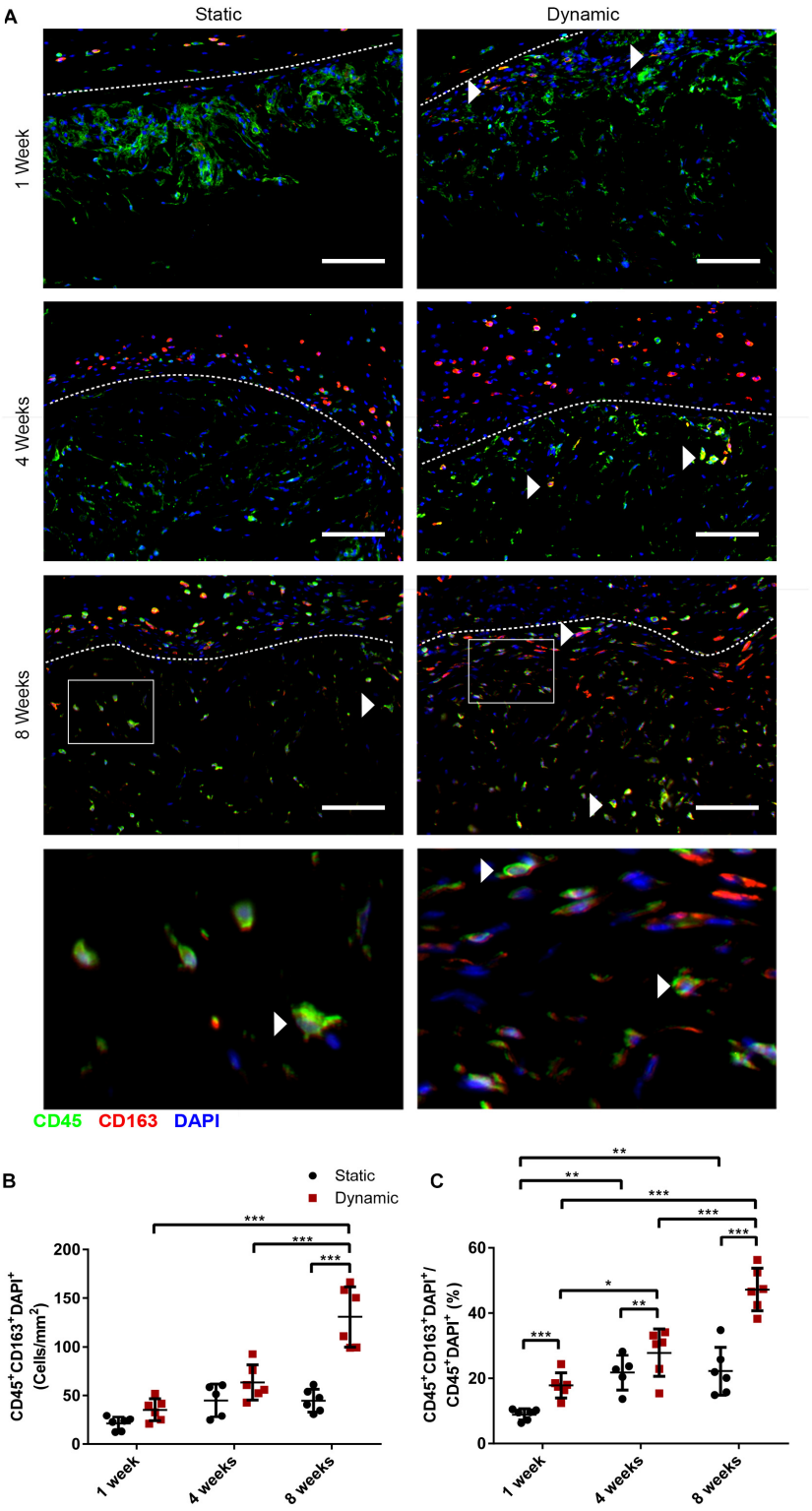

FIGURE 7 | Dynamic culture of human ASCs on the DAT scaffolds enhanced the percentage of cells expressing the pro-regenerative macrophage marker CD163 in the $CD45^+$ host cell population at 8 weeks post-implantation in the *nu/nu* mouse model. **(A)** Representative images showing CD45 (green), CD163 (red), and DAPI (blue). Dashed lines indicate the border between the fibrous capsule **(top)** and the DAT implant **(bottom)**. Scale bars represent 100 μm. Boxed regions in the 8-week images are shown at higher magnification below. White arrowheads highlight $CD45^+CD163^+$ cells. **(B)** $CD45^+CD163^+DAPI^+$ cell density within the DAT implants. **(C)** The percentage of $CD45^+CD163^+DAPI^+$ cells relative to the total $CD45^+DAPI^+$ population. $^*p < 0.05$, $^{**}p < 0.01$, $^{***}p < 0.001$.

larger dose of ASCs in the bioreactor cultured scaffolds relative to the statically cultured controls. However, there is evidence to support that culturing under shear stress can induce functional changes in MSC populations that may influence their capacity to stimulate regeneration (Bassaneze et al., 2010; Yuan et al., 2013; Becquart et al., 2016). As such, the current study sought to explore whether the phenotype and paracrine function of the ASCs on the DAT were altered by preconditioning the scaffolds within the bioreactor.

Inducible nitric oxide synthase and Arg-1 are enzymes involved in distinct pathways of arginine catabolism that have been commonly employed as functional markers of M1 and M2 macrophage polarization, respectively (Rath et al., 2014). In addition, previous studies have shown that iNOS expression is critical for the pro-regenerative immunomodulatory function of murine MSC populations (Ren et al., 2008; Li et al., 2012; Maria et al., 2018). Interestingly, iNOS expression was significantly enhanced in the human ASCs within the peripheral region of the DAT scaffolds in the dynamic group. Further, there was a significantly higher fraction of ASCs that co-expressed iNOS and Arg-1 in the peripheral region of the dynamic group, suggesting that bioreactor preconditioning modulated the ASC phenotype in the periphery of the DAT. In general, Arg-1 was found to be expressed by a high percentage of the ASCs cultured on the DAT scaffolds, which to the best of our knowledge, has not been explored as an MSC marker. However, a previous study reported that an isolated human $CD90^{+}CD45^{-}$ intraperitoneal cell population expressed high levels of Arg-1 and suppressed T-cell proliferation in culture, with the immunomodulatory effects regulated by the L-arginine concentration (Rath et al., 2014). While further investigation into the functional role of Arg-1 in human ASCs is warranted, it is possible that the observed expression may be associated with the known anti-inflammatory capacity of these cells (Ceccarelli et al., 2020).

The immunohistochemical analyses also demonstrated that a significantly higher fraction of the ASCs in the peripheral region of the DAT scaffolds in the dynamic group expressed TNF-α and IL-10, suggesting that bioreactor preconditioning promoted the localized production of these factors, which may have modulated the response of infiltrating host cell populations. Although TNF-α and other pro-inflammatory factors are often regarded negatively for their association with chronic inflammation and disease (Bulló et al., 2003; Maachi et al., 2004), it is becoming increasingly recognized that inflammation plays an important role in stimulating angiogenesis and tissue regeneration (Sainson et al., 2008; Kwon et al., 2013). It is important to note that the staining patterns demonstrating higher numbers of cells expressing the markers within the peripheral regions of the DAT (<200 μm from scaffold edge) suggest that media perfusion into the interior of the scaffolds was likely restricted over time within the bioreactor, which we also reported in our previous study (Han and Flynn, 2020). Despite this limitation, the perfusion bioreactor approach was effective at markedly enhancing *in vivo* adipose tissue regeneration within the DAT. While having a more homogeneous population of "activated" ASCs throughout the scaffold could potentially further augment regeneration, it is also possible that the locally enhanced expression of factors such as TNF-α was sufficient to initiate a regenerative response but not shift the overall microenvironment toward a more pro-inflammatory state that may not be conducive for regeneration.

To further assess whether culturing within the bioreactor modulated the paracrine profile of the ASCs on the DAT, a multiplex Luminex assay was performed to characterize the overall expression levels of a range of immunomodulatory factors expressed within adipose tissue. IL-10 expression, which has been shown to promote a more pro-regenerative macrophage phenotype (Mocellin et al., 2003; Boehler et al., 2014) and downregulate the expression of pro-inflammatory cytokines in immune cell populations (Peranteau et al., 2008; Martínez-Chaæon et al., 2018), was significantly enhanced in the dynamic group. In addition, the macrophage chemoattractant CXCL-10 (Petrovic-Djergovic et al., 2015), as well as the pro-angiogenic and anti-inflammatory factor HGF (Beilmann et al., 2004; Ceccarelli et al., 2020), were also detected at significantly higher levels in the lysates from the dynamic group. HGF can regulate endothelial cell survival, proliferation and migration (Kawaguchi and Kataoka, 2014), as well as endothelial tube formation (Beilmann et al., 2004). As such, the enhanced expression of this factor may have played a role in the increased $CD31^{+}$ cell recruitment observed in the *in vivo* model. Further, HGF has also been shown to have immunomodulatory effects on monocytes and macrophages, promoting a more pro-regenerative response (Chen et al., 2014; Choi et al., 2019). The expression of IL-6, which is known to promote the pro-inflammatory polarization of monocytes (Mori et al., 2011; Scheller et al., 2014), was significantly downregulated in the dynamic group. However, no significant differences were observed in the overall protein expression levels of the pro-inflammatory factors TNF-α and CXCL-2 within the lysates between the static and dynamic groups, supporting that the enhanced TNF-α expression observed in the IHC studies was highly localized.

It is possible that shear stress stimulation induced by media perfusion within the bioreactor may have altered the ASC phenotype and secretory profile. Shear forces can activate mechanosignaling pathways, including the MAPK and JNK pathways, through integrin activation, tensegrity-mediated mechanosensing, and by inducing changes in the fluidity of the cell membrane (Stolberg and McCloskey, 2009). Human ASCs have also been shown to possess a primary cilium (Hilgendorf et al., 2019), which has the potential to function as a shear stress sensor and signal transducer. Most studies to date exploring biomechanical stimulation on MSCs have focused on differentiation, rather than on possible effects on pro-angiogenic or immunomodulatory capacities. However, mechanical stimulation through intermittent fluid flow has previously been reported to increase the production of a range of pro-angiogenic and immunomodulatory factors including VEGFA, HGF, G-CSF, and IL-8 in cultured human ASCs (Bravo et al., 2017). Similarly, Becquart et al. (2016) demonstrated that intermittent shear stress stimulated the production of nitric oxide (NO) and enhanced mRNA expression of *VEGFA*, *FGF2*, and *IGF1* in cultured human bone marrow-derived MSCs. In addition, Lee et al. (2017) recently demonstrated that human

bone marrow-derived MSCs cultured under physiological shear stress within a microfluidic system showed enhanced anti-inflammatory function, with the effects regulated through focal adhesion kinase (FAK) signaling.

Notably, in addition to shear stress other factors could have contributed to the altered protein expression levels observed between the groups in the current study, including differences in the cell density, variations in the local concentration of nutrients, oxygen or other metabolites, as well as a cascading effect of other growth factors or cytokines. For example, in lipopolysaccharide (LPS)-induced macrophages *in vitro* and in interstitial macrophages in C57BL/6J mice, the enhanced expression of HGF was found to decrease IL-6 and increase IL-10 expression (Kamimoto et al., 2009). Further studies using alternative bioreactor platforms would be required to more specifically assess the effects of fluid shear stress on the pro-angiogenic and immunomodulatory functionality of the ASCs.

Building from the *in vitro* data, *in vivo* studies were performed to assess the effects of bioreactor preconditioning on host cell recruitment. Consistent with our previous findings that there was a significant increase in the density of erythrocyte-containing blood vessels in the DAT implants in the dynamic group at 4 and 8 weeks (Han and Flynn, 2020), $CD31^+$ endothelial cell recruitment was significantly enhanced in the dynamic group at all three timepoints in the current study, suggesting that culturing within the bioreactor augmented the capacity of the ASCs to stimulate angiogenesis within the implants. As it is well-recognized that the induction of angiogenesis is required for stable adipose tissue formation within engineered bioscaffolds (Ceccarelli et al., 2020), this may have contributed to the increased adipogenesis observed within this group (Han and Flynn, 2020).

The infiltration of host-derived $CD26^+$ cells was probed as a marker that has been associated with an adipocyte precursor phenotype. More specifically, Merrick et al. (2019) demonstrated that a $CD26^+$ interstitial progenitor population within murine adipose tissue could give rise to an intermediate population that was committed to the adipogenic lineage and could differentiate into mature adipocytes *in vivo*. The higher density of host-derived $CD26^+$ cells observed at 1 week post-implantation in the dynamic group, combined with the previously characterized adipo-inductive effects of this group (Han and Flynn, 2020), suggests that the dynamically cultured DAT scaffolds have the potential to both recruit progenitors and drive their differentiation toward an adipogenic state, associated with downregulation of CD26 expression (Merrick et al., 2019). However, it should be noted that other cell types can express CD26, including dendritic cells (Gliddon and Howard, 2002; Zhong et al., 2013), macrophages (Zhong et al., 2013), and natural killer cells (Bühling et al., 1994), and future studies should more fully characterize the $CD26^+$ population and its involvement in adipogenesis within the DAT.

Macrophages have been indicated to play an important role in mediating both angiogenesis and adipose tissue regeneration within ECM-derived bioscaffolds (Debels et al., 2013; Han et al., 2015). As such, the effects of dynamic culture on host macrophage recruitment were probed through co-staining for CD45, F4/80, and CD68, which showed no significant differences in terms of cell densities between the groups at any of the timepoints. Similarly, we previously found that seeding with ASCs modulated macrophage phenotype but did not specifically alter macrophage recruitment into the DAT implants in immunocompetent rat and mouse models (Han et al., 2015; Robb et al., 2020). Notably, there was an increased percentage of $CD45^+$ cells that were $F4/80^-$ and $CD68^-$ within both implant groups at 8 weeks. These cells may be other myeloid cell populations or their precursors, or potentially T cells (Kennedy et al., 1992) or natural killer cells (Krzywinska et al., 2016). It would be interesting to more fully characterize these cells to better understand their potential effects within the implants in future studies, including additional markers with quantitative analysis of digested explants using multicolor flow cytometry.

While there was no difference in total macrophage recruitment, analysis of CD163 expression in the $CD45^+$ cell population suggested that dynamic preconditioning of the ASCs on the DAT ultimately led to a shift toward a more pro-regenerative macrophage phenotype. In particular, $CD163^+$ macrophages have been associated with both angiogenesis and ECM remodeling in implanted biomaterials (Spiller et al., 2014). The increased presence of $CD163^+$ macrophages within the dynamically cultured implants is similar to our previous findings on the effects of ASC seeding in the immunocompetent rat and mouse models (Han et al., 2015; Robb et al., 2020), and these cells may have contributed to the enhanced remodeling of the DAT into host-derived adipose tissue (Han and Flynn, 2020).

Based on the *in vitro* and *in vivo* data in the current study, we postulate that the markedly enhanced adipose tissue regeneration observed following implantation of bioreactor preconditioned DAT scaffolds was due to the combined effects of (i) the delivery of a larger number of cells and (ii) alterations in the ASC phenotype and paracrine function within the periphery of the DAT. Addressing limitations in the current study, future work should focus on decoupling these effects and verifying that the ASCs that expressed the markers such as iNOS did indeed have enhanced pro-angiogenic and/or immunomodulatory capacities. These studies should include functional assays, for example, probing specific effects on endothelial cell proliferation and tubule formation, as well as macrophage polarization. For follow-up *in vivo* studies, especially those focused on characterizing the immunomodulatory effects of the ASCs, testing in humanized mouse models should be considered (Mehler et al., 2019). Using these models, it would be interesting to more fully characterize the phenotype of the infiltrating macrophages over time, and assess the role of other immune cell populations including T-cells. It would also be beneficial to perform studies using human ASCs engineered to stably express luciferase to enable more accurate tracking of the viable cells within the living animals through longitudinal bioluminescence imaging.

Although preconditioning the cells within the 3-D perfusion bioreactor system on the same scaffold on which they were delivered was effective within our pre-clinical model, it

may be worthwhile to consider separate platforms for cell preconditioning versus cell delivery as a potentially more scalable approach to advance toward future clinical translation as a cell-based therapy for large volume soft tissue augmentation. More specifically, alternative bioreactor systems could be designed that combine shear stress stimulation with culturing on ECM-derived bioscaffolds where the cells could be more uniformly subjected to the applied forces to avoid the heterogeneity that was observed in the cellular response in the current study. For example, our previously established stirred bioreactor system for expanding the ASCs on DAT microcarriers could hold promise as a dynamic preconditioning platform (Yu et al., 2017). The preconditioned cells could subsequently be incorporated within other biomaterial scaffolds designed to provide structural support and maintain the volume as host adipose tissue regeneration progresses, such as the intact DAT scaffolds used in the current study.

CONCLUSION

The findings of the current study support that dynamic preconditioning of human ASCs on the DAT scaffolds within the perfusion bioreactor under 2% O_2 altered their phenotype and paracrine profile relative to controls cultured under static conditions. Interestingly, a substantial fraction of the ASCs within the peripheral region of the DAT implants in the dynamic group simultaneously expressed iNOS and Arg-1, as well as both TNF-α and IL-10, suggesting they had a complex phenotype. Analysis in the *in vivo* model indicated that culturing within the bioreactor prior to implantation enhanced the recruitment of $CD31^+$ endothelial cells, as well as $CD26^+$ host cells, into the implants, which likely contributed to the increased angiogenesis and adipogenesis previously reported in this group. While there was no significant difference in total macrophage recruitment between the groups, greater infiltration of $CD163^+$ macrophages was observed in the dynamic group, indicative of a shift toward a more pro-regenerative macrophage response favorable for implant remodeling. Taken together with our previous work, the *in vitro* and *in vivo* findings suggest that bioreactor preconditioning can augment the capacity of human ASCs to stimulate adipose tissue regeneration within the DAT, and that these effects are likely mediated by a combination of increased expansion resulting in the delivery of a larger number of ASCs, as well as alterations in the paracrine functionality of the delivered ASCs. Overall, the current study supports the further investigation of dynamic culture under shear stress as a means to precondition ASCs and enhance their capacity to stimulate tissue regeneration through paracrine-mediated mechanisms.

DATA AVAILABILITY STATEMENT

The raw data supporting the conclusions of this article will be made available by the authors, without undue reservation.

ETHICS STATEMENT

The studies involving human participants were reviewed and approved by the Health Sciences Research Ethics Board, Western University. The patients/participants provided their written informed consent to participate in this study. The animal study was reviewed and approved by the Animal Care Committee, Western University.

AUTHOR CONTRIBUTIONS

LF and TH conceptualized and designed the study, with input from GD on macrophage characterization and AG on translational perspectives. AG provided clinical tissue samples for cell isolation and scaffold fabrication. TH performed the experimental studies and analyzed the data in collaboration with JW and LF, and in consultation with GD. TH and LF wrote the manuscript, with editorial feedback provided by JW, GD, and AG. All authors contributed to the article and approved the submitted version.

FUNDING

Funding for this study was provided by the Canadian Institutes of Health Research (CIHR) (Operating Grant # 119394), with infrastructure support from the Canada Foundation for Innovation (CFI) and the Ontario Research Fund (ORF). Scholarship funding was provided for TH from the Natural Sciences and Engineering Research Council of Canada (NSERC). Funding for this project was provided by an operating grant awarded to LF, with GD and AG as co-applicants.

ACKNOWLEDGMENTS

We would like to acknowledge Dr. Eric Arts for access to his MAGPIX system, as well as Dr. Brian Evans, Dr. Robert Richards, and Dr. Damir Matic for providing adipose tissue samples for this project. In addition, Dr. Pascal Morissette Martin, Dr. Laura Juignet, and Ms. Anna Kornmuller are thanked for their technical support with the animal surgeries. A version of this manuscript has been published as a preprint and is available on SSRN at: http://dx.doi.org/10.2139/ssrn.3732500.

SUPPLEMENTARY MATERIAL

The Supplementary Material for this article can be found online at: https://www.frontiersin.org/articles/10.3389/fbioe.2021.642465/full#supplementary-material

REFERENCES

Allard, J., Li, K., Lopez, X. M., Blanchard, S., Barbot, P., Rorive, S., et al. (2014). Immunohistochemical toolkit for tracking and quantifying xenotransplanted human stem cells. *Regen. Med.* 9, 437–452. doi: 10.2217/rme.14.26

Alvarez-Barreto, J. F., Landy, B., VanGordon, S., Place, L., DeAngelis, P. L., and Sikavitsas, V. I. (2011). Enhanced osteoblastic differentiation of mesenchymal stem cells seeded in RGD-Functionalized PLLA scaffolds and cultured in a flow perfusion bioreactor. *J. Tissue Eng. Regen. Med.* 5, 464–475. doi: 10.1002/term.338

Bassaneze, V., Barauna, V. G., Lavini-Ramos, C., Kalil, J., Schettert, I. T., Miyakawa, A. A., et al. (2010). Shear stress induces nitric oxide-mediated vascular endothelial growth factor production in human adipose tissue mesenchymal stem cells. *Stem Cells Dev.* 19, 371–378. doi: 10.1089/scd.2009.0195

Bates, D., Mächler, M., Bolker, B. M., and Walker, S. W. (2015). Fitting linear mixed-effects models using Lme4. *J. Stat. Softw.* 67:1. doi: 10.18637/jss.v067.i01

Becquart, P., Cruel, M., Hoc, T., Sudre, L., Pernelle, K., Bizios, R., et al. (2016). Human mesenchymal stem cell responses to hydrostatic pressure and shear stress. *Eur. Cells Mater.* 31, 160–173. doi: 10.22203/ecm.v031a11

Beilmann, M., Birk, G., and Lenter, M. C. (2004). Human primary co-culture angiogenesis assay reveals additive stimulation and different angiogenic properties of VEGF and HGF. *Cytokine* 26, 178–185. doi: 10.1016/j.cyto.2004.03.003

Boehler, R. M., Kuo, R., Shin, S., Goodman, A. G., Pilecki, M. A., Gower, R. M., et al. (2014). Lentivirus delivery of IL-10 to promote and sustain macrophage polarization towards an anti-inflammatory phenotype. *Biotechnol. Bioeng.* 111, 1210–1221. doi: 10.1002/bit.25175

Bourin, P., Bunnell, B. A., Casteilla, L., Dominici, M., Katz, A. J., March, K. L., et al. (2013). Stromal cells from the adipose tissue-derived stromal vascular fraction and culture expanded adipose tissue-derived stromal/stem cells: a joint statement of the international federation for adipose therapeutics and science (IFATS) and the international society for cellular therapy (ISCT). *Cytotherapy* 15, 641–648. doi: 10.1016/j.jcyt.2013.02.006

Braune, J., Weyer, U., Hobusch, C., Mauer, J., Brüning, J. C., Bechmann, I., et al. (2017). IL-6 regulates M2 polarization and local proliferation of adipose tissue macrophages in obesity. *J Immunol.* 198, 2927–2934. doi: 10.4049/jimmunol.1600476

Bravo, B., García, de Durango, C., González, A., Gortázar, A. R., Santos, X., et al. (2017). Opposite effects of mechanical action of fluid flow on proangiogenic factor secretion from human adipose-derived stem cells with and without oxidative stress. *J. Cell Physiol.* 232, 2158–2167. doi: 10.1002/jcp.25712

Brett, E., Chung, N., Leavitt, W. T., Momeni, A., Longaker, M. T., and Wan, D. C. (2017). A review of cell-based strategies for soft tissue reconstruction. *Tissue Eng. Part B Rev.* 23, 336–346. doi: 10.1089/ten.teb.2016.0455

Bühling, F., Kunz, D., Reinhold, D., Ulmer, A. J., Ernst, M., Flad, H. D., et al. (1994). Expression and functional role of dipeptidyl peptidase IV (CD26) on human natural killer cells. *Nat. Immun.* 13, 270–279.

Bulló, M., García-Lorda, P., Megias, I., and Salas-Salvadó, J. (2003). Systemic inflammation, adipose tissue tumor necrosis factor, and leptin expression. *Obes Res.* 11, 525–531. doi: 10.1038/oby.2003.74

Cai, L., Johnstone, B. H., Cook, T. G., Liang, Z., Traktuev, D., Cornetta, K., et al. (2007). Suppression of hepatocyte growth factor production impairs the ability of adipose-derived stem cells to promote ischemic tissue revascularization. *Stem Cells.* 25, 3234–3243. doi: 10.1634/stemcells.2007-2388

Ceccarelli, S., Pontecorvi, P., Anastasiadou, E., Napoli, C., and Marchese, C. (2020). Immunomodulatory effect of adipose-derived stem cells: the cutting edge of clinical application. *Front. Cell Dev. Bio.* 8:236. doi: 10.3389/fcell.2020.00236

Chazenbalk, G., Bertolotto, C., Heneidi, S., Jumabay, M., Trivax, B., Aronowitz, J., et al. (2011). Novel pathway of adipogenesis through cross-talk between adipose tissue macrophages, adipose stem cells and adipocytes: evidence of cell plasticity. *PLoS One* 6:e17834. doi: 10.1371/journal.pone.0017834

Chen, P. M., Liu, K. J., Hsu, P. J., Wei, C. F., Bai, C. H., Ho, L. J., et al. (2014). Induction of immunomodulatory monocytes by human mesenchymal stem cell-derived hepatocyte growth factor through ERK1/2. *J. Leukoc Biol.* 96, 295–303. doi: 10.1189/jlb.3a0513-242r

Choi, J. S., Yang, H. J., Kim, B. S., Kim, J. D., Kim, J. Y., Yoo, B., et al. (2009). Human Extracellular Matrix (ECM) powders for injectable cell delivery and adipose tissue engineering. *J. Control Release* 139, 2–7. doi: 10.1016/j.jconrel.2009.05.034

Choi, W., Lee, J., Lee, J., Lee, S. H., and Kim, S. (2019). Hepatocyte growth factor regulates macrophage transition to the M2 phenotype and promotes murine skeletal muscle regeneration. *Front. Physiol.* 10:914. doi: 10.3389/fphys.2019.00914

Debels, H., Galea, L., Han, X. L., Palmer, J., Van Rooijen, N., Morrison, W. A., et al. (2013). Macrophages play a key role in angiogenesis and adipogenesis in a mouse tissue engineering model. *Tissue Eng Part A.* 19, 2615–2625. doi: 10.1089/ten.tea.2013.0071

Dos Santos, F., Campbell, A., Fernandes-Platzgummer, A., Andrade, P. Z., Gimble, J. M., Wen, Y., et al. (2014). A xenogeneic-free bioreactor system for the clinical-scale expansion of human mesenchymal stem/stromal cells. *Biotechnol. Bioeng.* 111, 1116–1127. doi: 10.1002/bit.25187

Flynn, L. E. (2010). The use of decellularized adipose tissue to provide an inductive microenvironment for the adipogenic differentiation of human adipose-derived stem cells. *Biomaterials* 31, 4715–4724. doi: 10.1016/j.biomaterials.2010.02.046

Gliddon, D. R., and Howard, C. J. (2002). CD26 is expressed on a restricted subpopulation of dendritic cells in vivo. *Eur. J. Immunol.* 32, 1472–1481. doi: 10.1002/1521-4141(200205)32:5<1472::aid-immu1472>3.0.co;2-q

Haddad, S. M. H., Omidi, E., Flynn, L. E., and Samani, A. (2016). Comparative biomechanical study of using decellularized human adipose tissues for post-mastectomy and post-lumpectomy breast reconstruction. *J. Mech. Behav. Biomed. Mater.* 57, 235–245. doi: 10.1016/j.jmbbm.2015.12.005

Han, T. T. Y., and Flynn, L. E. (2020). Perfusion bioreactor culture of human adipose-derived stromal cells on decellularized adipose tissue scaffolds enhances in vivo adipose tissue regeneration. *J. Tissue Eng. Regen. Med.* 14, 1827–1840. doi: 10.1002/term.3133

Han, T. T. Y., Toutounji, S., Amsden, B. G., and Flynn, L. E. (2015). Adipose-Derived stromal cells mediate in vivo adipogenesis, angiogenesis and inflammation in decellularized adipose tissue bioscaffolds. *Biomaterials* 72, 125–137. doi: 10.1016/j.biomaterials.2015.08.053

Hilgendorf, K. I., Johnson, C. T., Mezger, A., Rice, S. L., Norris, A. M., Demeter, J., et al. (2019). Omega-3 fatty acids activate ciliary FFAR4 to control adipogenesis. *Cell* 179, 1289–1305. doi: 10.1016/j.cell.2019.11.005

Hothorn, T., Bretz, F., and Westfall, P. (2008). Simultaneous inference in general parametric models. *Biom. J.* 50, 346–363. doi: 10.1002/bimj.200810425

Hsiao, S. T., Lokmic, Z., Peshavariya, H., Abberton, K. M., Dusting, G. J., Lim, S. Y., et al. (2013). Hypoxic conditioning enhances the angiogenic paracrine activity of human adipose-derived stem cells. *Stem Cells Dev.* 22, 1614–1623. doi: 10.1089/scd.2012.0602

Kamimoto, M., Mizuno, S., and Nakamura, T. (2009). Reciprocal regulation of IL-6 and IL-10 balance by HGF via recruitment of heme oxygenase-1 in macrophages for attenuation of liver injury in a mouse model of endotoxemia. *Int. J. Mol. Med.* 24, 837–843. doi: 10.3892/ijmm_00000219

Kang, S., Kim, S. M., and Sung, J. H. (2014). Cellular and molecular stimulation of adipose-derived stem cells under hypoxia. *Cell Biol. Int.* 38, 553–562. doi: 10.1002/cbin.10246

Kapur, S. K., and Katz, A. J. (2013). Review of the adipose derived stem cell secretome. *Biochimie* 95, 2222–2228. doi: 10.1016/j.biochi.2013.06.001

Kawaguchi, M., and Kataoka, H. (2014). Mechanisms of hepatocyte growth factor activation in cancer tissues. *Cancers* 6, 1890–1904. doi: 10.3390/cancers6041890

Kennedy, J. D., Pierce, C. W., and Lake, J. P. (1992). Extrathymic T Cell maturation. phenotypic analysis of t cell subsets in nude mice as a function of age. *J. Immunol.* 148, 1620–1629.

Kochumon, S., Madhoun, A. A., Al-Rashed, F., Azim, R., Al-Ozairi, E., Al-Mulla, F., et al. (2020). Adipose tissue gene expression of CXCL10 and CXCL11 modulates inflammatory markers in obesity: implications for metabolic inflammation and insulin resistance. *Ther. Adv. Endocrin. Metab.* 11:2042018820930902. doi: 10.1177/2042018820930902

Krzywinska, E., Cornillon, A., Allende-Vega, N., Vo, D. N., Rene, C., Lu, Z. Y., et al. (2016). CD45 isoform profile identifies natural killer (NK) subsets with differential activity. *PLoS One* 11:e0150434. doi: 10.1371/journal.pone.0150434

Kuljanin, M., Brown, C. F. C., Raleigh, M. J., Lajoie, G. A., and Flynn, L. E. (2017). Collagenase treatment enhances proteomic coverage of low-abundance proteins in decellularized matrix bioscaffolds. *Biomaterials* 144, 130–143. doi: 10.1016/j.biomaterials.2017.08.012

Kusuyama, J., Komorizono, A., Bandow, K., Ohnishi, T., and Matsuguchi, T. (2016). CXCL3 positively regulates adipogenic differentiation. *J. Lipid Res.* 57, 1806–1820. doi: 10.1194/jlr.M067207

Kwon, Y. W., Heo, S. C., Jeong, G. O., Yoon, J. W., Mo, W. M., Lee, M. J., et al. (2013). Tumor necrosis factor-α-activated mesenchymal stem cells promote endothelial progenitor cell homing and angiogenesis. *Biochim. Biophys. Acta* 1832, 2136–2144. doi: 10.1016/j.bbadis.2013.08.002

Laschke, M. W., Harder, Y., Amon, M., Martin, I., Farhadi, J., et al. (2006). Angiogenesis in tissue engineering: breathing life into constructed tissue substitutes. *Tissue Eng.* 12, 2093–2104. doi: 10.1089/ten.2006.12.2093

Lee, H. J., Diaz, M. F., Ewere, A., Olsen, S. D., Cox, C. S. Jr., and Wenzel, P. M. (2017). Focal adhesion kinase signaling regulates anti-inflammatory function of bone marrow mesenchymal stromal cells induced by biomechanical force. *Cell Signal.* 38, 1–9. doi: 10.1016/j.cellsig.2017.06.012

Li, W., Ren, G., Huang, Y., Su, J., Han, Y., Li, J., et al. (2012). Mesenchymal stem cells: a double-edged sword in regulating immune responses. *Cell Death Differ.* 19, 1505–1513. doi: 10.1038/cdd.2012.26

Maachi, M., Piéroni, L., Bruckert, E., Jardel, C., Fellahi, S., Hainque, B., et al. (2004). Systemic low-grade inflammation is related to both circulating and adipose tissue TNFα, leptin and IL-6 levels in obese women. *Int. J. Obes. Relat. Metab. Disord.* 28, 993–997. doi: 10.1038/sj.ijo.0802718

Maria, A. T. J., Rozier, P., Fonteneau, G., Sutra, T., Maumus, M., Toupet, K., et al. (2018). INOS activity is required for the therapeutic effect of mesenchymal stem cells in experimental systemic sclerosis. *Front. Immunol.* 9:3056. doi: 10.3389/fimmu.2018.03056

Martínez-Chaæon, G., Brown, K. A., Docanto, M. M., Kumar, H., Salminen, S., Saarinen, N., et al. (2018). IL-10 suppresses TNF-A-Induced expression of human aromatase gene in mammary adipose tissue. *FASEB J.* 32, 3361–3370. doi: 10.1096/fj.201700938RRR

Mehler, V. J., Burns, C., and Moore, M. L. (2019). Concise review: exploring immunomodulatory features of mesenchymal stromal cells in humanized mouse models. *Stem Cells.* 37, 298–305. doi: 10.1002/stem.2948

Merrick, D., Sakers, A., Irgebay, Z., Okada, C., Calvert, C., Morley, M. P., et al. (2019). Identification of a mesenchymal progenitor cell hierarchy in adipose tissue. *Science* 364:eaav2501. doi: 10.1126/science.aav2501

Mocellin, S., Panelli, M. C., Wang, E., Nagorsen, D., and Marincola, F. M. (2003). The dual role of IL-10. *Trends Immunol.* 24, 36–43. doi: 10.1016/S1471-4906(02)00009-1

Mohiuddin, O. A., Campbell, B., Poche, J. N., Thomas-Porch, C., Hayes, D. A., Bunnell, B. A., et al. (2019). Decellularized adipose tissue: biochemical composition, in vivo analysis and potential clinical applications. *Adv. Exp. Med. Biol.* 1212, 57–70. doi: 10.1007/5584_2019_371

Mori, T., Miyamoto, T., Yoshida, H., Asakawa, M., Kawasumi, M., Kobayashi, T., et al. (2011). IL-1β and TNFα-Initiated IL-6-STAT3 pathway is critical in mediating inflammatory cytokines and RANKL expression in inflammatory arthritis. *Int. Immunol.* 23, 701–712. doi: 10.1093/intimm/dxr077

Peranteau, W. H., Zhang, L., Muvarak, N., Badillo, A. T., Radu, A., Zoltick, P. W., et al. (2008). IL-10 overexpression decreases inflammatory mediators and promotes regenerative healing in an adult model of scar formation. *J. Invest. Dermatol.* 128, 1852–1860. doi: 10.1038/sj.jid.5701232

Petrovic-Djergovic, D., Popovic, M., Chittiprol, S., Cortado, H., Ransom, R. F., and Partida-Sánchez, S. (2015). CXCL10 induces the recruitment of monocyte-derived macrophages into kidney, which aggravate puromycin aminonucleoside nephrosis. *Clin. Exp. Immunol.* 180, 305–315. doi: 10.1111/cei.12579

Pizzute, T., Lynch, K., and Pei, M. (2015). Impact of tissue-specific stem cells on lineage-specific differentiation: a focus on the musculoskeletal system. *Stem Cell Rev. Rep.* 11, 119–132. doi: 10.1007/s12015-014-9546-9548

R Core Team (2017). *R: A Language and Environment for Statistical Computing*. Vienna: R Foundation for Statistical Computing.

Rath, M., Müller, I., Kropf, P., Closs, E. I., and Munder, M. (2014). Metabolism via arginase or nitric oxide synthase: two competing arginine pathways in macrophages. *Front. Immunol.* 5:532. doi: 10.3389/fimmu.2014.00532

Ren, G., Zhang, L., Zhao, X., Xu, G., Zhang, Y., Roberts, A. I., et al. (2008). Mesenchymal stem cell-mediated immunosuppression occurs via concerted action of chemokines and nitric oxide. *Cell Stem Cell* 2, 141–150. doi: 10.1016/j.stem.2007.11.014

Robb, K. P., Juignet, L., Morissette Martin, P., Walker, J. T., Brooks, C., Barreira, C., et al. (2020). Adipose stromal cells enhance decellularized adipose tissue remodeling through multimodal mechanisms. *Tissue Eng Part A* doi: 10.1089/ten.tea.2020.0180 Online ahead of print.

Sainson, R. C. A., Johnston, D. A., Chu, H. C., Holderfield, M. T., Nakatsu, M. N., Crampton, S. P., et al. (2008). TNF primes endothelial cells for angiogenic sprouting by inducing a tip cell phenotype. *Blood* 111, 4997–5007. doi: 10.1182/blood-2007-08-108597

Scheller, J., Garbers, C., and Rose-John, S. (2014). Interleukin-6: from basic biology to selective blockade of pro-inflammatory activities. *Sem. Immunol.* 26, 2–12. doi: 10.1016/j.smim.2013.11.002

Siebert, A., Goren, I., Pfeilschifter, J., and Frank, S. (2016). Anti-Inflammatory effects of rosiglitazone in obesity-impaired wound healing depend on adipocyte differentiation. *PLoS One* 11:e0168562. doi: 10.1371/journal.pone.0168562

Spiller, K. L., Anfang, R. R., Spiller, K. J., Ng, J., Nakazawa, K. R., Daulton, J. W., et al. (2014). The role of macrophage phenotype in vascularization of tissue engineering scaffolds. *Biomaterials* 35, 4477–4488. doi: 10.1016/j.biomaterials.2014.02.012

Stolberg, S., and McCloskey, K. (2009). Can shear stress direct stem cell fate? *Biotechnol. Prog.* 25, 10–19. doi: 10.1002/btpr.124

Suga, H., Eto, H., Aoi, N., Kato, H., Araki, J., Doi, K., et al. (2010). Adipose tissue remodeling under ischemia: death of adipocytes and activation of stem/ progenitor cells. *Plast Reconstr. Surg.* 126, 1911–1923. doi: 10.1097/PRS.0b013e3181f4468b

Suga, H., Glotzbach, J. P., Sorkin, M., Longaker, M. T., and Gurtner, G. C. (2014). Paracrine mechanism of angiogenesis in adipose-derived stem cell transplantation. *Ann. Plast. Surg.* 72, 234–241. doi: 10.1097/SAP.0b013e318264fd6a

Thangarajah, H., Vial, I. N., Chang, E., El-Ftesi, S., Januszyk, M., Chang, E. I., et al. (2009). IFATS collection: adipose stromal cells adopt a proangiogenic phenotype under the influence of hypoxia. *Stem Cells* 27, 266–274. doi: 10.1634/stemcells.2008-2276

Trujillo, M. E., Sullivan, S., Harten, I., Schneider, S. H., Greenberg, A. S., and Fried, S. K. (2004). Interleukin-6 regulates human adipose tissue lipid metabolism and leptin production in vitro. *J. Clin. Endocrinol. Metab.* 89, 5577–5582. doi: 10.1210/jc.2004-0603

Wang, L., Johnson, J. A., Zhang, Q., and Beahm, E. K. (2013). Combining decellularized human adipose tissue extracellular matrix and adipose-derived stem cells for adipose tissue engineering. *Acta Biomater.* 9, 8921–8931. doi: 10.1016/j.actbio.2013.06.035

Young, D. A., Bajaj, V., and Christman, K. L. (2014). Decellularized adipose matrix hydrogels stimulate in vivo neovascularization and adipose formation. *J. Biomed. Mater. Res. A.* 102, 1641–1651. doi: 10.1002/jbm.a.35109

Yu, C., Kornmuller, A., Brown, C., Hoare, T., and Flynn, L. E. (2017). Decellularized adipose tissue microcarriers as a dynamic culture platform for human adipose-derived stem/stromal cell expansion. *Biomaterials* 120, 66–80. doi: 10.1016/j.biomaterials.2016.12.017

Yuan, L., Sakamoto, N., Song, G., and Sato, M. (2013). High-Level shear stress stimulates endothelial differentiation and VEGF secretion by human mesenchymal stem cells.". *Cell. Mol. Bioeng.* 6, 220–229. doi: 10.1007/s12195-013-0275-x

Zhao, F., and Ma, T. (2005). Perfusion bioreactor system for human mesenchymal stem cell tissue engineering: dynamic cell seeding and construct development. *Biotechnol. Bioeng.* 91, 482–493. doi: 10.1002/bit.20532

Zhong, J., Rao, X., Deiuliis, J., Braunstein, Z., Narula, V., Hazey, J., et al. (2013). A potential role for dendritic cell/macrophage-expressing DPP4 in obesity-induced visceral inflammation. *Diabetes* 62, 149–157. doi: 10.2337/db12-0230

Conflict of Interest: The authors declare that the research was conducted in the absence of any commercial or financial relationships that could be construed as a potential conflict of interest.

frontiers in Bioengineering and Biotechnology

ORIGINAL RESEARCH
published: 19 March 2021
doi: 10.3389/fbioe.2021.650289

Nanofiber-Based Delivery of Bioactive Lipids Promotes Pro-regenerative Inflammation and Enhances Muscle Fiber Growth After Volumetric Muscle Loss

*Cheryl L. San Emeterio[1†], Lauren A. Hymel[1†], Thomas C. Turner[1], Molly E. Ogle[1], Emily G. Pendleton[2], William Y. York[1], Claire E. Olingy[1], Alan Y. Liu[3], Hong Seo Lim[1], Todd A. Sulchek[1,3,4,5], Gordon L. Warren[6], Luke J. Mortensen[2,7], Peng Qiu[1,4], Young C. Jang[4,5], Nick J. Willett[1,4,8,9] and Edward A. Botchwey[1,4]**

[1] Department of Biomedical Engineering, Georgia Institute of Technology, Atlanta, GA, United States, [2] Regenerative Bioscience Center, Rhodes Center for ADS, University of Georgia, Athens, GA, United States, [3] School of Mechanical Engineering, Georgia Institute of Technology, Atlanta, GA, United States, [4] Petit Institute for Bioengineering and Bioscience, Georgia Institute of Technology, Atlanta, GA, United States, [5] School of Biological Sciences, Georgia Institute of Technology, Atlanta, GA, United States, [6] Department of Physical Therapy, Georgia State University, Atlanta, GA, United States, [7] School of Chemical, Materials, and Biomedical Engineering, University of Georgia, Athens, GA, United States, [8] Department of Orthopedics, Emory University, Atlanta, GA, United States, [9] Atlanta Veterans Affairs Medical Center, Decatur, GA, United States*

Volumetric muscle loss (VML) injuries after extremity trauma results in an important clinical challenge often associated with impaired healing, significant fibrosis, and long-term pain and functional deficits. While acute muscle injuries typically display a remarkable capacity for regeneration, critically sized VML defects present a dysregulated immune microenvironment which overwhelms innate repair mechanisms leading to chronic inflammation and pro-fibrotic signaling. In this series of studies, we developed an immunomodulatory biomaterial therapy to locally modulate the sphingosine-1-phosphate (S1P) signaling axis and resolve the persistent pro-inflammatory injury niche plaguing a critically sized VML defect. Multiparameter pseudo-temporal 2D projections of single cell cytometry data revealed subtle distinctions in the altered dynamics of specific immune subpopulations infiltrating the defect that were critical to muscle regeneration. We show that S1P receptor modulation via nanofiber delivery of Fingolimod (FTY720) was characterized by increased numbers of pro-regenerative immune subsets and coincided with an enriched pool of muscle stem cells (MuSCs) within the injured tissue. This FTY720-induced priming of the local injury milieu resulted in increased myofiber diameter and alignment across the defect space followed by enhanced revascularization and reinnervation of the injured muscle. These findings indicate that localized modulation of S1P receptor signaling via nanofiber scaffolds, which resemble the native extracellular matrix ablated upon injury, provides great potential as an immunotherapy for bolstering endogenous mechanisms of regeneration following VML injury.

Keywords: immunomodulation, inflammation, tissue engineering, regeneration, sphingolipid

OPEN ACCESS

Edited by:
Daniel Alge,
Texas A&M University, United States

Reviewed by:
Ngan F. Huang,
Stanford University, United States
Lorenzo Fassina,
University of Pavia, Italy
Chris Rathbone,
The University of Texas at San Antonio, United States

****Correspondence:***
Edward A. Botchwey
edward.botchwey@bme.gatech.edu

[†]These authors share first authorship

Specialty section:
This article was submitted to Tissue Engineering and Regenerative Medicine, a section of the journal Frontiers in Bioengineering and Biotechnology

Received: *06 January 2021*
Accepted: *01 March 2021*
Published: *19 March 2021*

Citation:
San Emeterio CL, Hymel LA, Turner TC, Ogle ME, Pendleton EG, York WY, Olingy CE, Liu AY, Lim HS, Sulchek TA, Warren GL, Mortensen LJ, Qiu P, Jang YC, Willett NJ and Botchwey EA (2021) Nanofiber-Based Delivery of Bioactive Lipids Promotes Pro-regenerative Inflammation and Enhances Muscle Fiber Growth After Volumetric Muscle Loss. Front. Bioeng. Biotechnol. 9:650289. doi: 10.3389/fbioe.2021.650289

INTRODUCTION

Though skeletal muscle possesses robust potential for healing after injury, large volumetric wounds that occur during combat, accidents or surgical resection often do not heal completely, resulting in fibrotic scarring and limited range of motion (Garg et al., 2015). Current standard of care involves the autologous transfer of tissue but this treatment produces limited functional restoration and also results in complications at both the donor and injury site (Beth and Pollot, 2016). Moreover, extensive soft tissue injury and concomitant damage to collateral blood vessels results in inadequate vascularization to the regenerating or grafted tissue. Recently, this unsuccessful muscle regeneration outcome following a traumatic injury has been linked to a dysfunctional immune response. Specifically, the immune response is overwhelmed by pro-inflammatory myeloid cells that exacerbate the pro-inflammatory phase of inflammation to a point where regeneration is not able to take place. Instead, the prolonged pro-inflammatory phase induces fibrosis and long-term loss of function (Aguilar et al., 2018; Larouche et al., 2018).

Monocytes and macrophages have become increasingly recognized as key regulators of microenvironmental cues within injured skeletal muscle (Arnold et al., 2007; Saclier et al., 2013). Tightly coordinated signals from monocyte/macrophages subpopulations govern the endogenous muscle stem cell (MuSC) niche and dictate the dynamic switch between either regenerative or fibrotic healing outcomes. Monocytes and macrophages are highly plastic immune cells that display a range of phenotypes *in vivo*. The classical, inflammatory monocyte is Ly6C^{hi} whereas non-classical, anti-inflammatory monocytes are Ly6C^{lo} (Geissmann et al., 2003). Ly6C^{hi} monocytes are rapidly recruited to the injury, where they can convert *in situ* into Ly6C^{lo} monocytes and become the primary contributors toward polarizing the macrophage population to a pro-regenerative ("M2") phenotype instead of an inflammatory ("M1") phenotype (Arnold et al., 2007). The presence of M2 macrophages marks the beginning of the regenerative phase of muscle healing; during this stage, M2 macrophages secrete IGF-1 to promote MuSC proliferation and subsequently secrete key growth factors, including growth differentiation factor 3 (GDF3), to promote myogenic differentiation (Tonkin et al., 2015; Juban and Chazaud, 2017). We have previously demonstrated that non-classical anti-inflammatory Ly6C^{lo} monocytes express relatively high levels of sphingosine-1-phosphate receptor 3 (S1PR3), which can be leveraged to modulate their response *in vivo* to promote the onset of the regenerative phase of muscle healing (Awojoodu et al., 2013).

Sphingosine-1-phosphate (S1P), a product of membrane sphingolipid metabolism, is a pleiotropic bioactive signaling lipid that activates signaling through five known G protein-coupled receptors, S1PR1-5 (Rivera et al., 2008). Extracellular gradients of S1P, achieved through the use of S1P chaperones, S1P neutralizing agents, sphingolipid metabolic enzymes, and biased agonists or antagonists of S1PR isotypes, can control fundamental processes such as immune cell fate and vascular integrity (Cartier and Hla, 2019). Additionally, the S1P signaling axis has been implicated in stimulating proliferation, motility and survival of MuSCs and inducing myogenic differentiation of myoblasts (Donati et al., 2013). Thus, S1P receptors have become an attractive pharmacological target in various autoimmune and inflammatory diseases including those affecting muscle repair and regeneration. This is perhaps most evident with the synthesis of Fingolimod (FTY720) from myriocin and its subsequent passing of all clinical trials and approval for the treatment of relapsing-remitting multiple sclerosis (Kappos et al., 2006). FTY720 is a small molecule agonist of S1PR1 and S1PR3-5 along with being a selective functional antagonist of S1PR1 by inducing irreversible S1PR1 internalization and degradation (Maceyka et al., 2012). We have shown previously that biomaterial-based gradients of S1P are short-lived in the tissue due to S1P degradation by S1P lyase. However, the active, phosphorylated form of FTY720, FTY720-P, is not catabolized by S1P lyase and can undergo multiple rounds of signaling due to its ability to be reversibly phosphorylated; this provides a more stable and sustained gradient in the tissue as observed in our previous work (Ogle et al., 2014). We have shown that local delivery of FTY720 recruits non-classical Ly6C^{lo} monocytes upon local delivery to inflamed skin injuries and promotes microvascular growth in an S1PR3-dependent manner (Olingy et al., 2017). Release of FTY720 from polymer nanofibers to mandibular bone defects increases the frequency of Ly6C^{lo} anti-inflammatory monocytes, promotes re-vascularization, and facilitates boney ingrowth (Das et al., 2013). Thus, the local delivery of an S1PR modulator, like FTY720, has emerged as a small molecule approach that can orchestrate the inflammatory response and subsequent healing of musculoskeletal injuries (Das et al., 2014; San Emeterio et al., 2017; Hymel et al., 2020).

In this series of studies, we investigated the immunomodulatory response and muscle regeneration outcome in a murine volumetric muscle loss (VML) injury after FTY720-loaded nanofiber implantation. The nanofiber implant was manufactured using 50/50 poly(lactic-co-glycolic acid) (PLGA)/Polycaprolactone (PCL) and was characterized using scanning electron microscopy (SEM) and atomic force microscopy (AFM) (**Supplementary Figure 1**). We used traditional "manually gated" immune populations, where regions of interest (manual gates) were drawn over a series of bivariate plots, for further analysis (**Supplementary Figure 1A**–I). Due to their ability to resolve subtly different cell populations, we applied both uniform manifold approximation and projection (UMAP) and spanning tree progression of density normalized events (SPADE) for dimension reduction and unbiased cluster identification (**Supplementary Figure 1A**–II,III) (Becht et al., 2018). SPADE is unique in its ability to reconstruct complex cellular hierarchies of immune cell transitions in order to reveal rare cell states before and after perturbations, such as injury or drug delivery (Qiu et al., 2011). Thus, we took advantage of this utility to classify the nodes of SPADE dendrograms to an immune cell subset and calculated how the cell frequency of these subsets is affected by FTY720 nanofiber treatment (**Supplementary Figure 1A**–IV,V). In addition to the single-cell analysis we performed whole mount immunohistochemistry to describe the functional muscle healing outcome after FTY720 nanofiber treatment (**Supplementary Figure 1B**–I). Using

two-photon confocal microscopy along with second harmonic generation (SHG) imaging and 3D reconstruction of images using Imaris software, we were able to characterize the muscle fiber alignment, collagen deposition, myeloid cell infiltration and reinnervation of muscle tissue (**Supplementary Figure 1B**–II,V). We hypothesized that local S1PR signaling modulation via nanofiber-based delivery of FTY720 from nanofiber scaffolds in murine VML defect models would shift the milieu to a more pro-regenerative microenvironment, leading to improved muscle regeneration and thus providing a promising therapeutic strategy to ameliorate the clinical burden VML presents.

RESULTS

Characterization of FTY720-Loaded Electrospun Nanofiber Scaffolds

In order to provide a biomaterial-mediated release of S1PR modulator, FTY720, to the local injury milieu, we fabricated PLGA/PCL nanofibers via electrospinning. FTY720 was released from the nanofiber scaffolds *in vitro* for 75 h, with approximately 96% of drug release occurring within the first 24 h (**Figure 1A**–I,II). After 75 h, about 97% of incorporated FTY720 had been released with only 0.065 ± 0.004 μg remaining in the scaffold. SEM and AFM were utilized to assess the morphology and mechanical properties between unloaded, blank nanofibers and those loaded with FTY720 to ensure that any differences in healing outcomes after injury were not attributed to variations in biomaterial characterization (**Figures 1B,C**). Scanning electron micrographs of blank nanofibers (**Figure 1B**–I) revealed a similar randomly oriented morphology to those loaded with FTY720 (**Figure 1B**–II). To evaluate the surface of the nanofibers with high resolution, we performed AFM to confirm that the topography of FTY720-loaded nanofibers was consistent with those that were not loaded with an immunomodulatory drug (**Figure 1C**–I,IV). Further, Young's modulus values were obtained over multiple contact points on the nanofibers, showing similar distribution profiles between unloaded and loaded scaffolds (**Figure 1C**–II,III,V,VI). These techniques establish that both surface and mechanical properties of blank versus FTY720-loaded nanofibers were unaffected by incorporation of this S1P analog, consistent with our previous studies utilizing nanofibers loaded with small molecule S1P receptor modulators (Hymel et al., 2020).

Localized S1P Receptor Modulation Primes the Injury Milieu for Inflammation Resolution

In order to study how local modulation of S1P receptors impacts timely resolution of inflammation and tissue regeneration, we made a 2 mm full-thickness defect to the murine spinotrapezius muscle (**Supplementary Figures 2A,B**). This VML model enables whole-mount visualization of cell populations and tissue microstructures involved in muscle repair. Following injury, mice were either left untreated, or underwent implantation of 3 mm blank or FTY720-loaded nanofiber scaffolds over the defect area (**Supplementary Figure 2C**). Because systemically administered FTY720 is known to induce lymphopenia by suppression of lymphocyte egress from lymph nodes (Blaho and Hla, 2014), we sought to determine whether localized administration of the drug resulted in any system-level effects. Analysis of blood lymphocyte populations by flow cytometry 1-day post injury revealed that both $CD4^+$ and $CD8^+$ T cell subsets were significantly decreased in the circulation of FTY720 nanofiber treated animals compared to no implant controls yet returned to similar levels by day 3 post injury (**Supplementary Figures 3A,B**). Systemic $Ly6C^{hi}$ inflammatory monocytes were not affected by local FTY720 release, but $Ly6C^{lo}$ anti-inflammatory monocytes showed a relative increase in the blood at later timepoints (**Supplementary Figures 3C,D**).

We hypothesized that local targeting of S1PR1 within the injury niche would prevent over accumulation of inflammatory immune cells by regulating timely tissue egress while simultaneously participating in the recruitment and polarization of pro-reparative cellular players. We performed flow cytometry of cells extracted from the muscle tissue 1 and 3 days after critical injury. At 1-day post injury, recruited monocytes overwhelm the immune cell population within the injured muscle. The heterogeneity underlying the monocyte population, based primarily on Ly6C expression, is demonstrated by their distant island locations within 2D UMAP projections. Distinct T cell islands distinguishing CD4 and CD8 antigen expression were also illustrated by UMAP analysis, although T cells were largely not present in the injured tissue at day 1, likely due to suppressed lymphocyte egress resulting from functional antagonism of S1PR1 (**Figures 2A,B**).

Because traditional strategies for analyzing multiparameter flow cytometry data are prone to user error and limited in its capacity to visualize the correlations among several markers from a series of bi-plots, the complexity of immune cell states may be severely undermined. We employed an unbiased clustering algorithm (SPADE) which preserves the inherent structure of the data and generates nodes to represent clusters of cells with similar marker expression. These nodes are positioned along an inferred trajectory, or "pseudotime" in order to visualize dynamics changes in (pseudo)temporal biological processes, such as cellular transitions, when longitudinal time series data is not available. To assess how local delivery of FTY720 biases immune cell phenotype at early timepoints, we generated SPADE dendrograms made of cells extracted from the muscle tissue 1 day after injury (**Figure 3**). SPADE dendrograms are comprised of live, single cells gated as $CD11b^+CD64^+MerTK^-$ monocytes (**Figures 3A,B**) or $CD3^+$ T cells (**Figure 3C**) from untreated (no implant) animals as well as those treated with blank or FTY720-loaded nanofiber scaffolds. The SPADE dendrograms were further annotated by overlaying manually gated monocyte or T cell subsets, including $Ly6C^{hi}$ inflammatory and $Ly6C^{lo}$ anti-inflammatory monocytes onto the greater monocyte dendrogram (**Figures 3A,B**, respectively) in addition to $CD4^+$ and $CD8^+$ T cell subsets overlaid onto the T cell dendrogram (**Figure 3C**). Nodes in the SPADE tree are colored in a gradient of cell frequency to illustrate where each manually overlaid cellular subset resides. For the pooled treatment monocyte SPADE

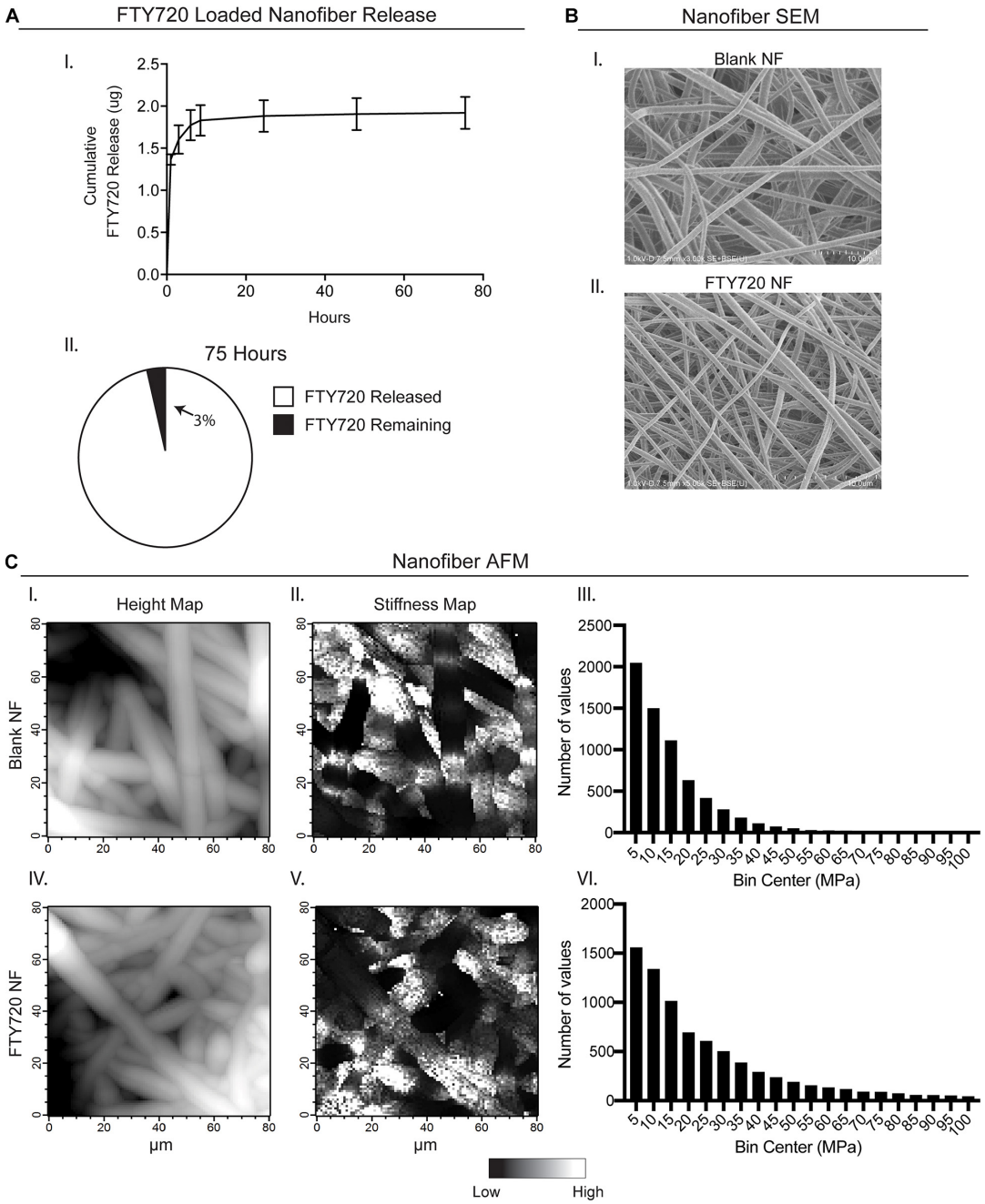

FIGURE 1 | Characterization of electrospun FTY720-loaded nanofiber scaffolds. Release of FTY720 from PLGA-PCL nanofiber (NF) scaffolds and biomaterial characterization via scanning electron microscopy (SEM) and atomic force microscopy (AFM). **(A)** *In vitro* cumulative release profile of FTY720 (I) with percentage of drug released after 75 h (II). **(B)** Scanning electron micrographs of unloaded, blank PLGA-PCL nanofibers (I) and nanofibers loaded with FTY720 (II). **(C)** AFM surface topology (I, IV) and stiffness (II, V) maps of blank and FTY720-loaded nanofibers where white regions represent areas of greater height and stiffness, respectively. Histograms of Young's moduli (MPa) obtained over multiple contact points on blank nanofibers (III) and FTY720-loaded nanofibers (VI).

dendrogram, Ly6C^{hi} inflammatory monocytes are annotated as nodes 1–7 (**Figure 3A**–II) while Ly6C^{lo} anti-inflammatory monocytes are annotated as nodes 8–19 (**Figure 3B**–II), each subset clustering in different SPADE nodes and trajectories to demonstrate their unique protein signatures. These protein signatures are further represented with SPADE node heatmaps that graphically represent heterogenous marker expressions characteristic of each monocyte subset (**Figures 3A**–I, **B**–I). For each identified monocyte subpopulation, we generated stacked bar graphs to visualize cell frequency differences within annotated nodes amongst treatment groups (**Figures 3A**–III, **B**–III). Each segment of the bar graphs corresponds to an annotated

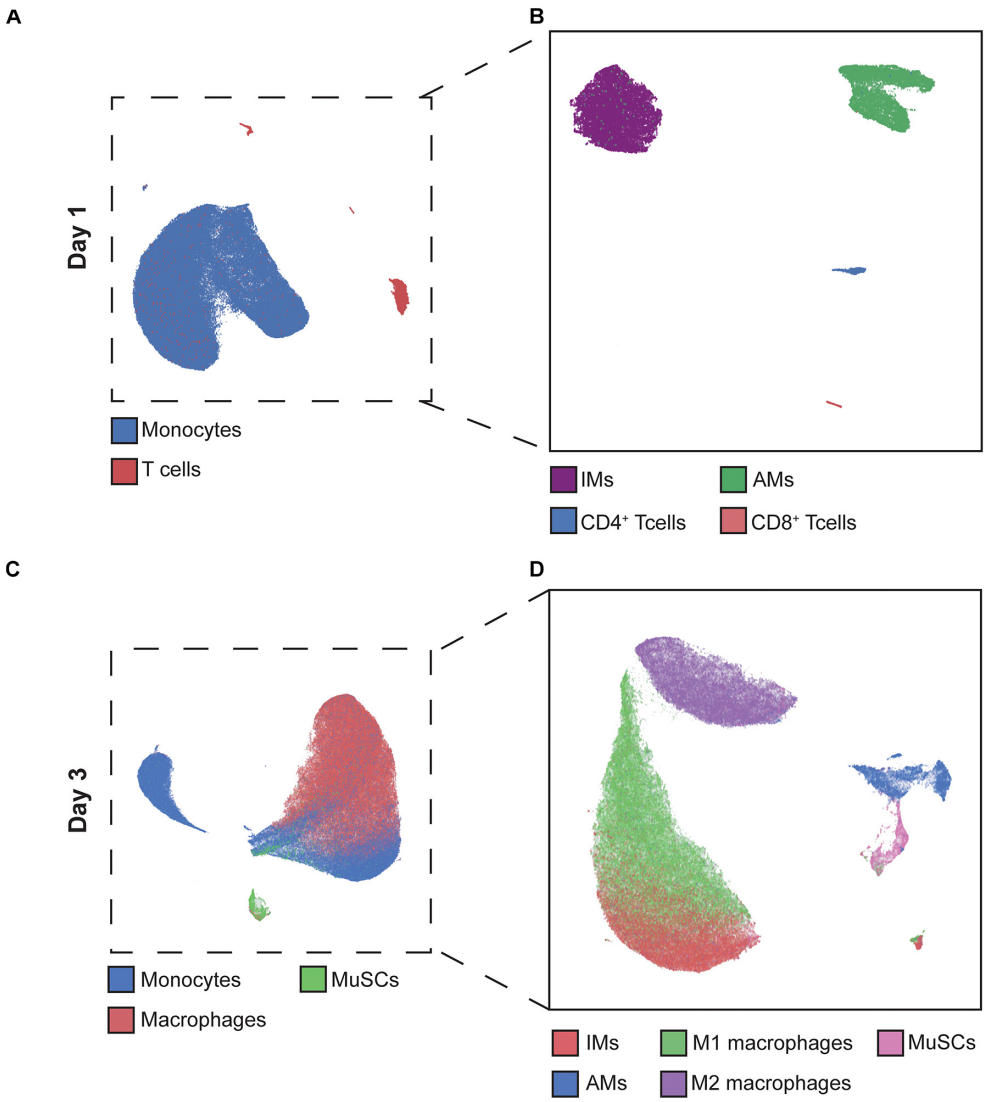

FIGURE 2 | UMAP projections reveal heterogeneous cell subpopulations present in spinotrapezius tissue 1 and 3 days after injury. 2D UMAP projections of single cells taken from explanted spinotrapezius tissues 1 and 3 days post injury. **(A)** UMAP of monocytes and T cells within the muscle at day 1 after injury where these larger cell types are broken down into their respective subpopulations (Ly6C^{hi} and Ly6C^{lo} monocytes, CD4^{+} and CD8^{+} T cells) in a separate UMAP **(B)**. **(C)** Monocyte, macrophage, and MuSCs comprise the cell composition of muscle tissue 3 days post injury with monocyte and macrophage cells types further examined for heterogeneous subpopulations in panel **(D)**.

SPADE node (colored and stacked numerically by node) for direct comparison of cell frequency in nodes across treatments.

No changes in cell frequency of Ly6C^{hi} inflammatory monocytes were evident across treatment groups at day 1, whereas local FTY720 delivery resulted in an early relative increase of Ly6C^{lo} anti-inflammatory monocytes compared to blank nanofiber and no implant control groups (**Figures 3A**–III, **B**–III). We have previously shown that these Ly6C^{lo} anti-inflammatory monocytes are biased progenitors of regenerative M2-like macrophages and are critical to regenerative processes in other tissues (Olingy et al., 2017; San Emeterio et al., 2017). Manually gated CD8^{+} T cells were overlaid onto the pooled treatment CD3^{+} SPADE dendrogram, located in nodes 1–3, while CD4^{+} helper T cells were positioned in nodes 4–13 (**Figure 3C**–II). Distinct dendrogram locations between these T cell subsets result from their protein expression differences that is visualized in an accompanying annotated SPADE node heatmap (**Figure 3C**–I). While collective CD4^{+} and CD8^{+} T cell numbers in injured tissue was not significantly different across treatments, we note that FTY720 treated animals had reduced T cell infiltration compared to those treated with blank nanofibers (**Figure 3C**–III). This was presumably a result

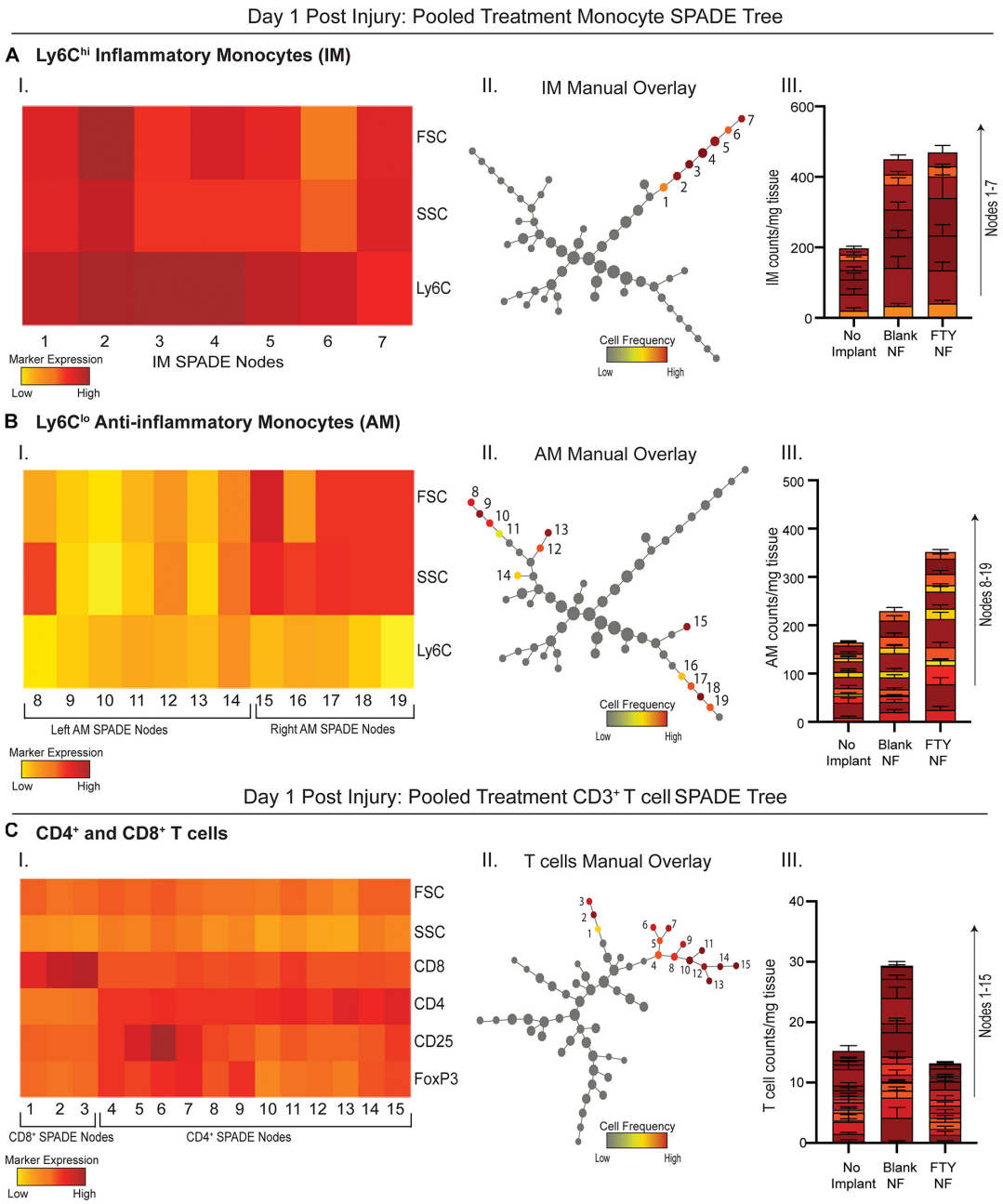

FIGURE 3 | Pseudotime analysis of immune cell infiltration into muscle defect area 1-day post VML injury. SPADE dendrograms consist of live, single cellular events gated as monocytes **(A,B)** and T cells **(C)** extracted from spinotrapezius muscle 1 day after VML injury from all treatment groups. Specific pre-gated cell subpopulations are overlaid onto their respective SPADE dendrograms where overlaid cells are color annotated by normalized cell frequency within the SPADE nodes. SPADE nodes of high frequency of a particular cellular subset (color annotated) are given a node number assignment to present a grouping of nodes distinguishing a certain cell subpopulation within the greater dendrogram trajectory (**A–C** II). The protein signature of the annotated SPADE nodes representing a specific subpopulation of cells is provided as a heatmap (**A–C** I). The number of cells in a given subpopulation per mg of tissue across all treatment groups quantified per annotated SPADE node and represented with a stacked bar graph where each segment of the bar graph corresponds to a given node number assignment (**A–C** III). Data presented as mean ± S.E.M per annotated node where all annotated nodes for a specified subset are stacked vertically in a bar graph for each treatment group. Statistical analysis performed includes one-way ANOVA with Tukey's multiple comparison. *n* = 6 samples for FTY720 and blank nanofiber (NF) groups and four samples for no implant (untreated) group.

of the acute lymphopenia induced at day 1 (**Supplementary Figure 3**). These results indicate that while immune cell recruitment into the tissue microenvironment was not yet significantly affected by therapeutic S1P receptor modulation at day 1 post injury, we see rising pro-regenerative monocyte subsets and decreased lymphocyte invasion which may play a

vital role in priming the injury niche toward timely resolution of inflammation.

Nanofiber-Based Delivery of a Pharmacological S1P Analog Enriches Pro-regenerative Immune Subsets and MuSC Population at 3 Days Post Injury

With local S1P receptor modulation beginning to shift the injury microenvironment from pro-inflammatory to pro-regenerative at day 1, we aimed to evaluate the therapeutic effect on key cellular players underlying ongoing muscle regeneration at 3 days post injury. Single cells were extracted from muscle tissue at 3 days post injury and analyzed by flow cytometry. Referring back to **Figure 2**, UMAP projections were again generated with cells extracted from injured muscle at day 3 (**Figures 2C,D**) and overlaid with select manually gated subsets to visualize the population of monocytes (blue) and macrophages (red) along with a group of resident MuSCs (green) present in the injured muscle (**Figure 2C**). **Figure 2D** shows the phenotypic variations between these immune populations, as the distance between M1 and M2-like macrophage clusters and between $Ly6C^{hi}$ inflammatory and $Ly6C^{lo}$ anti-inflammatory monocyte groupings indicate the innate protein expression differences distinguishing subsets existing within bulk cell types.

To evaluate more discrete heterogeneities within subpopulations of cells infiltrating the site of injury in response to S1P receptor agonism at a later stage in the initial inflammatory cascade, we generated SPADE dendrograms consisting of single, live cells from muscle tissue 3 days post VML injury (**Figure 4**). These SPADE dendrograms provide visual 2D representations of the heterogeneity within pre-gated monocytes (**Figure 4A**), macrophages (**Figure 4B**), and Lineage $(Lin)^-$ cells (**Figure 4C**) from animals treated with either blank or FTY720-loaded nanofibers. Select gated populations of interest ($Ly6C^{lo}$ anti-inflammatory monocytes, M2-like macrophages, and MuSCs) were overlaid onto their corresponding SPADE dendrograms (**Figures 4A**–II,**B**–II,**C**–II, respectively). Any node which occupies cells of the overlaid subset is annotated via a node assignment number and color coded by cell frequency within the given SPADE dendrogram. $Ly6C^{lo}$ anti-inflammatory monocytes occupy nodes labeled 1–13 within the monocyte SPADE dendrogram (**Figure 4A**–II), and their low Ly6C signature is confirmed by its accompanying SPADE node heatmap (**Figure 4A**–I). Stacked SPADE node bar graphs show that localized nanofiber-mediated release of FTY720 drastically increased the number of $Ly6C^{lo}$ anti-inflammatory monocytes infiltrating the tissue compared to blank nanofiber controls (**Figure 4A**–III) without any significant difference in the number of $Ly6C^{hi}$ inflammatory monocytes between treatments (**Supplementary Figure 4**). We further observed significantly more pro-regenerative M2-like macrophages, occupying nodes 1–17 in the macrophage dendrogram (**Figure 4B**–II), from FTY720 treated animals compared to those treated with blank nanofiber scaffolds (**Figure 4B**–III). Because macrophages are known to play a role in MuSC proliferation and differentiation, we identified $CXCR4^+$ $CD29^+$ MuSCs (**Figure 4C**–I) and overlaid these resident muscle cells onto the Lin^- SPADE dendrogram (**Figure 4C**–II). We found that modulating S1P receptors locally within the muscle tissue significantly enriched resident MuSCs (**Figure 4C**–III) which is a vital component to successful regeneration given that VML injury results in a catastrophic loss of the MuSC niche (Wosczyna and Rando, 2018). Our results suggest that FTY720 demonstrates its effectiveness as an immunomodulatory therapy after critical injury not only through its recruitment of pro-resolving immune subsets, but additionally by increasing the MuSC numbers four-fold within the injury environment.

S1P Receptor Immunotherapy Leads to Improved Metrics of Skeletal Muscle Regeneration

We assessed regeneration of muscle fibers 14 days post VML injury with confocal imaging to determine if the observed FTY720-induced immune cell recruitment dynamics underlie overall muscle repair and regeneration. Whole mount confocal images of injured spinotrapezius muscles were stained with desmin (green) to identify muscle fibers and CD68 (blue) to identify macrophages within and around the site of injury; representative images across all treatments groups were rendered in Imaris for 3D visualization of muscle fiber healing (**Supplementary Figure 5**). While untreated animals and those treated with blank nanofibers presented with large defect areas remaining 14 days post VML injury, muscle treated locally with FTY720 demonstrated accelerated wound healing with regenerating myofibers bridging across the defect area (**Supplementary Figures 5A–C**). A side view of the 3D muscle renderings showed the qualitative differences notable in $CD68^+$ macrophage infiltration into the defect area with untreated and blank nanofiber groups overwhelmed with persistent immune cell presence characterizing chronic, non-resolving inflammation (**Supplementary Figures 5D,E**). To the contrary, FTY720 delivery to the injured muscle resulted in qualitatively less macrophage crowding in and around the defect (**Supplementary Figure 5F**), indicating that S1PR modulation plays a pivotal role in efficient immune cell egress from the tissue in a timely manner.

We then examined the relationship between regenerating muscle fibers and their alignment with healthy fibers during injury repair (**Figure 5**). We measured the angle between centrally nucleated regenerating muscle fibers and the axis of original, uninjured muscle fibers (denoted in **Supplementary Figure 6**); a higher angle measurement (ranging from 0 to 90°) indicates poor alignment of the new muscle fibers. Untreated and unloaded nanofiber groups presented with disorganized fibers in random orientations (**Figures 5A,B,D,E**). Defects treated with FTY720 showed orderly elongation of myofibers across the injury site (**Figures 5C,F**). FTY720-treated defects exhibited significantly lower angle measurements ($17.82° \pm 5.4°$) compared to both untreated and blank nanofiber treated defects ($50.07° \pm 3.2°$ and $43.1° \pm 8.79°$, respectively), indicating improved alignment of newly developed myofibers (**Figure 5G**). Surface rendered cross sections of the

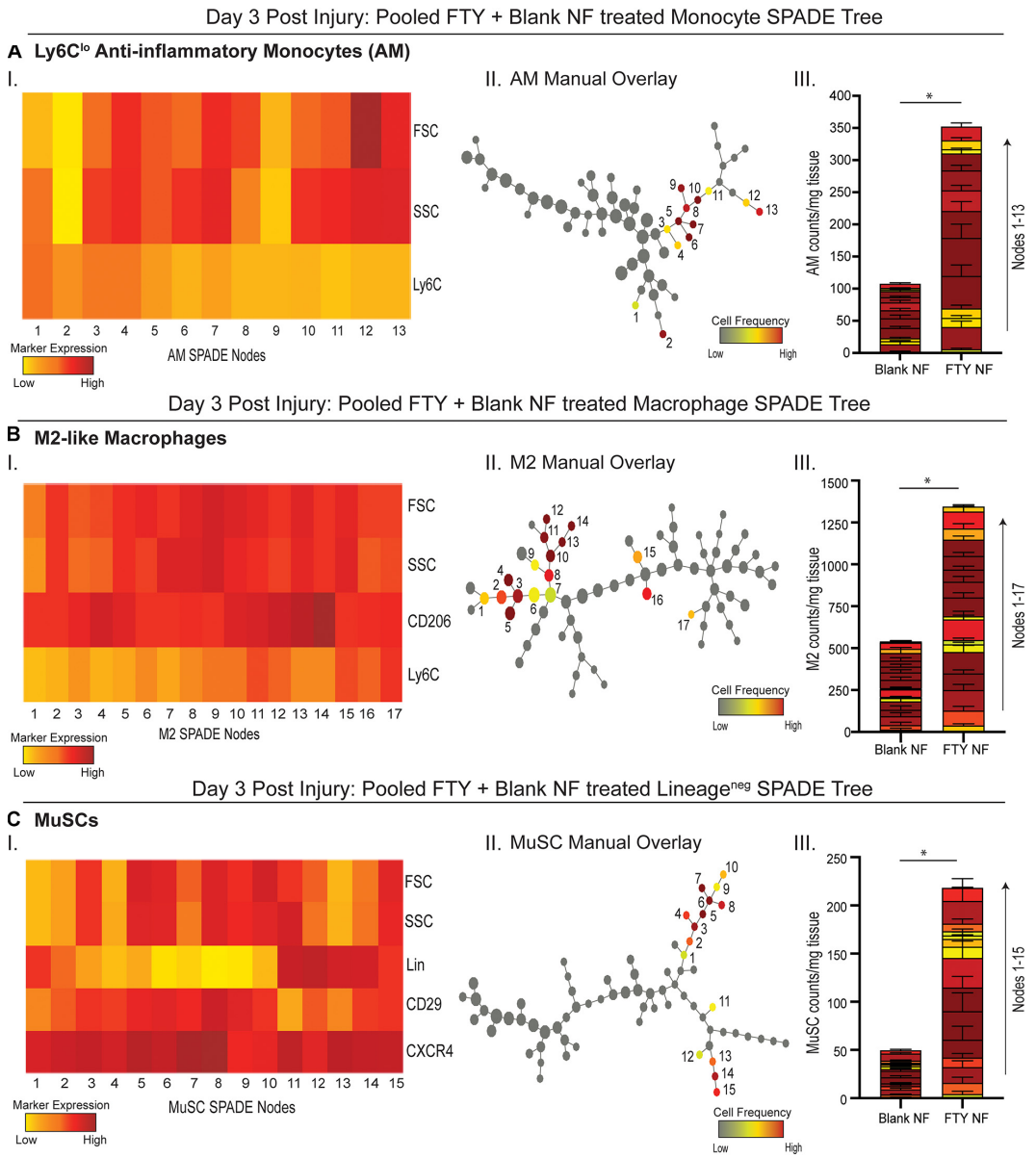

FIGURE 4 | Pseudotime visualization of cellular composition at the site of injury reveals an FTY720-induced increase in pro-regenerative subsets 3 days post VML injury. SPADE dendrograms consist of live, single cellular events gated as monocytes **(A)**, macrophages **(B)**, and Lin$^-$ cells **(C)** extracted from spinotrapezius muscle 3 days after VML injury from animals treated with blank or FTY720-loaded nanofibers (NF). Specific pre-gated cell subpopulations (Ly6C^{lo} anti-inflammatory monocytes, M2-like macrophages, and MuSCs) are overlaid onto their respective SPADE dendrograms where overlaid cells are color annotated by normalized cell frequency within the SPADE nodes. SPADE nodes of high frequency of a particular cellular subset (color annotated) are given a node number assignment to present a grouping of nodes distinguishing a certain cell subpopulation within the greater dendrogram trajectory (**A–C** II). The protein signature of the annotated SPADE nodes representing a specific subpopulation of cells is provided as a heatmap (**A–C** I). The number of cells in a given subpopulation per mg of tissue across all treatment groups quantified per annotated SPADE node and represented with a stacked bar graph where each segment of the bar graph corresponds to a given node number assignment (**A–C** III). Data presented as mean ± S.E.M per annotated node where all annotated nodes for a specified subset are stacked vertically in a bar graph for each treatment group. Statistical analysis performed includes unpaired *t*-tests. $n = 8$ samples per treatment group. $^*p < 0.05$.

regenerating muscle fibers surrounding the defect space showed that in addition to enhanced alignment, FTY720 treated fibers had improved circular morphology along with significantly increased fiber diameter compared to untreated and blank nanofiber groups (**Figures 5H,I**). These improved regenerative metrics observed in muscle treated with immunomodulatory FTY720 could be in part attributed to increased collagen deposition around new myofibers in the FTY720 treated animals (**Figure 5J**).

To further probe how collagen and muscle fibers align as the defect heals, we performed SHG imaging 2 weeks post injury to analyze the angular differences between the dominant axes

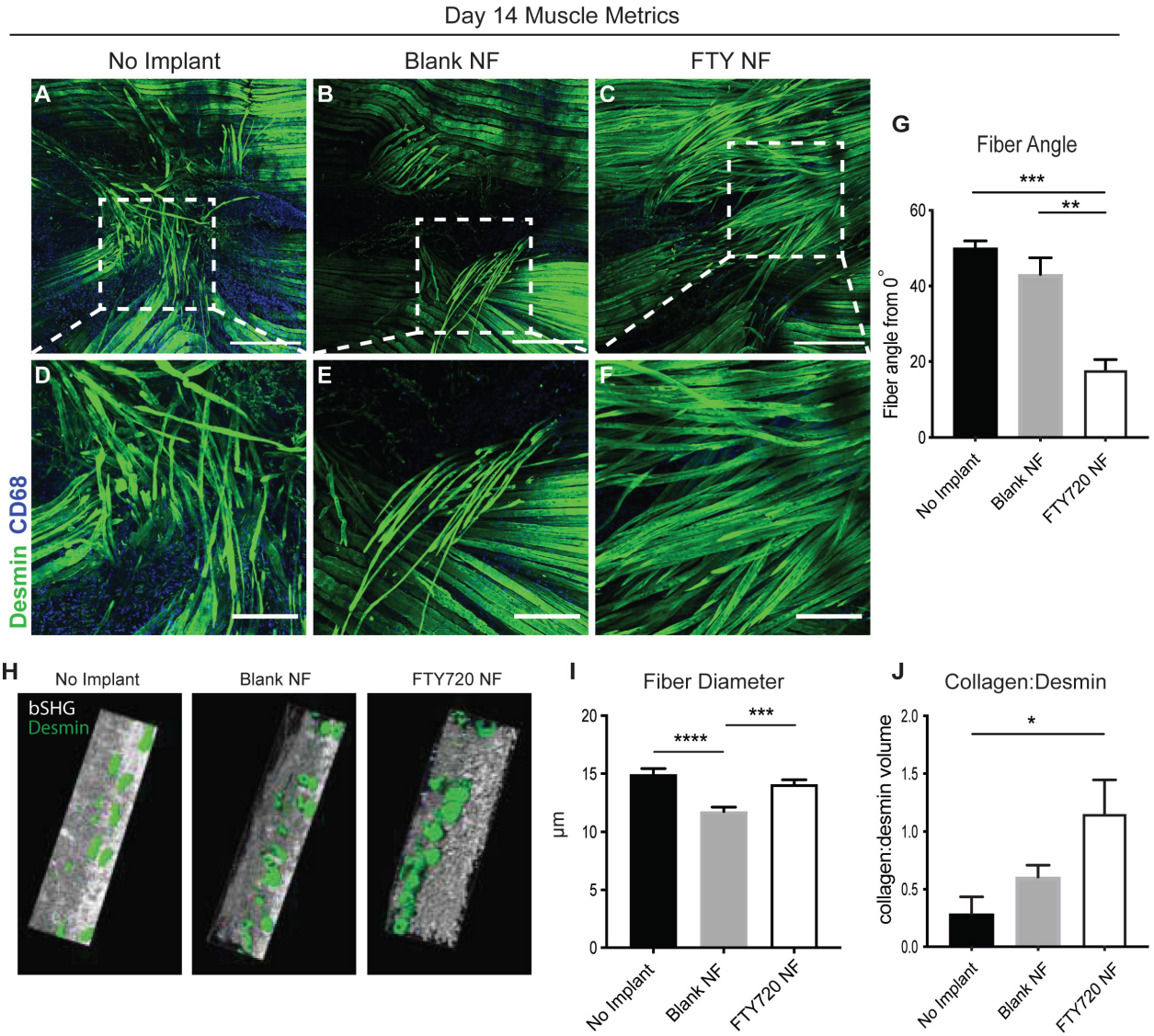

FIGURE 5 | Localized release of S1P analog from nanofiber scaffold enhances metrics of skeletal muscle healing and regeneration. Whole mount IHC of explanted spinotrapezius muscle 14 days post injury. Representative confocal images centered around the defect area from each treatment group stained with desmin (green) and CD68 (blue) **(A–C)** with a zoomed in ROI from each treatment group, denoted with dotted white boxes, presented in the second row **(D–F)**. **(G)** Fiber angle of regenerating muscle fibers measured from 0 to 90° degrees with respect to the pre-injury fiber axis. **(H)** Imaris generated cross-sectional view of regenerating muscle fibers for assessment of fiber morphology. **(I)** Fiber diameter measurements from animals across all treatment groups. **(J)** Volume ratio of collagen:desmin quantified for animals of each treatment group. Scale bars of 500 μm **(A–C)** and 200 μm **(D–F)**. Ordinary one-way ANOVA with Tukey's multiple comparisons conducted for statistical analysis and data is presented as mean ± S.E.M. n = 3–5 animals per treatment group. *$p < 0.05$, **$p < 0.01$, ***$p < 0.001$, ****$p < 0.0001$. bSHG = backward second harmonic generation, NF = nanofiber.

of collagen and muscle fiber orientation (**Figure 6**). We found that animals treated with FTY720-loaded nanofibers displayed collagen fibrils highly aligned with one another and with the regenerating muscle fibers within the defect area which was not observed in the untreated or blank nanofiber control groups (**Figure 6A**). In representative images, the maximum intensity angles of SHG signal are color coded for polarimetric distinction between collagen and muscle fibers where purple represents the actin/myosin banding and green represents areas of collagen alignment with the muscle fibers. We graphed the orientation angle of each pixel within the image with orientations of 0 and 180 aligned with the main direction of the muscle fibers. Distribution of the pixel orientations in each field of view had similar shapes in the uninjured and FTY720-treated animals, confirming collagen and muscle fiber alignment during the regenerative process (**Figure 6B**). Thus, increased collagen deposition induced by FTY720 may be vital to providing a remodeled extracellular matrix and an architectural conduit along which fibers can elongate in an aligned manner vital to mature skeletal muscle structure and function.

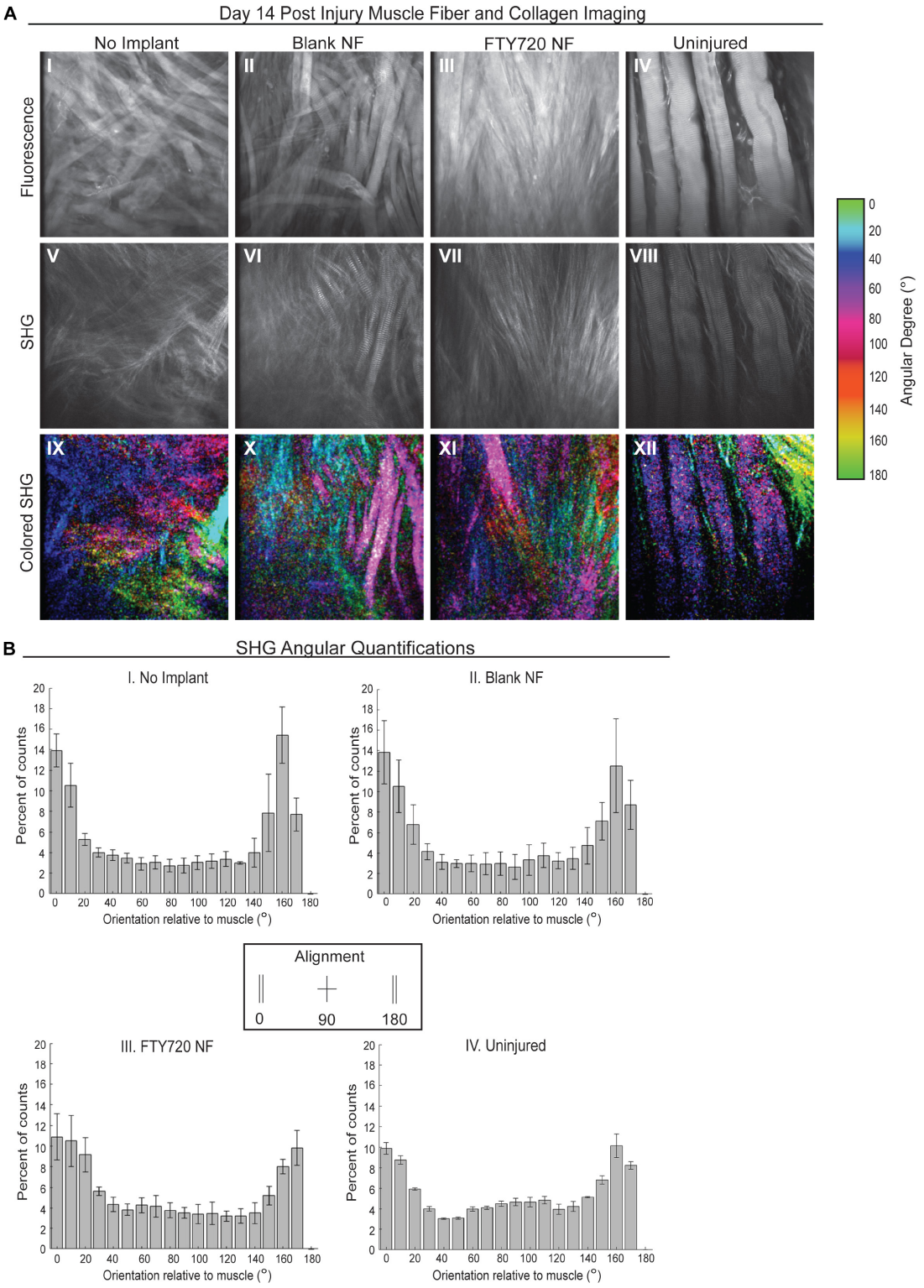

FIGURE 6 | Second harmonic generation (SHG) reveals collagen alignment in regenerating muscle fibers when treated with FTY720-loaded nanofiber scaffolds. **(A)** Second harmonic imaging of muscle fibers from untreated muscle, blank nanofiber (NF) treated muscle, FTY720-loaded nanofiber treated muscle, and uninjured muscle. Representative fluorescence images from each treatment group shown in the first row of images (I–IV), SHG imaging of the same animals per treatment shown in the second row (V–VIII), and the last row represents a color-coded maximum intensity projection in which the color key is annotated based on angular orientation (IX–XII). **(B)** Angular quantifications of collagen in relation to the muscle fiber axes measured via SHG. $n = 4$ per treatment group and data represented as mean ± S.D. SHG = second harmonic generation.

FTY720 Delivery Stimulates Re-vascularization and Regeneration of Damaged Neuromuscular Junctions

Restoration of functional properties of skeletal muscle relies on the revascularization and reinnervation of regenerated myofibers, two major challenges to a full recovery following traumatic injury. Representative images of muscle defects across all experimental conditions were stained for desmin (green), CD68 (blue), and CD31 (red) in order to characterize the vascular network present at 14 days post injury (**Figure 7**). Whereas untreated and blank nanofiber treated animals displayed an immature vascular network of disorganized small-diameter vessels (**Figures 7A,B,D,E**), FTY720 nanofiber treated animals were distinguished by distinctly formed, branching vasculature amongst regenerating fibers (**Figures 7C,F**). This result demonstrates the temporal coupling of myogenesis with vascular remodeling processes crucial for successful skeletal muscle regeneration (Borselli et al., 2010; Latroche et al., 2017).

To assess the reinnervation of myofibers around the defect area, FTY720 nanofibers were implanted into VML injured Thy1-YFP mice. In this mouse model, $Thy1^+$ motor neurons were labeled with YFP and detectable via immunofluorescence (**Figure 8**). At the 28 days post injury timepoint, regenerated neuromuscular junctions were detected by identifying regions of overlap of $Thy1^+$ pre-synaptic junctions (white) and acetylcholine $receptor^+$ post-synaptic junctions (red). While acetylcholine receptor clusters were present in untreated muscle, their morphology appeared fragmented and there was little association with motor axons indicative of frank denervation underlying severe VML trauma (**Figures 8B,E,H**). However, when treated with immunomodulatory FTY720, acetylcholine receptors appeared to begin recovering the pretzel-like morphology (denoted with white arrow) typical of mature, healthy neuromuscular junctions and displayed greater axonal density compared to untreated muscle (**Figures 8C,F**). The topological maturation of FTY720-treated acetylcholine receptors combined with an overlapping $Thy1^+$ axonal network (**Figure 8I**) suggests that FTY720 promotes regeneration of damaged neuromuscular junctions as soon as 28 days following severe trauma. The improved vascular network development and neuromuscular junction regeneration seen in animals treated locally with FTY720 highlights the promise of S1P receptor modulation toward boosting endogenous repair mechanisms imperative to functional recovery after severe musculoskeletal injury.

DISCUSSION

Volumetric muscle defect injuries comprise 50–70% of combat injuries and are the cause of 80% of limb amputations in soldiers (Grogan et al., 2011). The therapeutic options for critically sized muscle defects are few and exhibit poor clinical prognosis due to donor site morbidity, and inadequate integration of donor tissue into the local vascular and motor neural network, resulting in permanent functional deficits and disabilities. While extracellular matrix derived scaffolds have been utilized as void filling substitutes for autografts and promote M2-like macrophage polarization in the injury niche, the reported efficacy is highly variable (Qazi et al., 2015; Dziki et al., 2016). Although there have been several regenerative efforts made toward treating VML, the dysregulated immune response following critical VML injury is poorly understood. Subcritical, healing muscle defects exhibit an initial inflammatory phase, with pro-inflammatory immune cells such as $Ly6C^{hi}$ monocytes and M1-like macrophages peaking around days 2–3 post injury. Following this stage, M2-like macrophages and their biased progenitors, $Ly6C^{lo}$ monocytes, will predominate around 4–7 days post injury, marking the resolution of inflammation and bringing forth the restorative phase (∼8–14 days post injury) in which angiogenesis and matrix deposition coupled with MuSC differentiation contribute to desirable muscle healing (Chazaud, 2020). In contrast, critically sized VML injuries, as studied here, present with a dysregulated inflammatory cascade (**Supplementary Figure 7**). This often leads to chronic inflammation that does not successfully resolve which may result in pathological fibrosis instead of functional recovery. Employing small molecule, regenerative immunotherapies which influence the phenotype and function of endogenous pro-regenerative cell types represents a promising strategy for local immunomodulation of innate and adaptive immune response following critical VML.

In this study, we utilized a murine spinotrapezius VML model to investigate how local delivery of a pharmacological S1PR modulator influences endogenous cellular reprogramming within the injury milieu to foster enhanced myofiber regeneration coupled with revascularization and reinnervation of the muscle tissue. Nanofiber scaffolds fabricated from biocompatible polymers are an easily tunable platform that enables the incorporation of bioactive molecules suited to mediate S1PR signaling pathways critical to leukocyte trafficking and subsequent tissue repair. The nanofibrillar structure of the scaffolds not only resembles the native extracellular matrix that is lost upon traumatic injury, but further, the nanoscale topography and high surface-to-volume ratio improves interactions with cellular components infiltrating the defect (Das et al., 2013). Here, we engineered PLGA/PCL nanofiber scaffolds encapsulating FTY720, an immunomodulatory molecule known to redirect anti-inflammatory $Ly6C^{lo}$ monocytes from peripheral circulation into injured tissues when locally applied (Awojoodu et al., 2013). We have shown previously that nanofiber topography acted synergistically with FTY720 delivery in critically sized bone defects as evidenced by neovascularization within the defect site and recruitment of endogenous progenitor cells to enhance bone regeneration (Das et al., 2013).

While our study aims to target S1PR signaling to regulate the clearance and regenerative polarization of immune cells following VML, conventional methods of analyzing the immune response severely undermine its functional diversity. Cell populations captured at a single moment in time may include several distinct phenotypic transition states, yet this is often masked by averaging properties existing within bulk cell types and thus losing trends of single cells (Trapnell et al., 2014). New analytical and visualization techniques have

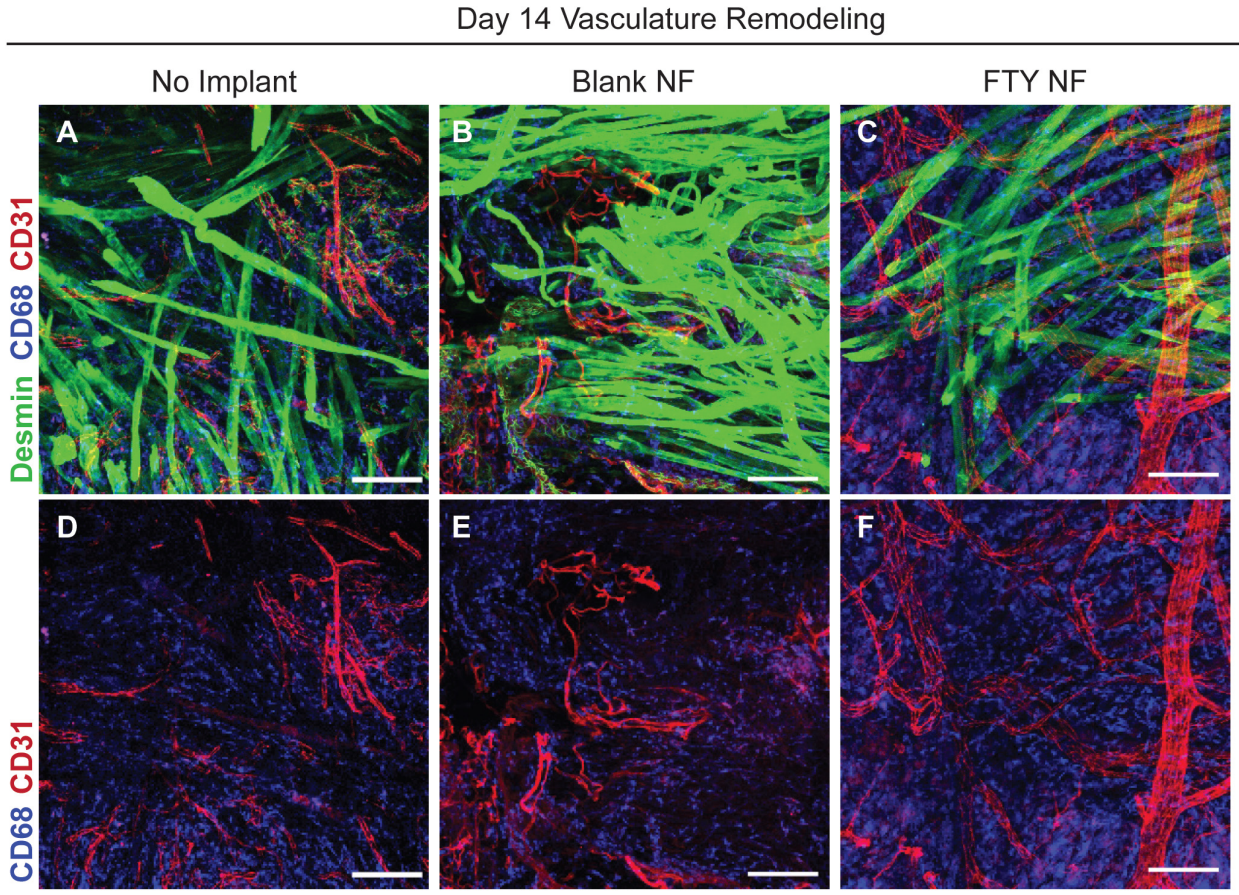

FIGURE 7 | Delivery of FTY720 stimulates re-vascularization within injured skeletal muscle. Whole mount IHC imaging of explanted spinotrapezius muscle 14 days post injury. Representative images within the defect space shown for each experimental condition stained for desmin (green), CD68 (blue), and CD31 (red) to identify muscle fibers, macrophages, and vasculature, respectively **(A–C)**. Second row of images **(D–F)** only depict CD68 and CD31 staining to clearly visualize the vascular network underlying regenerating muscle fibers after VML injury. Scale bars of 100 μm in each image. *n* = 2–3 animals per treatment group.

been developed to allow greater exploration into the diverse populations of immune cells underlying non-healing injuries and their response to therapeutic perturbations. We harness these technological advancements with SPADE, a dimensionality reduction and pseudotime trajectory tool that allows us to assess the immune cell recruitment and differentiation kinetics within an inflammatory, traumatic defect and investigate myeloid and lymphoid responses in this VML injury to the delivery of FTY720. Specifically, we find that while early Ly6C^{hi} inflammatory monocyte infiltration at day 1 post injury was unchanged between treatment groups, there were increases in the number of Ly6C^{lo} anti-inflammatory monocytes within animals treated with FTY720-loaded nanofibers compared to controls (**Figures 3A,B**). The Ly6C^{hi} inflammatory and Ly6C^{lo} anti-inflammatory monocytes occupy nodes in different trajectories of the SPADE dendrogram, illustrating SPADE's ability to distinguish varying protein signatures within bulk cell types (i.e., monocytes) and visualize the immune cell diversity central to wound healing. The upward trend of Ly6C^{lo} anti-inflammatory monocytes at day 1 with FTY720 treatment may account for robust M2-like macrophage increases seen at day 3, as this result aligns with other studies showing S1P's role in modulating macrophage polarization within the local injury milieu (Weigert et al., 2019).

Furthermore, there was a clear reduction in CD4^{+} and CD8^{+} T cell infiltration at day 1 post injury with FTY720 treatment, likely as a result of irreversible surface S1PR1 internalization and degradation (**Figure 3C**). Although the role of CD4^{+} and CD8^{+} T cells in volumetric muscle defect healing remains unclear, these cell subsets may secrete cytokines that could influence the polarization of myeloid subsets. CD4^{+} T cells produce IL-4 and IL-13 (Anthony et al., 2007) which may lead to pro-regenerative M2-like macrophage polarization (Spiller et al., 2016) while CD8^{+} lymphocytes secrete INF-γ (Schoenborn and Wilson, 2007), promoting an inflammatory M1-like macrophage phenotype (Spiller et al., 2016). While invasion of both T cell populations was reduced in muscle treated with FTY720, the complex interplay between lymphoid and myeloid cells is such that even slight shifts in cytokine balance due to decreases in these lymphoid populations could results in a tissue microenvironment more favorable to promoting regeneration.

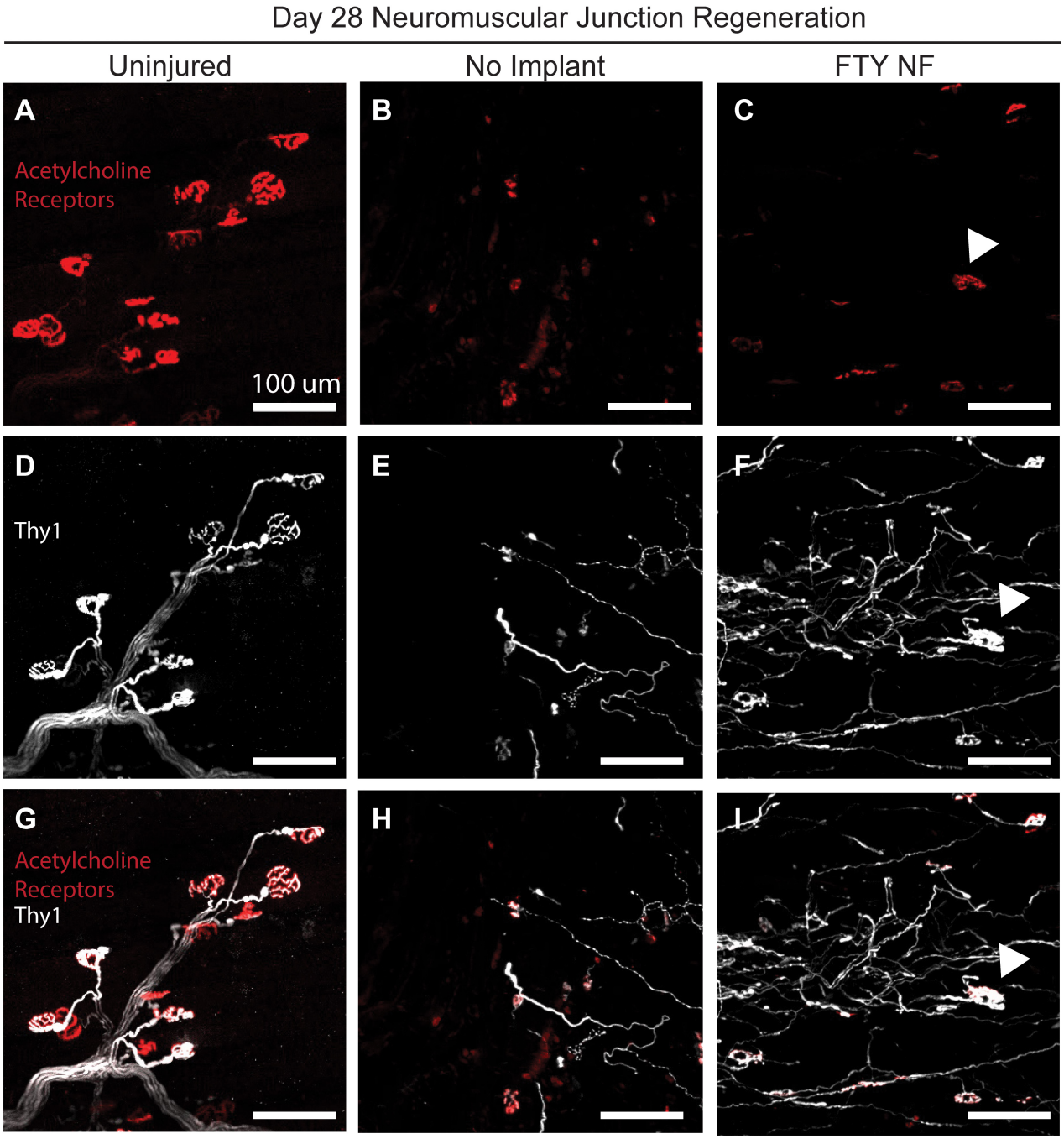

FIGURE 8 | Localized FTY720 delivery induces regeneration of damaged neuromuscular junctions following traumatic injury to the muscle. High powered immunofluorescence images of spinotrapezius muscle explanted 28 days post injury from uninjured muscle **(A,D,G)**, untreated muscle **(B,E,H)**, and muscle treated with FTY720-loaded nanofibers **(C,F,I)**. Thy1-YFP mice enabled labeling of motor neurons with YFP (white) and staining with rhodamine alpha-bungarotoxin (red) permits identification of post-synaptic acetylcholine receptors. Regenerated neuromuscular junctions identified by detecting overlapping regions of $Thy1^{+}$ pre-synaptic and acetylcholine $receptor^{+}$ post-synaptic junctions as indicated with white arrow. Scale bars of 100 μm. *n* = 2–3 animals per experimental group.

To assess whether the FTY720-mediated decreasing trends in T cell infiltration and simultaneous increasing trends in $Ly6C^{lo}$ anti-inflammatory monocytes at an early day 1 timepoint primes myeloid phenotypes at later timepoints, we again employ novel, pseudotime trajectory profiling of cell types comprising the injury niche at day 3 post VML. With significant increases in $Ly6C^{lo}$ anti-inflammatory monocytes and M2-like macrophages compared to blank nanofiber treatment (**Figures 4A,B**), it is concluded that pharmacological agonism of the S1P/S1PR signaling axis preferentially recruits immune cells which drive

inflammation resolution to ultimately set the stage for successful wound healing. While the transition from M1 to M2-like macrophages is not binary but rather a continuum of phenotypes, innovative high dimensional analytical tools such as SPADE are indispensable to identifying discrete macrophage subpopulations vital to fostering myogenesis. Both M1 and M2-like macrophages are known to influence MuSC proliferation and differentiation, so we decided to evaluate the effect of S1P receptor modulation on MuSC numbers at day 3 after injury. Interestingly, upon treatment with FTY720, injured spinotrapezius muscle harbored four times as many MuSCs compared to blank nanofiber treated muscle (**Figure 4C**). M1-like macrophages secrete cytokines such as TNFα and INF-γ which stimulate MuSC proliferation. M2-like macrophages promote the ongoing MuSC proliferation via initial IGF-1 secretion, but they also secrete GDF3 and TGFβ to stimulate MuSC differentiation and fusion to mature myofibers (Wosczyna and Rando, 2018). Thus, a tightly regulated switch in macrophage phenotype is critical for timely MuSC proliferation and myofiber maturation. We believe that the FTY720-mediated M1 to M2-like macrophage switch had a direct influence on MuSC differentiation via paracrine signaling, thus representing a vital therapeutic opportunity to intervene in the initial inflammatory cascade. Importantly, we observed similar increases in M2-like macrophages and MuSC numbers following local delivery of VPC01091 (local S1PR3 antagonist) to injured muscle in our previous studies (Hymel et al., 2020). Further studies exploring the cytokine profile after muscle injury in response to S1P receptor modulators are needed to examine the complex paracrine signaling between various myeloid cell subsets with muscle resident progenitor populations driving endogenous repair mechanisms.

To explore whether the immunological profile and increased MuSC numbers induced by FTY720 treatment influenced subsequent muscle repair and regeneration, we assessed various healing parameters. Rendering whole-mount confocal images of the muscle fibers surrounding the defect area into 3D surfaces, we qualitatively observe enhanced myofiber bridging across the defect space in FTY720 treated muscle compared to control groups which still present with large void areas 14 days post injury (**Supplementary Figure 5**). Intriguingly, there was an obvious decreased accumulation of $CD68^+$ macrophages in the FTY720 treated muscle. This finding is supported by our previous work in which the local delivery of S1P receptor modulator VPC01091 to injured muscle also resulted in decreased macrophage infiltration and more regenerating muscle fibers closing the defect area compared to controls (Hymel et al., 2020). We believe that the role of S1P signaling in regulating immune cell egress from non-lymphoid tissues rids the microenvironment of chronic inflammation, thus accelerating repair and regeneration as seen here with FTY720 treatment as well as with VPC0191 treatment (Baeyens and Schwab, 2020; Hymel et al., 2020). We observe that FTY720 nanofiber treated animals displayed increased fiber diameter compared to control animals, and increased collagen:desmin ratio (**Figures 5H–J**). Though we have previously attributed high collagen:desmin ratio to an increased fibrotic response, those observations were made in 1 mm volumetric defects which heal around 7 days (San Emeterio et al., 2017). In this 2 mm defect model, tissue must regenerate over three-fold more area than the 1 mm defect model, thus increased matrix deposition may be beneficial in this context to guide and support the growth of muscle fibers.

Because skeletal muscle fibers produce maximum force along a single axis, it is crucial for injured fibers to regenerate in alignment with pre-existing, healthy fibers. We observed a lower angle between regenerating fibers and the original fiber axis in animals treated with FTY720-loaded nanofiber scaffolds, indicating improved alignment of the muscle fibers themselves (**Figure 5G**) and their alignment with the surrounding extracellular matrix (**Figure 6**). We can conclude that the higher alignment is primarily due to the effects of FTY720, and not the presence of nanoarchitecture within the scaffold, due to the significantly higher fiber angle found in the blank nanofiber group. The mechanism by which FTY720 mediates fiber alignment is unknown at this point. However, M2-like macrophages have been shown to promote extracellular matrix synthesis within fibroblasts (Knipper et al., 2015) and fibroadipogenic progenitors (Lemos et al., 2015), and it has been recently shown that fibroblasts within a collagen matrix rapidly generate tensile forces to close surgically induced defects (Sakar et al., 2016). An interesting hypothesis is that the increase in M2-like macrophages mediated by FTY720 enhances fibroblast activity to generate contractile forces over the defect void that encourage muscle cell alignment as demonstrated *in vitro* (Liao et al., 2008). Further, it is likely that M2-like macrophages play an important role in guiding muscle fiber growth as they secrete matrix metalloproteinases which remodel the surrounding matrix, but further studies are necessary to determine whether specialized macrophage populations play a direct role in regulating newly formed muscle fiber morphology and orientation. Future studies probing matrix remodeling at later time points with FTY720 treated defects will be crucial to ensure that increased matrix deposition remodels sufficiently so that persistent fibrosis does not occur.

Lastly, we investigated whether our small molecule S1PR modulating immunotherapy could enhance revascularization and reinnervation after volumetric defect injury-two of the most prominent clinical barriers to regaining full muscle function. Within the localized injury area, FTY720 treated animals present a distinct vascular network among regenerating fibers compared to the smaller, immature vessels displayed by control groups at 14 days post injury (**Figure 7**). In evaluating the ability of FTY720 to regenerate damaged neuromuscular junctions, we found that treated animals exhibit greater $Thy1^+$ axonal density than untreated animals. Most importantly, these pre-synaptic junctions are spatially associated with morphologically maturing post-synaptic acetylcholine receptors, indicating ongoing regeneration of the motor neural network just 28 days after critical injury which is not observed in the untreated control (**Figure 8**). While FTY720's impact in resolving chronic inflammation and promoting MuSC differentiation likely paves the way for successful reinnervation to occur, FTY720 may also act

directly on neuromuscular junctions, as previous work has linked FTY720 to directly regulating synaptic function (Darios et al., 2017). While the qualitative assessment of FTY720-induced revascularization and reinnervation of injured muscle is promising, the lack of quantitative analysis remains a limitation of this work, and further studies are necessary to characterize these regenerative outcomes more thoroughly. Further, determining whether improved revascularization and reinnervation mediated by S1PR modulation can translate to greater contractile forces generated by regenerating muscle is an exciting future direction for ensuring successful functional outcomes.

Taken together, our work demonstrates the ability of utilizing biomaterial-mediated delivery of FTY720 to locally modulate the overwhelming and dysregulated immune response characterizing critical volumetric muscle injuries. We show that S1P receptor modulation results in increased pro-regenerative immune cell infiltration into the defect area in the early phases of the inflammatory cascade with simultaneous increases in activated MuSCs vital to regeneration of muscle fibers. By harnessing the capabilities of multiparameter pseudotime technologies, we are able to detect subtle cellular phenotype transitions mediated by therapeutic perturbations that are crucial to priming the injury milieu for enhanced regeneration. Therefore, as the identification and targeting of specific cellular players is critical to developing successful immunotherapies, this S1PR modulating strategy provides a platform for targeting distinct cellular responses with small molecule therapeutics that can be applied to a wide range of injuries and diseases.

MATERIALS AND METHODS

Nanofiber Scaffold Fabrication

Electrospun nanofiber scaffolds were fabricated as previously described (Das et al., 2013). PCL (Sigma) and PLGA were combined in a 1:1 weight/weight ratio at 18% polymer concentration for blank fibers and 20% polymer concentration for FTY720 (Cayman Chemical, crystalline solid formulation) loaded fibers. Polymers were dissolved in a 1:3 volume ratio solution of methanol to chloroform and vortexed for 2+ hour prior to spinning. For FTY720 loaded fibers, FTY720 was weighed out and directly added to the polymer solution at a 1:200 drug: polymer weight ratio. Two mL of either polymer solution was loaded into a 3 mL syringe with diameter of 10 mm. Electrospinning was performed at an applied voltage of 19 kV, and flow rate of 1 mL/h for both blank and FTY720 fibers. Working distance was set at 10 cm for blank fibers and 12 cm for FTY720 fibers. After 2 mL of polymer was spun, fibers were wrapped in low-binding plastic folders and stored at −20°C.

Drug Release From Nanofiber Scaffolds

Circular biopsy punches were used to punch out 3 mm discs from electrospun nanofiber sheets. Discs were placed in 100 μL of stimulated body fluid containing 4% fatty acid-free bovine serum albumin. Releasate was collected at the defined timepoints and replaced with fresh release medium.

Mass Spectrometry Quantification of FTY720 Release Samples

Fingolimod was extracted from release samples using a long chain base sphingolipid extraction protocol (Ogle et al., 2014). 100 μL of release media was placed in glass culture tubes with screw caps (tubes: Kimble-Chase 73750-13100, caps: Kimble-Chase 73802-13415) and 50 μL of phosphate buffered saline was added to bring total sample volume to 150 μL. 1.5 mL of 2:1 methanol to dichloromethane (by volume) extraction solvent was added to each tube. 50 picomoles of C17 sphingosine was added to each tube to serve as an internal standard. Tubes were capped, sonicated for 1 min, vortexed briefly, and incubated overnight at 48°C. The following day, tubes were allowed to cool to room temperature. Potassium hydroxide (150 μL of 1N) was added to each tube, sonicated for 1 min, vortexed briefly, and tubes were incubated at 37°C for 2 h. Samples were allowed to cool to room temperature, and 8 μL of glacial acetic acid was added to each tube before being sonicated for 1 min, and vortexed briefly. Each sample was checked to ensure a neutral (7.0) pH. Samples were centrifuged at 3000 rpm and supernatant collected in separate open top glass tubes. Extraction solvent (0.5 mL) was added to each original sample tube, and samples were sonicated for 1 min and vortexed briefly before being centrifuged again at 3000 rpm. The second supernatant was collected and added to first supernatant. Extraction solvent was evaporated off overnight by a vacuum concentrator (SpeedVac). The next day, 300 μL of mass spectrometry analysis solvent was added to each tube before being sonicated for 2 min. Samples were transferred to microcentrifuge tubes and centrifuged at 18,000 × *g* for 10 min. Supernatant (200 μL) was transferred to mass spectrometry sample vials. Samples were analyzed on a Micromass Quattro LC mass spectrometer.

Force Mapping of S1PR Modulating Nanofibers With AFM

All AFM measurements were performed with a MFP-3D Bio-AFM (Asylum Research, Santa Barbara, CA, United States). Nanofiber scaffolds were prepared as described and fixed on glass slides with double-sided tape. For stiffness measurements, 9.6 μm spherical PMMA particles (modulus ∼3 GPa) were attached to tipless silicon cantilevers (NSC35-C, Mikromasch, Sofia, Bulgaria) using a two-part epoxy and dried for at least 24 h. We use the thermal equipartition method (Hutter and Bechhoefer, 1993) to calibrate the cantilever spring constant immediately prior to use by indenting a glass substrate and performing a Lorentzian fit to the thermal spectrum. Topological images and accompanying stiffness characterizations of nanofibers were obtained from regions of 80 × 80 μm^2 force maps with 96 × 96 force curves per image. All the force-distance measurements were performed with 2 μm/sec approach velocity using a 500 nN force trigger. Force-distance plots were transformed into force-indentation depth plots and then 10–100% indentation depth was used to evaluate Young's modulus using a Hertzian contact model.

SEM of Nanofibers

Nanofiber scaffolds were sputter coated with gold for 30 sec and imaged on a Hitachi SU8010 Scanning Electron Microscope.

Spinotrapezius Volumetric Muscle Loss Surgery and Nanofiber Scaffold Implantation

All animal procedures were conducted according to protocols approved by Georgia Institute of Technology Institutional Animal Care and Use Committee. Male C57BL/6J (The Jackson Laboratory) of age 8–12 weeks old were used for all animal studies with the exception of neuromuscular regeneration assessment for which B6.Cg-Tg (Thy1-YFP)16Jrs/J (Jackson Laboratories #003709) mice were used. A 2 mm-diameter full thickness defect in the spinotrapezius muscle was created as previously described (San Emeterio et al., 2017). Briefly, a longitudinal 1-inch incision as made just after the bony prominence of the shoulder blade. The overlying fascia was dissected away and the spinotrapezius muscle was identified. The edge of the spinotrapezius was reflected and positioned against a sterile piece of wood and a 2 mm biopsy punch was made through the muscle. A 3 mm-diameter nanofiber scaffold implant was placed over the defect and sutured at the top to the muscle with a 10-0 suture. The skin incision was closed with wound clips.

Tissue Harvest and Flow Cytometry

To collect blood and tissue for flow cytometry analysis, mice were euthanized via CO_2 asphyxiation. Blood was then collected via cardiac puncture. Red blood cells were lysed in ammonium chloride (1-part blood, 9-parts ammonium chloride) prior to immunostaining for flow cytometry. For analysis of cell composition in spinotrapezius muscles, a 6 mm biopsy punch of muscle tissue centered on the defect was taken and weighed and then digested with 5,500 U/ml collagenase II and 2.5 U/ml Dispase II for 1.5 h in a shaking 37°C water bath. The digested muscles were filtered through a cell strainer to obtain a single cell suspension. Single-cell suspensions were stained for live cells using either Zombie Green or Zombie NIR (BioLegend) dyes in cell-culture grade PBS per manufacturer instructions. Cells were then stained with cell phenotyping antibodies in a 1:1 volume ratio of 3% FBS and Brilliant Stain Buffer (BD Biosciences) according to standard procedures and analyzed on a FACS Aria III flow cytometer (BD Biosciences). The following antibodies were used for cell phenotyping: BV605-conjugated anti-CD4 (BioLegend), BV785-conjugated anti-CD8 (BioLegend), PE-Cy7-conjugated CD3ε (BioLegend), PE-conjugated anti-CD115 (BioLegend), PerCP-Cy5.5-conjugated anti-CD115 (BioLegend), PE-conjugated anti-CD25, FITC-conjugated anti-FoxP3 (eBioscience), BV510-conjugated anti-CD11b (BioLegend), BV421-conjugated anti-CD11b (BioLegend), APC conjugated anti-Ly6C (BioLegend), BV711-conjugated anti-CD64 (BioLegend), PE-conjugated anti-MerTK (BioLegend), APC-Cy7-conjugated anti-Ly6G (BioLegend), PE-Cy7 conjugated anti-CD206 (BioLegend), FITC-conjugated anti-CD206 (BioLegend), PE-Cy5 conjugated anti-CD29 (BioLegend), PerCP-Cy5.5-conjugated anti-CXCR4 (BioLegend), and APC-conjugated Lineage antibody cocktail containing antibodies for mouse CD3e, CD11b, CD45R/B220, Ly-76, Ly6G, and Ly6C (BD Pharmingen). Additionally, 30 μL of AccuCheck Counting Beads (Invitrogen) were added per sample for absolute quantification of cell populations. Single, live cells were selected in FlowJo software for subsequent analysis. Myeloid cells were gated as $CD11b^+$ and lymphoid cells as $CD3^+$ cells. Unless indicated otherwise, macrophages were gated as $CD11b^+CD64^+MerTK^+$ cells, where M1-like macrophages were further characterized by their $CD206^{lo}Ly6C^{hi}$ signature and M2-like macrophages were characterized with a $CD206^{hi}Ly6C^{lo}$ protein signature. Monocytes were gated as $CD11b^+CD64^+MerTK^-$ cells, with inflammatory monocytes defined as $Ly6C^{hi}$ monocytes and anti-inflammatory as $Ly6C^{lo}$ monocytes. $CD3^+$ T cells were gated as $CD4^+$ or $CD8^+$ T cells based on their high expression of CD4 and CD8, respectively. MuSCs were gated as Lineage negative (Lin^-) $CD29^+$ $CXCR4^+$ cells.

High Dimensional Analysis of Flow Cytometry Data

Uniform Manifold Approximation and Projection (UMAP)

Uniform manifold approximation and projection is a non-linear dimensionality reduction algorithm. UMAP is able to embed high-dimensional data into a space of two or three dimensions, and cells are visualized in a scatter plot, where similarity is demonstrated via proximity to other points (Becht et al., 2018). Prior to UMAP dimensional reduction, we pre-gated each flow cytometry sample to select cellular subsets of interest and then imported into Python 3.7 using fcsparser[1] and Pandas 2.5. Each was normalized by applying arcsinh/150, and UMAP parameters of n_neighbors = 15 and min_dist = 0.1 were applied for compliance with UMAP assumptions. A composite UMAP projection that utilized data points from all desired samples was generated using Matplotlib. Each cell was then phenotyped by overlaying the pre-gated cell subset onto the UMAP projection[2].

Spanning-Tree Progression Analysis of Density-Normalized Events (SPADE)

Spanning tree progression of density normalized events is a visualization tool creating a 2D minimum spanning tree organized into nodes representing clusters of cells similar in their surface marker expressions. The size and color of each node are relative to the number of cells present and the median marker expression (Qiu et al., 2011). SPADE was performed through MATLAB and the source code is available at http://pengqiu.gatech.edu/software/SPADE/. MATLAB-based SPADE automatically generates the tree by performing density-dependent down-sampling, agglomerative clustering, linking clusters with a minimum spanning-tree algorithm and up-sampling based on user input. The SPADE tree was generated by exporting select pre-gated cellular subsets. The following SPADE parameters were used: Apply compensation matrix in FCS

[1]https://github.com/eyurtsev/fcsparser

[2]https://github.com/lmcinnes/umap

header, Arcsinh transformation with cofactor 150, neighborhood size 5, local density approximation factor 1.5, max allowable cells in pooled downsampled data 50000, target density 20000 cells remaining. Number of desired clusters ranged from 60 to 70.

Whole Mount Immunofluorescence of Spinotrapezius Tissues

Mice were euthanized 14 or 28 days after surgery via CO_2 asphyxiation. Post-euthanasia, mouse vasculature was perfused with warm saline followed by 4% PFA until tissues were fixed. The entire spinotrapezius muscle was explanted and permeabilized overnight with 0.2% saponin, then blocked overnight in 10% mouse serum. For immunofluorescence, tissues were incubated at 4°C overnight in a solution containing 0.1% saponin, 5% mouse serum, 0.5% bovine serum albumin, and the following conjugated fluorescent antibodies: Alexa Fluor 488 or Alexa Fluor 650 anti-desmin (1:200 dilution, Abcam), Alexa Fluor 594 anti-CD31 (1:100 dilution, BioLegend), Alexa Fluor 650 anti-CD68 (1:200 dilution, Bio-Rad), Alexa Fluor 488 anti-GFP tag (1:200 dilution, BioLegend), rhodamine alpha-bungarotoxin (1:200 dilution, Life Technologies). Following immunostaining, tissues were washed four times for 30 min each in 0.2% saponin for the first two washes, 0.1% saponin for the third wash, and PBS for the final wash, and then mounted in 50/50 glycerol/PBS.

Imaging and Quantification of Whole-Mount Immunofluorescence

Three-dimensional, tiled scans of whole-mount spinotrapezius muscles were performed on a Zeiss LSM 710 confocal microscope. Immunofluorescence imaging parameters were kept similar across all samples, with adjustments made only to keep image quality similar. Full-thickness Z-stacks (2 μm step size) were collected across the entire x-y plane analyzed. Max intensity projections were generated from 3D confocal images for 2D analysis in Zen software (Zeiss). Second harmonic generated signal was collected via 40× objective using a Chameleon laser to excite tissues at 790 nm and signal collected over 380–420 nm with acquisition parameters kept identical across animals. Desmin, CD68, and SHG signal from 3D z-stacks were rendered in Imaris as surfaces. For desmin surfaces the following parameters were used: auto-smoothing, thresholding set to 14 units, surfaces selected by eye. For SHG surfaces, the following parameters were used: no smoothing, auto-threshold set, all surfaces selected. $CD68^+$ surfaces were identified by smoothing with a 1.5 μm grain size and an automatic threshold on absolute intensity. Touching objects were split using a seed points diameter of 13.8 μm. Muscle fiber and collagen alignment (**Figure 6**) were analyzed using a home-built 2 photon imaging system as described previously (Forouhesh Tehrani et al., 2020; Pendleton et al., 2020). In brief, SHG images (512 × 512 pixels) of collagen and actin muscle structure were produced with linearly polarized excitation rotated at 10° intervals. The SHG signal was normalized and averaged over 20 frames, then color-coded based on the maximum intensity angle of each pixel. Each color serves to represent the dominant orientation of the underlying SHG sensitive structures (e.g., actin/myosin bands and collagen). We captured simultaneous 2 photon fluorescence images of sarcomere structure using Alexa Fluor 488 anti-desmin. The orientation in relation to the direction of the muscle was quantified in four images from each treatment group. Quantification of collagen deposition was performed in ImageJ software. Quantification of 2-dimensional fiber diameter was performed by measuring the widest portion of each regenerated muscle fiber (determined based on the morphology of desmin-positive regions) within the defect region from the day 14 2D maximum intensity projections in Zen software. To quantify fiber alignment, a parallel grid was overlaid on the 2D maximum intensity projection of desmin, following the axis of uninjured fibers. The angle between regenerated fibers (determined based on morphology of desmin positive regions) and the parallel lines in the grid was measured in FIJI. All angles were measured to be between 0 and 90°.

SPADE Node Heatmap

Spanning tree progression of density normalized events dendrogram heatmaps were constructed with calculated z-scores of fluorescence marker expression intensities for each surface marker used to immunophenotype a specific cell type across all nodes occupied by the cell type. Each row of the heatmap corresponds to a specific surface marker while each column represents an individual annotated SPADE node for a specified cellular subset.

Statistical Analysis

All statistical analysis was performed in GraphPad Prism software. Data presented as mean ± standard error of the mean (S.E.M.) unless otherwise indicated. For pairwise comparisons, unpaired *t*-test (according to experimental design) with Welch's correction if variance was significantly different was used. For grouped analyses, one-way ANOVA with Tukey's post-test was used for multiple comparisons. Unless otherwise noted, $p < 0.05$ was considered statistically significant.

DATA AVAILABILITY STATEMENT

The original contributions presented in the study are included in the article/**Supplementary Material**, further inquiries can be directed to the corresponding author/s.

ETHICS STATEMENT

The animal study was reviewed and approved by Georgia Institute of Technology Institutional Animal Care and Use Committee.

AUTHOR CONTRIBUTIONS

CS, LH, TS, GW, LM, PQ, YJ, NW, and EB designed the research, analyzed the data, and wrote the manuscript. CS, LH, and TT performed the research and wrote the manuscript. CS, LH, TT,

MO, EP, WY, CO, AL, and HL performed research, analyzed the data, and reviewed the manuscript. All authors contributed to the article and approved the submitted version.

FUNDING

This material is based upon work supported by the National Science Foundation Graduate Research Fellowship under Grant Nos. DGE-1650044 and DGE-1148903 as well as by the NIH under award numbers R01AR071708 and R56DE029703, the NIH Cell and Tissue Engineering Training grant under award number GM008433, and the American Heart Association Grant 15PRE25090024.

ACKNOWLEDGMENTS

We thank the core facilities at the Parker H. Petit Institute for Bioengineering and Bioscience at the Georgia Institute of Technology for the use of their shared equipment, services, and expertise.

SUPPLEMENTARY MATERIAL

The Supplementary Material for this article can be found online at: https://www.frontiersin.org/articles/10.3389/fbioe.2021.650289/full#supplementary-material

REFERENCES

Aguilar, C. A., Greising, S. M., Watts, A., Goldman, S. M., Peragallo, C., Zook, C., et al. (2018). Multiscale analysis of a regenerative therapy for treatment of volumetric muscle loss injury. *Cell Death Discov.* 4:33.

Anthony, R. M., Rutitzky, L. I., Urban, J. F., Stadecker, M. J., and Gause, W. C. (2007). Protective immune mechanisms in helminth infection. *Nat. Rev. Immunol.* 7, 975–987. doi: 10.1038/nri2199

Arnold, L., Henry, A., Poron, F., Baba-Amer, Y., van Rooijen, N., Plonquet, A., et al. (2007). Inflammatory monocytes recruited after skeletal muscle injury switch into antiinflammatory macrophages to support myogenesis. *J. Exp. Med.* 204, 1057–1069. doi: 10.1084/jem.20070075

Awojoodu, A. O., Ogle, M. E., Sefcik, L. S., Bowers, D. T., Martin, K., Brayman, K. L., et al. (2013). Sphingosine 1-phosphate receptor 3 regulates recruitment of anti-inflammatory monocytes to microvessels during implant arteriogenesis. *Proc. Natl. Acad. Sci. U.S.A.* 110, 13785–13790. doi: 10.1073/pnas.1221309110

Baeyens, A. A. L., and Schwab, S. R. (2020). Finding a way out: S1P signaling and immune cell migration. *Annu. Rev. Immunol.* 38, 759–784. doi: 10.1146/annurev-immunol-081519-083952

Becht, E., McInnes, L., Healy, J., Dutertre, C. A., Kwok, I. W. H., Ng, L. G., et al. (2018). Dimensionality reduction for visualizing single-cell data using UMAP. *Nat. Biotechnol.* 37, 38–44. doi: 10.1038/nbt.4314

Beth, E., and Pollot, B. T. C. (2016). *Volumetric Muscle Loss*. New York, NY: Springer.

Blaho, V. A., and Hla, T. (2014). An update on the biology of sphingosine 1-phosphate receptors. *J. Lipid Res.* 55, 1596–1608. doi: 10.1194/jlr.r046300

Borselli, C., Storrie, H., Benesch-Lee, F., Shvartsman, D., Cezar, C., Lichtman, J. W., et al. (2010). Functional muscle regeneration with combined delivery of angiogenesis and myogenesis factors. *Proc. Natl. Acad. Sci. U.S.A.* 107, 3287–3292. doi: 10.1073/pnas.0903875106

Cartier, A., and Hla, T. (2019). Sphingosine 1-phosphate: lipid signaling in pathology and therapy. *Science* 366:eaar5551. doi: 10.1126/science.aar5551

Chazaud, B. (2020). Inflammation and skeletal muscle regeneration: leave it to the macrophages! *Trends Immunol.* 41, 481–492. doi: 10.1016/j.it.2020.04.006

Darios, F. D., Jorgacevski, J., Flasker, A., Zorec, R., Garcia-Martinez, V., Villanueva, J., et al. (2017). Sphingomimetic multiple sclerosis drug FTY720 activates vesicular synaptobrevin and augments neuroendocrine secretion. *Sci. Rep.* 7:5958.

Das, A., Segar, C. E., Hughley, B. B., Bowers, D. T., and Botchwey, E. A. (2013). The promotion of mandibular defect healing by the targeting of S1P receptors and the recruitment of alternatively activated macrophages. *Biomaterials* 34, 9853–9862. doi: 10.1016/j.biomaterials.2013.08.015

Das, A., Tanner, S., Barker, D. A., Green, D., and Botchwey, E. A. (2014). Delivery of S1P receptor-targeted drugs via biodegradable polymer scaffolds enhances bone regeneration in a critical size cranial defect. *J. Biomed. Mater. Res. A* 102, 1210–1218. doi: 10.1002/jbm.a.34779

Donati, C., Cencetti, F., and Bruni, P. (2013). Sphingosine 1-phosphate axis: a new leader actor in skeletal muscle biology. *Front. Physiol.* 4:338. doi: 10.3389/fphys.2013.00338

Dziki, J. L., Sicari, B. M., Wolf, M. T., Cramer, M. C., and Badylak, S. F. (2016). Immunomodulation and mobilization of progenitor cells by extracellular matrix bioscaffolds for volumetric muscle loss treatment. *Tissue Eng. Part A* 22, 1129–1139. doi: 10.1089/ten.tea.2016.0340

Forouhesh Tehrani, K., Pendleton, E. G., Southern, W. M., Call, J. A., and Mortensen, L. J. (2020). Spatial frequency metrics for analysis of microscopic images of musculoskeletal tissues. *Connect. Tissue Res.* 62, 4–14. doi: 10.1080/03008207.2020.1828381

Garg, K., Corona, B. T., and Walters, T. J. (2015). Therapeutic strategies for preventing skeletal muscle fibrosis after injury. *Front. Pharmacol.* 6:87. doi: 10.3389/fphar.2015.00087

Geissmann, F., Jung, S., and Littman, D. R. (2003). Blood monocytes consist of two principal subsets with distinct migratory properties. *Immunity* 19, 71–82. doi: 10.1016/s1074-7613(03)00174-2

Grogan, B. F., Hsu, J. R., and Consortium, S. T. R. (2011). Volumetric muscle loss. *J. Am. Acad. Orthop. Surg.* 19, S35–S37.

Hutter, J. L., and Bechhoefer, J. (1993). Calibration of atomic-force microscope tips. *Rev. Sci. Instrum.* 64, 1868–1873. doi: 10.1063/1.1143970

Hymel, L. A., Ogle, M. E., Anderson, S. E., San Emeterio, C. L., Turner, T. C., York, W. Y., et al. (2020). Modulating local S1P receptor signaling as a regenerative immunotherapy after volumetric muscle loss injury. *J. Biomed. Mater. Res. A* 109, 695–712. doi: 10.1002/jbm.a.37053

Juban, G., and Chazaud, B. (2017). Metabolic regulation of macrophages during tissue repair: insights from skeletal muscle regeneration. *FEBS Lett.* 591, 3007–3021. doi: 10.1002/1873-3468.12703

Kappos, L., Antel, J., Comi, G., Montalban, X., O'Connor, P., Polman, C. H., et al. (2006). Oral fingolimod (FTY720) for relapsing multiple sclerosis. *N. Engl. J. Med.* 355, 1124–1140.

Knipper, J. A., Willenborg, S., Brinckmann, J., Bloch, W., Maass, T., Wagener, R., et al. (2015). Interleukin-4 receptor alpha signaling in myeloid cells controls collagen fibril assembly in skin repair. *Immunity* 43, 803–816. doi: 10.1016/j.immuni.2015.09.005

Larouche, J., Greising, S. M., Corona, B. T., and Aguilar, C. A. (2018). Robust inflammatory and fibrotic signaling following volumetric muscle loss: a barrier to muscle regeneration. *Cell Death Dis.* 9:409.

Latroche, C., Weiss-Gayet, M., Muller, L., Gitiaux, C., Leblanc, P., Liot, S., et al. (2017). Coupling between myogenesis and angiogenesis during skeletal muscle regeneration is stimulated by restorative macrophages. *Stem Cell Rep.* 9, 2018–2033. doi: 10.1016/j.stemcr.2017.10.027

Lemos, D. R., Babaeijandaghi, F., Low, M., Chang, C. K., Lee, S. T., Fiore, D., et al. (2015). Nilotinib reduces muscle fibrosis in chronic muscle injury by promoting TNF-mediated apoptosis of fibro/adipogenic progenitors. *Nat. Med.* 21, 786–794. doi: 10.1038/nm.3869

Liao, I. C., Liu, J. B., Bursac, N., and Leong, K. W. (2008). Effect of electromechanical stimulation on the maturation of myotubes on aligned electrospun fibers. *Cell. Mol. Bioeng.* 1, 133–145. doi: 10.1007/s12195-008-0021-y

Maceyka, M., Harikumar, K. B., Milstien, S., and Spiegel, S. (2012). Sphingosine-1-phosphate signaling and its role in disease. *Trends Cell Biol.* 22, 50–60. doi: 10.1016/j.tcb.2011.09.003

Ogle, M. E., Sefcik, L. S., Awojoodu, A. O., Chiappa, N. F., Lynch, K., Peirce-Cottler, S., et al. (2014). Engineering in vivo gradients of sphingosine-1-phosphate receptor ligands for localized microvascular remodeling and inflammatory cell positioning. *Acta Biomater.* 10, 4704–4714. doi: 10.1016/j.actbio.2014.08.007

Olingy, C. E., Emeterio, C. L., Ogle, M. E., Krieger, J. R., Bruce, A. C., Pfau, D. D., et al. (2017). Non-classical monocytes are biased progenitors of wound healing macrophages during soft tissue injury. *Sci. Rep.* 7:447.

Pendleton, E. G., Tehrani, K. F., Barrow, R. P., and Mortensen, L. J. (2020). Second harmonic generation characterization of collagen in whole bone. *Biomed. Opt. Express* 11, 4379–4396. doi: 10.1364/boe.391866

Qazi, T. H., Mooney, D. J., Pumberger, M., Geissler, S., and Duda, G. N. (2015). Biomaterials based strategies for skeletal muscle tissue engineering: existing technologies and future trends. *Biomaterials* 53, 502–521. doi: 10.1016/j.biomaterials.2015.02.110

Qiu, P., Simonds, E. F., Bendall, S. C., Gibbs, K. D. Jr., Bruggner, R. V., Linderman, M. D., et al. (2011). Extracting a cellular hierarchy from high-dimensional cytometry data with SPADE. *Nat. Biotechnol.* 29, 886–891. doi: 10.1038/nbt.1991

Rivera, J., Proia, R. L., and Olivera, A. (2008). The alliance of sphingosine-1-phosphate and its receptors in immunity. *Nat. Rev. Immunol.* 8, 753–763. doi: 10.1038/nri2400

Saclier, M., Yacoub-Youssef, H., Mackey, A. L., Arnold, L., Ardjoune, H., Magnan, M., et al. (2013). Differentially activated macrophages orchestrate myogenic precursor cell fate during human skeletal muscle regeneration. *Stem Cells* 31, 384–396. doi: 10.1002/stem.1288

Sakar, M. S., Eyckmans, J., Pieters, R., Eberli, D., Nelson, B. J., and Chen, C. S. (2016). Cellular forces and matrix assembly coordinate fibrous tissue repair. *Nat. Commun.* 7:11036.

San Emeterio, C. L., Olingy, C. E., Chu, Y., and Botchwey, E. A. (2017). Selective recruitment of non-classical monocytes promotes skeletal muscle repair. *Biomaterials* 117, 32–43. doi: 10.1016/j.biomaterials.2016.11.021

Schoenborn, J. R., and Wilson, C. B. (2007). Regulation of interferon−γ during innate and adaptive immune responses. *Adv. Immunol.* 96, 41–101. doi: 10.1016/S0065-2776(07)96002-2

Spiller, K. L., Wrona, E. A., Romero-Torres, S., Pallotta, I., Graney, P. L., Witherel, C. E., et al. (2016). Differential gene expression in human, murine, and cell line-derived macrophages upon polarization. *Exp. Cell Res.* 347, 1–13. doi: 10.1016/j.yexcr.2015.10.017

Tonkin, J., Temmerman, L., Sampson, R. D., Gallego-Colon, E., Barberi, L., Bilbao, D., et al. (2015). Monocyte/Macrophage-derived IGF-1 orchestrates murine skeletal muscle regeneration and modulates autocrine polarization. *Mol. Ther.* 23, 1189–1200. doi: 10.1038/mt.2015.66

Trapnell, C., Cacchiarelli, D., Grimsby, J., Pokharel, P., Li, S., Morse, M., et al. (2014). The dynamics and regulators of cell fate decisions are revealed by pseudotemporal ordering of single cells. *Nat. Biotechnol.* 32, 381–386. doi: 10.1038/nbt.2859

Weigert, A., Olesch, C., and Brune, B. (2019). Sphingosine-1-phosphate and macrophage biology-how the sphinx tames the big eater. *Front. Immunol.* 10:1706. doi: 10.3389/fimmu.2019.01706

Wosczyna, M. N., and Rando, T. A. (2018). A muscle stem cell support group: coordinated cellular responses in muscle regeneration. *Dev. Cell* 46, 135–143. doi: 10.1016/j.devcel.2018.06.018

Conflict of Interest: The authors declare that the research was conducted in the absence of any commercial or financial relationships that could be construed as a potential conflict of interest.

frontiers in Bioengineering and Biotechnology

ORIGINAL RESEARCH
published: 27 April 2021
doi: 10.3389/fbioe.2021.652055

Electrospun Polydioxanone Loaded With Chloroquine Modulates Template-Induced NET Release and Inflammatory Responses From Human Neutrophils

*Allison E. Fetz, Shannon E. Wallace and Gary L. Bowlin**

Department of Biomedical Engineering, University of Memphis, Memphis, TN, United States

OPEN ACCESS

Edited by:
Ryang Hwa Lee,
Texas A&M University, United States

Reviewed by:
Yves Bayon,
A Medtronic Company, France
Masoud Mozafari,
University of Toronto, Canada
Judite Barbosa,
University of Porto, Portugal

***Correspondence:**
Gary L. Bowlin
glbowlin@memphis.edu

Specialty section:
This article was submitted to Tissue Engineering and Regenerative Medicine, a section of the journal Frontiers in Bioengineering and Biotechnology

Received: *11 January 2021*
Accepted: *19 March 2021*
Published: *27 April 2021*

Citation:
Fetz AE, Wallace SE and Bowlin GL (2021) Electrospun Polydioxanone Loaded With Chloroquine Modulates Template-Induced NET Release and Inflammatory Responses From Human Neutrophils. Front. Bioeng. Biotechnol. 9:652055. doi: 10.3389/fbioe.2021.652055

The implantation of a biomaterial quickly initiates a tissue repair program initially characterized by a neutrophil influx. During the acute inflammatory response, neutrophils release neutrophil extracellular traps (NETs) and secrete soluble signals to modulate the tissue environment. In this work, we evaluated chloroquine diphosphate, an antimalarial with immunomodulatory and antithrombotic effects, as an electrospun biomaterial additive to regulate neutrophil-mediated inflammation. Electrospinning of polydioxanone was optimized for rapid chloroquine elution within 1 h, and acute neutrophil-biomaterial interactions were evaluated *in vitro* with fresh human peripheral blood neutrophils at 3 and 6 h before quantifying the release of NETs and secretion of inflammatory and regenerative factors. Our results indicate that chloroquine suppresses NET release in a biomaterial surface area–dependent manner at the early time point, whereas it modulates signal secretion at both early and late time points. More specifically, chloroquine elution down-regulates interleukin 8 (IL-8) and matrix metalloproteinase nine secretion while up-regulating hepatocyte growth factor, vascular endothelial growth factor A, and IL-22 secretion, suggesting a potential shift toward a resolving neutrophil phenotype. Our novel repurposing of chloroquine as a biomaterial additive may therefore have synergistic, immunomodulatory effects that are advantageous for biomaterial-guided *in situ* tissue regeneration applications.

Keywords: tissue regeneration, electrospinning, tissue engineering, neutrophils, neutrophil extracellular traps, NETs, chloroquine

INTRODUCTION

Biomaterial-guided *in situ* tissue regeneration utilizes a tissue engineering approach to guide the regeneration of diseased, damaged, or missing tissues (Li et al., 2015). However, compared to exogenous delivery in traditional tissue engineering, *in situ* tissue regeneration relies on the body's endogenous cells and signals to drive the repair and regeneration processes. Electrospun biomaterials have great potential for guiding *in situ* tissue regeneration because their extracellular

matrix (ECM)–mimicking fibers can be fabricated from a variety of biocompatible polymers and modified to suit tissue-specific applications (Lannutti et al., 2007; Kelleher and Vacanti, 2010). Additionally, fabrication of electrospun biomaterials is relatively simple, cost-effective, and easy to scale up for mass production. As such, electrospun templates are an excellent platform for developing biomaterials that guide *in situ* tissue regeneration with the potential for a far-reaching clinical impact.

Independent of location, the implantation of a biomaterial quickly initiates a tissue repair program to restore homeostasis that is initially characterized by an influx of neutrophils (Anderson et al., 2008; Chen and Nuñez, 2010). During the acute inflammatory response, neutrophils condition the microenvironment through multiple mechanisms before recruiting additional immune cells in the tissue repair program. Two of their most significant effector functions include the extrusion of neutrophil extracellular traps (NETs) and the secretion of soluble signals (Brinkmann et al., 2004; Lacy, 2006; Selders et al., 2017). Together, these mechanisms shape the microenvironment for resolution and healing or further perturbations of homeostasis.

NETs are composed of DNA that is complexed with antibacterial neutrophil-derived proteins, including histones, neutrophil elastase, and myeloperoxidase (MPO) (Brinkmann et al., 2004). They are released in response to bacterial signals for the purpose of killing pathogens and are also released in response to inflammatory mediators, such as interleukin 8 (IL-8) and tissue necrosis factor α (TNF-α), activated endothelial cells, and platelets (Gupta et al., 2005, 2010; Clark et al., 2007; Neeli et al., 2008). While they are indispensable for preventing pathogen dissemination, the dysregulated release of NETs is associated with aberrant effects in sterile inflammation due to the localization of noxious cargo that can damage host cells (Gupta et al., 2010; Kaplan and Radic, 2012; Chrysanthopoulou et al., 2014; Gregory et al., 2015). Of particular interest to tissue engineers is the ability of NETs to initiate thrombosis and fibrosis, both of which can be detrimental to functional tissue regeneration (Maugeri et al., 2006; Fuchs et al., 2010; Martinod et al., 2013; Chrysanthopoulou et al., 2014; Gregory et al., 2015; Riehl et al., 2016). In fact, our group has previously shown that NETs are released in response to the surface area–dependent, topographical cues of electrospun polydioxanone (PDO) biomaterials, functioning as a preconditioning event in the tissue repair program (Fetz et al., 2017).

Similar to the release of NETs, neutrophil degranulation and the secretion of soluble signals are meant to neutralize pathogens and initiate the tissue repair program, but they can become dysregulated, leading to tissue damage (Lacy, 2006; Selders et al., 2017). The combination of neutrophil recruitment and tissue damage is typically attributed to the release of proteinases that break down the ECM, such as matrix metalloproteinase 9 (MMP-9), and the release of proinflammatory chemotactic factors, such as IL-8 (Harada et al., 1994; Nagaoka and Hirota, 2000; Martinez et al., 2004; Rayment et al., 2008; Liu et al., 2009). With continual neutrophil recruitment and degranulation, the acute response can develop into a nonresolving, chronic response through a perpetual cycle of recruitment and activation (Martinez et al., 2004; Rayment et al., 2008). Despite these potential deleterious outcomes, neutrophil degranulation and the secretion of signaling molecules have also been shown to be tissue-restorative and proangiogenic (Ardi et al., 2007; Deryugina et al., 2014; Phillipson and Kubes, 2019). Neutrophils secrete vascular endothelial growth factor A (VEGF-A) and hepatocyte growth factor (HGF), both of which support and guide angiogenesis (Taichman et al., 1997; McCourt et al., 2001). Moreover, MMP-9 is also proangiogenic and has been shown to initiate and guide endothelial cell sprouting (Ardi et al., 2007; Christoffersson et al., 2012). Taken together, these data suggest that regulating neutrophil NET release and their secretion of signaling molecules at the onset of the tissue repair program is pertinent for regulating acute neutrophil-driven inflammation (Jhunjhunwala et al., 2015; Herath et al., 2017; Lin et al., 2017; Fetz et al., 2020).

In this work, we evaluated chloroquine diphosphate as an electrospun biomaterial additive to regulate *in vitro* NET release and the secretion of proinflammatory and prohealing mediators from human neutrophils. Chloroquine is a Food and Drug Administration–approved, antimalarial drug that has more recently been investigated as an immunomodulatory and antithrombotic drug for treating rheumatoid arthritis, systemic lupus erythematosus, and cancer (Wozniacka et al., 2006; Manic et al., 2014; Schrezenmeier and Dörner, 2020; Roldan et al., 2020). Furthermore, chloroquine has been shown to inhibit NET formation, indicating its potential benefit as an additive for regulating biomaterial-induced NET release and inflammation (Smith et al., 2014; Boone et al., 2015, 2018; Murthy et al., 2019). Here, we show that electrospun PDO biomaterials loaded with chloroquine modulate template-induced NET release and the inflammatory response from human neutrophils. We found that chloroquine suppresses NET release in a surface area–dependent manner at early time points while modulating proinflammatory and healing signals at both early and late time points. Ultimately, our findings demonstrate a novel repurposing of chloroquine as a template additive for *in situ* tissue engineering that modulates the *in vitro* acute inflammatory response to biomaterials.

MATERIALS AND METHODS

Biomaterial Fabrication

PDO (cat. no. 6100, Bezwada Biomedical, Hillsborough, NJ, United States) was dissolved overnight in 1,1,1,3,3,3-hexafluoro-2-propanol (cat. no. 003409-1KG, Oakwood Chemical, Estill, SC, United States) at varying concentrations (**Table 1**) to generate biomaterials composed of small and large fibers, previously shown to regulate NET release through their surface area–dependent, topographical cues (Fetz et al., 2017, 2018). Chloroquine diphosphate (cat. no. 0219391910, MP Biomedicals, Solon, OH, United States) was added to the solutions at a concentration of 0.07 mg/mL and dissolved for 1.5 h with gentle agitation before electrospinning. Then, the solutions were loaded into a syringe with a 22.5-gauge blunt needle for the 67 mg/mL PDO solution and an 18-gauge blunt needle for all other solutions and electrospun with optimized parameters (**Table 1**) to produce

small and large fibers as desired (Fetz et al., 2018). Fibers were collected on a 20 × 75 × 5-mm grounded, stainless-steel rectangular mandrel that was rotating 1,250 revolutions/min and translating 6.5 cm/s over 13 cm. Additional higher concentrations of chloroquine were incorporated into the electrospun biomaterials during optimization (**Supplementary Methods**). For all experiments, 8-mm-diameter discs of the electrospun biomaterials were cut using a biopsy punch (cat. no. P825, Acuderm Inc., Ft. Lauderdale, FL, United States) and stored in a desiccator until use. Prior to cell culture, the biomaterials were irradiated with ultraviolet light at a wavelength of 365 nm using an 8-W lamp (cat. no. EN280L, Spectroline, Westbury, NY, United States) at a working distance of 9.5 cm. The samples were disinfected for 10 min on each side in a sterile, laminar flow hood and kept disinfected until cell culture.

Biomaterial Characterization

The biomaterials were imaged with a scanning electron microscope, and scanning electron micrographs (SEMs) were analyzed in FibraQuant 1.3 software (nanoTemplate Technologies, LLC) to quantify fiber diameter as previously described (Fetz et al., 2018). Briefly, 150 semiautomated random measurements per SEM were taken to determine the average and corresponding standard deviation for fiber diameter.

Chloroquine Elution From Biomaterials

The elution of chloroquine from the biomaterials was quantified over the first 24 h using a microplate reader to measure absorbance as described (Lima et al., 2018). The biomaterials ($n = 4$) were placed in a 96-well cell culture plate, and 150 μL of 1 × Hanks buffered salt solution (HBSS, calcium, magnesium, and phenol red free, cat. no. 14175095, Thermo Fisher Scientific, Waltham, MA, United States) was added to each well. After incubating at 37°C for 30 min, 1, 3, 6, and 24 h, the supernatant was removed and refreshed with 150 μL of HBSS. The absorbance of the collected supernatant was read on a SpectraMax i3x Multi-Mode Microplate Reader at 330 nm, and the chloroquine concentration was interpolated from a standard dilution ranging from 333 to 0 μg/mL in HBSS (**Supplementary Figure 1**). In addition to concentration, the average percent release and standard deviation were calculated for each biomaterial.

Isolation and Culture of Primary Human Neutrophils

Heparinized whole blood from healthy donors was obtained by venipuncture from Tennessee Blood Services. As purchased or donated samples are not traceable back to the donor, it does not qualify as human subjects research as determined by the University of Memphis Institutional Review Board on November 22, 2016. Neutrophils were then isolated as previously described using Isolymph® density separation (Neeli and Radic, 2013; Fetz et al., 2017, 2018). After isolation, neutrophils were resuspended in HBSS with 10 mM HEPES and 0.2% autologous serum at a concentration of 1 million neutrophils/mL. The disinfected biomaterials ($n = 3$) were placed in a 96-well plate, and 40 μL of the cell culture media was added to each well to hydrate the biomaterials. Negative and positive tissue culture plastic (TCP) wells ($n = 3$) received 30 μL of the cell culture media prior to cell seeding. Subsequently, 100 μL of cell culture media containing 100,000 neutrophils was added to each well followed by 10 μL of heparin (cat. no. H3393, Sigma–Aldrich, St. Louis, MO, United States) at a final concentration of 10 U/mL heparin. Heparin was added to dissociate NET-associated MPO as previously described (Parker et al., 2012; Minden-Birkenmaier et al., 2020). The negative vehicle and positive controls added to TCP wells were 0.15% dimethylsulfoxide in 10 μL of HBSS and 100 nM phorbol 12-myristate 13-acetate (cat. no. P8139, Sigma–Aldrich, St. Louis, MO, United States) in 10 μL of HBSS, respectively. The neutrophils were cultured at 37°C and 5% CO_2 for 3 and 6 h. Following incubation, the samples were placed on ice for 10 min to inhibit neutrophil stimulation prior to processing. Three experiments were performed with unique donors (male, between 18 and 40 years of age), and the results were pooled for analysis.

Quantification of NETs and Secreted Signals

Supernatants were collected and assayed using a ProcartaPlex multiplex immunomagnetic assay (cat. no. PPX, Thermo Fisher Scientific, Waltham, MA, United States) on a MAGPIX® microplate reader (Luminex Corporation, Austin, TX, United States). The assayed analytes included angiopoietin, fibroblast growth factor 2, granulocyte colony-stimulating factor (CSF), HGF, IL-1β, IL-1 receptor antagonist, IL-6, IL-8, IL-10, IL-22, monocyte chemoattractant protein 1, MMP-9, MPO, TNF-α, and VEGF-A. To quantify percent NET release, the concentration of MPO was normalized to the concentration of MPO in the positive control at 6 h (Parker et al., 2012; Minden-Birkenmaier et al., 2020).

Fluorescent Microscopy

Samples were fixed with 10% buffered formalin (cat. no. SF1004, Thermo Fisher Scientific, Waltham, MA, United States) and stained with 5 μM SYTOX orange (cat. no. S34861, Thermo Fisher Scientific, Waltham, MA, United States) and NucBlue™ Fixed Cell ReadyProbes™ Reagent (DAPI, cat. no. R37606, Thermo Fisher Scientific, Waltham, MA, United States) as described (Minden-Birkenmaier et al., 2020). Briefly, samples were sequentially incubated with each stain for 5 min at room temperature. Three washes with 1 × phosphate-buffered saline for 5 min each were performed between each step. Cells and NETs were visualized on an Olympus BX43 fluorescent microscope.

Statistical Analysis

Statistical significance between fiber diameters was tested with a Kruskal–Wallis and Dunn multiple-comparisons test. All other statistical significance was tested with an analysis of variance and Holm–Sidak multiple-comparisons test. Statistical analyses were performed in Prism version 8.4.3 (GraphPad Software, San Diego, CA, United States) at a significance level of 0.05. Data are reported as mean ± standard deviation.

TABLE 1 | Electrospun biomaterials were fabricated with optimized parameters.

	Polymer concentration (mg/mL)	Chloroquine concentration (mg/mL)	Flow rate (mL/h)	Airgap distance (cm)	Applied voltage (+kV)
Small fibers	67	0	0.25	13	14
	70	0.07	0.5	12	13
Large fibers	138	0	4.0	28	25
	138	0.07	3.2	28	25

RESULTS

Electrospun PDO Rapidly Elutes Chloroquine

PDO was electrospun to create biomaterials with small and large fibers (**Figure 1A**). Based on our previous work, the small- and large-fiber biomaterials in this study represent materials that trigger two distinct neutrophil NET responses and two distinct potentials for tissue regeneration (Fetz et al., 2017, 2018). In order to make comparisons independent of fiber size, the polymer concentration was adjusted for the small- and large-fiber biomaterials so that the addition of chloroquine did not alter the resulting fibers (**Figure 1B**). Any differences in the neutrophil inflammatory response can therefore be attributed to chloroquine elution. Both the small- and large-fiber biomaterials rapidly eluted chloroquine with near 100% elution within the first hour and no detectable increase after 3 h (**Figure 1C**), which is ideal and desired for targeting the acute neutrophil response during inflammation (Lammermann et al., 2013). The burst elution, driven by segregation of the charged drug to the outer surface of the electrospun fibers (Sun et al., 2008), equated to a concentration of 11.8 $\pm$ 1.33 μM and 12.2 $\pm$ 1.63 μM chloroquine for the small- and large-fiber biomaterials, respectively (**Figure 1D**). This elution was optimized by changing chloroquine incorporation during biomaterial fabrication to achieve an eluted concentration near those previously reported in the literature (Smith et al., 2014; Germic et al., 2017). Additional biomaterials were also fabricated to elute higher concentrations of chloroquine (**Supplementary Figure 2**).

Chloroquine Elution Inhibits NET Release on Small Fibers

Neutrophils were isolated from the whole blood of healthy donors and seeded on electrospun biomaterials with or without chloroquine to trigger biomaterial-induced NET release. As anticipated, neutrophils had an increased propensity to form NETs on the small fibers compared to the large fibers at 3 h (**Figure 2A**). More importantly, the elution of chloroquine from the small-fiber biomaterials significantly reduced NET release to the level of the large fibers at 3 h while having no effect upon elution from the large fibers (**Figure 2B**). By 6 h, the difference between small and large fibers was less pronounced, and increased NET release was observed on both chloroquine-eluting biomaterials, suggesting a temporal, therapeutic window for inhibiting acute NET release (**Figure 2B**).

Chloroquine Elution Decreases Inflammatory Signal Secretion

Given the documented anti-inflammatory effects, we also evaluated if chloroquine elution would modulate the inflammatory response through the secretion of soluble signals using a multiplexed immunomagnetic assay. Of the assayed inflammatory analytes, only IL-8 and MMP-9 were detected in the supernatant (**Figure 3**). IL-8 is the archetypal neutrophil chemoattractant secreted by damaged cells as well as neutrophils during an acute inflammatory response. At both 3 and 6 h, IL-8 secretion was significantly greater on the small-fiber biomaterials compared to the large fibers (**Figure 3A**). As the small fibers appear to up-regulate NET release in a proinflammatory response, it is not surprising that IL-8 secretion mimicked the trends in NET release. However, despite observing a temporal inhibition of acute NET release at 3 h only, the elution of chloroquine from both small and large fibers continued to significantly suppress IL-8 secretion at 6 h. These data suggest there is independent regulation of NET release and IL-8 synthesis and secretion in the context of biomaterial-induced activation, which may be important for reducing aberrant neutrophil recruitment during the tissue repair program (Fujishima et al., 1993; de Oliveira et al., 2013; Degroote et al., 2020). Similar to IL-8, MMP-9 secretion was significantly greater on the small-fiber biomaterials compared to the large fibers with chloroquine elution suppressing secretion at 3 h (**Figure 3B**). However, unlike IL-8, MMP-9 secretion was near equivalent on all biomaterials by 6 h, suggesting a temporal modulation of MMP-9. As a promiscuous endopeptidase, elevated MMP-9 is correlated with tissue degradation and chronic inflammation, so its acute suppression by chloroquine may prevent triggering a continuum of matrix destruction during the initial inflammatory response (Nagaoka and Hirota, 2000; Rayment et al., 2008; Liu et al., 2009).

Chloroquine Elution Increases Regenerative Signal Secretion

Although well characterized for its anti-inflammatory effects, chloroquine is not well studied for its potential regenerative effects. Therefore, we also evaluated if chloroquine elution would regulate the secretion of regenerative signals from biomaterial-interacting neutrophils. While several regenerative and anti-inflammatory analytes were assayed, only HGF, VEGF-A, and IL-22 were detected (**Figure 4**). The secretion of HGF (**Figure 4A**) and VEGF-A (**Figure 4B**) followed very similar trends at 3 h, with both having significantly greater secretion on large fibers compared to small fibers, which is the inverse of NET release.

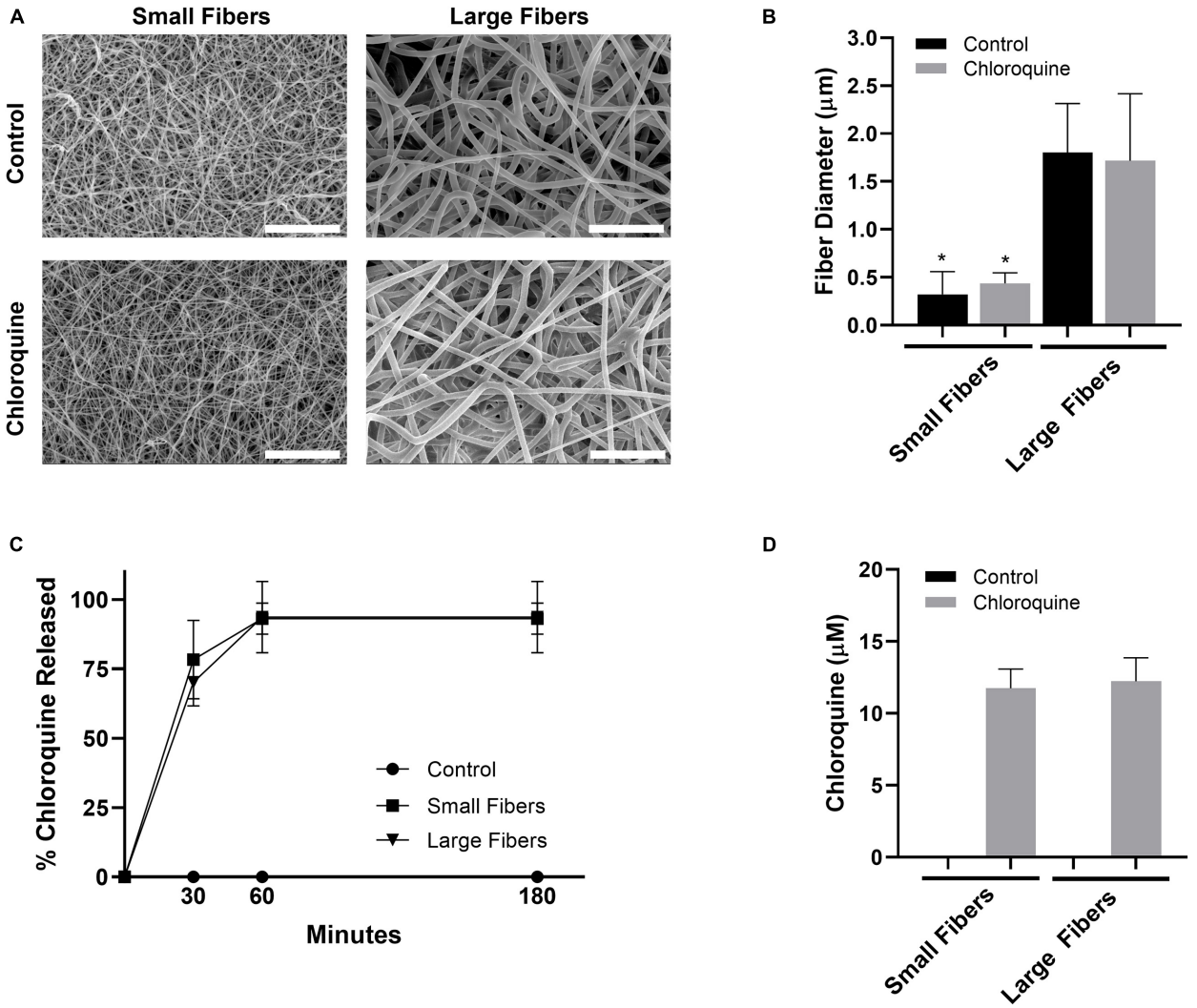

FIGURE 1 | Chloroquine incorporation into electrospun biomaterials results in uniform fibers that rapidly elute the additive. **(A)** Representative SEMs of the control and chloroquine-loaded biomaterials. Micrographs were acquired at 1,000× magnification and scale bars are 30 μm. **(B)** Fiber diameters of the electrospun biomaterials. Measurements ($n = 150$) were taken in FibraQuant 1.3 software. **(C)** Percent chloroquine released from the biomaterials and **(D)** eluted chloroquine concentration at 3 h. There was no increase in concentration after 3 h. See **Supplementary Figure 1** for the standard curve used to interpolate concentration ($n = 4$) from absorbance. Graphs show mean ± standard deviation. *$p < 0.0001$ was determined using a Kruskal–Wallis and Dunn multiple-comparisons test. Raw data are available in **Supplementary Spreadsheet 1**.

Additionally, the elution of chloroquine from the small fibers increased the secretion of HGF and VEGF-A to the level of the large fibers. By 6 h, the trends remained the same with an overall increase in the magnitude of secretion. As they are classic angiogenic signals (Taichman et al., 1997; McCourt et al., 2001; Wislez et al., 2003; Fridlender et al., 2009; He et al., 2016), these data indicate that chloroquine elution may help establish a more regenerative microenvironment around a biomaterial. Likewise, IL-22 secretion followed the same trends as HGF and VEGF-A, but its secretion was not detectable until 6 h, suggesting an absence of readily available stores (Dyring-Andersen et al., 2017). Nonetheless, as a proliferative and proangiogenic signal (Dyring-Andersen et al., 2017; Protopsaltis et al., 2019), the increased IL-22 secretion observed in response to chloroquine elution from the small fibers further suggests that chloroquine modulates the neutrophil phenotype toward healing and regeneration.

DISCUSSION

Electrospun biomaterials are excellent candidates for guided *in situ* tissue regeneration applications because they have a biomimetic structure that can also function as a drug delivery system to modulate acute inflammation (Kelleher and Vacanti, 2010; Minden-Birkenmaier et al., 2017). In recent years, neutrophils have gained attention as an important part of the acute inflammatory response to a biomaterial and the initiation of the tissue repair program (Fetz et al., 2017, 2020;

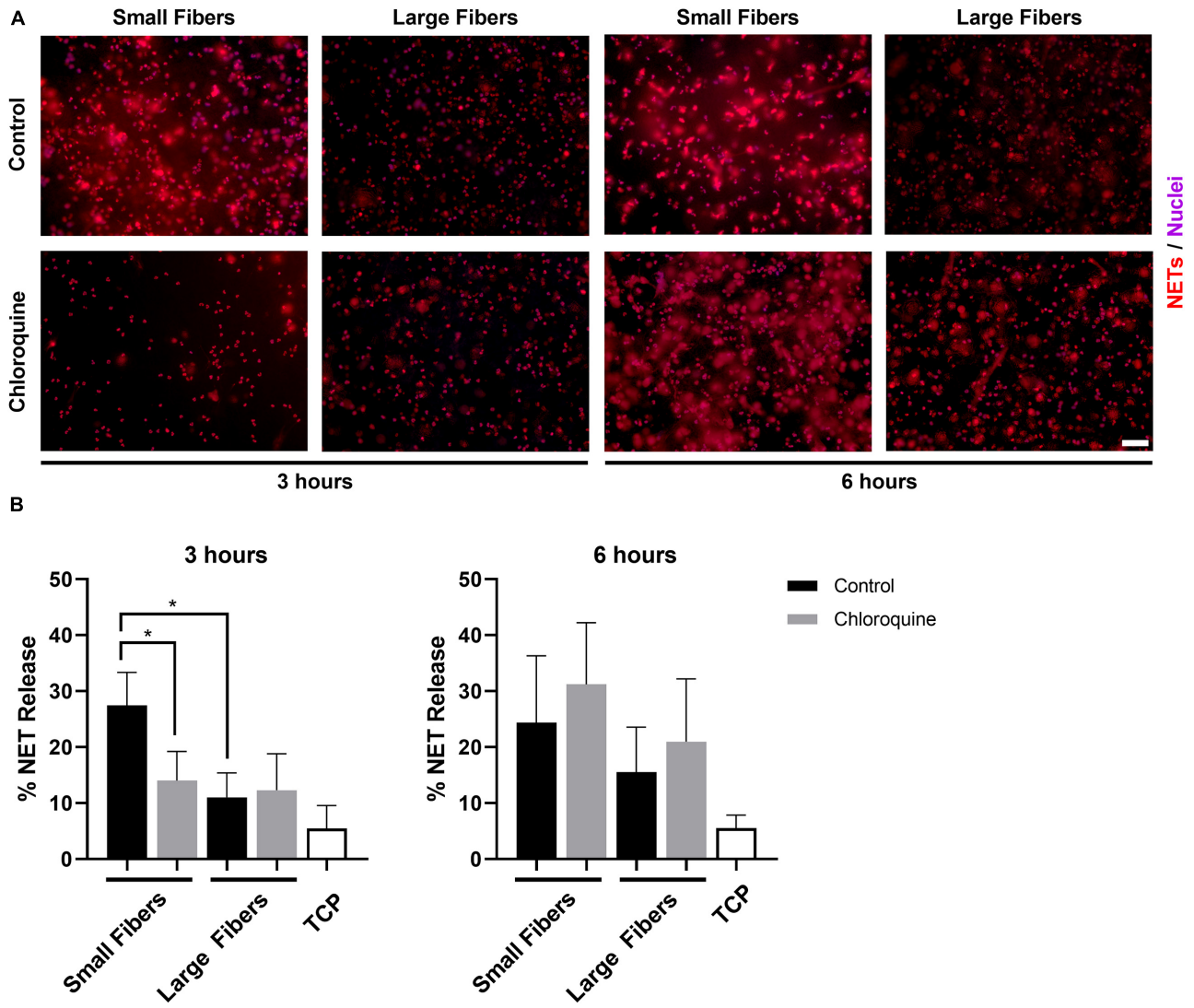

FIGURE 2 | Chloroquine elution inhibits NET release on small fibers but has no effect on large fibers. **(A)** Fluorescent micrographs of neutrophils on the electrospun biomaterials at 3 and 6 h after seeding. Staining of NETs (red) and nuclei (purple) reveals that chloroquine elution from the small fibers attenuates NET formation at the early time point, but not at the late time point. Conversely, chloroquine elution from the large fibers does not modulate NET release. Scale bar is 50 μm. **(B)** Percent NET release at 3 h (left) and 6 h (right) as quantified by the ELISA for NET-disassociated MPO. The quantification of percent NET release ($n = 3$) indicates that chloroquine elution from the small fibers reduces NET release to the level of the large fibers at 3 h with no effect at 6 h. The data represent the mean ± standard deviation of three independent experiments with unique donors. *$p < 0.0001$ was determined using an analysis of variance (ANOVA) and Holm–Sidak multiple-comparisons test. Raw data are available in **Supplementary Spreadsheet 1**.

Selders et al., 2017; Minden-Birkenmaier et al., 2020). Neutrophil recruitment, the release of NETs, and the secretion of soluble mediators can have diametrically opposed effects, leading to the resolution of inflammation and healing or chronic inflammation and fibrosis (Selders et al., 2017). Indeed, seminal work in neutrophil biology has highlighted the phenotypic plasticity of neutrophils and their ability to regulate the tissue environment (Buckley et al., 2006; Fridlender et al., 2009; Horckmans et al., 2016). Given the emphasis on endogenous cells for *in situ* tissue regeneration, regulation of the neutrophil response during acute inflammation is of utmost importance for cell integration and regeneration.

In this work, we developed electrospun PDO biomaterials that elute chloroquine to regulate biomaterial-induced neutrophil activation. PDO is an appealing polymer for electrospun biomaterials because of its biocompatibility, degradation rate, and mechanical properties (Boland et al., 2005; McClure et al., 2009). Additionally, chloroquine is an inexpensive drug historically used to treat malaria that has more recently garnered attention for its immunomodulatory and antithrombotic effects (Wozniacka et al., 2006; Moore et al., 2011; Manic et al., 2014; Schrezenmeier and Dörner, 2020). As a weak base that concentrates in acidic vesicles, it is classified as an inhibitor of lysosomes, lysosomal degradation, and endosomal Toll-like

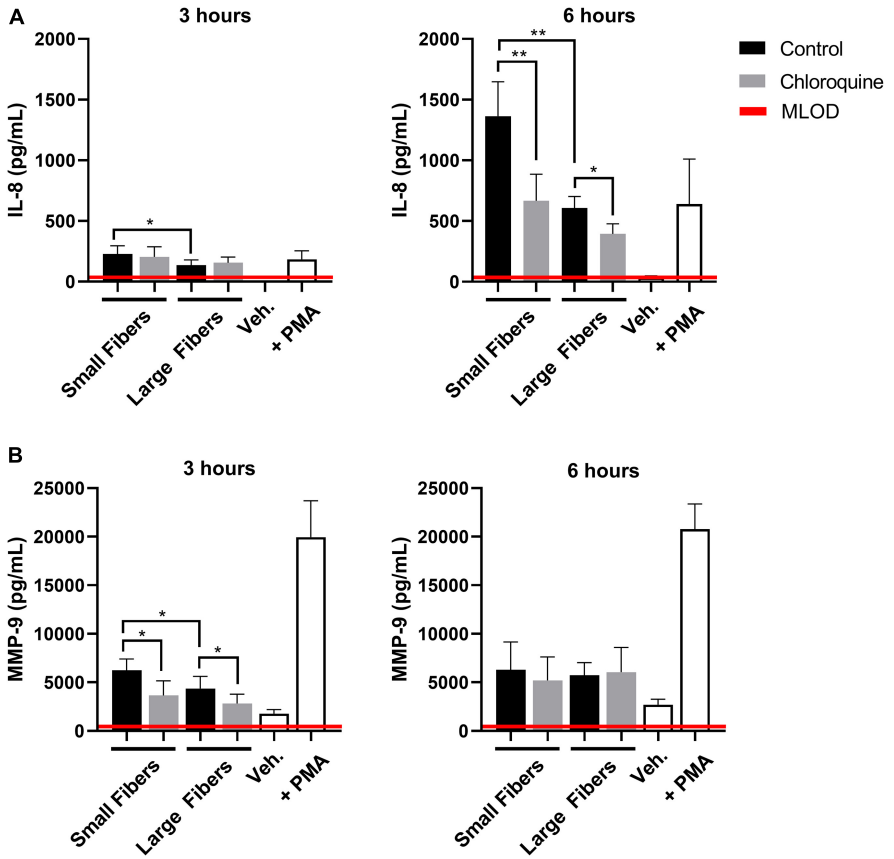

FIGURE 3 | Chloroquine-eluting biomaterials suppress inflammatory IL-8 and MMP-9 secretion from neutrophils. **(A)** IL-8 and **(B)** MMP-9 secretion at 3 h (left) and 6 h (right) after neutrophil seeding. Chloroquine elution down-regulated IL-8 secretion at both time points, whereas it only attenuates the acute secretion of MMP-9. The data ($n = 3$) represent the mean ± standard deviation of three independent experiments with unique donors. *$p < 0.05$ and **$p < 0.0001$ were determined using an analysis of variance (ANOVA) and Holm–Sidak multiple-comparisons test. Raw data are available in **Supplementary Spreadsheet 1**.

receptor signaling, as well as an inhibitor of autophagy (Sundelin and Terman, 2002; Frustaci et al., 2012; Mauthe et al., 2018). Recently, several groups have shown that chloroquine can be used to inhibit NET release (Smith et al., 2014; Boone et al., 2015, 2018; Germic et al., 2017; Murthy et al., 2019). As it is implicated in tissue fibrosis and thrombosis, NET formation is an appealing pharmacological target, especially in the context of biomaterial-induced NET release (Demers et al., 2012; Chrysanthopoulou et al., 2014; Gregory et al., 2015; Döring et al., 2017; Meng et al., 2017). Our group has shown that neutrophils have an increased propensity to form NETs on the surface of small-fiber electrospun biomaterials, leading to fibrotic encapsulation, whereas large-fiber biomaterials down-regulate NET release and guide tissue integration (Fetz et al., 2017). Jhunjhunwala et al. observed similar outcomes with implanted microcapsules that up-regulated NET release (Jhunjhunwala et al., 2015), thus indicating the need to engineer biomaterials that attenuate NET formation during the acute inflammatory response.

In these experiments, we incorporated chloroquine into the electrospun biomaterials to modulate NET release. At a dose 99.9% lower than the daily oral dose for malaria prophylaxis (Solitro and MacKeigan, 2016; Della Porta et al., 2020), we found that chloroquine eluted from small-fiber biomaterials down-regulated NET release to the level of the large-fiber biomaterials, whereas chloroquine elution from large fibers had no effect on NET release at the early time point. These findings are quite interesting, given that both materials eluted the same concentration of drug with near-identical release profiles. We observed a similar effect upon incorporating Cl-amidine into the electrospun biomaterials, which inhibits the enzyme peptidyl arginine deiminase 4 that is involved in NET formation (Leshner et al., 2012; Fetz et al., 2018). In both cases, these data suggest several mechanisms may be governing the release of NETs on electrospun biomaterials. Additionally, by the later time point, increased NET release was observed on both chloroquine-eluting biomaterials, suggesting a temporal, therapeutic window for inhibiting acute NET release. As the half-life of chloroquine is estimated to be 13–55 days, the observed increase in NET formation at 6 h again suggests that other regulatory mechanisms are involved in biomaterial-induced NET release (Moore et al., 2011; Della Porta et al., 2020). Last, biomaterials that eluted higher concentrations of chloroquine (**Supplementary Figure 2**) were developed to determine the therapeutic range of NET inhibition by chloroquine. Our

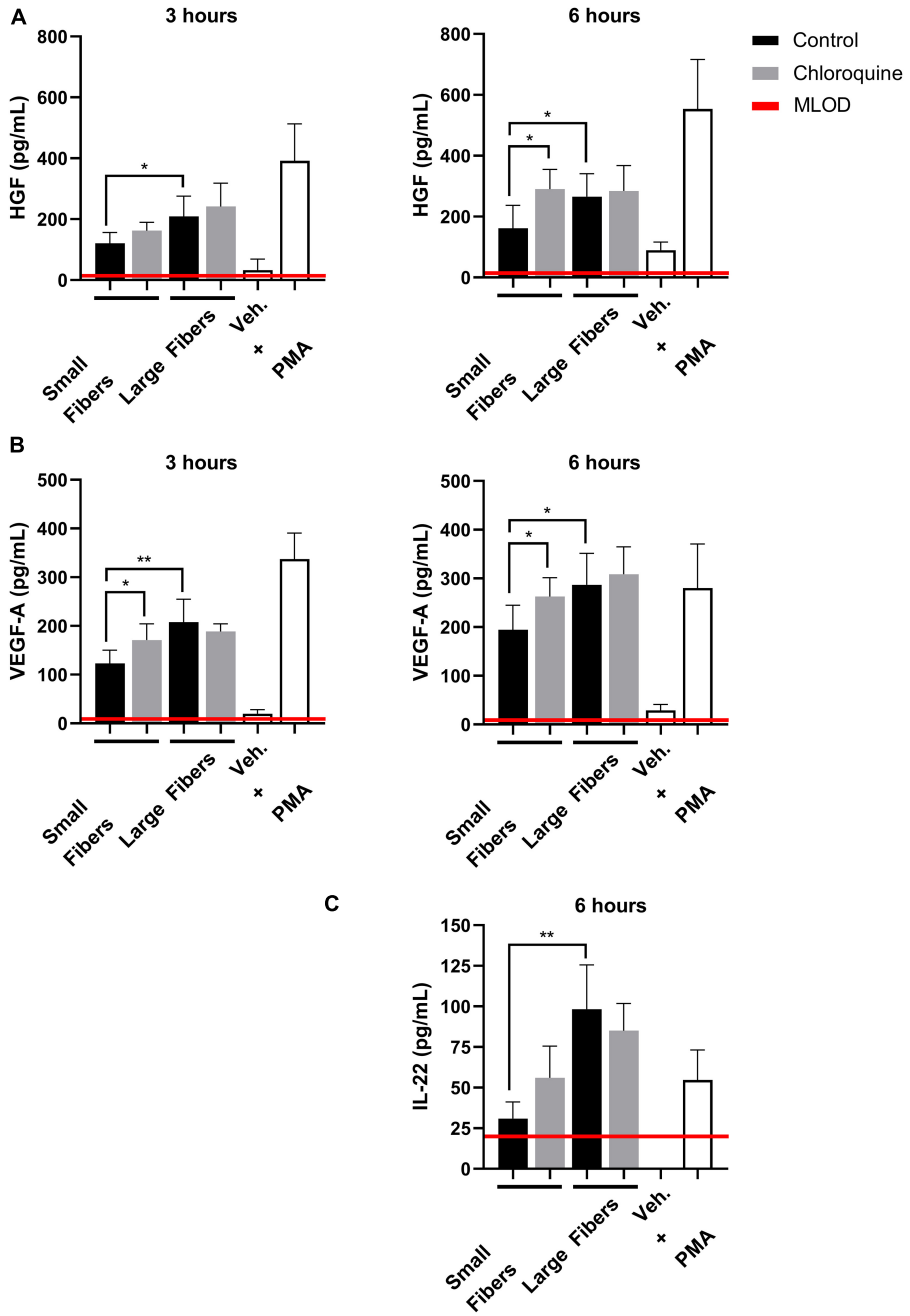

FIGURE 4 | Chloroquine-eluting biomaterials increase regenerative HGF, VEGF-A, and IL-22 secretion from neutrophils. **(A)** HGF and **(B)** VEGF-A were up-regulated with chloroquine elution at 3 h (left) and 6 h (right) after seeding, whereas **(C)** IL-22 was only detectable and up-regulated at 6 h after seeding. The data ($n = 3$) represent the mean ± standard deviation of three independent experiments with unique donors. *$p < 0.05$ and **$p < 0.0001$ were determined using an analysis of variance (ANOVA) and Holm–Sidak multiple-comparisons test. Raw data are available in **Supplementary Spreadsheet 1**.

data (**Supplementary Figure 3**) indicate that increasing the chloroquine concentration did not inhibit biomaterial-induced NET release and may have resulted in cytotoxic effects as previously reported (Pliyev and Menshikov, 2012).

Although we and others have shown that chloroquine can inhibit NET release, one group has found that a concentration of chloroquine similar to ours did not inhibit NET formation (Smith et al., 2014; Boone et al., 2015, 2018; Germic et al., 2017; Murthy et al., 2019). When chloroquine was shown to be effective at blocking NET release, neutrophils were stimulated with platelet activating factor, lipopolysaccharide, or our electrospun biomaterials (Smith et al., 2014; Boone et al., 2015). When chloroquine was shown to be ineffective, neutrophils were primed with granulocyte–macrophage CSF and stimulated with C5a,

which initiates distinctly different, vital NET release, or the release of mitochondrial NETs (Yousefi et al., 2009; Germic et al., 2017). These data indicate that the therapeutic efficacy of chloroquine for inhibiting NET formation is stimuli dependent and that there may be some overlap in the signaling pathways for biomaterial-induced NET release and other reported triggers of NET release (Farley et al., 2012; Alemán et al., 2016; Khan et al., 2017). Further work is needed to determine the specific signaling pathway involved in biomaterial-induced NET release, but our current data suggest involvement of surface-adsorbed IgG (Fetz et al., 2019).

In addition to inhibiting NETs, chloroquine has been reported to have immunomodulatory effects by altering the secretion of proinflammatory mediators. IL-1β, IL-8, MMP-9, and transforming growth factor β have all been shown to decrease with chloroquine treatment to attenuate inflammation (Delgado et al., 2006; Zhang et al., 2010; Sharma et al., 2017; Fujita et al., 2019). Likewise, in this work, we found that IL-8 and MMP-9 secretions were suppressed on the chloroquine-eluting biomaterials. IL-8 secretion is significantly up-regulated in neutrophils several hours after stimulation before returning to baseline levels, after which monocytes become the major source of IL-8 *in vivo* (Fujishima et al., 1993). Although neutrophils are necessary for tissue healing (Stirling et al., 2009; Horckmans et al., 2016; Lin et al., 2017), these data suggest that suppression of IL-8 by chloroquine at both early and later time points may down-regulate acute inflammation by reducing pernicious neutrophil chemotaxis (Végran et al., 2011). Similar to IL-8, MMP-9 is robustly secreted from neutrophils during acute inflammation and functions to degrade the ECM for enhanced cell motility (Lu et al., 2011; Deryugina et al., 2014). Consequently, MMP-9 can drive both tissue destruction through excessive ECM degradation and the rapid induction of angiogenesis (Ladwig et al., 2002; Ardi et al., 2007, 2009; Rayment et al., 2008; Liu et al., 2009; Hsu et al., 2015). While angiogenesis is paramount for tissue regeneration, elevated levels of MMP-9 could perpetuate inflammation and cyclic matrix destruction, so its suppression by chloroquine may approximate levels more conducive to regeneration, although this remains to be determined.

In conjunction with proinflammatory signals, we also evaluated the potential impact of chloroquine elution on regenerative signals. To our knowledge, no one has yet to explore this aspect of chloroquine's anti-inflammatory effects. We found that both HGF and VEGF-A secretions were increased with chloroquine elution from the biomaterials. HGF is a proangiogenic growth factor that promotes regeneration and homeostasis while inhibiting chronic inflammation and fibrosis in various tissues (McCourt et al., 2001; Wislez et al., 2003; Matsumoto et al., 2014; He et al., 2016). Similarly, VEGF-A is the canonical angiogenic signal secreted by neutrophils that has also been shown to recruit a proangiogenic subset of neutrophils (Taichman et al., 1997; Fridlender et al., 2009; Christoffersson et al., 2012, 2017). IL-22 closely followed the trends for HGF and VEGF-A, but was only detectable at the later time point, likely because of the time needed to up-regulate synthesis and secretion (Chen et al., 2016). IL-22 has been shown to be both protective and inflammatory, depending on the disease and model (Zindl et al., 2013; Dyring-Andersen et al., 2017; Zenewicz, 2018). However, it was more recently found to support angiogenesis in the tumor microenvironment by inducing endothelial cell proliferation, survival, and chemotaxis (Protopsaltis et al., 2019). Together, the increased secretion of HGF, VEGF-A, and IL-22 on chloroquine-eluting biomaterials suggests a previously unrecognized aspect of chloroquine's immunomodulatory effects.

Taken together, our novel incorporation of chloroquine into electrospun biomaterials illustrates the potential therapeutic benefit of this drug for biomaterial-guided, *in situ* tissue regeneration applications. Although we are the first to repurpose it as an electrospun template additive for tissue engineering applications, chloroquine has been incorporated into a coating for urine catheters to reduce sterile inflammation by reducing neutrophil necrosis and IL-8 secretion (Puyo et al., 2018). Likewise, our data indicate that local delivery through electrospun PDO biomaterials may down-regulate acute neutrophil-driven inflammation while simultaneously up-regulating their regenerative phenotype. The mechanisms underlying chloroquine's regulation of NET formation and signal secretion as well as its impact on macrophage phenotype and its *in vivo* efficacy are the subject of further investigations. Additional future work includes evaluation of these biomaterials with platelets and platelet–neutrophil interactions to begin elucidating if chloroquine's antithrombotic properties are correlated with its inhibition of NET formation (Ouseph et al., 2015; Boone et al., 2018). In conclusion, we have shown that our chloroquine-eluting biomaterials regulate acute neutrophil-driven inflammatory responses *in vitro* by down-regulating NET release and inflammatory signals while up-regulating regenerative signals. These responses may have synergistic effects that are advantageous for biomaterial-guided *in situ* tissue regeneration.

DATA AVAILABILITY STATEMENT

The original contributions presented in the study are included in the article/**Supplementary Material**, further inquiries can be directed to the corresponding author/s.

ETHICS STATEMENT

The studies involving human participants were reviewed by the University of Memphis Institutional Review Board. Written informed consent for participation was not required for this study in accordance with the national legislation and the institutional requirements.

AUTHOR CONTRIBUTIONS

AF and GB: conceptualization and funding acquisition. AF and SW: methodology and data curation. AF: writing—original draft preparation. AF, SW, and GB: writing—review and editing. GB:

supervision and project administration. All authors have read and agreed to the published version of the manuscript.

FUNDING

This research was funded by the National Institute of Biomedical Imaging and Bioengineering of the National Institutes of Health under Award No. R15EB022345. Additionally, this work was supported by the National Science Foundation Graduate Research Fellowship Program under Grant no. 1451514.

SUPPLEMENTARY MATERIAL

The Supplementary Material for this article can be found online at: https://www.frontiersin.org/articles/10.3389/fbioe.2021.652055/full#supplementary-material

REFERENCES

Alemán, O. R., Mora, N., Cortes-Vieyra, R., Uribe-Querol, E., and Rosales, C. (2016). Transforming growth factor-β-activated kinase 1 is required for human FcγRIIIb-induced neutrophil extracellular trap formation. *Front. Immunol.* 7:277. doi: 10.3389/fimmu.2016.00277

Anderson, J. M., Rodriguez, A., and Chang, D. T. (2008). Foreign body reaction to biomaterials. *Proc. Semin. Immunol* 20, 86–100.

Ardi, V. C., Kupriyanova, T. A., Deryugina, E. I., and Quigley, J. P. (2007). Human neutrophils uniquely release TIMP-free MMP-9 to provide a potent catalytic stimulator of angiogenesis. *Proc. Natl. Acad. Sci. U.S.A.* 104, 20262–20267. doi: 10.1073/pnas.0706438104

Ardi, V. C., Van den Steen, P. E., Opdenakker, G., Schweighofer, B., Deryugina, E. I., and Quigley, J. P. (2009). Neutrophil MMP-9 proenzyme, unencumbered by TIMP-1, undergoes efficient activation in vivo and catalytically induces angiogenesis via a basic fibroblast growth factor (FGF-2)/FGFR-2 pathway. *J. Biol. Chem.* 284, 25854–25866. doi: 10.1074/jbc.M109.033472

Boland, E. D., Coleman, B. D., Barnes, C. P., Simpson, D. G., Wnek, G. E., and Bowlin, G. L. (2005). Electrospinning polydioxanone for biomedical applications. *Acta Biomater.* 1, 115–123. doi: 10.1016/j.actbio.2004.09.003

Boone, B. A., Murthy, P., Miller-Ocuin, J., Doerfler, W. R., Ellis, J. T., Liang, X., et al. (2018). Chloroquine reduces hypercoagulability in pancreatic cancer through inhibition of neutrophil extracellular traps. *BMC Cancer.* 18:678. doi: 10.1186/s12885-018-4584-2

Boone, B. A., Orlichenko, L., Schapiro, N. E., Loughran, P., Gianfrate, G. C., Ellis, J. T., et al. (2015). The receptor for advanced glycation end products (RAGE) enhances autophagy and neutrophil extracellular traps in pancreatic cancer. *Cancer Gene. Ther.* 22:326. doi: 10.1038/cgt.2015.21

Brinkmann, V., Reichard, U., Goosmann, C., Fauler, B., Uhlemann, Y., Weiss, D. S., et al. (2004). Neutrophil extracellular traps kill bacteria. *Science* 303, 1532–1535. doi: 10.1126/science.1092385

Buckley, C. D., Ross, E. A., McGettrick, H. M., Osborne, C. E., Haworth, O., Schmutz, C., et al. (2006). Identification of a phenotypically and functionally distinct population of long-lived neutrophils in a model of reverse endothelial migration. *J. Leuko. Biol.* 79, 303–311. doi: 10.1189/jlb.0905496

Chen, F., Cao, A., Yao, S., Evans-Marin, H. L., Liu, H., Wu, W., et al. (2016). mTOR mediates IL-23 induction of neutrophil IL-17 and IL-22 production. *J. Immunol.* 196, 4390–4399. doi: 10.4049/jimmunol.1501541

Chen, G. Y., and Nuñez, G. (2010). Sterile inflammation: sensing and reacting to damage. *Nat. Rev. Immunol.* 10, 826–837. doi: 10.1038/nri2873

Christoffersson, G., Lomei, J., O'Callaghan, P., Kreuger, J., Engblom, S., and Phillipson, M. (2017). Vascular sprouts induce local attraction of proangiogenic neutrophils. *J. Leuko. Biol.* 102, 741–751. doi: 10.1189/jlb.1MA0117-018R

Christoffersson, G., Vågesjö, E., Vandooren, J., Lidén, M., Massena, S., Reinert, R. B., et al. (2012). VEGF-A recruits a proangiogenic MMP-9-delivering neutrophil subset that induces angiogenesis in transplanted hypoxic tissue. *Blood* 120, 4653–4662. doi: 10.1182/blood-2012-04-421040

Chrysanthopoulou, A., Mitroulis, I., Apostolidou, E., Arelaki, S., Mikroulis, D., Konstantinidis, T., et al. (2014). Neutrophil extracellular traps promote differentiation and function of fibroblasts. *J. Pathol.* 233, 294–307. doi: 10.1002/path.4359

Clark, S. R., Ma, A. C., Tavener, S. A., McDonald, B., Goodarzi, Z., Kelly, M. M., et al. (2007). Platelet TLR4 activates neutrophil extracellular traps to ensnare bacteria in septic blood. *Nat. Med.* 13, 463–469. doi: 10.1038/nm1565

de Oliveira, S., Reyes-Aldasoro, C. C., Candel, S., Renshaw, S. A., Mulero, V., and Calado, Â (2013). Cxcl8 (IL-8) mediates neutrophil recruitment and behavior in the zebrafish inflammatory response. *J. Immunol.* 190, 4349–4359. doi: 10.4049/jimmunol.1203266

Degroote, R. L., Weigand, M., Hauck, S. M., and Deeg, C. A. (2020). IL8 and PMA trigger the regulation of different biological processes in granulocyte activation. *Front. Immunol.* 10:3064. doi: 10.3389/fimmu.2019.03064

Delgado, M. A., Poschet, J. F., and Deretic, V. (2006). Nonclassical pathway of *Pseudomonas aeruginosa* DNA-induced interleukin-8 secretion in cystic fibrosis airway epithelial cells. *Infect. Immun.* 74, 2975–2984. doi: 10.1128/IAI.74.5.2975-2984.2006

Della Porta, A., Bornstein, K., Coye, A., Montrief, T., Long, B., and Parris, M. A. (2020). Acute chloroquine and hydroxychloroquine toxicity: a review for emergency clinicians. *Am. J. Emerg. Med.* 38, 2209–2217. doi: 10.1016/j.ajem.2020.07.030

Demers, M., Krause, D. S., Schatzberg, D., Martinod, K., Voorhees, J. R., Fuchs, T. A., et al. (2012). Cancers predispose neutrophils to release extracellular DNA traps that contribute to cancer-associated thrombosis. *Proc. Natl. Acad. Sci. U.S.A.* 109, 13076–13081. doi: 10.1073/pnas.1200419109

Deryugina, E. I., Zajac, E., Juncker-Jensen, A., Kupriyanova, T. A., Welter, L., and Quigley, J. P. (2014). Tissue-infiltrating neutrophils constitute the major in vivo source of angiogenesis-inducing MMP-9 in the tumor microenvironment. *Neoplasia* 16, 771–788. doi: 10.1016/j.neo.2014.08.013

Döring, Y., Soehnlein, O., and Weber, C. (2017). Neutrophil extracellular traps in atherosclerosis and atherothrombosis. *Circ. Res.* 120, 736–743. doi: 10.1161/CIRCRESAHA.116.309692

Dyring-Andersen, B., Honoré, T. V., Madelung, A., Bzorek, M., Simonsen, S., Clemmensen, S. N., et al. (2017). IL-17A and IL-22 producing neutrophils in psoriatic skin. *Br. J. Dermatol.* 177:e321. doi: 10.1111/bjd.15533

Farley, K., Stolley, J. M., Zhao, P., Cooley, J., and Remold-O'Donnell, E. (2012). A serpinB1 regulatory mechanism is essential for restricting neutrophil extracellular trap generation. *J. Immunol.* 189, 4574–4581. doi: 10.4049/jimmunol.1201167

Fetz, A. E., Fantaziu, C. A., Smith, R. A., Radic, M. Z., and Bowlin, G. L. (2019). Surface area to volume ratio of electrospun polydioxanone templates regulates the adsorption of soluble proteins from human serum. *Bioengineering* 6:78. doi: 10.3390/bioengineering6030078

Fetz, A. E., Neeli, I., Buddington, K. K., Read, R. W., Smeltzer, M. P., Radic, M. Z., et al. (2018). Localized delivery of Cl-amidine from electrospun polydioxanone templates to regulate acute neutrophil NETosis: a preliminary evaluation of the PAD4 inhibitor for tissue engineering. *Front. Pharmacol.* 9:289. doi: 10.3389/fphar.2018.00289

Fetz, A. E., Neeli, I., Rodriguez, I. A., Radic, M. Z., and Bowlin, G. L. (2017). Electrospun template architecture and composition regulate neutrophil NETosis in vitro and in vivo. *Tissue Engin. Part A* 23, 1054–1063. doi: 10.1089/ten.TEA.2016.0452

Fetz, A. E., Radic, M. Z., and Bowlin, G. L. (2020). Neutrophils in biomaterial-guided tissue regeneration: Matrix reprogramming for angiogenesis. *Tissue Engin. Part B* doi: 10.1089/ten.TEB.2020.0028. [Epub ahead of print].

Fridlender, Z. G., Sun, J., Kim, S., Kapoor, V., Cheng, G., Ling, L., et al. (2009). Polarization of tumor-associated neutrophil phenotype by TGF-β:"N1" versus "N2". *TAN. Cancer Cell* 16, 183–194. doi: 10.1016/j.ccr.2009.06.017

Frustaci, A., Morgante, E., Antuzzi, D., Russo, M. A., and Chimenti, C. (2012). Inhibition of cardiomyocyte lysosomal activity in hydroxychloroquine cardiomyopathy. *Int. J. Cardiol.* 157, 117–119. doi: 10.1016/j.ijcard.2012.03.112

Fuchs, T. A., Brill, A., Duerschmied, D., Schatzberg, D., Monestier, M., Myers, D. D., et al. (2010). Extracellular DNA traps promote thrombosis. *Proc. Natl. Acad. Sci. U.S.A.* 107, 15880–15885. doi: 10.1073/pnas.1005743107

Fujishima, S., Hoffman, A. R., Vu, T., Kim, K. J., Zheng, H., Daniel, D., et al. (1993). Regulation of neutrophil interleukin 8 gene expression and protein secretion by LPS, TNF-α, and IL-1β. *J. Cell. Physiol.* 154, 478–485. doi: 10.1002/jcp.1041540305

Fujita, Y., Matsuoka, N., Temmoku, J., Furuya, M. Y., Asano, T., Sato, S., et al. (2019). Hydroxychloroquine inhibits IL-1β production from amyloid-stimulated human neutrophils. *Arthritis Res. Ther.* 21:250. doi: 10.1186/s13075-019-2040-6

Germic, N., Stojkov, D., Oberson, K., Yousefi, S., and Simon, H. U. (2017). Neither eosinophils nor neutrophils require ATG 5-dependent autophagy for extracellular DNA trap formation. *Immunology* 152, 517–525. doi: 10.1111/imm.12790

Gregory, A. D., Kliment, C. R., Metz, H. E., Kim, K. H., Kargl, J., Agostini, B. A., et al. (2015). Neutrophil elastase promotes myofibroblast differentiation in lung fibrosis. *J. Leuko. Biol.* 98, 143–152. doi: 10.1189/jlb.3HI1014-493R

Gupta, A. K., Hasler, P., Holzgreve, W., Gebhardt, S., and Hahn, S. (2005). Induction of neutrophil extracellular DNA lattices by placental microparticles and IL-8 and their presence in preeclampsia. *Hum. Immunol.* 66, 1146–1154.

Gupta, A. K., Joshi, M. B., Philippova, M., Erne, P., Hasler, P., Hahn, S., et al. (2010). Activated endothelial cells induce neutrophil extracellular traps and are susceptible to NETosis-mediated cell death. *FEBS Lett.* 584, 3193–3197. doi: 10.1016/j.febslet.2010.06.006

Harada, A., Sekido, N., Akahoshi, T., Wada, T., Mukaida, N., and Matsushima, K. (1994). Essential involvement of interleukin-8 (IL-8) in acute inflammation. *J. Leuko. Biol.* 56, 559–564.

He, M., Peng, A., Huang, X. Z., Shi, D. C., Wang, J. C., Zhao, Q., et al. (2016). Peritumoral stromal neutrophils are essential for c-Met-elicited metastasis in human hepatocellular carcinoma. *Oncoimmunology* 5:e1219828. doi: 10.1080/2162402X.2016.1219828

Herath, T. D., Larbi, A., Teoh, S. H., James Kirkpatrick, C., and Goh, B. T. (2017). Neutrophil-mediated enhancement of angiogenesis and osteogenesis in a novel triple cell co-culture model with endothelial cells and osteoblasts. *J. Tissue Eng. Regen. Med.* 12:e1221–e1236. doi: 10.1002/term.2521

Horckmans, M., Ring, L., Duchene, J., Santovito, D., Schloss, M. J., Drechsler, M., et al. (2016). Neutrophils orchestrate post-myocardial infarction healing by polarizing macrophages towards a reparative phenotype. *Eur. Heart J.* 38, 187–197. doi: 10.1093/eurheartj/ehw002

Hsu, A. T., Barrett, C. D., DeBusk, M. G., Ellson, C. D., Gautam, S., Talmor, D. S., et al. (2015). Kinetics and role of plasma matrix metalloproteinase-9 expression in acute lung injury and the acute respiratory distress syndrome. *Shock* 44, 128–136. doi: 10.1097/SHK.0000000000000386

Jhunjhunwala, S., Aresta-DaSilva, S., Tang, K., Alvarez, D., Webber, M. J., Tang, B. C., et al. (2015). Neutrophil responses to sterile implant materials. *PLoS One.* 10:e0137550. doi: 10.1371/journal.pone.0137550

Kaplan, M. J., and Radic, M. (2012). Neutrophil extracellular traps: Double-edged swords of innate immunity. *J. Immunol.* 189, 2689–2695. doi: 10.4049/jimmunol.1201719

Kelleher, C. M., and Vacanti, J. P. (2010). Engineering extracellular matrix through nanotechnology. *J. R. Soc. Interface.* 7, S717–S729. doi: 10.1098/rsif.2010.0345.focu

Khan, M. A., Farahvash, A., Douda, D. N., Licht, J.-C., Grasemann, H., Sweezey, N., et al. (2017). JNK activation turns on LPS-and Gram-negative bacteria-induced NADPH oxidase-dependent suicidal NETosis. *Sci. Rep.* 7:3409. doi: 10.1038/s41598-017-03257-z

Lacy, P. (2006). Mechanisms of degranulation in neutrophils. *Allergy Asthma Clin. Immunol.* 2:98. doi: 10.1186/1710-1492-2-3-98

Ladwig, G. P., Robson, M. C., Liu, R., Kuhn, M. A., Muir, D. F., and Schultz, G. S. (2002). Ratios of activated matrix metalloproteinase-9 to tissue inhibitor of matrix metalloproteinase-1 in wound fluids are inversely correlated with healing of pressure ulcers. *Wound Repair Regen.* 10, 26–37. doi: 10.1046/j.1524-475x.2002.10903.x

Lammermann, T., Afonso, P. V., Angermann, B. R., Wang, J. M., Kastenmuller, W., Parent, C. A., et al. (2013). Neutrophil swarms require LTB4 and integrins at sites of cell death in vivo. *Nature* 498, 371–375. doi: 10.1038/nature12175

Lannutti, J., Reneker, D., Ma, T., Tomasko, D., and Farson, D. (2007). Electrospinning for tissue engineering scaffolds. *Mater. Sci. Eng. C* 27, 504–509. doi: 10.1016/j.msec.2006.05.019

Leshner, M., Wang, S., Lewis, C., Zheng, H., Chen, X. A., Santy, L., et al. (2012). PAD4 mediated histone hypercitrullination induces heterochromatin decondensation and chromatin unfolding to form neutrophil extracellular trap-like structures. *Front. Immunol.* 3:307. doi: 10.3389/fimmu.2012.00307

Li, Q., Ma, L., and Gao, C. (2015). Biomaterials for in situ tissue regeneration: development and perspectives. *J. Mater. Chem.* 3, 8921–8938. doi: 10.1039/C5TB01863C

Lima, T., Feitosa, R., dos Santos-Silva, E., dos Santos-Silva, A., Siqueira, E., Machado, P., et al. (2018). Improving encapsulation of hydrophilic chloroquine diphosphate into biodegradable nanoparticles: a promising approach against herpes virus simplex-1 infection. *Pharmaceutics* 10:255. doi: 10.3390/pharmaceutics10040255

Lin, R. Z., Lee, C. N., Moreno-Luna, R., Neumeyer, J., Piekarski, B., Zhou, P., et al. (2017). Host non-inflammatory neutrophils mediate the engraftment of bioengineered vascular networks. *Nat. Biotechnol.* 1:0081. doi: 10.1038/s41551-017-0081

Liu, Y., Min, D., Bolton, T., Nubé, V., Twigg, S. M., Yue, D. K., et al. (2009). Increased matrix metalloproteinase-9 predicts poor wound healing in diabetic foot ulcers. *Diabetes Care* 32, 117–119. doi: 10.2337/dc08-0763

Lu, P., Takai, K., Weaver, V. M., and Werb, Z. (2011). Extracellular matrix degradation and remodeling in development and disease. *Cold Spring Harb. Perspect. Biol.* 3:a005058. doi: 10.1101/cshperspect.a005058

Manic, G., Obrist, F., Kroemer, G., Vitale, I., and Galluzzi, L. (2014). Chloroquine and hydroxychloroquine for cancer therapy. *Mol. Cell Oncol.* 1:e29911. doi: 10.4161/mco.29911

Martinez, F. O., Sironi, M., Vecchi, A., Colotta, F., Mantovani, A., and Locati, M. (2004). IL-8 induces a specific transcriptional profile in human neutrophils: synergism with LPS for IL-1 production. *Eur. J. Immunol.* 34, 2286–2292. doi: 10.1002/eji.200324481

Martinod, K., Demers, M., Fuchs, T. A., Wong, S. L., Brill, A., Gallant, M., et al. (2013). Neutrophil histone modification by peptidylarginine deiminase 4 is critical for deep vein thrombosis in mice. *Proc. Natl. Acad. Sci. U.S.A.* 110, 8674–8679. doi: 10.1073/pnas.1301059110

Matsumoto, K., Funakoshi, H., Takahashi, H., and Sakai, K. (2014). HGF–Met pathway in regeneration and drug discovery. *Biomedicine* 2, 275–300. doi: 10.3390/biomedicines2040275

Maugeri, N., Brambilla, M., Camera, M., Carbone, A., Tremoli, E., Donati, M., et al. (2006). Human polymorphonuclear leukocytes produce and express functional tissue factor upon stimulation 1. *J. Thromb. Haemost.* 4, 1323–1330. doi: 10.1111/j.1538-7836.2006.01968.x

Mauthe, M., Orhon, I., Rocchi, C., Zhou, X., Luhr, M., Hijlkema, K.-J., et al. (2018). Chloroquine inhibits autophagic flux by decreasing autophagosome-lysosome fusion. *Autophagy* 14, 1435–1455. doi: 10.1080/15548627.2018.1474314

McClure, M. J., Sell, S. A., Simpson, D. G., and Bowlin, G. L. (2009). Electrospun polydioxanone, elastin, and collagen vascular scaffolds: uniaxial cyclic distension. *J. Eng. Fibers Fabr.* 4, 18–25. doi: 10.1177/155892500900400204

McCourt, M., Wang, J., Sookhai, S., and Redmond, H. (2001). Activated human neutrophils release hepatocyte growth factor/scatter factor. *Eur. J. Surg. Oncol.* 27, 396–403. doi: 10.1053/ejso.2001.1133

Meng, H., Yalavarthi, S., Kanthi, Y., Mazza, L. F., Elfline, M. A., Luke, C. E., et al. (2017). In vivo role of neutrophil extracellular traps in antiphospholipid antibody–mediated venous thrombosis. *Arthritis Rheum.* 69, 655–667. doi: 10.1002/art.39938

Minden-Birkenmaier, B., Selders, G., Fetz, A., Gehrmann, C., and Bowlin, G. (2017). "Electrospun systems for drug delivery," in *Electrospun Materials for Tissue Engineering and Biomedical Applications*, eds T. Uyar and E. Kny (Amsterdam: Elsevier), 117–145.

Minden-Birkenmaier, B. A., Smith, R. A., Radic, M. Z., van der Merwe, M., and Bowlin, G. L. (2020). Manuka honey reduces NETosis on an electrospun template within a therapeutic window. *Polymers* 12:1430. doi: 10.3390/polym12061430

Moore, B. R., Page-Sharp, M., Stoney, J. R., Ilett, K. F., Jago, J. D., and Batty, K. T. (2011). Pharmacokinetics, pharmacodynamics, and allometric scaling of chloroquine in a murine malaria model. *Antimicrob. Agents Chemother.* 55, 3899–3907. doi: 10.1128/AAC.00067-11

Murthy, P., Singhi, A. D., Ross, M. A., Loughran, P., Paragomi, P., Papachristou, G. I., et al. (2019). Enhanced neutrophil extracellular trap (NET) formation in acute pancreatitis contributes to disease severity and is reduced by chloroquine. *Front. Immunol.* 10:28. doi: 10.3389/fimmu.2019.00028

Nagaoka, I., and Hirota, S. (2000). Increased expression of matrix metalloproteinase-9 in neutrophils in glycogen-induced peritoneal inflammation of guinea pigs. *Inflamm. Res.* 49, 55–62. doi: 10.1007/s000110050559

Neeli, I., Khan, S. N., and Radic, M. (2008). Histone deimination as a response to inflammatory stimuli in neutrophils. *J. Immunol.* 180, 1895–1902. doi: 10.4049/jimmunol.180.3.1895

Neeli, I., and Radic, M. (2013). Opposition between PKC isoforms regulates histone deimination and neutrophil extracellular chromatin release. *Front. Immunol.* 4:38. doi: 10.3389/fimmu.2013.00038

Ouseph, M. M., Huang, Y., Banerjee, M., Joshi, S., MacDonald, L., Zhong, Y., et al. (2015). Autophagy is induced upon platelet activation and is essential for hemostasis and thrombosis. *Blood* 126, 1224–1233. doi: 10.1182/blood-2014-09-598722

Parker, H., Albrett, A. M., Kettle, A. J., and Winterbourn, C. C. (2012). Myeloperoxidase associated with neutrophil extracellular traps is active and mediates bacterial killing in the presence of hydrogen peroxide. *J. Leuko. Biol.* 91, 369–376. doi: 10.1189/jlb.0711387

Phillipson, M., and Kubes, P. (2019). The healing power of neutrophils. *Trends Immunol.* 40, 635–647. doi: 10.1016/j.it.2019.05.001

Pliyev, B. K., and Menshikov, M. (2012). Differential effects of the autophagy inhibitors 3-methyladenine and chloroquine on spontaneous and TNF-α-induced neutrophil apoptosis. *Apoptosis* 17, 1050–1065. doi: 10.1007/s10495-012-0738-x

Protopsaltis, N. J., Liang, W., Nudleman, E., and Ferrara, N. (2019). Interleukin-22 promotes tumor angiogenesis. *Angiogenesis* 22, 311–323. doi: 10.1007/s10456-018-9658-x

Puyo, C. A., Earhart, A., Staten, N., Huang, Y., Desai, A., Lai, H., et al. (2018). Mitochondrial DNA induces Foley catheter related bladder inflammation via Toll-like receptor 9 activation. *Sci. Rep.* 8:6377. doi: 10.1038/s41598-018-24818-w

Rayment, E. A., Upton, Z., and Shooter, G. K. (2008). Increased matrix metalloproteinase-9 (MMP-9) activity observed in chronic wound fluid is related to the clinical severity of the ulcer. *Br. J. Dermatol.* 158, 951–961. doi: 10.1111/j.1365-2133.2008.08462.x

Riehl, D. R., Roewe, J., Klebow, S., Esmon, N. L., Eming, S., Colucci, G., et al. (2016). Neutrophil extracellular traps drive bleomycin-induced lung fibrosis by regulating TGFβ1-dependent interactions of platelets and macrophages. *FASEB J.* 30:665.13. doi: 10.1096/fasebj.30.1_supplement.50.1

Roldan, E. Q., Biasiotto, G., Magro, P., and Zanella, I. (2020). The possible mechanisms of action of 4-aminoquinolines (chloroquine/hydroxychloroquine) against Sars-Cov-2 infection (COVID-19): a role for iron homeostasis? *Pharmacol. Res.* 158:104904. doi: 10.1016/j.phrs.2020.104904

Schrezenmeier, E., and Dörner, T. (2020). Mechanisms of action of hydroxychloroquine and chloroquine: implications for rheumatology. *Nat. Rev. Rheumatol* 16, 155–166. doi: 10.1038/s41584-020-0372-x

Selders, G. S., Fetz, A. E., Radic, M. Z., and Bowlin, G. L. (2017). An overview of the role of neutrophils in innate immunity, inflammation and host-biomaterial integration. *Regen. Biomat.* 4, 55–68. doi: 10.1093/rb/rbw041

Sharma, P., Yi, R., Nayak, A. P., Wang, N., Tang, F., Knight, M. J., et al. (2017). Bitter taste receptor agonists mitigate features of allergic asthma in mice. *Sci. Rep.* 7:46166. doi: 10.1038/srep46166

Smith, C. K., Vivekanandan-Giri, A., Tang, C., Knight, J. S., Mathew, A., Padilla, R. L., et al. (2014). Neutrophil extracellular trap–derived enzymes oxidize high-density lipoprotein: an additional proatherogenic mechanism in systemic lupus erythematosus. *Arthritis Rheum.* 66, 2532–2544. doi: 10.1002/art.38703

Solitro, A. R., and MacKeigan, J. P. (2016). Leaving the lysosome behind: novel developments in autophagy inhibition. *Future Med. Chem.* 8, 73–86. doi: 10.4155/fmc.15.166

Stirling, D. P., Liu, S., Kubes, P., and Yong, V. W. (2009). Depletion of Ly6G/Gr-1 leukocytes after spinal cord injury in mice alters wound healing and worsens neurological outcome. *J. Neurosci.* 29, 753–764. doi: 10.1523/JNEUROSCI.4918-08.2009

Sun, X. Y., Nobles, L. R., Borner, H. G., and Spontak, R. J. (2008). Field-driven surface segregation of biofunctional species on electrospun PMMA/PEO microfibers. *Macromol. Rapid Comm.* 29, 1455–1460. doi: 10.1002/marc.200800163

Sundelin, S. P., and Terman, A. (2002). Different effects of chloroquine and hydroxychloroquine on lysosomal function in cultured retinal pigment epithelial cells. *APMIS* 110, 481–489. doi: 10.1034/j.1600-0463.2002.100606.x

Taichman, N. S., Young, S., Cruchley, A. T., Taylor, P., and Paleolog, E. (1997). Human neutrophils secrete vascular endothelial growth factor. *J. Leuko. Biol.* 62, 397–400. doi: 10.1002/jlb.62.3.397

Végran, F., Boidot, R., Michiels, C., Sonveaux, P., and Feron, O. (2011). Lactate influx through the endothelial cell monocarboxylate transporter MCT1 supports an NF-κB/IL-8 pathway that drives tumor angiogenesis. *Cancer Res.* 71, 2550–2560. doi: 10.1158/0008-5472.CAN-10-2828

Wislez, M., Rabbe, N., Marchal, J., Milleron, B., Crestani, B., Mayaud, C., et al. (2003). Hepatocyte growth factor production by neutrophils infiltrating bronchioloalveolar subtype pulmonary adenocarcinoma: role in tumor progression and death. *Cancer Res.* 63, 1405–1412.

Wozniacka, A., Lesiak, A., Narbutt, J., McCauliffe, D., and Sysa-Jedrzejowska, A. (2006). Chloroquine treatment influences proinflammatory cytokine levels in systemic lupus erythematosus patients. *LUPUS* 15, 268–275. doi: 10.1191/0961203306lu2299oa

Yousefi, S., Mihalache, C., Kozlowski, E., Schmid, I., and Simon, H. U. (2009). Viable neutrophils release mitochondrial DNA to form neutrophil extracellular traps. *Cell Death Differ.* 16, 1438–1444. doi: 10.1038/cdd.2009.96

Zenewicz, L. A. (2018). IL-22: there is a gap in our knowledge. *Immunohorizons* 2, 198–207. doi: 10.4049/immunohorizons.1800006

Zhang, Q., Itagaki, K., and Hauser, C. J. (2010). Mitochondrial DNA is released by shock and activates neutrophils via p38 map kinase. *Shock* 34, 55–59. doi: 10.1097/SHK.0b013e3181cd8c08

Zindl, C. L., Lai, J. F., Lee, Y. K., Maynard, C. L., Harbour, S. N., Ouyang, W., et al. (2013). IL-22–producing neutrophils contribute to antimicrobial defense and restitution of colonic epithelial integrity during colitis. *Proc. Natl. Acad. Sci. U.S.A.* 110, 12768–12773. doi: 10.1073/pnas.1300318110

Conflict of Interest: The authors declare that the research was conducted in the absence of any commercial or financial relationships that could be construed as a potential conflict of interest.

frontiers in Bioengineering and Biotechnology

REVIEW
published: 02 June 2021
doi: 10.3389/fbioe.2021.679525

Clinical Use of the Self-Assembling Peptide RADA16: A Review of Current and Future Trends in Biomedicine

Sharanya Sankar[1†], Kate O'Neill[2†], Maurice Bagot D'Arc[3], Florian Rebeca[1], Marie Buffier[1], Elton Aleksi[4], Melanie Fan[2], Noriaki Matsuda[5], Eun Seok Gil[4] and Lisa Spirio[4]*

[1] 3-D Matrix Europe SAS, Caluire-et-Cuire, France, [2] 3-D Matrix UK Ltd., London, United Kingdom, [3] BLUEPHARM SAS, Paris, France, [4] 3-D Matrix Inc., Newton, MA, United States, [5] 3-D Matrix, Ltd., Tokyo, Japan

OPEN ACCESS

Edited by:
Carl Austin Gregory, Texas A&M Health Science Center, United States

Reviewed by:
Tzu-Wei Wang, National Tsing Hua University, Taiwan
Marie-noelle Giraud, Université de Fribourg, Switzerland

***Correspondence:**
Lisa Spirio
lisa@3dmatrix.com

† These authors have contributed equally to this work and share first authorship

Specialty section:
This article was submitted to Tissue Engineering and Regenerative Medicine, a section of the journal Frontiers in Bioengineering and Biotechnology

Received: *12 March 2021*
Accepted: *10 May 2021*
Published: *02 June 2021*

Citation:
Sankar S, O'Neill K, Bagot D'Arc M, Rebeca F, Buffier M, Aleksi E, Fan M, Matsuda N, Gil ES and Spirio L (2021) Clinical Use of the Self-Assembling Peptide RADA16: A Review of Current and Future Trends in Biomedicine. Front. Bioeng. Biotechnol. 9:679525. doi: 10.3389/fbioe.2021.679525

RADA16 is a synthetic peptide that exists as a viscous solution in an acidic formulation. In an acidic aqueous environment, the peptides spontaneously self-assemble into β-sheet nanofibers. Upon exposure and buffering of RADA16 solution to the physiological pH of biological fluids such as blood, interstitial fluid and lymph, the nanofibers begin physically crosslinking within seconds into a stable interwoven transparent hydrogel 3-D matrix. The RADA16 nanofiber hydrogel structure closely resembles the 3-dimensional architecture of native extracellular matrices. These properties make RADA16 formulations ideal topical hemostatic agents for controlling bleeding during surgery and to prevent post-operative rebleeding. A commercial RADA16 formulation is currently used for hemostasis in cardiovascular, gastrointestinal, and otorhinolaryngological surgical procedures, and studies are underway to investigate its use in wound healing and adhesion reduction. Straightforward application of viscous RADA16 into areas that are not easily accessible circumvents technical challenges in difficult-to-reach bleeding sites. The transparent hydrogel allows clear visualization of the surgical field and facilitates suture line assessment and revision. The shear-thinning and thixotropic properties of RADA16 allow its easy application through a narrow nozzle such as an endoscopic catheter. RADA16 hydrogels can fill tissue voids and do not swell so can be safely used in close proximity to pressure-sensitive tissues and in enclosed non-expandable regions. By definition, the synthetic peptide avoids potential microbiological contamination and immune responses that may occur with animal-, plant-, or mineral-derived topical hemostats. *In vitro* experiments, animal studies, and recent clinical experiences suggest that RADA16 nanofibrous hydrogels can act as surrogate extracellular matrices that support cellular behavior and interactions essential for wound healing and for tissue regenerative applications. In the future, the unique nature of RADA16 may also allow us to use it as a depot for precisely regulated drug and biopharmaceutical delivery.

Keywords: self-assembling peptide hydrogel, nanofiber, RADA16, hemostasis, tissue regeneration, wound healing, surgery, endoscopy

INTRODUCTION TO SELF-ASSEMBLING PEPTIDES (SAPs)

Self-assembling peptides (SAPs) are short oligopeptides that often contain repeating amino acid sequences, which, under appropriate environmental conditions spontaneously self-assemble into distinct nanostructures (Edwards-Gayle and Hamley, 2017; Lee et al., 2019). Explorations into the characteristics and biomedical utility of SAPs followed the discovery in 1989 of a native yeast protein containing repeated amino acid sequences, zuotin, that self-assembled into 3-dimensional (3D) structures in specific fluid environments (Zhang et al., 1992). This process of molecular self-assembly found in nature inspired scientists to develop unique SAPs for research and medical product development, including RADA16 (Zhang, 2017). The SAP monomeric constitution can be purposefully selected so that spontaneous self-assembly forms distinct well-ordered supramolecular structures with desired configurations including sheets, vesicles, tubes, and interlinking fibrous networks resembling natural extracellular matrix (ECM). Self-assembly of SAP peptide molecules into discrete structures primarily involves non-covalent interactions including hydrogen bonding, electrostatic interactions, hydrophobic/hydrophilic relationships, and van der Waals forces (Edwards-Gayle and Hamley, 2017).

Various subclasses of SAPs have been identified and characterized (Hartgerink et al., 2001; Chen, 2005; Choi et al., 2012; Argudo et al., 2018; Qiu et al., 2018). One well-studied SAP subgroup are the ionic-complementary SAPs, characterized by an alternating sequence of positively and negatively charged amino acids (Chen, 2005). Ionic-complementary SAPs are further categorized by specific residue charge distribution patterns into Type I, +−+−; Type II, ++−−; Type III, +++−−−; or Type IV, +++−−−− monomers, with the subclass defined by the number of similarly charged peptides occurring in sequence. Type-1 ionic-complementary peptides have β-strand periodicity and their regular charge patterns allow their spontaneous interlinking assembly by hydrophobic effect and hydrogen bonding into predictable complex β-sheet suprastructures. The specific charge pattern of SAP peptides determines their interlocking assembly configuration, allowing scientists to generate different polymeric structures with distinct biological behavior and interactions. This review focuses on one such Type-I peptide, RADA16-I (hereafter referred to as RADA16), a SAP that spontaneously self-assembles into nanofibrous structure and that under physiological conditions forms a complex hydrogel of interwoven networks. RADA16 has demonstrated clinical utility as a highly effective hemostatic agent for controlling surgical bleeding and shows great promise as a surrogate ECM for wound healing and tissue regeneration, and as an efficient drug delivery platform.

Abbreviations: 3D, 3-dimensional; AE, adverse event; AGIB, acute gastrointestinal bleeding; ECM, extracellular matrix; EMR, endoscopic mucosal resection; ESD, endoscopic submucosal dissection; GI, gastrointestinal; IPB, intraprocedural bleeding; RADA16, $(arginine\text{-}alanine\text{-}arginine\text{-}aspartic\ acid)_4$; RP, radiation proctopathy; SAP, self-assembling peptide; VEGF, vascular endothelial growth factor.

MECHANISM OF ACTION OF RADA16

RADA16 is a 16-amino acid Type I-SAP containing repeated R (positively charged arginine), A (hydrophobic alanine), and D (negatively charged aspartic acid) amino acid residues (**Figure 1**). A single RADA16 peptide is a ∼6 nm-length monomeric oligopeptide.

RADA16 peptides are manufactured in an acidic environment (pH ≈2) and spontaneously self-assemble to form nanofibers in water. At pH 2, the net charge of a RADA16 peptide is positive because the side carboxylic acids of its four aspartic acids are protonated in water (i.e., no charge under their pKa of ≈3.7) while the side guanidine groups of its four arginines are positively charged. The presence of hydrophobic amino acid groups and positively charged sequences along the RADA16 peptide allows monomer organization into stable β-sheet nanofiber with a positively charged surface in this aqueous acidic environment (**Figure 2**; Yokoi et al., 2005). Therefore, the RADA16 nanofibers are flowable in an acidic aqueous condition due to electric repulsion among the positively charged nanofibers, while they generate high viscosity due to their fibrous structure. The diameter of the RADA16 nanofibers is smaller than the wavelength of visual light (i.e., 380–740 nm) so the solution appears transparent. The action of self-assembly is spontaneous and reversible, so the peptides can disassemble upon exposure to external shearing force and spontaneously reassemble after removal of the force (**Figure 3**). This property allows for easy application and coverage of wounds due to partial disassembly of RADA16 peptides as the material is applied but its viscosity immediately returns after application via molecular reassembly. In clinical practice, these shear-thinning and thixotropic properties make RADA16 solutions suitable for application through a narrow applicator and allow the product to flow easily into wounds (**Figure 3**).

When the peptide solution is neutralized and buffered by the physiological pH and ionic characteristics of bodily fluids (e.g., blood, lymph, cerebrospinal fluid) or tissue culture media, the side carboxylic acids of the RADA16 four aspartic acids are deprotonated (i.e., negatively charged over their pKa of ≈3.7, which creates both four positive charges and four negative charges on the RADA16 peptide, and the net charge becomes zero). The surface of the nanofibers becomes hydrophobic; thus, the neighboring nanofibers are physically cross-linked via hydrophobic interactions to become a complex mesh-like hydrogel structure (**Figure 3**) that resembles native ECM architecture (Yokoi et al., 2005; Cormier et al., 2013; Zhang, 2017; Wang et al., 2019).

These unique properties of RADA16 have been adapted by researchers and surgeons for diverse experimental and clinical applications. RADA16 has been commercialized as PuraMatrix™ (3-D Matrix Ltd., Tokyo, Japan), a 1% peptide solution for use as an ECM surrogate for laboratory evaluation of cell adhesion, chemotaxis, proliferation and development, and

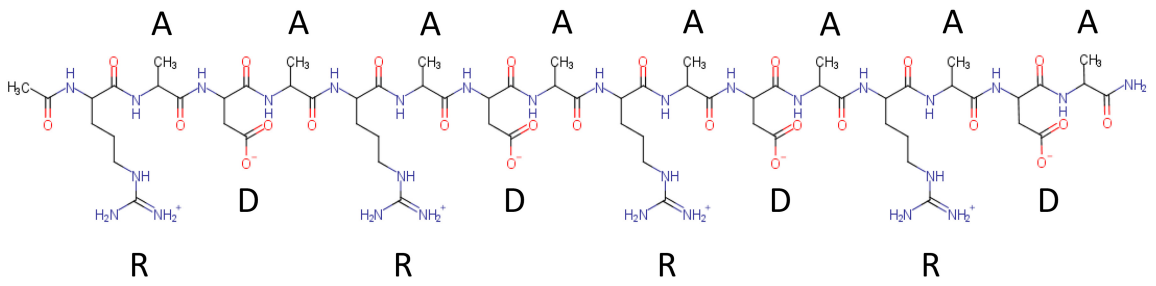

FIGURE 1 | Chemical structure of RADA16 peptide. RADA16 peptide chemical structure showing the 16 amino acids organized as sequentially repeated 4-amino acid sequences containing R (positively charged arginine), A (hydrophobic alanine), and D (negatively charged aspartic acid) residues.

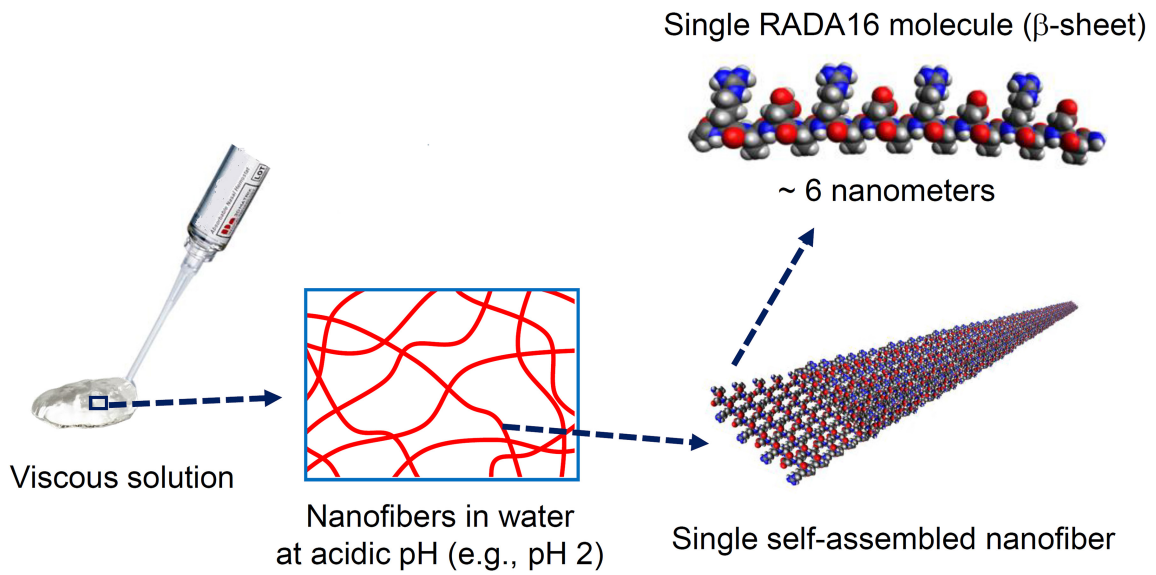

FIGURE 2 | Macro, micro, and nanostructures of RADA16 in an aqueous solution. Spontaneous and reversible self-assembly of RADA16 molecules occurs in acidic solutions to generate nanofibers. RADA16 molecules with β-sheet conformation interact through face-to-face hydrophobic interactions and edge-to-edge hydrogen bonding to form layered and extended nanofibers, ~6 nm in width. These ECM-like nanofibers form a viscous and transparent aqueous solution at a relatively low concentration range (e.g., 0.1~2.5% weight/volume).

as an *in vitro* and pre-clinical *in vivo* 3D scaffold for hemostasis, wound healing, and tissue engineering investigations (Wang et al., 2019; Corning Life Sciences Inc, 2021).

In the clinic or operating room, the SAP products PuraStat® and PuraBond® (3-D Matrix Europe SAS, Caluire-et-Cuire, France), are delivered by pre-filled syringes as viscous aqueous solutions of synthetic 2.5% RADA16, that spreads across the surface of the wound. When RADA16 comes in to contact with blood or other physiological fluids, it forms a hydrogel. The hydrogel formation acts as a barrier and blocks the flow of the blood from the wound and thereby, demonstrates excellent topical hemostatic control of intra- and post-operative bleeding associated with diverse surgical procedures, including oozing from wound surfaces of the skin and other organs (**Figure 4**) and from suture lines of vascular anastomoses (**Figure 5**; 3-D Matrix Europe SAS, 2014; Wang et al., 2019). The hemostatic mechanism of action of the RADA16 products is *in situ* formation of a transparent hemostatic hydrogel barrier on bleeding wound surfaces upon contact with physiological fluids present at the surgical site (**Figure 5**). A sister product cleared in the United States, PuraSinus™ (also 2.5% RADA16), is an intraoperatively applied hemostatic wound dressing that also prevents adhesion formation and acts as an adjunct to wound healing after nasal surgery or trauma (US Food and Drug Administration, 2021). Finally, PuraDerm™ has been cleared in the United States as topical wound dressing for the management of partial and full-thickness wounds such as pressure sores, leg ulcers, diabetic ulcers, and surgical wounds.

One other SAP is currently approved for clinical use by regulatory authorities besides RADA16, an 11 amino acid peptide (QQRFEWEFEQQ) known as PF_{11}-4 (commercial name Curodont™ Repair) that promotes remineralization and regression in early dental caries (Alkilzy et al., 2018; Sedlakova Kondelova et al., 2020). This review focuses on the evolution of applying RADA16 for surgical bleeding control and provides an overview of studies indicating the great potential of this unique

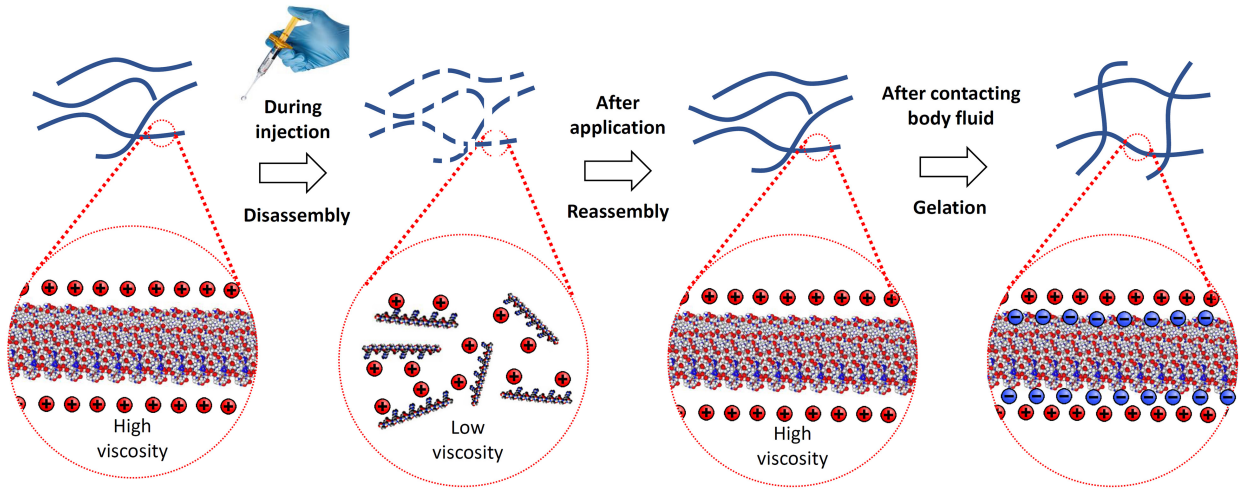

FIGURE 3 | Illustration of RADA16 structure and properties as it is applied to and gels on a wound site. Acidic aqueous solutions of RADA16 are viscous and exhibit shear-thinning and thixotropic disassembly/reassembly, which allows their easy administration to wound sites through catheters and syringes with viscosity returning immediately after administration. Upon contact with the physiological pH of body fluids including blood and interstitial fluid, the surface net charges of RADA16 nanofibers become zero resulting in the physical crosslinking by hydrophobic interactions between neighboring RADA16 nanofibers, so that RADA16 solution forms *in situ* hydrogels on the wound site and act as a physical barrier to bleeding.

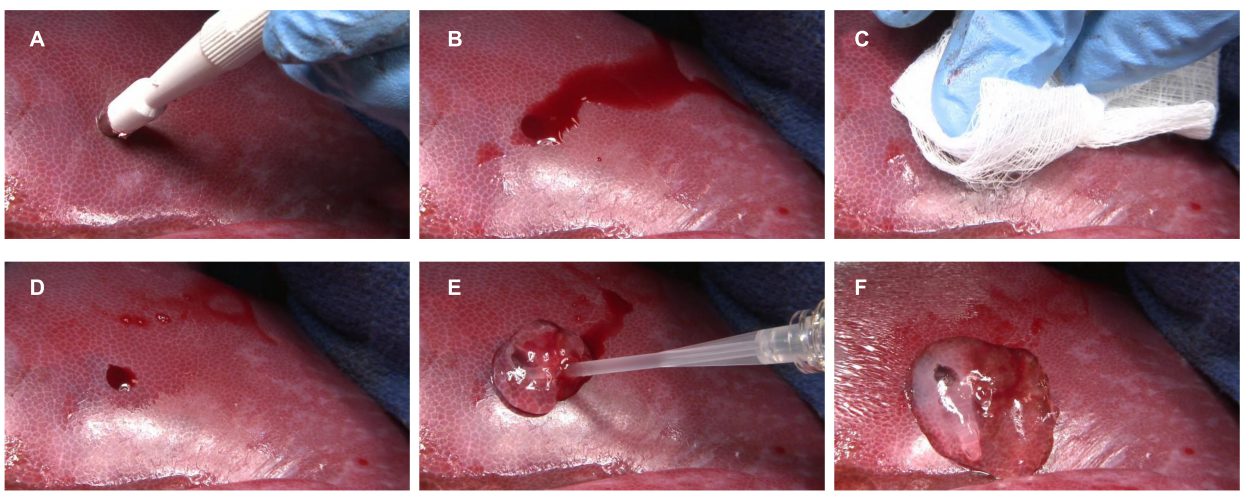

FIGURE 4 | Hemostatic use of RADA16 self-assembling peptide hydrogel to control bleeding from wound surfaces of the liver. In a porcine model, punch biopsy of the liver surface **(A)** results in frank bleeding **(B)**. After site irrigation and drying **(C)**, residual bleeding **(D)** is stopped by the easy single-syringe application of RADA16 solution **(E)**, which rapidly forms a transparent hemostatic *in situ* hydrogel barrier upon contact with physiological fluids **(F)**. This approach can be used to stop topical bleeding at surgical and wound sites in skin, organs, vessels, and other tissues.

formulation in facilitating wound healing, tissue regeneration, and as a drug-delivery depot.

TOPICAL HEMOSTATIC AGENTS FOR SURGICAL BLEEDING

Intraoperative and post-operative bleeding is a risk of all surgical procedures (Dagi, 2005), and appropriate treatment depends upon the site, cause, and extent of blood loss. Ongoing rapidly evolving technological advances have provided surgeons with an expanding diversity of innovative approaches for achieving intraoperative and post-operative hemostasis in their patients. Standard hemostatic methods range from simple pressure application, electrocautery, vessel ligation, and suturing for primary wound closure, intravenous administration of blood products, and systemic or topical delivery of procoagulation agents.

Modern biotechnology has developed many new topical hemostats for surgical use, including formulations based on oxidized cellulose, gelatin, collagen, fibrin and thrombin, hyaluronic acid, and cyanoacrylates. All of these topical

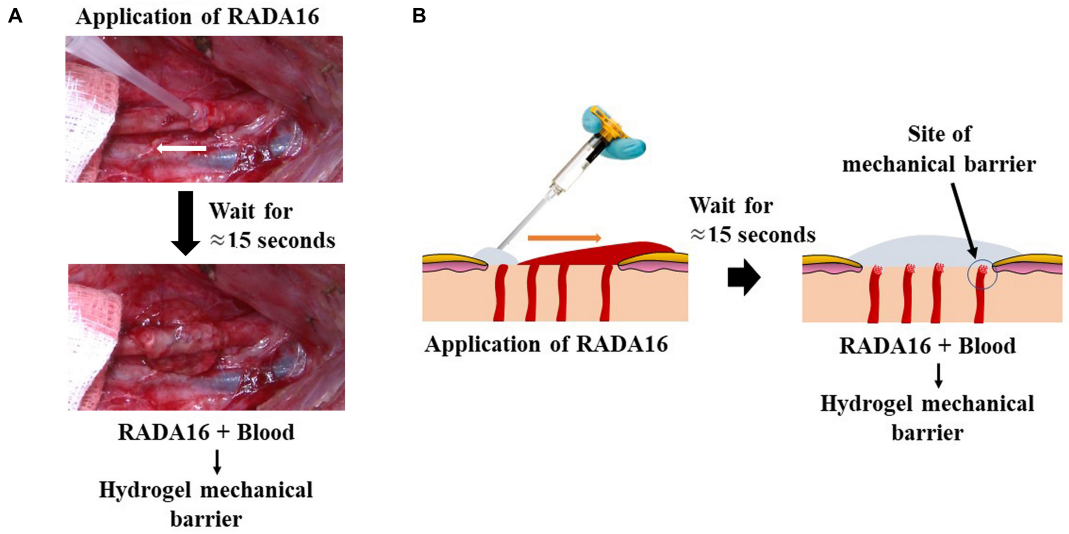

FIGURE 5 | Hemostatic mechanism of action of RADA16 self-assembling peptide hydrogel on bleeding wound surfaces. Upon contact with physiological fluids present at the surgical site, the RADA16 solution rapidly forms a transparent hemostatic *in situ* hydrogel barrier on the oozing suture lines of vascular anastomoses **(A)** and the topical/surgical oozing sites such as ulcer and resected tissue after surgery **(B)**. In a porcine model using the femoral artery, a longitudinal suture line was conventionally irrigated and sponge-dried, and RADA16 was syringe-applied to the suture line on the vessel's outer surface. The white arrow shows the direction of syringe movement during application. RADA16 solution can stop residual bleeding at blood vessel suture lines and anastomoses sites during cardiothoracic and vascular surgeries **(A)**. In a general topical/surgical bleeding site, *in situ* hemostatic hydrogel formation is initiated at the interface between the bleeding site and the applied RADA16 layer. This is represented diagrammatically **(B)**. The transparent nature of the hydrogel allows easy visualization of the surgical field and underlying sutures and bleeding sites, thus enabling the surgeon to evaluate the surgical site for satisfactory hemostasis and the possible need to perform revisions.

hemostatic classes have unique strengths and limitations (Achneck et al., 2010; Pereira et al., 2018). An ideal topical hemostatic agent would be easy to administer in diverse surgical and post-operative scenarios, rapid-acting, effective, completely biocompatible, non-animal derived, resorbable, easy to use, and cost-effective. A newer class of self-assembling topical hemostats including RADA16 may best satisfy all of these requirements.

SURGICAL HEMOSTASIS USING RADA16

PuraStat and PuraBond are 2.5% RADA16 formulations that are CE-marked as Class III medical devices for hemostatic use in humans. They are indicated as adjunctive hemostatic supplements to intraoperative ligation and suturing, to control exudative bleeding from small blood vessels and parenchyma of solid organs, at vascular anastomoses, and in the case of PuraStat from small vessels of the gastrointestinal (GI) tract mucosa following endoscopic and laparoscopic tissue resection (**Figures 4–6**; 3-D Matrix Europe SAS, 2014). A related product, PuraSinus (also a 2.5% aqueous RADA16 formulation), was cleared by the FDA in 2019 as an intraoperatively applied wound dressing for achieving hemostasis, preventing adhesion formation, and as an adjunct to wound healing after nasal surgery or trauma repair (**Figure 4–6**; US Food and Drug Administration, 2021).

Sterile-filtered acidic RADA16 hemostatic solutions exhibit long-term stability during storage at refrigerator temperatures (3-D Matrix Europe SAS, 2014; US Food and Drug Administration, 2021). Syringe delivery of SAP solutions facilitates easy one-handed application in most circumstances, without the need to mix or dissolve components before application as with some fibrin-based hemostats (Spotnitz, 2010), for example. Thus, it is "ready to use," with no preparation requirements or complicated handling that may prove cumbersome for surgeon or nurses.

The RADA16 aqueous formulations can be precisely applied within tight surgical fields; their fluidity conforms to irregular tissue surfaces, and their viscosity allows filling tissue voids and prevents unwanted migration away from the application site. Unlike some topical hemostats, RADA16 does not absorb bodily fluids and expand in volume after application, which avoids the risk of compressive injury when used in pressure-sensitive tissues or physically constrained structures such as the coronary arteries and nerves (Schonauer et al., 2004; Tomizawa, 2005; Pereira et al., 2018). The RADA16 hydrogel remains transparent even after gelation (**Figures 4**, **5**), so clear visualization of the surgical site and suture lines is maintained. This facilitates continuous surveillance of the operative area to evaluate the need for wound closure repair or revision, because any residual bleeding is instantly identifiable. Hemostats based on RADA16 can be used in combination with electrosurgical coagulation forceps, and clips and sutures may be placed through the hydrogel after application. Prophylactic administration of RADA16 solutions can also be used to reduce the likelihood of delayed-onset bleeding after surgical procedures such as endoscopic resection (Subramaniam et al., 2019).

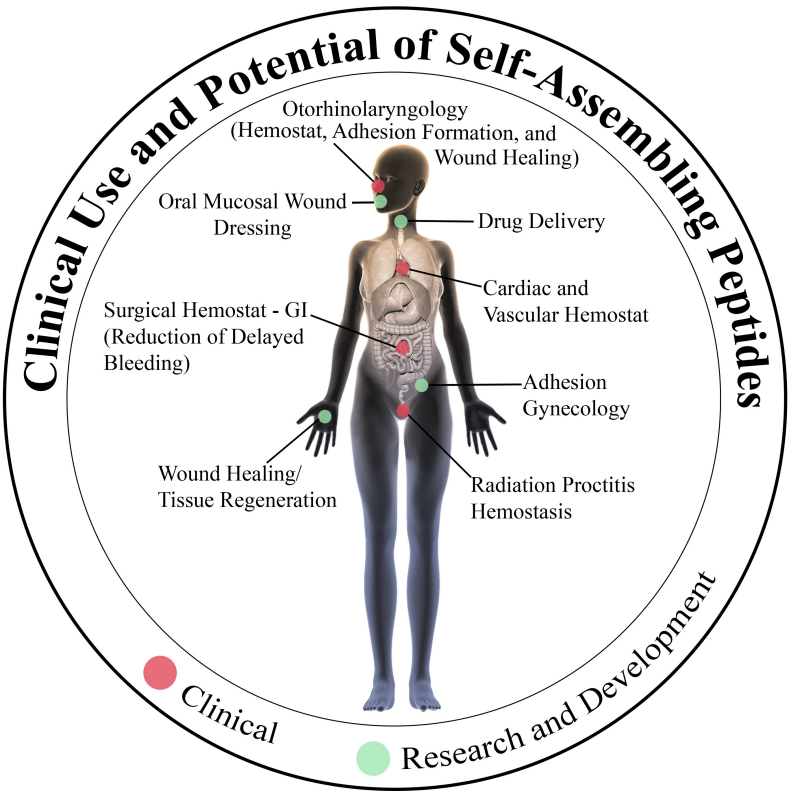

FIGURE 6 | Current and future clinical uses of the self-assembling peptide RADA16. Hemostatic RADA16 formulations are currently in use for stopping intraoperative bleeding and preventing delayed/rebleeding in cardiovascular, gastrointestinal, and otorhinolaryngological surgical procedures. Experimentation is underway to determine if RADA16 can act as a surrogate extracellular matrix to improve wound healing and tissue regeneration in diverse tissues and organs, and possibly act as a precisely regulated drug delivery depot.

Gelation of applied aqueous RADA16 begins upon contact with physiological fluid which buffers the acidic aqueous solution and provides an appropriate ionic microenvironment for hydrogel formation (Ellis-Behnke et al., 2006a; Wang et al., 2012). Exposure to tissue interstitial fluids in the absence of frank bleeding will also initiate RADA16 gelation (Subramaniam et al., 2019). Compared to animal- and plant-derived hemostats such as collagen and cellulose agents, pure synthetic SAP formulations such as RADA16 carry no risk of containing unwanted contaminants that may be pyrogenic or present other safety concerns (Genove et al., 2005). The RADA16 3D meshwork pore sizes are small enough (50–200 nm) to restrict platelet (2–3-μm diameter) and erythrocyte (6–8-μm diameter) penetration and achieve hemostasis. Instead, the blood-contacting RADA16 solution begins rapid gelation (as quickly as 15–20 s) from its surface and presents a hemocompatible surface for platelets and erythrocytes to accumulate on and initiate hemostasis, thereby enhancing the hemostasis achieved by the RADA16 matrix's physical barrier function alone (**Figure 5**; Saini et al., 2016; Taghavi et al., 2018). The hydrogel components themselves, however, do not appear to directly activate either platelets or complement C3a/C4, but do provide a substratum upon which physiological coagulation reactions, likely initiated by wound-released factors, may proceed (Saini et al., 2016; Taghavi et al., 2018). The PuraStat matrix contains 97.5% water, which allows the unhindered diffusion of soluble nutrients, growth factors, and oxygen that are essential mediators of healing at the wound surfaces.

Unlike some topical hemostatic agents, neither RADA16 hydrogel nor its constituents induce inflammatory or immune reactions (Genove et al., 2005; Wang et al., 2019). Over time, applied PuraStat and PuraSinus^{TM} are degraded to their constituent natural and entirely biocompatible L-amino acids by endogenous proteolytic/hydrolytic mechanisms, the fragments of which are then either metabolized or recycled, ultimately removing all residual RADA16 from the surgical site.

Topical hemostatic formulations should be convenient to administer in diverse operative settings, act quickly to efficiently staunch bleeding, be non-allergenic and non-inflammatory, facilitate and not inhibit wound healing, be resorbable, and cost-effective. Members of the SAP family such as RADA16 may best fulfill these criteria, and eventually become a standard-of-care for controlling and preventing mild-to-moderate bleeding associated with many surgical scenarios.

Indeed, following the approval of RADA16 for clinical use as a topical hemostatic agent, its utility has been demonstrated in multiple surgeries that are commonly performed in, for example but not limited to, cardiothoracic and vascular

surgery, gastroenterology, and otorhinolaryngology specialties (**Figure 6**).

RADA16 Hemostasis in Cardiac and Vascular Surgery

After demonstrating excellent hemostasis with 2–2.5% RADA16 solutions (from 3-D Matrix Inc.) in pre-clinical models of rabbit aortic puncture and dog aortic graft anastomoses, RADA16 was evaluated for safety and hemostatic effectiveness in human subjects undergoing cardiovascular surgery (Masuhara et al., 2012). Subjects comprised 25 individuals (22 male/3 female; age 54–80 years), who underwent coronary artery bypass grafting ($n = 9$), abdominal aortic graft replacement ($n = 4$), or peripheral artery bypass ($n = 12$) at two Japanese medical centers. The target sites for 2.5% RADA16 application were mild-to-moderate remnant bleeding at vessel-to-vessel anastomoses, graft anastomoses, and autologous vein patch plasty sites; other hemostatic approaches were employed if bleeding was copious or spurting. All subjects had been heparinized during surgery, which was reversed by protamine sulfate injection immediately after RADA16 application. Of 33 total bleeding sites, the mean application area was 3.3 cm^2 using an average of 1.5 mL (range 0.5–3.0 mL) RADA16 solution at each site. Approximately 1 mL of RADA16 was applied to coronary anastomoses, 2 mL to aortic anastomoses, and 1 mL to other peripheral vascular anastomotic sites. The immediate hemostasis effectiveness rate was 88% (29/33 sites), and mean hemostasis time was 154 ± 39 s. Effectiveness was 100% if a second treatment was used to treat post-operative bleeding. No RADA16-related safety issues were observed. The researchers concluded that RADA16 is an efficacious hemostatic agent for stopping oozing bleeding in cardiovascular surgery.

The safety, performance, and ease of use of RADA16 (PuraStat) as a hemostatic agent during left ventricular assist device (LVAD) implantation was evaluated in a prospective study of 15 patients at a single center in Germany (Morshuis et al., 2019). Application sites included the apical cannulation, and the outflow graft anastomoses. Hemostatic effectiveness was confirmed in 93% (27/29) of evaluated bleeding sites, with a rapid average time to hemostasis of 19.4 ± 13.0 s. There were no RADA16-related adverse events (AEs), and no inflammation, excessive granulation, or foreign body reaction was observed through post-operative 24 months.

Thoracic surgeons were queried about experiences using RADA16 for hemostasis in 50 consecutive cardiovascular surgery patients (mean age 72 years) at two medical centers in the United Kingdom who underwent various procedures including coronary artery bypass, valve repair or replacement, sometimes with grafting, and aortic repair or replacement (Giritharan et al., 2018). The most common application sites for RADA16 were aortotomy closures (62%) and graft suture lines (18%). Other areas of RADA16 application included oozing bleeding at cannulation sites, patch repairs, needle hole bleeds from prosthetic grafts, and at the top end anastomosis of vein grafts during coronary artery bypass. Surgeons rated the syringe-delivered product as easy-to-use, even in hard-to-reach surfaces. Hemostasis was achieved with RADA16 alone in 84% of applications and it worked well in conjunction with other hemostatic agents (e.g., Bioglue® and Fibrillar®). The distinctive transparent nature of PuraStat was appreciated because it allowed clear visualization of suture lines after its application. Mean blood product use of packed red cells, platelets, fresh-frozen plasma, and cryoprecipitate was below the national average for these procedures. No RADA16-related AEs were reported.

RADA16 Hemostasis in Gastrointestinal Endoscopic Surgery

Intraprocedural bleeding (IPB) and delayed bleeding or rebleeding are significant challenges encountered during endoscopic resection of lesions or endoscopic intervention for acute GI bleeding (Kataoka et al., 2016). Current standard treatment modalities such as electrocoagulation, argon plasma coagulation, and mechanical clip placement pose a risk of thermal injury or perforation and can be technically challenging depending on the bleeding site and endoscopist experience (Chetcuti Zammit and Sidhu, 2018). Recently, topical hemostatic powders have been introduced as additional options for managing bleeding in the GI tract (Mourad and Leong, 2018; de Rezende et al., 2019). However, these powders do not precisely cover the target lesion, but typically are dispersed well beyond the margins of the bleeding defect. Additionally, existing hemostatic powders are opaque, which can block the surgeon's view of the operative field and hinder evaluation of the bleeding source and are prone to premature gel formation that may clog the catheter (de Nucci et al., 2020). The bleeding in the GI tract can also be treated with RADA16-based hemostats, which can staunch unwanted bleeding while the transparent nature of the hydrogel maintains excellent visualization of the surgical field, and premature gelation within the catheter does not occur (Yoshida et al., 2014; Pioche et al., 2016; Subramaniam et al., 2019).

The hemostatic utility of RADA16 was reported in 12 subjects who experienced oozing bleeding during interventional endoscopic mucosal resection (EMR) or endoscopic submucosal dissection (ESD) for gastric tumors (Yoshida et al., 2014). Hemostasis with RADA16 was deemed "remarkably effective" in 11 patients and "effective" in 1 patient. Time-to-hemostasis was 105 ± 87 s, using an average of 3.3 ± 2.1 ml of RADA16 per lesion. No secondary hemorrhages occurred in any subject. Following this initial proof-of-concept study that indicated good feasibility and effectiveness, these surgeons indicated the need to perform further studies involving a larger number of patients in Japan and in Europe.

A study at two centers in France evaluated the hemostatic effectiveness of RADA16 on delayed bleeding in 56 subjects (age 67 ± 11 years) with 65 diverse GI lesions (22 stomach, 15 rectum, 10 duodenum, 8 esophagus, 7 colon, and 3 ampullary) (Pioche et al., 2016). Forty patients underwent ESD procedures and 18 EMR procedures. The rate of delayed bleeding after RADA16 use was only 6% despite 45% of lesions (29/65) having been considered at high-risk of rebleeding. No device-related AEs occurred, and endoscopists reported easy administration of the peptide solution through the catheter and continuous visualization of the resection bed.

The effectiveness of RADA16 was evaluated for preventing delayed bleeding in 45 consecutive patients (51 lesions) who underwent gastric ESD in Japan (1% RADA16 was used, termed PuraMatrix by the authors) (Uraoka et al., 2016). RADA16 was applied to the resected base at the end of the procedure. The rate of post-ESD bleeding was 2% (1/51 lesions), defined as any case requiring endoscopic or surgical intervention or having a decrease in hemoglobin level of 2 g/dL. Endoscopic follow-up was performed at 1, 4, and 8 weeks after ESD and no AEs related to RADA16 occurred. The rate of healing at week 1 and the rate of scarring at weeks 4 and 8 were higher than rates reported in the literature, suggesting that the peptide facilitated ulcer healing.

Safety, effectiveness, and technical feasibility of using RADA16 (as PuraStat; 3-D Matrix Europe SAS., France) as a topical GI hemostat was reported in a study of 100 subjects (mean age 69.3 years; 32% female) undergoing complex endoscopic resection (ER) (79 ESD, 21 EMR) procedures at a single United Kingdom medical center (Subramaniam et al., 2019). Surgeries comprised 48 esophageal, 31 colorectal, 11 gastric, and 10 duodenal sites, and 30% of the patients were on antithrombotic therapy. Mean lesion size was 3.7 ± 2.1 cm and the mean resection base area was 14.1 ± 16.5 cm^2. RADA16 was used to control IPB that occurred in 64% of cases (33 esophageal, 5 gastric, 6 duodenal, 20 colorectal), and was applied prophylactically to cover the resection base in all 100 cases. Diathermy was employed when RADA16 alone did not completely stop bleeding. RADA16 was delivered through the endoscope channel via 3-mL pre-filled syringes connected to 1600-mm (gastric) or 2200-mm (colonic) custom catheters (PuraStat Nozzle System Type-E, Top Corporation, Tokyo, Japan). RADA16 alone was an effective hemostat in 75% of these cases (73% of venous type mild oozing-to-moderate bleeding, and 50% of spurting bleeds). Thus, while having some utility for adjunctively controlling spurting bleeds, SAP-based hemostasis is best suited for controlling mild-to-moderate surgical bleeding, and for prophylactically preventing delayed bleeding onset. Only a small volume of RADA16, mean 1.8 ± 1.4 mL per lesion, was required for hemostasis of IPBs, whereas 2.6 ± 1.8 mL was used to completely cover the resection base. Hemostasis with RADA16 occurred in 70 ± 69 s. The delayed bleeding rate of 3% (two antral gastric cancer ESDs and one esophageal cancer ESD) was lower than anticipated in this high-risk cohort. Resection sites were clearly visible at all stages before, during, and after RADA16 application. The transparent and viscous nature of the RADA16 solution and resultant hydrogel permits its use as an adjunct therapy to traditional hemostatic methods such as clips or coagulation to control complex bleeding. There were no reported technical challenges such as catheter blockage and RADA16 was delivered successfully to the desired site in all cases with no technical challenges. No RADA16-associated AEs occurred.

The same United Kingdom group subsequently designed a randomized trial to compare RADA16 (PuraStat) adjunctive use (interventional group) against thermal coagulation-only (control group) for controlling IPB during ESD (Subramaniam et al., 2020). No other treatments (prophylactic coagulation or clipping) were performed in either group. This was a single-center study of 101 treatment-blinded subjects ($N = 91$ analyzed in the modified intention-to-treat cohort after exclusions and withdrawals) who underwent esophageal or colorectal ESD for lesions sized between 2 and 5 cm. Mean subject age was 71.5 ± 11.2 years in the diathermy-only control group ($n = 45$) and 68.6 ± 10.6 years in the RADA16 group ($n = 46$). Uninterrupted single antiplatelet therapy with aspirin was allowed, and all other anticoagulants were discontinued per local guidelines. Learning from their previous study (Subramaniam et al., 2019), grade 3 spurting bleeds were excluded and treated with other modalities. Fifty percent of the RADA16 group and 38% of Controls had significant comorbidities, and 40% of study participants had anticoagulant therapy stopped prior to their procedure. Lesion locations for the RADA16 group were 61% esophageal ($n = 28$) and 39% colorectal ($n = 18$), and 44% esophageal ($n = 20$) and 56% colorectal ($n = 25$) for the Control group.

The Control group had 269 IPBs in 45 subjects and RADA16 group experienced 232 IPBs in 46 patients (Subramaniam et al., 2020). The RADA16 group demonstrated a 50% reduction in the use of diathermy, with an overall 92.6% hemostatic effectiveness rate. Time-to-hemostasis was 70 ± 76 s in the RADA16 group and 78 ± 274 s in thermocoagulation-only Controls ($p = 0.14$). Total procedure times were similar in the RADA16 group at 74.2 ± 48.7 min and Controls at 80.7 ± 56.6 min. The RADA16 group received prophylactic hydrogel application to the resection base, and there was no difference in delayed bleed rates from lesions between the two groups (≈4% in both groups). Resection base healing was a secondary study end point and was significantly faster in RADA16-treated subjects than control subjects (detailed below in section "RADA16 to Enhance Wound Healing and Tissue Regeneration").

Acute gastrointestinal bleeding (AGIB) is associated with significant morbidity and mortality (Gralnek et al., 2015). Depending on the cause and location of bleeding, managing AGIB can prove challenging. A recent retrospective observational study performed at three Italian hospitals evaluated endoscopically applied RADA16 (as PuraStat; 3-D Matrix Europe SAS) as an adjunct hemostatic method in 77 patients (41 upper GI, 36 lower GI) with AGIB (de Nucci et al., 2020). Cases in which RADA16 was used for primary hemostasis or prophylactically to prevent delayed bleeding after polypectomy, EMR, or ESD were excluded. The primary outcome was immediate hemostatic effectiveness with a secondary outcome being re-bleed rate within 7 days. Bleed types were defined as either spurting ($n = 13$) or oozing ($n = 64$). Sixty-five percent (50/77) of patients had an iatrogenic bleed, primarily as delayed bleeds following EMR ($n = 29$) and IPBs during EMR ($n = 14$). Of the 27 cases with non-iatrogenic bleeds, most were due to peptic ulcer ($n = 19$) and cancer ($n = 5$). Immediate hemostasis was achieved in 90% (70/77) of cases using adjunctive RADA16. Hemostatic failure was observed in 7 of the 13 spurting bleeds, comprising duodenal ulcer ($n = 2$), gastric ulcer ($n = 2$), and post-EMR ($n = 1$ each for colonic, gastric, and duodenal sites). Of these seven spurting-bleeding cases, bleeding was slowed enough with RADA16 in five cases to allow hemostasis achievement by another approach. The rebleeding rate within 7 days post-operatively was 10% (8/77 patients), consisting of

gastric cancer ($n = 3$), gastric ulcer ($n = 2$), post-EMR gastric bleeds ($n = 2$), and duodenal ulcer ($n = 1$). Six of the eight rebleed patients were stabilized after RADA16 re-application, and the remaining two patients (both cancer) underwent surgery for bleeding. These data suggest the likely utility of RADA16 for treating AGIB, which will be assessed in more depth in planned prospective trials.

RADA16 Hemostasis in Gastrointestinal Laparoscopic Surgery

Post-operative lymphorrhea can occur following lymphadenectomy during pelvic laparoscopic or open surgery (Ghezzi et al., 2012). Colorectal dissection often exposes large raw pre-sacral surfaces and can transect lymphatics and blood vessels, causing fluid leakage into the peritoneal cavity (White et al., 1985). Excess peritoneal fluid is usually reabsorbed; however, it can cause AEs including secondary infection from colorectal anastomosis leakage, sepsis, and thrombosis from vascular compression (Rudralingam et al., 2017). Several studies have investigated the utility of hemostatic RADA16 during laparoscopic colorectal resection, to staunch bleeding and exudative fluid flow into the peritoneal cavity.

A single-center Japanese study of 20 subjects that underwent laparoscopic pelvic surgery for rectal cancer reported reduced peritoneal effusion in the half of subjects ($n = 10$) who received 1% RADA16 (as PuraMatrix) treatment (Kondo et al., 2014). RADA16 was applied to the bleeding wound at 2 mL/5-cm^2 surface area, twice, and this procedure was repeated if hemostasis was not initially achieved. Both groups were statistically similar in age, disease stage, and tumor location. Hemostasis was achieved within 5 min in all 10 RADA16-treated individuals. Operation time, bleeding volumes during surgery, hospitalization duration, and time with drain insertion were similar in both groups. Subjects receiving 1% RADA16 displayed significantly less post-operative pelvic drainage fluid (≈170 mL) compared with control subjects (≈350 mL; $p < 0.01$). No AEs occurred during the 2–3-month follow-up that were related to RADA16. The researchers concluded that 1% RADA16 was a safe and effective sealing material for preventing lymphorrhea after pelvic surgery.

A prospective observational study of 20 consecutive subjects (mean age 61 ± 2 years, range 52–70 years; 40% female) who underwent laparoscopic colorectal surgery was performed at one United Kingdom medical center (Ortenzi and Haji, 2020). Procedures included anterior resection (55%), sigmoidectomy (25%), and right hemicolectomy (20%). RADA16 (as PuraStat) was used as a method of hemostasis when conventional methods such as pressure application or thermal ablation were either insufficient or not recommended due to proximity to the ureter, pelvic/sacral veins, or other delicate structures. Mean overall surgery time was 185 ± 45 min. Mean RADA16 application time was 40 ± 17 s, and mean time to achieving hemostasis was 17.5 ± 3.5 s after treatment. Wound beds averaged 5.4 ± 2.3 cm^2. No RADA16-related post-operative complications were observed; no delayed post-operative bleeding occurred.

In an abstract presented at the 2019 European Colorectal Congress, robust hemostasis was reported when RADA16 (PuraStat) was used in laparoscopic and robotic bowel resections (Stefan et al., 2019). Of 20 consecutive rectal cancer surgical cases, 10 received RADA16 adjunctive intraoperative hemostasis; controls used traditional hemostatic approaches only. Median drain output on Day 1 was 70 mL in the RADA16 group compared with 103 mL in the No-RADA16 group, indicating superior control of wound oozing and fluid exudate accumulation with the hydrogel. Median hospitalization duration was 5 days in both groups. Post-operative septic complications occurred in one RADA16 case and four conventional hemostasis-only cases. Post-operative ileus occurred in two RADA16 subjects and five patients in the No-RADA16 group. R0 resection was achieved in all patients. The authors appreciated the utility and effectiveness of RADA16 in significantly reducing pelvic oozing and bleeding after rectal cancer surgery.

RADA16 Hemostasis for Radiation-Induced Proctitis

Radiation therapy is a common treatment modality for diverse pelvic cancers including prostate, bladder, cervical, uterine, rectal, and anal malignancies (Trzcinski et al., 2018). Radiation proctitis or proctopathy (RP) is a radiation-induced injury most commonly to the rectum seen in patients who have undergone pelvic radiotherapy (Tabaja and Sidani, 2018). Radiation proctitis can present as an acute inflammatory response involving only the superficial mucosa, or as a chronic pathogenic change in bowel function due to progressive endothelial dysfunction and vascular sclerosis, which includes bleeding, ischemia, and subsequent fibrosis (Weiner et al., 2016; White and Henson, 2021). Acute RP affects up to 75% of patients receiving pelvic radiotherapy, appearing within 1–6 weeks of treatment and with symptoms typically resolving within 3 months (Weiner et al., 2016). Chronic RP can occur months to years after radiation treatment, with a variably reported incidence ranging between 2.5 and 30%. Rectal bleeding is the most frequent symptom of chronic RP, occurring in 29–90% of patients (Tabaja and Sidani, 2018).

A report described a case series of 21 RP subjects (18 men; 17 prostate, 2 vaginal, 2 rectal; median age 76 years, range 47–84 years) who were administered RADA16 (as PuraStat) for hemostasis after rectal bleeding that remained refractory to standard treatment with sucralfate enema, hyperbaric oxygen therapy, and/or argon plasma photocoagulation (White and Henson, 2021). RADA16 was applied endoscopically at weekly intervals up to three times, with further treatments as determined by symptoms. Even in subjects with the most severe cases of RP, treatment with RADA16 improved self-recorded rectal bleeding amounts. Median episodes of bleeding reduced from 4.5 (range 0–27) to 2 (range 0–16) in the 7 days prior to the first and third treatment, respectively; Eight patients (38%) had no rectal bleeding following treatment, and 14 patients (67%) reported reduced bleeding episodes. Endoscopic grade defined by the Zinicola score (Zinicola et al., 2003) improved in 12 patients and 9 showed no change; however, 4/9 patients with no change in endoscopic grade started the study at the lowest grade and 5/9 with no grade change experienced a reduced number of bleeding episodes. Mean hemoglobin levels increased by 3.7 g/L

from baseline to third treatment, and by 6.7 g/L from baseline to last follow up (median 12 months; range 3–18 months). Of patients followed up >12 months beyond their first RADA16 treatment, only one had recurrence of significant bleeding. Of 6 blood transfusion-dependent patients, four required no further transfusions; of the two patients that required additional transfusions, one had thrombocytopenia secondary to cirrhosis and the other had recurrent severe bleeding upon resuming aspirin monotherapy, which was then stopped.

Additional early data has been collected in a United Kingdom registry of prospective endoscopic studies to evaluate the role of RADA16 in diverse GI bleeding events, including RP. Initial data were presented at the 2019 European Society of Gastroenterology Congress detailed 226 procedures across three indications, including 22 RP cases (Arndtz et al., 2020). In these RP cases, RADA16 was used as a sole therapy in 14 individuals and secondary therapy in 8, and all resulted in a recorded improvement in patient-reported symptom score and measured hemoglobin levels. These results with RP cases support the expanded use of RADA16-based hemostasis to effectively treat bleeding sequelae arising from diverse iatrogenic causes, including pathologies arising from therapeutic radiation administration.

RADA16 for Otorhinolaryngological Surgery

A case series report was the first to evaluate using RADA16 (as PuraStat) as a hemostatic agent in endonasal procedures (Lee et al., 2017). In that study, 60 subjects with severe allergic rhinitis and intractable nasal obstruction underwent endoscopic turbinoplasty by a single surgeon at three Australian hospitals. Remnant bleeding commonly occurs after turbinate resection surgery because the tissues are highly vascularized. This is typically an outpatient procedure and, after attempting conventional hemostatic approaches, patients are frequently discharged with nasal packaging tamponade to control bleeding. Nasal packing can cause discomfort, endonasal adhesions and infection, and delay healing (Fairbanks, 1986). One mL of RADA16 could cover an area of 1 cm^2, so a single 5-mL syringe was sufficient for each bilateral turbinoplasty. The fluidity and transparent nature of the RADA16 solution allowed easy vertical application that ensured thorough coverage of the resected area while maintaining good wound visibility. No subject experienced adhesion formation or rebleeding, and all demonstrated normal operative site healing. Subsequently, another group reported the successful application of RADA16 for hemostasis in a 49-year-old man who underwent endoscopic endonasal surgery in Australia to divide a severe nasopharyngeal stenosis that arose secondary to chemoradiotherapy for squamous cell cancer of the tongue base (Wong et al., 2020). The patient was discharged the same day, having reported immediate post-operative improvement in subjective nasal patency. At 2 months follow-up, no rebleeding was reported by the patient, and complete resolution of his nasal obstructive symptoms was maintained. No evidence of recurrence or residual adhesion tissue was noted. These initial results suggest that RADA16 is suitable for consideration as an appropriate hemostatic agent in endonasal surgery. As mentioned previously, PuraSinus^{TM} has been cleared in the United States as a sinus hemostat but is also indicated for the prevention of adhesion formation and as an adjunct to wound healing (**Figure 6**).

RADA16 FOR WOUND HEALING AND TISSUE REGENERATION

Appropriate wound healing and tissue regeneration relies on a complex orchestration of multiple influences within the wound microenvironment, including cytokine, chemokine, and growth factor signals that recruit and activate cellular participants, vascularization and oxygenation status, mechanical forces, and the construction and remodeling of an ECM scaffolding (Rodrigues et al., 2019). The composition and structure of synthetic mesh-like ECM biomimetics, such as the interwoven fibers of the RADA16 hydrogel, may provide a favorable template for the repair of tissues damaged by surgery, pathology or trauma, including those of skin, bone, nerve, heart, liver, and other organs (**Figure 6**; Yi et al., 2017; Lee et al., 2019; Wang et al., 2019; Gelain et al., 2020).

Support for using RADA16 as an ECM surrogate for wound healing has been strengthened by numerous *in vitro* models in which RADA16 hydrogel supported proliferation, and differentiation of diverse cell types (Kakiuchi et al., 2013; Wang et al., 2019; Song et al., 2020). The simple peptide structure of RADA16 allows easy addition of various chemical moieties, which can then be rapidly screened for functional effects in wound-healing models (Bradshaw et al., 2014). An elegant 3D laboratory model of human skin was created by embedding human dermal fibroblasts and keratinocytes within a collagen type-I matrix (Schneider et al., 2008). Punchouts of these model tissue constructs underwent re-epithelialization at an accelerated rate when overlaid with 1% RADA16 hydrogel compared to healing observed without treatment, and even more so when epidermal growth factor was embedded within the RADA16 matrix. Thus, in addition to assisting wound healing by providing a physical 3D scaffold resembling native ECM, the RADA16 nanoporous matrix might also serve as a useful reservoir for the regulated release of therapeutic drugs and biologics (**Figure 4**).

Cartilage and bone defects might also be amenable to RADA16-mediated regenerative approaches. For example, chondrocytes embedded in RADA16 hydrogels maintained their differentiated status and expressed collagen type-II and glycosaminoglycans, with expression continuing to intensify through 3 weeks of culture (Liu et al., 2010). Scaffolds of RADA16 hydrogel containing co-embedded osteogenic adipose-derived stem cells and endothelial adipose-derived stem cells in a 1:1 ratio demonstrated both strong osteogenic and angiogenic differentiation, as gauged by expression of multiple cell-specific markers (Yang et al., 2018). Thus, RADA16 may serve as a useful scaffold for treating damaged or eroded cartilage and bone defects.

Animal studies have also supported a promising role for RADA16 not only as a hemostatic agent, but to facilitate

wound healing, tissue regeneration, and angiogenesis (Cheng et al., 2013a,b; Wang et al., 2017, 2019; Gelain et al., 2020; Han et al., 2020). In a rat model of middle ear mucosal damage, cultured middle-ear mucosal epithelial cells were able to successfully repopulate and heal mucosal defects when cells were administered within a 2.5% RADA16 hydrogel matrix (as PuraStat), but instillation of cells suspended in culture media alone were unable to survive and repair the damaged mucosa (Akiyama et al., 2013). Purposefully created periodontal defects in rats showed significant healing and bone regeneration at 4 weeks when defects were initially filled with 2.5% RADA16 solution compared to defects filled with Matrigel (a mouse-derived ECM-like product) or left unfilled (Takeuchi et al., 2016). In a rat model of inflammatory colitis simulated by chemically induced colon mucosal ulceration, topical application of 1% RADA16 (as PuraMatrix) significantly suppressed colonic injury as viewed by endoscopy, downregulated expression of inflammatory cytokines, and increased expression of wound-healing factors (Araki et al., 2021). Topical application of RADA16 in an assessor-blinded porcine EMR study suggested enhanced neomucosal coverage and less submucosal damage with RADA16 versus no-RADA16 treatment, at 6 days after lesion creation (Tsiamoulos et al., 2017). Furthermore, a more recent study demonstrated that RADA16 reduces the incidence of esophageal stricture after 5-cm circumferential ESD in a porcine model by facilitating re-epithelialization (Oumrani et al., 2019, 2021). In a rat bone defect model, RADA16 formulations supported osteoregeneration, and showed utility as a depot for fibroblast growth factor (He et al., 2017). Human-induced pluripotent stem cells were encapsulated within RADA16 microspheres before induction toward a neural phenotype and transplantation into the brains of immunocompromised mice (Francis et al., 2016). The RADA16-encapsulated neurons displayed robust survival and neurite outgrowth *in vivo*, outnumbering surviving neurons that had been transplanted in suspension by two orders of magnitude. When injected at the injury site in rats with transected sciatic nerves, RADA16 hydrogel supported axonal outgrowth from damaged neurons, and the addition of functional motifs to the peptide monomers enhanced this activity. Similarly, the RADA16 meshwork is a permissive milieu for axonal regrowth from the severed optic tract of adult hamsters, sufficient to restore vision at least partially (Ellis-Behnke et al., 2006b). These observations suggest that RADA16 and related SAPs might deserve consideration as potentially effective reprogramming and transplantation vehicles for neurons and other cell types in future regenerative medicine studies (**Figure 6**).

Peptide chemistry allows the precise attachment of various functional moieties to RADA16 to confer novel biological activities to the hydrogel including enhanced tissue regenerative capacity. For example, GRGDS and YIGSR are peptide sequences unique to the ECM proteins fibronectin and laminin-1, respectively, which mediate cell adhesion to the matrix. In a rat liver injury model, application of 1% RADA16, either alone or coupled to either ECM moiety, resulted in more extensive wound healing after 2 weeks versus thermocautery control sites (Cheng et al., 2013a). The number of proliferating hepatocytes was greater in wounds managed with RADA16 coupled to either ECM sequence than in the RADA16-alone or control groups. In this model, dissolution of all three hydrogel scaffolds was obvious within 3–7 days and was complete by 2 weeks. In a rat traumatic brain injury model (forebrain punch biopsy), neural stem cells were suspended in either plain 1% RADA16 or in RADA16 coupled to another functional laminin motif IKVAV, and suspensions were applied to wound sites to polymerize (Cheng et al., 2013b). Addition of the ECM motif to RADA16 enhanced stem cell differentiation in hydrogels toward a neuronal phenotype and minimized astrocyte formation at 3 and 6 weeks compared to cells encapsulated in unmodified RADA16, suggesting enhanced regenerative capacity in functionalized RADA16 hydrogels. Histological analysis of the wound sites revealed hydrogel presence at 1 week, which was not visible at 3 weeks suggesting complete scaffold dissolution by this time. A subsequent study demonstrated enhanced endogenous neural stem cell differentiation, neurogenesis and functional recovery, and neovascularization in a zebrafish brain injury model when 1% RADA16 alone or coupled to SVVYGLR, an angiogenic α-integrin-binding sequence derived from osteopontin, was applied to wound sites (Wang et al., 2017). Thus, diverse pre-clinical experiments have demonstrated the unique potential of RADA16 and several of its variants in facilitating the recruitment, proliferation, and differentiation of multiple cell types, resulting in effective wound healing, neurogenesis, and angiogenesis. Future trials will capitalize on these observations to explore potential new clinical uses for RADA16 as a surrogate ECM in human regenerative medicine.

Several of the clinical trials mentioned earlier also explored RADA16 effects beyond achieving hemostasis, including observations on wound healing in humans. Gastric ESD ulcer healing by was assessed by evaluating mucosal coverage and margins of the ulcer (Uraoka et al., 2016), according to the Sakita classification (Sakita et al., 1971). An increased healing rate was observed after 1 week, and scarring was more extensive than anticipated between 4 and 8 weeks post-operatively, leading the authors to conclude that RADA16 might improve healing of ESD-induced gastric ulcers. In the randomized control trial that explored RADA16 use during esophageal and colorectal ESD (Subramaniam et al., 2020), resection base healing was a secondary study end point. At 4 weeks post-procedure, 75% of RADA16 ulcers showed either complete wound healing or scarring compared with only 54% of ulcers in the diathermy-only group. At Week 4, significantly more RADA16 subjects, 49%, achieved complete wound healing compared with 25% of control subjects. In a series of individuals who underwent bilateral turbinectomy, RADA16 was associated not only with effective hemostasis but also with the lack of adhesion formation during healing (Lee et al., 2017). Taken together, it appears that the porous meshwork of the RADA16 hydrogel not only functions as an effective barrier to bleeding, but also might support wound healing by acting as a temporary scaffold that facilitates the integration, proliferation, and maturation of the cells needed to create new tissue. Incorporating specific structural modifications into the

RADA16 molecule might allow us to tailor hydrogel biological activities to provide optimal regenerative environments for different clinical applications.

RADA16 HYDROGELS AS DRUG RESERVOIR AND DELIVERY SYSTEMS

The RADA16 nanoporous matrix might also serve as a useful reservoir for the regulated release of therapeutic drugs and biologics, to enhance various biological processes such as angiogenesis and neurogenesis that are important in wound healing and tissue regeneration. Sections of surrogate human skin tissue were created *in vitro* by embedding human dermal fibroblasts within a collagen type-I matrix and overlaying these with a stratified layer of keratinocytes (Schneider et al., 2008). After punch-out "wounding" of the skin construct, a drop of 1% RADA16 suspension was placed into and above the wound to polymerize. Inclusion of recombinant epidermal growth factor (10 μg/mL) in the RADA16 hydrogel caused an ≈4-fold increase in re-epithelialization over the wounded region versus RADA16 alone. Sequential measurements of the tissue culture media indicated that growth factor was released from the RADA16 hydrogel in a linear fashion through 24 h, at which point 65% of incorporated cytokine had been released, and significant addition growth factor egress from the hydrogel was not observed afterward. Furthermore, in a rat myocardial infarction model, injection of 1% RADA16-II (RARADADARARADADA) suspension containing platelet-derived growth factor-BB (PDGF) into the infarct border zone immediately after infarction was cardioprotective and resulted in improved cardiac function and reduced cardiomyocyte apoptosis measured 2 weeks post-infarction (Hsieh et al., 2006). Myocardial cell proliferation, neovascularization, regional blood flow, and local inflammation were not changed by RADA/PDGF treatment. Without the SAP scaffold, PDGF-BB injected alone rapidly disappeared from injected sites within 24 h, and only a negligible amount of PDGF-BB could be detected after 3 days. In contrast, when PDGF-BB was co-administered with RADA16-II, the resultant hydrogel scaffolding facilitated controlled growth factor release, and 16.1 ± 2.4% of PDGF-BB remained at the targeted delivery sites after 14 days.

Converse to regenerative and wound healing applications, RADA16 has also been explored as a potential delivery vehicle for antineoplastic agents, to destroy solid tumors. Syringe-delivery of a liquid therapeutic/RADA16 mixture directly into a solid tumor might polymerize into a biodegradable hydrogel that restricts gradual drug release to the local environment. This might be a promising approach to effectively obliterate individual tumors while minimizing the systemic toxicity associated with many cancer drugs. When the potent antitumor drug paclitaxel was embedded in RADA16 matrices, drug release kinetics were dependent upon RADA16 concentrations used to form the hydrogels, and controlled release from 1% RADA16 markedly inhibited proliferation of the human breast cancer cell line MDA-MB-435S for at least 1 week (Liu et al., 2011). Another group performed pre-clinical studies to explore the idea of loading RADA16 with tamoxifen and injecting it directly within the breast following lumpectomy, to exert cytotoxicity on any remnant breast cancer cells (Wu et al., 2017). Other peptide-based hydrogels and nanogels have also been explored *in vitro* to deliver doxorubicin, an antineoplastic drug used in stomach, bladder, breast, lung, and ovarian cancer therapies (Gallo et al., 2021).

Structural modifications to RADA16 can alter its function as a hydrogel drug delivery system. One group created hydrogels out of two differently modified RADA16 peptides with different functions (Huang et al., 2019). One peptide was end-linked to a QLK motif that facilitates crosslinking of the peptides by transglutaminase activity. Microbial transglutaminase was used to mimic the bioactivity expected from the intrinsic coagulation factor XIIIa, an endogenous enzyme activated by thrombin cleavage. Subsequent covalent crosslinks are resistant to proteolytic degradation thus providing increased mechanical stability of the hydrogel. The second RADA peptide was modified by the attachment of an LRK moiety, which regulates binding to heparan sulfates that are integral glycosaminoglycan components of native ECM. Importantly, heparan sulfates form non-covalent complexes with potent angiogenic molecules such as vascular endothelial growth factor (VEGF) and growth promoters such as hepatocyte growth factor (Rajangam et al., 2006). *In vitro*, enzyme crosslinking of 2% RADA16-QLK/LRK resulted in a 5-fold increase in hydrogel rheological stiffness. Crosslinked hydrogels were more resistant to degradation, showing 20% dissolution in 3 days versus 40% in non-crosslinked gels. At the 35-day study terminus, 61% of crosslinked and 82% of control gel volumes were degraded. Modified RADA16 hydrogels spiked with heparan-binding cytokines before polymerization displayed reproducible release kinetics *in vitro*. With VEGF, 32% of total cytokine was released within 3 days, and 62% through 28 days. In a chick chorioallantoic membrane assay, the modified RADA16 formulation resulted in significantly greater angiogenesis with larger-caliber vessels, when the applied hydrogel contained angiogenic growth factors. Thus, two minor RADA16 modifications resulted in significantly strengthened hydrogels with sustained growth factor release over 4 weeks. In a rodent myocardial infarction model, RADA16 was modified by attachment of a LRK-containing sequence and injected with VEGF into infarction-damaged hearts resulted in increased angiogenesis, better cell survival, less scar formation, and improved cardiac function at 1 month than injecting unmodified RADA16 plus VEGF (Guo et al., 2012). Such studies demonstrate the feasibility of modulating RADA16 structure to sequester and regulate the controlled release of therapeutic agents that drive wound healing and tissue regeneration.

Release kinetics of cytokines and other therapeutic agents from RADA-based hydrogels can likely be fine-tuned by altering the peptide concentration and chemistry (Gelain et al., 2020). Thus, in addition to assisting wound healing by providing a physical 3D scaffold resembling native ECM, both unmodified and structurally tailored RADA16 hydrogels might have unique abilities to direct specific tissue healing and reconstruction events through the selective presentation and release of incorporated biologics (Lee et al., 2019; Wang et al., 2019; Gelain et al., 2020).

POTENTIAL LIMITATIONS OF RADA16 HYDROGELS

For hemostatic applications, RADA16 formulations are currently approved as topical agents to halt oozing and low-pressure bleeding. Unmodified RADA16's shear-thinning/thixotropic nature probably precludes its utility in high shear environments (e.g., intra-arterial) where strong hemodynamic and rheological forces might inordinately increase the hydrogel's disassembly rate. Hydrogel resistance to shear stress can be increased by either increasing the peptide concentration to form more durable hydrogels or by modifying the RADA16 structure by attaching motifs that enhance crosslinking or adhesion to surrounding tissues or endogenous coagulation components to provide additional anchoring strength. Still, for currently approved hemostatic applications, predictable RADA16 hydrogel dissolution to non-toxic metabolites occurs comfortably after the risk of delayed bleeding has passed and is a desirable trait.

As a surrogate ECM scaffolding for facilitating wound healing and tissue regeneration, the ability of RADA16 hydrogels to fill tissue voids and easy syringe and catheter application to difficult-to-reach sites are positive attributes. In some highly mobile or load-bearing sites such as joints and bones, different resident tissues and structures (e.g., tendon/sheath appositions within tendon sheaths, ligament insertions, long bone appositions after repair/reconstruction) are subject to variable and often strong mechanical forces. In these environments, the limited mechanical strength of RADA16-based hydrogels might risk damage to the structural integrity of the surrogate hydrogel ECM, and potentially compromise or delay regenerative outcomes. Although modifications to the RADA16 peptide concentration or chemistry might appreciably increase intrinsic gel strength and strengthen hydrogel attachments to surrounding tissues, hydrogel-based wound healing/regenerative approaches will still probably remain suitable only for environments where physical forces are either not extreme or can be temporarily restrained, for example by splinting/casting/anchoring (joint and long bone applications) or suturing (soft but mobile tissue applications).

Alternatively, to strengthen RADA16-based hydrogels, RADA16 might be co-polymerized with more mechanically durable polymeric scaffold materials. For example, composite nanoscaffolds created with functionalized RADA16 blended and co-polymerized within electrospun poly (L-lactic-co-glycolic acid) nanofibers generates a 3D matrix that displays stronger mechanical properties and slower degradation than RADA16 alone and promoted expression of molecular indicators of nerve repair and cell survival in an *in vitro* rat Schwann cell model (Nune et al., 2016). Similarly, a composite of 1% RADA16 modified with an RGD integrin binding motif was polymerized interspersed with a 5% photocrosslinkable polyester nanofiber suspension, and the resulting hydrogel was nearly three-fold stronger (storage modulus, G′) than 1% RADA16-only hydrogels and also had a reduced degradation rate (Zhai et al., 2020). Additionally, this combination improved wound healing in a rat spinal cord transection model. The ability to easily modulate RADA16-based hydrogel structure, cell and molecular interactions, and physical durability offer diverse possibilities for creative design of new hemostatic, tissue regenerative, and drug delivery platforms.

CONCLUSION

Synthetic SAPs, exemplified in this review by RADA16, are unique in both character and in potential clinical utility. The ability of SAPs to spontaneously form higher-order structures, and our growing aptitude at customizing these peptides to selectively modify their polymeric architecture and associated biological interactions, together allow diverse new opportunities for biomedical exploration and therapeutic development. RADA16 has proven utility as an effective topical hemostatic agent in a variety of surgical and pathological scenarios. Now, accelerating research continues to clarify the functionality of RADA16 as a surrogate ECM that may have meaningful practical implications for wound healing in diverse organs. Additionally, the permissive microenvironment provided by the RADA16 nanofiber meshwork might be harnessed and modified to optimally synchronize the complex mechanics of cell and tissue development that are necessary for regenerative medicine applications. The unique and customizable nature of RADA16 and other SAPs also provides new prospects for use as a depot and targeted delivery system for drugs and biopharmaceuticals.

AUTHOR CONTRIBUTIONS

All authors were involved in all facets of literature review, manuscript construction and content, and critical revisions and approved the submitted version.

FUNDING

This work was supported by 3-D Matrix, Ltd., Tokyo, Japan.

ACKNOWLEDGMENTS

The authors thank Subinoy Das, MD, FACS (U.S. Institute for Advanced Sinus Care and Research, Columbus, Ohio) and Hiroyuki Aihara, MD, Ph.D. (Brigham and Women's Hospital, Boston, MA) for their suggestions and critical review of the manuscript. The authors also thank Matthew Silverman, Ph.D. (Writing Assistance Inc., Plymouth, MN, United States and Biomedical Publishing Solutions, Delray Beach, FL, United States) for expert writing and editorial assistance. Silverman's fees were paid by 3-D Matrix, Ltd.

REFERENCES

Achneck, H. E., Sileshi, B., Jamiolkowski, R. M., Albala, D. M., Shapiro, M. L., and Lawson, J. H. (2010). A comprehensive review of topical hemostatic agents: efficacy and recommendations for use. *Ann. Surg.* 251, 217–228. doi: 10.1097/SLA.0b013e3181c3bcca

Akiyama, N., Yamamoto-Fukuda, T., Takahashi, H., and Koji, T. (2013). In situ tissue engineering with synthetic self-assembling peptide nanofiber scaffolds, PuraMatrix, for mucosal regeneration in the rat middle-ear. *Int. J. Nanomed.* 8, 2629–2640. doi: 10.2147/IJN.S47279

Alkilzy, M., Santamaria, R., Schmoeckel, J., and Splieth, C. (2018). Treatment of carious lesions using self-assembling peptides. *Adv. Den Res.* 29, 42–47. doi: 10.1177/0022034517737025

Argudo, P. G., Contreras-Montoya, R., Álvarez de Cienfuegos, L., Cuerva, J. M., Cano, M., et al. (2018). Unravelling the 2D self-assembly of Fmoc-dipeptides at fluid interfaces. *Soft Matter* 14, 9343–9350. doi: 10.1039/c8sm01508b

Araki, T., Mitsuyama, K., Yamasaki, H., Morita, M., Tsuruta, K., Mori, A., et al. (2021). Therapeutic potential of a self-assembling peptide hydrogel to treat colonic injuries associated with inflammatory bowel disease. *J. Crohns. Colitis* jjab033. doi: 10.1093/ecco-jcc/jjab033 [Epub ahead of print].

Arndtz, S., Subramaniam, S., Hossain, E., Abdelrahim, M., Ang, Y., Beintaris, I., et al. (2020). Outcomes from the UK PuraStat registry – a multi-centre prospective observational study to evaluate the role of PuraStat in the management of gastrointestinal bleeding (POPS). Abstract (virtual). ESGE Days Congress, April 23–25, 2020. *Endoscopy* 52, S1–S350. doi: 10.1055/s-0040-1704116

Bradshaw, M., Ho, D., Fear, M. W., Gelain, F., Wood, F. M., and Iyer, K. S. (2014). Designer self-assembling hydrogel scaffolds can impact skin cell proliferation and migration. *Sci. Rep.* 4:6903. doi: 10.1038/srep06903

Chen, P. (2005). Self-assembly of ionic-complementary peptides: a physicochemical viewpoint. *Colloids Surf.* 261, 3–24.

Cheng, T. Y., Chen, M. H., Chang, W. H., Huang, M. Y., and Wang, T. W. (2013b). Neural stem cells encapsulated in a functionalized self-assembling peptide hydrogel for brain tissue engineering. *Biomaterials* 34, 2005–2016. doi: 10.1016/j.biomaterials.2012.11.04

Cheng, T. Y., Wu, H. C., Huang, M. Y., Chang, W. H., Lee, C. H., and Wang, T. W. (2013a). Self-assembling functionalized nanopeptides for immediate hemostasis and accelerative liver tissue regeneration. *Nanoscale* 5, 2734–2744. doi: 10.1039/c3nr33710c

Chetcuti Zammit, S., and Sidhu, R. (2018). Small bowel bleeding: cause and the role of endoscopy and medical therapy. *Curr. Opin. Gastroenterol.* 34, 165–174. doi: 10.1097/MOG.0000000000000429

Choi, S. J., Jeong, W. J., Kang, S. K., Lee, M., Kim, E., Ryu, et al. (2012). Differential self-assembly behaviors of cyclic and linear peptides. *Biomacromolecules* 13, 1991–1995. doi: 10.1021/bm3005947

Cormier, A. R., Lopez-Majada, J. M., Alamo, R. G., and Paravastu, A. K. (2013). Distinct solid and solution state self-assembly pathways of RADA16-I designer peptide. *J. Pept. Sci.* 19, 477–484. doi: 10.1002/psc.2524

Corning Life Sciences Inc (2021). *Corning® PuraMatrix™ Peptide Hydrogel: Frequently Asked Questions*. Available online at: https://www.corning.com/media/worldwide/global/documents/faq_DL_028_Corning_PuraMatrix_Peptide_Hydrogel.pdf (accessed April 22, 2021).

3-D Matrix Europe SAS (2014). *PuraStat® Absorbable Haemostatic Material Instructions for Use*. Available online at: https://www.nicolai-medizintechnik.de/anweisungen/544_IFU_PuraStat_03_2014.pdf (accessed April 22, 2021).

Dagi, T. F. (2005). The management of postoperative bleeding. *Surg. Clin. North Am.* 85, 1191–1213. doi: 10.1016/j.suc.2005.10.013

de Nucci, G., Reati, R., Arena, I., Bezzio, C., Devan, M., della Corte, C., et al. (2020). Efficacy of a novel self-assembling peptide hemostatic gel as a rescue therapy for refractory acute gastrointestinal bleeding. *Endoscopy* 52, 773–779. doi: 10.1055/a-1145-34

de Rezende, D. T., Brunaldi, V. O., Bernardo, W. M., Ribeiro, I. B., Mota, R. C. L., Baracat, F. I., et al. (2019). Use of hemostatic powder in treatment of upper gastrointestinal bleeding: a systematic review and meta-analysis. *Endosc. Int. Open* 7, E1704–E1713. doi: 10.1055/a-0977-2897

Edwards-Gayle, C. J. C., and Hamley, I. W. (2017). Self-assembly of bioactive peptides, peptide conjugates, and peptide mimetic materials. *Org. Biomol. Chem.* 15, 5867–5876. doi: 10.1039/c7ob01092c

Ellis-Behnke, R. G., Liang, Y., Tay, D., Kau, P., Schneider, G., Zhang, S., et al. (2006a). Nano hemostat solution, immediate hemostasis at the nanoscale. *Nanomed* 2, 207–215.

Ellis-Behnke, R. G., Liang, Y. X., You, S. W., Tay, D. K., Zhang, S., So, K. F., et al. (2006b). Nano neuro knitting: peptide nanofiber scaffold for brain repair and axon regeneration with functional return of vision. *Proc. Natl. Acad. Sci. U.S.A.* 103, 5054–5059. doi: 10.1073/pnas.0600559103

Fairbanks, D. N. (1986). Complications of nasal packing. *Otolaryngol. Head Neck Surg.* 94, 412–415. doi: 10.1177/019459988609400337

Francis, N. L., Bennett, N. K., Halikere, A., Pang, Z. P., and Moghe, P. V. (2016). Self-assembling peptide nanofiber scaffolds for 3-D reprogramming and transplantation of human pluripotent stem cell-derived neurons. *ACS Biomater. Sci. Eng.* 2, 1030–1038. doi: 10.1021/acsbiomaterials.6b00156

Gallo, E., Diaferia, C., Rosa, E., Accardo, A., and Morelli, G. (2021). Peptide-based hydrogels as delivery systems for doxorubicin. *J. Pept. Sci.* 16, 1617–1630. doi: 10.1002/psc.3301

Gelain, F., Luo, Z., and Zhang, S. (2020). Self-assembling peptide EAK16 and RADA16 nanofiber scaffold hydrogel. *Chem. Rev.* 120, 13434–13460. doi: 10.1021/acs.chemrev.0c00690

Genove, E., Shen, C., Zhang, S. G., and Semino, C. E. (2005). The effect of functionalized self-assembling peptide scaffolds on human aortic endothelial cell function. *Biomaterials* 26, 3341–3351.

Ghezzi, F., Uccella, S., Cromi, A., Bogani, G., Robba, C., Serati, M., et al. (2012). Lymphoceles, lymphorrhea, and lymphedema after laparoscopic and open endometrial cancer staging. *Ann. Surg. Oncol.* 19, 259–267. doi: 10.1245/s10434-011-1854-5

Giritharan, S., Salhiyyah, K., Tsang, G. M., and Ohri, S. K. (2018). Feasibility of a novel, synthetic, self-assembling peptide for suture-line haemostasis in cardiac surgery. *J. Cardiothorac. Surg.* 13:68. doi: 10.1186/s13019-018-0745-2

Gralnek, I. M., Dumonceau, J. M., Kuipers, E. J., Lanas, A., Sanders, D. S., Kurien, M., et al. (2015). Diagnosis and management of nonvariceal upper gastrointestinal hemorrhage: European Society of Gastrointestinal Endoscopy (ESGE) Guideline. *Endoscopy* 47, a1–46. doi: 10.1055/s-0034-1393172

Guo, H. D., Cui, G. H., Yang, J. J., Wang, C., Zhu, J., Zhang, L. S., et al. (2012). Sustained delivery of VEGF from designer self-assembling peptides improves cardiac function after myocardial infarction. *Biochem. Biophys. Res. Commun.* 424, 105–111. doi: 10.1016/j.bbrc.2012.06.080

Han, C., Zhang, Z., Sun, J., Li, K., Li, Y., Ren, C., et al. (2020). Self-asssembling peptide-based hydrogels in angiogenesis. *Int. J. Nanomed.* 15, 10257–10269. doi: 10.2147/IJN.S277046

Hartgerink, J. D., Beniash, E., and Stupp, S. I. (2001). Self-assembly and mineralization of peptide-amphiphile nanofibers. *Science* 294, 1684–1688. doi: 10.1126/science.1063187

He, B., Ou, Y., Chen, S., Zhao, W., Zhou, A., Zhao, J., et al. (2017). Designer bFGF-incorporated d-form self-assembly peptide nanofiber scaffolds to promote bone repair. *Mater. Sci. Eng. C. Mater. Biol. Appl.* 74, 451–458. doi: 10.1016/j.msec.2016.12.042

Hsieh, P. C., Davis, M. E., Gannon, J., MacGillivray, C., and Lee, R. T. (2006). Controlled delivery of PDGF-BB for myocardial protection using injectable self-assembling peptide nanofibers. *J. Clin. Invest.* 116, 237–248. doi: 10.1172/JCI25878

Huang, L. C., Wang, H. C., Chen, L. H., Ho, C. Y., Hsieh, P. H., Huang, M. Y., et al. (2019). Bioinspired self-assembling peptide hydrogel with proteoglycan-assisted growth factor delivery for therapeutic angiogenesis. *Theranostics* 9, 7072–7087. doi: 10.7150/thno.35803

Kakiuchi, Y., Hirohashi, N., and Murakami-Murofushi, K. (2013). The macroscopic structure of RADA16 peptide hydrogel stimulates monocyte/macrophage differentiation in HL60 cells via cholesterol synthesis. *Biochem. Biophys. Res. Commun.* 433, 298–304. doi: 10.1016/j.bbrc.2013.02.105

Kataoka, Y., Tsuji, Y., Sakaguchi, Y., Minatsuki, C., Asada-Hirayama, I., Niimi, K., et al. (2016). Bleeding after endoscopic submucosal dissection: risk factors and preventive methods. *World J. Gastroenterol.* 22, 5927–5935. doi: 10.3748/wjg.v22.i26.5927

Kondo, Y., Nagasaka, T., Kobayashi, S., Kobayashi, N., and Fujiwara, T. (2014). Management of peritoneal effusion by sealing with a self-assembling nanofiber polypeptide following pelvic surgery. *Hepatogastroenterology* 61, 349–353.

Lee, S., Trinh, T. H. T., Yoo, M., Shin, J., Lee, H., Kim, J., et al. (2019). Self-assembling peptides and their application in the treatment of diseases. *Int. J. Mol. Sci.* 20:5850. doi: 10.3390/ijms20235850

Lee, M., Ma, Z., and Ananda, A. (2017). A novel haemostatic agent based on self-assembling peptides in the setting of nasal endoscopic surgery, a case series. *Int. J. Surg. Case. Rep.* 41, 461–464. doi: 10.1016/j.ijscr.2017.11.024

Liu, J., Song, H., Zhang, L., Xu, H., and Zhao, X. (2010). Self-assembly-peptide hydrogels as tissue-engineering scaffolds for three-dimensional culture of chondrocytes in vitro. *Macromol. Biosci.* 10, 1164–1170. doi: 10.1002/mabi.200900450

Liu, J., Zhang, L., Yang, Z., and Zhao, X. (2011). Controlled release of paclitaxel from a self-assembling peptide hydrogel formed in situ and antitumor study in vitro. *Int. J. Nanomed.* 6, 2143–2153. doi: 10.2147/IJN.S24038

Masuhara, H., Fujii, T., Watanabe, Y., Koyama, N., and Tokuhiro, K. (2012). Novel infectious agent-free hemostatic material (TDM-621) in cardiovascular surgery. *Ann. Thorac. Cardiovasc. Surg.* 18, 444–451.

Morshuis, M., Schönbrodt, M., and Gummert, J. (2019). Safety and performance of a self-assembling peptide haemostat for the management of bleeding after left ventricular assist device implantation: outcomes of a post market clinical follow-up study. *J. Heart Lung Transplant.* 38:S194. doi: 10.1016/j.healun.2019.01.469

Mourad, F. H., and Leong, R. W. (2018). Role of hemostatic powders in the management of lower gastrointestinal bleeding: a review. *J. Gastroenterol. Hepatol.* 33, 1445–1453. doi: 10.1111/jgh.14114

Nune, M., Krishnan, U. M., and Sethuraman, S. (2016). PLGA nanofibers blended with designer self-assembling peptides for peripheral neural regeneration. *Mater. Sci. Eng. C.* 62, 329–337.

Ortenzi, M., and Haji, A. (2020). Safety and feasability of PuraStat in laparoscopic colorectal surgery. *Minim. Invasive. Ther. Allied. Technol.* 2020, 1–6. doi: 10.1080/13645706.2020.1739711

Oumrani, S., Barret, M., Bordaçahar, B., Beuvon, F., Hochart, G., Pagnon-Minot, A., et al. (2019). Application of a self-assembling peptide matrix prevents esophageal stricture after circumferential endoscopic submucosal dissection in a porcine model. *PLoS One* 14:e0212362. doi: 10.1371/journal.pone.0212362

Oumrani, S., Barret, M., Beuvon, F., Nicco, C., Chene, C., Batteaux, F., et al. (2021). Prevention of esophageal stricture after circumferential endoscopic submucosaldissection using a modified self-assembling peptide. *Dis. Esophagus* 1–7. doi: 10.1093/dote/doaa133

Pereira, B. M., Bortoto, J. B., and Fraga, G. P. (2018). Topical hemostatic agents in surgery: review and prospects. *Rev. Col. Bras. Cir.* 45:e1900. doi: 10.1590/0100-6991e-20181900

Pioche, M., Camus, M., Rivory, J., Leblanc, S., Lienhart, I., Barret, M., et al. (2016). A self-assembling matrix-forming gel can be easily and safely applied to prevent delayed bleeding after endoscopic resections. *Endosc. Int. Open* 4, E415–419. doi: 10.1055/s-0042-102879

Qiu, F., Chen, Y., Tang, C., and Zhao, X. (2018). Amphiphilic peptides as novel nanomaterials: design, self-assembly and application. *Int. J. Nanomed.* 13, 5003–5022. doi: 10.2147/IJN.S166403

Rajangam, K., Behanna, H. A., Hui, M. J., Han, X. Q., Hulvat, J. F., Lomasney, J. W., et al. (2006). Heparin binding nanostructures to promote growth of blood vessels. *Nano Lett.* 6, 2086–2090.

Rodrigues, M., Kosaric, N., Bonham, C. A., and Gurtner, G. C. (2019). Wound healing: a cellular perspective. *Physiol. Rev.* 99, 665–706. doi: 10.1152/physrev.00067.2017

Rudralingam, V., Footitt, C., and Layton, B. (2017). Ascites matters. *Ultrasound* 25, 69–79. doi: 10.1177/1742271X16680653

Sedlakova Kondelova, P., Mannaa, A., Bommer, C., Abdelaziz, M., Daeniker, L., di Bella, E., et al. (2020). Efficacy of P11-4 for the treatment of initial buccal caries: a randomized clinical trial. *Sci. Rep.* 10:20211. doi: 10.1038/s41598-020-77057-3

Saini, A., Serrano, K., Koss, K., and Unsworth, L. D. (2016). Evaluation of the hemocompatibility and rapid hemostasis of (RADA)4 peptide-based hydrogels. *Acta Biomater.* 31, 71–79. doi: 10.1016/j.actbio.2015.11.059

Sakita, T., Oguro, Y., Takasu, S., Fukutomi, H., and Miwa, T. (1971). Observations on the healing of ulcerations in early gastric cancer. The life cycle of the malignant ulcer. *Gastroenterology* 60, 835–839.

Schneider, A., Garlick, J. A., and Egles, C. (2008). Self-assembling peptide nanofiber scaffolds accelerate wound healing. *PLoS One* 3:e1410. doi: 10.1371/journal.pone.0001410

Schonauer, C., Tessitore, E., Barbagallo, G., Albanese, V., and Moraci, A. (2004). The use of local agents: bone wax, gelatin, collagen, oxidized cellulose. *Eur. Spine J.* 13, S89–96. doi: 10.1007/s00586-004-0727-z

Song, H., Cai, G., Liang, J., Ao, D. S., Wang, H., and Yang, Z. (2020). Three-dimensional culture and clinical drug responses of a highly metastatic human ovarian cancer HO-8910PM cells in nanofibrous microenvironments of three hydrogel biomaterials. *J. Nanobiotechnol.* 18:90. doi: 10.1186/s12951-020-00646-x

Spotnitz, W. (2010). Fibrin sealant: past, present, and future: a brief review. *World J. Surg.* 34, 632–634. doi: 10.1007/s00268-009-0252-7

Stefan, S., Siddiqi, N., Naqvi, S., Rawlinson, E., and Khan, J. (2019). *The Innovative Use of a Haemostatic gel to Reduce the Incidence of Pelvic Collection After Rectal Cancer Surgery – Can We Enhance the Enhanced Recovery Program? European Colorectal Congress. 1–5 December, 2019. St. Gallen, Switzerland. Abstract 1667. Techniques Coloproctology. 24, 655. On page 75*. Available online at: https://www.colorectalsurgery.eu/custom/media/ECC2019/Abstracts/ECC2019_Abstractbook.pdf (accessed April 22, 2021).

Subramaniam, S., Kandiah, K., Thayalasekaran, S., Longcroft-Wheaton, G., and Bhandari, P. (2019). Haemostasis and prevention of bleeding related to ER: the role of a novel self-assembling peptide. *United Eur. Gastroenterol. J.* 7, 155–162. doi: 10.1177/2050640618811504

Subramaniam, S., Kandiah, K., Chedgy, F., Fogg, C., Thayalasekaran, S., Alkandari, A., et al. (2020). A novel self-assembling peptide for hemostasis during endoscopic submucosal dissection: a randomized controlled trial. *Endoscopy* 53, 27–35. doi: 10.1055/a-1198-0558

Tabaja, L., and Sidani, S. M. (2018). Management of radiation proctitis. *Dig. Dis. Sci.* 63, 2180–2188. doi: 10.1007/s10620-018-5163-8

Taghavi, L., Aramvash, A., Seyedkarimi, M. S., and Malek Sabet, N. (2018). Evaluation of the hemocompatibility of RADA 16-I peptide. *J. Biomat. Appl.* 32, 1024–1031. doi: 10.1177/0885328217748861

Takeuchi, T., Bizenjima, T., Ishii, Y., Imamura, K., Suzuki, E., Seshima, F., et al. (2016). Enhanced healing of surgical periodontal defects in rats following application of a self-assembling peptide nanofibre hydrogel. *J. Clin. Periodontol.* 43, 279–288. doi: 10.1111/jcpe.12515

Tomizawa, Y. (2005). Clinical benefits and risk analysis of topical hemostats: a review. *J. Artif. Organs* 8, 137–142. doi: 10.1007/s10047-005-0296-x

Trzcinski, R., Mik, M., Dziki, L., and Dziki, A. (2018). "Radiation proctitis," in *Proctological Diseases in Surgical Practice*, ed. P. Cianci (London: IntechOpen Ltd), 105–117. doi: 10.5772/intechopen.76200

Tsiamoulos, Z. P., Rajaratnam, R., Sibbons, P. D., and Saunders, B. P. (2017). Use of a novel synthetic, topical gel to enhance healing post endoscopic mucosal resection: a randomised, blinded preclinical study. *Gastrointest. Endoscopy* 85:AB512. doi: 10.1016/j.gie.2017.03.1181

Uraoka, T., Ochiai, Y., Fujimoto, A., Goto, O., Kawahara, Y., Kobayashi, N., et al. (2016). A novel fully synthetic and self-assembled peptide solution for endoscopic submucosal dissection-induced ulcer in the stomach. *Gastrointest. Endosc.* 83, 1259–1264. doi: 10.1016/j.gie.2015.11.015

US Food and Drug Administration (2021). *510(k) Premarket Notification K183015, Summary. "Polymer, Ear, Nose and Throat, Synthetic, Absorbable"; PuraSinus®; 3-D Matrix Inc*. Available online at: https://www.accessdata.fda.gov/scripts/cdrh/cfdocs/cfpmn/pmn.cfm?ID=K183015 (accessed April 22, 2021).

Wang, R., Wang, Z., Guo, Y., Li, H., and Chen, Z. (2019). Design of a RADA16-based self-assembling peptide nanofiber scaffold for biomedical applications. *J. Biomater. Sci. Polym. Ed.* 30, 713–736. doi: 10.1080/09205063.2019k

Wang, T., Zhong, X., Wang, S., Lv, L., and Zhao, X. (2012). Molecular mechanisms of RADA16-1 peptide on fast stop bleeding in rat models. *Int. J. Mol. Sci.* 13, 15279–15290.

Wang, T. W., Chang, K. C., Chen, L. H., Liao, S. Y., Yeh, C. W., and Chuang, Y. J. (2017). Effects of an injectable functionalized self-assembling nanopeptide hydrogel on angiogenesis and neurogenesis for regeneration of the central nervous system. *Nanoscale* 9, 16281–16292. doi: 10.1039/c7nr06528k

Weiner, J., Wong, A., Schwartz, D., Martinez, M., Aytaman, A., and Schreiber, D. (2016). Endoscopic and non-endoscopic approaches for the management of radiation-induced rectal bleeding. *World J. Gastroenterol.* 22, 6972–6986.

White, M., Mueller, P. R., Ferrucci, J. T. Jr., Butch, R. J., Simeone, J. F., Neff, C. C., et al. (1985). Percutaneous drainage of postoperative abdominal and pelvic lymphoceles. *AJR Am. J. Roentgenol.* 145, 1065–1069. doi: 10.2214/ajr.145.5

White, K., and Henson, C. C. (2021). Endoscopically delivered PuraStat for the treatment of severe haemorrhagic radiation proctopathy: a service evaluation of a new endoscopic treatment for a challanging condition. *Frontline Gastroenterol.* doi: 10.1136/flgastro-2020-101735 [Epub ahead of print].

Wong, E., Ho, J., Smith, M., Sritharan, N., Riffat, F., and Smith, M. C. (2020). Use of Purastat, a novel haemostatic matrix based on self-assembling peptides in the prevention of nasopharyngeal adhesion formation. *Int. J. Surg. Case Rep.* 70, 227–229. doi: 10.1016/j.ijscr.2020.04.027

Wu, H., Zhou, T., Tian, L., Xia, Z., and Xu, F. (2017). Self-assembling RADA16-I peptide hydrogel scaffold loaded with tamoxifen for breast reconstruction. *Biomed. Res. Int.* 2017:3656193. doi: 10.1155/2017/3656193

Yang, H., Hong, N., Liu, H., Wang, J., Li, Y., and Wu, S. (2018). Differentiated adipose-derived stem cell cocultures for bone regeneration in RADA16-I in vitro. *J. Cell. Physiol.* 233, 9458–9472. doi: 10.1002/jcp.26838

Yi, S., Ding, F., Gong, L., and Gu, X. (2017). Extracellular matrix scaffolds for tissue engineering and regenerative medicine. *Curr. Stem Cell Res. Ther.* 12, 233–246. doi: 10.2174/1574888X11666160905092513

Yokoi, H., Kinoshita, T., and Zhang, S. (2005). Dynamic reassembly of peptide RADA16 nanofiber scaffold. *Proc. Natl. Acad. Sci. U.S.A.* 102, 8414–8419. doi: 10.1073/pnas.0407843102 k

Yoshida, M., Goto, N., Kawaguchi, M., Koyama, H., Kuroda, J., Kitahora, T., et al. (2014). Initial clinical trial of a novel hemostat, TDM-621, in the endoscopic treatments of the gastric tumors. *J Gastroenterol. Hepatol.* 29, 77–79. doi: 10.1111/jgh.12798

Zhai, H., Zhou, J., Xu, J., Sun, X., Xu, Y., and Qiu, X. (2020). Mechanically strengthened hybrid peptide-polyester hydrogel and potential applications in spinal cord injury repair. *Biomed. Mater.* 15:055031. doi: 10.1088/1748-605X/ab9e45

Zhang, S., Lockshin, C., Herbert, A., Winter, E., and Rich, A. (1992). Zuotin, a putative Z-DNA binding protein in Saccharomyces cerevisiae. *EMBO J.* 11, 3787–3796.

Zhang, S. (2017). Discovery and design of self-assembling peptides. *Interface Focus* 7:20170028. doi: 10.1098/rsfs.2017.0028

Zinicola, R., Rutter, M. D., Falasco, G., Brooker, J. C., Cennamo, V., Contini, S., et al. (2003). Haemorrhagic radiation proctitis: endoscopic severity may be useful to guide therapy. *Int. J. Colorectal. Dis.* 18, 439–444. doi: 10.1007/s00384-003-0487-y

Conflict of Interest: SS, KO'N, FR, MB, EA, MF, NM, EG, and LS are employees of 3-D Matrix, Ltd. MBD'A is a consultant for 3-D Matrix, Ltd.

frontiers in Bioengineering and Biotechnology

OPINION
published: 21 July 2021
doi: 10.3389/fbioe.2021.712685

Creating a Pro-Regenerative Tissue Microenvironment: Local Control is the Key

*Nadya Lumelsky**

National Institute of Dental and Craniofacial Research (NIDCR), National Institutes of Health (NIH), Bethesda, MD, United States

Keywords: pro-regenerative microenvironment, biomaterials, stem cell niche, regenerative medicine, scaffolds

INTRODUCTION

The potential of regenerative medicine to restore tissues and organs compromised or lost due to disease, injury or aging has captured the public imagination and attracted many multidisciplinary researchers to the field. However, despite significant promise, translation to the clinic has so far been modest. This slow progress might at least in part be due to the technical complexity of traditional cell-based approaches, which require *in vitro* manufacturing of large quantities of high-quality clinical grade cells for transplantation, ensuring targeted delivery and survival of these cells *in vivo*, as well as promoting functional morphogenesis of the new tissues and their integration with host tissues. The regulatory path for Food and Drug Administration (FDA) approval of such complex therapies could be arduous. While cell-based therapies remain an important goal for the future of regenerative medicine, an alternative class of therapies—referred to as autotherapies (Lumelsky et al., 2018)—that does not rely on exogenous cell transplantation, but instead attempts to pattern a pro-regenerative tissue microenvironment to optimize endogenous regeneration, might have a simplified regulatory path, and holds significant promise for achieving functional tissue regeneration *in vivo*. While the autotherapies idea is not new (Krzyszczyk et al., 2018; Liu and Segura, 2020; Fetz and Bowlin, 2021), it is particularly important and timely now. Many recent scientific and technical advances, including those in the basic biology of tissue regeneration, single-cell analyses, data science, and bioinformatics, as well as in material science and bioengineering, could propel the field forward and fulfill the therapeutic promise of this class of therapies.

Multiple Players in the Pro-Regenerative Microenvironment

It is widely recognized that tissue maintenance and regeneration in mammals is controlled by multi-component microenvironmental systems collectively referred to as stem cell niches. In these niches, stem and progenitor cells, various somatic cell types, extracellular matrices (ECMs), and signaling mediators reciprocally interact with each other (Durand et al., 2018; Ruddy and Morshead, 2018). The niches generally remain quiescent under normal adult homeostasis, but injury or disease remodel their regulatory landscapes, and in some cases, induce elements of embryonic or early postnatal regulatory states. This creates a pro-regenerative microenvironment that allows activation, proliferation and differentiation of stem and progenitor cells to build new functional tissues (Nusse et al., 2018; Abbasi et al., 2020; Fuchs and Blau, 2020; Massenet et al., 2021). The regenerative potential of tissues varies widely depending on the species, age, and type of tissue. In some lower vertebrates, new body parts can be completely reconstituted following resection. In mammals, including humans, some tissues, including skin, liver, and oral and intestinal mucosa, regenerate well, while others -such as heart, pancreas, and teeth hardly regenerate at all (Iismaa et al., 2018). Biological age is also a key factor in determining regeneration outcome independent of tissue type, with progressively diminishing regenerative capacity throughout a lifespan (Sousounis et al., 2014).

OPEN ACCESS

Edited by:
Bryan Brown,
University of Pittsburgh, United States

Reviewed by:
Frederick Schoen,
Brigham and Women's Hospital and Harvard Medical School, United States
Chase Cornelison,
University of Massachusetts Amherst, United States
Fei Liu,
Texas A&M University, United States

***Correspondence:**
Nadya Lumelsky
nadyal@nidcr.nih.gov

Received: *21 May 2021*
Accepted: *09 July 2021*
Published: *21 July 2021*

Citation:
Lumelsky N (2021) Creating a Pro-Regenerative Tissue Microenvironment: Local Control is the Key. Front. Bioeng. Biotechnol. 9:712685. doi: 10.3389/fbioe.2021.712685

An extensive body of work has identified numerous biochemical and biophysical mediators, signaling pathways and cell types responsible for control of the pro-regenerative microenvironment in the niche across different species. Many of these mediators and signaling pathways are shared among lower vertebrates and mammals Progress in this field has been greatly facilitated by recent advances in single cell analyses, bioinformatics, and system biology using a variety of organs and animal regeneration models in lower vertebrates, zebrafish and mice, as well as *in vitro* 3-dimensional tissue models such as organoids and tissue chips (Godwin et al., 2013; Mahmoud et al., 2015; Nowoshilow and Tanaka, 2020; Brezitski et al., 2021; Thompson and Takebe, 2021). These studies revealed that regeneration outcomes are determined by a combination of numerous interdependent niche parameters, which precisely align in a spatial and temporal fashion for maintenance and restoration of tissue structure and function. These parameters include the availability and homing of stem and other cell types, including immune cells to the site of injury (Wu et al., 2017; Yin et al., 2017), specific patterns of the ECM remodeling and degradation (Hematti et al., 2018), a timely resolution of acute inflammation and prevention of the onset of chronic inflammation (Kizil et al., 2015), and the establishment of effective vascular supply and neuronal input to the regenerating tissue (Rezza et al., 2014; Mahmoud et al., 2015; Ribatti et al., 2021).

Interestingly, recent results in a variety of model systems strongly suggest that a contribution of the immune system to endogenous tissue regeneration extends beyond its modulation of post-injury inflammation, and also includes direct crosstalk between the innate and adaptive immune systems and the regenerative machinery of the niche to promote or inhibit regeneration (Naik et al., 2018). Failure to achieve a proper patterning of the pro-regenerative microenvironment results in defective regeneration, which manifests itself in tissue fibrosis and scarring instead of productive restoration of functional tissue.

Given the complexity of endogenous tissue regeneration mechanisms, it is not surprising that the outcomes of regenerative medicine therapies in human populations have been variable, as it is now known that they are highly impacted by genetics, age and co-morbidities, including diabetes, obesity and disfunctions of the immune system (Fadini et al., 2020; Masson and Krawetz, 2020). Thus, for the clinical success of regenerative medicine, it will be important to develop and test promising therapies in disease-relevant animal models, including large animal models, that reflect elements of the heterogeneity of human populations (Ribitsch et al., 2020).

Orchestrating a Pro-Regenerative Microenvironment With Biomaterials

Optimizing endogenous tissue regeneration requires dynamic and predictable spaciotemporal control of the *in vivo* microenvironment. Our current limited ability to achieve such control represents a major roadblock in the field. However, recent progress in biomaterial design lends hope for the future. Over the years, biomaterials employed by regenerative medicine have evolved from inert compounds to powerful effectors of the tissue microenvironment and cellular phenotype. Biomaterials can now be endowed with multiple functionalities that augment tissue regeneration *in vivo*, including: delivery and release of biomolecules with pre-determined kinetics; manipulating stem and progenitor cell lineage commitment, proliferation and differentiation; controlling cellular migration and adhesion; mimicking properties of natural ECMs; exerting local mechanical forces; and modulating immune responses (Wu et al., 2017; Ma and Huang, 2020). Chemists and engineers can now generate predictable and quantitative frameworks for developing new biomaterials with desired functionalities, optimize these functionalities through innovative fabrication approaches and bioassays, and engineer their nanoscale topography, adhesion sites and optimized growth factor presentation to cells (Di Cio and Gautrot, 2016; Vegas et al., 2016; Darnell and Mooney, 2017; Donnelly et al., 2018). Below I offer several examples of promising biomaterial design advances.

Early work showed that biomolecules could be encapsulated into polymeric particles and hydrogels with tunable properties to allow preservation of these biomolecules' activity for delivery and extended controlled release in tissues. More recent efforts have aimed at designing systems to fit the requirements of a dynamic microenvironment of diseased or injured tissues and release multiple mediators in a spaciotemporal fashion (Hettiaratchi and Shoichet, 2019). For example, in a spinal cord injury (SCI), insufficient axonal growth across an astrocyte scar, which forms as a result of SCI and the absence of growth supporting substrates and cell homing cues, are thought to contribute to failed regeneration. Anderson *et al.* used a multiprong approach in which they treated SCIs in rodents with a combination of viral vectors and hydrogels applied sequentially to the injury site for targeted temporal delivery of multiple growth factors (Anderson et al., 2018). They promoted axon growth with osteopontin, insulin-like growth factor 1 and ciliary-derived neurotrophic factor; induced axon growth supporting substrate with fibroblast growth factor 2 and epidermal growth factor and used glial-derived neurotrophic factor as a homing signal for the growing axons. Providing these three types of stimuli in combination, but not individually, stimulated robust axon regrowth through astrocyte scar borders and across the lesion that was over 100-fold greater than in controls. While this approach is relatively cumbersome and may face obstacles in clinical translation, the study supports the feasibility of endogenous regeneration of complex injuries.

Sophisticated delivery systems in which biomolecule release can be triggered in a combinatorial, sequential or pulsative manner by external stimuli, such as ultrasound, light, temperature, or magnetic/electric fields have also been developed (Cheah et al., 2021; Rapp and DeForest, 2021). Each stimulus has advantages and disadvantages depending on the specific application, but in principle, such approaches provide superior flexibility by assuring tunable and targeted biomolecule release patterns on demand. In the future, it should be possible to couple biomolecule release with biosensing to build feedback

systems in which a biomolecule concentration is flexibly adjusted in response to regeneration dynamics.

At this time triggered release studies are primarily conducted in preclinical animal models, and numerous examples of such studies are offered in the excellent recent Reviews referenced above. For example, Zhao et al. used UV light for an on-demand epidermal growth factor release from the hyaluronic acid-based supramolecular hydrogels. Application of this technology to a full thickness rodent skin wound model, resulted in a superior wound healing with respect to granulation tissue formation, and improved angiogenesis compared to controls (Zhao et al., 2020). In another study, Chen et al. used temperature as a trigger for fibroblast growth factor (FGF) release from the chitosan scaffolds incorporating three-dimensionally ordered macroporous particles—inverse opal particles—in a rodent infected skin wound model. The release of the encapsulated FGF from the inverse opal particles was triggered by a high temperature at the inflamed wound site. Because FGF release induced special light reflection changes in the inverse opal particles, the investigators were able to monitor the process in real time. This on-demand release system augmented cell migration and homing at the wound site and ensured the efficient transport of oxygen, nutrients, and metabolic wastes resulting in down-regulation of inflammatory markers, increased collagen deposition and improved granulation tissue formation compared to controls (Chen et al., 2018).

Another promising approach involves building modular chemical frameworks with hydrogels of specifically-designed chemical crosslinker architecture endowing them with precise degradative properties in response to external stimuli, which can be programmed using Boolean logic (Badeau et al., 2018). The authors of this work demonstrated the applicability of their system to the complex spaciotemporal demands of biomolecule delivery by synthesizing 17 distinct hydrogels that collectively yielded all possible YES/OR/AND logic outputs in response to proteases, chemical reducing agents and UV light. The utility of these types of materials for regenerative medicine, is in their potential to pattern tissue microenvironment in response to a combination of exogenous spatiotemporal cues and endogenous cell generated signals. One example of such application is offered by Arakawa et al. who engineered programmable hydrogel photodegradation scheme to generate a customizable vasculature (Arakawa et al., 2017).

In addition to biomolecule delivery, biomaterials also hold promise to improve viral vector-mediated gene delivery by providing more targeted and controllable means for delivering gene cargo to tissues (Wang et al., 2021). These approaches have the potential to overcome the current limitations of uncontrolled virion release and transgene expression as well as undesirable immune response and off-target viral toxicity. Moreover, biomaterial-augmented micro-RNA, small interfering RNA and mRNA delivery approaches show promise for achieving robust and precise control of gene expression. These biomaterial-enabled nucleic acid therapeutics can either induce or inhibit the expression of specific genes and transcription factors involved in control of stem cell niches thereby augmenting endogenous regeneration (Lee et al., 2019; Patel et al., 2019; Yu et al., 2020).

Mechanical forces have been recognized as powerful players in the niche, affecting lineage commitment of stem cells as well as their self-renewal and differentiation during embryonic development and postnatally (Vining and Mooney, 2017; Argentati et al., 2019). Cells in tissues exert internal mechanical forces on their microenvironment—the niche-through adhesive interactions of their cytoskeleton with the ECM and neighboring cells. Reciprocally, external sheer, tensile, and compressive forces act as powerful effectors of niche's function, cells' phenotype and ECM properties. Much progress has been made in unravelling molecular mechanisms and signaling pathways associated with internal and external mechanical cues in the niche. These advances provide hope that this knowledge can be harnessed for regenerative medicine applications. Active biomaterials designed for such applications can modulate their physical and chemical properties and transmit mechanical forces *in vivo* in response to a variety of internal and external stimuli. Such biomaterials can be programmed to exert dynamic mechanical forces on cells and tissues in a controllable manner, thereby mimicking the native tissue microenvironment. These biomaterials thus have a capacity to pattern physiological processes, including tissue morphogenesis and regeneration (Özkale et al., 2021).

A strategy capitalizing on mechanical force modulation to promote vascular morphogenesis has recently been described by Wei et al. (2020). In this study, the investigators developed dynamic hydrogel (D-hydrogel) networks in which chemical crosslinks are remodeled in response to traction forces imposed by the cells encapsulated in these hydrogels. The investigators show that the D-hydrogels increased the contractility of human endothelial cells, leading through a series of steps to the activation of focal adhesion kinase, metalloproteinase expression and angiogenesis when the encapsulated cells were transplanted subcutaneously into a mouse. The non-dynamic hydrogels lacking remodeling crosslinks failed to promote angiogenesis. These results suggest that D-hydrogels and other biomaterials that respond to mechanical forces could serve as valuable tools for promoting the endogenous vascular morphogenesis required for successful regeneration of numerous tissues.

In the past, the design of biomaterials was primarily driven by the goals of achieving controlled degradation and superior biocompatibility that would prevent foreign body and fibrotic responses at the site of implantation. These are still important goals, but more recent studies also strive to engineer immunomodulatory biomaterials that control the innate and adaptive immune system responses to pattern a tissue pro-regenerative microenvironment (Chung et al., 2017). This new direction emerged from works demonstrating that the immune system actively participates in tissue regeneration, and that biomaterials can be designed to elicit predictable regenerative responses through the mediation of crosstalk between different immune cells and stem and progenitor cells in the niche (Mariani et al., 2019; Li et al., 2021).

An interesting example of a promising immunomodulatory material was described recently by Griffin et al. (2021). This group developed injectable D-enantiomeric peptide crosslinked Microporous Annealed Particle hydrogels that accelerated the healing of cutaneous wounds and inhibited fibrosis *in vivo*. Importantly, this effect was completely dependent on the generation of an adaptive immune response to the D-enantiomeric peptides, without addition of cells, growth factors or adjuvants. Such immunomodulatory biomaterials, which tip the balance toward regeneration rather than foreign body response and fibrosis, may provide powerful means for achieving minimally invasive endogenous tissue regeneration. Further, predictable modulation of the inflammatory tissue microenvironment can be achieved by delivering extracellular vehicles (EVs) to tissues. It has been shown that EVs derived from mesenchymal stem cells can be used to functionalize biomaterials, to endow them with immunomodulatory and tissue regenerative properties (Brennan et al., 2020).

CONCLUSION

Autotherapies have the potential to bring regenerative medicine advances to the clinic. The success of this endeavor, however, is critically dependent on the integration of advances in cellular and molecular regenerative mechanisms with those in bioengineering and material science. Together, these advances could enable robust and predictable control and monitoring of the tissue microenvironment *in vivo*. Significant discoveries have been made in these fields during the last decade, but additional effort is needed to capitalize on these discoveries *via* productive cross-disciplinary collaborations. Given the exquisite complexity of the regenerative mechanisms, multi-prong bioengineering approaches are needed to enable spaciotemporal control of stem cell niches. The new autotherapies will counteract chronic inflammation and tissue destruction and augment regeneration, thereby shifting the diseased tissue homeostasis from fibrosis and scarring to restoration of normal structure and function. Practical application of autotherapies still faces many challenges, but a critical mass of basic science knowledge and technical knowhow is already in place to overcome these challenges and to revolutionize regenerative medicine.

AUTHOR CONTRIBUTIONS

The author confirms being the sole contributor of this work and has approved it for publication.

REFERENCES

Abbasi, S., Sinha, S., Labit, E., Rosin, N. L., Yoon, G., Rahmani, W., et al. (2020). Distinct Regulatory Programs Control the Latent Regenerative Potential of Dermal Fibroblasts during Wound Healing. *Cell Stem Cell* 27, 396–412. doi:10.1016/j.stem.2020.07.008

Anderson, M. A., O'Shea, T. M., Burda, J. E., Ao, Y., Barlatey, S. L., Bernstein, A. M., et al. (2018). Required Growth Facilitators Propel Axon Regeneration across Complete Spinal Cord Injury. *Nature* 561, 396–400. doi:10.1038/s41586-018-0467-6

Arakawa, C. K., Badeau, B. A., Zheng, Y., and DeForest, C. A. (2017). Multicellular Vascularized Engineered Tissues through User-Programmable Biomaterial Photodegradation. *Adv. Mater.* 29, 1703156. doi:10.1002/adma.201770266

Argentati, C., Morena, F., Tortorella, I., Bazzucchi, M., Porcellati, S., Emiliani, C., et al. (2019). Insight into Mechanobiology: How Stem Cells Feel Mechanical Forces and Orchestrate Biological Functions. *Int. J. Mol. Sci.* 20, 5337. doi:10.3390/ijms20215337

Badeau, B. A., Comerford, M. P., Arakawa, C. K., Shadish, J. A., and DeForest, C. A. (2018). Engineered Modular Biomaterial Logic gates for Environmentally Triggered Therapeutic Delivery. *Nat. Chem.* 10, 251–258. doi:10.1038/nchem.2917

Brennan, M. A., Layrolle, P., and Mooney, D. J. (2020). Biomaterials Functionalized with MSC Secreted Extracellular Vesicles and Soluble Factors for Tissue Regeneration. *Adv. Funct. Mater.* 30, 1909125. doi:10.1002/adfm.201909125

Brezitski, K. D., Goff, A. W., DeBenedittis, P., and Karra, R. (2021). A Roadmap to Heart Regeneration through Conserved Mechanisms in Zebrafish and Mammals. *Curr. Cardiol. Rep.* 23, 29. doi:10.1007/s11886-021-01459-6

Cheah, E., Wu, Z., Thakur, S. S., O'Carroll, S. J., and Svirskis, D. (2021). Externally Triggered Release of Growth Factors - A Tissue Regeneration Approach. *J. Controlled Release* 332, 74–95. doi:10.1016/j.jconrel.2021.02.015

Chen, C., Liu, Y., Wang, H., Chen, G., Wu, X., Ren, J., et al. (2018). Multifunctional Chitosan Inverse Opal Particles for Wound Healing. *ACS Nano* 12, 10493–10500. doi:10.1021/acsnano.8b06237

Chung, L., Maestas, D. R., Jr., Housseau, F., and Elisseeff, J. H. (2017). Key Players in the Immune Response to Biomaterial Scaffolds for Regenerative Medicine. *Adv. Drug Deliv. Rev.* 114, 184–192. doi:10.1016/j.addr.2017.07.006

Darnell, M., and Mooney, D. J. (2017). Leveraging Advances in Biology to Design Biomaterials. *Nat. Mater* 16, 1178–1185. doi:10.1038/nmat4991

Di Cio, S., and Gautrot, J. E. (2016). Cell Sensing of Physical Properties at the Nanoscale: Mechanisms and Control of Cell Adhesion and Phenotype. *Acta Biomater.* 30, 26–48. doi:10.1016/j.actbio.2015.11.027

Donnelly, H., Dalby, M. J., Salmeron-Sanchez, M., and Sweeten, P. E. (2018). Current Approaches for Modulation of the Nanoscale Interface in the Regulation of Cell Behavior. *Nanomedicine: Nanotechnology, Biol. Med.* 14, 2455–2464. doi:10.1016/j.nano.2017.03.020

Durand, C., Charbord, P., and Jaffredo, T. (2018). The Crosstalk Between Hematopoietic Stem Cells and Their Niches. *Curr. Opin. Hematol.* 25, 285–289. doi:10.1097/moh.0000000000000438

Fadini, G. P., Spinetti, G., Santopaolo, M., and Madeddu, P. (2020). Impaired Regeneration Contributes to Poor Outcomes in Diabetic Peripheral Artery Disease. *Arterioscler Thromb. Vasc. Biol.* 40, 34–44. doi:10.1161/atvbaha.119.312863

Fetz, A. E., and Bowlin, G. L. (2021). Neutrophil Extracellular Traps: Inflammation and Biomaterial Preconditioning for Tissue Engineering. *Tissue Eng. Part. B Rev.* doi:10.1089/ten.teb.2021.0013

Fuchs, E., and Blau, H. M. (2020). Tissue Stem Cells: Architects of Their Niches. *Cell Stem Cell* 27, 532–556. doi:10.1016/j.stem.2020.09.011

Godwin, J. W., Pinto, A. R., and Rosenthal, N. A. (2013). Macrophages are Required for Adult Salamander Limb Regeneration. *Proc. Natl. Acad. Sci. USA* 110, 9415–9420. doi:10.1073/pnas.1300290110

Griffin, D. R., Archang, M. M., Kuan, C.-H., Weaver, W. M., Weinstein, J. S., Feng, A. C., et al. (2021). Activating an Adaptive Immune Response from a Hydrogel Scaffold Imparts Regenerative Wound Healing. *Nat. Mater.* 20, 560–569. doi:10.1038/s41563-020-00844-w

Hematti, P. (2018). "Role of Extracellular Matrix in Cardiac Cellular Therapies," in *Cardiac Extracellular Matrix: Fundamental Science to Clinical Applications*. Editors E. G. Schmuck, P. Hematti, and A. N. Raval (Cham: Springer International Publishing), 173–188. doi:10.1007/978-3-319-97421-7_9

Hettiaratchi, M. H., and Shoichet, M. S. (2019). Modulated Protein Delivery to Engineer Tissue Repair. *Tissue Eng. A* 25, 925–930. doi:10.1089/ten.tea.2019.0066

Iismaa, S. E., Kaidonis, X., Nicks, A. M., Bogush, N., Kikuchi, K., Naqvi, N., et al. (2018). Comparative Regenerative Mechanisms Across Different Mammalian Tissues. *NPJ Regen. Med.* 3, 6. doi:10.1038/s41536-018-0044-5

Kizil, C., Kyritsis, N., and Brand, M. (2015). Effects of Inflammation on Stem Cells: Together They Strive?. *EMBO Rep.* 16, 416–426. doi:10.15252/embr.201439702

Krzyszczyk, P., Schloss, R., Palmer, A., and Berthiaume, F. (2018). The Role of Macrophages in Acute and Chronic Wound Healing and Interventions to Promote Pro-wound Healing Phenotypes. *Front. Physiol.* 9, 419. doi:10.3389/fphys.2018.00419

Lee, S. W. L., Paoletti, C., Campisi, M., Osaki, T., Adriani, G., Kamm, R. D., et al. (2019). MicroRNA Delivery through Nanoparticles. *J. Controlled Release* 313, 80–95. doi:10.1016/j.jconrel.2019.10.007

Li, J., Jiang, X., Li, H., Gelinsky, M., and Gu, Z. (2021). Tailoring Materials for Modulation of Macrophage Fate. *Adv. Mater.* 33, e2004172. doi:10.1002/adma.202004172

Liu, Y., and Segura, T. (2020). Biomaterials-Mediated Regulation of Macrophage Cell Fate. *Front. Bioeng. Biotechnol.* 8, 609297. doi:10.3389/fbioe.2020.609297

Lumelsky, N., O'Hayre, M., Chander, P., Shum, L., and Somerman, M. J. (2018). Autotherapies: Enhancing Endogenous Healing and Regeneration. *Trends Mol. Med.* 24, 919–930. doi:10.1016/j.molmed.2018.08.004

Ma, J., and Huang, C. (2020). Composition and Mechanism of Three-Dimensional Hydrogel System in Regulating Stem Cell Fate. *Tissue Eng. B: Rev.* 26, 498–518. doi:10.1089/ten.teb.2020.0021

Mahmoud, A. I., O'Meara, C. C., Gemberling, M., Zhao, L., Bryant, D. M., Zheng, R., et al. (2015). Nerves Regulate Cardiomyocyte Proliferation and Heart Regeneration. *Develop. Cel.* 34, 387–399. doi:10.1016/j.devcel.2015.06.017

Mariani, E., Lisignoli, G., Borzi, R. M., and Pulsatelli, L. (2019). Biomaterials: Foreign Bodies or Tuners for the Immune Response? *Int. J. Mol. Sci.* 20, 636. doi:10.3390/ijms20030636

Massenet, J., Gardner, E., Chazaud, B., and Dilworth, F. J. (2021). Epigenetic Regulation of Satellite Cell Fate during Skeletal Muscle Regeneration. *Skelet Muscle* 11, 4. doi:10.1186/s13395-020-00259-w

Masson, A. O., and Krawetz, R. J. (2020). Understanding Cartilage protection in OA and Injury: a Spectrum of Possibilities. *BMC Musculoskelet. Disord.* 21, 432. doi:10.1186/s12891-020-03363-6

Naik, S., Larsen, S. B., Cowley, C. J., and Fuchs, E. (2018). Two to Tango: Dialog Between Immunity and Stem Cells in Health and Disease. *Cell* 175, 908–920. doi:10.1016/j.cell.2018.08.071

Nowoshilow, S., and Tanaka, E. M. (2020). Introducing www.axolotl-omics.Org-an Integrated -Omics Data portal for the Axolotl Research Community. *Exp. Cel Res.* 394, 112143. doi:10.1016/j.yexcr.2020.112143

Nusse, Y. M., Savage, A. K., Marangoni, P., Rosendahl-Huber, A. K. M., Landman, T. A., de Sauvage, F. J., et al. (2018). Parasitic Helminths Induce Fetal-like Reversion in the Intestinal Stem Cell Niche. *Nature* 559, 109–113. doi:10.1038/s41586-018-0257-1

Özkale, B., Sakar, M. S., and Mooney, D. J. (2021). Active Biomaterials for Mechanobiology. *Biomaterials* 267, 120497. doi:10.1016/j.biomaterials.2020.120497

Patel, S., Athirasala, A., Menezes, P. P., Ashwanikumar, N., Zou, T., Sahay, G., et al. (2019). Messenger RNA Delivery for Tissue Engineering and Regenerative Medicine Applications. *Tissue Eng. Part A* 25, 91–112. doi:10.1089/ten.tea.2017.0444

Rapp, T. L., and DeForest, C. A. (2021). Targeting Drug Delivery with Light: A Highly Focused Approach. *Adv. Drug Deliv. Rev.* 171, 94–107. doi:10.1016/j.addr.2021.01.009

Rezza, A., Sennett, R., and Rendl, M. (2014). Adult Stem Cell Niches. *Curr. Top. Dev. Biol.* 107, 333–372. doi:10.1016/b978-0-12-416022-4.00012-3

Ribatti, D., Tamma, R., and Annese, T. (2021). The Role of Vascular Niche and Endothelial Cells in Organogenesis and Regeneration. *Exp. Cel Res.* 398, 112398. doi:10.1016/j.yexcr.2020.112398

Ribitsch, I., Baptista, P. M., Lange-Consiglio, A., Melotti, L., Patruno, M., Jenner, F., et al. (2020). Large Animal Models in Regenerative Medicine and Tissue Engineering: To Do or Not to Do. *Front. Bioeng. Biotechnol.* 8, 972. doi:10.3389/fbioe.2020.00972

Ruddy, R. M., and Morshead, C. M. (2018). Home sweet home: the Neural Stem Cell Niche throughout Development and after Injury. *Cell Tissue Res* 371, 125–141. doi:10.1007/s00441-017-2658-0

Sousounis, K., Baddour, J. A., and Tsonis, P. A. (2014). Aging and Regeneration in Vertebrates. *Curr. Top. Dev. Biol.* 108, 217–246. doi:10.1016/b978-0-12-391498-9.00008-5

Thompson, W. L., and Takebe, T. (2021). Human Liver Model Systems in a Dish. *Develop. Growth Differ.* 63, 47–58. doi:10.1111/dgd.12708

Vegas, A. J., Veiseh, O., Doloff, J. C., Ma, M., Tam, H. H., Bratlie, K., et al. (2016). Combinatorial Hydrogel Library Enables Identification of Materials that Mitigate the Foreign Body Response in Primates. *Nat. Biotechnol.* 34, 345–352. doi:10.1038/nbt.3462

Vining, K. H., and Mooney, D. J. (2017). Mechanical Forces Direct Stem Cell Behaviour in Development and Regeneration. *Nat. Rev. Mol. Cel Biol.* 18, 728–742. doi:10.1038/nrm.2017.108

Wang, Y., Bruggeman, K. F., Franks, S., Gautam, V., Hodgetts, S. I., Harvey, A. R., et al. (2021). Is Viral Vector Gene Delivery More Effective Using Biomaterials?. *Adv. Healthc. Mater.* 10, e2001238. doi:10.1002/adhm.202001238

Wei, Z., Schnellmann, R., Pruitt, H. C., and Gerecht, S. (2020). Hydrogel Network Dynamics Regulate Vascular Morphogenesis. *Cell Stem Cell* 27, 798–812. doi:10.1016/j.stem.2020.08.005

Wu, R. X., Yin, Y., He, X. T., Li, X., and Chen, F. M. (2017). Engineering a Cell Home for Stem Cell Homing and Accommodation. *Adv. Biosyst.* 1, e1700004. doi:10.1002/adbi.201700004

Yin, Y., Li, X., He, X. T., Wu, R. X., Sun, H. H., and Chen, F. M. (2017). Leveraging Stem Cell Homing for Therapeutic Regeneration. *J. Dent Res.* 96, 601–609. doi:10.1177/0022034517706070

Yu, T., Wang, H., Zhang, Y., Wang, X., and Han, B. (2020). The Delivery of RNA-Interference Therapies Based on Engineered Hydrogels for Bone Tissue Regeneration. *Front. Bioeng. Biotechnol.* 8, 445. doi:10.3389/fbioe.2020.00445

Zhao, W., Li, Y., Zhang, X., Zhang, R., Hu, Y., Boyer, C., et al. (2020). Photo-Responsive Supramolecular Hyaluronic Acid Hydrogels for Accelerated Wound Healing. *J. Controlled Release* 323, 24–35. doi:10.1016/j.jconrel.2020.04.014

Conflict of Interest: The author declares that the research was conducted in the absence of any commercial or financial relationships that could be construed as a potential conflict of interest.

frontiers in Bioengineering and Biotechnology

ORIGINAL RESEARCH
published: 21 July 2021
doi: 10.3389/fbioe.2021.697671

Indomethacin Treatment Post-irradiation Improves Mouse Parotid Salivary Gland Function via Modulation of Prostaglandin E_2 Signaling

Kristy E. Gilman[1], Jean M. Camden[2], Lucas T. Woods[2], Gary A. Weisman[2] and Kirsten H. Limesand[1]**

[1] Department of Nutritional Sciences, University of Arizona, Tucson, AZ, United States, [2] Department of Biochemistry and Christopher S. Bond Life Sciences Center, University of Missouri, Columbia, MO, United States

OPEN ACCESS

Edited by:
Fei Liu,
Texas A&M University, United States

Reviewed by:
Changyu Zheng,
National Institutes of Health, United States
Sarah Knox,
University of California, San Francisco, United States

***Correspondence:**
Kristy E. Gilman
gilmankr@arizona.edu
Kirsten H. Limesand
limesank@u.arizona.edu

Specialty section:
This article was submitted to Tissue Engineering and Regenerative Medicine, a section of the journal Frontiers in Bioengineering and Biotechnology

Received: *20 April 2021*
Accepted: *28 June 2021*
Published: *21 July 2021*

Citation:
Gilman KE, Camden JM, Woods LT, Weisman GA and Limesand KH (2021) Indomethacin Treatment Post-irradiation Improves Mouse Parotid Salivary Gland Function via Modulation of Prostaglandin E_2 Signaling. Front. Bioeng. Biotechnol. 9:697671. doi: 10.3389/fbioe.2021.697671

Annually, >600,000 new cases of head and neck cancer (HNC) are diagnosed worldwide with primary treatment being surgery and radiotherapy. During ionizing radiation (IR) treatment of HNC, healthy salivary glands are collaterally damaged, leading to loss of function that severely diminishes the quality of life for patients due to increased health complications, including oral infections and sores, cavities, and malnutrition, among others. Therapies for salivary hypofunction are ineffective and largely palliative, indicating a need for further research to uncover effective approaches to prevent or restore loss of salivary gland function following radiotherapy. Previous work in our lab implicated prostaglandin E_2 (PGE_2) as an inflammatory mediator whose release from radiation-exposed cells promotes salivary gland damage and loss of function. Deletion of the P2X7 purinergic receptor for extracellular ATP reduces PGE_2 secretion in irradiated primary parotid gland cells, and salivary gland function is enhanced in irradiated $P2X7R^{-/-}$ mice compared to wild-type mice. However, the role of PGE_2 signaling in irradiated salivary glands is unclear and understanding the mechanism of PGE_2 action is a goal of this study. Results show that treatment of irradiated mice with the non-steroidal anti-inflammatory drug (NSAID) indomethacin, which reduces PGE_2 production via inhibition of cyclooxygenase-1 (COX-1), improves salivary gland function compared to irradiated vehicle-treated mice. To define the signaling pathway whereby PGE_2 induces salivary gland dysfunction, primary parotid gland cells treated with PGE_2 have increased c-Jun N-terminal Kinase (JNK) activation and cell proliferation and reduced amylase levels and store-operated calcium entry (SOCE). The *in vivo* effects of blocking PGE_2 production were also examined and irradiated mice receiving indomethacin injections have reduced JNK activity at 8 days post-irradiation and reduced proliferation and increased amylase levels at day 30, as compared to irradiated mice without indomethacin. Combined, these data suggest a mechanism whereby irradiation-induced PGE_2 signaling to JNK blocks critical steps in saliva secretion

manifested by a decrease in the quality (diminished amylase) and quantity (loss of calcium channel activity) of saliva, that can be restored with indomethacin. These findings encourage further attempts evaluating indomethacin as a viable therapeutic option to prevent damage to salivary glands caused by irradiation of HNC in humans.

Keywords: radiation, head and neck cancer, salivary glands, xerostomia, prostaglandin E_2, indomethacin, immunomodulation, regeneration

INTRODUCTION

Each year, >600,000 new cases of head and neck cancer (HNC) are diagnosed across the world (Johnson et al., 2020). Effective approaches to treat HNC include surgical excision of the tumor followed by IR, with or without chemotherapy (Cramer et al., 2019). During radiation treatment, salivary glands, located proximal to tumors, are collaterally damaged leading to reduced salivary gland function. Reduced saliva output causes numerous health complications, including increased rates of oral infections, cavities, and malnutrition and an overall poorer quality of life (Grundmann et al., 2009). Current treatment options for salivary hypofunction are palliative, relatively ineffective and costly to patients, indicating a need for further research to improve the quality of life for HNC patients (Jensen et al., 2019).

Wound healing is a complex regenerative process that occurs in three sequential but overlapping phases following tissue damage: (i) hemostasis/inflammation, (ii) proliferation/re-epithelialization, and (iii) remodeling. While each phase of the response is essential for adequate wound repair, dysregulation at any stage can lead to insufficient repair or chronic inflammation and excessive scarring. Hemostasis/inflammatory responses begin immediately following a wounding event and typically last for about 3 days (Reinke and Sorg, 2012). Radiation-induced inflammatory responses have been studied in salivary glands but present conflicting results (Jasmer et al., 2020). Research suggests that interleukin (IL)-6 mediates induction of cellular senescence in irradiated (13 Gy) submandibular glands (SMGs), with elevated levels seen at 3 h and 14 days post-IR. However, both IL-6 knockdown and IL-6 treatment prior to radiation exposure unexpectedly protected SMGs from senescence at 8 weeks post-IR, leaving the role of IL-6 during the inflammatory response to radiation difficult to understand (Marmary et al., 2016). Interestingly, treatment of SMGs with an adenovirus containing the neurotrophic factor, neurturin, prevents hypofunction in irradiated (6 Gy fractions × 5 days) salivary glands, when given pre- but not post-IR (Lombaert et al., 2020). Radiation treatment also resulted in a significant increase in inflammation-associated gene expression in irradiated mice (300 days post-IR) and minipigs (16 weeks post-IR) that was reduced by neurturin-expressing adenovirus administration prior to radiation exposure and was associated with normalized morphology and increased size and function of the salivary gland (Lombaert et al., 2020). In contrast, another study demonstrated that there is a decrease in immune-related gene expression and reduced macrophage numbers in irradiated (15 Gy) SMGs at days 7–28 post-IR, whereas adenoviral-induced activation of the Sonic hedgehog (Shh) pathway at day 3 post-IR increased immune gene expression and macrophage numbers (Zhao et al., 2020). These studies suggest that an effective therapy to prevent salivary gland dysfunction due to radiation should target the hemostasis/inflammation phase of tissue damage, i.e., 0–3 days post-IR.

The second phase of the wound healing response, cell proliferation, is necessary to replace cells lost following damage; however, the homeostatic regulation of proliferation and differentiation is necessary to promote functional tissue repair. It has previously been proposed that the proliferative phase encompasses days 3–21 of the wound healing process, with transition to the remodeling phase occurring from day 21 through 1 year post-damage (Reinke and Sorg, 2012). In irradiated salivary glands, it has been shown that compensatory proliferation begins at day 5 post-IR and is mediated by activation of c-Jun N-terminal kinase (JNK) signaling (Wong et al., 2019). However, cell proliferation rates in irradiated salivary glands remain elevated compared to non-irradiated glands at chronic timepoints, days 30, 60, and 90 post-IR (Grundmann et al., 2010). Despite the increase in cell proliferation rates in irradiated salivary glands, the cells remain undifferentiated, as indicated by decreased amylase levels (Grundmann et al., 2010; Hill et al., 2014; Morgan-Bathke et al., 2014). Various pharmacological agents have been evaluated for restoration of irradiated parotid glands, where reducing the proliferative response correlates with increased salivary gland function *in vivo* (Grundmann et al., 2010; Hill et al., 2014; Morgan-Bathke et al., 2014). These data suggest that dysregulated signaling during the transition from the proliferative to remodeling phases of the wound healing process should be targeted to enhance salivary gland function following radiation damage.

The P2X7 receptor (P2X7R) for extracellular ATP released from damaged cells is a component of the innate immune system. Previous work from our lab showed that deletion or pharmacological antagonism of the P2X7R prevents salivary gland dysfunction in mice caused by radiation exposure (Gilman et al., 2019). Interestingly, mouse primary parotid gland cells lacking the P2X7R secrete significantly lower levels of the biologically active lipid, prostaglandin E_2 (PGE_2), basally and following radiation exposure, which suggests that P2X7R-mediated PGE_2 release may lead to salivary gland dysfunction that could be reversed by blocking the P2X7R (Gilman et al., 2019). PGE_2 is produced from plasma membrane phospholipid-derived arachidonic acid that is first converted to prostaglandin H_2 by cyclooxygenases (COXs), COX-1 and COX-2, and then to

PGE_2 by microsomal PGE synthase-1 (mPGES-1), mPGES-2 or cytosolic PGE synthase (cPGES) (Gilman and Limesand, 2020). PGE_2 acts by binding to four different E-prostanoid receptors (EPRs), EP1-4R, to induce the activation of multiple G proteins (Gilman and Limesand, 2020). EPRs, typically EP2R and EP4R, also can transactivate the epidermal growth factor receptor (EGFR) (Jiang et al., 2017). Based on their ability to activate G protein and EGFR signaling, PGE_2-bound EPRs regulate multiple physiological processes, including, proliferation, differentiation, survival, cytokine production, immune cell migration and vasodilation/vasoconstriction (Dennis and Norris, 2015; Gilman and Limesand, 2020). PGE_2 also induces the phosphorylation of intracellular c-Jun terminal kinase (JNK) and it's downstream target c-Jun (Zeng et al., 2015; Zhong et al., 2015), which we have previously shown mediates the induction of compensatory proliferation in irradiated salivary glands (Wong et al., 2019). Indomethacin is a non-steroidal anti-inflammatory drug (NSAID) that functions via nonselective and reversible inhibition of COXs to reduce the synthesis of eicosanoids, including PGE_2 (Lucas, 2016). Due to the postulated role of PGE_2 in the induction of radiation-induced salivary gland dysfunction, we evaluated the hypothesis that indomethacin treatment would restore irradiated salivary gland function by blocking PGE_2 production and subsequent activation of JNK-mediated compensatory proliferation.

MATERIALS AND METHODS

Mice

Animals were maintained according to the University of Arizona Institutional Animal Care and Use Committee (IACUC) regulations with protocols approved by the IACUC. Four to eight week-old C57BL/6J (stock no. 000664) or FVB/NJ mice (stock no. 001800) were purchased from Jackson Labs (Bar Harbor, ME, United States). Age- and sex-matched mice of the same genotype were randomly assigned to treatment groups. Mice were on 12 h light/dark cycles and housed in vented cages with food and water *ad libitum*. Where indicated, mice received intraperitoneal (IP) injections of vehicle (sterile saline with 10% ethanol) or indomethacin (1 mg/kg body weight, Sigma, no. I7378, St. Louis, MO, United States) prepared from a 10 mg/mL stock solution in 100% ethanol, warmed at 55°C for 5 min, diluted to 1 mg/mL in saline and sterilized by passage through a 0.22 μm Polyvinylidene difluoride (PVDF) filter.

Radiation Treatment

Mice were sedated via an IP injection of a mixture of ketamine/xylazine (50–10 mg/kg), constrained in 50 mL tubes and shielded with >6 mm lead, leaving only the head and neck region exposed. Mice or cells were placed in the radiation field and received a single 5 Gy dose of radiation from a ^{60}Co Teletherapy unit at 80 cm distance from the source and ∼0.3–0.4 Gy/min (Theatron-80, Atomic Energy of Canada, Ottawa, ON, Canada) or a 225 kV X-ray unit at 48 cm distance from the source and 1.4 Gy/min (RS2000, Rad Source Technologies, Buford, GA, United States).

Saliva Collection

Salivary flow rates were evaluated on days 3, 10, or 30 following radiation. Saliva production was stimulated with an IP injection of carbachol (0.25 mg/kg body weight) and whole saliva was collected for 5 min via vacuum aspiration into pre-weighed tubes and then snap-frozen. Salivary flow was calculated by taking the difference in tube weight (post-collection minus pre-collection) and dividing by 5 min to express saliva secretion in milligrams per minute. Saliva flow rates were normalized to the average of the non-irradiated, vehicle-injected group on each day of collection.

Primary Cell Preparation

Parotid glands were removed from four to eight week-old C57BL/6J mice, prepared as previously described (Gilman et al., 2019) and suspended in primary cell culture media: DMEM/F12 containing (in wt/vol, except where noted) epidermal growth factor (0.4%; Fisher Scientific), insulin (0.125%; Invitrogen), glutamine (1.25%; Invitrogen), nonessential amino acids (1%; Invitrogen), transferrin (0.125%, Invitrogen), retinoic acid (0.05%; Sigma-Aldrich), trace elements (1%; Thermo Fisher Scientific), gentamycin (0.5%; Thermo Fisher Scientific), fungizone (0.2%; Invitrogen), hydrocortisone (0.04%; Sigma-Aldrich), and fetal bovine serum (10% vol/vol; Thermo Fisher Scientific, unless the use of serum-free media was indicated). Cells were used immediately as dispersed parotid cell aggregates or seeded onto 35 mm collagen-coated plates and grown for 2 days prior to use. Primary parotid cells or aggregates from independent preparations are considered as a single replicate for assays and at least three replicates were performed from separate preparations for all experiments.

Cyclooxygenase Activity Assay

Primary cells were prepared as described above. On day 2 of culture, cells were treated with indomethacin (25 μM in saline from the 100% ethanol stock solution) or vehicle (saline with 0.1% ethanol) and cells were collected 24 h later. Protein was extracted as described below and COX activity was measured via a COX activity assay (Abcam, no. ab204699, Cambridge, United Kingdom) following the manufacturer's instructions.

Prostaglandin E_2 Enzyme-Linked Immunosorbent Assay

Primary cells were prepared as described above. On day 2 of culture, media was replaced and cells were treated with indomethacin (25 μM in saline) or vehicle (saline with 0.1% ethanol) 1 h prior to receiving a 5 Gy dose of radiation. Cell-free supernatants were collected at indicated timepoints following radiation and the PGE_2 concentrations were determined with an enzyme-linked immunosorbent assay (PGE_2 ELISA, R&D Systems, no. KGE004B, Minneapolis, MN) following the manufacturer's instructions, where PGE_2 was normalized to the protein concentration of the corresponding cell culture dish.

Prostaglandin E_2 Treatment

Vehicle (DMSO) or varying doses (10 nM, 100 nM, 1 μM, 10 μM) of PGE_2 (Cayman Chemical, no. 14010, Ann Arbor, MI,

United States) were diluted in serum-free primary cell media and used to treat dispersed parotid cell aggregates at the indicated timepoints for dose-response and kinetic analyses. For amylase staining, PGE_2 was diluted to 10 μM in serum-complete primary cell media and cells were treated on culture plates for 24 h prior to collection. Cells were centrifuged and resuspended in lysis buffer to extract proteins as described below.

Protein Isolation and Quantification

Parotid glands were harvested and snap-frozen from untreated and irradiated mice at day 8 or 30 post-IR. Tissues were homogenized in radioimmunoprecipitation assay (RIPA) buffer, with protease inhibitor cocktail (30 μL/mL; Sigma, no. P8340), sodium orthovanadate (5 mM) and phenylmethylsulfonyl fluoride (PMSF, 1 mM). Tissue homogenates were incubated on ice for 30 min, sonicated for 1–2 min and centrifuged at 12,000 RPM for 10 min at 4°C to remove cell debris. Cells or aggregates were collected by scraping, centrifuged, resuspended in tissue protein extraction reagent (T-PER, Thermo no. 78510) with protease inhibitor cocktail (30 μL/mL), sodium orthovanadate (5 mM), and PMSF (1 mM), incubated on ice for 10–15 min and centrifuged at 12,000 rpm for 10 min at 4°C to remove cell debris. Protein content was measured with the Pierce Coomassie Plus Bradford assay (Thermo, no. 23236, Waltham, MA, United States) or the Bicinchoninic acid (BCA) assay (Thermo, no. 23225).

Immunoblotting

Five to fifty micrograms of protein were added to 2X Laemmli sample buffer and boiled for 5–10 min at 95–100°C. Sample proteins were separated via electrophoresis on 10% polyacrylamide gels. Proteins were transferred to PVDF membranes (Millipore, no. IPVH00010) at 100 volts for 1 h. Membranes were blocked in either 5% (w/v) nonfat milk or 5% (w/v) bovine serum albumin (BSA, Fisher Bioreagents, no. BP1600-100) dissolved in tris-buffered saline with Tween 20 (TBS-T, 20 mM Tris base, 137 mM NaCl, 0.05% Tween 20 (v/v), pH 7.6) for 1 h at room temperature, washed in TBS-T three times for 5 min each and incubated in primary antibody overnight at 4°C. The following rabbit-anti-mouse primary antibodies were used: phospho-JNK/SAPK (p54/p46)$^{T183/Y185}$ (1:1,000, Cell Signaling, no. 4668, Danvers, MA, United States), JNK/SAPK (p54/p46, 1:1,000, Cell Signaling, no. 9252) phospho-c-Jun^{S73} (1:1,000, Abcam, no. ab30620), c-Jun (1:1,000, Cell Signaling, no. 9165), amylase (1:3,000 in 3% BSA, Sigma, no. A8273), Aquaporin 5 (AQP5; 1:1,000, Millipore-Sigma, no. AB3559-50UL), muscle, intestine and stomach expression 1 (MIST1; 1:1,000, Cell Signaling, no. 14896), EP1 (1:500; Cayman Chemical no. 101740), EP2 (1:200; Cayman Chemical no. 101750), EP3 (1:200; Cayman Chemical no. 101760), EP4 (1:200; Cayman Chemical no. 101775), ERK1/2 (1:1,000; Cell Signaling, no. 9102) or β-tubulin (1:1,000, Cell Signaling, no. 2128). Membranes were washed three times for 5 min each in TBS-T then incubated in HRP-conjugated goat anti-rabbit IgG antibody (1:10,000 in 5% nonfat milk TBS-T; Cell Signaling, no. 7074S) for 1 h at room temperature. Membranes were washed three times for 5 min each in TBS-T then incubated with Pierce ECL Western Blotting Substrate (Thermo, no. 32109) for 1 min or SuperSignal West Pico Plus Chemiluminescent Substrate (Thermo, no. 34577) for 5 min. Membranes were exposed to autoradiography film (Genesee, no. 30-810) and developed using an Srx-101A X-ray film processor (Konica). Membranes were stripped using Restore Western Blotting Stripping Buffer (Fisher, no. 21063), blocked in 5% nonfat milk and re-probed for loading controls. Densitometry was performed using ImageJ software (NIH).

5-Ethynyl-2′-Deoxyuridine Incorporation Assay

Primary parotid gland cells were prepared as described above and were cultured on 18 mm collagen-coated glass coverslips (Neuvitro, no. H-18-collagen, Vancouver, WA, United States). On day 4 of culture, cells were treated with vehicle (DMSO), PGE_2 (Cayman Chemical, no. 14010), or EP receptor-selective (EP1R-EP4R) agonists at indicated doses: 17-phenyl trinor PGE_2 (EP1R agonist; Cayman Chemical, no. 14810), AH13205 (EP2R agonist; Santa Cruz Biotechnology, no. sc-214513), sulprostone (EP3R agonist; Cayman Chemical, no. 14765) and CAY10598 (EP4R agonist; Cayman Chemical, no. 13281). Cells were serum-starved for 2 h prior to treatment. All compounds were solubilized in DMSO, mixed into serum-free primary cell culture media (described above) and cells were treated for 24 h. During the last hour of EPR agonist treatment, cells were incubated with 5-ethynyl-2'-deoxyuridine (EdU) from the Click iT EdU cell proliferation kit (Invitrogen, no. 10337). EdU was fluorescently labeled following the manufacturer's instructions. Coverslips were mounted on glass slides with Prolong Gold Antifade Mountant (Thermo Fisher Scientific, no. 36934). Images were captured on a Leica DM5500 fluorescence microscope (Leica Microsystems, Wetzlar, Germany) with 4-megapixel Pursuit camera (Diagnostic Instruments, Inc.) at 200× magnification. EdU positive cells and total cells were manually counted. Groups were quantified by averaging the number of positive cells out of the total number of cells from 5 fields of view/slide and 3 slides per treatment. Graphs depict the average number of positive cells/total number of cells. Each symbol represents an independent sample.

Intracellular Calcium Quantification

Intracellular free Ca^{2+} concentration ($[Ca^{2+}]_i$) in isolated parotid epithelial cells was quantified as previously described (Woods et al., 2018). Briefly, primary parotid gland cells untreated or treated with 10 μM PGE_2 for 24 h in serum-free DMEM/F12 media containing gentamycin (50 μg/ml) were washed with assay buffer (120 mM NaCl, 4 mM KCl, 1.2 mM KH_2PO_4, 1.2 mM $MgSO_4$, 1 mM $CaCl_2$, 10 mM glucose, 15 mM HEPES, 1% (w/v) BSA, pH 7.4) and then adhered to chambered coverslips using Cell-Tak cell adhesive (Corning Inc., Corning, NY, United States) and loaded with 2 μM of the calcium indicating dye, fura-2-AM (Life Technologies, Carlsbad, CA, United States) in assay buffer for 30 min at 37°C, washed and incubated in dye-free assay buffer for 30 min. Prior to use, cells were washed again and placed in calcium-free assay buffer containing 0.2 mM EDTA and baseline fluorescence values were

collected for 60 s prior to stimulation with carbachol (100 μM) for 210 s to evaluate muscarinic type 3 receptor functionality. Then, 3 mM calcium was added for the final 90 s to quantitate store-operated calcium entry (SOCE) into cells. Changes in the 340/380 nm fluorescence excitation ratio (505 nm emission) were detected using an InCyt Dual-Wavelength Fluorescence Imaging System (Intracellular Imaging, Cincinnati, OH, United States). Resulting fluorescence ratios were converted to $[Ca^{2+}]_i$ (nM) using a standard curve created with solutions containing known concentrations of Ca^{2+}.

Histology

Salivary glands were harvested from mice at indicated timepoints post-IR and submerged in 10% neutral buffered formalin overnight. Tissues were sent to IDEXX Bioanalytics (Columbia, MO, United States) for processing where they were dehydrated with ethanol and xylene, embedded in paraffin and sectioned at 4 μm.

Immunofluorescence

Salivary gland sections were incubated at 37°C for 20 min, submerged in Histoclear (National Diagnostics, no. HS-200) for 10 min and rehydrated in ethanol gradations (100, 95, 70, and 50%) and deionized water for 10 min each. Sections were permeabilized for 15 min in 0.2% (v/v) Triton X-100 in PBS, then washed with PBS three times for 5 min each. Next, antigen retrieval was completed by microwaving sections in citric acid (pH 6.0) for 10 min and then cooling for 20 min. Sections were washed with PBS three times for 5 min each, blocked in 0.5% New England nuclear blocking agent (Perkin Elmer, no. 2346249) for 1 h at room temperature and then incubated in anti-amylase antibody (1:1,000 in 1% BSA; Sigma, no. A8273) or anti-Ki67 antibody [1:400 in 1% BSA, Cell Signaling, no. 9129] overnight at 4°C. Slides were washed three times for 10 min each, incubated in fluorophore-conjugated goat anti-rabbit IgG antibody (Alexa Fluor 488, 1:500 in 1% BSA; Thermo, no. A-11008) for 1 h at room temperature, washed again three times for 10 min each and then rinsed in water for 5 min. Cell nuclei were stained with 4',6-diamidino-2-phenylindole (DAPI, 1 μg/mL; Invitrogen, no. D1306) for 3 min then washed with water for 10 min. Amylase-stained sections were mounted with 50% glycerol in 10 mM Tris–HCl (pH 8.0), and Ki67-stained sections were mounted with ProLong Gold Antifade mounting agent (Invitrogen, no. P36934) and imaged the following day. Images were captured on a Leica DM5500 with 4-megapixel Pursuit camera at 400× magnification with identical camera settings used for all images. Quantification was done using ImageJ software with images from 20 fields of view per mouse with 5 mice per treatment for amylase area, or 5 fields of view per mouse with 4 mice per treatment for Ki67. Graphs depict the mean percentage of amylase positive area or the average percentage of Ki67 positive cells out of the total cell number. Each point represents an independent mouse.

Statistical Analysis

Statistical tests were run using GraphPad Prism 9 software (San Diego, CA, United States). Normally distributed data was assessed by Brown-Forsythe test. To determine significance between groups, a student's *t*-test, or a one-way analysis of variance (ANOVA) was used, followed by Dunnett's *post hoc* comparisons when comparing to a control group, or Bonferroni's *post hoc* comparisons when comparing all groups. A *p*-value of less than 0.05 is considered statistically significant. Specific *p*-values are indicated by the number of asterisks above groups ($^{*}p < 0.05$, $^{**}p < 0.01$, $^{***}p < 0.001$, $^{****}p < 0.0001$).

RESULTS

Post-radiation Indomethacin Treatment Restores Salivary Gland Function in Mice

FVB/NJ (**Figures 1A–D**) or C57BL/6J (**Figures 1E,F**) mice were exposed to 5 Gy of radiation and were injected with the NSAID, indomethacin (1 mg/kg body weight), 1 h prior to IR only (**Figures 1A,B**, IR+1 Indo) or again at days 1 and 2 post-IR (**Figures 1A,B**, IR+3 Indo). Alternatively, mice received injections of indomethacin at days 3, 5, and 7 post-IR (**Figures 1C–F**). Stimulated salivary flow rates were measured on day 3, representative of an acute timepoint post-IR damage, and day 30, representative of a chronic timepoint post-IR damage (Grundmann et al., 2010). The results indicate that a single injection of indomethacin (1 Indo) prior to IR exposure does not preserve salivary gland function post-IR (**Figures 1A,B**). Interestingly, mice receiving both pre- and post-IR indomethacin (3 Indo) injections have reduced stimulated saliva output on day 3 that is only modestly improved by day 30 (**Figures 1A,B**). In contrast, FVB/NJ (**Figures 1C,D**) and C57BL/6 (**Figures 1E,F**) mice receiving indomethacin injections on days 3, 5, and 7 post-IR (**Figures 1C–F**) show salivary flow rates at days 10 and 30 post-IR similar to untreated, vehicle injected (UT+Veh) mice (**Figures 1C,D**). In addition, indomethacin treatment alone does not alter salivary gland function in mice not treated with IR (**Figures 1C,D**). Combined, these data suggest that inhibiting eicosanoid synthesis with indomethacin following radiation exposure leads to restoration of salivary gland function.

Indomethacin Treatment of Primary Parotid Gland Cells Reduces COX-1 Activity and Prostaglandin E_2 Secretion Induced by Radiation

Indomethacin inhibits both COX-1 and COX-2 functions (Tanaka et al., 2002), but has greater selectivity for COX-1 (Warner et al., 1999; Brown et al., 2001). To evaluate whether indomethacin is COX-1- or COX-2-selective in salivary glands, parotid acinar cells were treated with vehicle or indomethacin (25 μM) for 24 h and COX-1 and COX-2 activities were measured. Results indicate that indomethacin preferentially inhibits COX-1 in primary parotid acinar cells (**Figure 2A**). We have previously shown that there are elevated levels of PGE_2 secreted from primary parotid gland cells following IR exposure, with lower PGE_2 levels detected in IR-exposed $P2X7R^{-/-}$ cells that correlate with improved salivary gland function (Gilman et al., 2019). To determine if indomethacin treatment modulates PGE_2 secretion, primary parotid gland cells were exposed to

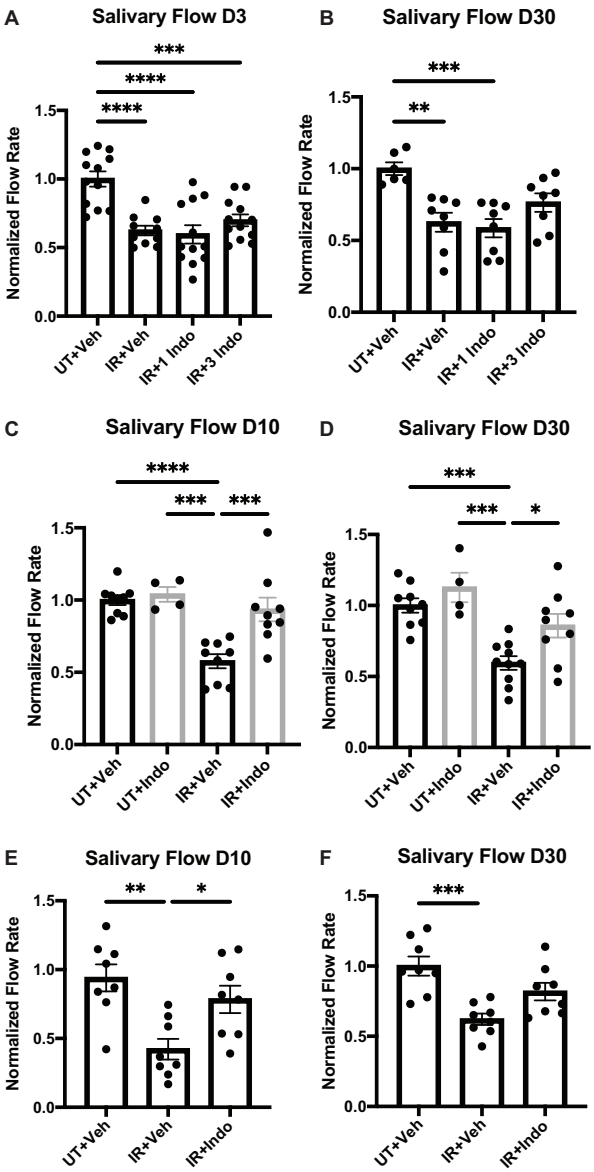

FIGURE 1 | Pre- versus post-radiotherapy indomethacin treatment differentially modulates salivary flow rates in mice. **(A–D)** FVB or **(E,F)** C57BL/6J mice were untreated (UT) or treated with 5 Gy ionizing radiation (IR) and intraperitoneal injections of vehicle (Veh, saline with 10% ethanol) or indomethacin (Indo, 1 mg/kg body weight) **(A,B)** 1 h prior to radiation (1 Indo) or again at days 1 and 2 post-IR (3 Indo) or **(C–F)** at days 3, 5 and 7 post-IR. **(A–F)** Carbachol-stimulated (0.25 mg/kg body weight) saliva was collected on **(A)** day 3, **(C,E)** day 10 and **(B,D,F)** day 30 post-IR, as described in section "Materials and Methods." Graphs represent the mean ± standard error of the mean (SEM). Each closed circle represents an independent sample. Significant differences were determined via a one-way ANOVA followed by Bonferroni's *post hoc* comparisons (*$p < 0.05$, **$p < 0.01$, ***$p < 0.001$, ****$p < 0.0001$). Groups with no asterisks are not significantly different from each other.

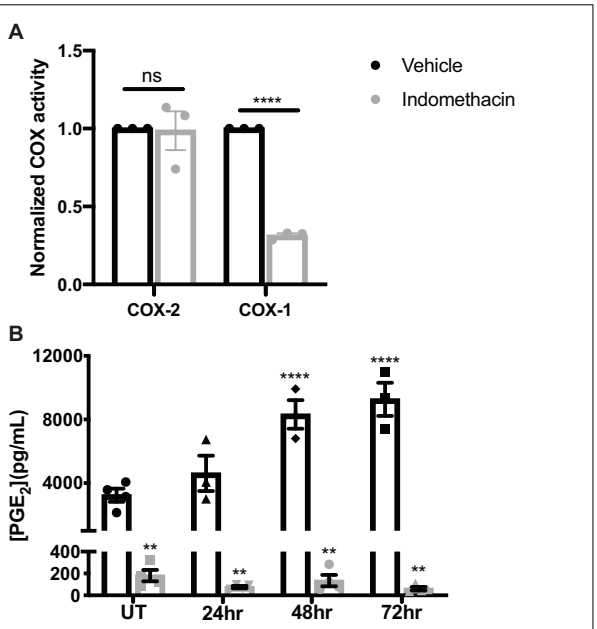

FIGURE 2 | Indomethacin treatment reduces cyclooxygenase-1 (COX) function and PGE_2 release in irradiated primary parotid acinar cells. Primary parotid acinar cells were prepared from C57BL/6J mice as described in section "Materials and Methods" and were untreated (UT) or treated with 5 Gy radiation (IR) with vehicle (Veh, saline with 0.1% ethanol) or indomethacin (Indo, 25 μM) for 1 h prior to IR. **(A)** Untreated cells were collected after 24 h of indomethacin treatment, protein was extracted and COX activities were measured with a COX assay kit selective for COX-1 and COX-2. **(B)** Cell-free supernatants from vehicle or indomethacin treated cells were collected at indicated timepoints post-IR and PGE_2 secretion was measured with a PGE_2 enzyme-linked immunosorbent assay. **(A,B)** Graphs represent the mean ± SEM. Each symbol represents an independent sample. Significant differences from UT+ Veh treated cells were determined via **(A)** a student's *t*-test or **(B)** a one-way ANOVA followed by Bonferroni's *post hoc* comparisons (**$p < 0.01$, ****$p < 0.0001$; ns is not significant).

5 Gy radiation with or without indomethacin pre-treatment (25 μM). Results indicate that indomethacin significantly reduces PGE_2 secretion into primary parotid cell-free supernatants at 24–72 h post-IR, whereas PGE_2 secretion is also inhibited by indomethacin in cells not treated with IR (**Figure 2B**). These data show that indomethacin functions by inhibiting COX-1 activity and reduces constitutive and radiation-induced production of PGE_2 in primary parotid gland cells.

Prostaglandin E_2 Treatment Activates JNK Signaling in Primary Parotid Gland Cells

We have previously shown that the JNK pathway is activated at day 5 post-IR and promotes radiation-induced compensatory cell proliferation that correlates with the loss of saliva secretion (Grundmann et al., 2010; Hill et al., 2014; Wong et al., 2019). PGE_2 has been shown to stimulate JNK and c-Jun phosphorylation in human endometrial stromal cells (Zeng et al., 2015) and primary human skin fibroblasts (Arasa et al., 2019). To evaluate whether PGE_2 activates JNK signaling in salivary glands, primary parotid cell aggregates were treated with varying doses of PGE_2 for 10 min and phosphorylation of the JNK p54 and p46 isoforms and their downstream target, c-Jun, were assessed

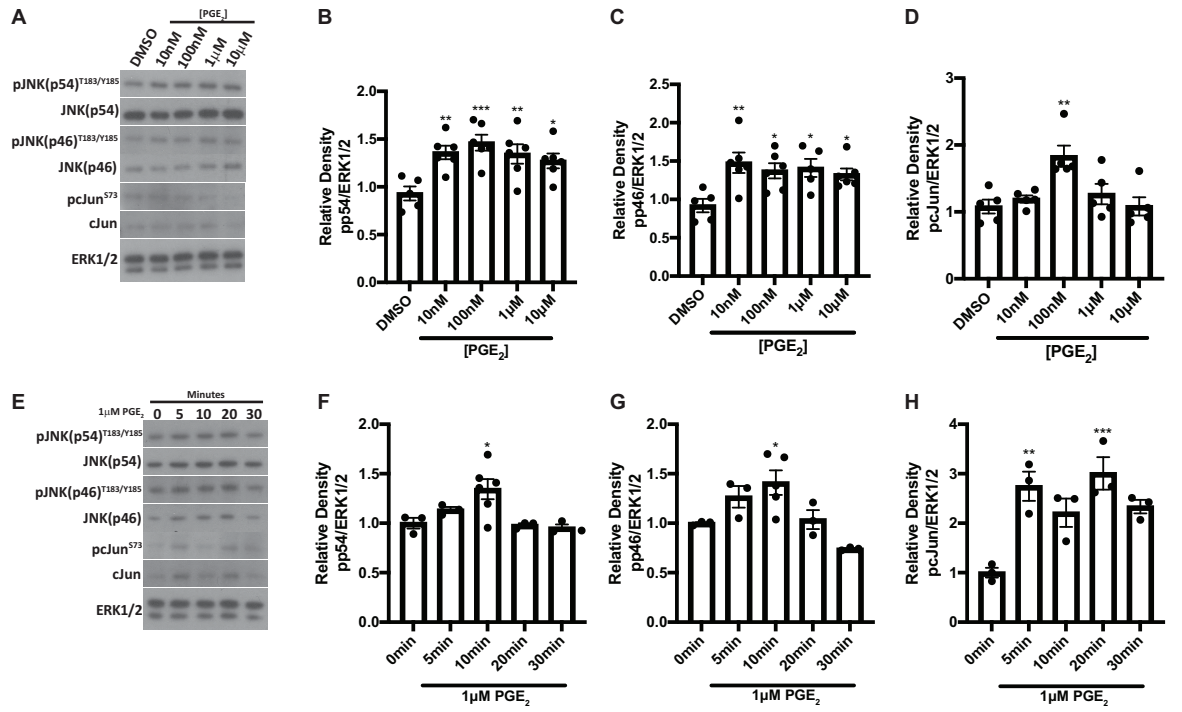

FIGURE 3 | PGE_2 treatment activates JNK pathways in primary parotid acinar cells. Primary parotid acinar cells were prepared from C57BL/6J mice as described in section "Materials and Methods." **(A–D)** Dispersed parotid cell aggregates were treated with vehicle (DMSO) or varying doses of PGE_2 (10 nM, 100 nM, 1 or 10 μM) in serum-free media for 10 min. **(A)** Representative Western blot images of phosphorylated JNK signaling molecules following PGE_2 treatment at the indicated concentrations. **(B–D)** Densitometry of Western blots represented in panel **(A)**. **(E–H)** Dispersed parotid cell aggregates were treated with vehicle (DMSO) or 1 μM PGE_2 in serum-free media for 5, 10, 20, or 30 min. **(E)** Representative Western blot images of the kinetics of PGE_2-mediated phosphorylation of JNK signaling molecules following 1 μM PGE_2 treatment. **(F–H)** Densitometry of Western blots represented in panel **(E)**. **(A–H)** Immunoblots were generated from cell lysates using anti-phospho-JNK/SAPK (p54/p46)$^{T183/Y185}$ or anti-phospho-c-Jun^{S73} antibodies, which were stripped and re-probed for JNK/SAPK (p54/p46) or c-Jun and then ERK1/2 as a loading control. Densitometry was performed using ImageJ software and protein content was normalized to the average of DMSO-treated cells **(A–D)** or cells treated for 0 min **(E–H)**. Graphs represent the mean ± SEM. Each closed circle represents an independent sample. Significant differences from DMSO-treated cells or cells treated for 0 min were determined via a one-way ANOVA followed by Dunnett's *post hoc* comparisons (*$p < 0.05$, **$p < 0.01$, ***$p < 0.001$).

via Western analysis. Phosphorylation of both p54 and p46 JNK are enhanced following treatment with all doses of PGE_2 tested (**Figures 3A–C**), whereas c-Jun phosphorylation is modestly increased following 100 nM PGE_2 treatment (**Figures 3A,D**). To determine kinetic changes in JNK and c-Jun phosphorylation induced by PGE_2, primary parotid cell aggregates were treated with 1 μM PGE_2 and phosphorylation of JNK p54 and p46 and c-Jun were assessed after 0, 5, 10, 20, and 30 min. Results indicate that phosphorylation of p54 and p46 JNK are elevated at 10 min following 1 μM PGE_2 treatment (**Figures 3E–G**). Interestingly, c-Jun phosphorylation is increased at all timepoints measured, with significantly higher levels observed at 5 and 20 min following PGE_2 treatment as compared to the 0 timepoint (**Figures 3E,H**). These data show that PGE_2 activates the JNK/c-Jun pathway in parotid glands.

Prostaglandin E_2 and EP2, 3, and 4 Receptor Agonism Induce Proliferation of Primary Parotid Gland Cells

It has been shown that JNK activation mediates compensatory proliferation in parotid glands at day 5 post-IR (Wong et al., 2019) and PGE_2-induced JNK signaling is able to stimulate proliferation of pulmonary epithelial tumor cells (Zhong et al., 2015) and human mesenchymal stem cells (Yun et al., 2011). To evaluate whether PGE_2 treatment or selective EP receptor (EP1R-EP4R) activation is able to induce cell proliferation in salivary glands, primary parotid gland cells were treated with PGE_2 or selective agonists for EP1R (17-phenyl trinor PGE_2; 1 μM), EP2R (AH13205; 1 or 10 μM), EP3R (sulprostone; 0.01 or 1 μM) or EP4R (CAY10598; 1 or 10 μM) for 24 h and EdU incorporation was determined during the last hour of treatment as a measure of cell proliferation. The number of EdU positive cells increases following PGE_2 treatment (0.01 or 0.03 μM), EP2R agonism (1 or 10 μM AH13205), EP3R agonism (0.01 or 1 μM sulprostone) or EP4R agonism (1 or 10 μM CAY10598) as compared to DMSO-treated cells (**Figures 4A,B** and **Supplementary Figures 1A,B**). EP1R agonism (1 μM 17-phenyl trinor PGE_2) did not increase proliferation levels compared to DMSO-treated controls (**Figures 4A,B**). These data indicate PGE_2 increases proliferation in parotid gland cells via either EP2, 3 or 4 receptor activation, which is likely mediating the induction of the compensatory proliferation response seen post-IR (Grundmann et al., 2010; Hill et al., 2014;

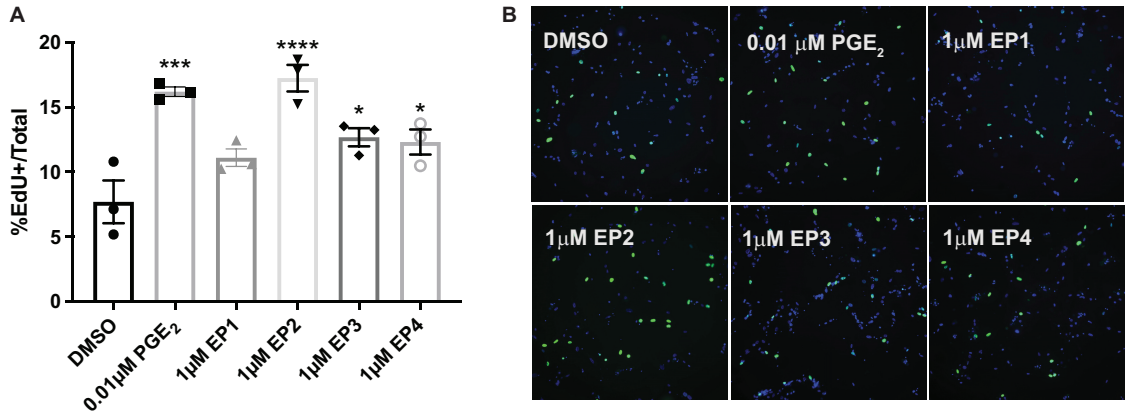

FIGURE 4 | PGE_2 and EP2, 3 and 4 receptor agonism induce proliferation of primary parotid gland cells. Primary parotid cells were prepared from C57BL/6J mice, serum-starved for 2 h and treated with vehicle (DMSO), PGE_2 (0.01 μM) or the EP receptor-selective (EP1R-EP4R) agonists for EP1R: 17-phenyl trinor PGE_2 (1 μM), EP2R: AH13205 (1 μM), EP3R: sulprostone (1 μM) or EP4R: CAY10598 (1 μM). All compounds were solubilized in DMSO, mixed with serum-free primary cell culture media and incubated with cells for 24 h with EdU added during the last hour of treatment to monitor proliferating cells, as described in section "Materials and Methods." **(A)** Groups were quantified by averaging the number of positive cells out of the total number of cells from 5 fields of view/slide. Graphs represent the mean ± SEM. Each symbol represents an independent sample. Significant differences from DMSO-treated cells were determined via a one-way ANOVA followed by Dunnett's *post hoc* comparisons (*$p < 0.05$, ***$p < 0.001$, ****$p < 0.0001$). **(B)** Representative fields of view are shown.

Wong et al., 2019), downstream of radiation-induced PGE_2 secretion (Gilman et al., 2019).

Prostaglandin E_2 Decreases Amylase Levels and Store-Operated Calcium Entry in Primary Parotid Cells

Amylase is a marker for differentiated acinar cells and, following radiation damage, amylase levels are reduced in parotid glands, which correlates with reduced gland function (Grundmann et al., 2010; Hill et al., 2014; Morgan-Bathke et al., 2014). To evaluate whether PGE_2 influences amylase production in parotid glands, primary parotid cells were treated with 10 μM PGE_2 for 24 h and amylase levels were determined via Western analysis. Amylase levels are reduced in PGE_2-treated cells when compared to vehicle-treated cells (**Figures 5A,B**). To identify other mechanisms by which PGE_2 mediates alterations in salivary gland function, primary parotid cells were treated with PGE_2 for 24 h and loaded with the calcium indicating dye, fura-2. Intracellular calcium concentration ($[Ca^{2+}]_i$) was measured for 6 min following carbachol (100 μM) stimulation in media lacking calcium, and 3 mM calcium was added 4.5 min after carbachol stimulation. The peak $[Ca^{2+}]_i$ in parotid gland cells following carbachol stimulation is not different between vehicle and PGE_2-treated cells, indicating normal functionality of muscarinic type 3 receptors on parotid cells and no effect of PGE_2 on the $[Ca^{2+}]$ in intracellular stores (**Figures 5C,D**). Following addition of 3 mM calcium into the media, there is reduced re-entry of calcium in PGE_2-treated cells indicated by a reduction in $[Ca^{2+}]_i$ as compared to vehicle-treated cells, suggesting that PGE_2 signaling blocks SOCE in parotid glands (**Figures 5C,D**). Taken together, these data illustrate that PGE_2 reduces amylase levels and inhibits SOCE in primary parotid cells.

Indomethacin Treatment Reduces JNK Signaling *in vivo* at Day 8 Post-IR

We have previously shown that IR activates JNK signaling 5 days post-IR, which partially regulates the compensatory proliferation response in parotid glands (Wong et al., 2019). It is well described that JNK activation induces c-Jun phosphorylation (Johnson and Nakamura, 2007). To determine if indomethacin treatment modulates JNK signaling *in vivo*, mice with or without 5 Gy IR exposure were injected with vehicle or indomethacin (1 mg/kg body weight) at days 3, 5 and 7 post-IR. Parotid glands were harvested at day 8 and used for immunoblots. Phosphorylation of JNK p54 and p46 are increased in irradiated parotid tissues at day 8 post-IR, a response reduced with indomethacin treatment (**Figures 6A–C**). Further, phosphorylation of c-Jun that is significantly increased at day 8 post-IR is reversed with indomethacin treatment (**Figures 6A,D**). These data illustrate that post-IR indomethacin treatment blocks JNK activation in parotid glands, supporting a role for indomethacin in protection from IR-induced salivary gland damage.

Post-radiation Indomethacin Treatment Enhances Parotid Gland Amylase Levels and Reduces Compensatory Proliferation at Day 30

To confirm the *in vitro* findings that PGE_2 decreases amylase secretion, mice were untreated or exposed to 5 Gy radiation with vehicle or indomethacin injections at days 3, 5, and 7 post-IR and parotid glands were collected at day 30, representing a chronic timepoint following damage (Grundmann et al., 2010). Protein was extracted for immunoblot analysis, which shows that total amylase levels are reduced in irradiated, vehicle-injected mice (**Figures 7A,B**), whereas indomethacin treatment

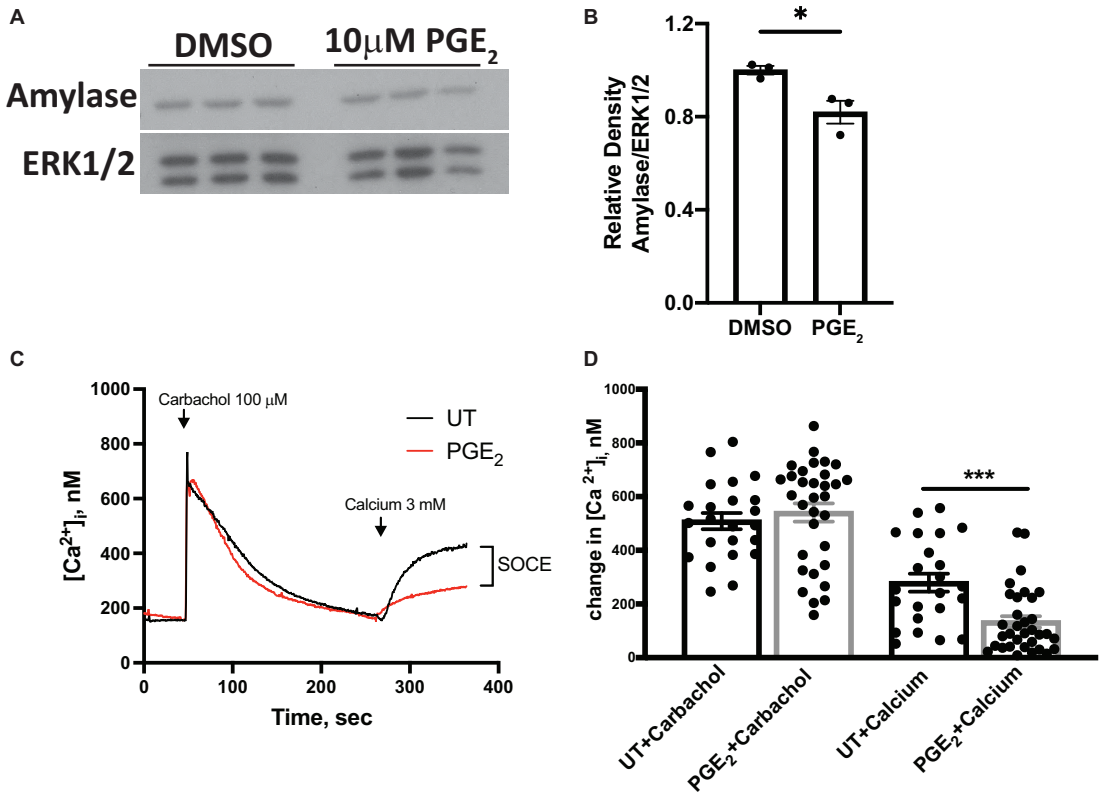

FIGURE 5 | PGE_2 treatment decreases amylase levels and store-operated calcium entry (SOCE) in primary parotid acinar cells. Primary parotid acinar cells were prepared from C57BL/6J mice as described in section "Materials and Methods." **(A–D)** Primary parotid gland cells were untreated (UT) or treated with vehicle (DMSO) or PGE_2 (10 μM) for 24 h. **(A)** Representative Western blot images of changes in amylase levels following PGE_2 treatment. **(B)** Densitometry of Western blots represented in panel **(A)**. **(A,B)** Immunoblots were prepared from cell lysates with an anti-amylase antibody which were stripped and re-probed for ERK1/2 as a loading control. Densitometry was done using ImageJ software and protein content was normalized to the average of DMSO-treated cells. Graphs represent the mean ± SEM. Each closed circle represents an independent sample. Significant differences from DMSO-treated cells were determined via a student's *t*-test (*$p < 0.05$). **(C)** Representative tracings of time-dependent fura-2 fluorescence in mouse primary parotid acinar cells pretreated with or without PGE_2 (10 μM) for 24 h, stimulated with carbachol (100 μM) in calcium-free media followed by addition of calcium (3 mM) where indicated. **(D)** Peak changes in $[Ca^{2+}]_i$ induced by carbachol and the indicated addition of 3 mM calcium. Values are mean ± SEM of results from 23 to 33 cells from two separate cell preparations as shown with closed circles. Significant differences from untreated cells were determined via a student's *t*-test (***$p < 0.001$).

increases amylase levels in irradiated mice to similar levels as unirradiated, vehicle-injected mice (**Figures 7A,B**). To confirm these findings and evaluate the proportion of amylase producing acinar cells *in vivo*, parotid glands were collected at day 30 for histological analysis and immunohistochemistry was used to determine the area of salivary gland tissue staining positive for amylase (graphed as percent of total area). The proportion of amylase secreting acinar cells is reduced at day 30 in irradiated, vehicle-injected mice, but indomethacin restored amylase levels to those in unirradiated, vehicle-injected mice (**Figures 7C,D**). To evaluate whether or not indomethacin exerts modulatory effects on other proteins that influence salivary gland secretion, whole tissue homogenates were used for immunoblots to assess levels of aquaporin 5 (AQP5) and muscle, intestine, and stomach expression 1 (MIST1). Irradiated, vehicle-injected mice have reduced levels of AQP5 in parotid gland homogenates when compared to untreated glands, with indomethacin-treated glands having levels that were not statistically different from either group (**Supplementary Figures 2A–C**). Unexpectedly, MIST1 levels were not significantly different across treatment groups (**Supplementary Figures 2A–C**). PGE_2 is able to induce proliferation following EP2-4 activation (**Figure 4** and **Supplementary Figure 1**) and compensatory proliferation that occurs in irradiated salivary glands correlates with loss of function (Grundmann et al., 2010; Hill et al., 2014; Morgan-Bathke et al., 2014). However, the evaluation of indomethacin as a compensatory proliferation modulator post-radiation has not been previously explored. Parotid gland tissue sections were stained for the proliferation marker Ki67 to evaluate differences in compensatory proliferation following radiation in vehicle and indomethacin-treated mice. Ki67 positive cells are significantly increased in irradiated, vehicle-injected mice and reduced with post-radiation indomethacin treatment (**Figures 7E,F**). These data demonstrate that indomethacin treatment reduces the compensatory proliferation response and increases the concentration of the major enzyme amylase in irradiated parotid glands indicating improved differentiation of acinar cells, which suggests that this pharmaceutical should be further tested for

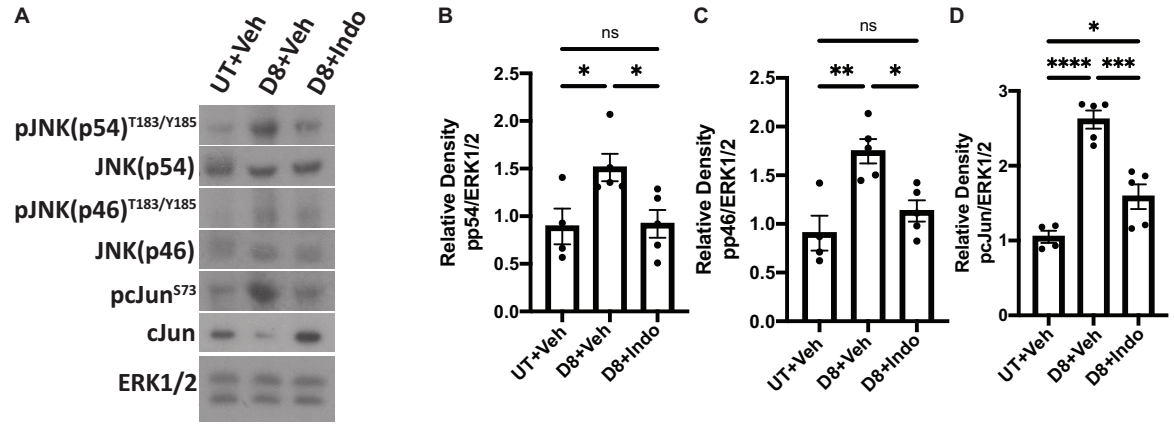

FIGURE 6 | Indomethacin reduces JNK signaling *in vivo* at day 8 post-IR. **(A–D)** C57BL/6J mice were untreated (UT) or received 5 Gy radiation with intraperitoneal injections of vehicle (Veh, saline with 10% ethanol) or indomethacin (Indo, 1 mg/kg body weight) at days 3, 5, and 7 post-IR. Parotid glands were collected at day 8 post-IR. **(A)** Representative Western blot images of phosphorylated JNK signaling molecules following radiation and indomethacin treatments. **(B–D)** Densitometry of Western blots represented in panel **(A)**. **(A–D)** Immunoblots were generated from tissue lysates using antibodies against phospho-JNK/SAPK (p54/p46)$^{T183/Y185,}$ or phospho-c-Jun^{S73}, which were stripped and re-probed for JNK/SAPK (p54/p46) or c-Jun and then ERK1/2 as a loading control. Densitometry was performed using ImageJ software and protein content was normalized to the average of UT + Veh-treated mice. Graphs represent the mean ± SEM. Each closed circle represents an independent sample. Significant differences were determined via a one-way ANOVA followed by Bonferroni's *post hoc* comparisons (*$p < 0.05$, **$p < 0.01$, ***$p < 0.001$, ****$p < 0.0001$, ns = not significant).

restoration of the normal protein composition of saliva in patients undergoing radiotherapy for HNC.

DISCUSSION

Wound healing is a highly complex process that requires delicately coordinated signaling for adequate repair to occur. In irradiated salivary glands, there is conflicting data regarding induction of inflammatory responses (Marmary et al., 2016; Lombaert et al., 2020; Zhao et al., 2020). However, it is well characterized that excessive cell proliferation occurs, but without adequate production of functional differentiated cells (Grundmann et al., 2010; Hill et al., 2014; Morgan-Bathke et al., 2014), suggesting that inhibition of the pathways responsible for compensatory proliferation may improve salivary gland function post-IR. Indomethacin is an NSAID that inhibits both COX-1 and COX-2 functions, but COX-1 has a 10-fold lower IC_{50} value for indomethacin than COX-2 (COX-1 IC_{50}: 13 nM; COX-2 IC_{50}: 130 nM) (Warner et al., 1999). These findings are consistent with our data from primary parotid gland cells, where 25 μM indomethacin caused a significant reduction in COX-1 activity after 24 h but had no effect on COX-2 activity (**Figure 2A**). Our previous studies demonstrated reduced PGE_2 secretion from primary parotid gland cells of $P2X7R^{-/-}$ compared to wild type mice that correlated with the preservation of salivary gland function post-IR, although the differences observed in expression levels or activity of COX isoforms did not correlate with changes in PGE_2 secretion (Gilman et al., 2019). Here, we show that indomethacin reduces PGE_2 production and secretion in both untreated and irradiated primary parotid cells, which correlates with reduced COX-1 activity (**Figures 2A,B**). PGE_2 has many physiological roles under homeostatic and inflammatory conditions. However, in the context of radiation damage to salivary glands, the generation of PGE_2 appears to be detrimental to the cell regenerative response, suggesting that NSAIDs are a possible therapeutic modality for restoring salivary gland function post-IR (Goldberg, 1986; Dennis and Norris, 2015; Gilman and Limesand, 2020).

While suppressing PGE_2 production appears to be protective for irradiated salivary glands (**Figures 1**, **2**) (Gilman et al., 2019), how PGE_2 influences salivary gland dysfunction has not been clearly delineated. Previous work on pancreatitis, an inflammatory disorder that is associated with high serum amylase content, found that PGE_2 treatment blocks amylase secretion from pancreatic acini (Mössner et al., 1991). Furthermore, canines with allograft pancreatic transplants that were treated with dimethyl-PGE_2 had reduced amylase levels in urine compared to untreated controls, indicative of improved pancreatic function with PGE_2 (Garvin et al., 1989). Indomethacin treatment has been shown to increase isoproterenol (ISO)-induced amylase secretion from rat parotid gland tissue, where enhanced amylase secretion observed following ISO (0.1 μM) stimulation was abrogated by co-treatment with PGE_2 (Hata et al., 1990). Here, we show that PGE_2 treatment of primary parotid gland cells reduces amylase levels (**Figures 5A,B**) and that post-IR indomethacin treatment of mice increased amylase levels in whole parotid tissue (**Figure 7**). We also show that although carbachol-induced Ca^{2+} release from intracellular stores was unaffected, PGE_2 decreases SOCE in primary parotid gland cells (**Figures 5C,D**). Research on the mechanism whereby PGE_2 inhibits SOCE is limited, although studies have linked production of PGE_2 to activation of SOCE (Kuda et al., 2011; Jairaman et al., 2015). One previous study found that PGE_2 treatment (2 h) modulated

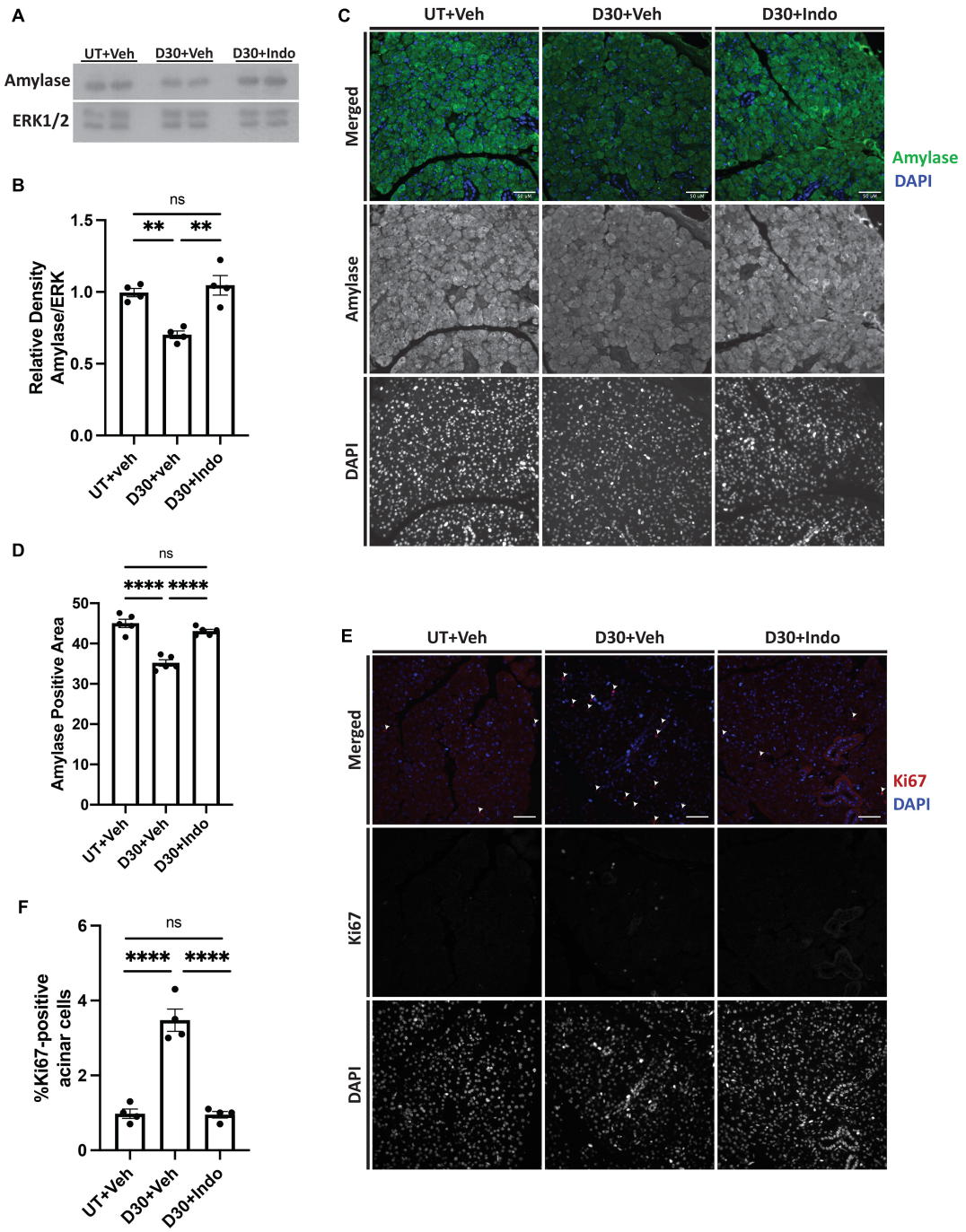

FIGURE 7 | Indomethacin treatment enhances amylase levels and reduces compensatory proliferation in whole parotid glands at day 30 post-IR. **(A,B)** C57BL/6J or (C-F) FVB mice were untreated (UT) or received 5 Gy ionizing radiation (IR) with intraperitoneal injections of vehicle (Veh, saline with 10% ethanol) or indomethacin (Indo, 1 mg/kg body weight) at days 3, 5, and 7 post-IR. Parotid glands were extracted at day 30 post-IR. **(A,B)** Immunoblots were generated from tissue lysates and an anti-amylase antibody, which were stripped and re-probed for ERK1/2 as a loading control. **(A)** Representative Western blot images of changes in amylase levels following radiation and indomethacin treatments. **(B)** Densitometry was performed using ImageJ software and protein content was normalized to the average of the UT + Veh group. **(C–F)** Parotid glands were fixed, sectioned and immunohistochemistry was performed with **(C,D)** an anti-amylase antibody or **(E,F)** an anti-Ki67 antibody, as described in section "Materials and Methods." **(C)** Representative images of amylase positive area (40× magnification, scale bar: 50 μm). **(D)** Percent positive amylase area was determined using ImageJ software. The graph represents the amylase positive area as a percentage of the total area. **(E)** Representative images of Ki67 positive area (white arrows indicate Ki67+, DAPI+ cells; 40× magnification, scale bar: 50 μm). **(F)** Ki67 positive and total cell numbers were manually counted from 5 fields of view/mouse. The graph represents the Ki67 positive cell number as a percentage of the total cell number. **(B,D,F)** Graphs represent the mean ± SEM. Each closed circle represents an independent sample. Significant differences were determined via a one-way ANOVA followed by Bonferroni's *post hoc* comparisons (**$p < 0.01$, ****$p < 0.0001$; ns = not significant).

T cell receptor activation-induced calcium mobilization and SOCE in T cells (Choudhry et al., 1999), which express all EPR isoforms (EP1-4Rs) (Nataraj et al., 2001). In the current study, we show that PGE_2 treatment (24 h) of primary mouse parotid cells that express EP1, EP2, EP3, and EP4 receptors (**Supplementary Figure 3**) had no effect on carbachol-induced release of intracellular stores but did reduce subsequent SOCE (**Figures 5C,D**). Radiation has been shown to cause a loss of SOCE in salivary gland cells due to STIM1 cleavage through activation of the TRPM2 pathway (Liu et al., 2017), although there have been no reports on interactions between PGE_2 and its receptors (EP1-EP4) and this pathway. Further investigation of how PGE_2 modulates amylase production and SOCE in salivary glands is warranted and this information may be applicable to other exocrine organs, such as the pancreas and lacrimal glands.

PGE_2 has been shown to activate the JNK/c-Jun pathway (Zeng et al., 2015; Arasa et al., 2019) and induces proliferation of pulmonary tumors (Zhong et al., 2015) and human mesenchymal stem cells (Yun et al., 2011). Previous work from our lab indicated that JNK/c-Jun activation leads to compensatory proliferation at day 5 post-IR (Wong et al., 2019) that remains elevated through day 90 (Grundmann et al., 2010) and reducing this dysregulated compensatory proliferation correlates with improved salivary gland function post-IR (Grundmann et al., 2010; Hill et al., 2014; Wong et al., 2019). The mediators responsible for radiation-induced cell proliferation in salivary glands are not well defined. Here, we show that PGE_2 treatment of primary parotid gland cells activates the JNK/c-Jun pathway (**Figure 3**) and PGE_2 or selective EP2, EP3, or EP4 receptor agonists induce cell proliferation (**Figure 4**), suggesting that PGE_2 mediates the compensatory proliferation response observed in parotid glands *in vivo*. Further supporting this observation, post-radiation indomethacin treatment significantly reduced JNK pathway activation in parotid glands of mice (**Figure 6**) and Ki67 positive staining at day 30 (**Figures 7E,F**), which correlates with the ability of indomethacin to improve salivary gland function in irradiated salivary glands (**Figures 1C–F**). Taken together, our data suggest that indomethacin treatment is a viable pharmacotherapeutic approach to protect salivary glands from IR-induced damage by blocking PGE_2 production and its activation of the JNK/c-Jun pathway leading to dysregulated proliferation. Relevantly, excessive PGE_2 production has been implicated in the progression of cancer (Nakanishi and Rosenberg, 2013). In multiple HNC models there is evidence that increased production of PGE_2 increases tumor cell proliferation that can be inhibited with NSAID treatment (Zweifel et al., 2002; Pelzmann et al., 2004; Ye et al., 2004). In HNC xenografts with head and neck squamous cell carcinoma-1483 (SCC-1483) cells, increased COX-2-mediated PGE_2 production was observed and treatment with a COX-2 selective inhibitor or a PGE_2-neutralizing antibody reduced tumor growth (Zweifel et al., 2002). Interestingly, treatment of oral SCC-25 cells with genistein, celecoxib or indomethacin reduced PGE_2 production and cell proliferation levels compared to controls (Ye et al., 2004). Lastly, indomethacin treatment of SCC-25 or SCC-9 cell lines reduced cell growth and induced apoptosis *in vitro* (Pelzmann et al., 2004). Therefore, the use of NSAIDs, such as indomethacin, may be a general means to restrict the growth of cells that become dedifferentiated, as is the case with irradiated salivary gland acinar cells and metastatic tumor cells, both of epithelial origin.

DATA AVAILABILITY STATEMENT

The original contributions presented in the study are included in the article/**Supplementary Material**, and further inquiries can be directed to the corresponding author/s.

ETHICS STATEMENT

The animal study was reviewed and approved by the University of Arizona Institutional Animal Care and Use Committee.

AUTHOR CONTRIBUTIONS

KG curated and visualized data and drafted the manuscript. KG and JC designed and conducted the experiments. KG, KL, and GW obtained funding for completion of this work. All authors conceptualized experiments, edited the manuscript and approved the final version of the manuscript.

FUNDING

This work was supported by the NIH R01 grant DE023342 to KL and GW, and the F31 grant DE028737 to KG. The funding agency had no role in study design, data collection, data analysis, the decision to publish this study or the preparation of this manuscript.

ACKNOWLEDGMENTS

We would like to thank Sean Limesand for the use of the Leica DM5500 microscope and Partha Samadder for technical assistance.

SUPPLEMENTARY MATERIAL

The Supplementary Material for this article can be found online at: https://www.frontiersin.org/articles/10.3389/fbioe.2021.697671/full#supplementary-material

Supplementary Figure 1 | Additional doses of PGE_2 and EP2R, EP3R and EP4R agonists induce proliferation of primary parotid gland cells. Primary parotid cells were prepared from C57BL/6J mice, serum-starved for 2 h and treated with vehicle (DMSO), PGE_2 (0.03 μM), or EP-receptor-selective (EP2R-EP4R) agonists for EP2R: AH13205 (10 μM), EP3R: sulprostone (0.01 μM) or EP4R: CAY10598 (10 μM). All compounds were solubilized in DMSO, mixed with serum-free primary cell culture media and incubated with cells for 24 h with EdU added during the last hour of treatment to monitor proliferating cells, as described in section "Materials and Methods." **(A)** Groups were quantified by averaging the number of positive cells out of the total number of cells from 5 fields of view/slide. Graphs represent the mean ± SEM. Each symbol represents an independent sample. Significant differences from DMSO-treated cells were determined via a one-way ANOVA

followed by Dunnett's *post hoc* comparisons (*$p < 0.05$, **$p < 0.01$). **(B)** Representative fields of view are shown.

Supplementary Figure 2 | The effect of indomethacin treatment on AQP5 and MIST1 levels in irradiated parotid glands. **(A–C)** C57BL/6J mice were untreated (UT) or received 5 Gy ionizing radiation (IR) with intraperitoneal injections of vehicle (Veh, saline with 10% ethanol) or indomethacin (Indo, 1 mg/kg body weight) at days 3, 5, and 7 following IR and parotid glands were extracted at day 30. Immunoblots were generated from tissue lysates using anti-AQP5 or anti-MIST1 antibodies, and blots were stripped and re-probed for β-tubulin as a loading control. **(A)** Representative Western blot of changes in AQP5 and MIST1 levels following radiation and indomethacin treatments. **(B,C)** Densitometry was performed using ImageJ software and protein content was normalized to the average of the UT + Veh group (*$p < 0.05$; ns = not significant).

Supplementary Figure 3 | EP1-4 receptors are present in murine parotid glands. Parotid glands were harvested from untreated (UT) C57BL/6J mice and used for immunoblots. The figure contains representative images of immunoblots for EPRs using antibodies against EP1R, EP2R, EP3R, and EP4R, which were stripped and re-probed for ERK1/2 as a loading control.

REFERENCES

Arasa, J., Terencio, M. C., Andrés, R. M., Marín-Castejón, A., Valcuende-Cavero, F., Payá, M., et al. (2019). Defective induction of COX-2 expression by Psoriatic fibroblasts promotes pro-inflammatory activation of macrophages. *Front. Immunol.* 10:536. doi: 10.3389/fimmu.2019.00536

Brown, W. A., Skinner, S. A., Malcontenti-Wilson, C., Vogiagis, D., and Brien, P. E. (2001). Non-steroidal anti-inflammatory drugs with activity against either cyclooxygenase 1 or cyclooxygenase 2 inhibit colorectal cancer in a DMH rodent model by inducing apoptosis and inhibiting cell proliferation. *Gut* 48, 660–666. doi: 10.1136/gut.48.5.660

Choudhry, M. A., Hockberger, P. E., and Sayeed, M. M. (1999). PGE2 suppresses mitogen-induced Ca2+ mobilization in T cells. *Am. J. Physiol.* 277, R1741–R1748. doi: 10.1152/ajpregu.1999.277.6.R1741

Cramer, J. D., Burtness, B., Le, Q. T., and Ferris, R. L. (2019). The changing therapeutic landscape of head and neck cancer. *Nat. Rev. Clin. Oncol.* 16, 669–683. doi: 10.1038/s41571-019-0227-z

Dennis, E. A., and Norris, P. C. (2015). Eicosanoid storm in infection and inflammation. *Nat. Rev. Immunol.* 15, 511–523. doi: 10.1038/nri3859

Garvin, P. J., Niehoff, M., and Burton, F. (1989). The effect of dimethyl PGE2 on canine pancreatic autograft exocrine secretion. *J. Surg. Res.* 46, 502–506. doi: 10.1016/0022-4804(89)90168-6

Gilman, K. E., Camden, J. M., Klein, R. R., Zhang, Q., Weisman, G. A., and Limesand, K. H. (2019). P2X7 receptor deletion suppresses γ-radiation-induced hyposalivation. *Am. J. Physiol. Regul. Integr. Comp. Physiol.* 316, R687–R696. doi: 10.1152/ajpregu.00192.2018

Gilman, K. E., and Limesand, K. H. (2020). The complex role of prostaglandin E(2)-EP receptor signaling in wound healing. *Am. J. Physiol. Regul. Integr. Comp. Physiol.* 320, R287–R296. doi: 10.1152/ajpregu.00185.2020

Goldberg, R. I. (1986). Protection of irradiated parotid by prostaglandin synthesis inhibitors. *J. Am. Dent. Assoc.* 112, 179–181.

Grundmann, O., Fillinger, J. L., Victory, K. R., Burd, R., and Limesand, K. H. (2010). Restoration of radiation therapy-induced salivary gland dysfunction in mice by post therapy IGF-1 administration. *BMC Cancer* 10:417. doi: 10.1186/1471-2407-10-417

Grundmann, O., Mitchell, G. C., and Limesand, K. H. (2009). Sensitivity of salivary glands to radiation: from animal models to therapies. *J. Dent. Res.* 88, 894–903. doi: 10.1177/0022034509343143

Hata, F., Takeuchi, T., Asano, M., and Yagasaki, O. (1990). Effects of indomethacin and prostaglandin E2 on amylase secretion by rat parotid tissue. *Biochem. Pharmacol.* 40, 390–393. doi: 10.1016/0006-2952(90)90707-R

Hill, G., Headon, D., Harris, Z. I., Huttner, K., and Limesand, K. H. (2014). Pharmacological activation of the EDA/EDAR signaling pathway restores salivary gland function following radiation-induced damage. *PLoS One* 9:e112840. doi: 10.1371/journal.pone.0112840

Jairaman, A., Yamashita, M., Schleimer, R. P., and Prakriya, M. (2015). Store-operated Ca2+ release-activated Ca2+ channels regulate PAR2-activated Ca2+ signaling and cytokine production in airway epithelial cells. *J. Immunol.* 195, 2122–2133. doi: 10.4049/jimmunol.1500396

Jasmer, K. J., Gilman, K. E., Muñoz Forti, K., Weisman, G. A., and Limesand, K. H. (2020). Radiation-induced salivary gland dysfunction: mechanisms, therapeutics and future directions. *J. Clin. Med.* 9:4095. doi: 10.3390/jcm9124095

Jensen, S. B., Vissink, A., Limesand, K. H., and Reyland, M. E. (2019). Salivary gland hypofunction and xerostomia in head and neck radiation patients. *J. Natl. Cancer Inst. Monogr.* 2019:lgz016. doi: 10.1093/jncimonographs/lgz016

Jiang, J., Qiu, J., Li, Q., and Shi, Z. (2017). Prostaglandin E2 signaling: alternative target for glioblastoma? *Trends Cancer* 3, 75–78. doi: 10.1016/j.trecan.2016.12.002

Johnson, D. E., Burtness, B., Leemans, C. R., Lui, V. W. Y., Bauman, J. E., and Grandis, J. R. (2020). Head and neck squamous cell carcinoma. *Nat. Rev. Dis. Primers* 6:92. doi: 10.1038/s41572-020-00224-3

Johnson, G. L., and Nakamura, K. (2007). The c-jun kinase/stress-activated pathway: regulation, function and role in human disease. *Biochim. Biophys. Acta* 1773, 1341–1348. doi: 10.1016/j.bbamcr.2006.12.009

Kuda, O., Jenkins, C. M., Skinner, J. R., Moon, S. H., Su, X., Gross, R. W., et al. (2011). CD36 protein is involved in store-operated calcium flux, phospholipase A2 activation, and production of prostaglandin E2. *J. Biol. Chem.* 286, 17785–17795. doi: 10.1074/jbc.M111.232975

Liu, X., Gong, B., de Souza, L. B., Ong, H. L., Subedi, K. P., Cheng, K. T., et al. (2017). Radiation inhibits salivary gland function by promoting STIM1 cleavage by caspase-3 and loss of SOCE through a TRPM2-dependent pathway. *Sci. Signal.* 10:eaal4064. doi: 10.1126/scisignal.aal4064

Lombaert, I. M. A., Patel, V. N., Jones, C. E., Villier, D. C., Canada, A. E., Moore, M. R., et al. (2020). CERE-120 prevents irradiation-induced hypofunction and restores immune homeostasis in porcine salivary glands. *Mol. Ther. Methods Clin. Dev.* 18, 839–855. doi: 10.1016/j.omtm.2020.07.016

Lucas, S. (2016). The pharmacology of indomethacin. *Headache* 56, 436–446. doi: 10.1111/head.12769

Marmary, Y., Adar, R., Gaska, S., Wygoda, A., Maly, A., Cohen, J., et al. (2016). Radiation-induced loss of salivary gland function is driven by cellular senescence and prevented by IL6 modulation. *Cancer Res.* 76, 1170–1180. doi: 10.1158/0008-5472.CAN-15-1671

Morgan-Bathke, M., Harris, Z. I., Arnett, D. G., Klein, R. R., Burd, R., Ann, D. K., et al. (2014). The Rapalogue, CCI-779, improves salivary gland function following radiation. *PLoS One* 9:e113183. doi: 10.1371/journal.pone.0113183

Mössner, J., Secknus, R., Spiekermann, G. M., Sommer, C., Biernat, M., Bahnsen, H., et al. (1991). Prostaglandin E2 inhibits secretagogue-induced enzyme secretion from rat pancreatic acini. *Am. J. Physiol.* 260(Pt 1), G711–G719. doi: 10.1152/ajpgi.1991.260.5.G711

Nakanishi, M., and Rosenberg, D. W. (2013). Multifaceted roles of PGE2 in inflammation and cancer. *Semin. Immunopathol.* 35, 123–137. doi: 10.1007/s00281-012-0342-8

Nataraj, C., Thomas, D. W., Tilley, S. L., Nguyen, M. T., Mannon, R., Koller, B. H., et al. (2001). Receptors for prostaglandin E(2) that regulate cellular immune responses in the mouse. *J. Clin. Invest.* 108, 1229–1235. doi: 10.1172/JCI13640

Pelzmann, M., Thurnher, D., Gedlicka, C., Martinek, H., and Knerer, B. (2004). Nimesulide and indomethacin induce apoptosis in head and neck cancer cells. *J. Oral Pathol. Med.* 33, 607–613. doi: 10.1111/j.1600-0714.2004.00216.x

Reinke, J. M., and Sorg, H. (2012). Wound repair and regeneration. *Eur. Surg. Res.* 49, 35–43. doi: 10.1159/000339613

Tanaka, A., Hase, S., Miyazawa, T., Ohno, R., and Takeuchi, K. (2002). Role of cyclooxygenase (COX)-1 and COX-2 inhibition in nonsteroidal anti-inflammatory drug-induced intestinal damage in rats: relation to various pathogenic events. *J. Pharmacol. Exp. Ther.* 303:1248. doi: 10.1124/jpet.102.041715

Warner, T. D., Giuliano, F., Vojnovic, I., Bukasa, A., Mitchell, J. A., and Vane, J. R. (1999). Nonsteroid drug selectivities for cyclo-oxygenase-1 rather than cyclo-oxygenase-2 are associated with human gastrointestinal toxicity: a full in vitro analysis. *Proc. Natl. Acad. Sci. U. S. A.* 96, 7563–7568. doi: 10.1073/pnas.96.13.7563

Wong, W. Y., Allie, S., and Limesand, K. H. (2019). PKCζ and JNK signaling regulate radiation-induced compensatory proliferation in parotid salivary glands. *PLoS One* 14:e0219572. doi: 10.1371/journal.pone.0219572

Woods, L. T., Camden, J. M., Khalafalla, M. G., Petris, M. J., Erb, L., Ambrus, J. L. Jr., et al. (2018). P2Y(2) R deletion ameliorates sialadenitis in IL-14α-transgenic mice. *Oral Dis.* 24, 761–771. doi: 10.1111/odi.12823

Ye, F., Wu, J., Dunn, T., Yi, J., Tong, X., and Zhang, D. (2004). Inhibition of cyclooxygenase-2 activity in head and neck cancer cells by genistein. *Cancer Lett.* 211, 39–46. doi: 10.1016/j.canlet.2004.03.043

Yun, S. P., Ryu, J. M., Jang, M. W., and Han, H. J. (2011). Interaction of profilin-1 and F-actin via a β-arrestin-1/JNK signaling pathway involved in prostaglandin E(2)-induced human mesenchymal stem cells migration and proliferation. *J. Cell. Physiol.* 226, 559–571. doi: 10.1002/jcp.22366

Zeng, C., Xu, J. N., Zhou, Y., Yang, H. X., Zhou, Y. F., and Xue, Q. (2015). C-Jun NH2-terminal kinase and p38 inhibition suppresses prostaglandin E2-stimulated aromatase and estrogen receptor levels in human endometriosis. *J. Clin. Endocrinol. Metab.* 100, E1404–E1414. doi: 10.1210/jc.2015-2031

Zhao, Q., Zhang, L., Hai, B., Wang, J., Baetge, C. L., Deveau, M. A., et al. (2020). Transient activation of the Hedgehog-Gli pathway rescues radiotherapy-induced dry mouth via recovering salivary gland resident macrophages. *Cancer Res.* 80, 5531–5542. doi: 10.1158/0008-5472.CAN-20-0503

Zhong, X., Fan, Y., Ritzenthaler, J. D., Zhang, W., Wang, K., Zhou, Q., et al. (2015). Novel link between prostaglandin E2 (PGE2) and cholinergic signaling in lung cancer: the role of c-Jun in PGE2-induced α7 nicotinic acetylcholine receptor expression and tumor cell proliferation. *Thorac. Cancer* 6, 488–500. doi: 10.1111/1759-7714.12219

Zweifel, B. S., Davis, T. W., Ornberg, R. L., and Masferrer, J. L. (2002). Direct evidence for a role of cyclooxygenase 2-derived prostaglandin E2 in human head and neck xenograft tumors. *Cancer Res.* 62, 6706–6711.

Conflict of Interest: The authors declare that the research was conducted in the absence of any commercial or financial relationships that could be construed as a potential conflict of interest.

frontiers in Bioengineering and Biotechnology

ORIGINAL RESEARCH
published: 08 September 2021
doi: 10.3389/fbioe.2021.659742

Platelet-Rich Plasma Induces Autophagy and Promotes Regeneration in Human Dental Pulp Cells

Hanxin Xu[1,2,3†], *Fen Xu*[1,2,3†], *Jiajia Zhao*[1,2,3], *Caixia Zhou*[1,2,3] *and Jiarong Liu*[1,2,3*]

[1]Department of Stomatology, Union Hospital, Tongji Medical College, Huazhong University of Science and Technology, Wuhan, China, [2]School of Stomatology, Tongji Medical College, Huazhong University of Science and Technology, Wuhan, China, [3]Hubei Province Key Laboratory of Oral and Maxillofacial Development and Regeneration, Wuhan, China

OPEN ACCESS

Edited by:
Ryang Hwa Lee,
Texas A&M University, United States

Reviewed by:
Ahmed El-Fiqi,
Dankook University, South Korea
Carl Austin Gregory,
Texas A&M Health Science Center, United States

***Correspondence:**
Jiarong Liu
kqyyljr@aliyun.com

[†]These authors have contributed equally to this work and share first authorship

Specialty section:
This article was submitted to Tissue Engineering and Regenerative Medicine, a section of the journal Frontiers in Bioengineering and Biotechnology

Received: 28 January 2021
Accepted: 05 August 2021
Published: 08 September 2021

Citation:
Xu H, Xu F, Zhao J, Zhou C and Liu J (2021) Platelet-Rich Plasma Induces Autophagy and Promotes Regeneration in Human Dental Pulp Cells. Front. Bioeng. Biotechnol. 9:659742. doi: 10.3389/fbioe.2021.659742

Regenerative endodontic procedures using autologous platelet-rich plasma (PRP) can improve the biologic outcome of treatment. However, its mechanism of action on improving pulp regeneration is not fully elucidated. Autophagy was recently shown to be related to tissue repair and osteogenesis. Therefore, the objective of this study was to investigate the effect of PRP in dental pulp regeneration and to elucidate the role of autophagy involved in this process. Human dental pulp cells (hDPCs) were isolated from healthy dental pulp and co-cultured with an increasing concentration of PRP. Cellular migration and proliferation were determined by scratch assay, transwell assay, and cell-counting kit 8 assay. Osteogenic differentiation was clarified by using alkaline phosphatase staining, alizarin red staining, and real-time polymerase chain reaction (RT-PCR) to measure the gene expression levels of alkaline phosphatase, collagen-1, osteocalcin, dentin matrix protein 1, and dentin sialophosphoprotein. Autophagic bodies were observed by transmission electron microscopy and the expression of autophagy marker light chain 3B (LC3B) was determined by immunofluorescence staining. The mRNA and protein expression level of LC3B and Beclin-1 were quantified by qRT-PCR and western blotting. The effect of PRP on cellular migration, proliferation, and osteogenic differentiation was further investigated in the milieu of autophagy activator, rapamycin, and inhibitor, 3-methyladenine. Results showed that PRP promoted cell migration, proliferation, and osteogenic differentiation. Autophagic bodies were strongly activated and the expression level of LC3B and Beclin-1 was significantly promoted by PRP. Autophagy inhibition suppressed PRP-induced hDPCs migration, proliferation, and osteogenic differentiation, whereas autophagy activator substantially augmented PRP-stimulated migration, proliferation, and differentiation. Taken together, these findings suggested that PRP could effectively promote regenerative potentials associated with autophagy.

Keywords: platelet-rich plasma, autophagy, osteogenic differentiation, human dental pulp cells, dental pulp regeneration

INTRODUCTION

If immature teeth have a diffuse pulp infection or periapical periodontitis with an open apex, apexification with calcium hydroxide or apical barrier with mineral trioxide aggregate was adapted according to the traditional methods (Bonte et al., 2015). However, neither method above could promote root development (Andreasen et al., 2002). Regenerative endodontic methods mainly including revascularization and regeneration could enable these roots to continue growing in width and length (Sun et al., 2011). Recent reports demonstrated that revitalization of these infected immature teeth using platelet-rich plasma (PRP) provided a desirable outcome (Sachdeva et al., 2015). PRP separated from whole blood has been described as platelet concentrates. When these platelets are activated, they could release amounts of growth factors. These growth factors are confirmed to accelerate the healing process and promote pulp repair (Altaii et al., 2017). PRP also presented benefits as a natural scaffold for cell proliferation, migration, and differentiation in pulp regeneration (Torabinejad and Faras, 2012; Bezgin et al., 2015).

Although numerous reports indicated that PRP provided a promising choice in regenerative endodontic procedures, the mechanism of action remains to be fully determined. Autophagy is an intracellular catabolic process of self-degradation of cellular components (Sotthibundhu et al., 2018). It plays an important role in cellular nutrition supply, functions maintaining, growth, and removing anomalous cellular components that are accumulated in aging (Mizushima and Levine, 2010). Several proteins, including microtubule-associated protein light chain 3 B (LC3B) and Beclin-1, have been implicated in the process of autophagy. LC3B is located in both the inner and outer membranes of autophagosomes. Autophagy increases the conversion of LC3B I into LC3B II, so the accumulation of LC3B II is the most widely used marker for autophagy. Beclin-1 is an autophagy-initiated protein and therefore increases in Beclin-1 also accompany activation of the process (Mizushima, 2018). Autophagy was reported to be involved in cell proliferation, differentiation, and migration (Yang et al., 2015) and supposed to have an essential role in tissue repair and regeneration (Xiao et al., 2013).

We hypothesize that autophagy might be involved in PRP-mediated dental pulp regeneration. Therefore, this study aimed to evaluate the effect of PRP on migration, proliferation, and osteogenic differentiation of human dental pulp cells (hDPCs). We also explored the effects of PRP in the autophagic activity of hDPCs and the role of autophagy in PRP-induced migration, proliferation, and differentiation.

MATERIALS AND METHODS

hDPCs Isolation and Culture

Dental pulp tissues were collected from healthy caries-free premolars or third molars from 13-to-25-year-old patients. Informed consent was obtained from the patients and the protocol was approved by the Ethics Committee of Union Hospital, Tongji Medical College, Huazhong University of Science and Technology. Briefly, under the sterile condition, tooth surfaces were cleaned by 75% ethanol; debris and periodontal ligament were then cleaned off by a scalpel blade. The tooth was slowly cut along cemento-enamel junction and pulp tissue was gently separated from the crown and root. Pulp tissue was then cut into small pieces and digested in a solution containing 3 mg/ml collagenase type I (Invitrogen) and 4 mg/ml dispase (Roche) for 1 h at 37°C. Digested pieces were cultured in DMEM supplemented with 20% FBS (Fetal Bovine Serum) and 1% penicillin-streptomycin (Huang et al., 2008; Karamzadeh et al., 2012). Cells were passaged three to four times and used in subsequent experiments.

PRP Preparation and Activation

Human whole blood samples were harvested with informed consent from 6 (mean age 20 ± 15 years) healthy volunteer donors. The blood sample collection was also approved by the Institutional Research Ethics Committee of Union Hospital. PRP was separated from the blood samples by secondary centrifugation. The blood collection was firstly centrifugalized at 550 g for 10 min; the top plasma and middle platelet layers were then carefully transferred to a new tube. After secondly centrifugalizing the blood collection at 1,230 g for 15 min, the upper layer was discarded carefully and 1 ml of PRP containing precipitated platelets was obtained. Before each use, calcium chloride was added to PRP at a ratio of 1:9, and thrombin was added at 500 IU per 1 ml volume of PRP (Marx et al., 1998; Mizushima, 2018).

Cell Migration Assay

Cell migration was firstly assessed by scratch assay. In short, hDPCs (7×10^5) were seeded into 6-well plates and incubated for 24 h. The cells were scored with a sterile pipette tip to leave a plus shape scratch of approximately 0.4–0.5 mm in width. The culture medium was then changed into DMEM containing 1 and 10% FBS and 1, 5, 10, and 20% PRP separately in different groups. The cell migration was observed with an inverted microscope at 24 h.

In transwell assay, hDPCs (6×10^4) were suspended in 200 uL of serum-free DMEM and were added to the upper chamber of the insert (transwell plates are 6.5 mm in diameter with 8 μm pore filters; Corning Costar, Cambridge, MA). The culture medium in the lower chamber was changed into 500 uL of DMEM with 1 and 10% FBS and 1, 5, 10, and 20% PRP, respectively. After 24 h, the upper chambers were washed with PBS and the cells inside the chamber were gently wiped off by a cotton swab. The cells beneath the filter were fixed with 4% paraformaldehyde and then stained with crystal violet for 30 min. The number of the migration cells was observed and counted under an inverted microscope. All experiments were done in triplicate.

Proliferation Assay

The effect of PRP on the proliferation of hDPCs was evaluated by using a cell-counting kit 8 assay (CCK-8, Dojindo, Japan). Briefly,

hDPCs (3×10^3) were seeded into 96-well plates and divided into six groups. After overnight incubation, the medium was changed into different concentrations of FBS (1 and 10%) and PRP (1, 5, 10, and 20%) respectively. At the indicated time points (1, 3, 5 days), cells were quantified using CCK-8 assay and absorbance was measured at 450 nm in quintuplicate wells per condition.

To further explore the effect of autophagy on cell migration and proliferation in PRP-treated hDPCs, autophagy modulation was employed. Cells were pre-treated with rapamycin (RAP) (100 nM, MCE, China) or 3-methyladenine (3-MA) (5 mM, MCE, China) before incubation with 5% PRP in scratch assay, transwell assay, and CCK-8 assay.

Immunofluorescence Staining

For immunofluorescence detection, hDPCs were seeded on top of coverslips in 12-well plates. After overnight incubation, the culture medium was changed into DMEM with 1 and 10% FBS and 1, 5, 10, and 20% PRP separately in different groups. After incubation for 24h, the cells were fixed in 4% paraformaldehyde, permeabilized with 0.5% Triton X-100, and blocked with 1% BSA. LC3B (1:500, Abclone, China) was added as primary antibody and incubated overnight at 4°C. Alexa Fluor 488 (Proteintech) green fluorescence conjugate goat anti-mouse was used as a secondary antibody (1:200). Alexa Fluor cy3 phalloidin red fluorescence conjugate (1:500) was then applied to mark the actin cytoskeleton, and subsequently, the DPSCs were treated with 4′, 6-diamidino-2-phenylindole (DAPI, 1:1,000, Biosharp, China). The coverslips were mounted on a microscope slide with an embedding medium and observed under a laser scanning confocal microscope. To investigate the effect of autophagy on immunofluorescence, cells were cultured in the presence of an inhibitor or agonist of autophagy.

Transmission Electron Microscopy

hDPCs (5×10^6) were cultured with 10% FBS or 5% PRP for 24 h, digested with 2.5% trypsin/EDTA (HyClone, America), centrifuged, and fixed with 2.5% glutaraldehyde (Sigma) overnight at 4°C. The samples were examined using a transmission electron microscope (Hitachi HT7700-SS, Hitachi, Japan) operating at 75 kV.

Alkaline Phosphatase (ALP) Staining

hDPCs were cultivated in mineralized medium containing 10% FBS and 1, 5, 10, and 20% PRP for 7 days and fixed with 4% paraformaldehyde. The cells were stained with an ALP assay kit (Jiancheng Bioengineering Institute, China) according to the manufacturer's instructions. To investigate the role of autophagy in PRP-induced cell osteogenic differentiation, autophagy inhibitor or enhancer was also introduced.

Alizarin Red Staining

hDPCs (4×10^4) were seeded into 24-well culture plates and cultured in osteogenic induction medium (Cyagen, China). The cells were divided into five groups and in each group 10% FBS and 1, 5, 10, and 20% PRP were added, respectively. Cultures were stained with Alizarin Red (Servicebio, China) on day 21 to show deposits of calcium phosphate according to the manufacturer's instructions. Shortly, the cells were fixed with 4% paraformaldehyde for 30 min and stained by the Alizarin Red (Servicebio, China) for 15 min.

RNA Isolation and Quantitative Real-Time Polymerase Chain Reaction (qRT-PCR)

Total RNA was isolated from hDPCs after 3 weeks of incubation (LC3B, Beclin-1 for 24 h, ALP for 7 days) and reversely transcribed into complementary DNA using the RNA Isolation Total RNA Extraction Reagent (Vazyme, China) and HiScript III RT SuperMix for qPCR (Vazyme, China). qRT-PCR was performed in triplicate using an AceQ Universal SYBR qPCR Master Mix (Vazyme, China). The reaction conditions were as follows: polymerase activation at 95°C for 10 min, 40 cycles of denaturation at 95°C for 15 s, and annealing and extension at 60°C for 1 min. The primers for the reference gene β-actin and for the target genes ALP, collagen-1(COL 1), osteocalcin (OCN), dentin matrix protein 1 (DMP-1), dentin sialophosphoprotein (DSPP), LC3B, and Beclin-1 are shown in **Table 1**.

Western Blot Analysis

hDPCs were cultured in 10% PBS, 5%PRP, RAP, or 5%3-MA for 24 h; protein was extracted using RIPA buffer with fresh protease inhibitors (InvivoGen). Protein concentration was measured by the BCA kit (Beyotime). The proteins were separated by electrophoresis on an SDS-PAGE gel and then transferred onto a PVDF membrane. After blocking for 1 h with skim milk, the membranes were incubated with primary antibodies against LC3B (1:1,000; Abclonal), Beclin-1 (1:1,000; Abclonal), and GAPDH (1:1,0000; Proteintech) overnight at 4°C. Then, the membranes were incubated with secondary antibodies for more than 1 h. The protein-antibody complexes were then visualized using the enhanced chemiluminescence detection system.

Statistical Analysis

Data from different experiments were represented as mean ± standard deviation and analyzed by SPSS 20.0. Student's *t*-test or one-way ANOVA was used to analyze the significant difference. $p < 0.05$ was considered statistically significant.

RESULTS

Cell Migration and Proliferation of hDPCs

In scrape assay, the results showed that 5, 10, and 20% PRP significantly promoted cell migration of hDPCs (**Figure 1A**) and 5% PRP showed the best effect. Simultaneously, in the transwell assay (**Figures 1A,B**), the number of cells that migrated toward 10% FBS and 1, 5, 10, and 20% PRP was significantly higher than the control group (1% FBS) (**Figures 1A,B**). The number of migrating cells toward 5% PRP was also the highest (**Figure 1B**).

TABLE 1 | The primers for the reference genes.

Gene name	Forward (5'-3')	Reverse (5'-3')
GAPDH	ATTCCATGGCACCGTCAAGG	TCGCCCCACTTGATTTTGGA
ALP	TGAGAGTGACGAGAAAGCCAGG	TTCCGTGCGGTTCCAGATGAA
OCN	TCACACTCCTCGCCCTATTG	TGCTTGGACACAAAGGCTG
COL-1	TACCGGGCTGATGATGCCAAT	ATCTTGAGGTCACGGCAGGT
DSPP	GGGCCATTCCAGTTCCTCAAA	TTCATGCACCAGGACACCACT
DMP-1	ATCCTGTGCTCTCCCAGTAACC	ATGACTCACTGCTCTCCAAGGG
Beclin-1	CCATGCAGGTGAGCTTCGT	GAATCTGCGAGAGACACCATC
LC3B	GATGTCCGACTTATTCGAGAGC	TTGAGCTGTAAGCGCCTTCTA

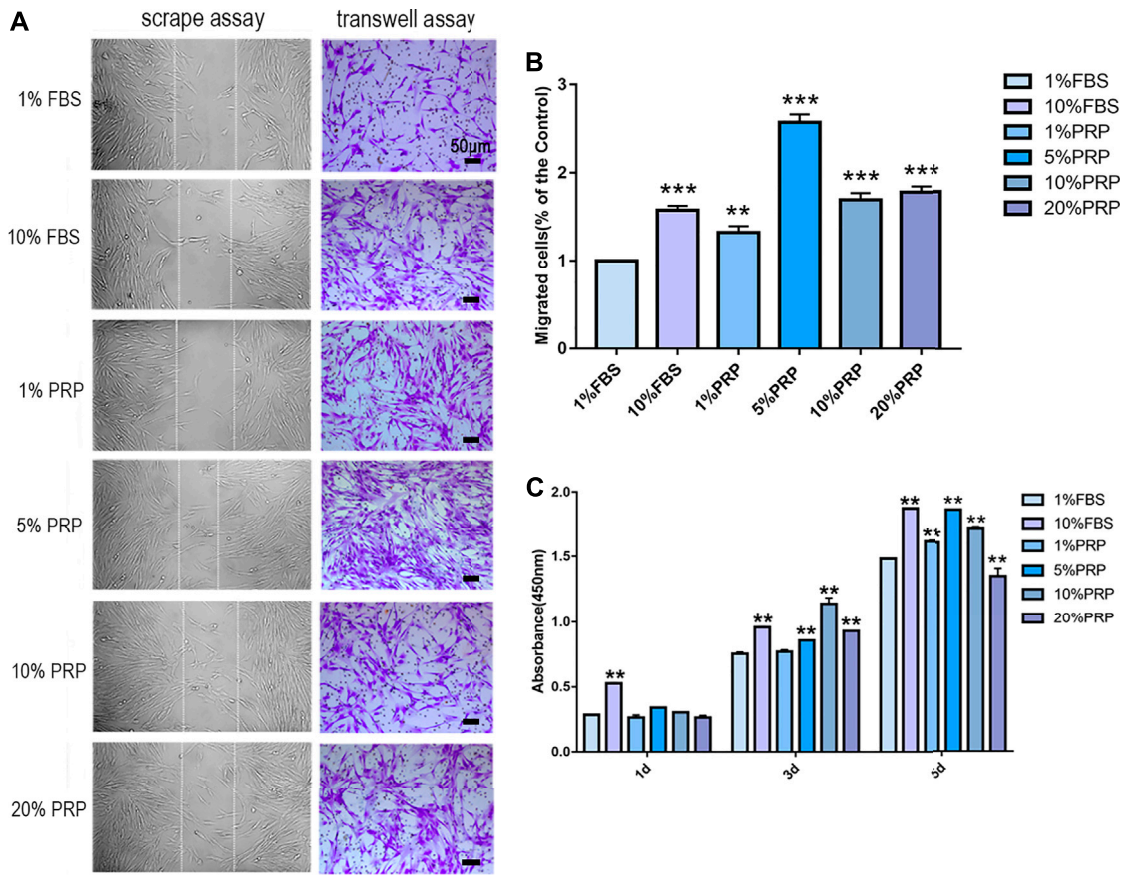

FIGURE 1 | PRP enhanced cell migration and proliferation of hDPCs. **(A)** In scrape assay, hDPCs were seeded into 6-well plates in the presence of 1 and 10% FBS and 1, 5, 10, and 20% PRP for 24 h. In transwell assay, hDPCs were seeded into the upper chamber of transwell plates, with different concentrations of FBS or PRP in the lower chamber for 24 h (scale bar, 50 μm). **(B)** Measurement of the number of migrated hDPCs in a transwell assay. **(C)** The proliferation of hDPCs was assessed by a CCK-8 assay. Data in **(B)** and **(C)** are representative of three independent experiments. Data are presented as mean ± standard deviation. Significantly different groups, $^{*}p < 0.05$, $^{**}p < 0.001$.

To examine the effect of PRP on cell proliferation, a CCK-8 test was performed. The results demonstrated that there were no significant differences in cell proliferation rates between groups on day 1. On day 3, PRP at 5, 10, and 20% concentration significantly increased cell proliferation rates. On day 5, the cell cultured in 1, 5, and 10% PRP showed significantly higher

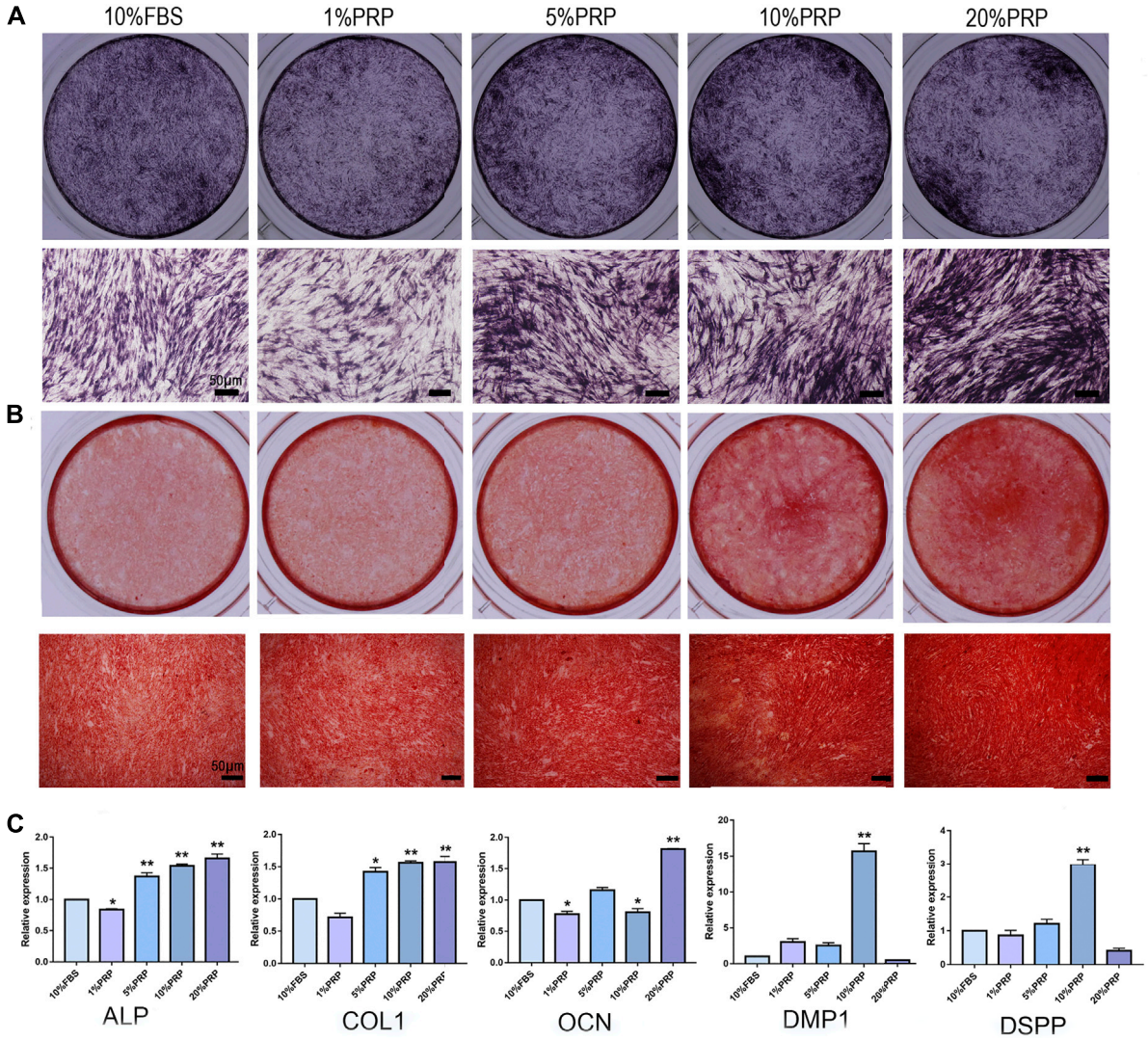

FIGURE 2 | Effect of PRP on cell osteogenic differentiation of hDPCs was assessed by ALP, alizarin red staining, and real-time quantitative PCR. **(A)** Cells cultured in the presence of different concentrations of PRP were fixed and stained for ALP (scale bar, 50 μm). **(B)** Cells were fixed and stained with alizarin red (scale bar, 50 μm). **(C)** Real-time quantitative-PCR analysis of ALP, COL 1, OCN, DMP-1, DSPP mRNA expression in different groups. Data in **(C)** are representative of five independent experiments. Data are presented as mean ± standard deviation. Significantly different groups, $^{*}p < 0.05$, $^{**}p < 0.001$.

proliferation rates, while a significant reduction in cell proliferation was observed with 20% PRP concentration than the control group (1% FBS) (**Figure 1C**).

Osteogenic Differentiation of hDPCs

To explore the effects of PRP on osteogenic differentiation, ALP and alizarin red staining were analyzed. The hDPCs cultured in 5, 10, and 20% PRP increased the level of ALP staining than the control group (10% FBS) (**Figure 2A**). The alizarin red results showed that PRP increased mineralized nodule formation (5, 10, and 20%) (**Figure 2B**). The group treated with 20% PRP demonstrated the highest osteogenic induction capacities.

To determine the transcriptomic changes accompanied by PRP treatment, we performed qRT-PCR. ALP, Col-1, OCN, DMP-1, and DSPP are important genes for osteogenic differentiation. The expression levels of ALP and Col-1 were highly elevated in 5, 10, and 20% PRP-treated group (**Figure 2C**). The expression level of OCN was dramatically increased in the 20% PRP group, while DSPP and DMP-1 expression were significantly induced by 10% PRP (**Figure 2C**).

Autophagy Activation by PRP

To investigate the activation of autophagy by PRP treatment, immunofluorescence staining was firstly employed to detect the expression of the autophagy-associated protein (LC3B). As shown in **Figures 3A,B**, the expression of LC3B was increased significantly by PRP at 5% concentration. The results of the transmission electron microscope showed that a large number of autophagic vacuoles (arrows in **Figure 3C**) were observed in hDPCs incubated with 5% PRP (**Figure 3D**). Consistent with the

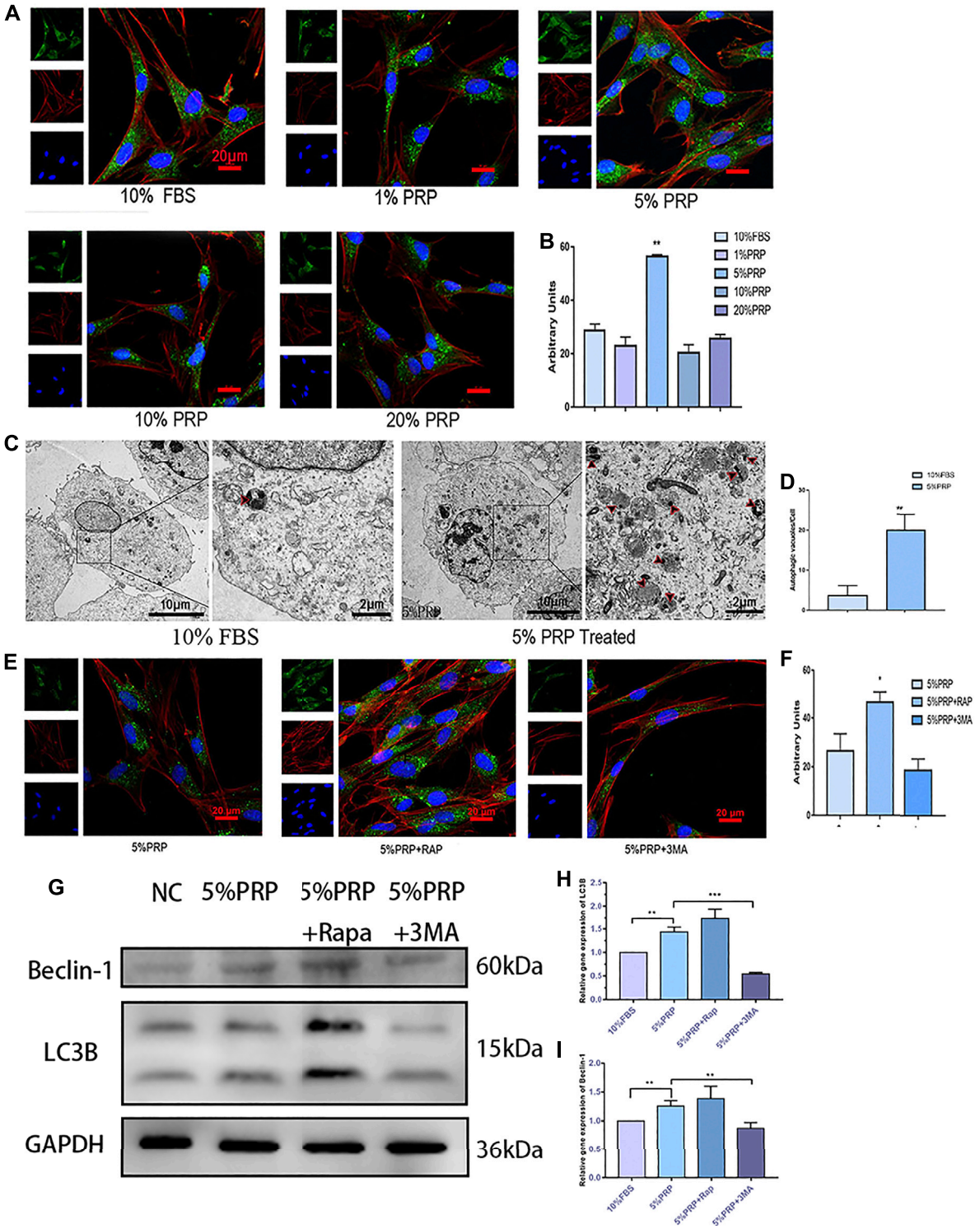

FIGURE 3 | (A) Autophagy activation by PRP. By immunofluorescence staining, 5% PRP obviously increased the expression of LC3B (scale bar, 20 μm). **(B)** The graph shows the quantitative analysis of LC3B fluorescence by Image J. **(C)** By transmission electron microscope, 5% PRP-treated hDPCs showed a large number of autophagic vacuoles. **(D)** The number of autophagic vacuoles per cell. Experiments were repeated three times. **(E)** Immunofluorescence staining of autophagy-associated protein was elevated by rapamycin, whereas it was reduced by 3-MA (scale bar, 20 μm). **(F)** Quantitative analysis of LC3B fluorescence was estimated by Image J. **(G)** Western blot analysis of the autophagy-associated proteins levels in the hDPCs treated with 5% PRP, rapamycin (RAP) (100 nM) + 5% PRP, or 3-methyladenine (3-MA) (5 mM) + 5% PRP for 24 h. **(H)** LC3B and Beclin-1 **(I)** mRNA expression were analyzed by quantitative PCR. Data in **(B)**, **(C)**, **(D)**, **(F)**, **(H),** and **(I)** are presented as mean ± standard deviation. Significantly different groups, $^{*}p < 0.05$, $^{**}p < 0.001$.

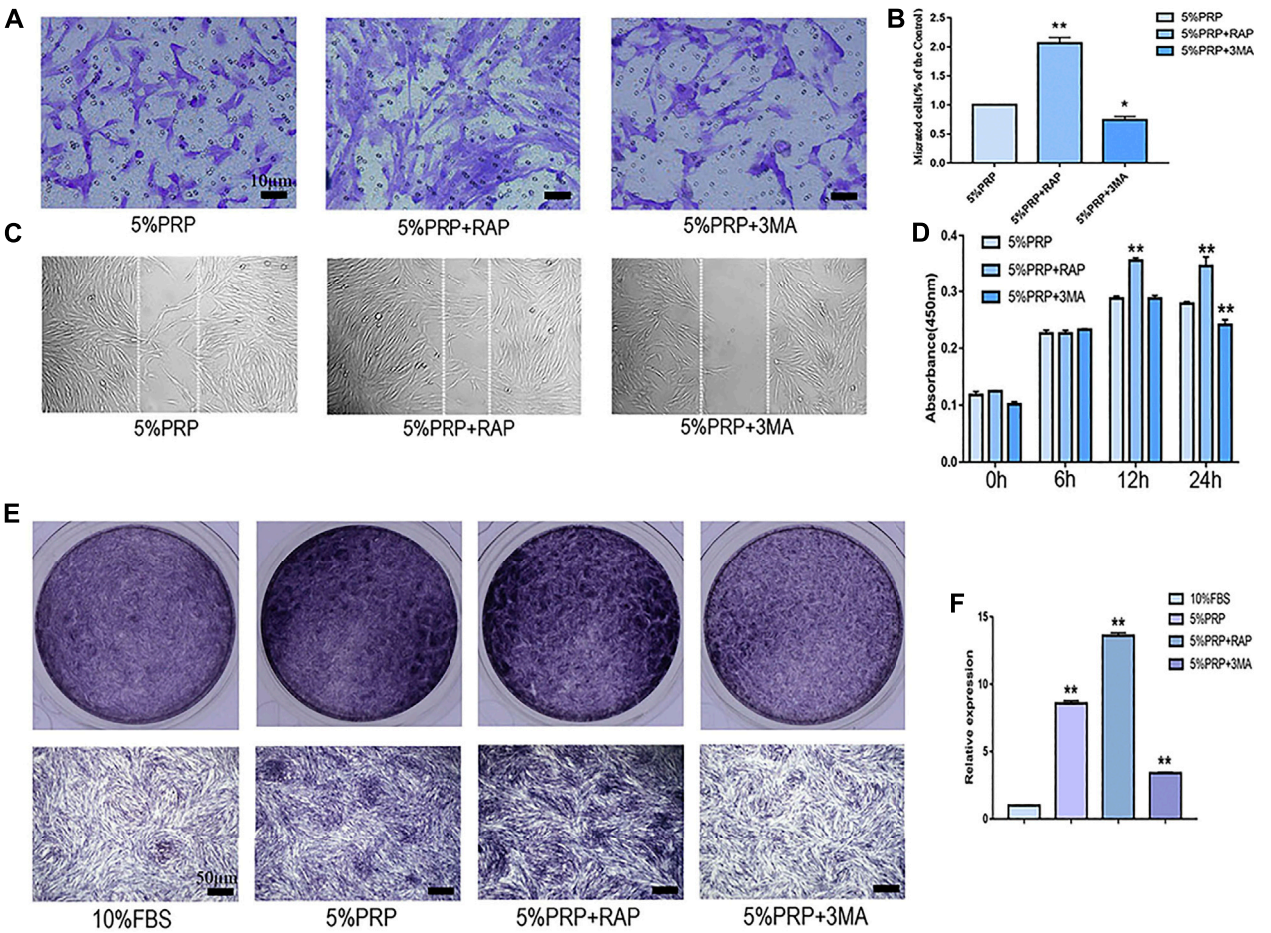

FIGURE 4 | Cell migration, proliferation, and osteogenic differentiation were suppressed by autophagy inhibitor and promoted by autophagy agonist. hDPCs were treated with 5% PRP, rapamycin (RAP) (100 nM) + 5% PRP, or 3-methyladenine (3-MA) (5 mM) + 5% PRP. **(A)** By transwell assay, representative images of the migrated cells in different groups (scale bar, 10 μm). **(B)** The graph shows the number of migrated cells in different groups by transwell assay. **(C)** Representative images of the migrated cells were evaluated by scrape assay. **(D)** The CCK-8 assay was used to assess the proliferation ratio up to 24 h. **(E)** ALP staining of the four groups on day 7 (scale bar, 50 μm). **(F)** ALP mRNA expression was analyzed by quantitative PCR. Experiments were repeated three times. Data in **(B), (D), (E)** are presented as mean ± standard deviation. Significantly different groups, $^{*}p < 0.05$, $^{**}p < 0.001$.

immunofluorescence staining results, the western blotting and qRT-PCR results showed that expression of autophagy-associated proteins, LC3B and Beclin-1, were increased by 5% PRP (**Figures 3G–I**). The result suggested that autophagy was strongly activated by PRP treatment.

After the agonist and inhibitor of autophagy were added, the immunofluorescence staining of LC3B was increased in the presence of rapamycin and decreased by 3-MA (**Figures 3E,F**). The expression level of autophagy-related genes and protein expressions, LC3B and Beclin-1, was also elevated by rapamycin and reduced by 3-MA (**Figures 3G–I**).

In the presence of an autophagy activator (RAP), cell migration was promoted in both transwell (**Figures 4A,B**) and scratch assay (**Figure 4C**). In the presence of inhibitor (3-MA), the migration of hDPCs was weakened in both scrape and transwell assay (**Figures 4A–C**). In the CCK-8 assay, the proliferation of hDPCs was enhanced after treatment with autophagy activator at 12 and 24 h time points. Cell proliferation was weakened in the presence of autophagy inhibitor at 24 h (**Figure 4D**). The ALP staining and quantitative-PCR results revealed that autophagy inhibition suppressed PRP-induced hDPCs osteogenic differentiation, whereas autophagy activator augmented PRP-stimulated differentiation (**Figures 4E,F**). These data suggested that autophagy was involved in cell migration, proliferation, and differentiation induced by PRP.

DISCUSSION

Endodontic treatments are widely used in clinical work (Ng et al., 2007; 2008). However, for incompletely developed teeth, conventional root canal therapy would have a poor prognosis (Harlamb, 2016). On one hand, these teeth often have open and divergent apices, and it is difficult to clean and obturate these roots with traditional techniques and materials. On the other

hand, the dentinal walls of these teeth are very thin and weak, which makes them prone to fracture with stress-overload (Lawley et al., 2004). The regenerative endodontic procedure can regenerate pulp-like tissue and promote root development of these teeth (Sachdeva et al., 2015; Kim et al., 2018; Staffoli et al., 2019). PRP contains many growth factors and provides desirable outcomes for the revitalization of immature teeth (Li et al., 2014; Diogenes and Ruparel, 2017). Therefore, there is wide interest in the PRP-mediated regeneration of dental pulp (Otero et al., 2017; Chai et al., 2019).

Dentinal regeneration requires the involvement of several physiological processes in hDPCs, including cell migration, proliferation, and osteogenic differentiation (Yeom et al., 2016; Zhang et al., 2017). The present study investigated the regenerative activity of hDPCs cultured with different concentrations of PRP and we demonstrated that PRP showed significant regenerative potential. We firstly demonstrated that cell migration and proliferation were significantly induced by PRP. The osteogenic experiments showed that PRP induced significantly greater mineralization of hDPCs. Some recent studies have developed culture conditions for in vitro expansion of cells treated by PRP (Lucarelli et al., 2003; Yeom et al., 2016; Pandey et al., 2019; Hahn et al., 2020). These research articles also focused on optimizing concentrations of PRP used for treatments (Lucarelli et al., 2003; Pandey et al., 2019; Wang et al., 2019; Hahn et al., 2020). Pandey et al. reported that 2.5–20% PRP (v/v) concentrations promoted cell migration and proliferation *in vitro*, while 40% PRP suppressed their migration and proliferation (Pandey et al., 2019). Another study demonstrated that PRP at 1–5% (v/v) concentration induced cell proliferation, while PRP at 30–100% concentrations suppressed cell proliferation (Choi et al., 2005). PRP with different concentrations was also found to have different capacities for MSC osteogenesis (Wang et al., 2019). Compared with the previously published results, we observed that PRP concentrations with up to 20% (v/v) could promote cell migration of hDPCs, with a PRP concentration of 5% to be the most optimal. Our data also demonstrated that PRP concentrations with up to 10% stimulated proliferation of hDPCs *in vitro*, while a significant reduction in cell proliferation was observed with 20% PRP concentration at day 5. Our osteogenic differentiation results showed that the osteogenic mineralization of hDPCs was stimulated by PRP ranging from 5 to 20%, with a PRP concentration of 20% to be the most optimal. The reported optimal concentrations for cell migration, proliferation, and differentiation varied between studies. These differences can be attributed to a variety of preparation procedures and methodology of PRP (Pandey et al., 2019). Furthermore, the difference can also be affected by the health status difference and personal condition of donors (Pandey et al., 2019). In our observations, PRP with up to 20% (v/v) concentration was beneficial for the regenerative potential of hDPCs.

However, to the best of our knowledge, we still have limited information on the action mechanism of PRP. Autophagy is an intracellular catabolic process by which protein aggregates and the damaged organelles are degraded. Autophagy was reported to have been involved in various cell procedures, such as cell migration, osteogenic differentiation of MSC, and odontoblast differentiation (Pantovic et al., 2013; Pei et al., 2016). To our knowledge, no study was done to evaluate the role of autophagy in PRP-induced pulp regeneration. Several studies have been published about the involvement of autophagy in the process of PRP treatment. Moussa et al. demonstrated that PRP increased significantly the cell proliferation of chondrocytes and promoted autophagosome and cartilage formation in osteoarthritic chondrocytes (Moussa et al., 2017). While another study demonstrated that PRP inhibited autophagic pathways and highlighted the regenerative effects against induced arthritis (Shafik et al., 2019).

In the present study, we hypothesized that autophagy might be involved in PRP-mediated cell migration, proliferation, and osteogenic differentiation in hDPCs. We firstly demonstrated that the expression of autophagy marker (including LC3B and Beclin-1) was increased significantly in 5% PRP-treated hDPCs. We also observed increased autophagosome formation by transmission electron microscope. These results suggested that autophagy was induced by PRP. In the following study, we proved that cell migration, proliferation, and osteogenic differentiation were upregulated in the presence of autophagy activator and downregulated in the presence of inhibitor. These results indicated that autophagy might be a crucial contributor to the regenerative ability of PRP. Former studies showed that autophagy was observed during odontoblast differentiation (Wang et al., 2017; Zhang and Chen, 2018) and even more in cells with LPS stimulation (Pei et al., 2016). These results suggested that autophagy modulated the odontoblast differentiation. Our results also demonstrated that PRP treatment could effectively promote regenerative potential associated with autophagy. Further studies are required to understand the molecular mechanism in PRP-mediated regeneration.

However, we have several limitations in the study. Firstly, the experiment was conducted in cultured hDPCs, and we speculate that, *in vivo*, the reaction of the cells to PRP stimulation might be more complex and varied compared with that in *in vitro* environment. So, further studies were required like a study in an animal model and we hope that it could provide new insights into the biology of PRP in dental pulp regeneration. Secondly, platelet and growth factor levels in PRP varied greatly due to individual differences in the donor and this may influence the research results. Thirdly, the autophagy inhibitory drug 3-MA was used in this study. 3-Methyladenine was a widely used autophagy inhibitor and elicited a significant reduction in cell viability (Chicote et al., 2020). According to Chicote J et al., the cytotoxicity induced by 3-MA correlated with massive DNA damage in many culture cell lines. We measured the effects of DNA damage by 3-MA in hDPCs and our results showed that 5 mM were non-cytotoxic concentrations of 3-MA for hDPCs (**Supplementary Figure S1**). Even though, 3-MA is called for cautionary usage in the future study.

In conclusion, our study suggested cell migration, proliferation, and osteogenic differentiation of hDPCs were promoted by PRP ranging from 5 to 20% concentration.

Autophagy was triggered by PRP and might be a crucial contributor to the regenerative ability of PRP. This study will provide useful therapeutic strategies for the application of PRP in dental pulp regeneration.

DATA AVAILABILITY STATEMENT

The original contributions presented in the study are included in the article/**Supplementary Material**; further inquiries can be directed to the corresponding author.

ETHICS STATEMENT

The studies involving human participants were reviewed and approved by the Ethics Committee of Union Hospital, Tongji Medical College, Huazhong University of Science and Technology. Written informed consent to participate in this study was provided by the participants' legal guardian/next of kin.

AUTHOR CONTRIBUTIONS

HX and FX contributed equally to this article. JL and JZ designed the study. HX and FX conducted the experiment. HX, FX, and JZ drafted the manuscript. CZ and FX analyzed the data, performed the statistical analysis, and edited the manuscript.

FUNDING

This work was supported by the project from the Science Foundation of Hubei Provincial Health Committee (No. WJ 2019M157 to JL) and the National Natural Science Foundation of China (No. 81700946 to JZ).

SUPPLEMENTARY MATERIAL

The Supplementary Material for this article can be found online at: https://www.frontiersin.org/articles/10.3389/fbioe.2021.659742/full#supplementary-material

REFERENCES

Altaii, M., Kaidonis, X., Koblar, S., Cathro, P., and Richards, L. (2017). Platelet Rich Plasma and Dentine Effect on Sheep Dental Pulp Cells Regeneration/Revitalization Ability (*In Vitro*). *Aust. Dent. J.* 62, 39–46. doi:10.1111/adj.12426

Andreasen, J. O., Farik, B., and Munksgaard, E. C. (2002). Long-Term Calcium Hydroxide as a Root Canal Dressing May Increase Risk of Root Fracture. *Dent. Traumatol.* 18, 134–137. doi:10.1034/j.1600-9657.2002.00097.x

Bezgin, T., Yilmaz, A. D., Celik, B. N., Kolsuz, M. E., and Sonmez, H. (2015). Efficacy of Platelet-Rich Plasma as a Scaffold in Regenerative Endodontic Treatment. *J. Endod.* 41, 36–44. doi:10.1016/j.joen.2014.10.004

Bonte, E., Beslot, A., Boukpessi, T., and Lasfargues, J. J. (2015). MTA versus Ca(OH)2 in Apexification of Non-Vital Immature Permanent Teeth: a Randomized Clinical Trial Comparison. *Clin. Oral Investig.* 19, 1381–1388. doi:10.1007/s00784-014-1348-5

Chai, J., Jin, R., Yuan, G., Kanter, V., Miron, R. J., and Zhang, Y. (2019). Effect of Liquid Platelet-Rich Fibrin and Platelet-Rich Plasma on the Regenerative Potential of Dental Pulp Cells Cultured Under Inflammatory Conditions: A Comparative Analysis. *J. Endod.* 45, 1000–1008. doi:10.1016/j.joen.2019.04.002

Chicote, J., Yuste, V. J., Boix, J., and Ribas, J. (2020). Cell Death Triggered by the Autophagy Inhibitory Drug 3-Methyladenine in Growing Conditions Proceeds With DNA Damage. *Front. Pharmacol.* 11, 580343. doi:10.3389/fphar.2020.580343

Choi, B. H., Zhu, S. J., Kim, B. Y., Huh, J. Y., Lee, S. H., and Jung, J. H. (2005). Effect of Platelet-Rich Plasma (PRP) Concentration on the Viability and Proliferation of Alveolar Bone Cells: an *In Vitro* Study. *Int. J. Oral Maxillofac. Surg.* 34, 420–424. doi:10.1016/j.ijom.2004.10.018

Diogenes, A., and Ruparel, N. B. (2017). Regenerative Endodontic Procedures: Clinical Outcomes. Dent. *Clin. North. Am.* 61, 111–125. doi:10.1016/j.cden.2016.08.004

Hahn, O., Kieb, M., Jonitz-Heincke, A., Bader, R., Peters, K., and Tischer, T. (2020). Dose-Dependent Effects of Platelet-Rich Plasma Powder on Chondrocytes *In Vitro*. *Am. J. Sport.s Med.* 48, 1727–1734. doi:10.1177/0363546520911035

Harlamb, S. C. (2016). Management of Incompletely Developed Teeth Requiring Root Canal Treatment. *Aust. Dent. J.* 61 (Suppl. 1), 95–106. doi:10.1111/adj.12401

Huang, A. H., Chen, Y. K., Lin, L. M., Wang, S., Shieh, T. Y., Chan, A. W., et al. (2008). Isolation and Characterization of Dental Pulp Stem Cells from a Supernumerary Tooth. *J Oral Pathol Med.* 37 (9), 571–574. doi:10.1111/j.1600-0714

Kim, S. G., Malek, M., Sigurdsson, A., Lin, L. M., and Kahler, B. (2018). Regenerative Endodontics: a Comprehensive Review. *Int. Endod. J.* 51, 1367–1388. doi:10.1111/iej.12954

Karamzadeh, R., Eslaminejad, M. B., Aflatoonian, R., et al. (2012). Isolation, Characterization and Comparative Differentiation of Human Dental Pulp Stem Cells Derived from Permanent Teeth by Using Two Different Methods. *J Vis Exp.* 69 (9), 4372. doi:10.3791/4372

Lawley, G. R., Schindler, W. G., Walker, W. R., and Kolodrubetz, D. (2004). Evaluation of Ultrasonically Placed MTA and Fracture Resistance With Intracanal Composite Resin in a Model of Apexification. *J. Endod.* 30, 167–172. doi:10.1097/00004770-200403000-00010

Li, X., Hou, J., Wu, B., Chen, T., and Luo, A. (2014). Effects of Platelet-Rich Plasma and Cell Coculture on Angiogenesis in Human Dental Pulp Stem Cells and Endothelial Progenitor Cells. *J. Endod.* 40, 1810–1814. doi:10.1016/j.joen.2014.07.022

Lucarelli, E., Beccheroni, A., Donati, D., Sangiorgi, L., Cenacchi, A., Del, V. A., et al. (2003). Platelet-Derived Growth Factors Enhance Proliferation of Human Stromal Stem Cells. *Biomaterials.* 24, 3095–3100. doi:10.1016/s0142-9612(03)00114-5

Marx, R. E., Carlson, E. R., Eichstaedt, S. R., Schimmele, R. M., Strauss, J. E., Georgeff, K. R., et al. (1998). Plateletrich Plasma: Growth Factor Enhancement for Bone Grafts. *Oral Surg Oral Med Oral Pathol Oral Radiol Endod.* 85 (6), 638–646. doi:10.1016/s1079-2104(98)90029-4

Mizushima, N. (2018). A Brief History of Autophagy from Cell Biology to Physiology and Disease. *Nat. Cel. Biol.* 20, 521–527. doi:10.1038/s41556-018-0092-5

Mizushima, N., and Levine, B. (2010). Autophagy in Mammalian Development and Differentiation. *Nat. Cel. Biol.* 12, 823–830. doi:10.1038/ncb0910-823

Moussa, M., Lajeunesse, D., Hilal, G., El, A. O., Haykal, G., Serhal, R., et al. (2017). Platelet Rich Plasma (PRP) Induces Chondroprotection via Increasing Autophagy, Anti-inflammatory Markers, and Decreasing Apoptosis in Human Osteoarthritic Cartilage. *Exp. Cel. Res.* 352, 146–156. doi:10.1016/j.yexcr.2017.02.012

Ng, Y. L., Mann, V., Rahbaran, S., Lewsey, J., and Gulabivala, K. (2007). Outcome of Primary Root Canal Treatment: Systematic Review of the Literature - Part 1. Effects of Study Characteristics on Probability of success. *Int. Endod. J.* 40, 921–939. doi:10.1111/j.1365-2591.2007.01322.x

Ng, Y. L., Mann, V., Rahbaran, S., Lewsey, J., and Gulabivala, K. (2008). Outcome of Primary Root Canal Treatment: Systematic Review of the Literature -- Part 2. Influence of Clinical Factors. *Int. Endod. J.* 41, 6–31. doi:10.1111/j.1365-2591.2007.01323.x

Otero, L., Carrillo, N., Calvo-Guirado, J. L., Villamil, J., and Delgado-Ruíz, R. A. (2017). Osteogenic Potential of Platelet-Rich Plasma in Dental Stem-Cell Cultures. *Br. J. Oral Maxillofac. Surg.* 55, 697–702. doi:10.1016/j.bjoms.2017.05.005

Pandey, S., Hickey, D. U., Drum, M., Millis, D. L., and Cekanova, M. (2019). Platelet-Rich Plasma Affects the Proliferation of Canine Bone Marrow-Derived Mesenchymal Stromal Cells *In Vitro*. *Bmc. Vet. Res.* 15, 269. doi:10.1186/s12917-019-2010-x

Pantovic, A., Krstic, A., Janjetovic, K., Kocic, J., Harhaji-Trajkovic, L., Bugarski, D., et al. (2013). Coordinated Time-Dependent Modulation of AMPK/Akt/MTOR Signaling and Autophagy Controls Osteogenic Differentiation of Human Mesenchymal Stem Cells. *Bone.* 52, 524–531. doi:10.1016/j.bone.2012.10.024

Pei, F., Wang, H. S., Chen, Z., and Zhang, L. (2016). Autophagy Regulates Odontoblast Differentiation by Suppressing NF-Kb Activation in an Inflammatory Environment. *Cell. Death Dis.* 7, e2122. doi:10.1038/cddis.2015.397

Mizushima, N. (2018). A brief history of autophagy from cell biology to physiology and disease. *Nat. Cell. Biol.* 20, 521–527. doi:10.1038/s41556-018-0092-5

Sachdeva, G. S., Sachdeva, L. T., Goel, M., and Bala, S. (2015). Regenerative Endodontic Treatment of an Immature Tooth with a Necrotic Pulp and Apical Periodontitis Using Platelet-Rich Plasma (PRP) and mineral Trioxide Aggregate (MTA): a Case Report. *Int. Endod. J.* 48, 902–910. doi:10.1111/iej.12407

Shafik, N. M., El-Esawy, R. O., Mohamed, D. A., Deghidy, E. A., and El-Deeb, O. S. (2019). Regenerative Effects of Glycyrrhizin And/or Platelet Rich Plasma on Type-II Collagen Induced Arthritis: Targeting Autophay Machinery Markers, Inflammation and Oxidative Stress. *Arch. Biochem. Biophys.* 675, 108095. doi:10.1016/j.abb.2019.108095

Sotthibundhu, A., Promjuntuek, W., Liu, M., Shen, S., and Noisa, P. (2018). Roles of Autophagy in Controlling Stem Cell Identity: a Perspective of Self-Renewal and Differentiation. *Cell. Tissue Res.* 374, 205–216. doi:10.1007/s00441-018-2829-7

Staffoli, S., Plotino, G., Nunez, T. B., Grande, N. M., Bossù, M., Gambarini, G., et al. (2019). Regenerative Endodontic Procedures Using Contemporary Endodontic Materials. *Materials (Basel).* 12, 908. doi:10.3390/ma12060908

Sun, H. H., Jin, T., Yu, Q., and Chen, F. M. (2011). Biological Approaches Toward Dental Pulp Regeneration by Tissue Engineering. *J. Tissue Eng. Regen. Med.* 5, e1–e16. doi:10.1002/term.369

Torabinejad, M., and Faras, H. (2012). A Clinical and Histological Report of a Tooth With an Open apex Treated With Regenerative Endodontics Using Platelet-Rich Plasma. *J. Endod.* 38, 864–868. doi:10.1016/j.joen.2012.03.006

Wang, K., Li, Z., Li, J., Liao, W., Qin, Y., Zhang, N., et al. (2019). Optimization of the Platelet-Rich Plasma Concentration for Mesenchymal Stem Cell Applications. *Tissue Eng. Part. A.* 25, 333–351. doi:10.1089/ten.TEA.2018.0091

Wang, X., Wu, T. T., Jiang, L., Rong, D., and Zhu, Y. Q. (2017). Deferoxamine-Induced Migration and Odontoblast Differentiation via ROS-dependent Autophagy in Dental Pulp Stem Cells. *Cell. Physiol. Biochem.* 43, 2535–2547. doi:10.1159/000484506

Xiao, M., Li, L., Hu, Q., Ma, L., Liu, L., Chu, W., et al. (2013). Rapamycin Reduces Burn Wound Progression by Enhancing Autophagy in Deep Second-Degree Burn in Rats. *Wound Repair Regen.* 21, 852–859. doi:10.1111/wrr.12090

Yang, J. W., Zhang, Y. F., Wan, C. Y., Sun, Z. Y., Nie, S., Jian, S. J., et al. (2015). Autophagy in SDF-1α-Mediated DPSC Migration and Pulp Regeneration. *Biomaterials.* 44, 11–23. doi:10.1016/j.biomaterials.2014.12.006

Yeom, K. H., Ariyoshi, W., Okinaga, T., Washio, A., Morotomi, T., Kitamura, C., et al. (2016). Platelet-Rich Plasma Enhances the Differentiation of Dental Pulp Progenitor Cells into Odontoblasts. *Int. Endod. J.* 49, 271–278. doi:10.1111/iej.12443

Zhang, L., and Chen, Z. (2018). Autophagy in the Dentin-Pulp Complex Against Inflammation. *Oral Dis.* 24, 11–13. doi:10.1111/odi.12749

Zhang, M., Jiang, F., Zhang, X., Wang, S., Jin, Y., Zhang, W., et al. (2017). The Effects of Platelet-Derived Growth Factor-BB on Human Dental Pulp Stem Cells Mediated Dentin-Pulp Complex Regeneration. *Stem Cell Transl. Med.* 6, 2126–2134. doi:10.1002/sctm.17-0033

Conflict of Interest: The authors declare that the research was conducted in the absence of any commercial or financial relationships that could be construed as a potential conflict of interest.

Publisher's Note: All claims expressed in this article are solely those of the authors and do not necessarily represent those of their affiliated organizations, or those of the publisher, the editors, and the reviewers. Any product that may be evaluated in this article, or claim that may be made by its manufacturer, is not guaranteed or endorsed by the publisher.

frontiers in Bioengineering and Biotechnology

ORIGINAL RESEARCH
published: 24 September 2021
doi: 10.3389/fbioe.2021.729180

Laminin-1 Peptides Conjugated to Fibrin Hydrogels Promote Salivary Gland Regeneration in Irradiated Mouse Submandibular Glands

*Kihoon Nam[1,2], Harim T. dos Santos[1,2], Frank Maslow[1,2], Bryan G. Trump[3], Pedro Lei[4], Stelios T. Andreadis[4,5,6,7] and Olga J. Baker[1,2,8]**

[1]Bond Life Sciences Center, University of Missouri, Columbia, MO, United States, [2]Department of Otolaryngology-Head and Neck Surgery, School of Medicine, University of Missouri, Columbia, MO, United States, [3]School of Dentistry, University of Utah, Salt Lake City, UT, United States, [4]Department of Chemical and Biological Engineering, University at Buffalo, The State University of New York, Buffalo, NY, United States, [5]Department of Biomedical Engineering, University at Buffalo, The State University of New York, Buffalo, NY, United States, [6]Center of Bioinformatics and Life Sciences, University at Buffalo, The State University of New York, Buffalo, NY, United States, [7]Center of Cell, Gene and Tissue Engineering, University at Buffalo, The State University of New York, Buffalo, NY, United States, [8]Department of Biochemistry, University of Missouri, Columbia, MO, United States

OPEN ACCESS

Edited by:
Carl Austin Gregory, Texas A&M Health Science Center, United States

Reviewed by:
Fei Liu, Texas A&M University, United States
Menekse Ermis Sen, Middle East Technical University, Turkey

***Correspondence:**
Olga J. Baker
bakero@health.missouri.edu

Specialty section:
This article was submitted to Tissue Engineering and Regenerative Medicine, a section of the journal Frontiers in Bioengineering and Biotechnology

Received: *22 June 2021*
Accepted: *23 August 2021*
Published: *24 September 2021*

Citation:
Nam K, dos Santos HT, Maslow F, Trump BG, Lei P, Andreadis ST and Baker OJ (2021) Laminin-1 Peptides Conjugated to Fibrin Hydrogels Promote Salivary Gland Regeneration in Irradiated Mouse Submandibular Glands. Front. Bioeng. Biotechnol. 9:729180. doi: 10.3389/fbioe.2021.729180

Previous studies demonstrated that salivary gland morphogenesis and differentiation are enhanced by modification of fibrin hydrogels chemically conjugated to Laminin-1 peptides. Specifically, Laminin-1 peptides (A99: CGGALRGDN-amide and YIGSR: CGGADPGYIGSRGAA-amide) chemically conjugated to fibrin promoted formation of newly organized salivary epithelium both *in vitro* (*e.g.,* using organoids) and *in vivo* (*e.g.,* in a wounded mouse model). While these studies were successful, the model's usefulness for inducing regenerative patterns after radiation therapy remains unknown. Therefore, the goal of the current study was to determine whether transdermal injection with the Laminin-1 peptides A99 and YIGSR chemically conjugated to fibrin hydrogels promotes tissue regeneration in irradiated salivary glands. Results indicate that A99 and YIGSR chemically conjugated to fibrin hydrogels promote formation of functional salivary tissue when transdermally injected to irradiated salivary glands. In contrast, when left untreated, irradiated salivary glands display a loss in structure and functionality. Together, these studies indicate that fibrin hydrogel-based implantable scaffolds containing Laminin-1 peptides promote secretory function of irradiated salivary glands.

Keywords: biomaterial, hydrogel, regeneration, tissue engineering, saliva, irradiated salivary glands

INTRODUCTION

According to the American Cancer Society, each year more than 80,000 people develop head and neck cancer in the United States (Siegel et al., 2021). A first-line treatment for head and neck cancer is radiation therapy (Sroussi et al., 2017), but ionizing radiation typically leads to chronic oral complications such as xerostomia (i.e., hyposalivation) (Chambers et al., 2004; Grundmann et al., 2010; Jensen et al., 2010; Pinna et al., 2015; Sroussi et al., 2017; Jensen et al., 2019; Haderlein et al., 2020; Jasmer et al., 2020). This condition contributes to oral microbial infections and impairs activities of daily life such as speaking, chewing, and swallowing (Lovelace et al., 2014; Brook, 2021). Existing treatments for hyposalivation are limited to the use

of muscarinic receptor agonists (e.g., cevimeline and pilocarpine) (Braga et al., 2009; Turner, 2016) that induce saliva secretion from the few remaining acinar cells as well as use of saliva substitutes (Silvestre et al., 2009; Rocchi and Emmerson, 2020); however, these therapies target surface-level symptoms and provide only temporary relief (Jaguar et al., 2017; Jensen et al., 2019; Lung et al., 2021). Therefore, development of alternative treatments to restore salivary gland secretory function is critical. Several experimental therapies including the use of stem cells (Nanduri et al., 2011; Nanduri et al., 2013; Pringle et al., 2013; Mitroulia et al., 2019; Su et al., 2020), embryonic organ culture (Ogawa et al., 2013; Ogawa and Tsuji, 2015; Ikeda et al., 2019), organ bioprinting (Ferreira et al., 2016; Adine et al., 2018), cell sheets (Nam et al., 2019a; dos Santos et al., 2020), gene therapy (Zheng et al., 2011; Baum et al., 2012; Arany et al., 2013) and bioengineered scaffolds (Peters et al., 2014; Foraida et al., 2017; Patil and Nanduri, 2017; Nam et al., 2019b) have offered the promise of more advanced solutions as detailed below.

Regarding stem cells/progenitors, previous studies showed that c-Kit$^+$ cells, which normally are found in very low numbers within salivary gland specimens (Nanduri et al., 2011; Nanduri et al., 2013) can be expanded *ex vivo* for restoring salivary gland function; however, further characterization (e.g., how they incorporate into host tissue as well as long term secondary effects such as tumorigenesis and survival rates) must be determined before translating this approach into humans. Another technology involves the use of embryonic organ culture transplantation, where embryonic salivary cells grown in culture can be transplanted *in vivo* (Ogawa et al., 2013); nonetheless, a diminished gland size and an absence of studies showing long-term outcomes following treatment significantly decrease the utility of this model for translational applications. Bioprinting strategies have shown the possibility of assembling glandular compartments (e.g., acinar/ductal epithelial, myoepithelial, endothelial, and neuronal) into salivary gland organotypic cultures; however, this technology does not mimic the salivary gland native architecture (e.g., cell polarity and organization (Ferreira et al., 2016; Adine et al., 2018)). Cell sheets made of salivary gland cells have demonstrated positive results, as they promote cell differentiation and tissue integrity in wounded mouse submandibular gland (SMG) models, yet the main challenge facing this technology is the need to standardize cell composition within the sheets and thereby achieve greater reproducibility (Nam et al., 2019a; dos Santos et al., 2020). Regarding scaffolds other than the Fibrin Hydrogels (FH), various biomaterials (Aframian et al., 2000; Sun et al., 2006; Cantara et al., 2012; Soscia et al., 2013; Hsiao and Yang, 2015; Yang and Hsiao, 2015) have been shown to promote cell growth and attachment but the degree of structural organization, as demonstrated by hollow multi-lumen formation, cell polarity and functionality, has been modest. Likewise, studies have shown that human cells grown on a hyaluronic acid-based scaffold and transplanted into a wounded mouse parotid gland lead to improved secretory function (Pradhan-Bhatt et al., 2014); nevertheless, these results included neither monitoring for degradation of the scaffold nor evidence of new tissue formation, thus raising concerns with the stability of the biomaterial and capacity for regeneration, respectively. Together, these technologies offer the potential for more advanced solutions to hyposalivation due to head and neck radiation therapy but have yet to truly deliver.

In response to these needs and challenges, we developed FH with conjugated Laminin-1 peptides (L_{1p}) A99 and YIGSR that were used successfully to repair salivary gland tissue in a wounded SMG mouse model (Nam et al., 2017a; Nam et al., 2017b; Nam et al., 2019b). To apply these results to a more translational setting, the goal of the current study is to determine whether transdermal injection with the L_{1p} A99 and YIGSR chemically conjugated to FH can promote secretory function in irradiated salivary glands.

MATERIALS AND METHODS

Materials

Lyophilized human fibrinogen, tris base, ethylenediaminetetraacetic acid (EDTA), pilocarpine, isoproterenol, goat serum, hydrochloric acid, hematoxylin, eosin Y solution, Tween® 20, calcium chloride ($CaCl_2$) and ε-aminocaproic acid (εACA) were purchased from MilliporeSigma (Burlington, MA). Rabbit anti-zonula occludens 1 (ZO-1) antibody, rabbit anti-induced nitric oxide synthase (iNOS) antibody, Alexa Fluor 488 conjugated anti-rabbit IgG secondary antibody, Alexa Fluor 568 conjugated anti-rabbit IgG secondary antibody and Alexa Fluor 568 conjugated anti-mouse IgG secondary antibody were purchased from Invitrogen (Carlsbad, CA). Rabbit anti-transmembrane Protein 16A (TMEM16A) antibody and mouse anti-intercellular adhesion molecule (ICAM-1) antibody were purchased from Abcam (Cambridge, MA). Rabbit anti-vascular cell adhesion molecule 1 (VCAM-1) antibody and rabbit Arginase-1 (Arg-1) antibody were purchased from Cell Signaling Technology (Danvers, MA). Mouse anti-Na^+/K^+-ATPase antibody was purchased from Santa Cruz Biotechnology (Dallas, TX). Mouse anti-E-cadherin antibody was purchased from BD Biosciences (San Jose, CA). Phosphate buffered saline (PBS), DyLight™ 680 NHS-ester, 4′,6-diamidino-2-phenylindole (DAPI), Triton X-100, sodium citrate, xylene and ethanol were purchased from Thermo Fisher Scientific (Waltham, MA). Ketamine and xylazine were purchased from VetOne (Boise, ID). Insulin syringes (28G) were purchased from BD (Franklin Lakes, NJ). Peptides were synthesized by University of Utah DNA/Peptide synthesis core facility, as previously described (Nam et al., 2016; Nam et al., 2017a; Nam et al., 2017b).

Animals

Female 6-week-old C57BL/6J mice weighing ~17–20 g were purchased from Jackson Laboratory (Bar Harbor, ME). Power analysis was performed to determine mouse numbers using G*Power 3.1.9.7 software (Heinrich-Heine-Universität Düsseldorf, Düsseldorf, Germany; http://www.gpower.hhu.de/). All calculations were conducted using a significance level of 0.05 with 95% power. Then, 105 mice were randomly distributed into

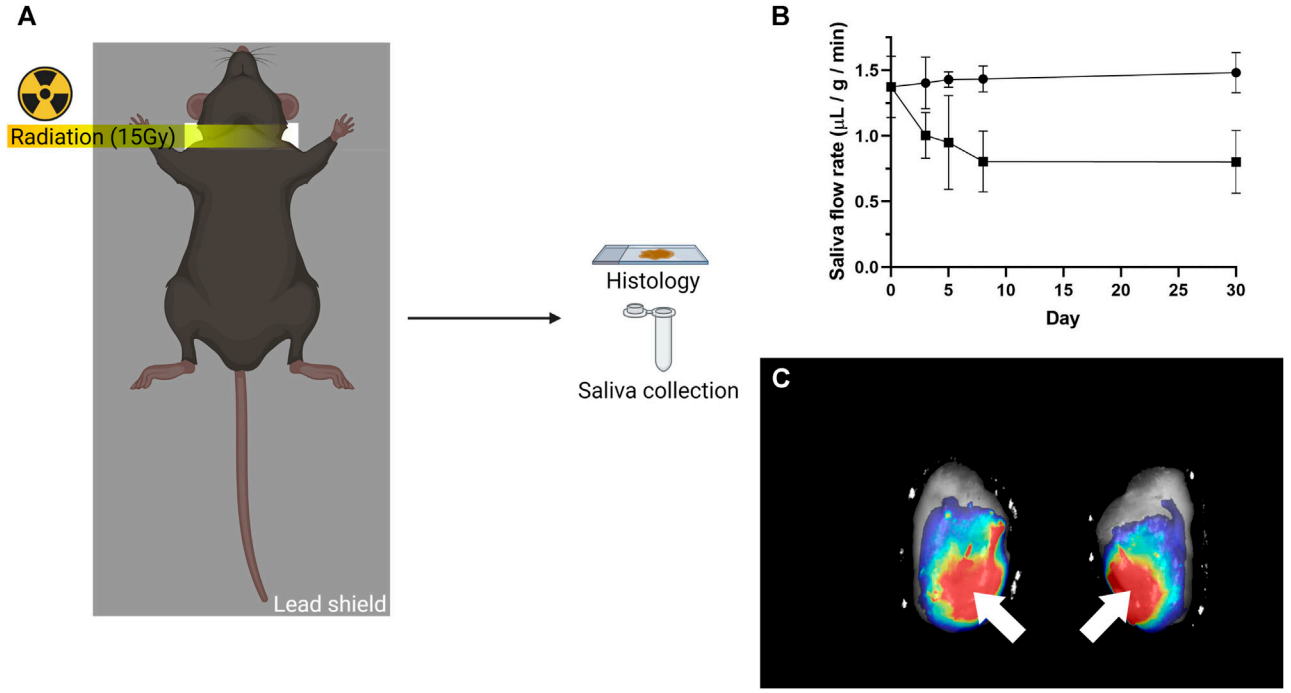

FIGURE 1 | Radiation treatment and local L_{1P}-FH delivery used in this study. **(A)** Mice received a single 15 Gy radiation dose with a customized lead shield having a 1 cm slit aligned to the mouse's neck. **(B)** Radiation treatment caused saliva flow rates to be significantly reduced. The symbol (●) indicates non-irradiated group, while the symbol (■) indicates irradiated group. **(C)** DyLight 680 conjugated L_{1P}-FH were successfully delivered to the mouse submandibular glands when applied via transdermal injection. White arrows indicate the site of L_{1P}-FH injection.

three groups to receive the following treatments: non-irradiated (40 mice), irradiated without L_{1p}-FH injection (40 mice), and irradiated while also receiving the L_{1p}-FH injection (25 mice), comprising treatment groups 1–3, respectively. All animal usage, anesthesia and surgeries were conducted with the approval of the University of Utah Institutional Animal Care and Use Committee (IACUC) in compliance with the ARRIVE guidelines.

Radiation Treatment

Salivary gland tissue damage is a late degenerative response observed after radiation therapy (Wu and Leung, 2019; Jasmer et al., 2020). To confirm L_{1p}-FH regenerative effects in a more clinically relevant animal model, a widely accepted head and neck irradiated mouse model was used for this study (Deasy et al., 2010; Varghese et al., 2018). Briefly, mice were anesthetized with ketamine (100 mg/kg) and xylazine (5 mg/kg) solution administered intraperitoneally with the head and neck area positioned over the 1 cm slit of a customized lead shield, thereby protecting other areas of the body from radiation. SMGs then received a single 15 Gy radiation dose using a JL Shepherd ^{137}Cs irradiator (**Figure 1A**). Animals were allowed to recover for 3 days and received hydrogel treatment soon after, as detailed below.

Hydrogel Preparation

Peptides and DyLight 680 conjugated fibrinogen were prepared, as previously described (Nam et al., 2017a; Nam et al., 2017b). Briefly, two Laminin-1 peptides (A99 and YIGSR) were synthesized on a peptide synthesizer. Peptides were then conjugated to the fibrinogen using sulfo-LC-SPDP and cysteine residue in peptides. In addition, fibrinogen was chemically labeled with a fluorescent dye through NHS ester of DyLight 680. Finally, laminin-1 peptide conjugated fibrinogens and DyLight 680 labeled fibrinogen were dialyzed against ultrapure water, lyophilized, and stored at −80°C until use. L_{1p}-FH were prepared similar to previous studies (Nam et al., 2017a; Nam et al., 2017b) except for the use of exogenous thrombin (thereby preventing rapid polymerization inside the syringe) as follows: YIGSR-conjugated fibrinogen (1.2 mg/ml), A99-conjugated fibrinogen (1.2 mg/ml), DyLight 680 conjugated fibrinogen (0.1 mg/ml), $CaCl_2$ (2.5 mM) and εACA (2 mg/ml) were mixed in a tris buffered saline (TBS) solution. Polymerization of L_{1p}-FH was confirmed from fluorescence in the SMG of randomly selected mice (**Figure 1C**).

Transdermal Injection

C57BL/6J mice were anesthetized with 3% isoflurane using an oxygen flow rate set at 2.0 L/min, and 10 µL of freshly mixed L_{1p}-FH solution was transdermally injected using insulin syringe (G 28) to irradiated mouse SMGs at post-radiation day 3. L_{1p}-FH effects were studied at days 8 and 30. Using thrombin prior transdermal injection causes rapid polymerization of L_{1p}-FH which clogs the needle. To overcome this issue, the mixture was applied in a liquid form using endogenous thrombin for internal polymerization. To confirm scaffold implantation *in*

vivo, FH was labeled with DyLight 680 and quantified within dissected glands using a Bio-Rad Chemi-Doc™ MP imaging system (**Figure 1C**).

Hematoxylin and Eosin and Masson's Trichrome Stain

SMGs were fixed in 10% formalin at room temperature overnight, dehydrated in 70% ethanol solution, embedded in paraffin wax and cut into 3 μm sections. Sections were then deparaffinized with xylene and rehydrated with serial ethanol solutions (100%, 95% 80, 70 and 50%, v/v) and distilled water. For hematoxylin and eosin staining, the rehydrated sections were stained with hematoxylin for 5 min, washed with distilled water for 5 min, tap water for 5 min and distilled water for 2 min. Next, slides were stained with eosin for 30 s, washed with tap water for 5 min and distilled water for 2 min. Finally, hematoxylin and eosin stained gland sections were dehydrated with 95 and 100% ethanol (v/v), cleared in xylene and mounted with a xylene-based mounting medium. As for Masson's trichrome staining, the rehydrated sections were re-fixed in Bouin's solution at 60°C for 1 h then washed with running tap water for 10 min and distilled water for 5 min. Next, sections were stained with Weigert's iron hematoxylin solution for 10 min then washed with running warm tap water for 10 min and distilled water for 5 min. For cytoplasm staining, sections were incubated with Biebrich scarlet acid fuchsine solution for 5 min and washed three times with distilled water for 2 min. Regarding collagen staining, sections were incubated in phosphotungstic/phosphomolybdic acid for 15 min, stained with aniline blue solution for 5 min and washed three times with distilled water for 2 min. Stained sections were then differentiated in 1% acetic acid solution for 1 min and washed two times with distilled water for 2 min. Finally, Masson's trichrome stained sections were dehydrated with serial ethanol solutions (95 and 100%), cleared in xylene and mounted with a xylene-based mounting medium. Finally, the samples were analyzed using a Leica DMI6000B (Leica Microsystems, Wetzlar, Germany) to determine tissue morphology.

Confocal Analysis

For antigen retrieval, the rehydrated and fixed tissue sections were incubated in Tris-EDTA buffer [10 mM Tris, 1 mM EDTA, 0.05% (v/v) Tween® 20, pH 9.0] for ZO-1 and E-cadherin or with sodium citrate buffer [10 mM sodium citrate, 0.05% (v/v) Tween® 20, pH 6.0] for TMEM16A, Na^+/K^+-ATPase, iNOS, Arg-1, VCAM-1 and ICAM-1 at 95°C for 30 min. Next, samples were permeabilized with 0.1% (v/v) triton X-100 in PBS at room temperature for 45 min. Specimens were then blocked in 5% (v/v) goat serum in PBS for 1 h at room temperature and incubated at 4°C with the following primary antibodies overnight: rabbit anti-ZO-1, mouse anti-E-cadherin, rabbit anti-TMEM16A, mouse anti-Na^+/K^+-ATPase, rabbit anti-VCAM-1 or mouse anti-ICAM-1. At that time, sections were incubated with anti-rabbit Alexa Fluor 488 and anti-mouse Alexa Fluor 568 secondary antibodies in 5% goat serum at room temperature for 1 h followed by 300 nM DAPI staining at room temperature for 5 min. For M1 and M2 marker staining, specimens were blocked in 3% (w/v) bovine serum albumin (BSA) in PBS for 1 h at room temperature and incubated with primary antibodies (rabbit anti-iNOS or rabbit anti-Arg-1) at 37°C for 1 h. Then, sections were incubated with anti-rabbit Alexa Fluor 568 in 3% BSA at room temperature for 1 h followed by 300 nM DAPI staining at room temperature for 5 min. Finally, specimens were analyzed using a STELLARIS Confocal Microscope (Leica Microsystems, Wetzlar, Germany).

Macrophage Ratio

M1 and M2 macrophage cells were determined using ImageJ. Specifically, the color threshold was set to isolate the colocalized signal of nuclei and M1 (**Figure 4**, white arrows)/M2 (**Figure 4**, red arrows) positive cells, which were counted and normalized by area. Statistical significance was assessed using one-way ANOVA ($^*p < 0.01$) and Dunnett's post-hoc test for multiple comparisons to group 2 (irradiated with no L_{1p}-FH injection at day 30).

Saliva Flow Rate Measurements

Mice were anesthetized with ketamine (100 mg/kg) and xylazine (5 mg/kg) followed by intraperitoneal injection with pilocarpine (25 mg/kg) and isoproterenol (0.5 mg/kg). Then, whole saliva was collected using a micropipette for 5 min and flow rate was calculated using the following formula:

$$\text{Saliva flow rate} = \frac{\text{Stimulated saliva } (\mu L)}{\text{Body weight of mouse } (g) \text{ x collection time } (5 min)}$$

Statistical Analysis

Experimental data were analyzed using one-way ANOVA and Dunnett's post hoc test for multiple comparisons to the non-irradiated group 1 at day 30. All values represent means ± SD ($n = 5$), where p values <0.01 were considered statistically significant. Finally, these calculations were performed using GraphPad Prism 6.

RESULTS

A Head and Neck Irradiated Mouse Model was Achieved

To investigate whether L_{1p}-FH could restore irradiated SMG structure and function, C57BL/6J mice were subjected to a single radiation treatment as described in Materials and Methods (**Figure 1A**). Mice treated with a single 15 Gy radiation dose displayed a significant reduction in saliva flow rates as compared to non-irradiated controls (i.e., from 1.43 to 0.80 μL/g/min, $n = 5$, $p < 0.01$) in the first 8 days and remained steady thereafter until day 30 (**Figure 1B**). These results demonstrated that the radiation dose utilized here caused significant loss of salivary secretory function and can thus be used as a head and neck irradiated preclinical model, consistent with previous studies (Lombaert et al., 2008; Varghese et al., 2018; Weng et al., 2018).

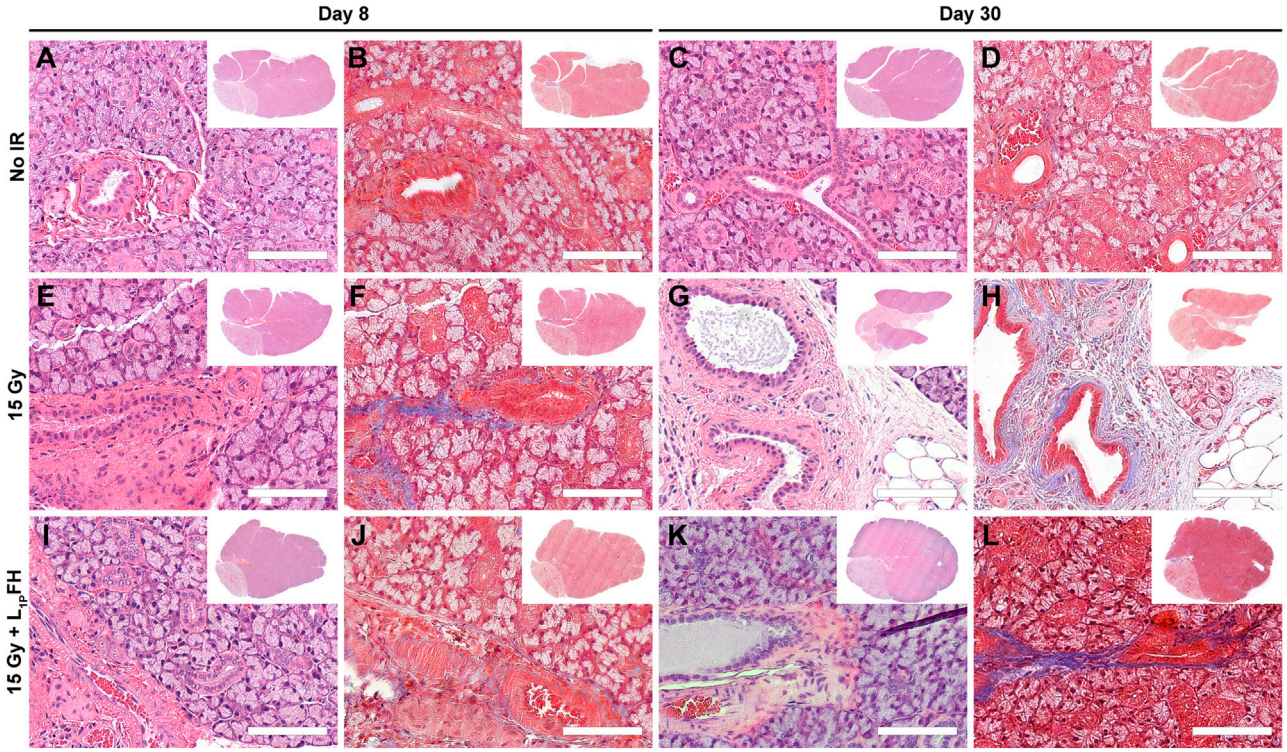

FIGURE 2 | Treatment with L_{1p}-FH preserves epithelial integrity when applied after radiation treatment. Hematoxylin and eosin **(A,C,E,G,I,K)** as well Masson's trichrome **(B,D,F,H,J,L)** staining of mouse submandibular glands from group 1 [non-irradiated, **(A–D)**], group 2 [irradiated without L_{1p}-FH injection, **(E–H)**] and group 3 [irradiated with L_{1p}-FH injection, **(I–L)**] were performed and tissue morphology was analyzed using a Leica DMI6000B. Scale bars represent 100 μm. Representative image from a total of five mice per group.

L_{1p}-FH was Successfully Implanted in Irradiated Mouse Submandibular Glands

Our previous studies showed the biocompatibility of L_{1p}-FH with host tissue when surgically implanted in a wounded mouse model (Nam et al., 2017a; Nam et al., 2017b). To avoid an open wound surgery, we attempted to deliver the L_{1p}-FH to irradiated mouse SMG via transdermal injection as described in Materials and Methods. For these experiments, we used a fluorescently labeled hydrogel using DyLight 680 and successfully implanted L_{1p}-FH in irradiated mouse SMG *via* transdermal injection (**Figure 1C**, white arrows).

L_{1p}-FH Preserved Epithelial Integrity After Radiation Treatment

Our previous studies showed that L_{1p}-FH promoted tissue repair in a wounded SMG mouse model (Nam et al., 2017a; Nam et al., 2017b; Nam et al., 2019b). To determine whether these effects occur in the head and neck irradiated mouse model, we randomly distributed mice in three groups and applied this scaffold as follows: non-irradiated, irradiated without L_{1p}-FH injection and irradiated that received the L_{1p}-FH injection, comprising treatment groups 1–3, respectively (see Material and Methods section). As shown in **Figure 2**, group 1 (non-irradiated glands) displayed intact lobules where the parenchyma was separated by areas of thin connective tissue at days 8 (**Figures 2A,B**) and 30 (**Figures 2C,D**). As for cytologic features, serous acini cells showed a typical pyramidal shape with basophilic cytoplasm and basal nuclei. In contrast, mucous cells showed a pale cytoplasm with flat basilar nuclei, intercalated ducts were lined by cuboidal and/or flat cells, striated ducts showed cuboidal to low columnar cells and granular convoluted ducts were lined by tall columnar cells containing intracytoplasmic eosinophilic granules. Together, these features indicate that the non-irradiated glands in group 1 showed the morphology of a healthy epithelium. In contrast, group 2 (irradiated with no L_{1p}-FH injection) demonstrated glandular parenchyma separated by thicker connective tissue strands, ductal areas with ectasia, intraluminal depositions and increased presence of fibrosis when compared to controls (**Figures 2E,F**). Furthermore, tissue damage was even more severe at day 30 (**Figures 2G,H**), where SMG showed an extensive disruption of the lobular architecture as indicated by the replacement of acini and ducts with sheets of vacuolated cells, adipocytes and fibrosis. Together, these results indicated that irradiated glands with no L_{1p}-FH injection (group 2) dramatically lost epithelial integrity. Remarkably, mice in group 3 (irradiated with L_{1p}-FH injection) recovered many of the features of healthy glands. For instance, we observed the presence of serous acinar units with organized ductal structures surrounded by thin connective tissue strands

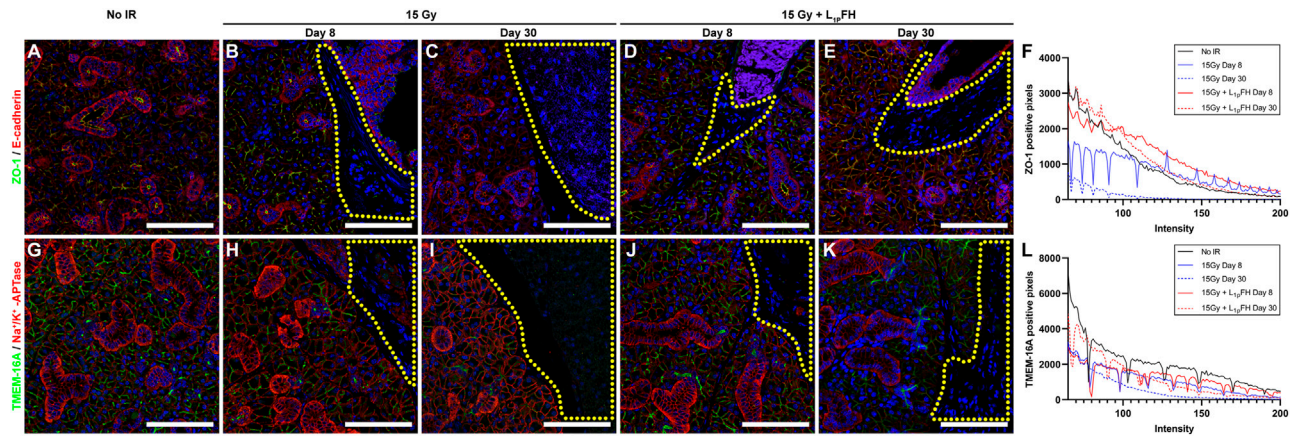

FIGURE 3 | Treatment with L_{1p}-FH maintains epithelial polarity and functional marker expression. Salivary structural and functional marker organization was analyzed using confocal microscopy with specific antibodies against ZO-1 [green; **(A–E)**], E-cadherin [red; **(A–E)**], TMEM16A [green; **(G–K)**], Na^+/K^+-ATPase [red; **(G–K)**], and DAPI (blue; everywhere). Scale bars represent 100 μm. Yellow-dotted areas indicate fibroblast-like areas. Representative image from a total of five mice per group. ZO-1 **(F)** and TMEM-16A **(L)** positive pixels were analyzed using ImageJ.

similar to the non-irradiated group 1 at both days 8 (**Figures 2I,J**) and 30 (**Figures 2K,L**). These changes indicate that group 3 (irradiated glands treated with L_{1p}-FH) had a morphology consistent with a healthy salivary gland epithelium and results in this section indicate that L_{1p}-FH is a suitable scaffold for promoting epithelial integrity in irradiated SMG.

L_{1p}-FH Maintained Epithelial Polarity and Preserved Ion Transporter Expression

To determine whether L_{1p}-FH maintained epithelial polarity in an irradiated mouse model, we stained the SMG sections with the apical tight junction marker ZO-1 and basolateral marker E-cadherin. As shown in **Figure 3A**, group 1 (non-irradiated glands) displayed apical ZO-1 (green) and basolateral E-cadherin (red) after 30 days. However, in group 2 (irradiated glands with no L_{1p}-FH injection), a mild residual ZO-1 signal was detected at day 8 (**Figures 3B,F**, blue solid line), and a weaker ZO-1 signal was expressed at day 30 (**Figure 3F**, blue dotted line), together with ZO-1 disorganization (**Figure 3C**), thereby indicating loss of epithelial polarity. In contrast, group 3 (irradiated glands treated with L_{1p}-FH) showed apical ZO-1 and basolateral E-cadherin signals both at days 8 (**Figure 3D**) and 30 (**Figure 3E**), indicating that the scaffold treatment helps to maintain epithelial polarity (**Figure 3F**, red line and red dotted line). Regarding the presence of functional markers, group 1 (non-irradiated SMG) showed apical TMEM16A (**Figure 3G**, green) and basolateral Na^+/K^+-ATPase localization (**Figure 3G**, red) at day 30, consistent with a healthy salivary epithelium. In contrast, group 2 (irradiated glands with no L_{1p}-FH injection) showed a moderate TMEM16A signal (**Figure 3L**, blue solid line) at day 8 (**Figure 3H**, green) and weaker TMEM16A signal (**Figure 3L**, blue dotted line) at day 30 (**Figure 3I**, green). Interestingly, group 3 (irradiated glands treated with L_{1p}-FH) expressed strong apical TMEM16 (**Figures 3J,K**, green; **Figure 3L**, red line and red dotted line) and basolateral Na^+/K^+-ATPase similar to non-irradiated glands, thus suggesting that L_{1p}-FH treatment helps to maintain epithelial polarity and preserve ion transport expression, both of which are critical for saliva secretion.

L_{1p}-FH Promoted Macrophage Polarization

Our previous studies indicated that treatment with L_{1p}-FH promoted macrophage polarization in a wounded SMG female mouse model (Brown et al., 2020). To determine whether similar effects occur in an irradiated mouse model, we identified the presence of M1 and M2 subtypes within the SMG using macrophage-specific antibodies (i.e., iNOS and Arg-1, corresponding to M1 and M2, respectively). As shown in **Figures 4A,F**, group 1 (non-irradiated glands) expressed iNOS-positive cells with approximately 0.94 macrophages per 100,000 μm (Sroussi et al., 2017). In contrast, group 2 (irradiated glands with no L_{1p}-FH injection) showed a significant increase in M1 macrophages (approximately 28.65 iNOS-positive cells) at day 30 (**Figures 4C,F**). Notably, group 3 (irradiated glands treated with L_{1p}-FH) showed a significant decrease of M1 macrophages (approximately 5.92 iNOS-positive cells) at day 30 (**Figures 4E,F**) compared to group 2. Regarding the presence of M2 markers, group 2 (irradiated glands with no L_{1p}-FH injection) expressed Arg-1-positive cells with approximately 5.92 macrophages at day 30 (**Figures 2I,L**), which is not a significant difference from group 1 (**Figures 4G,L**, 2.60 macrophages). Interestingly, group 3 (irradiated glands treated with L_{1p}-FH) expressed a significant increase of Arg-1-positive cells at day 30 (approximately 11.37 macrophages, **Figure 4K,L**). Together, these results indicate that L_{1p}-FH causes a decrease in M1 macrophages together with an increase in M2 macrophages in SMG following radiation treatment.

L_{1p}-FH Increased Saliva Secretion After Radiation Treatment

Our previous studies indicate that treatment with L_{1p}-FH enhances saliva secretion in a wounded SMG mouse model

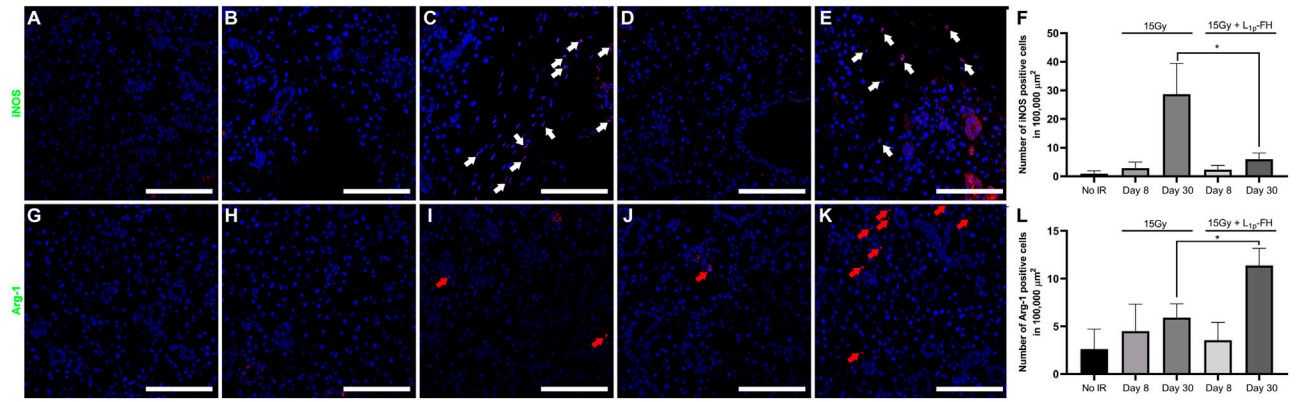

FIGURE 4 | L_{1p}-FH promotes macrophage polarization. Macrophage marker expression was analyzed using confocal microscopy with specific antibodies against iNOS **(A–F)**, Arg-1 **(G–L)**, and DAPI (blue; everywhere). Scale bars represent 100 μm. White and red arrows indicate iNOS or Arg-1 positive cells, respectively. Representative image from a total of five mice per group. iNOS **(F)** and Arg-1 **(L)** positive cells were analyzed using ImageJ and GraphPad Prism 6. Data represent the means ± SD of $n = 5$ mice per condition with statistical significance assessed using one-way ANOVA (*$p < 0.01$) and Dunnett's post-hoc test for multiple comparisons to group 2 (irradiated with no L_{1p}-FH injection at day 30).

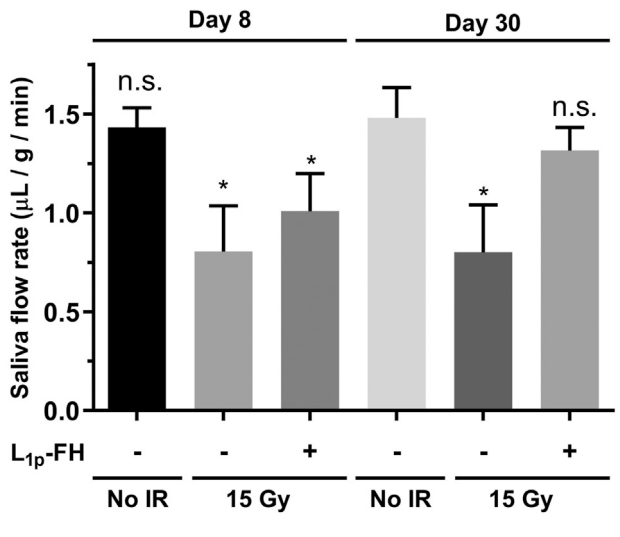

FIGURE 5 | L_{1p}-FH increases saliva secretion after radiation treatment. Mice were anesthetized and stimulated with pilocarpine and isoproterenol at days 8 and 30 with saliva collected for 5 min. Data represent the means ± SD of $n = 5$ mice per condition with statistical significance assessed using one-way ANOVA (*$p < 0.01$) and Dunnett's post-hoc test for multiple comparisons to group 1 (non-irradiated mice at day 30). The symbol (+) indicates L_{1p}-FH injection, while the symbol (–) indicates no L_{1p}-FH injection, and n. s indicates no significant differences from group 1 (non-irradiated mice at day 30).

(Nam et al., 2017a; Nam et al., 2017b; Nam et al., 2019b). To determine whether similar effects occur in an irradiated mouse model, we treated irradiated SMG with a transdermal injection of L_{1p}-FH as described in Materials and Methods. As shown in **Figure 5**, group 1 (non-irradiated glands) showed intact saliva flow rates (i.e., 1.43 μL/g/min), as expected. In contrast, group 2 (irradiated untreated glands) exhibited a significant reduction in saliva flow rates (i.e., 0.80 μL/g/min, $n = 5$, $p < 0.01$). Notably, group 3 (irradiated glands treated with L_{1p}-FH) showed a significant increase of saliva flow rates (1.32 μL/g/min, $n = 5$, $p < 0.01$) at day 30, thereby demonstrating that L_{1p}-FH restores saliva secretion after radiation treatment.

DISCUSSION

Our previous studies indicated that treatment with FH alone promotes neither cell polarity nor differentiation in salivary gland epithelium, both *in vitro or in vivo* (Nam et al., 2016; Nam et al., 2017a; Nam et al., 2017b; Nam et al., 2019b; Dos Santos et al., 2021). However, specific L_{1p} sequences (A99: CGGALRGDN-amide, YIGSR: CGGADPGYIGSRGAA-amide) proved to be useful for improving salivary gland regeneration (Hoffman et al., 1998). Specifically, freshly isolated SMG cells grown on L_{1p} chemically attached to FH induced lumen formation and secretory function (Nam et al., 2016). Moreover, L_{1p}-FH promoted salivary gland regeneration in an *in vivo* wound-healing mouse model (Nam et al., 2017a; Nam et al., 2017b), thus leading to increased saliva secretion. Such functional recovery indicates that FH-based scaffolds can be used to promote salivary gland function in radiation-induced hyposalivation. Additionally, we developed a transdermal delivery system specifically for this study with the aim of using the patient's own blood for polymerization to increase biocompatibility (Froelich et al., 2010; Dietrich et al., 2013) and having the ancillary benefits of displaying optimal rheological properties (i.e., softness) and being less invasive than other delivery methods (i.e., retro-ductal delivery (Nair et al., 2016) and surgical application (Ogawa et al., 2013)), all of which indicates a greater degree of clinical applicability for our newly designed mouse model.

Regarding results of the current study, salivary gland morphology was significantly improved by L_{1p}-FH

(**Figures 2I–L** and **Figure 3D,E**) and saliva secretion (**Figure 5**) was likewise restored by day 30 post-radiation; however, such treatment gains cannot be counted on to persist, given the residual fibrosis noted (**Figure 2L**). Additionally, future studies will use growth factors specifically targeted for angiogenesis (i.e., VEGF and FGF9) (Nam et al., 2019b) in response to current results demonstrating L_{1p}-FH promoted macrophage polarization (**Figure 4**) but gave rise to no blood vessel formation (**Supplementary Figure S1**). Moreover, should such gains in fact prove persistent (e.g., maintained over long periods of time), we as yet have limited knowledge of the mechanisms responsible for this recovery. These issues notwithstanding, the results to date are important because they are the first time that L_{1p}-FH has been used in irradiated glands to restore their form and function.

It is noteworthy to mention three major differences between our previous studies and the current work. First, our previous studies used L_{1p} in trimeric form (Dos Santos et al., 2021) and in combination with growth factors (Nam et al., 2019b), while the current work employs only monomeric forms and no growth factors. Next, our previous studies used a more invasive SMG surgical punch model (Nam et al., 2017a; Nam et al., 2017b; Nam et al., 2019b) as compared to currently used transdermal injection implantation method. Finally, we replaced the SMG wounded mouse model of our prior studies with a radiation model for greater specificity in terms of clinical features and increased translational application.

To expand on this work, future studies will perform extended saliva secretion studies and track the appearance of fibrosis at multiple time points via histological studies and investigate how L_{1p} used here (i.e., A99 (Mochizuki, 2003; Rebustini et al., 2007; David et al.,2008) and YIGSR (Caiado and Dias, 2012; Frith et al., 2012; Huettner et al., 2018; Motta et al., 2019)) bind to specific integrins, thus addressing the questions noted above in relation to treatment duration and mechanisms. Finally, should this treatment near the stage of clinical trials, it would be important to replace the current single dose of radiation used for proof of concept and early exploration with more clinically appropriate fractionated doses.

DATA AVAILABILITY STATEMENT

The original contributions presented in the study are included in the article/**Supplementary Material**, further inquiries can be directed to the corresponding author.

ETHICS STATEMENT

The animal study was reviewed and approved by University of Utah IACUC.

AUTHOR CONTRIBUTIONS

KN, SA, and OB conceived the idea; KN, HS, and OB designed the study, and wrote the manuscript; KN, HS, FM, and BT performed all the experiments and/or analyzed the data; KN, SA, and OB directed the project; PL, SA, KN, and OB provided technical support, and corrections to the manuscript; KN and OB revised the manuscript according to the comments of all co-authors. All authors reviewed the manuscript and approved the submitted version.

FUNDING

This study is supported by the National Institutes of Health–National Institute of Dental and Craniofacial Research (grant R01DE022971 to OB and SA and grant R01DE027884 to OB).

SUPPLEMENTARY MATERIAL

The Supplementary Material for this article can be found online at: https://www.frontiersin.org/articles/10.3389/fbioe.2021.729180/full#supplementary-material

Supplemental Figure S1 | L_{1p}-FH does not enhance angiogenesis after radiation treatment. VCAM-1 (green) and ICAM-1 (red) were analyzed using confocal microscopy. Scale bars represent 100 μm. Representative image from a total of 5 mice per group.

REFERENCES

Adine, C., Ng, K. K., Rungarunlert, S., Souza, G. R., and Ferreira, J. N. (2018). Engineering Innervated Secretory Epithelial Organoids by Magnetic Three-Dimensional Bioprinting for Stimulating Epithelial Growth in Salivary Glands. *Biomaterials* 180, 52–66. doi:10.1016/j.biomaterials.2018.06.011

Aframian, D. J., Cukierman, E., Nikolovski, J., Mooney, D. J., Yamada, K. M., and Baum, B. J. (2000). The Growth and Morphological Behavior of Salivary Epithelial Cells on Matrix Protein-Coated Biodegradable Substrata. *Tissue Eng.* 6, 209–216. doi:10.1089/10763270050044380

Arany, S., Benoit, D. S., Dewhurst, S., and Ovitt, C. E. (2013). Nanoparticle-mediated Gene Silencing Confers Radioprotection to Salivary Glands *In Vivo*. *Mol. Ther.* 21, 1182–1194. doi:10.1038/mt.2013.42

Baum, B. J., Alevizos, I., Zheng, C., Cotrim, A. P., Liu, S., McCullagh, L., et al. (2012). Early Responses to Adenoviral-Mediated Transfer of the Aquaporin-1 cDNA for Radiation-Induced Salivary Hypofunction. *Proc. Natl. Acad. Sci.* 109, 19403–19407. doi:10.1073/pnas.1210662109

Braga, M., Tarzia, O., Bergamaschi, C., Santos, F., Andrade, E., and Groppo, F. (2009). Comparison of the Effects of Pilocarpine and Cevimeline on Salivary Flow. *Int. J. Dent Hyg.* 7, 126–130. doi:10.1111/j.1601-5037.2008.00326.x

Brook, I. (2021). *Early Side Effects of Radiation Treatment for Head and Neck Cancer*. Cancer/Radiothérapie.

Brown, C. T., Nam, K., Zhang, Y., Qiu, Y., Dean, S. M., Dos Santos, H. T., et al. (2020). Sex-dependent Regeneration Patterns in Mouse Submandibular Glands. *J. Histochem. Cytochem.* 68, 305–318. doi:10.1369/0022155420922948

Caiado, F., and Dias, S. (2012). Endothelial Progenitor Cells and Integrins: Adhesive Needs. *Fibrogenesis Tissue Repair* 5, 4. doi:10.1186/1755-1536-5-4

Cantara, S. I., Soscia, D. A., Sequeira, S. J., Jean-Gilles, R. P., Castracane, J., and Larsen, M. (2012). Selective Functionalization of Nanofiber Scaffolds to Regulate Salivary Gland Epithelial Cell Proliferation and Polarity. *Biomaterials* 33, 8372–8382. doi:10.1016/j.biomaterials.2012.08.021

Chambers, M. S., Garden, A. S., Kies, M. S., and Martin, J. W. (2004). Radiation-induced Xerostomia in Patients with Head and Neck Cancer: Pathogenesis, Impact on Quality of Life, and Management. *Head Neck* 26, 796–807. doi:10.1002/hed.20045

David, R., Shai, E., Aframian, D. J., and Palmon, A. (2008) Isolation and Cultivation of Integrin α6β1–Expressing Salivary Gland Graft Cells: A Model for Use with an Artificial Salivary Gland. *Tissue Eng. A* 14, 331–337. doi:10.1089/tea.2007.0122

Deasy, J. O., Moiseenko, V., Marks, L., Chao, K. S. C., Nam, J., and Eisbruch, A. (2010). Radiotherapy Dose-Volume Effects on Salivary Gland Function. *Int. J. Radiat. Oncology*Biology*Physics* 76, S58–S63. doi:10.1016/j.ijrobp.2009.06.090

Dietrich, M., Heselhaus, J., Wozniak, J., Weinandy, S., Mela, P., Tschoeke, B., et al. (2013). Fibrin-based Tissue Engineering: Comparison of Different Methods of Autologous Fibrinogen Isolation. *Tissue Eng. C: Methods* 19, 216–226. doi:10.1089/ten.tec.2011.0473

dos Santos, H. T., Kim, K., Okano, T., Camden, J. M., Weisman, G. A., Baker, O. J., et al. (2020). Cell Sheets Restore Secretory Function in Wounded Mouse Submandibular Glands. *Cells* 9, 2645. doi:10.3390/cells9122645

Dos Santos, H. T., Nam, K., Brown, C. T., Dean, S. M., Lewis, S., Pfeifer, C. S., et al. (2021). Trimers Conjugated to Fibrin Hydrogels Promote Salivary Gland Function. *J. Dent Res.* 100, 268–275. doi:10.1177/0022034520964784

Ferreira, J. N., Rungarunlert, S., Urkasemsin, G., Adine, C., and Souza, G. R. (2016). Three-Dimensional Bioprinting Nanotechnologies towards Clinical Application of Stem Cells and Their Secretome in Salivary Gland Regeneration. *Stem Cell Int.* 2016, 7564689. doi:10.1155/2016/7564689

Foraida, Z. I., Kamaldinov, T., Nelson, D. A., Larsen, M., and Castracane, J. (2017). Elastin-PLGA Hybrid Electrospun Nanofiber Scaffolds for Salivary Epithelial Cell Self-Organization and Polarization. *Acta Biomater.* 62, 116–127. doi:10.1016/j.actbio.2017.08.009

Frith, J. E., Mills, R. J., Hudson, J. E., and Cooper-White, J. J. (2012). Tailored Integrin-Extracellular Matrix Interactions to Direct Human Mesenchymal Stem Cell Differentiation. *Stem Cell Develop.* 21, 2442–2456. doi:10.1089/scd.2011.0615

Froelich, K., Pueschel, R. C., Birner, M., Kindermann, J., Hackenberg, S., Kleinsasser, N. H., et al. (2010). Optimization of Fibrinogen Isolation for Manufacturing Autologous Fibrin Glue for Use as Scaffold in Tissue Engineering. *Artif. Cell Blood Substitutes, Biotechnol.* 38, 143–149. doi:10.3109/10731191003680748

Grundmann, O., Fillinger, J. L., Victory, K. R., Burd, R., and Limesand, K. H. (2010). Restoration of Radiation Therapy-Induced Salivary Gland Dysfunction in Mice by post Therapy IGF-1 Administration. *BMC Cancer* 10, 417. doi:10.1186/1471-2407-10-417

Haderlein, M., Speer, S., Ott, O., Lettmaier, S., Hecht, M., Semrau, S., et al. (2020). Dose Reduction to the Swallowing Apparatus and the Salivary Glands by De-intensification of Postoperative Radiotherapy in Patients with Head and Neck Cancer: First (Treatment Planning) Results of the Prospective Multicenter DIREKHT Trial. *Cancers (Basel)* 12, doi:10.3390/cancers12030538

Hoffman, M. P., Nomizu, M., Roque, E., Lee, S., Jung, D. W., Yamada, Y., et al. (1998). Laminin-1 and Laminin-2 G-Domain Synthetic Peptides Bind Syndecan-1 and Are Involved in Acinar Formation of a Human Submandibular Gland Cell Line. *J. Biol. Chem.* 273, 28633–28641. doi:10.1074/jbc.273.44.28633

Hsiao, Y.-C., and Yang, T.-L. (2015). Data Supporting Chitosan Facilitates Structure Formation of the Salivary Gland by Regulating the Basement Membrane Components. *Data in brief* 4, 551–558. doi:10.1016/j.dib.2015.07.006

Huettner, N., Dargaville, T. R., and Forget, A. (2018). Discovering Cell-Adhesion Peptides in Tissue Engineering: Beyond RGD. *Trends Biotechnol.* 36, 372–383. doi:10.1016/j.tibtech.2018.01.008

Ikeda, E., Ogawa, M., Takeo, M., and Tsuji, T. (2019). Functional Ectodermal Organ Regeneration as the Next Generation of Organ Replacement Therapy. *Open Biol.* 9, 190010. doi:10.1098/rsob.190010

Jaguar, G. C., Prado, J. D., Campanhã, D., and Alves, F. A. (2017). Clinical Features and Preventive Therapies of Radiation-Induced Xerostomia in Head and Neck Cancer Patient: a Literature Review. *Appl. Cancer Res.* 37, 31. doi:10.1186/s41241-017-0037-5

Jasmer, K. J., Gilman, K. E., Muñoz Forti, K., Weisman, G. A., and Limesand, K. H. (2020). Radiation-Induced Salivary Gland Dysfunction: Mechanisms, Therapeutics and Future Directions. *J. Clin. Med.* 9, 4095. doi:10.3390/jcm9124095

Jensen, S. B., Vissink, A., Limesand, K. H., and Reyland, M. E. (2019). Salivary Gland Hypofunction and Xerostomia in Head and Neck Radiation Patients. *J. Natl. Cancer Inst. Monogr.* doi:10.1093/jncimonographs/lgz016

Jensen, S. B., au, fnm., Pedersen, A. M. L., Vissink, A., Andersen, E., Brown, C. G., et al. (2010). A Systematic Review of Salivary Gland Hypofunction and Xerostomia Induced by Cancer Therapies: Prevalence, Severity and Impact on Quality of Life. *Support Care Cancer* 18, 1039–1060. doi:10.1007/s00520-010-0827-8

Lombaert, I. M. A., Brunsting, J. F., Wierenga, P. K., Kampinga, H. H., de Haan, G., and Coppes, R. P. (2008). Keratinocyte Growth Factor Prevents Radiation Damage to Salivary Glands by Expansion of the Stem/Progenitor Pool. *Stem Cells* 26, 2595–2601. doi:10.1634/stemcells.2007-1034

Lovelace, T. L., Fox, N. F., Sood, A. J., Nguyen, S. A., and Day, T. A. (2014). Management of Radiotherapy-Induced Salivary Hypofunction and Consequent Xerostomia in Patients with Oral or Head and Neck Cancer: Meta-Analysis and Literature Review. *Oral Surg. Oral Med. Oral Pathol. Oral Radiol.* 117, 595–607. doi:10.1016/j.oooo.2014.01.229

Lung, C. B., Watson, G. E., Verma, S., Feng, C., and Saunders, R. H. (2021). Duration of Effect of Biotène spray in Patients with Symptomatic Dry Mouth: A Pilot Study. *Oral Surg. Oral Med. Oral Pathol. Oral Radiol.* 131, 415–421. doi:10.1016/j.oooo.2020.12.002

Mitroulia, A., Gavriiloglou, M., Athanasiadou, P., Bakopoulou, A., Poulopoulos, A., and Andreadis, D. (2019). Salivary Gland Stem Cells and Tissue Regeneration: An Update on Possible Therapeutic Application. *J. Contemp. Dent Pract.* 20, 978–986. doi:10.5005/jp-journals-10024-2620

Mochizuki, M., (2003). Current Awareness. *Hydrol. Process* 17, 875–877. doi:10.1002/hyp.5037

Motta, C. M. M., Endres, K. J., Wesdemiotis, C., Willits, R. K., and Becker, M. L. (2019). Enhancing Schwann Cell Migration Using Concentration Gradients of Laminin-Derived Peptides. *Biomaterials* 218, 119335. doi:10.1016/j.biomaterials.2019.119335

Nair, R. P., Zheng, C., and Sunavala-Dossabhoy, G. (2016). Retroductal Submandibular Gland Instillation and Localized Fractionated Irradiation in a Rat Model of Salivary Hypofunction. *JoVE*, 53785. doi:10.3791/53785

Nam, K., Dean, S. M., Brown, C. T., Smith, R. J., Lei, P., Andreadis, S. T., et al. (2019). Synergistic Effects of Laminin-1 Peptides, VEGF and FGF9 on Salivary Gland Regeneration. *Acta Biomater.* 91, 186–194. doi:10.1016/j.actbio.2019.04.049

Nam, K., Jones, J. P., Lei, P., Andreadis, S. T., and Baker, O. J. (2016). Laminin-111 Peptides Conjugated to Fibrin Hydrogels Promote Formation of Lumen Containing Parotid Gland Cell Clusters. *Biomacromolecules* 17, 2293–2301. doi:10.1021/acs.biomac.6b00588

Nam, K., Kim, K., Dean, S. M., Brown, C. T., Davis, R. S., Okano, T., et al. (2019). Using Cell Sheets to Regenerate Mouse Submandibular Glands. *NPJ Regen. Med.* 4, 16. doi:10.1038/s41536-019-0078-3

Nam, K., Maruyama, C. L., Wang, C.-S., Trump, B. G., Lei, P., Andreadis, S. T., et al. (2017). Laminin-111-derived Peptide Conjugated Fibrin Hydrogel Restores Salivary Gland Function. *PLoS One* 12, e0187069. doi:10.1371/journal.pone.0187069

Nam, K., Wang, C.-S., Maruyama, C. L. M., Lei, P., Andreadis, S. T., and Baker, O. J. (2017). L1 Peptide-Conjugated Fibrin Hydrogels Promote Salivary Gland Regeneration. *J. Dent Res.* 96, 798–806. doi:10.1177/0022034517695496

Nanduri, L. S. Y., Lombaert, I. M. A., van der Zwaag, M., Faber, H., Brunsting, J. F., van Os, R. P., et al. (2013). Salisphere Derived C-Kit+ Cell Transplantation Restores Tissue Homeostasis in Irradiated Salivary Gland. *Radiother. Oncol.* 108, 458–463. doi:10.1016/j.radonc.2013.05.020

Nanduri, L. S. Y., Maimets, M., Pringle, S. A., van der Zwaag, M., van Os, R. P., and Coppes, R. P. (2011). Regeneration of Irradiated Salivary Glands with Stem Cell Marker Expressing Cells. *Radiother. Oncol.* 99, 367–372. doi:10.1016/j.radonc.2011.05.085

Ogawa, M., Oshima, M., Imamura, A., Sekine, Y., Ishida, K., Yamashita, K., et al. (2013). Functional Salivary Gland Regeneration by Transplantation of a Bioengineered Organ Germ. *Nat. Commun.* 4, 2498. doi:10.1038/ncomms3498

Ogawa, M., and Tsuji, T. (2015). Reconstitution of a Bioengineered Salivary Gland Using a Three-Dimensional Cell Manipulation Method. *Curr. Protoc. Cel Biol.* 66, 19. doi:10.1002/0471143030.cb1917s66

Patil, S. V., and Nanduri, L. S. Y. (2017). Interaction of Chitin/chitosan with Salivary and Other Epithelial Cells-An Overview. *Int. J. Biol. Macromolecules* 104, 1398–1406. doi:10.1016/j.ijbiomac.2017.03.058

Peters, S. B., Naim, N., Nelson, D. A., Mosier, A. P., Cady, N. C., and Larsen, M. (2014). Biocompatible Tissue Scaffold Compliance Promotes Salivary Gland Morphogenesis and Differentiation. *Tissue Eng. Part A* 20, 1632–1642. doi:10.1089/ten.tea.2013.0515

Pinna, R., Campus, G., Cumbo, E., Mura, I., and Milia, E. (2015). Xerostomia Induced by Radiotherapy: an Overview of the Physiopathology, Clinical Evidence, And management of the Oral Damage. *Tcrm* 11, 171–188. doi:10.2147/tcrm.s70652

Pradhan-Bhatt, S., (2014). A Novel *In Vivo* Model for Evaluating Functional Restoration of a Tissue-engineered Salivary Gland. *Laryngoscope* 124, 456–461. doi:10.1002/lary.24297

Pringle, S., Van Os, R., and Coppes, R. P. (2013). Concise Review: Adult Salivary Gland Stem Cells and a Potential Therapy for Xerostomia. *Stem Cells* 31, 613–619. doi:10.1002/stem.1327

Rebustini, I. T., Patel, V. N., Stewart, J. S., Layvey, A., Georges-Labouesse, E., Miner, J. H., et al. (2007). Laminin α5 Is Necessary for Submandibular Gland Epithelial Morphogenesis and Influences FGFR Expression through β1 Integrin Signaling. *Develop. Biol.* 308, 15–29. doi:10.1016/j.ydbio.2007.04.031

Rocchi, C., and Emmerson, E. (2020). Mouth-Watering Results: Clinical Need, Current Approaches, and Future Directions for Salivary Gland Regeneration. *Trends Mol. Med.* 26, 649–669. doi:10.1016/j.molmed.2020.03.009

Siegel, R. L., Miller, K. D., Fuchs, H. E., and Jemal, A. (2021). Cancer Statistics, 2021. *CA A. Cancer J. Clin.* 71, 7–33. doi:10.3322/caac.21654

Silvestre, F. J., Minguez, M. P., and Suñe-Negre, J. M. (2009). Clinical Evaluation of a New Artificial Saliva in spray Form for Patients with Dry Mouth. *Med. Oral Patol Oral Cir Bucal* 14, E8–E11.

Soscia, D. A., Sequeira, S. J., Schramm, R. A., Jayarathanam, K., Cantara, S. I., Larsen, M., et al. (2013). Salivary Gland Cell Differentiation and Organization on Micropatterned PLGA Nanofiber Craters. *Biomaterials* 34, 6773–6784. doi:10.1016/j.biomaterials.2013.05.061

Sroussi, H. Y., Epstein, J. B., Bensadoun, R.-J., Saunders, D. P., Lalla, R. V., Migliorati, C. A., et al. (2017). Common Oral Complications of Head and Neck Cancer Radiation Therapy: Mucositis, Infections, Saliva Change, Fibrosis, Sensory Dysfunctions, Dental Caries, Periodontal Disease, and Osteoradionecrosis. *Cancer Med.* 6, 2918–2931. doi:10.1002/cam4.1221

Su, X., Liu, Y., Bakkar, M., ElKashty, O., El-Hakim, M., Seuntjens, J., et al. (2020). Labial Stem Cell Extract Mitigates Injury to Irradiated Salivary Glands. *J. Dent Res.* 99, 293–301. doi:10.1177/0022034519898138

Sun, T., Zhu, J., Yang, X., and Wang, S. (2006). Growth of Miniature Pig Parotid Cells on Biomaterials *In Vitro*. *Arch. Oral Biol.* 51, 351–358. doi:10.1016/j.archoralbio.2005.10.001

Turner, M. D. (2016). Hyposalivation and Xerostomia. *Dental Clin. North America* 60, 435–443. doi:10.1016/j.cden.2015.11.003

Varghese, J. J., Schmale, I. L., Mickelsen, D., Hansen, M. E., Newlands, S. D., Benoit, D. S. W., et al. (2018). Localized Delivery of Amifostine Enhances Salivary Gland Radioprotection. *J. Dent Res.* 97, 1252–1259. doi:10.1177/0022034518767408

Weng, P.-L., Aure, M. H., Maruyama, T., and Ovitt, C. E. (2018). Limited Regeneration of Adult Salivary Glands after Severe Injury Involves Cellular Plasticity. *Cel Rep.* 24, 1464–1470. doi:10.1016/j.celrep.2018.07.016

Wu, V. W. C., and Leung, K. Y. (2019). A Review on the Assessment of Radiation Induced Salivary Gland Damage after Radiotherapy. *Front. Oncol.* 9, 1090. doi:10.3389/fonc.2019.01090

Yang, T.-L., and Hsiao, Y.-C. (2015). Chitosan Facilitates Structure Formation of the Salivary Gland by Regulating the Basement Membrane Components. *Biomaterials* 66, 29–40. doi:10.1016/j.biomaterials.2015.06.028

Zheng, C., Cotrim, A. P., Rowzee, A., Swaim, W., Sowers, A., Mitchell, J. B., et al. (2011). Prevention of Radiation-Induced Salivary Hypofunction Following hKGF Gene Delivery to Murine Submandibular Glands. *Clin. Cancer Res.* 17, 2842–2851. doi:10.1158/1078-0432.ccr-10-2982

Conflict of Interest: The authors declare that the research was conducted in the absence of any commercial or financial relationships that could be construed as a potential conflict of interest.

Publisher's Note: All claims expressed in this article are solely those of the authors and do not necessarily represent those of their affiliated organizations, or those of the publisher, the editors and the reviewers. Any product that may be evaluated in this article, or claim that may be made by its manufacturer, is not guaranteed or endorsed by the publisher.

frontiers in Bioengineering and Biotechnology

ORIGINAL RESEARCH
published: 02 November 2021
doi: 10.3389/fbioe.2021.764703

Canine Mesenchymal Stromal Cell-Mediated Bone Regeneration is Enhanced in the Presence of Sub-Therapeutic Concentrations of BMP-2 in a Murine Calvarial Defect Model

Lauren K. Dobson[1], *Suzanne Zeitouni*[2], *Eoin P. McNeill*[2], *Robert N. Bearden*[1], *Carl A. Gregory*[2] *and W. Brian Saunders*[1]*

[1]*Department of Small Animal Clinical Sciences, College of Veterinary Medicine and Biomedical Sciences, Texas A&M University, College Station, TX, United States,* [2]*Department of Molecular and Cellular Medicine, Institute for Regenerative Medicine, Texas A&M Health Science Center, College Station, TX, United States*

OPEN ACCESS

Edited by:
Bin Li,
Soochow University, China

Reviewed by:
Zoran Ivanovic,
Établissement Français du Sang (EFS), France
Feng-Huei Lin,
National Taiwan University, Taiwan

***Correspondence:**
W. Brian Saunders
bsaunders@cvm.tamu.edu

Specialty section:
This article was submitted to Tissue Engineering and Regenerative Medicine, a section of the journal Frontiers in Bioengineering and Biotechnology

Received: *25 August 2021*
Accepted: *27 September 2021*
Published: *02 November 2021*

Citation:
Dobson LK, Zeitouni S, McNeill EP, Bearden RN, Gregory CA and Saunders WB (2021) Canine Mesenchymal Stromal Cell-Mediated Bone Regeneration is Enhanced in the Presence of Sub-Therapeutic Concentrations of BMP-2 in a Murine Calvarial Defect Model. Front. Bioeng. Biotechnol. 9:764703. doi: 10.3389/fbioe.2021.764703

Novel bone regeneration strategies often show promise in rodent models yet are unable to successfully translate to clinical therapy. Sheep, goats, and dogs are used as translational models in preparation for human clinical trials. While human MSCs (hMSCs) undergo osteogenesis in response to well-defined protocols, canine MSCs (cMSCs) are more incompletely characterized. Prior work suggests that cMSCs require additional agonists such as IGF-1, NELL-1, or BMP-2 to undergo robust osteogenic differentiation *in vitro*. When compared directly to hMSCs, cMSCs perform poorly *in vivo*. Thus, from both mechanistic and clinical perspectives, cMSC and hMSC-mediated bone regeneration may differ. The objectives of this study were twofold. The first was to determine if previous *in vitro* findings regarding cMSC osteogenesis were substantiated *in vivo* using an established murine calvarial defect model. The second was to assess *in vitro* ALP activity and endogenous BMP-2 gene expression in both canine and human MSCs. Calvarial defects (4 mm) were treated with cMSCs, sub-therapeutic BMP-2, or the combination of cMSCs and sub-therapeutic BMP-2. At 28 days, while there was increased healing in defects treated with cMSCs, defects treated with cMSCs and BMP-2 exhibited the greatest degree of bone healing as determined by quantitative μCT and histology. Using species-specific qPCR, cMSCs were not detected in relevant numbers 10 days after implantation, suggesting that bone healing was mediated by anabolic cMSC or ECM-driven cues and not *via* engraftment of cMSCs. In support of this finding, defects treated with cMSC + BMP-2 exhibited robust deposition of Collagens I, III, and VI using immunofluorescence. Importantly, cMSCs exhibited minimal ALP activity unless cultured in the presence of BMP-2 and did not express endogenous canine BMP-2 under any condition. In contrast, human MSCs exhibited robust ALP activity in all conditions and expressed human BMP-2 when cultured in control and osteoinduction media. This is the first *in vivo* study in support of previous *in vitro* findings regarding cMSC

osteogenesis, namely that cMSCs require additional agonists to initiate robust osteogenesis. These findings are highly relevant to translational cell-based bone healing studies and represent an important finding for the field of canine MSC-mediated bone regeneration.

Keywords: canine, bone, regeneration, calvarial, BMP-2, *in vivo*, MSC

INTRODUCTION

Non-union bone defects are a major challenge in orthopaedics. It has previously been estimated that approximately 10% of fractures result in non-union (Marsh 1998). In some patients, poor bone quality and inadequate fixation provide insufficient biomechanical stabilization and result in non-union (Bishop et al., 2012). In other patients, age and other co-morbidities lead to impaired endogenous bone repair and an insufficient biologic response to achieve union (Hak et al., 2014). In many patients, a combination of biomechanical and biologic factors contribute equally to the development of non-unions. Development of methods to achieve rapid, reliable healing of large bone defects will reduce the incidence of implant failure, reoperation, patient-morbidity, and the burden on the healthcare system.

For decades, autografts have been the gold standard for treatment and prevention of non-unions due to their ability to provide osteogenic, osteoinductive, and osteoconductive stimuli to the defect (Kao and Scott 2007). Disadvantages of autografting include a paucity of osteogenic cells, limited osteoconductivity, poor host-cell adhesion properties, insufficient biomechanical properties, incomplete osteointegration, and untoward immune response (Boden, 2002; Cuomo et al., 2009). Therefore, a clear need exists for the development of an effective technology with efficacy similar to autografting but without the associated limitations. The most feasible form for this technology is a cell-scaffold composite; however, achieving clinical efficacy, reproducibility, biocompatibility, and an effective production pipeline have hampered development of this strategy (McNeill et al., 2020).

Mesenchymal stromal cells (MSCs) are promising agents for bone repair and regeneration. MSCs isolated from adult tissues such as bone marrow, synovium, adipose, and other tissues possess the capacity to differentiate into numerous connective tissue lineages including osteoblasts, adipocytes, and chondrocytes. MSCs also possess the ability to provide stromal support through deposition of anabolic matrices, deliver trophic factors to repairing tissues, and exhibit immunomodulatory properties. However, the use of human MSCs for bone repair in animal models and the clinical setting has been disappointing due to donor variability and inconsistent outcomes. For these reasons, much work is in progress to optimize the osteoregenerative potential of MSCs via modulation of the canonical Wnt pathway, co-administration of MSCs with osteogenic extracellular matrices, and the use of iPS-derived MSCs (Zeitouni et al., 2012; McNeill et al., 2020).

A major hurdle for novel MSC-scaffold constructs is the successful translation from *in vitro* and rodent model findings to demonstration of efficacy in clinical patients. Large animal models are often utilized as an intermediary toward clinical therapy in human beings (Hatsushika et al., 2014; Cong et al., 2019). While sheep, pig, dog, and goat models are well-described, the dog represents an under-represented model species for orthopaedic regenerative studies (Hoffman and Dow 2016). Dogs exhibit similar orthopaedic physiology and biomechanics to human beings, have complex immune systems, are recognized by regulatory agencies, exhibit more genetic diversity than domestic livestock species, and are amenable to functional outcome measures such as gait analysis. Another advantage of the dog as a translational model species is the ability to perform veterinary clinical trials using naturally occurring non-union fractures with outcome measures identical to future human clinical trials. Moreover, there is precedent for using naturally occurring diseases in the canine model to evaluate novel therapeutics for use in human beings (Hubbard et al., 2018).

While hMSCs have been intensely characterized and consistently undergo *in vitro* osteogenesis in response to well-defined differentiation protocols, a relative handful of studies have focused on canine MSC [cMSCs; (Volk et al., 2005; Levi et al., 2011; Bearden et al., 2017; James et al., 2017; Gasson et al., 2021)]. In regards to osteogenic differentiation, a growing body of work suggests that cMSCs do not respond to hMSC osteogenic protocols without addition of agonists such as bone morphogenic protein 2 (BMP-2), insulin-like growth factor-1 (IGF-1), or neural epidermal growth factor-like 1 protein [NELL-1; (Volk et al., 2005; Levi et al., 2011; Bearden et al., 2017; James et al., 2017; Gasson et al., 2021)]. Importantly, the reduced *in vitro* performance of cMSCs was previously documented *in vivo* in a nude mouse calvarial defect model (Levi et al., 2011). Defects treated with human adipose-derived MSCs exhibited significant bone healing, whereas defects treated with murine or canine MSCs exhibited minimal bone healing and were not different than untreated controls (Levi et al., 2011). These results suggest that the mechanisms that control osteogenesis in cMSCs and hMSCs may be somewhat different.

BMP-2 has undoubtedly demonstrated the most clinical promise as an alternative to autografting (Boden et al., 2000; Hecht et al., 2000; Liu et al., 2019). When applied on a compression resistant calcium phosphate matrix, recombinant human BMP-2 (rhBMP-2) enhances lumbar spinal fusions and improves long-bone fracture healing (Glassman et al., 2005; Dimar et al., 2006). Importantly, rhBMP-2 is also effective in other species such as sheep and dogs has been used in canine bone healing models (Kandziora et al., 2002; Schmoekel et al., 2004; Kinsella et al., 2011). Concerns have surfaced with BMP-2 therapy due to reports of uncontrollable/ectopic bone formation, respiratory difficulty, osteolysis, cervical and soft

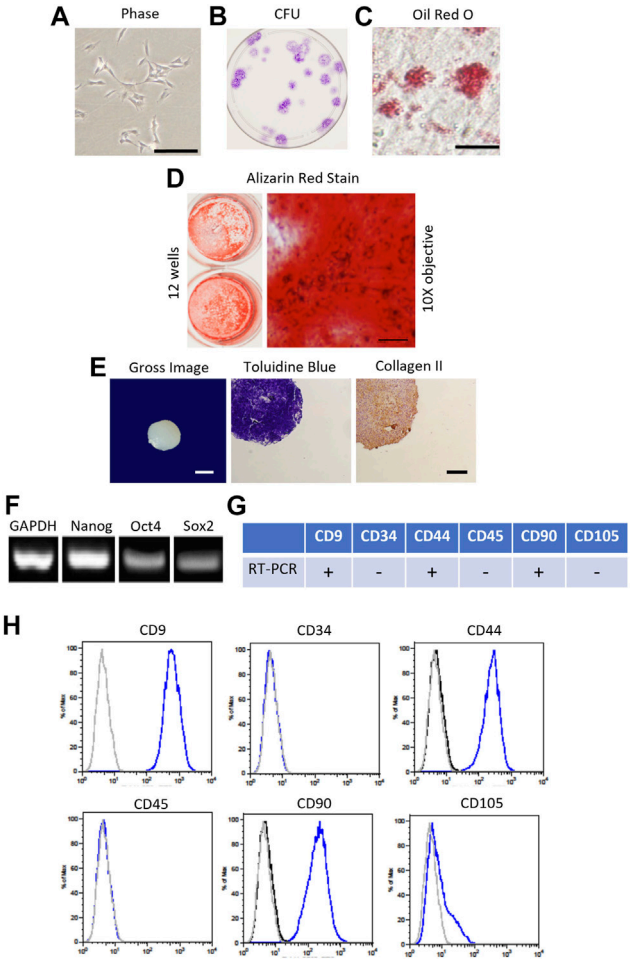

FIGURE 1 | Characterization of canine bone marrow-derived mesenchymal stromal cell (cMSC). **(A)**: Passage 1 cMSCs were expanded at 100 cells/cm^2 in CCM with media exchange every 48 h until cMSCs reached 70–80% Representative phase contrast microscopy image of cMSCs exhibiting a spindle-shaped, mesenchymal phenotype (bar = 250 μm). **(B)**: cMSCs were assessed with the classic colony forming unit (CFU) assay to demonstrate ability to form distinct colonies in the absence of media exchange over a 21 days time course. **(C)**: Adipogenic differentiation was confirmed *via* Oil Red O staining after 21 days of culture in adipogenic differentiation medium (bar = 25 μm). **(D)**: Osteogenic differentiation was confirmed *via* Alizarin Red Stain after 21 days of culture in osteogenic differentiation medium (ODM) supplemented with + 200 ng/ml of rh-BMP-2. Gross photography of representative wells are provided (left) in conjunction with transmitted light microscopy images (right, bar = 125 μm). **(E)**: Chondrogenic differentiation was confirmed using the traditional micromass assay. Gross image of a representative cMSC chondrogenic spheroid (bar = 300 μm) is provided on the left, with Toluidine Blue for and Collagen Type II immunohistochemistry shown at center and right (bar = 150 μm). **(F)**: cMSCs were assessed for endogenous expression of the plasticity-associated genes Nanog, Oct4, and Sox2 using RT-PCR. Canine GAPDH was used as a housekeeping gene. **(G, H)**: Real-time PCR and flow cytometry analysis of cMSCs demonstrating expression of CD9, CD44, and CD90 and the absence of CD34, CD45, and CD105. Using these characterization methods, the cMSCs met the criteria for MSCs.

tissue inflammation, adipogenic activation, urogenital events and bone cyst formation (Carragee, Hurwitz, and Weiner 2011; Faundez et al., 2016). As such, efforts are underway to refine BMP-2 dosing or develop alternative BMP-2 treatment strategies. Using a rat lumbar spinal fusion model, Bae and colleagues demonstrated that delivery of a sub-therapeutic concentration of BMP-2 in combination with fresh bone marrow allografts led to improved lumbar fusion rates, suggesting that cells could be combined with a low dose of BMP-2 to achieve clinical unions (Bae et al., 2013).

Given the prior studies demonstrating that cMSCs fail to undergo robust *in vitro* osteogenesis without supplemental BMP-2 *in vitro* (Volk et al., 2005; Levi et al., 2011; Bearden et al., 2017; James et al., 2017; Gasson et al., 2021), the objective of this study was to determine whether bone marrow-derived cMSCs were capable of inducing a healing response in an established murine calvarial defect model in the absence or presence of BMP-2, and to determine whether a combination of sub-therapeutic rhBMP-2 and cMSCs behaved synergistically similar to the findings of Bae et al. We hypothesized that cMSCs co-administered with a sub-therapeutic concentration of rhBMP-2 would induce superior bone healing as compared to untreated defects or defects treated with either cMSCs or sub-therapeutic rhBMP-2 alone.

MATERIALS AND METHODS

Culture and Differentiation of cMSCs and hMSCs

Canine MSCs were obtained from a bone marrow aspirate from the proximal humerus of a haematologically healthy canine donor under an approved Animal Use Protocol (2011-149) with the supervision of the Institutional Animal Care and Use Committee at Texas A&M University. Using Ficoll centrifugation and plastic adherence, mononuclear cells were plated at 30,000 cells/cm^2 on 150 cm^2 dishes to isolate Passage 0 (P0) cells in complete culture medium (CCM) consisting of alpha minimal essential medium (α-MEM, Invitrogen, Waltham, MA) containing 10% premium select fetal bovine serum (Atlanta Biologicals, Norcross, GA), 2 mM L-glutamine, 100 units/ml penicillin, and 100 ug/ml streptomycin (Invitrogen) (Bearden et al., 2017). Plates were washed daily with PBS for 3 days and media exchange was performed at 48 h intervals until colonies of P0 cells were visible. Cells were washed, trypsinized, and Passage 1 (P1) cells were expanded at clonal density 100 cells/cm^2 in CCM with media exchange every 48 h until cells reached 70% confluence. Cells were characterized and confirmed to be cMSCs as defined by Dominici with slight modifications for the canine species **Figure 1**; (Dominici et al., 2006; Bearden et al., 2017). The preparation of cMSCs used in the present study was selected due to its representative performance in osteogenic differentiation assays (Bearden et al., 2017). P1 cells were cryopreserved in 1 × 10^6/ml aliquots in α-MEM with 30% FBS and 5% DMSO (Hybrimax, Sigma-Aldrich, St. Louis, MO). For subsequent experiments, cells were thawed and expanded to Passage 2 (P2) cells at 100 cells/cm^2 in CCM.

Human MSCs (hMSCs) were obtained from the iliac crest of two haematologically healthy human donors under a Texas A&M/Baylor Scott and White Hospital (Temple, TX)

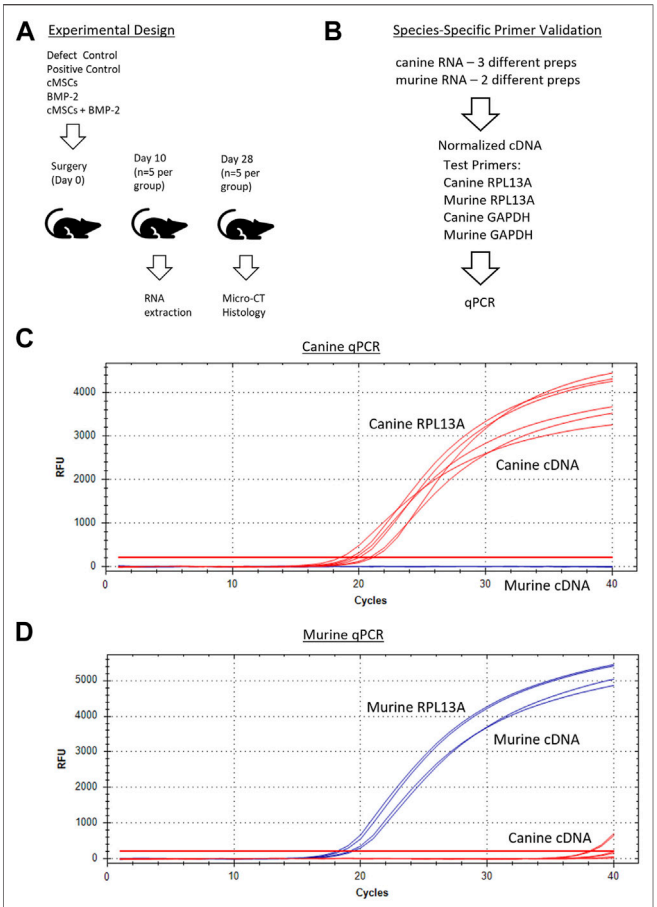

FIGURE 2 | Overall experimental design and species-specific primer development and validation. **(A)**: Surgical treatment groups included a negative control (defect control), positive control (100 μg/ml BMP-2), 2 × 10^6 cMSCs, sub-therapeutic BMP-2 (6 μg/ml), or cMSCs + BMP-2 (6 μg/ml). Mice were terminated for RNA extraction (Day 10) or μCT and histology (Day 28). **(B)**: qPCR primer design and validation schematic for canine and murine RNA samples. Primer pairs that amplified RPL13A and GAPDH in a species-dependent manner were selected for further use. **(C, D)**: Canine and murine RPL13a qPCR amplification curves for canine cDNA (red lines) and murine cDNA (blue lines). Canine and murine RPL13a primer-pairs resulted in species-specific amplification and were used in subsequent analyses.

Institutional Review Board-approved protocol. hMSCs were isolated, expanded, and cryopreserved using identical methods to the cMSCs, with the exception that the CCM used to isolate and expand the hMSCs contained 20% premium select FBS (Atlanta Biologicals). The hMSCs were selected for the present study due to their representative performance in osteogenic differentiation assays (Clough et al., 2015).

Murine Calvarial Defect Model

Murine calvarial defect studies were conducted under an approved AUP (2016-0144) with the supervision of the Texas A&M University Institutional Animal Care and Use Committee. 60-days female Nu/J mice were acquired from Jackson Laboratories (Bar Harbor, ME) and housed in sterile conditions. Mice (n = 10/group) were anesthetized using isoflurane inhalant anesthesia in 100% O_2 with whole body warming at 37°C. Post-operative care consisted of buprenex administration twice a day for 3 days and a hydrogel diet to encourage caloric intake. After sterile surgical preparation with chlorhexidine and alcohol, 4 mm unilateral calvarial defects were created with an osteotomy burr (Roboz Surgical, Gaithersburg, MD) under continuous saline irrigation. To ensure consistent defect placement, each defect was created 1–2 mm from the sagittal and coronal sutures.

P1 cMSCs were thawed, washed, plated at 100 cells/cm^2, and cultured in CCM until P2 cells were 70–80% confluent on the day of surgical implantation. P2 cMSCs were washed in PBS, trypsinized, neutralized with CCM, washed in α-MEM to remove residual serum, and suspended in sterile filtered PBS in 2 × 10^6 cell aliquots per defect. cMSC aliquots were stored on ice in the surgical suite until the time of administration. Calvarial defects were treated with either 2 × 10^6 cMSCs in murine plasma, 6 μg/ml recombinant human BMP-2 (rhBMP-2, R and D systems, Minneapolis, MN) in murine plasma [BMP-2; (Bae et al., 2013)], or the combination of 2 × 10^6 cMSCs and 6 μg/ml rhBMP-2 in murine plasma (cMSCs + BMP-2; **Figure 2A**). At the time of defect creation, the aliquots of cMSCs were centrifuged, resuspended in 20 μL of 4°C murine plasma (Sigma-Aldrich), added to 20 μL of 4°C 2X thromboplastin C (Fisher Scientific, Waltham, MA), and immediately pipetted onto each calvarial defect. For the cMSC treatment groups that also received 6 μg/ml rhBMP-2, after combination of murine plasma and thromboplastin, 6 μL of rhBMP-2 was added to the pipette for implantation into the defect. Gelation of the murine plasma was confirmed by manual agitation of the solution with the pipette tip. A positive control group received 100 μg/ml rhBMP-2 on a gelatin surgical sponge (positive control) based on previous work (Bae et al., 2013) (Gelfoam, Baxter International, Deerfield, IL). A negative control group [defect control group (n = 4 mice/group)] did not receive inductive treatment but did receive 40 μL of plasma and thromboplastin to confirm that co-administration of murine plasma had no effect on defect healing. Mice were recovered from anesthesia and housed in group cages until termination at Day 10 (RNA isolation and quantification of cMSCs) or Day 28 (assessment of healing *via* microCT and histology; **Figure 2A**).

Canine and Murine Cell Titration Standard Curve

In order to screen calvarial defects for the presence of canine cells post-implantation, murine and canine RNA were first used to create species-specific primers for real-time quantitative PCR (qPCR). Murine fibroblasts (C3H10T1/2, ATCC, Manassas, VA) and cMSCs were cultured in CCM. Two preparations of C3H10T1/2 and three preparations of cMSCs (1 × 10^6 cells/prep) were isolated and used to extract RNA using the High Pure RNA Isolation Kit (Roche Diagnostics, Basel, Switzerland). RNA samples were quantified *via* nanodrop (Thermofisher, Waltham, MA) to determine RNA yields and were normalized to identical RNA values prior to generation of cDNA (SuperScript III cDNA kit, Invitrogen). For qPCR, cDNA was amplified in a

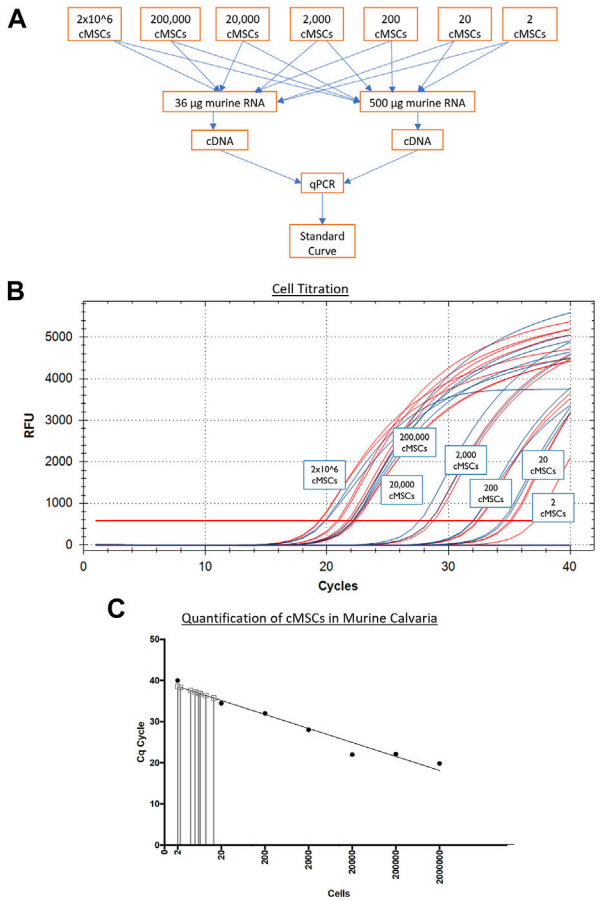

FIGURE 3 | Generation of a qPCR-based cMSC standard curve to detect cMSCs in calvarial defects at Day 10. **(A)**: Serial dilutions of RNA were performed on RNA extracted from 2×10^6 total cMSCs. RNA samples were added to individual sample tubes containing either 36 or 500 µg of murine RNA to determine if the amount of murine RNA would affect the ability to identify canine RPL13A. cDNA samples were generated and qPCR was performed. **(B)**: qPCR amplification curves are shown for canine RPL13A from cDNA samples generated with either 36 µg (red lines) or 500 µg (blue lines) of murine RNA. **(C)**: Cycle thresholds from Panel A (red lines) were used to generate a standard curve using a linear curve fit technique. RNA samples were isolated from the calvarial defects treated with cMSCs or cMSCs + BMP-2. These samples contained both murine and canine RNA. cDNA samples were generated and qPCR performed for canine RPL13A. Cycle threshold results were interpolated on the standard curve. At Day 10 post implantation, only 2–20 total cMSCs were detected.

20 µL reaction containing SYBR Green PCR master mix (Fast SYBR Green, Applied Biosystems, City, State) on a CFX96 Real-Time System (Bio-Rad, City, State). Canine RPL13A and GAPDH (Peters et al., 2007), murine RPL13A and GAPDH made using primer-blast (Ye et al., 2012), were used to create species-specific housekeeping primers (Sigma, St. Louis, MO; **Figure 2B**). The two murine and three canine cDNA preparations were assessed in duplicate with qPCR using both murine and canine RPL13A and GAPDH (4 primer pairs) to confirm species specificity.

Next, murine and canine RNA were used to determine a correlation of threshold cycles and create a standard curve for minimum and maximum numbers of detectable cells. Murine fibroblasts (C3H10T1/2) or cMSCs (2×10^6) were used to extract RNA using the High Pure RNA isolation kit (Roche Diagnostics). Samples were quantified using the nanodrop to obtain RNA concentrations. Once the RNA concentrations for 2×10^6 cMSCs was determined, cMSC RNA samples were titrated from 2×10^6 cells in serial dilutions down to the equivalent of two cells. Titrated canine RNA samples were placed into 36 or 500 µg murine RNA to represent a low or high background of murine RNA (**Figure 3A**). Each of the mixed canine and murine RNA samples were used to create cDNA (SuperScript III cDNA kit, Invitrogen). qPCR was performed as described above using canine RPL13Aand cycle threshold data for each cell titration were interpolated to a standard curve in Prism version 8.00 for Mac (GraphPad Software, La Jolla, CA). qPCR amplification of canine RPL13A (**Figure 3B**) was similar in either the low concentration of background murine RNA (36 µg; red lines) or the high concentration of background murine RNA (500 µg; blue lines). Therefore, the standard curve to interpolate detection of cMSCs at day 10 was based on the cMSC cell titrations mixed with low concentration of murine RNA (**Figure 3C**).

Real-Time Quantitative PCR Detection of cMSCs at Day 10

At Day 10, mice (n = 5) from cell therapy groups (cMSCs and cMSCs + BMP-2) were terminated. Dissection instruments and the workspace were treated with RNAse Zap (Invitrogen) prior to harvesting calvaria. Individual calvaria were removed using a rotary tool fitted with a 10 mm diameter diamond-cutting wheel. Calvarial samples were washed in PBS and snap frozen in liquid nitrogen (**Figure 2A**). RNA was extracted the day of calvarial harvest using a Roche High Pure RNA isolation kit (Roche Diagnostics). Samples were thawed in 800 µL lysis buffer in their respective 50 ml conical tubes and were rocked for 30 min at room temperature after the addition of 400 µL of sterile room temperature PBS. The PBS and lysis buffer mixture was then passed through High Pure RNA isolation kit purification columns following manufacturers protocol and then eluted in 50 µL in elution buffer (Roche Diagnostics).

Individual eluents were then assayed for the number of cMSCs present within each calvarial defect using qPCR for the canine housekeeping gene RPL13A. For each sample, 40 ng of RNA was used to generate cDNA using the SuperScript III cDNA kit (Invitrogen). For quantitative RT-PCR, cDNA samples were amplified in a 20 µL reaction containing SYBR Green PCR master mix (Fast SYBR Green, Applied Biosystems) on a CFX96 Real-Time System (Bio-Rad). Threshold cycles for each specimen were plotted against the previously described standard curve (**Figures 3A,B**) to quantify the number of cMSC in each defect at Day 10. Values were interpolated in Prism version 8.00 for Mac (GraphPad Software).

Micro-Computed Tomography Analysis

At 28 days, mice (n = 5/group) were terminated and calvaria were excised and placed in 10% neutral buffered formalin (NBF) for fixation. Samples were removed from the 10% NBF, dried with a

Kimwipe, and wrapped in Parafilm (VWR International, Radnor, PA) in preparation for μCT. Samples were imaged 360° using a 28 kV beam with image pixel size of 16 μM, flat field correction, and frame averaging with a SkyScan 1,275 μCT (Bruker; Germany). Individual tiff files from each scan were converted to axial bitmap files for further reconstruction analysis using NRecon (Micro Photonics, Allentown, PA). To minimize scanning artifacts, misalignment compensation, ring artifact reduction, beam hardening, and cross-sectional rotation were optimized and kept constant for all samples. Hounsfield units (HU) were set between −934 and 6297 HU for all reconstructions. Control groups were used to optimize the scanning and reconstruction parameters. Mimics 20.0 (Materialise, Plymouth, MI) was used to generate 3-D reconstructions and quantify bone healing. First, cylinders were generated on each calvarial defect reconstruction using a 4 mm diameter cylinder placed around the margin of each defect. Thresholding was set to 70–255 HU to capture mineralized woven bone. Data were reported as both volume (mm^3) and surface area (mm^2). Threshold settings were determined based on previous work (Samsonraj et al., 2017).

Histological Analysis

Upon completion of μCT, calvaria were removed from 10% NBF and decalcified in 1 M dibasic EDTA, pH 8.0 (Sigma). The solution was changed every 2 days until decalcification was confirmed by manual palpation and survey μCT. Samples were dehydrated via increasing alcohol gradations, cleared with Sub-X clearing agent (Surgipath Medical Industries, Richmond, IL) and embedded in paraffin (Thermo Scientific Richard-Allan Scientific, San Diego, CA). Paraffin-embedded samples were cut to 4 μm sections and floated onto Gold Seal Ultra stick slides (Thermo Scientific, San Diego, CA). Prior to staining, sections were heated to 60°C for 20 min in deparaffinized HiPur Xylene (Thermo Scientific Richard-Allan Scientific) and rehydrated. For H&E staining, sections were stained in Gill's hematoxylin II stain and counterstained with Eosin Y (Poly Scientific R and D, Bay Shore, NY) before clearing and dehydration. Masson's trichrome staining was performed using a commercially available kit (Thermo Scientific Richard-Allan Scientific) following the manufacturer's protocol. Slides were cover-slipped with mounting medium (Thermo Scientific Richard-Allan Scientific).

Immunoflourescence for Collagen Type I, III, VI, and XII

Immunoflourescence was performed to determine the presence of Collagen Type I, III, VI, and XII within calvarial defects. Prior to immunofluorescence, slides were heated to 60°C for 20 min, deparaffinized in HiPur Xylene (Thermo Scientific Richard-Allan Scientific) and rehydrated. Antigen retrieval was performed with 20 μL proteinase K (Agilent) per section followed by a 15-min incubation at 37°C (Dawson et al., 2019). Diluted Vectastain ABC Normal Goat serum was used as the blocking reagent [Vectastain Elite ABC Kit (Rabbit-IgG); Vector Laboratories, Burlingame, CA]. Primary antibodies were diluted in 1% BSA in sterile Tris Buffered Saline (TBS) at a dilution of 1:40 for Collagen I (PA127396, Invitrogen), 1:200 for Collagen III (227341AP, Proteintech Group, Inc., Rosemont, IL), 1:200 for Collagen VI (ab6588, Abcam, Cambridge, MA), and 1:200 for Collagen XII (NBP2-57420, Novus). Antibodies were applied at 20 μL per section and incubated overnight at 4°C. The following day slides were washed with 1X Tri-Buffered Saline with 0.1% Tween (TBST) (Dawson et al., 2019). Bound antibodies were detected by goat anti-rabbit Alexaflour 488 (green) conjugated secondary antibody (Invitrogen) at a 1:500 dilution for 1 h at room temperature. Slides were processed with 4′,6-diamidino-2-phenylindole (DAPI, Invitrogen) for 5 min in order to detect nuclei, rinsed in DI-H2O, dried, and mounted with Prolong Gold Antifade mountant (Invitrogen). Representative images were obtained using an Olympus IX70 Fluorescence microscope (Olympus, Tokyo, Japan) and fluorescent microscopy using SPOT software (version 5.1; Sterling Heights, MO).

Alkaline Phosphatase Activity and BMP-2 Gene Expression

cMSCs and human bone marrow MSCs (hMSCs; hMSC-7, hMSC-25) were used to compare inherent differences in cMSC and hMSC alkaline phosphatase (ALP) activity. Passage 1 cMSCs and hMSCs were thawed and plated as described above to reach 80% confluent P2's. P2 cMSCs and hMSCs were washed, trypsinized, and plated at 1×10^4 cells/cm^2 in 12-well plates (Corning) (n = 6 wells/condition). P2 cMSC and hMSCs were also reserved and used for RNA extraction for day 0 time point using High Pure RNA Isolation Kit following manufacturers protocol (Roche). Cells were cultured in 10% CCM, osteogenic differentiation medium (ODM) consisting of α-MEM with 10% FBS, 10 μg/ml β-glycerophosphate (Sigma), 50 mg/ml ascorbate-2-phosphate (Sigma), or ODM + 100 ng/μL of recombinant human bone morphogenic protein-2 [rhBMP-2; ODM + 100 BMP-2; R and D Systems (Krause et al., 2011)]. Media were exchanged twice weekly. At 7 days, wells (n = 3/condition) were washed twice with PBS and incubated with 500 μL cold (4°C) ALP activity buffer containing 1 mM magnesium chloride (Sigma), 0.1% Triton-X (Sigma), and 100 mM sodium chloride (Sigma) in PBS (Volk et al., 2005; Krause et al., 2011; Bearden et al., 2017; Gasson et al., 2021). 500 μL cold (4°C) ALP substrate, p-nitrophenylphosphate (PNPP, Thermo Fisher, Waltham, MA), was added to each well to initiate the ALP activity reaction. Absorbance for each well was determined at 405 nm in 1-min intervals for 20 min at 37°C using an automated plate reader (Cytation 5, BioTek, Winooski, VT) and Gen5Bio software. Kinetic curves were generated for each well and the ALP activity of each well was calculated by determining the slope of each kinetic curve using a linear curve fit method. ALP activity was normalized to number of cells per well using DNA quantification as previously described (Krause et al., 2011; Bearden et al., 2017).

The remaining wells were washed twice with PBS prior to RNA extraction using the High Pure RNA Isolation Kit (Roche

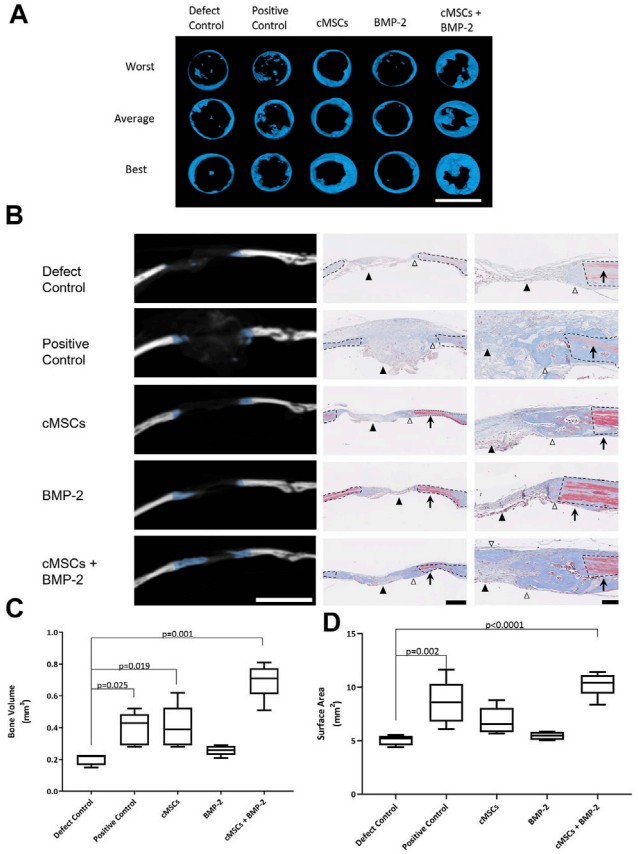

FIGURE 4 | Micro-computed tomography (μCT) and histological analysis of bone healing in murine calvarial defects. **(A)**: μCT was performed at 28 days and used to create coronal plane 3D reconstructions of all calvaria. Reconstructions representing the worst, average, and best bone healing response for each treatment group are provided (bar = 4 mm). Subjectively, the bone healing responses were the greatest for the cMSC and cMSC + BMP-2 treatment groups. **(B)**: Frontal plane μCT images from "average" specimens in panel A are depicted at the widest portion of the defect (bar = 4 mm). Corresponding histology images were obtained at low (bar = 500 μm) or high (bar = 100 μm) magnification. Masson's Trichrome staining allows identification of fibrous tissue (light blue, black arrowheads), woven bone associated with bone healing (dark blue, white arrowheads), or mature, lamellar bone (red, arrows) adjacent to the calvarial defects. Dashed lines denote the margin of the surgical defect. Consistent with the coronal reconstructions in panel A, the cMSC and cMSC + BMP-2 treatment group exhibited the greatest degree of woven bone formation in the histologic sections, confirming the μCT findings. **(C)**: Quantification of bone volume (mm^3) at calvarial defect sites are provided for all treatment groups (box and whisker plots denote mean, 25th and 75th percentile, and range). There was no significant difference in bone volume between sub-therapeutic BMP-2 (BMP-2) and the negative control (Defect Control). There was a significant increase in bone volume for the therapeutic concentration of BMP-2 (Positive control), cMSCs alone (cMSCs), and cMSCs with sub-therapeutic BMP-2 (cMSCs + BMP-2). The cMSCs + BMP-2 treatment group exhibited the greatest bone volume of all groups. Data were analyzed with one-way ANOVA followed by Dunnett's multiple comparison test. **(D)**: Quantification of bone surface area (mm^2) for all treatment groups as described in panel C. There was no significant difference in bone surface area between cMSCs alone (cMSCs), sub-therapeutic BMP-2 (BMP-2), and negative controls (Defect Control). Bone surface area for the therapeutic concentration of BMP-2 (Positive Control) and cMSCs with sub-therapeutic BMP-2 (cMSCs + BMP-2) was

(*Continued*)

FIGURE 4 | significantly greater than negative controls (Defect Control). The cMSCs + BMP-2 treatment group exhibited the greatest bone surface area of all groups. These results demonstrate that while cMSCs are capable of inducing a bone healing response superior to un-treated defects, co-administration of cMSCs with a sub-therapeutic concentration of BMP-2 initiates a more robust healing response, confirming our hypothesis that cMSCs may require additional agonists to maximize bone regeneration *in vivo*.

Life Science, Penzberg, Germany). 300 μL of sterile PBS was pipetted into each well followed by manual dissociation of the monolayer with a pipette tip. Monolayers from replicate wells were combined in 1.7 ml tubes (900 μL/tube) and centrifuged for 3 min at 500 g. Supernatant was removed and pellets were resuspended with 200 μL PBS. 400 μL Lysis Binding Buffer was added following manufacturer's protocol (Roche High Pure RNA Isolation Kit). All samples were treated with DNase to remove contaminating DNA and quantified using a NanoDropTM 1000 Spectrophotometer (ThermoFisher).

Complementary DNA (cDNA) was synthesized from 300 ng RNA (normalized across all samples for each cell preparation) using the SuperScript III RT Kit (Invitrogen) according to the manufacturer's protocol. Canine BMP-2 cDNA ORF Clone (SinoBiological cat #DG70088-G, Wayne, PA) was used as a positive PCR control. P1 cMSC and canine bone marrow RNA (Zyagen #DR704, San Diego, CA) were also assessed for BMP-2 expression. cDNA was used to perform reverse transcription PCR (RT-PCR) in a 15 μL reaction. Canine and human BMP-2 forward (F) and reverse (R) primer sequences were generated with primer-blast (Ye et al., 2012) and are as follows: canine F 5′ CGGTCTCATTACGGAGCTGG 3′, canine R 5′ CTCCGGGTT GTTTTCCCACT 3′, human F 5′ ATGCAAGCAGGTGGGAAA GT 3′ and human R 5′ TGGCCTTATCTGTGACCAGC 3′. Ethidium bromide agarose gel electrophoresis (110 V and 400 amps for 40 min) was used to identify bands for BMP-2 expression at 324 base pairs for canine BMP-2 and 188 bp for human BMP-2 expression.

Identical primer pairs and cDNA samples were used for qPCR of canine or human BMP-2 expression using a CFX96 Real-Time System (Bio-Rad, Hercules, CA). cMSC expression was normalized to the housekeeping genes RPL13A and RPL32 using cDNA extracted from cells used to set up the ALP Assay at day 0 as a baseline (Peters et al., 2007). hMSCs were normalized to β2M and GAPDH housekeeping genes using either hMSC-7 or hMSC-25 days 0 cDNA as a baseline (Kumar et al., 2009; Ye et al., 2012). Once threshold (CT) levels were normalized they were used to provide relative gene expression using the $2^{-\Delta\Delta Ct}$ method (Livak and Schmittgen 2001).

Statistics

Descriptive statistics were reported as mean ± standard deviation (SD) for all data. Analytical statistics were performed using Prism version 8.00 for Mac (GraphPad). Data were analyzed using either one-way ANOVA with Dunnett's multiple comparisons post-test or two-way ANOVA with Tukey's post-hoc test. Significance was established at $p < 0.05$.

RESULTS

Detection of cMSCs in Murine Calvarial Defects at Day 10

RNA samples obtained from the treatment groups that received cells (cMSC and cMSCs + BMP-2) were assessed *via* qPCR for cMSCs at Day 10. RNA samples from the positive control group (BMP-2) were used as an internal control to ensure cMSCs were not detected, as this group did not receive cMSCs as treatment. Ten days after defect creation, of the 2×10^6 cMSCs applied to each defect, a miniscule number of cMSCs ranging from 2–20 cells were detected within each defect (**Figure 3C**). These results indicate that cMSCs, when delivered in a plasma/thromboplastin carrier in a murine calvarial defect model, do not remain within the defect site at relevant numbers for an extended period of time after implantation.

Micro-Computed Tomography and Histological Analyses

All treatment groups were evaluated for bone healing using μCT at Day 28. Coronal plane 3D reconstructions of the best, average, and worst calvarial defects are provided in **Figure 4A**. Subjectively, there were minimal islands of bone within the center of negative control defects (Defect Control) and the periphery of the defects remained smooth with well-defined margins (**Figure 4A**). There were increased islands of bone within the defect with some advancement of bone from the periphery of defects in the positive control group (100 μg/ml BMP-2, **Figure 4A**). Defects treated with cMSCs alone (cMSCs) or cMSCs and sub-therapeutic BMP-2 (cMSCs + BMP-2, **Figure 4A**) exhibited islands of bone within the defects and circumferential advancement of bone from the defect margins. Defects treated with sub-therapeutic BMP-2 alone (BMP-2) were subjectively similar to the negative controls (**Figure 4A**). Subjectively, defects treated with cMSCs and the sub-therapeutic concentration of BMP-2 exhibited the greatest degree of bone healing.

In order to assess bone healing histologically, frontal plane histologic sections were generated and assessed in conjunction with matched frontal plane μCT images (**Figure 4B**). Formation of new, woven bone at the margin of calvarial defects is indicated by blue overlay on the CT images. On adjacent histological sections, defect margins are denoted by black dashed lines. Mason's Trichrome staining allowed for the differentiation of lamellar bone containing crosslinked, mature collagen at the defect margin (red tissue) or new, woven bone containing more poorly organized collagen and is attempting to heal the defect (dark blue tissue). Histologically, there was fibrous tissue (light blue) with minimal bone formation at the defect margins of negative control defects. In positive controls, the gelatin sponge carrier was readily visible within the defect (light blue), however there was minimal woven bone at defect margins. As with the coronal reconstructions, the most robust bone healing was noted in the groups receiving cMSCs or cMSCs + sub-therapeutic BMP-2. The sub-therapeutic BMP-2 treatment group appeared similar to negative controls.

Bone healing was objectively quantified and results are provided in **Figures 4C,D**. Bone volume (mm^3) was as follows: defect control (0.205 ± 0.038), positive control (0.396 ± 0.103), cMSCs (cMSCs; 0.404 ± 0.136), sub-therapeutic BMP-2 (BMP-2; 0.258 ± 0.031), and cMSCs + BMP-2 (0.696 ± 0.111; **Figure 4C**). Bone surface area (mm^2) was as follows: defect control (5.06 ± 0.488), positive control (8.57 ± 0.2.06), cMSCs (6.85 ± 1.27), sub-therapeutic BMP-2 (BMP-2; 5.45 ± 0.374), and cMSCs + BMP-2 (10.29 ± 1.15; **Figure 4D**). Treatment groups that received cMSCs, cMSCs + BMP-2, and the positive controls exhibited significantly higher bone volume when compared to defect controls ($p = 0.019$, $p = 0.001$ and $p = 0.025$, respectively). Positive controls and the treatment group receiving cMSCs + BMP-2 exhibited significantly higher surface area values when compared to untreated controls ($p = 0.002$ and $p < 0.0001$, respectively). Collectively, these results demonstrate that while cMSCs are capable of inducing a bone healing response at Day 28 in an established murine calvarial defect model, the co-administration of cMSCs with a sub-therapeutic concentration of BMP-2 results in a more robust, consistent healing response.

Immunofluorescence for Collagen Type I, III, VI, and XII

As exhibited in **Figure 3C**, we were unable to detect relevant numbers of residual cMSCs within calvarial defects 10 days post-implantation. Despite this finding, treatment of calvarial defects with cMSCs or the combination of cMSCs and sub-therapeutic BMP-2 resulted in the greatest degree of defect healing (**Figure 4**). For these reasons, we elected to assess calvarial defects for ECM components known to contribute to bone healing (**Figure 5**). Collagen Type I, III, and VI were detected in all treatment groups. Collagen I was detected within the lamellae of the mature bone adjacent to defects, within the more poorly organized woven bone within healing defects, and sparsely within the fibrous tissue spanning the negative control defects. Subjectively, Collagen I staining was enhanced and diffusely present in the cMSC + BMP-2 treatment group, which is consistent with the enhanced bone healing response in this group. In contrast to Collagen Type I, Collagen III was limited to the fibrous tissue bridging defects or to the leading edge of healing bone, which is consistent with the known role of Collagen Type III in wound and bone healing (Volk et al., 2011; Izu et al., 2012; Garnero 2015; Miedel et al., 2015). Collagen III was subjectively increased in the cMSC + BMP-2 treatment group. Collagen VI exhibited a similar immunofluorescence pattern to Collagen III. Collagen VI was present in all treatment groups and was localized to the fibrous tissue bridging the center of calvarial defects or to the leading edge of healing bone, with the greatest degree of staining in the positive control, cMSC, and cMSC + BMP-2 treatment group. Collagen XII was not detectible within any of the treatment groups with the exception of the cMSCs + BMP-2 group in which it was weakly present both within the fibrous tissue bridging the defects and the leading edge of healing bone. In summary, Collagen I, III, VI, and XII exhibited distinct deposition patterns (Collagen I vs. III) and exhibited the greatest degree of staining in the cMSC + BMP-2 treatment group. These results suggest that enhanced ECM deposition of anabolic collagens may be one method by which

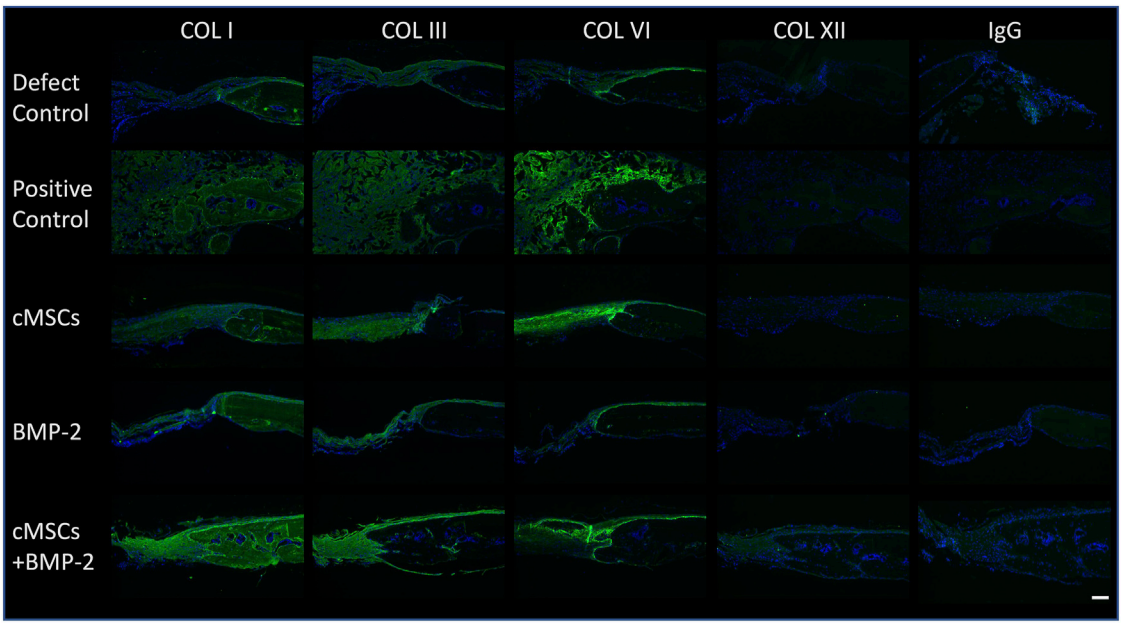

FIGURE 5 | Immunofluorescence of Collagens Type I, III, VI, and XII in murine calvarial defects. Immunofluorescence was performed to determine the presence of Collagen Type I, III, VI, and XII within calvarial defects. Bound primary antibodies were detected with a goat anti-rabbit Alexaflour 488 (green) secondary antibody. Slides were processed with 4′,6-diamidino-2-phenylindole (DAPI) to identify nuclei. Negative control sections (IgG) are provided for reference. Excitation range was 495 nm and emission 519 nm (bar = 100 μM). Representative images are provided for all treatment groups. Collagen Type I, III, and VI were detected in all treatment groups. Collagen I staining was diffusely present, whereas Collagen III was limited to the fibrous tissue bridging the defect and the leading edge of bone healing. Collagen VI was detected in all treatment groups, and co-localized with Collagen III. Collagen XII was not detectible in any of the treatment groups with the exception of the cMSC + BMP-2 treatment group, where it was weakly present and co-localized with Collagens III and VI. Collectively, Collagen I, III, VI, and XII staining was the greatest in the cMSC + BMP-2 treatment group, providing a potential mechanism for the treatment effect of this group.

cMSCs, which are transiently present within the defects, may enhance bone healing *in vivo*.

ALP Activity and BMP-2 Gene Expression

In order to further characterize these *in vivo* findings, ALP activity and endogenous BMP-2 gene expression were assessed in both cMSCs and hMSCs. Consistent with prior studies, cMSCs exhibited minimal ALP activity when cultured in control (CCM) or basal osteogenic medium (ODM). There was a significant increase in cMSC ALP activity in the presence of osteogenic medium containing BMP-2 (ODM + BMP-2) (**Figure 6**; $p < 0.0001$). (Bearden et al., 2017). In contrast, two preparations of hMSCs (hMSC-7 and hMSC-25) exhibited robust ALP activity in all media conditions, similar to previously published work (Diefenderfer et al., 2003a; Diefenderfer et al., 2003b; Clough et al., 2015) These results suggest that hMSC basal ALP activity is constitutively active, whereas cMSC ALP activity requires osteogenic induction media containing BMP-2.

To determine whether endogenous BMP-2 gene expression may play a role in this finding, Day 7 RNA samples were extracted from triplicate wells from the ALP assay in **Figure 6A** and assessed for canine or human BMP-2 expression using qPCR (**Figure 6B**). Gene expression of canine BMP-2 was minimally affected by osteogenic induction media. Expression of human BMP-2 was significantly increased when hMSCs were cultured in osteogenic induction medium (ODM) or medium containing BMP-2 (ODM + BMP-2). The relative expression of human BMP-2 was significantly greater than canine BMP-2 in the OBM + BMP-2 condition. These qPCR results indicate that the preparation of cMSCs used in the present study do not significantly increase endogenous canine BMP-2 expression in response to osteogenic induction media, even in the presence of BMP-2.

One explanation for the lack of endogenous BMP-2 expression in the cMSCs is that the cMSCs initially possessed the ability to express endogenous BMP-2, but lost this ability during isolation, culture expansion, or cryopreservation (Hass et al., 2011; Yang et al., 2018). Adult, canine, bone marrow cDNA and cDNA samples from P2 cMSCs at Day 0 or Day 7 of the ALP activity assay were assessed for BMP-2 expression using RT-PCR. A plasmid containing canine BMP-2 was used as a positive control (**Figure 7A**). RT-PCR of the positive control plasmid produced the expected canine BMP-2 band at 324 base pairs. There was no visible expression of canine BMP-2 in canine bone marrow, P2 cMSCs at Day 0 of the ALP activity assay, or P2 cMSCs after 7 days of culture in CCM, ODM, or ODM + BMP-2. These results suggest that canine BMP-2 is not expressed in bone marrow isolated from adult canines, nor is BMP-2 expressed in isolated, low passage cMSCs cultured in control or osteogenic induction media (with or without BMP-2).

Human BMP-2 gene expression was also evaluated using RT-PCR (**Figure 7B**) for the two preparations of hMSCs used for

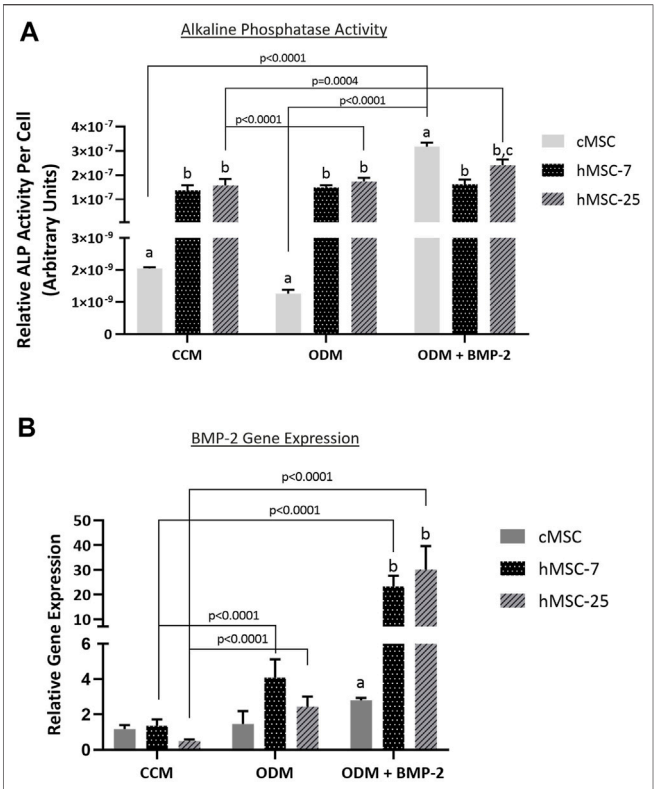

FIGURE 6 | Alkaline phosphatase (ALP) activity and endogenous BMP-gene expression in cMSCs and hMSCs. **(A)**: cMSCs and two preparations of hMSCs were examined using the classic ALP activity assay. Cells were cultured for 7 days in control (CCM), osteogenic medium (ODM), or osteogenic medium containing 100 ng/ml BMP-2 (ODM + BMP-2). ALP activity for each well was normalized to cell number by DNA quantification. Data were analyzed with two-way ANOVA and Tukey's post hoc test. cMSCs exhibited minimal ALP activity in CCM or ODM, but responded robustly when cultured in ODM + BMP-2. In contrast, ALP activity for both preparations of hMSCs was robust regardless of culture conditions. These results are consistent with prior work and demonstrate important differences between cMSC and hMSC *in vitro* osteogenic differentiation. **(B)**: qPCR results for canine and human bone morphogenic protein-2 (BMP-2) from the ALP activity assay in Panel A. Data were analyzed with two-way ANOVA and Tukey's post hoc test. In support of the ALP activity assay results, cMSCs did not initiate a significant increase in BMP-2 gene expression in response to ODM or ODM + BMP-2. In contrast, both preparations of hMSCs demonstrated significantly greater BMP-2 gene expression when cultured in ODM or ODM + BMP-2. Lastly, there was significantly reduced canine BMP-2 gene expression as compared to the human BMP-2 gene expression when cells were cultured in ODM + BMP-2.

comparative purposes in the ALP activity assay (**Figure 6**). In contrast to the cMSCs in which we were unable to detect canine BMP-2 expression, hMSCs expressed BMP-2 on Day 0 of the ALP activity assay, as well as after 7 days of culture in CCM, ODM, or ODM = BMP-2). Subjectively, there was increased expression in the hMSCs after 7 days of culture in ODM (**Figure 7B**; Lanes 3,7) and ODM + BMP-2 (**Figure 7B**; Lanes 4,8), consistent with the qPCR results reported in **Figure 6B**. RNA samples extracted from hMSCs at Day 0 (when cells were plated for ALP assay) exhibited slightly reduced BMP-2 expression. Negative controls did not produce BMP-2 bands (**Figure 7B**; Lanes 1,5, and 9). These RT-PCR results suggest that in contrast to cMSCs, hMSCs are capable of endogenous BMP-2 expression, and furthermore, that BMP-2 expression is increased when hMSCs are cultured in the presence of osteogenic induction media.

DISCUSSION

The dog represents a strong translational model for cell-based bone-healing (Hoffman and Dow 2016). However, key similarities and differences between canine and human MSC osteogenic differentiation must be defined if this model species is to be used most effectively. The primary objective of the present study was to determine if previous *in vitro* findings regarding cMSC osteogenic differentiation were relevant in the *in vivo* setting, specifically the observations by multiple investigators that cMSCs do not undergo robust osteogenic differentiation unless supplemented with additional growth factors such as IGF-1, NELL-1, or BMP-2 (Volk et al., 2005; Levi et al., 2011; Bearden et al., 2017; James et al., 2017; Gasson et al., 2021). A secondary objective was to characterize osteogenic differentiation and endogenous BMP-2 gene expression *in vitro* for both cMSCs and hMSCs. Using an established murine calvarial defect model, defects treated with cMSCs in a murine plasma carrier exhibited a modest bone healing response. As expected, defects treated with a sub-therapeutic concentration of BMP-2 (6 μg/ml) were not significantly different than negative controls. However, when cMSCs were co-administered with BMP-2, there was a marked increase in defect healing when assessed by quantitative μCT and histology. Interestingly, relevant numbers of cMSCs were not detectible in calvarial defects 10 days after implantation, suggesting that the cMSC and BMP-2 healing response was driven by paracrine cues or ECM-mediated signals. To that end, Collagen I, III, VI, and XII immunofluorescence was the greatest in defects treated with cMSC and BMP-2, providing evidence that key anabolic ECM-mediated signals were involved in the improved healing response. Consistent with prior work (Volk et al., 2005; Levi et al., 2011; Bearden et al., 2017; James et al., 2017; Gasson et al., 2021), cMSCs failed to undergo early-stage *in vitro* osteogenic differentiation when cultured under typical osteo-induction conditions and required supplementation of osteogenic medium with BMP-2 in order to exhibit ALP activity. Lastly, cMSCs did not express canine BMP-2 in response to osteogenic induction under any treatment condition, whereas hMSCs expressed human BMP-2 under control and osteogenic differentiation conditions.

When compared to the human MSC field, much less attention has been given to cMSCs. While some studies suggest that cMSCs undergo *in vitro* osteogenic differentiation in a manner similar to hMSCs, a growing body of work indicates cMSCs require additional agonists to consistently initiate osteogenic differentiation. Volk and colleagues initially reported that cMSCs isolated from bone marrow of multiple dogs exhibited little ALP activity unless the osteogenic medium was supplemented with BMP-2 and ascorbate-2-phosphate (Volk et al., 2005). This finding was subsequently confirmed in a large scale characterization study of cMSCs derived from

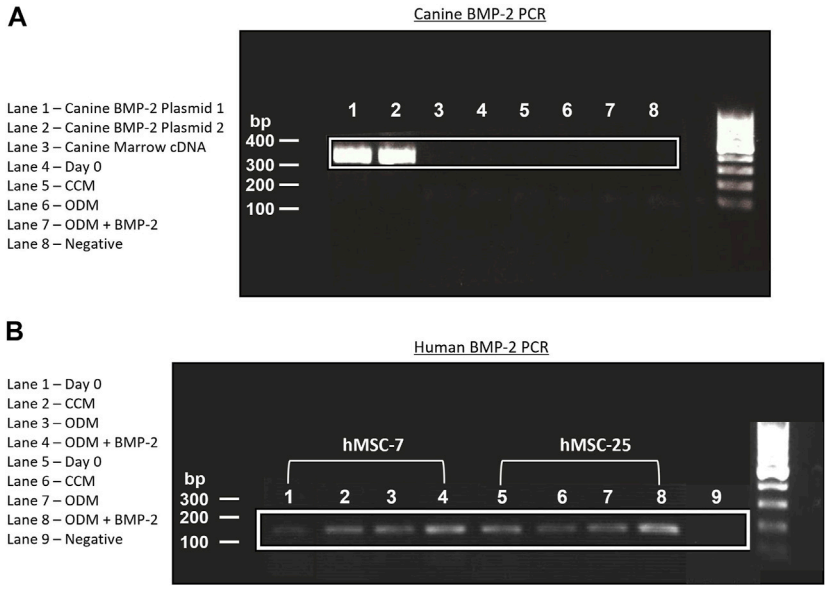

FIGURE 7 | Endogenous expression of canine and human BMP-2 by RT-PCR. **(A)**: A plasmid encoding the canine BMP-2 gene was acquired and two preparations of this plasmid cDNA were used for positive controls (Lanes 1, 2). RNA from canine bone marrow, or RNA samples obtained from cMSCs at Day 0 or Day 7 of the ALP activity assay (**Figure 6**) were used to create cDNA. All cDNA samples were assessed for canine BMP-2 gene expression using a primer pair designed to create a 324 bp transcript. There was robust expression of the canine BMP-2 gene in the control plasmids (Lanes 1 and 2). Canine bone marrow and cMSCs at Day 0 and Day 7 of the ALP activity assay did not exhibit detectible canine BMP-2 gene expression. **(B)**: RNA from the two preparations of hMSCs in **Figure 6** were used to create cDNA. Expression of human BMP-2 was evaluated in both preparations of hMSCs at Day 0 and Day 7 (CCM, ODM, and ODM + BMP-2) with a primer pair designed to create a 188 bp transcript. Human BMP-2 was present at both timepoints and in all conditions. There was an increase in BMP-2 signal in the samples isolated from Day 7 of the ALP activity assay, particularly in the cells treated with ODM + BMP-2. These findings are supportive of the results provided in **Figure 6** and demonstrate clear differences in endogenous BMP-2 gene expression of canine and human MSCs in response to osteogenic induction media.

synovial, adipose, or bone-marrow tissue (Bearden et al., 2017). While BMP-2 has most often been used to supplement cMSC osteogenic differentiation, other agonists such as NELL-1 and IGF-1 have also been used to improve *in vitro* osteogenic differentiation of cMSCs (Levi et al., 2011; James et al., 2017).

In a study evaluating the *in vitro* and *in vivo* osteogenic potential of adipose derived MSCs from murine, canine, and human donors, Levi and colleagues reported that cMSCs exhibited poor osteogenic differentiation *in vitro* unless osteogenic differentiation medium was supplemented with IGF-1 (Levi et al., 2011). Furthermore, cMSCs failed to induce healing of critically-sized murine calvarial defects whereas hMSCs induced a strong healing response. Based on the study results, it was suggested that cMSCs may need to be primed with IGF-1 or other agonists prior to *in vivo* administration, drawing into question the relevance of the canine translational model in bone healing studies.

There are important differences in the effective dose of recombinant human (rh)BMP-2 across species (Faria et al., 2007; Schmiedt et al., 2007). In rodents, it was previously shown that BMP-2 at a concentration of 100–160 μg/ml was optimal for inducing spinal fusion (Bae et al., 2013; McNeill et al., 2020). In a stepwise dilution experiment, it was determined that administration of 6 μg/ml BMP-2 was sub-therapeutic and did not lead to formation of *de novo* bone or spinal fusion. However, when 6 μg/ml of BMP-2 was co-administered with allogenic bone marrow aspirate into fusion sites, 89% of the sites achieved stable fusion. The results of Levi et al. as well as Bae et al., when considered in the context of prior work from our lab (Bearden et al., 2017; Gasson et al., 2021) collectively inspired the present study. The concentrations of BMP-2 selected in the present study for positive control (100 μg/ml) and sub-therapeutic (6 μg/ml) BMP-2 treatment groups were selected based on the results of Bae et al. Consistent with their findings, murine calvarial defects treated with 6 μg/ml BMP-2 alone did not have significantly different bone healing as compared to negative controls, supporting the use of this concentration of BMP-2 as a sub-therapeutic dose in the murine calvarial defect setting.

In order to provide some insight into the mechanism by which cMSCs contribute to bone healing in this model, mice were terminated 10 days post treatment and calvaria were examined for residual cMSCs using species-specific qPCR (**Figure 2A**). Murine and canine primers were developed to the housekeeping genes RPL13A and GAPDH (Peters et al., 2007; Ye et al., 2012). Primers were validated and dilutional experiments were performed in a background of low or high concentrations of murine RNA to detect RNA from 2×10^6 down to as few as two cMSCs (**Figures 2**, **3**). Using this technique, we were unable to detect relevant numbers of cMSCs within calvarial defects 10 days after implantation (**Figure 3C**), despite the fact that bone healing was observed in response to these two treatment groups (cMSCs alone, cMSCs with sub-therapeutic BMP-2).

It was initially believed that MSCs homed to site of injury, differentiated into cells of need, and permanently engrafted to

survive as reparative tissue (Prockop et al., 2003; Caplan 2005). A more recent proposed mechanism of action is that of the MSC as a medicinal supply cell or nurse cell. Under this concept, MSCs respond to local injury cues and produce autocrine and paracrine signals such as cytokines, growth factors, and ECM components that improve the host's endogenous healing abilities (Osugi et al., 2012; Freitas et al., 2019). Putative factors in the medicinal supply cell paradigm, include, but are not limited to, vascular endothelial growth factor (VEGF), basic fibroblast growth factor (bFGF), insulin-like growth factors (IGFs), hepatocyte growth factor (HCF), platelet-derived growth factor-ββ (PDGF-ββ), BMP-2, and stromal cell-derived factor-1 (SDF-1), and various provisional ECM components. Results of the present study suggest that cMSCs, when administered in a murine plasma carrier, likely initiate bone healing through this mechanism.

While much effort has been focused on administration of MSCs to accomplish skeletal regeneration, recent focus in the field has shifted away from cell delivery to the administration of MSC-derived exosomes or ECM components (Osugi et al., 2012; Zeitouni et al., 2012; Clough et al., 2015; McNeill et al., 2020). One compelling strategy to enhance bone healing in the clinical setting is the delivery of anabolic MSC-derived ECM scaffolds at the time of surgical stabilization. In support of this concept, it has been previously shown that MSCs can be induced to deposit anabolic ECM on gelatin surgical sponges and that these deposits contain a number of important collagens known to stimulate bone formation, namely Collagens I, III, VI, and XII (Zeitouni et al., 2012). This approach also resulted in improved healing of critically sized murine femoral defects (Clough et al., 2015) and when co-administered with hMSCs led to the greatest degree of defect healing. These studies provide evidence that anabolic ECM derived from osteogenically differentiated MSCs are capable of initiating bone healing even in the absence of cells. The authors of these studies hypothesized that Collagen VI and XII may serve as key biomarkers for treatment success. Collagen VI and XII have also been shown to co-localize to inter-cellular contacts and interference with Collagen VI or XII expression resulted in altered deposition of these collagens both within and adjacent to MSCs (Izu et al., 2016; McNeill et al., 2020).

Results of the present study provide additional evidence that Collagens I, III, VI, and XII are key ECM components for robust bone regeneration. While Collagen VI was detected in most treatment groups, the greatest degree of deposition was noted in the cMSC + BMP-2 treatment group, which was the only group in which Collagen XII was detectible. This treatment group also exhibited the greatest degree of bone healing. Collagen VI and XII have been shown to regulate development of osteoblasts during murine skeletal morphogenesis (Izu et al., 2012). Thus, the observation that Collagen VI and XII immunofluorescence were enhanced in the treatment group with the greatest degree of bone healing is consistent with what is currently known about these collagens. One potential mechanism to explain the effect of cMSCs and sub-therapeutic BMP-2 in the present study is the binding affinity of Collagen VI with BMP-2. cMSCs administered to the defects may have initiated increased Collagen VI deposition, which led to binding of BMP-2, trapping of BMP-2 in provisional ECM, and potentiating BMP-2 effects (McNeill et al., 2020).

The findings in the present study that cMSCs fail to initiate ALP activity in response to osteogenic induction media unless supplemented with BMP-2 is consistent with prior work (Volk et al., 2005; Bearden et al., 2017; Gasson et al., 2021). To the authors' knowledge, however; marrow-derived cMSCs have not been evaluated for expression of endogenous (canine) BMP-2 in response to osteogenic stimuli. While two different preparations of hMSCs expressed endogenous BMP-2 and expression was increased in response to osteogenic media, we were unable to detect endogenous expression of canine BMP-2 in cMSCs under any setting with the exception of a control plasmid. Moreover, we assessed canine bone marrow cDNA for BMP-2 gene expression and none was detected. The canonical Wnt/β-catenin pathway and the BMP/SMAD signaling pathways are both known to regulate osteoblastic differentiation (Yang et al., 2015; Zhao et al., 2020; Zhang et al., 2013). Complex, incompletely characterized cross-talk occurs between these two pathways. It is presently unclear whether the BMP-2 pathway is capable of providing upstream feedback to Wnt/β-catenin (Yang et al., 2015; Zhao et al., 2020), or whether Wnt/β-catenin is upstream of BMP-2 signaling (Zhang et al., 2013). There are likely multiple levels of cross-talk between the two pathways. The results presented in this study may suggest that in cMSCs, BMP-2 signaling functions to activate an insufficient or partially inhibited Wnt/β-catenin pathway. Another potential explanation is that cMSCs may express increased levels of Dkk-1, which is a known inhibitor of the Wnt/β-catenin pathway. Interestingly, Dkk-1 is unable to inhibit the Wnt pathway when it is transactivated by exogenous BMP-2 administration (Zhang et al., 2013).

It is presently unclear why the cMSCs examined in this study are incapable of expressing endogenous canine BMP-2. The RT-PCR results in which canine adult bone marrow cDNA were examined for canine BMP-2 expression suggest that the cMSCs did not lose the ability to express BMP-2 after isolation or cell expansion in response to an altered *in vitro* niche. As mentioned above, dogs respond to recombinant BMP-2 therapy in both induced- and spontaneous-injury settings (Faria et al., 2007; Boudrieau 2015). Due to the non-specific nature of BMP-2 receptor binding, it is possible that canine-derived cMSCs express a complete set of Type-I and -II BMP receptors but that in the canine species, other endogenous BMP's that are associated with skeletal development such as BMP-4, -6, or -7 are more physiologically relevant (Kim et al., 2018; Teunissen et al., 2018). The signaling cross-talk between canine BMP/SMAD and Wnt/β-catenin and their respective roles in cMSC osteogenic differentiation as well as endogenous BMP expression will be the focus of future studies.

As with all studies, the present study is not without limitations. While providing important *in vivo* support for previous *in vitro* findings, a single preparation of canine bone marrow-derived MSCs was used. This preparation of cMSCs was selected due to the fact that these cMSCs exhibited average *in vitro* osteogenic differentiation parameters and as such were representative of canine marrow MSCs. RNA extractions of harvested murine calvaria were used to screen for residual cMSCs 10 days post-implantation. It is possible that some cMSCs were present within deeper portions of healing osteoid and were not recovered during RNA extractions, although the extraction protocol described

above resulted in visible removal of all soft and some hard tissues from the defect sites. The immunofluorescence performed in the present study, while providing support for the concept of cMSC-driven ECM deposition of anabolic collagen molecules, did not exhaustively characterize all ECM components known to be stimulatory or inhibitory to the bone healing response. Documentation that cMSCs are unable to express endogenous BMP-2 represents an important observation, but the mechanistic explanations for this observation remain to be determined and will be the focus of future work. Lastly, while the present work represents an important *in vivo* finding, the athymic calvarial defect model is not representative of the more complex body systems of larger animals such as dogs or humans that contain well-developed immune systems and substantially different biomechanical environments.

In conclusion, this study demonstrates important differences between cMSC and hMSC *in vitro* osteogenic differentiation and endogenous BMP-2 expression. More importantly, it provides the first *in vivo* evidence that cMSCs may require supplemental agonists such as BMP-2 to accomplish *in vivo* healing. This strategy may also prove useful in order to reduce the cost and side effects associated with administration of high concentrations of BMP-2 (Carragee et al., 2011; Faundez et al., 2016).

DATA AVAILABILITY STATEMENT

The raw data supporting the conclusion of this article will be made available by the authors, without undue reservation.

ETHICS STATEMENT

The studies involving human participants were reviewed and approved by the Texas A&M/Baylor Scott and White Hospital (Temple, TX) Institutional Review Board. The patients/participants provided their written informed consent to participate in this study. The animal study was reviewed and approved by the Texas A&M University Institutional Animal Care and Use Committee.

AUTHOR CONTRIBUTIONS

WS and CG were responsible for experimental design. LD, SZ, EM, RB, CG, and WS performed the studies, analyzed the data, and contributed to the manuscript. All authors contributed to the article and approved the submitted version.

FUNDING

Funding provided by the CSTR Institute, Texas A&M University and the Bone and Joint Fund, Texas A&M Foundation.

ACKNOWLEDGMENTS

The authors would like to thank Alyssa Falck, Dr. Lindsey Dawson, and Dr. Miok Lee for their technical expertise.

REFERENCES

Bae, H. W., Zhao, L., Kanim, L. E., Wong, P., Marshall, D., and Delamarter, R. B. (2013). Bone Marrow Enhances the Performance of rhBMP-2 in Spinal Fusion. *The J. Bone Jt. Surgery-American Volume* 95, 338–347. doi:10.2106/jbjs.k.01118

Bearden, R. N., Huggins, S. S., Cummings, K. J., Gregory, C. A., Smith, R., and Saunders, W. B. (2017). *In-Vitro* Characterization of Canine Multipotent Stromal Cells Isolated from Synovium, Bone Marrow, and Adipose Tissue: A Donor-Matched Comparative Study. *Stem Cel. Res. Ther.* 8 (1), 1–22. doi:10.1186/s13287-017-0639-6

Bishop, J. A., Palanca, A. A., Bellino, M. J., and Lowenberg, D. W. (2012). Assessment of Compromised Fracture Healing. *J. Am. Acad. Orthopaedic Surgeons* 20 (5), 273–282. doi:10.5435/JAAOS-20-05-273

Boden, S. D. (2002). Overview of the Biology of Lumbar Spine Fusion and Principles for Selecting a Bone Graft Substitute. *Spine* 27 (16 Suppl. L), S26–S31. doi:10.1097/00007632-200208151-00007

Boden, S. D., Zdeblick, T. A., Sandhu, H. S., and Heim, S. E. (2000). The Use of rhBMP-2 in Interbody Fusion Cages. *Spine* 25 (3), 376–381. doi:10.1097/00007632-200002010-00020

Boudrieau, R. J. (2015). Initial Experience with RhBMP-2 Delivered in a Compressive Resistant Matrix for Mandibular Reconstruction in 5 Dogs. *Vet. Surg.* 44 (4), 443–458. doi:10.1111/j.1532-950X.2014.12171.x

Caplan, A. I. (2005). Review:Mesenchymal Stem Cells: Cell-Based Reconstructive Therapy in Orthopedics. *Tissue Engineeringtissue Eng.* 11, 1198–1211. doi:10.1089/ten.2005.11.1198

Carragee, E. J., Hurwitz, E. L., and Weiner, B. K. (2011). A Critical Review of Recombinant Human Bone Morphogenetic Protein-2 Trials in Spinal Surgery: Emerging Safety Concerns and Lessons Learned. *Spine J.* 11 (6), 471–491. doi:10.1016/j.spinee.2011.04.023

Clough, B. H., McCarley, M. R., Krause, U., Zeitouni, S., Froese, J. J., McNeill, E. P., et al. (2015). Bone Regeneration with Osteogenically Enhanced Mesenchymal Stem Cells and Their Extracellular Matrix Proteins. *J. Bone Miner Res.* 30 (1), 83–94. doi:10.1002/jbmr.2320

Cong, X., Zhang, S.-M., Ellis, M. W., and Luo, J. (2019). Large Animal Models for the Clinical Application of Human Induced Pluripotent Stem Cells. *Stem Cell Dev.* 28 (19), 1288–1298. doi:10.1089/scd.2019.0136

Cuomo, A. V., Virk, M., Petrigliano, F., Morgan, E. F., and Lieberman, J. R. (2009). Mesenchymal Stem Cell Concentration and Bone Repair: Potential Pitfalls from Bench to Bedside. *J. Bone Jt. Surgery-American Volume* 91 (5), 1073–1083. doi:10.2106/JBJS.H.00303

Dawson, L. A., Brunauer, R., Zimmel, K. N., Qureshi, O., Falck, A. R., Kim, P., et al. (2019). Adult Mouse Digit Amputation and Regeneration: A Simple Model to Investigate Mammalian Blastema Formation and Intramembranous Ossification. *J. Visualized Experiments* 2019 (149), e59749. doi:10.3791/59749

Diefenderfer, D. L., Osyczka, A. M., Garino, J. P., and Leboy, P. S. (2003a). Regulation of BMP-Induced Transcription in Cultured Human Bone Marrow Stromal Cells. *In J. Bone Jt. Surg. - Ser. A.* 85, 19–28. doi:10.2106/00004623-200300003-00005

Diefenderfer, D. L., Osyczka, A. M., Reilly, G. C., and Leboy, P. S. (2003b). BMP Responsiveness in Human Mesenchymal Stem Cells. *Connect. Tissue Res.* 44 (Suppl. 1), 305–311. doi:10.1080/03008200390181825

Dimar, J. R., Glassman, S. D., Burkus, K. J., and Carreon, L. Y. (2006). Clinical Outcomes and Fusion Success at 2 Years of Single-Level Instrumented Posterolateral Fusions with Recombinant Human Bone Morphogenetic Protein-2/Compression Resistant Matrix versus Iliac Crest Bone Graft. *Spine* 31 (22), 2534–2539. doi:10.1097/01.brs.0000240715.78657.81

Dominici, M., Le Blanc, K., Mueller, I., Slaper-Cortenbach, I., Marini, F. C., Krause, D. S., et al. (2006). Minimal Criteria for Defining Multipotent Mesenchymal Stromal Cells. The International Society for Cellular Therapy Position Statement. *Cytotherapy* 8 (4), 315–317. doi:10.1080/14653240600855905

Faria, M. L. E., Lu, Y., Heaney, K., Uthamanthil, R. K., Muir, P., and Markel, M. D. (2007). Recombinant Human Bone Morphogenetic Protein-2 in Absorbable Collagen Sponge Enhances Bone Healing of Tibial Osteotomies in Dogs. *Vet. Surg.* 36 (2), 122–131. doi:10.1111/j.1532-950X.2007.00242.x

Faundez, A., Tournier, C., Garcia, M., Aunoble, S., and Le Huec, J. C. (2016). Bone Morphogenetic Protein Use in Spine Surgery-Complications and Outcomes: A Systematic Review. *Int. Orthopaedics.* 40 (6), 1309–1319. doi:10.1007/s00264-016-3149-8

Freitas, G. P., Lopes, H. B., Alann, T., Souza, P., Paula, G., Oliveira, F. P., et al. (2019). Cell Therapy: Effect of Locally Injected Mesenchymal Stromal Cells Derived from Bone Marrow or Adipose Tissue on Bone Regeneration of Rat Calvarial Defects. *Scientific Rep.* 9 (1), 1–13. doi:10.1038/s41598-019-50067-6

Garnero, P. (2015). The Role of Collagen Organization on the Properties of Bone. *Calcified Tissue Int.* 97 (3), 229–240. doi:10.1007/s00223-015-9996-2

Gasson, S. B., Dobson, L. K., Chow, L., Dow, S., Gregory, C. A., and Saunders, W. B. (2021). Optimizing *In Vitro* Osteogenesis in Canine Autologous and Induced Pluripotent Stem Cell-Derived Mesenchymal Stromal Cells with Dexamethasone and BMP-2. *Stem Cell Dev.* 30 (4), 214–226. doi:10.1089/scd.2020.0144

Glassman, S. D., Dimar, J. R., Carreon, L. Y., Campbell, M. J., Puno, R. M., and Johnson, J. R. (2005). Initial Fusion Rates with Recombinant Human Bone Morphogenetic Protein-2/Compression Resistant Matrix and a Hydroxyapatite and Tricalcium Phosphate/Collagen Carrier in Posterolateral Spinal Fusion. *Spine* 30 (15), 1694–1698. doi:10.1097/01.brs.0000172157.39513.80

Hak, D. J., Fitzpatrick, D., Bishop, J. A., Marsh, J. L., Tilp, S., Schnettler, R., et al. (2014). Delayed Union and Nonunions: Epidemiology, Clinical Issues, and Financial Aspects. *Injury* 45 (Suppl. 2), S3–7. doi:10.1016/j.injury.2014.04.002

Hass, R., Kasper, C., Böhm, S., and Jacobs, R. (2011). Different Populations and Sources of Human Mesenchymal Stem Cells (MSC): A Comparison of Adult and Neonatal Tissue-Derived MSC. *Cell Commun. Signaling.* 9, 1–14. doi:10.1186/1478-811X-9-12

Hatsushika, D., Muneta, T., Nakamura, T., Horie, M., Koga, H., Nakagawa, Y., et al. (2014). Repetitive Allogeneic Intraarticular Injections of Synovial Mesenchymal Stem Cells Promote Meniscus Regeneration in a Porcine Massive Meniscus Defect Model. *Osteoarthritis. Cartilage* 22 (7), 941–950. doi:10.1016/j.joca.2014.04.028

Hecht, B. P., Fischgrund, J. S., Herkowitz, H. N., Penman, L., Toth, J. M., and Ali, S. (2000). The Use of Recombinant Human Bone Morphogenetic Protein 2 (RhBMP-2) to Promote Spinal Fusion in a Nonhuman Primate Anterior Interbody Fusion Model. *Spine* 25 (6 Suppl. L), 629–636. doi:10.1097/00007632-200003151-00014

Hoffman, A., and Dow, S. (2016). TRANSLATIONAL and CLINICAL Concise Review : Stem Cell Trials Using Companion Animal Disease Models. *Stem Cells Express*, 34 (7), 1709–1729. doi:10.1002/stem.2377

Hubbard, M. E., Arnold, S., Zahid, A. B., McPheeters, M., Gerard O'Sullivan, M., Tabaran, A. F., et al. (2018). Naturally Occurring Canine Glioma as a Model for Novel Therapeutics. *Cancer Invest.* 36 (8), 415–423. doi:10.1080/07357907.2018.1514622

Izu, Y., Ezura, Y., Koch, M., Birk, D. E., and Noda, M. (2016). Collagens VI and XII Form Complexes Mediating Osteoblast Interactions during Osteogenesis. *Cel Tissue Res.* 364 (3), 623–635. doi:10.1007/s00441-015-2345-y

Izu, Y., Ezura, Y., Mizoguchi, F., Kawamata, A., Nakamoto, T., Nakashima, K., et al. (2012). Type VI Collagen Deficiency Induces Osteopenia with Distortion of Osteoblastic Cell Morphology. *Tissue. Cell* 44 (1), 1–6. doi:10.1016/j.tice.2011.08.002

James, A. W., Zhang, X., Crisan, M., Hardy, W. R., Liang, P., Meyers, C. A., et al. (2017). Isolation and Characterization of Canine Perivascular Stem/Stromal Cells for Bone Tissue Engineering. *PLoS ONE* 12 (5), e0177308. doi:10.1371/journal.pone.0177308

Kandziora, F., Pflugmacher, R., Scholz, M., Knispel, C., Hiller, T., Schollmeier, G., et al. (2002). Comparison of BMP-2 and Combined IGF-I/TGF-B1 Application in a Sheep Cervical Spine Fusion Model. *Eur. Spine J.* 11 (5), 482–493. doi:10.1007/s00586-001-0384-4

Kao, S. T., and Scott, D. D. (2007). A Review of Bone Substitutes. *Oral Maxillofac. Surg. Clin. North America* 19 (4), 513–521. doi:10.1016/j.coms.2007.06.002

Kim, Y., Kang, B. J., Kim, W., Yun, H. S., and Kweon, O. K. (2018). Evaluation of Mesenchymal Stem Cell Sheets Overexpressing BMP-7 in Canine Critical-Sized Bone Defects. *Int. J. Mol. Sci.* 19 (7). doi:10.3390/ijms19072073

Kinsella, C. R., Bykowski, M. B., Lin, A. J., Cray, J. J., Durham, E. L., Smith, D. M., et al. (2011). BMP-2-Mediated Regeneration of Large-Scale Cranial Defects in the Canine: An Examination of Different Carriers. *Plast. Reconstr. Surg.* 127 (5), 1865–1873. doi:10.1097/PRS.0b013e31820cf2c9

Krause, U., Seckinger, A., and Gregory, C. A. (2011). Assays of Osteogenic Differentiation by Cultured Human Mesenchymal Stem Cells. *Methods Mol. Biol. (Clifton, N.J.)* 698, 215–230. doi:10.1007/978-1-60761-999-4_17

Kumar, S. A., Hu, X., Brown, M., Kuschak, B., Hernandez, T. A., Johnston, J. B., et al. (2009). Lysophosphatidic Acid Receptor Expression in Chronic Lymphocytic Leukemia Leads to Cell Survival Mediated Though Vascular Endothelial Growth Factor Expression. *Leuk. Lymphoma* 50 (12), 2038–2048. doi:10.3109/10428190903275586

Levi, B., Nelson, E. R., Brown, K., James, A. W., Xu, D., Dunlevie, R., et al. (2011). Differences in Osteogenic Differentiation of Adipose-Derived Stromal Cells from Murine, Canine, and Human Sources *In Vitro* and *In Vivo*. *Plast. Reconstr. Surg.* 128 (2), 373–386. doi:10.1097/PRS.0b013e31821e6e49

Liu, Q., Yu, Y., Reisdorf, R. L., Qi, J., Chun, K., Berglund, L. J., et al. (2019). Engineered Tendon-Fibrocartilage-Bone Composite and Bone Marrow-Derived Mesenchymal Stem Cell Sheet Augmentation Promotes Rotator Cuff Healing in a Non-weight-bearing Canine Model. *Biomaterials* 192 (September 2018), 189–198. doi:10.1016/j.biomaterials.2018.10.037

Livak, K. J., and Schmittgen, T. D. (2001). Analysis of Relative Gene Expression Data Using Real-Time Quantitative PCR and the 2-ΔΔCT Method. *Methods* 25 (4), 402–408. doi:10.1006/meth.2001.1262

Marsh, D. (1998). Concepts of Fracture Union, Delayed Union, and Nonunion. *Clin. Orthopaedics Relat. Res.* 355 (Suppl. L), 22–30. doi:10.1097/00003086-199810001-00004

McNeill, E. P., Zeitouni, S., Pan, S., Haskell, A., Cesarek, M., Tahan, D., et al. (2020). Characterization of a Pluripotent Stem Cell-Derived Matrix with Powerful Osteoregenerative Capabilities. *Nat. Commun.* 11 (1), 1–15. doi:10.1038/s41467-020-16646-2

Miedel, E. L., Brisson, B. K., Hamilton, T., Gleason, H., Swain, G. P., Lopas, L., et al. (2015). Type III Collagen Modulates Fracture Callus Bone Formation and Early Remodeling. *J. Orthopaedic Res.* 33 (5), 675–684. doi:10.1002/jor.22838

Osugi, M., Katagiri, W., Yoshimi, R., Inukai, T., Hibi, H., and Ueda, M. (2012). Conditioned Media from Mesenchymal Stem Cells Enhanced Bone Regeneration in Rat Calvarial Bone Defects. *Tissue Eng. - A.* 18 (13–14), 1479–1489. doi:10.1089/ten.tea.2011.0325

Peters, I. R., Peeters, D., Helps, C. R., and Day, M. J. (2007). Development and Application of Multiple Internal Reference (Housekeeper) Gene Assays for Accurate Normalisation of Canine Gene Expression Studies. *Vet. Immunol. Immunopathology* 117 (1–2), 55–66. doi:10.1016/j.vetimm.2007.01.011

Prockop, D. J., Gregory, C. A., and Spees, J. L. (2003). One Strategy for Cell and Gene Therapy: Harnessing the Power of Adult Stem Cells to Repair Tissues. *Proc. Natl. Acad. Sci. United States America* 100 (Suppl. 1), 11917–11923. doi:10.1073/pnas.1834138100

Samsonraj, R. M., Dudakovic, A., Zan, P., Pichurin, O., Cool, S. M., Andre, J., et al. (2017). A Versatile Protocol for Studying Calvarial Bone Defect Healing in a Mouse Model. *Tissue Eng. - C: Methods* 23 (11), 686–693. doi:10.1089/ten.tec.2017.0205

Schmiedt, C. W., Lu, Y., Heaney, K., Muir, P., Amodie, D. M., and Markel, M. D. (2007). Comparison of Two Doses of Recombinant Human Bone Morphogenetic Protein in Absorbable Collagen Sponges for Bone Healing in Dogs. *Am. J. Vet. Res.* 68 (8), 834–840. doi:10.2460/ajvr.68.8.834

Schmoekel, H., Schense, J. C., Weber, F. E., Grätz, K. W., Gnägi, D., Müller, R., et al. (2004). Bone Healing in the Rat and Dog with Nonglycosylated BMP-2 Demonstrating Low Solubility in Fibrin Matrices. *J. Orthopaedic Res.* 22 (2), 376–381. doi:10.1016/S0736-0266(03)00188-8

Teunissen, M., Riemers, F. M., van Leenen, D., Marian, J., Groot Koerkamp, A., Meij, B. P., et al. (2018). Growth Plate Expression Profiling: Large and Small Breed Dogs Provide New Insights in Endochondral Bone Formation. *J. Orthopaedic Res.* 36 (1), 138–148. doi:10.1002/jor.23647

Volk, S. W., Diefenderfer, D. L., Christopher, S. A., Haskins, M. E., and Leboy, P. S. (2005). Effects of Osteogenic Inducers on Cultures of Canine Mesenchymal Stem Cells. *Am. J. Vet. Res.* 66 (10), 1729–1737. doi:10.2460/ajvr.2005.66.1729

Volk, S. W., Wang, Y., Mauldin, E. A., Liechty, K. W., and Adams, S. L. (2011). Diminished Type III Collagen Promotes Myofibroblast Differentiation and

Increases Scar Deposition in Cutaneous Wound Healing. *Cells Tissues Organs* 194 (1), 25–37. doi:10.1159/000322399

Yang, J., Ye, L., Hui, T. Q., Yang, D. M., Huang, D. M., Zhou, X. D., et al. (2015). Bone Morphogenetic Protein 2-Induced Human Dental Pulp Cell Differentiation Involves P38 Mitogen-Activated Protein Kinase-Activated Canonical WNT Pathway. *Int. J. Oral Sci.* 7 (2), 95–102. doi:10.1038/ijos.2015.7

Yang, Y. H. K., Ogando, C. R., See, C. W., Chang, T. Y., and Barabino, G. A. (2018). Changes in Phenotype and Differentiation Potential of Human Mesenchymal Stem Cells Aging *In Vitro*. *Stem Cel Res. Ther.* 9 (1), 1–14. doi:10.1186/s13287-018-0876-3

Ye, J., Coulouris, G., Zaretskaya, I., Cutcutache, I., Rozen, S., and Madden, T. L. (2012). Primer-BLAST: A Tool to Design Target-specific Primers for Polymerase Chain Reaction. *BMC Bioinformatics* 13, 134. doi:10.1186/1471-2105-13-134

Zeitouni, S., Krause, U., Clough, B. H., Halderman, H., Falster, A., Blalock, D. T., et al. (2012). Human Mesenchymal Stem Cell-Derived Matrices for Enhanced Osteoregeneration (Science Translational Medicine (2012) 4. *Sci. Translational Med.* 4 (149), 1–11. doi:10.1126/scitranslmed.3004739

Zhang, R., Oyajobi, B. O., Harris, S. E., Chen, Di., Tsao, C., Deng, H. W., et al. (2013). Wnt/β-Catenin Signaling Activates Bone Morphogenetic Protein 2 Expression in Osteoblasts. *Bone* 52 (1), 145–156. doi:10.1016/j.bone.2012.09.029

Zhao, H. J., Chang, H. M., Klausen, C., Zhu, H., Li, Y., Peter, C., et al. (2020). Bone Morphogenetic Protein 2 Induces the Activation of WNT/β-Catenin Signaling and Human Trophoblast Invasion through Up-Regulating BAMBI. *Cell Signal.* 67 (44), 109489. doi:10.1016/j.cellsig.2019.109489

Conflict of Interest: The authors declare that the research was conducted in the absence of any commercial or financial relationships that could be construed as a potential conflict of interest.

Publisher's Note: All claims expressed in this article are solely those of the authors and do not necessarily represent those of their affiliated organizations, or those of the publisher, the editors and the reviewers. Any product that may be evaluated in this article, or claim that may be made by its manufacturer, is not guaranteed or endorsed by the publisher.

frontiers in Bioengineering and Biotechnology

REVIEW
published: 30 November 2021
doi: 10.3389/fbioe.2021.730938

Mobilizing Endogenous Repair Through Understanding Immune Reaction With Biomaterials

*Maria Karkanitsa, Parinaz Fathi, Tran Ngo and Kaitlyn Sadtler**

Section on Immuno-Engineering, National Institute of Biomedical Imaging and Bioengineering, National Institutes of Health, Bethesda, MD, United States

With few exceptions, humans are incapable of fully recovering from severe physical trauma. Due to these limitations, the field of regenerative medicine seeks to find clinically viable ways to repair permanently damaged tissue. There are two main approaches to regenerative medicine: promoting endogenous repair of the wound, or transplanting a material to replace the injured tissue. In recent years, these two methods have fused with the development of biomaterials that act as a scaffold and mobilize the body's natural healing capabilities. This process involves not only promoting stem cell behavior, but by also inducing activity of the immune system. Through understanding the immune interactions with biomaterials, we can understand how the immune system participates in regeneration and wound healing. In this review, we will focus on biomaterials that promote endogenous tissue repair, with discussion on their interactions with the immune system.

Keywords: biomaterials, immunoengineering, regenerative medicine, wound healing, hydrogels, foreign body response, skin regeneration, muscle regeneration

OPEN ACCESS

Edited by:
Ryang Hwa Lee,
Texas A&M University, United States

Reviewed by:
Tatiana Segura,
Duke University, United States
Yasuhiko Tabata,
Kyoto University, Japan

****Correspondence:***
Kaitlyn Sadtler
kaitlyn.sadtler@nih.gov

Specialty section:
This article was submitted to Tissue Engineering and Regenerative Medicine, a section of the journal Frontiers in Bioengineering and Biotechnology

Received: *25 June 2021*
Accepted: *10 September 2021*
Published: *30 November 2021*

Citation:
Karkanitsa M, Fathi P, Ngo T and Sadtler K (2021) Mobilizing Endogenous Repair Through Understanding Immune Reaction With Biomaterials. Front. Bioeng. Biotechnol. 9:730938. doi: 10.3389/fbioe.2021.730938

INTRODUCTION

Biomaterial properties such as mechanics, chemical composition, biodegradability, and others play a role in governing biomaterial-tissue interactions. Despite early attempts, it was quickly understood that an immune response to the biomaterial could not be avoided (Williams, 2008). The classical negative immune response to a biomaterial is termed the Foreign Body Response (FBR), which involves protecting the body from the invading material *via* a fibrous capsule around the material (Zhang et al., 2021). Recent efforts have focused on developing biomaterials that actively promote a regenerative environment and healing instead of a foreign body response. Fine-tuning these biomaterials to induce scar-free wound healing is a major undertaking, with potential applications in multiple diseases and conditions. This review focuses on the understanding of the immune response to biomaterials to suite the clinical need of promoting endogenous regeneration, with emphasis on muscle and skin tissues. A limitation of this review is that detailed discussion of biomaterials is provided only for applications in muscle and skin injuries. Despite this, many of the same considerations can be employed for biomaterial-based treatments of other tissues.

WOUND HEALING AND BIOMATERIALS

The process of wound healing consists of three main stages: an inflammatory phase, regenerative phase, and a remodeling/repair phase (Gonzalez et al., 2016). The result of wound healing can be

largely categorized in two different outcomes: full restoration of function or a chronic failure to remodel. A failure to remodel results in chronic fibrosis and scar tissue formation, which can also lead to chronic inflammation at the site of injury (Oishi and Manabe, 2018).

The process of wound healing is heavily dependent on immune signaling cues, which help in clearing of dead tissue, mobilization of local stem cells, and remodeling of extracellular matrix (Oishi and Manabe, 2018). Immune signaling can be modulated by biomaterials, that can also act to stabilize the injury site and aid in promoting repair.

Inflammatory Phase

The inflammatory phase is characterized by angiogenesis, deposition of collagen, production of a scaffold composed of extracellular matrix (ECM) proteins, cell growth, and myofibroblast contraction to minimize the size of the wound (Atala et al., 2010). Immediately after the trauma, blood fills the site of injury to achieve hemostasis (Tonkin et al., 2015). Circulating, inactive enzymes are activated to trigger the complement cascade and clotting (Medzhitov, 2008). Local immune cells such as mast cells and tissue-resident macrophages secrete chemokines, cytokines, vasoactive amines, eicosanoids, and products of the clotting and complement cascade to recruit immune cells and activate circulating plasma proteins (Medzhitov, 2008).

Activated platelets release platelet-derived growth factor (PDGF), CXCL8, TNF-α, and other immune mediators (Ellis et al., 2018). This enables immune cell recruitment and further inflammation. Additionally, activated platelets adhere to ECM proteins at the injury site and aid in formation of a clot to prevent excess blood loss and pathogen entry (Nurden et al., 2008). The clot is also formed of ECM proteins such as fibronectin, vitronectin, and more, which act as attachment points for migrating cells entering the injury site (Barrientos et al., 2008).

In addition to platelet activation, inflammation is triggered by injured host cells *via* release of immune mediators and breakdown of ECM (Medzhitov, 2008). The best-established pro-inflammatory ECM component is glycosaminoglycan hyaluronate, which activates Toll-Like Receptors (TLRs), which activate inflammatory cascades. Release of Danger Associated Molecular Patterns (DAMPs) such as alarmins induce recruitment of immune cells, particularly macrophages, to the site of the wound (Bianchi, 2007). Any pathogens that invade the wound additionally release pathogen-associated molecular patterns (PAMPs) which are recognized by tissue resident cells and trigger further inflammatory signaling *via* TLRs (Ellis et al., 2018).

Mast cells are often found at the injury site, which activate to release cytoplasmic granules filled with inflammatory mediators such as histamine (Raziyeva et al., 2021). It is believed that mast cells help promote neutrophil infiltration at the injury site, and persistence of mast cells at the injury site is correlated with elevated levels of scarring at the injury site (Wulff and Wilgus, 2013). As a result, is believed that mast cells function at the wound site to augment the inflammatory phase of wound healing, and apoptose or leave the injury site when the process of wound healing progresses (Wulff and Wilgus, 2013).

Neutrophils are one of the first immune cell types to extravasate and respond to the inflammatory signaling at the site of the injury (Ellis et al., 2018). In particular, CXCL8 acts as a chemoattractant and recruits neutrophils to the site of injury. Neutrophils also are capable of producing CXCL8 to create a positive feedback loop (Ellis et al., 2018). Once at the site of injury, neutrophils aid against invading pathogens *via* release of cytoplasmic granules and reactive oxygen species. They also aid to promote angiogenesis *via* release of pro-angiogenic factors such as VEGF, aid in recruitment of other immune cells such as monocytes *via* release of MCP-1, TNF-a, and more, and tissue remodeling *via* release of uPA (Ellis et al., 2018).

Other innate immune cells, such as basophils, also contribute to the inflammatory phase of wound healing (Raziyeva et al., 2021). Basophils, recruited by chemokines such as GM-CSF, secrete large volumes of IL-4, a cytokine that promotes fibroblast and macrophage activation (Ellis et al., 2018; Raziyeva et al., 2021).

Monocytes/macrophages are a key cell type in the inflammatory phase of wound repair (Minutti et al., 2017). While tissue-resident macrophages are activated by local inflammatory cues post-injury, monocytes extravasate and enter the injury site *via* inflammatory cues and then polarize into different phenotypes (Hesketh et al., 2017). While the phenotypical classifications of macrophages is a debated topic, it is largely accepted that macrophages lie on a spectrum of polarization between M1 "proinflammatory" macrophages and M2 "anti-inflammatory" macrophages.

Macrophage polarization is largely determined by extracellular cues in the microenvironment. As monocytes enter the site of injury, the inflammatory cues they receive induce polarization into the M1 phenotype (Krzyszczyk et al., 2018). As inflammatory macrophages, they phagocytose dead tissue and secrete cytokines that promote inflammation and recruit more immune cells such as natural killer cells, macrophages, and T helper cells (Krzyszczyk et al., 2018). They additionally phagocytose apoptosed neutrophils to help clear the wound (Ellis et al., 2018).

If the innate part of the immune system is not sufficient in clearing the wound, the inflammatory phase persists with larger infiltrate of monocytes that differentiate into macrophages and dendritic cells (Medzhitov, 2008; Muire et al., 2020). Differentiation of monocytes into dendritic cells enables antigen presentation to adaptive immune cells and, particularly, activation of $CD4^+$ T helper cells (Muire et al., 2020). In particular, $CD4^+$ $CD25^+$ T helper cells are found at the site of healing in various tissues (Campbell and Rudensky, 2020). However, there are also Th1, Th2, and Th17 helper cells found at the sites of tissue injury (Gause et al., 2013; Brockmann et al., 2017; Raziyeva et al., 2021). This will be elaborated on in the regenerative phase of wound healing.

Regenerative Phase

The regenerative phase is characterized by closure of the wound, angiogenesis, and replacement of the inflammatory scaffold produced by coagulation by ECM proteins and fibroblasts

(Gonzalez et al., 2016). Revascularization of the wounded site is a crucial part of regeneration, as the local tissue requires a source of nutrients. As blood vessels regenerate, a population of pericytes mediate their production and stability (Takakura, 2006). Interestingly, pericytes (also known as perivascular stem cells, or PVSCs) can also differentiate into cartilage, bone, or muscle precursors (Gonzalez et al., 2016). As a result, they play a crucial role in tissue repair. Cytokines and growth factors within the injury site recruit and activate fibroblasts, which secrete large volumes of ECM and contract further to completely seal the wound. The ECM components produced by fibroblasts, namely collagens, replace the hematoma formed in the inflammatory phase (Gonzalez et al., 2016). Precursor tissue cells began to rapidly proliferate and invade the margins of the wound site, to prepare for creation of fully functionalized tissue that will replace the ECM scaffold (Muire et al., 2020).

Macrophages play a crucial role in promoting endogenous repair of the site by directing stem cell activation and self-renewal (Chazaud et al., 2003; Minutti et al., 2017). In time, macrophages change from a proinflammatory phenotype to a regenerative, immunosuppressive phenotype (Oishi and Manabe, 2018). Not only does this aid in the transition from the inflammatory to the regenerative phase of tissue repair, but also provides cues for self-renewal and differentiation of the local stem cells (Arnold et al., 2007). By phagocytosing dead cell debris and promoting local stem cell function, macrophages play a crucial role in the transition from the regenerative to the repair phase of the healing process.

An important component of the regenerative phase is the tissue's adult stem cell population, which works to replace the damaged site with fully functional tissue that is histologically identical to the site prior to injury (Mann et al., 2011). Stem cells are characterized by their ability to self renew and differentiate into different cell populations (Dekoninck and Blanpain, 2019). Every tissue has a different regenerative capacity-skin, for instance, is capable of faster regeneration than neuronal tissue (Iismaa et al., 2018). While regenerative capacity is tissue-dependent, stem cell mobilization and function is highly dependent on immune cell dynamics. For the purpose of this review, we will be focusing on how the immune system regulates stem cells and their function in wound healing.

As mentioned previously, adaptive immune cells begin to infiltrate the site of injury and also act in various ways to promote wound healing processes. $CD4^+$ T cells, upon entry to the wound, polarize into different phenotypes depending on the cytokine signaling at the time of antigen presentation *via* antigen presenting cells such as macrophages and dendritic cells (Martinez-Sanchez et al., 2018). While there are multiple different subsets of $CD4^+$ T cells, the role of Th2, Th17, and Tregs are well established as playing a role in wound healing.

Th2 helper T cells are characterized by their expression of transcription factor GATA3 and production of IL-4, IL-5, and IL-13 (Raphael et al., 2015). Research on Th2 helper cells in wound healing is particularly well established in the context of parasite-induced tissue damage, such as those that come as a result of helminth infections (Allen and Wynn, 2011; Gause et al., 2013). While M1 macrophages and other pro-inflammatory cascades are effective at clearing the injury site of any invading pathogens, they are not effective at inducing wound healing and resolution of inflammation (Allen and Wynn, 2011). As a result, it is theorized that Th2 helper cells evolved to provide this type of brake on inflammation, by secreting IL-4 and IL-13 to promote repair and polarize different cell types to a more immunosuppressive phenotype. This includes promoting fibroblast activation/secretion of ECM and M2 macrophage polarization (Allen and Wynn, 2011).

Th17 cells are characterized by their expression of transcription factor RORγt and production of IL-17 and IL-22 (Raphael et al., 2015). Their role in wound healing appears to be very dependent on the tissue and location of injury, largely due to the pleiotropic effects of IL-17. For instance, IL-17 has been shown to work synergistically with FGF2 to promote epithelial lining repair in a mouse model of colitis (Song et al., 2015). Nonetheless, the inflammatory properties of IL-17 have also been demonstrated to hinder wound healing, as IL-17 knockout mice experience better skin wound healing than wild-type mice (Rodero et al., 2013).

While the role of IL-17 in wound healing is a grey area, IL-22 production by TH17 cells is known to promote wound repair in many tissues by regulating fibroblast activation and production of ECM (Brockmann et al., 2017). IL-22 has been shown in mice to promote wound repair in the skin, intestine, liver, and kidney (Arshad et al., 2020).

Regulatory T cells are believed to act to oppose TH17 cells to suppress the residual inflammation (Raphael et al., 2015; Muire et al., 2020). Regulatory T cells can be found in circulation and also as tissue resident cells, both of which are known to play an important role in wound healing (Zaiss et al., 2019). Local release of epidermal growth factor-like growth factor Amphiregulin by tissue-resident Tregs actively aids in resolving inflammation *via* local release of Transforming Growth Factor Beta (TGF-B) (Zaiss et al., 2019). Hui et al. (2017) also demonstrated that, in zebrafish, Tregs infiltrated injured organs and secreted organ-specific regeneration factors such as Insulin-like growth factor in the retina. Furthermore, knockout of regulatory T cells severely impaired the regenerative capacity of the heart, spinal cord, and retina of zebrafish, independent of the immunomodulatory capacities. Secretion of immunosuppressive cytokines by regulatory T cells has known to also promote tissue healing after heart attacks and protect against kidney ischemia-reperfusion injury in mouse models (Kinsey et al., 2009; Weirather et al., 2014). Additionally, regulatory T cells actively promote local cell differentiation and restoration of homeostasis in certain contexts. In a mouse model of demyelination, regulatory T cells were shown to actively promote myelin regeneration and oligodendrocyte differentiation (Dombrowski et al., 2017). The combination of ECM deposition, transition to an anti-inflammatory and pro-regenerative immune state, and promotion of local stem cell activity are crucial components of the regenerative phase.

Repair Phase

The repair phase of wound healing involves formation of functional tissue that is physiologically identical to the site

prior to injury. Stem cells continue to differentiate and utilize the deposited ECM to direct the proper tissue formation. Extracellular matrix proteins such as fibronectin provide attachments for cells to bind to and promotes migration into the deposited ECM (Yamada, 2000). In time, the blood vessels, fibroblasts, and inflammatory cells in the area either exit the tissue or undergo cell death *via* apoptosis/or by other unestablished mechanisms (Gonzalez et al., 2016).

Regeneration or repair are two outcomes of a wound (Oishi and Manabe, 2018). Regeneration results in full resolution of the injury, with the resulting tissue being conformationally identical to the pre-trauma tissue. When a tissue is unable to fully regenerate, the body responds to a chronic fibrotic stage in which a scar forms and the regenerative phase does not cease (Atala et al., 2010). The repair outcome of a wound leads to development of a scar that can severely affect tissue function and leave patients with permanent and costly conditions. The cost to treat a diabetic foot ulcer episode (DFU) in the clinic was found to average $24,226 (Hicks et al., 2019). In 2014, an estimated 14.5% of medicare beneficiaries had at least one wound/wound-related infection, with Medicare spending on treatment of these wounds costing a minimum of $28.1 billion dollars (Nussbaum et al., 2018). With the aging population of the United States, this number is believed to increase over time unless better therapeutics are developed (Nussbaum et al., 2018).

Use of Biomaterials in Wound Healing

Scientists have focused on developing ways to promote regeneration over repair, including creation of biomaterial scaffolds to support and guide this process. The ideal scaffold should meet the mechanical and physical needs of the native tissue, degrade as the new tissue is formed, integrate with the host tissue, and be reliably produced on a large scale (Sheikh et al., 2015). However, recent studies have also emphasized the need for the biomaterial to stimulate the regenerative capabilities of the immune system (Andorko and Jewell, 2017).

The immune system provides signaling cues for local stem cells and plays a crucial role in clearing the injury site (Strbo et al., 2014). This signaling is reviewed extensively elsewhere, but includes pro-regenerative signals such as Insulin-like Growth Factor-1 or pro-repair signals like TGF-B (Liu et al., 2016; Alcazar et al., 2020). The immune system is also incredibly sensitive to exogenous cues and can be utilized therapeutically to produce certain outcomes. By utilizing the immune system *via* biomaterials, the process of wound healing can be optimized, and the burden of long-term physical trauma can be ameliorated.

FOREIGN BODY RESPONSE

While biomaterials have great clinical promise, they can also have some off-target effects. Regardless of the classification of the biomaterial, virtually all biomaterials are capable of eliciting a foreign body response (Aramwit, 2016). There are four main steps of the Foreign Body Response: protein adsorption, acute inflammation, chronic inflammation, and collagen deposition around the implanted material (Zhang et al., 2021). These steps are outlined in **Figure 1**.

Protein Adsorption

Upon implantation, proteins in the interstitial fluid and blood immediately bind to the material, triggering downstream immune pathways. These proteins include but are not limited to complement proteins, clotting proteins, or immunoglobulins (Williams, 2008). There is no one protein that is deemed solely responsible for a foreign body response. However, there are some that are found more commonly on the surface of a biomaterial. Albumin, fibrinogen, fibronectin, C3 protein, and gammaglobulins are all implicated in the foreign body response (Anderson et al., 2008). These proteins can undergo conformational changes and trigger proinflammatory signaling cascades such as the clotting and complement cascades (Mödinger et al., 2018). These cascades induce local inflammation and recruit mast cells, neutrophils, and macrophages to the biomaterial surface.

Acute Inflammation

Neutrophils are one of the first cells recruited to the biomaterial site, as they are often the first cell to respond to inflammatory signals (Anderson et al., 2008). Mast cells are also a commonly found cell at the biomaterial surface. Both these cells degranulate to release more pro-inflammatory signals. IL-4 and IL-13 production by mast cells are known to play important roles in determining the extent of foreign body response mounted against the biomaterial (Anderson et al., 2008). Of all cell types, macrophages are one of the most crucial components of the Foreign Body Response (Williams, 2008; Sheikh et al., 2015; Mariani et al., 2019). Macrophages can bind to fibrinogen, fibronectin, and vitronectin *via* integrin receptors and thus latch on to the surface of the biomaterial (Anderson et al., 2008). IL-4 and IL-13 produced by mast cells drive macrophage activation (Sheikh et al., 2015).

Chronic Inflammation

Upon binding to the biomaterial surfaces, macrophages immediately attempt to phagocytose the biomaterial (Medzhitov, 2008). When the size or shape of the biomaterial makes it impossible to do so, macrophages become frustrated and form Foreign Body Giant cells (FBGCs) to attempt to further phagocytose the site. IL-4 and IL-13, two cytokines often present at the biomaterial interface, are known drivers of Foreign Body Giant Cell formation (McNally and Anderson, 1995; DeFife et al., 1997).

FBGCs are terminally differentiated and not as plastic as macrophages, and contain high numbers of lysosomes (Sheikh et al., 2015). They are known to attach to the biomaterial surface and release a host of inflammatory cytokines and Reactive Oxygen Species (ROS) (Hernandez-Pando et al., 2000; Anderson et al., 2008). The cytokines expressed and the formation of FBGCs are largely determined by the biomaterial's properties such as hydrophobicity or rigidity (Carnicer-Lombarte et al., 2021).

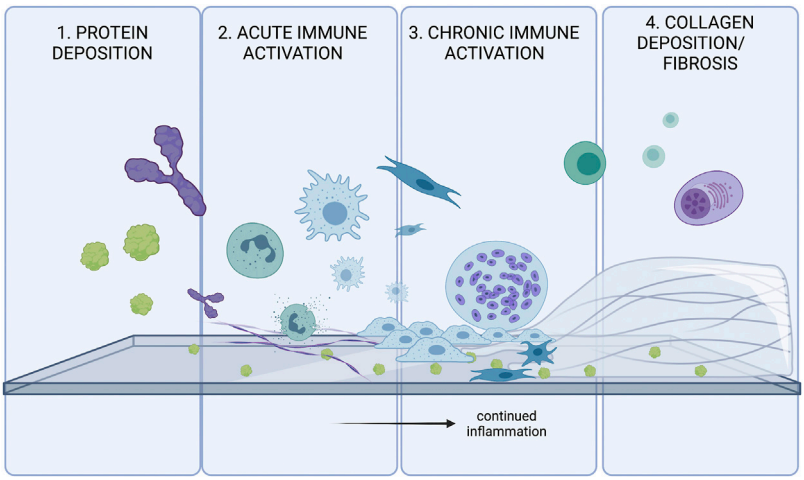

FIGURE 1 | The four stages of the Foreign Body Response (FBR). FBR is initially triggered by protein adsorption. and activation of various inflammatory cascades. Innate immune systems attempt to degrade/phagocytose the foreign body, and will continue to try eliminating the threat until collagen accumulates on the surface of the foreign body. The fibrosis acts as a barrier to protect the body from the threat of the foreign body.

In addition to innate immune cells, there has been evidence that biomaterial-specific, adaptive immune cells are primed by Antigen Presenting Cells in secondary lymphoid organs (Van Luyn et al., 1998; Chung et al., 2020; Adusei et al., 2021). Various classes of T cells contribute to the Foreign Body Response, including TH1 and TH2 type T helper cells. Both cell types act largely by stimulating macrophages by releasing cytokines, Interferon Gamma (IFNy) by TH1 cells and IL-4 and IL-13 by TH2 cells (Adusei et al., 2021). Th17 cells and production of IL-17 by nonconventional gamma-delta T cells has also been implicated in driving of the foreign body response (Wolfram et al., 2012; Chung et al., 2020).

Fibrous Capsule Formation

Upon unsuccessful phagocytosis of the biomaterial, the body forms a fibrous capsule around the biomaterial to block it off from the body (Anderson et al., 2008). Both M1 and M2 macrophages are believed to play a role in activating fibroblasts and promoting ECM secretion around the site (Witherel et al., 2019). Particularly, cytokines including VEGF, IL-6, TNF-alpha, and TGF-B1 are believed to be released by macrophages and promote fibrosis around the implanted biomaterial.

The fibrotic capsule around the implanted biomaterial is designed to protect the body from any harm the biomaterial may cause. Fibroblasts are recruited to the site by local inflammatory mediators, and their activation into myofibroblasts is characterized by production of alpha smooth muscle actin (a-SMA) (Witherel et al., 2019). The activated cells then produce large amounts of ECM on the surface of the material to block it off from the body. Monocyte coculture with various medical polymers and fibroblasts demonstrated that human IL-1 was responsible for monocyte-mediated fibroblast stimulatory potential (Miller and Anderson, 1989). Furthermore, the fibrous capsule around the biomaterial also consists of FBGCs, which continue to try and eliminate the biomaterial even after it is blocked off from the body (Anderson et al., 2008).

Mitigating the Foreign Body Response

It is estimated that the conservative failure rate of implants due to foreign body response is around 10%, and the cost of solving this need is around $10 billion per year (Zhang et al., 2021). There are countless approaches to mitigating the foreign body response, including use of endogenously found substances for biomaterials, changing the physical properties of the biomaterial, and codelivery of anti-inflammatory drugs.

Tissue-derived ECM scaffolds have long been used due to its natural role in promoting endogenous repair and proving to be well suited for the clinic (Hortensius and Harley, 2016). Despite the inherent biocompatibility of ECM proteins, however, studies indicate that collagen implants can elicit a foreign body response (Aamodt and Grainger, 2016). This shows that ECM matrix and derivatives could adversely affect the healing processes in some unknown ways. However, the collagen often degrades before any adverse effects due to the foreign body response are really seen.

Plant-derived alginates (a polysaccharide block co-polymer of β-D-mannuronate and α-L-guluronate) also elicit a severe foreign body response (Doloff et al., 2017). Since it is not degradable like collagen, a fibrous layer will coat the biomaterial and prevent proper function. Veiseh et al. (2015) demonstrated that the foreign body response to spheres made of SLG20, an alginate where over 60% of the monomer units are guluronate, is inversely correlated with the diameter of the spheres. Interestingly, this seems to be the case for a variety of materials, including steel, glass, polycaprolactone, and polystyrene (Veiseh et al., 2015).

In addition to changing the shape and size of the biomaterial, alginates are extremely easy to chemically modify. Papers such as that of Vegas et al. (2016) demonstrate that alginates can be chemically modified to evade the immune response. Doloff et al. (2017) highlighted the importance of CSF-1 in recruitment of

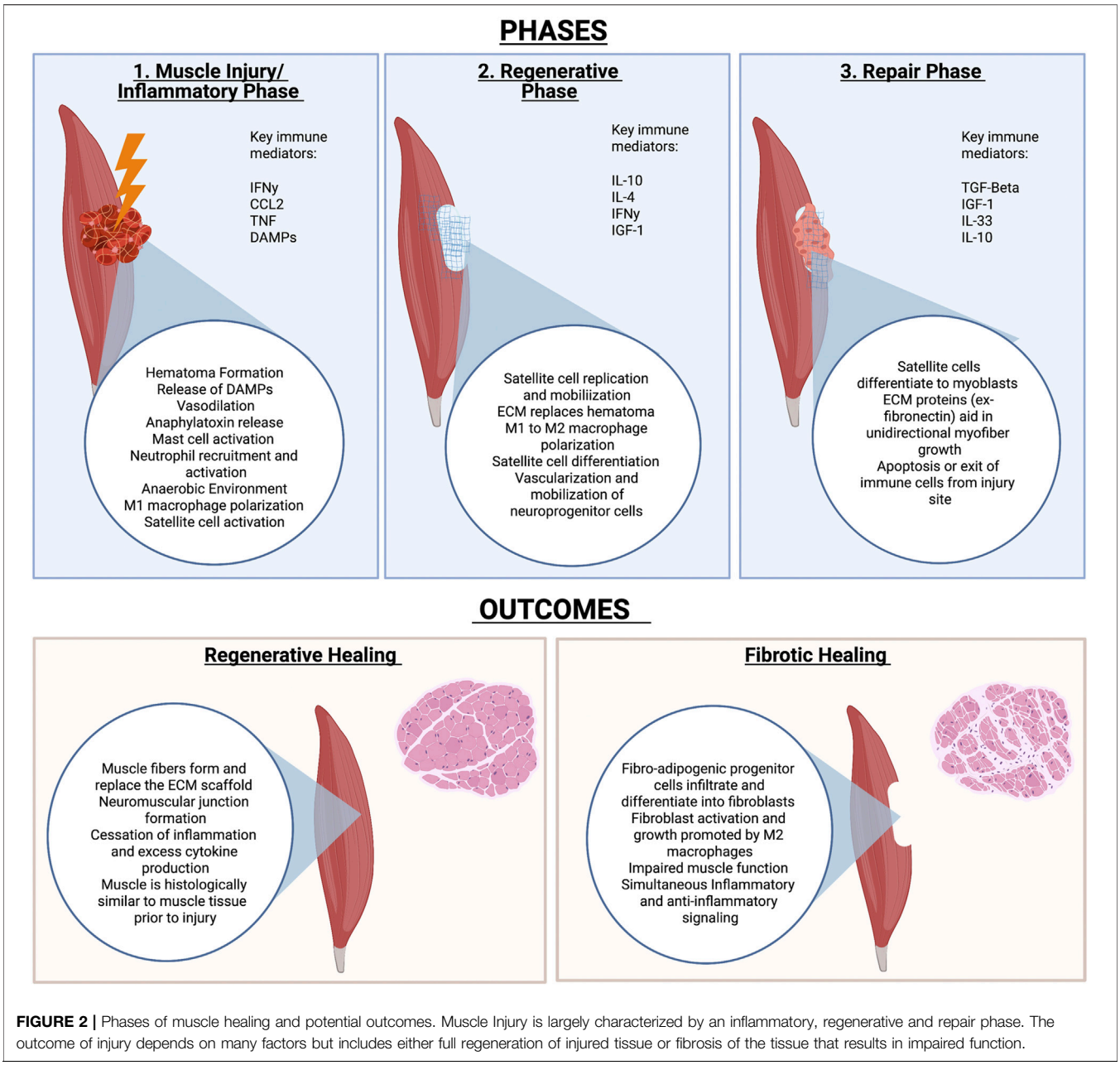

FIGURE 2 | Phases of muscle healing and potential outcomes. Muscle Injury is largely characterized by an inflammatory, regenerative and repair phase. The outcome of injury depends on many factors but includes either full regeneration of injured tissue or fibrosis of the tissue that results in impaired function.

immune cells to the implanted biomaterial and demonstrated that blocking the CSF-1 receptor prevented the foreign body response in non-human primates. CSF-1 receptor is a key regulatory of myeloid cell activation, and its blockage essentially mitigates the myeloid response to the biomaterial (Stanley and Chitu, 2014). Regulating the myeloid response to biomaterials, therefore, is a promising approach to mitigating foreign body response.

Regardless of chemical composition, however, the size and morphology of the biomaterial itself could lead to a foreign body response. Padmore et al. (2017) showed a linear correlation between length of glass fibers with production of Interleukin 1-a, COX-2, and TNF-a by alveolar macrophages. Additionally, studies analyzing the effect of biomimetic multi-scale wrinkles demonstrate that wrinkled biomaterials promoted an anti-inflammatory macrophage phenotype and minimized the extent of collagen deposition in comparison to flat materials (Wang et al., 2016) Therefore, it is incredibly important to consider the multitude of variables that determine the extent of the foreign body response to a specific biomaterial.

MUSCLE

Muscle tissue is highly structured and composed largely of long, multinucleated muscle fibers that are enclosed into bundles by extracellular matrix protein. Muscle precursor cells, named

satellite cells, the resulting tissue is strong but dynamic, and able to meet evolving physical demands.

According to the World Health Organization, there are 1.71 billion people in the world suffering from musculoskeletal disorders (Cieza et al., 2020). Prevalence of musculoskeletal disorders is rising, though a majority of these cases are treated with physical rehabilitation and minimal need for intensive care (Muire et al., 2020).

Courtesy of the regenerative nature of muscle tissue, healthy muscle is often able to heal in response to minor trauma. Significant issues come, however, when the extent of muscle trauma exceeds the regenerative capacity of the muscle. This triggers a dysregulated immune and regenerative response that involves scarring, deteriorated muscle function, and long-term health issues (Andrea Sass et al., 2018). A common example of this kind of injury is the volumetric muscle loss (VML), which involves damage to muscle adjacent to a fractured bone (Hurtgen et al., 2016). Often, VML injuries are left untreated due to the lack of viable therapies.

Muscle Healing

The process of muscle healing is extensively reviewed elsewhere (Muire et al., 2020) and briefly outlined in **Figure 2**. As mentioned previously, the healing process can be largely categorized into three major phases: the inflammatory, regenerative, and remodeling phases. The three phases are outlined in **Figure 2**.

The importance of the immune system in muscle homeostasis is emphasized by the estimated 10^9 leukocytes per liter in adult, rodent limb muscles (Tidball, 2017). Upon muscle injury, the site of injury fills with blood and a scaffold-like hematoma forms to recruit immune cells and protect the tissue from infection (Muire et al., 2020).

Activated platelets, neutrophils, and more recruit monocytes that activate to become macrophages (Muire et al., 2020). M1 macrophages and other innate immune cells act to clear the site. Once the clot is formed and there is no threat of pathogens, the immune system begins to focus on repair of the tissue instead of inflammation. This includes polarization of immune cells such as macrophages and T cells to a more immunoregulatory phenotype. M2 macrophages and TH2 T helper cells, in particular, promote myofibroblast activation to allow for ECM production and replacement of the hematoma with ECM. The ECM deposition and modelling acts to stabilize the wound site and promote proper myofiber growth to conform to the original tissue. This ensures formation of a muscle that is morphologically identical to the uninjured tissue (Muire et al., 2020).

In addition to promoting ECM deposition at the injury site, macrophages play a key role in muscle stem cell function. Muscle stem cells are present as satellite cells, which rapidly self-renew and then fuse together to form myofibers (Muire et al., 2020). While satellite cells are the main myofiber precursors, it is also important to note that perivascular stem cells (PVSC) located adjacent to blood vessels in skeletal muscle can also differentiate into myoblasts (Sicari et al., 2014a). It is well established that M1 macrophages promote satellite cell replication, while M2 macrophages induce M2 differentiation (Dziki et al., 2016). Furthermore, direct coculture of macrophages with muscle precursor cells decrease apoptosis of the precursor cells (Chazaud et al., 2003).

As myoblasts form into myofibers, the cells rely on ECM to guide their differentiation and rely on mechanical cues from ECM during this process (Muire et al., 2020). Interestingly, mechanical stimulation appears to promote the crosstalk between M2 macrophages and myoblasts during muscle formation in mice (Dziki et al., 2018).

When the injury is too large, ECM secretion persists as immune cells fail to properly regulate ECM deposition and myoblast differentiation. Excess deposition leads to failure of satellite cells to form proper myofibers, resulting in scar tissue formation instead of muscle tissue. Adipose tissue and fibroblasts invade the injured space, and seal the wound to protect the body from invading pathogens (Muire et al., 2020).

Traumas like VML injuries are immediately predisposed to a failure of resolution due to the massive immune cell influx that comes as a result of release of immune mediators by the injured tissue (Bianchi, 2007). Namely, Damage Associated Molecular Patterns (DAMPs) and Alarmins are highly elevated following a traumatic muscle injury. Satellite cells require mechanical stimulation to differentiate into muscle cells, so efforts to create biomaterials for muscle injuries have largely relied on creating scaffolds that aid in mechanical support for satellite cells. Additionally, a large focus of these materials is promotion of immunoregulation to prevent the continuation of inflammation that ultimately leads to fibrosis. These types of materials can be broadly characterized into Extracellular Matrix Proteins and derivatives, natural biomaterials, synthetic biomaterials, and cell-laden biomaterials. Common biomaterials, their immunomodulatory properties, and potential clinical obstacles are outlined in **Table 1**.

Extracellular Matrix Proteins/Derivatives

Extracellular matrix (ECM) and derivatives are a well-established class of biomaterials and have already shown great clinical success (Aamodt and Grainger, 2016). At its purest form, ECM biomaterials are protein-based, decellularized extracts from animal tissue and are largely composed of Collagen I by weight.

Extracellular matrix (ECM) and derivatives have already shown great clinical success in treating muscular injury (Aamodt and Grainger, 2016). Cheap, easy to produce, and effective, ECM biomaterials are protein-based, decellularized extracts from animal tissue. Type I Collagen is the main component of decellularized ECM, and has been used successfully for decades since it is readily degraded by the body (Aamodt and Grainger, 2016). This ensures that whatever foreign body response to the collagen is minimal.

While Type I collagen is not immunogenic, it is the various smaller components of ECM that succeed in triggering desirable cell stimulation, activation, or migration. This includes growth factors, ECM degradation products, or cell adhesion molecules (Dziki et al., 2017).

Porcine ECM scaffolds have been shown to promote muscle wound healing in mice and humans (Sicari et al., 2014b). Deeper research into the mechanism of action demonstrate that immune

TABLE 1 | Biomaterials for skeletal muscle tissue regeneration and their immunomodulatory properties.

Class	Name	Type of muscle injury	Immune modulation	Publication
ECM SCAFFOLDS/ DERIVATIVES	Xenogeneic ECM Scaffolds	Volumetric Muscle Loss	Promotes M1 to M2 macrophage transition M2 macrophages promote PVSC and neurogenic precursor cells migration ECM induces IL-4 production to promote Th2 T helper cell polarization (essential for wound healing) Induces release of VEGF, and IGF-1 to induce myogenesis and regulate inflammation	Hoganson et al. (2010); Sicari et al. (2014a); Sadtler et al. (2016)
	Hyaluronic acid	Primary mouse cells derived from tibialis anterior muscle	High molecular weight HA is known to promote cellular invasion and differentiation of epicardial cells *via* CD44 and MEKK1 High MW heparin retains growth factors and releases them slowly to promote regeneration and immune modulation (ex- TGF-B) Can be modified to include ECM components (ex- laminin and RGD peptides) promote invasion of myoblasts into hydrogel	(Craig et al., 2010; Jha et al., 2015; Silva Garcia et al., 2019; Schuurmans et al., 2021)
	Minced Muscle Grafts	Volumetric Muscle Loss	Significantly reduced cell infiltrate into injury site Graft elevated production of MCP-1, IL-10, and IGF-1 Minimized circulating levels of RAGE and other alarmins	Hurtgen et al. (2017)
Naturally-Derived Polymers	Alginate	Volumetric Muscle Loss	Alginate ferrogel planted near the site of injury was used to induce mechanical compression; mechanical stimulation of cells + clearance of inflammatory mediators promoted muscle healing Can be chemically modified to inhibit immune reactions or promote specific cell activity (ex- CSF-1 inhibitors, RGD)	Cezar et al. (2016); Sun and Tan (2013); Doloff et al. (2017)
	Silk Fibroin	*In-vitro* (human skeletal muscle myoblasts)	Silk fibroin scaffolds can promote myoblast ECM deposition and promote myofiber formation	Thurber et al. (2015); Chaturvedi et al. (2017)
Synthetic Biomaterials	Polyprolene mesh	Abdominal Wall Defect/ Hernia	Has the mechanical properties desired for many medical applications; can be coated with ECM to prevent foreign body response and promote repair *via* M2 macrophage polarization	Wolf et al. (2014); Wang See et al. (2020)
	Polyethylene Glycol (PEG)	*In-vitro* (Rat and Human Aortic Muscle Cell Lines)	Can be engineered to be proteolytically degradable and avoid foreign body response	Mann et al. (2001); Han et al. (2019)
		Cryo-injured tibialis anterior injury	Can be loaded with growth factors to induce immune effects and regeneration	
	Methacrylic Acid (MAA)	Intramuscular Injection	Promotes M2 macrophage polarization *via* IGF-1 Promotes sonic hedgehog signaling to increase vascularization and wound healing Upregulation of Arg and Fizz1	Lisovsky and Sefton (2016); Talior-Volodarsky et al. (2017); Carleton and Sefton (2019)

modulation by ECM scaffolds aids in the promotion of muscle repair.

Hoganson et al. (2010) demonstrated that cytokines encapsulated in porcine mesothelium aid in muscle repair, namely Vasoendothelial Growth Factor (VEGF), Insulin-like growth factor (IGF-1), and Transforming Growth Factor Beta TGF-β assay. This study also demonstrated that there was an unidentified factor released by porcine mesothelium that promoted VEGF production in fibroblasts, which is key in promoting revascularization of the wound.

Release of IGF-1 by ECM scaffolds also aids in M1 to M2 macrophage polarization during the transition from the inflammatory to repair phase in muscle wound healing (Tonkin et al., 2015). As mentioned previously, severe muscular trauma is likely to result in scarring as a result of the large amounts of alarmins released as a result of injury. Promoting transition of the inflammatory phase to the repair phase is a goal of many biomaterials designed to treat muscular trauma. Indeed, decellularized skeletal muscle ECM with encapsulated IGF-1 demonstrated increased muscle regeneration and minimized fibrosis in a rabbit animal model of VML injury (Lee et al., 2020).

In addition to M2 macrophages, myoblasts and neurogenic precursor cells were found to infiltrate to the center of the

implanted ECM. Researchers previously demonstrated that degradation products from ECM scaffolds promote M2 macrophage phenotype similarly to IL-4 (Sicari et al., 2014a). M2 macrophages then promote chemotaxis and myogenesis of satellite cells and PVSCs into the center of the scaffold.

Sadtler et al. (2016) highlighted the importance of T cells in ECM-mediated endogenous repair of muscle by demonstrating the inability of RAG1 deficient mice to heal in the same capacity as wild type mice in a model of VML injury. In this experiment, mice underwent a volumetric loss injury in the quadriceps muscle, which was then filled with tissue-derived ECM due to their immunomodulatory properties. In RAG1 deficient and RICTOR deficient mice, the immunomodulatory properties of ECM scaffolds were not apparent. When comparing the immune cell phenotypes, immunomodulatory, regenerative macrophages were downregulated in the RAG1 mouse. Interestingly, levels of CD206+ macrophages were restored upon wild-type $CD4^+$ transfer, but not with transfer of Rictr- T cells (Sadtler et al., 2016). Rictor is a component of the mTORC2 complex, which drives polarization of CD4 T cells to a Th2 phenotype. Sadtler et al. (2016) proposes that IL4 production initially induced by macrophages and innate immune cells is thus propagated by Th2 helper cells in the weeks after muscle injury, which drives healing and a pro-regenerative environment.

ECM scaffolds used for regenerative medicine have demonstrated varying results *in vivo* and highlight several important aspects of endogenous repair in muscle trauma. Human trials of porcine ECM transplanted into VML patients showed variable results (Sicari et al., 2014b). While 3 patients out of five experienced an increase in functional outcome variables, two saw no difference. Interestingly, the two patients with no improvement had the same injury type as a patient who improved, highlighting the variability of the outcomes. There are, however, several limitations to this trial. All patients enrolled in the trial had already gone through several rounds of physical therapy and were treated with ECM a year after injury. In contrast, the murine model in the paper received ECM treatment immediately after VML injury. It is unclear whether ECM treatment directly after injury could aid in VML repair.

Specific ECM components can be chemically modified to have different biological functions. Bencherif et al. (2008) created a photopolymerizable polymer made of hyaluronic acid and glycidyl methacrylate modified to include the RGD peptide of integrin, which promoted myoblast cell adhesion and differentiation *in vitro*. Expanding on this, researchers developed hyaluronic acid hydrogels chemically conjugated with peptide components of ECM, and showed that the CSGIKVAV peptide of laminin promoted cell adhesion and satellite cell migration into the scaffold (Silva Garcia et al., 2019).

In order to minimize the need for myoblast migration into the scaffold, researchers have demonstrated the efficacy of autologous minced muscle grafts in repairing VML injury in rats (Hurtgen et al., 2017). The addition of minced muscle grafts aided not only in restoring muscle function after injury to the Tibialis Anterior muscle, but also restored aggregation of mineralization at the fracture site of a neighboring bone. While promising, clinical feasibility of this therapy will rely heavily on finding an alternative source of muscle cells.

Natural Biomaterials

As mentioned before, ECM biomaterials have limitations that might be solved by differently sourced biomaterials. Several naturally-derived polymers have shown great promise as biomaterials to promote regeneration. Materials such as agarose, alginate, silk, fibrin, and more have all been manipulated to treat VML.

Fibrin is a key component of the clotting cascade and is a natural part of the wound healing process (Grasman et al., 2015; Muire et al., 2020). Additionally, the fibrillary structure of Fibrin promotes myoblast survival, proliferation, and differentiation (Matthias et al., 2018). Muscle derived stem cells encapsulated in fibrin gels effectively differentiated into myofibers and promoted effective VML repair (Matthias et al., 2018).

Grasman et al. (2015) developed a scaffold consisting of biopolymer microfibers using fibrinogen and thrombin crosslinked by carbodiimide. They also adsorbed Hepatocyte Growth Factor (HGF) to the surface of fibrin microfibers and demonstrated that myofiber growth was increased with the implants. It is important to note, however, that collagen deposition remained the same across all groups, meaning that the extent of fibrosis may not have necessarily been decreased by the implant. This could likely be caused by a foreign body response or recruitment of fibroblasts by the adsorbed Hepatocyte Growth Factor (HGF).

Studies on the immunomodulatory effects of fibrin as a biomaterial differ-while some studies suggest that fibrin minimizes monocyte/macrophage recruitment, others demonstrate that fibrin gels increase leukocyte recruitment and promote production of proinflammatory cytokines IL-1B and IL-6 (García-García and Martin, 2019). Encapsulation of different cytokines within fibrin gels could help increase the immunomodulatory effects of fibrin gels and counteract undesirable immune stimulation by the biomaterial.

Alginate is another very popular biomaterial, due to ease of chemical modification, crosslinking, and biocompatibility. Alginate is derived from seaweed and is a polymer formed from (1–4)-linked β-D-mannuronic acid (M) and α-L-guluronic acid (G) monomers (Sun and Tan, 2013). Alginate is easily crosslinked to form a gel from a fluid using cations such as calcium and barium, meaning that there are minimal adverse effects to cells encapsulated within the alginate in comparison to other crosslinking methods such as ultraviolet photopolymerization. It is also very easy to chemically modify with various peptides to stimulate certain cell behavior, the most common of which being the RGD peptide from integrins (Sun and Tan, 2013).

Unlike other biomaterials for muscle healing, alginate is unique because it does not degrade easily in the body (Sahoo and Biswal, 2021). However, it has still been used in various wound healing contexts. Cezar et al. (2016) developed a ferrogel using an alginate-based scaffold containing 7% iron oxide. Instead of implanting directly at the injury site, the device was implanted subcutaneously and used a magnet to trigger

mechanical compressions to stimulate the wounded muscle, as opposed to having a scaffold directly transplanted into the defect. A significant improvement in muscle healing and function with this was observed, likely due to mechanical stimulation of cells and physical clearance of inflammatory mediators like Reactive Oxygen Species (ROS) (Cezar et al., 2016). This work demonstrates that physical stimulation may aid in promoting the inflammatory to regenerative phase of trauma healing.

Silk biomaterials are an emerging trend in wound healing and regenerative medicine (Pollini and Paladini, 2020). Similar to alginates, silk biomaterials such as silk fibroin can be highly tunable and have shown great efficacy in promoting wound healing in the eye, nervous system, and more (Pollini and Paladini, 2020). Only recently have silk scaffolds been developed for muscle healing in particular. Chaturvedi et al. (2017) demonstrated that myoblasts can grow and differentiate effectively on various silk fibroin scaffolds. Interestingly, Chaturvedi observed that the silk aided in promoting deposition of ECM by the myoblasts and proposed that the method by which the fibroins were presented to the myoblasts mattered more than the chemical composition of the fibroins. There are few papers reporting *in vivo* function of silk biomaterials for muscle healing. However, reports indicate that there are certain derivatives of silk that are able to not trigger an adverse immune response and are able to be degraded by macrophages *in vivo* (Thurber et al., 2015).

Synthetic Biomaterials

Because of the limitations of ECM-derived scaffolds, alternative biomaterials with similar morphological or physical characteristics are desirable. An added benefit to these materials is that many of them can be fine-tuned with a lot more accuracy and precision, making it easier to alter their mechanical and biological properties.

A key aspect of synthetic biomaterials is their ability to be formed into various configurations. Synthetic materials can be formed into meshes, foams, hydrogels, and electrospun scaffolds (Wolf et al., 2015). These configurations can determine the cellular response to the biomaterial, such as providing better attachment points for myoblasts (McKeon-Fischer et al., 2011). These kinds of materials include Poly (lactic acid) (PLA), poly (glycolic acid), Poly (e-caprolactone) (PCL), and more (Wolf et al., 2015).

Polyprolene mesh has been used for hernia repair for over 50 years and is considered the standard of care to reinforce the abdominal wall muscles after a hernia. Nonetheless, there are a host of issues with polyprolene mesh, resulting in complications reviewed by Gavlin et al. (2020). Two common complications of synthetic meshes are infection and fibrosis, triggering chronic inflammation and discomfort to the patient (Wang See et al., 2020).

Because myoblasts have mechanical requirements for adhesion and myotube formation, the rigidity that synthetic biomaterial makes them an ideal material for muscle regeneration. The biggest flaw of most synthetic biomaterials, however, is the inherent lack of immunocompatibility, and thus highlights the importance of this trait in a regenerative biomaterial. For instance, myoblasts seeded in sheets of Poly (glycolic acid) fiber mesh successfully formed unidirectional myofibers *in vivo* (Saxena et al., 1999). However, invading fibroblasts and foreign body giant cells overwhelmed the construct and makes the PGA fiber mesh alone unsuitable for transplantation.

Polyethylene glycol (PEG) is a common synthetic biomaterial, largely because it was believed to not be as immunogenic as other synthetic biomaterials and has many physical characteristics that make it a desirable biomaterial (Gombotz et al., 1991). PEG hydrogels containing a preoteolytically degradable peptide sequence and the RGD peptide promoted muscle cell adherence and migration into the hydrogel (Mann et al., 2001). Similarly, a PEG hydrogel loaded with Wnt7a, a promyogenic factor, promoted skeletal muscle migration and also promoted myotube formation from transplanted myoblasts in mice (Han et al., 2019).

Methacrylic Acid (MAA) has shown great efficacy as a biomaterial in other tissues, and has recently been applied to skeletal muscle. Methacrylic acid promotes IGF-1 signaling and increases presence of Fizz-1+ macrophages in skeletal muscle (Carleton and Sefton, 2019). MAA also promotes sonic hedgehog (SHH) signaling and promotes vascularization (Talior-Volodarsky et al., 2017).

Applying electrospinning techniques to synthetic biomaterials has significantly increased the feasibility of synthetic scaffolds for tissue engineering by making them less immunogenic. This technique allows for easy and tunable manipulation of synthetic biomaterials to create scaffolds with similar properties as the natural extracellular matrix (Sill and von Recum, 2008). Electrospun scaffolds can also incorporate various drugs such as growth factors, RNA, antibiotics, and more in a safe and reliable manner. The process of electrospinning is summarized in various papers, but results in formation of highly tunable microfibers of polymers (Sill and von Recum, 2008). By changing the voltage, distance between the needle and collector, viscosity, and feed rate can be optimized to change properties of the biomaterial (Politi et al., 2020).

Electrospinning has greatly improved efficacy of synthetic biomaterials for muscle healing. PLGA fiber scaffolds laden with myoblasts showed aligned myofiber growth and development, indicating that PLGA was a suitable biomaterial to promote muscle formation (Narayanan et al., 2020). PLGA is a generally well tolerated synthetic material that degrades to lactic acid and glycolic acid (Wolf et al., 2015). Yang et al. (2014) demonstrated that patches made of nanopatterned PLGA and myoblasts successfully formed myofibers in a model of muscular dystrophy. In the future, incorporation of immunomodulatory components to synthetic biomaterials could bolster the efficacy of these materials even more.

Combinatorial Materials

As previously mentioned, each biomaterial type has its limitations. However, significant progress has been made in combining various materials to create a superior scaffold. While synthetic biomaterials may provide the best scaffolds for myoblasts to attach and differentiate upon, foreign body response to most of these materials is virtually unavoidable. While synthetic scaffolds have

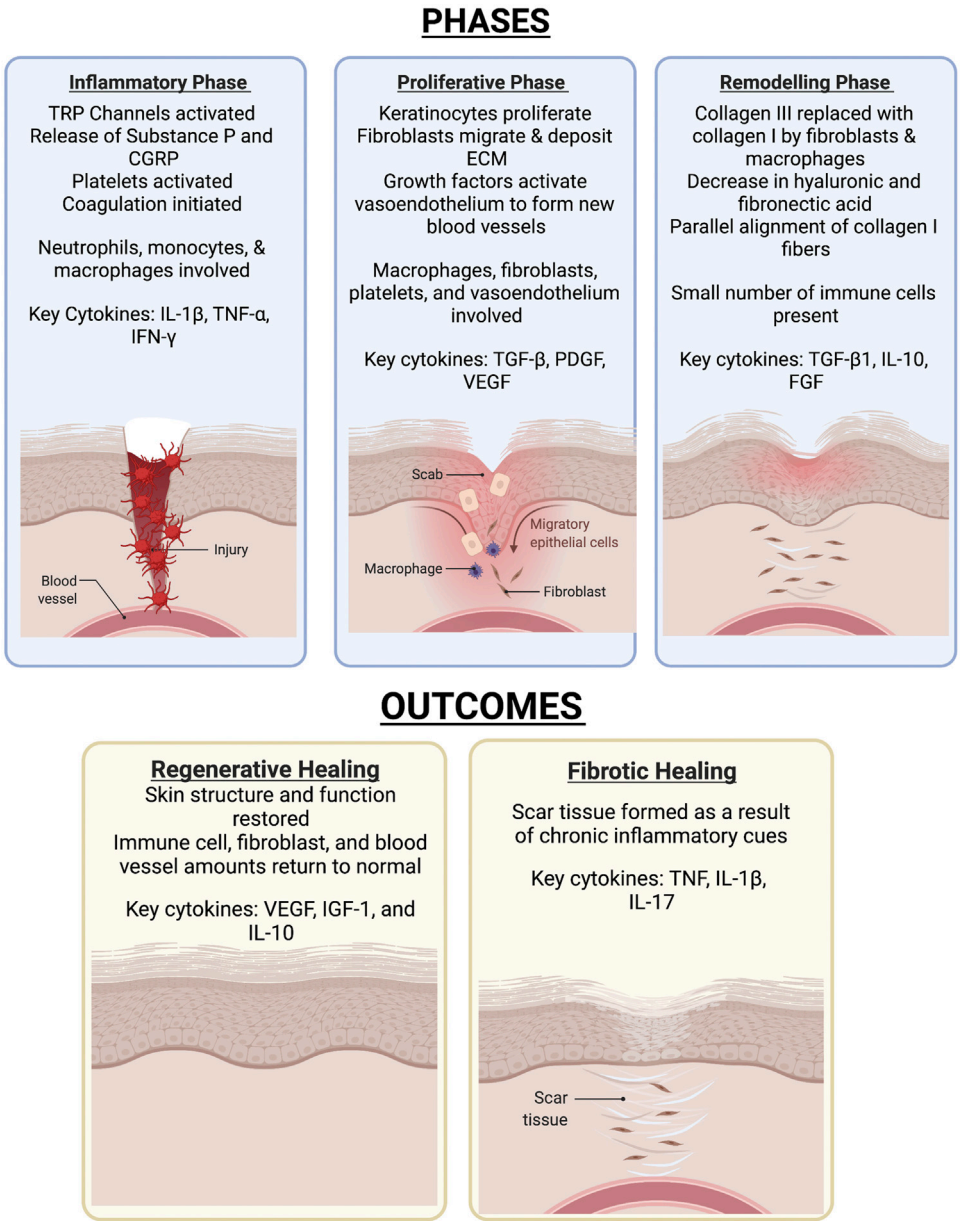

FIGURE 3 | The various phases of skin wound healing and the outcomes. Skin healing consists of three phases-the inflammatory, proliferative, then remodelling phase. The outcome of the healing process results in either full resolution of injury or formation of a scar.

been used in the clinic for decades, permanent implantation of these materials alone to treat an area where fibrosis is likely to trigger adverse effects in many patients. As a result, combinatorial materials made of both immunomodulatory and synthetic scaffolds are an emerging field.

To combat the M1 macrophage-mediated response against polypropylene mesh, Wolf et al. (2014) coated the polyprolene mesh with an ECM hydrogel before implantation. The surrounding ECM was sufficient to combat the highly inflammatory nature of the polyprolene mesh, particularly by reducing the number of M1 macrophages and Foreign Body Giant Cells present around the mesh.

Using ECM scaffolds to combat the foreign body response to synthetic biomaterials has also shown success with PCL scaffolds. Jin et al. (2021) demonstrated the efficacy of a combinatorial biomaterial composed of PCL and muscle-derived ECM in promoting VML repair.

SKIN

Skin Healing

Skin is comprised of two layers, the epidermis (upper layer) and dermis (lower layer), that are separated by the basement

membrane. These layers are in turn composed of sublayers with different cell types and structures (Rognoni and Watt, 2018). The epidermis contains epithelial cells such as keratinocytes and Merkel cells, melanocytes, and immune cells such as Langerhans cells, γδT-cells, and $CD8^+$ tissue-resident memory T cells, while the dermis contains dendritic cells, macrophages, innate lymphoid cells, natural killer (NK) cells $CD8^+$ tissue-resident memory T cells, fibroblasts, and pericytes (Rognoni and Watt, 2018; Ho and Kupper, 2019). The immune and endothelial cell populations within the dermis have been shown to change with age (Rognoni and Watt, 2018).

Detailed reviews of skin composition and the wound healing process have been written by others (Landén et al., 2016; Rognoni and Watt, 2018; Cañedo-Dorantes and Cañedo-Ayala, 2019). In brief, skin injuries trigger a three-phase process that has an inflammatory phase, proliferative phase, and a remodeling phase as seen in **Figure 3**. In the inflammatory phase, skin damage activates transient receptor potential (TRP) channels, stimulating sensory neurons to create action potentials (Gouin et al., 2017; Cañedo-Dorantes and Cañedo-Ayala, 2019). Many TRP channels such as those responding to temperature are expressed in skin keratinocyte cells (Patapoutian et al., 2009). This leads to the initiation of pain and the release of substance P and calcitonin gene-related peptide (CGRP) that play a variety of roles in increasing blood flow and vascular permeability, as well as attracting inflammatory cells (Schmelz and Petersen, 2001; Cañedo-Dorantes and Cañedo-Ayala, 2019). Indeed, the vasodilator activity of CGRP has been shown to be regulated by substance P (Brain and Williams, 1988). Vascular injury exposes blood platelets to basement membrane proteins such as collagen (Schmelz and Petersen, 2001; Bergmeier and Hynes, 2012), activating the platelets and leading to the initiation of the coagulation cascade. Platelet cell surface receptors interact with other cells and release growth factors to lead to pathogen detection and elimination (Tamagawa-Mineoka, 2015; Nami et al., 2016; Cañedo-Dorantes and Cañedo-Ayala, 2019).

The proliferative phase is characterized by fibroblast, keratinocyte, and endothelial cell migration and proliferation (Landén et al., 2016; Boothby et al., 2020). Keratinocytes respond to multiple signals and stimulatory factors by moving from the wound edge and proliferating to re-epithelialize the wound surface and rebuild the basement membrane (Jacinto et al., 2001; Barrientos et al., 2008; Landén et al., 2016). Fibroblasts from the surrounding area also migrate in response to multiple signals and stimulatory factors, leading to degradation of the provisional matrix and deposition of ECM components (Gill and Parks, 2008; Schultz and Wysocki, 2009; Nissinen and Kähäri, 2015; Xue and Jackson, 2015; Landén et al., 2016). Macrophage-fibroblast interactions in particular have been found to play an important role in myofibroblast proliferation and skin repair (Shook et al., 2018). This phase also involves angiogenesis to restore the tissue's vascular network. Growth factors at the wound site activate endothelial cells from existing vessels, leading to their migration and formation of new blood vessels, which then recruit pericytes and smooth muscle cells (Li et al., 2003; Landén et al., 2016). Macrophages, fibroblasts, platelets, and endothelial cells each play important roles in the proliferative phase (Cañedo-Dorantes and Cañedo-Ayala, 2019). During the remodeling phase, deposited Collagen III is replaced by Collagen I (Landén et al., 2016).

Stem cells play an important role throughout the skin wound healing process, with involvement of both stem cell proliferation and signaling in healing (Coalson et al., 2019). Studies in mouse skin epidermis have revealed that stem cell activation during the wound healing process leads to the generation of new stem cells and progenitors that promote tissue expansion (Aragona et al., 2017). Adult stem cells including endothelial progenitor cells, bone marrow-derived mesenchymal cells, and adipose tissue-derived stem cells can each contribute to skin wound healing (Kim and Suh, 2010). Bone marrow-derived mesenchymal stem cells are known to differentiate into several types of skin cells including keratinocytes, endothelial cells, pericytes, and even monocytes/macrophages (Sasaki et al., 2008). Endothelial progenitor cells and adipose tissue-derived stem cells are each involved in revascularization of injured tissue (Kim and Suh, 2010). Extensive studies have been conducted to apply stem cells for skin wound healing (Nourian Dehkordi et al., 2019), but detailed discussion of approaches that do not make use of biomaterials are beyond the scope of the present review.

Types of Skin Wounds and Biomaterial Approaches

The applications of skin wound healing include treatment of diabetic wounds, burn wounds, and full-thickness skin wounds. Traditional biomaterial-based approaches to skin wound healing typically focus on providing flexible mechanical properties while protecting the wound from infection. In this section, however, we will focus on biomaterial-based approaches that seek to modulate the body's immune response to aid in the healing process. Many skin wound healing studies include the use of polymeric nanofibers [reviewed by Miguel et al. (2019)], the use of polymeric scaffolds [reviewed by Dickinson and Gerecht (2016), Sahana and Rekha (2018)], or the use of hydrogels. A number of immune-focused skin healing approaches aid in macrophage transition from a pro-inflammatory phenotype to anti-inflammatory phenotype, but some address multiple stages of the skin healing process as seen in **Table 2**. We categorize these approaches based on their use of naturally derived biomaterials or a combination of natural and synthetic materials. The use of synthetic materials alone is unlikely to be favorable due to an increased immune response to synthetic materials.

Naturally-Derived Biomaterials

Many skin healing studies have been undertaken with naturally-derived biomaterials (Hortensius and Harley, 2016), but few studies on skin healing have conducted extensive examination of the immunomodulatory functions of these naturally-derived biomaterials.

Collagen-based wound dressings are a naturally-derived biomaterial commonly used in treating skin wounds. Collagen, a highly-abundant extracellular matrix component, represents a family of glycoproteins that are involved in a variety of physiological functions. For example, collagen VII is known to

TABLE 2 | Biomaterials for skin regeneration and their immunomodulatory properties.

Class	Name	Type of skin injury	Immune modulation	Publication
Combinatorial biomaterials	Sodium Alginate and Bioactive Glass hydrogels	Full-thickness skin wound	Macrophages promote migration of fibroblasts and mouse artery endothelial cells in skin	Zhu et al. (2020)
	Coaxial scaffolds of PLGA nanofibers + fibrinogen _ collagen I	Diabetic Wound	Combination of Fibrinogen + Collagen I exposure promoted M2 macrophage polarization and healed the wound by stopping inflammation	Sun et al. (2021)
	Stem cells loaded in biomaterials	Diabetic rat wound	Downregulation of pro-inflammatory cytokines; Increased M2/M1 ratio	Chen et al. (2021)
	Anti IL-6 eluting GelMA hydrogels	Mouse skin transplant	Promoted skin allograft survival by minimizing T cell and macrophage transplantation	Uehara et al. (2019)
	PEG hydrogels + Silver Ions and mangiferin liposomes	Mouse skin flap injury	Prevented infection, increased microvessel density, and the magniferin minimized macrophage recruitment	Mao et al. (2019)
	Microporous Annealed Particle Hydrogels with D-Amino acids	Mouse full-thickness incisional wounds	Increased immune cell recruitment lead to tissue regeneration and prevented scarring IL-33 production by local myeloid cells promoted healing	Griffin et al. (2021)
Natural biomaterials	Keratin	N/A (*in vitro*)	Low molecular weight keratin promoted M1 to M2 transition in macrophages	Waters et al. (2018)
	Me-HA hydrogels loaded with bFGF	Mouse full-thickness skin wounds	Improved re-epithelialization, granulation formation, collagen deposition, skin appendage regeneration, and vascularization	Chen et al. (2020)
	Electrospun Soy Protein Scaffolds	Pig model of full thickness excisional wound	Dermal papillae formation in the dermis, collagen formation, and a well-formed stratified epithelial layer; Formation of dermal appendages	Har-el et al. (2014)
	Electrospun tilapia skin collagen membranes	Sprague Dawley rat full-thickness skin wound models	Improvement in wound healing rate and reduced inflammation compared to Kaltostat and untreated controls	Zhou et al. (2016)

lead to re-epithelialization through organization of laminin-332 at the dermal-epidermal junction, in addition to supporting dermal fibroblast migration and regulating cytokine production (Nyström et al., 2013). In addition to providing 3D structure and favorable mechanical properties, collagen interacts with cells *via* mediation by proteins that bind with the Pro-Hyp-Gly unit, those that bind with the Phe-Hyp-Gly sequence, receptors for collagen's cryptic binding sites, and receptors for non-collagenous domains (Chattopadhyay and Raines, 2014). Zhou et al. (2016) derived collagen sponges from tilapia skin. Through *in vivo* implantation of the collagen sponges, they found that the material itself did not lead to immune activation. They further formed membranes by electrospinning the collagen sponges and determined that the *in vitro* adhesion and proliferation of human keratinocytes (HaCaTs) seeded on the nanofiber membranes were favorable. The collagen nanofibers were also found to lead to upregulation of involucrin, filaggrin, and TGase1 genes, indicating keratinocyte differentiation. *In vivo* placement of the collagen nanofibers in Sprague Dawley rat full-thickness skin wound models demonstrated an improvement in wound healing rate and reduced inflammation compared to Kaltostat and untreated controls. Other studies have primarily focused on the use of commercially-available collagen-based wound dressings such as Aplifraf, Dermagraft, Graftjacket, Integra, and others in human trials, for example for use in treating diabetic foot ulcers (Holmes et al., 2013).

Keratin, a protein that is a key component of skin, has been shown to aid in skin wound healing in multiple ways. Key factors that set keratin apart from other naturally-derived materials such as collagen include high homology between species to reduce immunogenicity of keratin-derived biomaterials, and a high degree of cystine presence to slow down degradation (Kelly, 2016). Cystine's role as a precursor to glutathione, an antioxidant, provides a further mechanism by which keratin-based biomaterials can support healing (Kelly, 2016). Waters et al. (2018) evaluated the anti-inflammatory effects of various keratin-derived coatings *in vitro*. The wound healing and regenerative abilities of keratin-based biomaterials have been extensively studied, and Waters et al. (2018) demonstrated that peptide-containing keratin fractions with lower molecular weights appear to be slightly more effective in inducing a transition from pro-inflammatory macrophage phenotype to anti-inflammatory phenotype than high molecular weight keratin fractions.

Hyaluronic acid (HA) is a non-sulfated glycosaminoglycan and extracellular matrix component that acts as an immune regulator in physiological and pathological conditions (Noble et al., 2011). HA accumulates at sites of injury and inflammation where it is degraded by reactive oxygen species and hylauronidases, engaging in complex interactions with the wound environment to regulate cytokine secretion and influence immune cell migration (Voinchet et al., 2006). Methacrylation of HA enables light-activated crosslinking for easy formation of HA-based hydrogels (Ondeck and Engler,

2016). Chen et al. (2020) used methacrylated hyaluronic acid (Me-HA) hydrogels loaded with basic fibroblast growth factor (bFGF) as an injectable bioactive wound dressing (bFGF@Me-HA). When applied to mouse full-thickness skin wounds, bFGF@Me-HA improved wound healing with accelerated re-epithelialization, granulation formation, collagen deposition, and skin appendage regeneration. The hydrogels also led to improved cell proliferation and vascularization, which was caused by upregulation of transforming growth factor-β and VEGF.

Another naturally-derived biomaterial, soy protein isolate, has been shown to act as an anti-inflammatory agent by inhibiting NF- κB-dependent expression of inflammatory cytokines and VCAM-1 *in vivo* in acute and chronic inflammation models (Burris et al., 2014). Har-el et al. (2014) used soy protein isolate to electrospin soy protein scaffolds (SPS) for wound healing. When applied to a porcine full thickness excisional wound healing model, SPS treatment led to the presence of fewer inflammatory/immune cells than untreated controls and development of the beginnings of a stratified epithelial layer just 2 weeks after wounding. By 4 weeks after wounding, SPS treatment had led to dermal papillae formation in the dermis, collagen formation, and a well-formed stratified epithelial layer. The treatment also led to the formation of dermal appendages such as sweat glands and hair follicles, which were not observed in untreated controls.

Combinatorial Biomaterials

Zhu et al. (2020) evaluated the anti-inflammatory effects of an injectable hydrogel composed of sodium alginate and bioactive glass (BG/SA hydrogel) that had previously been applied for skin tissue regeneration. They demonstrated that macrophages exposed to BG/SA hydrogels had enhanced gene expression of anti-inflammatory factors such as TGF-β, VEGF, bFGF, ARG and IL-10, and that cell culture media conditioned by BG/SA-treated macrophages led to increased migration of fibroblasts and mouse artery endothelial cells. Using a mouse full-thickness skin wound model in normal mice and macrophage-depleted mice, they found that the improvement in wound healing caused by BG/SA hydrogel was eliminated in the absence of macrophages, indicating the presence of macrophages played a direct role in *in vivo* wound healing with the BG/SA hydrogels.

A major concern with diabetic wounds is that they are persistently open due to slow healing, which can increase the potential for the development of infections. Acceleration of wound healing can reduce the opportunity for wound infection. In the context of diabetic wounds, even scarred healing would be an improved outcome compared to wound infection. PLGA is an FDA approved polymer that is biocompatible and biodegradable (Hirenkumar and Steven, 2012). While not commonly used by itself to induce immune effects, it is often used for applications in controlled drug delivery. Sun et al. (2021) sought to develop an immunomodulatory scaffold for diabetic wound management, mimicking the sequential appearance of fibrinogen and collagen I in the wound healing process. They developed coaxial scaffolds composed of PLGA nanofibers with fibrinogen incorporated into the shell and collagen I incorporated into the core, taking advantage of the PLGA degradation to expose collagen I over time. *In vitro*, the coaxial scaffolds were found to promote the secretion of growth factors associated with wound healing (TGF-b1, VEGF and bFGF), as well as immunosuppressive factors (COX-2 and TSG-6). Additionally, macrophages treated with media that had been conditioned by adipose-derived mesenchymal stromal cells (ASCs) exposed to the coaxial scaffolds had a greater M2/M1 ratio than those treated with PLGA scaffolds or PLGA scaffolds with only fibrinogen or only collagen I incorporated. When applied to an *in vivo* diabetic rat wound model, coaxial scaffolds were found to accelerate diabetic wound healing by resolving inflammation.

Materials based on methacrylic acid have shown great efficacy in treating various skin conditions, including diabetic wound healing (Fitzpatrick et al., 2012; Lisovsky and Sefton, 2016). Methacrylic acid biomaterials promote blood vessel formation *via* sonic hedgehog signaling and promote M2 macrophage polarization *via* an IGF-1 mediated pathway (Martin et al., 2010; Talior-Volodarsky et al., 2017). Plenty of theories as to how the methacrylic acid functions have been developed, but the full mechanism of action has not been fully detailed (Lisovsky et al., 2015).

The incorporation of cells or secretable factors involved in skin repair is another method by which biomaterials can be optimized for skin wound healing. In particular, stem cells are often used as immunomodulatory agents even if they do not develop into new tissue. The mechanisms behind immunomodulatory functions of stem cells are not entirely understood, but they likely result from a combination of soluble factor secretion and cell-to-cell interactions with immune cells (Kuo et al., 2012; Pumberger et al., 2016; Zhao et al., 2016). Chen et al. (2021) used cryogel/hydrogel biomaterials loaded with stem cells to generate an immunomodulatory response in a rat model of diabetic wound healing. The cell-seeded hydrogels/cryogels, which were formed from glycol chitosan and a biodegradable Schiff base crosslinker difunctional polyurethane, led to immunomodulation by down-regulating proinflammatory cytokines TNF-α and IL-1β and upregulating TGFβ-1. Chitosan, a cationic polysaccharide which is commonly derived from crustaceans, has been shown to have both pro-inflammatory and anti-inflammatory properties depending on conditions such as degree of deacetylation, molecular weight, form, and other factors (Fong and Hoemann, 2018). Anti-inflammatory effects of chitosan have been linked to intracellular signaling pathways involving cGAS-STING which can trigger a type 1 IFN response, inducing the release of anti-inflammatory factors such as IL-1ra (Fong and Hoemann, 2018). In the Chen et al. study, the combined effects of biomaterials and cells led wounds treated with cell-seeded biomaterials to also have a higher M2/M1 ratio than those of control wounds or wounds treated with stem cells alone, suggesting an anti-inflammatory function for the biomaterials. Uehara et al. (2019) developed anti-IL-6 antibody-eluting gelatin methacryloyl (GelMA) hydrogels to improve skin allograft survival (Uehara et al., 2019). GelMA is a commonly used biomaterial that is that is considered advantageous for its mechanical properties that can be

precisely tuned. GelMA has been shown to exert anti-inflammatory properties by suppressing TNF-α expression (Donaldson et al., 2018). By crosslinking GelMA/anti-IL-6 on the wound bed prior to skin allograft placement, Uehara et al. (2019) enabled the continual release of anti-IL-6 at the wound site to combat IL-6, which plays a role in innate and adaptive immune responses. Implantation of GelMA/anti-IL-6 approach reduced T cell and monocyte infiltration into the allograft skin and almost doubled graft survival compared to the control. Importantly, incorporation of anti-IL-6 into the biomaterial also provided an improvement in graft survival compared to systemic administration of anti-IL-6.

Mao et al. (2019) aimed to address multiple phases of the skin healing process by developing a hydrogel with both anti-inflammatory and pro-angiogenic properties. They developed a polyethylene glycol (PEG) hydrogel that was crosslinked with silver ions (Ag^+) and loaded with mangiferin liposomes (MF-Lip@PEG), with the goal of combining mangiferin's cytoprotective properties with the antimicrobial activity of Ag^+. When injected in a mouse skin flap injury model, the MF-Lip@PEG hydrogel was found to reduce tissue necrosis and increase microvessel density in the skin flaps. Furthermore, although PEG itself led to high macrophage recruitment, the MF-Lip@PEG hydrogel was able to reduce macrophage recruitment in a concentration-dependent manner.

In contrast to approaches that seek to dampen the immune response, Griffin et al. (2021) used the activation of specific immune responses by D-amino acid crosslinked Microporous annealed particle (MAP) hydrogels to elicit skin regeneration in murine models. They found that MAP hydrogels crosslinked with D-amino acids had faster degradation *in vivo* than those crosslinked with L-amino acids. This faster degradation was a result of enhanced immune cell recruitment, and was found to lead to tissue regeneration, in contrast to the formation of semi-fibrous dermal scar tissue when MAP hydrogels crosslinked with L-amino acids were used. These results suggest that the adaptive immune response can be exploited for skin wound healing.

CONCLUSIONS AND FURTHER DIRECTIONS

The fields of regenerative medicine and bioengineering have made great advances in developing biocompatible and regenerative scaffolds using biomaterials. As discussed, numerous biomaterials developed incorporate the immune system to naturally mediate regeneration and prevent scarring. Each of these approaches have their pros and cons, and it is likely that the best scaffold for regeneration will involve a combination of these materials. Understanding how these biomaterials promote regeneration *via* the immune system plays a crucial part in our understanding of how endogenous repair works. Countless papers highlight the role that various immune cells, particularly macrophages, play in mediating adult stem cell replication and differentiation into the target cell. By modulating the immune cell infiltrate into the injury site, it is possible to effectively modulate stem cell behavior. Hybrid biomaterials are a promising next step in regenerative medicine and will likely be able to combine the benefits of different materials. With hybrid materials come an exciting next step in understanding the healing process, creating more space for optimization. To achieve this goal, more research must be done on understanding all steps of the immune response to biomaterials, particularly *in vivo*.

AUTHOR CONTRIBUTIONS

MK outlined of the paper and contributed to the abstract, introduction, overview of wound healing, foreign body response, and the section on muscle and muscle biomaterials. PF wrote the section on skin wound healing and biomaterials for skin healing. TN and KS edited the manuscript.

ACKNOWLEDGMENTS

Figures 1–3 were made with Biorender biorender.com.

REFERENCES

Aamodt, J. M., and Grainger, D. W. (2016). Extracellular Matrix-Based Biomaterial Scaffolds and the Host Response. *Biomaterials* 86, 68–82. doi:10.1016/j.biomaterials.2016.02.003

Adusei, K. M., Ngo, T. B., and Sadtler, K. (2021). T Lymphocytes as Critical Mediators in Tissue Regeneration, Fibrosis, and the Foreign Body Response. *Acta Biomater.* S1742-7061, 00260–00269. doi:10.1016/j.actbio.2021.04.023

Alcazar, C. A., Hu, C., Rando, T. A., Huang, N. F., and Nakayama, K. H. (2020). Transplantation of Insulin-like Growth Factor-1 Laden Scaffolds Combined with Exercise Promotes Neuroregeneration and Angiogenesis in a Preclinical Muscle Injury Model. *Biomater. Sci.* 8, 5376–5389. doi:10.1039/d0bm00990c

Allen, J. E., and Wynn, T. A. (2011). Evolution of Th2 Immunity: A Rapid Repair Response to Tissue Destructive Pathogens. *Plos Pathog.* 7, e1002003. doi:10.1371/journal.ppat.1002003

Anderson, J. M., Rodriguez, A., and Chang, D. T. (2008). Foreign Body Reaction to Biomaterials. *Semin. Immunol.* 20, 86–100. doi:10.1016/j.smim.2007.11.004

Andorko, J. I., and Jewell, C. M. (2017). Designing Biomaterials with Immunomodulatory Properties for Tissue Engineering and Regenerative Medicine. *Bioeng. Translational Med.* 2, 139–155. doi:10.1002/btm2.10063

Aragona, M., Dekoninck, S., Rulands, S., Lenglez, S., Mascré, G., Simons, B. D., et al. (2017). Defining Stem Cell Dynamics and Migration during Wound Healing in Mouse Skin Epidermis. *Nat. Commun.* 8, 14684. doi:10.1038/ncomms14684

Aramwit, P. (2016). "Introduction to Biomaterials for Wound Healing," in *Wound Healing Biomaterials* (Woodhead Publishing), 3–38. doi:10.1016/B978-1-78242-456-7.00001-5

Arnold, L., Henry, A., Poron, F., Baba-Amer, Y., Van Rooijen, N., Plonquet, A., et al. (2007). Inflammatory Monocytes Recruited after Skeletal Muscle Injury Switch into Antiinflammatory Macrophages to Support Myogenesis. *J. Exp. Med.* 204, 1057–1069. doi:10.1084/jem.20070075

Arshad, T., Mansur, F., Palek, R., Manzoor, S., and Liska, V. (2020). A Double Edged Sword Role of Interleukin-22 in Wound Healing and Tissue Regeneration. *Front. Immunol.* 11, 2148. doi:10.3389/fimmu.2020.02148

Atala, A., Irvine, D. J., Moses, M., and Shaunak, S. (2010). Wound Healing versus Regeneration: Role of the Tissue Environment in Regenerative Medicine. *MRS Bull.* 35, 597–606. doi:10.1557/mrs2010.528

Barrientos, S., Stojadinovic, O., Golinko, M. S., Brem, H., and Tomic-Canic, M. (2008). PERSPECTIVE ARTICLE: Growth Factors and Cytokines in Wound Healing. *Wound Repair Regen.* 16, 585–601. doi:10.1111/j.1524-475X.2008.00410.x

Bencherif, S. A., Srinivasan, A., Horkay, F., Hollinger, J. O., Matyjaszewski, K., and Washburn, N. R. (2008). Influence of the Degree of Methacrylation on Hyaluronic Acid Hydrogels Properties. *Biomaterials* 29, 1739–1749. doi:10.1016/j.biomaterials.2007.11.047

Bergmeier, W., and Hynes, R. O. (2012). Extracellular Matrix Proteins in Hemostasis and Thrombosis. *Cold Spring Harbor Perspect. Biol.* 4, a005132. doi:10.1101/cshperspect.a005132

Bianchi, M. E. (2007). DAMPs, PAMPs and Alarmins: All We Need to Know about Danger. *J. Leukoc. Biol.* 81, 1–5. doi:10.1189/jlb.0306164

Boothby, I. C., Cohen, J. N., and Rosenblum, M. D. (2020). Regulatory T Cells in Skin Injury: At the Crossroads of Tolerance and Tissue Repair. *Sci. Immunol.* 5, eaaz9631–13. doi:10.1126/sciimmunol.aaz9631

Brain, S. D., and Williams, T. J. (1988). Substance P Regulates the Vasodilator Activity of Calcitonin Gene-Related Peptide. *Nature* 335, 73–75. doi:10.1038/335073a0

Brockmann, L., Giannou, A., Gagliani, N., and Huber, S. (2017). Regulation of TH17 Cells and Associated Cytokines in Wound Healing, Tissue Regeneration, and Carcinogenesis. *Ijms* 18, 1033. doi:10.3390/IJMS18051033,

Burris, R. L., Ng, H.-P., and Nagarajan, S. (2014). Soy Protein Inhibits Inflammation-Induced VCAM-1 and Inflammatory Cytokine Induction by Inhibiting the NF-κB and AKT Signaling Pathway in Apolipoprotein E-Deficient Mice. *Eur. J. Nutr.* 53, 135–148. doi:10.1007/s00394-013-0509-7

Campbell, C., and Rudensky, A. (2020). Roles of Regulatory T Cells in Tissue Pathophysiology and Metabolism. *Cel Metab.* 31, 18–25. doi:10.1016/j.cmet.2019.09.010

Cañedo-Dorantes, L., and Cañedo-Ayala, M. (2019). Skin Acute Wound Healing: A Comprehensive Review. *Int. J. Inflamm.* 2019, 1–15. doi:10.1155/2019/3706315

Carleton, M. M., and Sefton, M. V. (2019). Injectable and Degradable Methacrylic Acid Hydrogel Alters Macrophage Response in Skeletal Muscle. *Biomaterials* 223, 119477. doi:10.1016/j.biomaterials.2019.119477

Carnicer-Lombarte, A., Chen, S.-T., Malliaras, G. G., and Barone, D. G. (2021). Foreign Body Reaction to Implanted Biomaterials and its Impact in Nerve Neuroprosthetics. *Front. Bioeng. Biotechnol.* 9, 622524. doi:10.3389/fbioe.2021.622524

Cezar, C. A., Roche, E. T., Vandenburgh, H. H., Duda, G. N., Walsh, C. J., and Mooney, D. J. (2016). Biologic-free Mechanically Induced Muscle Regeneration. *Proc. Natl. Acad. Sci. USA* 113, 1534–1539. doi:10.1073/pnas.1517517113

Chattopadhyay, S., and Raines, R. T. (2014). Collagen-based Biomaterials for Wound Healing. *Biopolymers* 101, 821–833. doi:10.1002/bip.22486

Chaturvedi, V., Naskar, D., Kinnear, B. F., Grenik, E., Dye, D. E., Grounds, M. D., et al. (2017). Silk Fibroin Scaffolds with Muscle-like Elasticity Support *In Vitro* Differentiation of Human Skeletal Muscle Cells. *J. Tissue Eng. Regen. Med.* 11, 3178–3192. doi:10.1002/term.2227

Chazaud, B., Sonnet, C., Lafuste, P., Bassez, G., Rimaniol, A.-C., Poron, F., et al. (2003). Satellite Cells Attract Monocytes and Use Macrophages as a Support to Escape Apoptosis and Enhance Muscle Growth. *J. Cel Biol.* 163, 1133–1143. doi:10.1083/jcb.200212046

Chen, A., Huang, W., Wu, L., An, Y., Xuan, T., He, H., et al. (2020). Bioactive ECM Mimic Hyaluronic Acid Dressing via Sustained Releasing of bFGF for Enhancing Skin Wound Healing. *ACS Appl. Bio Mater.* 3, 3039–3048. doi:10.1021/acsabm.0c00096

Chen, T.-Y., Wen, T.-K., Dai, N.-T., and Hsu, S.-h. (2021). Cryogel/hydrogel Biomaterials and Acupuncture Combined to Promote Diabetic Skin Wound Healing through Immunomodulation. *Biomaterials* 269, 120608. doi:10.1016/j.biomaterials.2020.120608

Chung, L., Maestas, D. R., Lebid, A., Mageau, A., Rosson, G. D., Wu, X., et al. (2020). Interleukin 17 and Senescent Cells Regulate the Foreign Body Response to Synthetic Material Implants in Mice and Humans. *Sci. Transl. Med.* 12, eaax3799. doi:10.1126/scitranslmed.aax3799

Cieza, A., Causey, K., Kamenov, K., Hanson, S. W., Chatterji, S., and Vos, T. (2020). Global Estimates of the Need for Rehabilitation Based on the Global Burden of Disease Study 2019: a Systematic Analysis for the Global Burden of Disease Study 2019. *Lancet* 396, 2006–2017. doi:10.1016/S0140-6736(20)32340-0

Coalson, E., Bishop, E., Liu, W., Feng, Y., Spezia, M., Liu, B., et al. (2019). Stem Cell Therapy for Chronic Skin Wounds in the Era of Personalized Medicine: From Bench to Bedside. *Genes Dis.* 6, 342–358. doi:10.1016/j.gendis.2019.09.008

Craig, E A., Parker, P., Austin, A. F., Barnett, J. V., and Camenisch, T. D. (2010). Involvement of the MEKK1 Signaling Pathway in the Regulation of Epicardial Cell Behavior by Hyaluronan. *Cell. Signal.* 22 (6), 968–976. doi:10.1016/j.cellsig.2010.02.004

DeFife, K. M., Jenney, C. R., McNally, A. K., Colton, E., and Anderson, J. M. (1997). Interleukin-13 Induces Human Monocyte/macrophage Fusion and Macrophage Mannose Receptor Expression. *J. Immunol.* 158, 3385–3390. Available at: http://www.ncbi.nlm.nih.gov/pubmed/9120298 (Accessed June 23, 2021).

Dekoninck, S., and Blanpain, C. (2019). Stem Cell Dynamics, Migration and Plasticity during Wound Healing. *Nat. Cel Biol.* 21, 18–24. doi:10.1038/s41556-018-0237-6

Dickinson, L. E., and Gerecht, S. (2016). Engineered Biopolymeric Scaffolds for Chronic Wound Healing. *Front. Physiol.* 7, 341. doi:10.3389/fphys.2016.00341

Doloff, J. C., Veiseh, O., Vegas, A. J., Tam, H. H., Farah, S., Ma, M., et al. (2017). Colony Stimulating Factor-1 Receptor Is a central Component of the Foreign Body Response to Biomaterial Implants in Rodents and Non-human Primates. *Nat. Mater* 16, 671–680. doi:10.1038/nmat4866

Dombrowski, Y., O'Hagan, T., DIttmer, M., Penalva, R., Mayoral, S. R., Bankhead, P., et al. (2017). Regulatory T Cells Promote Myelin Regeneration in the central Nervous System. *Nat. Neurosci.* 20, 674–680. doi:10.1038/nn.4528

Donaldson, A. R., Tanase, C. E., Awuah, D., Vasanthi Bathrinarayanan, P., Hall, L., Nikkhah, M., et al. (2018). Photocrosslinkable Gelatin Hydrogels Modulate the Production of the Major Pro-inflammatory Cytokine, TNF-α, by Human Mononuclear Cells. *Front. Bioeng. Biotechnol.* 6, 1–11. doi:10.3389/fbioe.2018.00116

Dziki, J. L., Sicari, B. M., Wolf, M. T., Cramer, M. C., and Badylak, S. F. (2016). Immunomodulation and Mobilization of Progenitor Cells by Extracellular Matrix Bioscaffolds for Volumetric Muscle Loss Treatment. *Tissue Eng. Part A* 22, 1129–1139. doi:10.1089/ten.tea.2016.0340

Dziki, J. L., Huleihel, L., Scarritt, M. E., and Badylak, S. F. (2017). Extracellular Matrix Bioscaffolds as Immunomodulatory Biomaterials. *Tissue Eng. Part A* 23, 1152–1159. doi:10.1089/ten.tea.2016.0538

Dziki, J. L., Giglio, R. M., Sicari, B. M., Wang, D. S., Gandhi, R. M., Londono, R., et al. (2018). The Effect of Mechanical Loading Upon Extracellular Matrix Bioscaffold-Mediated Skeletal Muscle Remodeling. *Tissue Eng. A* 24, 34–46. doi:10.1089/ten.tea.2017.0011

Ellis, S., Lin, E. J., and Tartar, D. (2018). Immunology of Wound Healing. *Curr. Derm Rep.* 7, 350–358. doi:10.1007/S13671-018-0234-9

Fitzpatrick, L. E., Lisovsky, A., and Sefton, M. V. (2012). The Expression of Sonic Hedgehog in Diabetic Wounds Following Treatment with Poly(methacrylic Acid-Co-Methyl Methacrylate) Beads. *Biomaterials* 33, 5297–5307. doi:10.1016/j.biomaterials.2012.04.008

Fong, D., and Hoemann, C. D. (2018). Chitosan Immunomodulatory Properties: Perspectives on the Impact of Structural Properties and Dosage. *Future Sci. OA* 4, FSO225. doi:10.4155/fsoa-2017-0064

García-García, A., and Martin, I. (2019). Extracellular Matrices to Modulate the Innate Immune Response and Enhance Bone Healing. *Front. Immunol.* 10, 2256. doi:10.3389/FIMMU.2019.02256

Gause, W. C., Wynn, T. A., and Allen, J. E. (2013). Type 2 Immunity and Wound Healing: Evolutionary Refinement of Adaptive Immunity by Helminths. *Nat. Rev. Immunol.* 13, 607–614. doi:10.1038/nri3476

Gavlin, A., Kierans, A. S., Chen, J., Song, C., Guniganti, P., and Mazzariol, F. S. (2020). Imaging and Treatment of Complications of Abdominal and Pelvic Mesh Repair. *Radiographics* 40, 432–453. doi:10.1148/rg.2020190106

Gill, S., and Parks, W. (2008). Metalloproteinases and Their Inhibitors: Regulators of Wound Healing. *Int. J. Biochem. Cel Biol.* 40, 1334–1347. doi:10.1016/j.biocel.2007.10.024

Gombotz, W. R., Guanghui, W., Horbett, T. A., and Hoffman, A. S. (1991). Protein Adsorption to Poly(ethylene Oxide) Surfaces. *J. Biomed. Mater. Res.* 25, 1547–1562. doi:10.1002/jbm.820251211

Gonzalez, A. C. D. O., Costa, T. F., Andrade, Z. d. A., and Medrado, A. R. A. P. (2016). Wound Healing - A Literature Review. *Bras. Dermatol.* 91, 614–620. doi:10.1590/abd1806-4841.20164741

Gouin, O., L'Herondelle, K., Lebonvallet, N., Le Gall-Ianotto, C., Sakka, M., Buhé, V., et al. (2017). TRPV1 and TRPA1 in Cutaneous Neurogenic and Chronic Inflammation: Pro-Inflammatory Response Induced by Their Activation and Their Sensitization. *Protein Cell* 8, 644–661. doi:10.1007/s13238-017-0395-5

Grasman, J. M., Do, D. M., Page, R. L., and Pins, G. D. (2015). Rapid Release of Growth Factors Regenerates Force Output in Volumetric Muscle Loss Injuries. *Biomaterials* 72, 49–60. doi:10.1016/j.biomaterials.2015.08.047

Griffin, D. R., Archang, M. M., Kuan, C.-H., Weaver, W. M., Weinstein, J. S., Feng, A. C., et al. (2021). Activating an Adaptive Immune Response from a Hydrogel Scaffold Imparts Regenerative Wound Healing. *Nat. Mater.* 20, 560–569. doi:10.1038/s41563-020-00844-w

Han, W. M., Mohiuddin, M., Anderson, S. E., García, A. J., and Jang, Y. C. (2019). Co-delivery of Wnt7a and Muscle Stem Cells Using Synthetic Bioadhesive Hydrogel Enhances Murine Muscle Regeneration and Cell Migration during Engraftment. *Acta Biomater.* 94, 243–252. doi:10.1016/j.actbio.2019.06.025

Har-el, Y.-e., Gerstenhaber, J. A., Brodsky, R., Huneke, R. B., and Lelkes, P. I. (2014). Electrospun Soy Protein Scaffolds as Wound Dressings: Enhanced Reepithelialization in a Porcine Model of Wound Healing. *Wound Med.* 5, 9–15. doi:10.1016/j.wndm.2014.04.007

Hernandez-Pando, R., Bornstein, Q. L., Aguilar Leon, D., Orozco, E. H., Madrigal, V. K., and Martinez Cordero, E. (2000). Inflammatory Cytokine Production by Immunological and Foreign Body Multinucleated Giant Cells. *Immunology* 100, 352–358. doi:10.1046/j.1365-2567.2000.00025.x

Hesketh, M., Sahin, K. B., West, Z. E., and Murray, R. Z. (2017). Macrophage Phenotypes Regulate Scar Formation and Chronic Wound Healing. *Ijms* 18, 1545. doi:10.3390/ijms18071545

Hicks, C. W., Canner, J. K., Karagozlu, H., Mathioudakis, N., Sherman, R. L., Black, J. H., et al. (2019). Quantifying the Costs and Profitability of Care for Diabetic Foot Ulcers Treated in a Multidisciplinary Setting. *J. Vasc. Surg.* 70, 233–240. doi:10.1016/j.jvs.2018.10.097

Hirenkumar, M., and Steven, S. (2012). Poly Lactic-Co-Glycolic Acid (PLGA) as Biodegradable Controlled Drug Delivery Carrier. *Polymers (Basel)* 3, 1–19. doi:10.3390/polym3031377.Poly

Ho, A. W., and Kupper, T. S. (2019). T Cells and the Skin: from Protective Immunity to Inflammatory Skin Disorders. *Nat. Rev. Immunol.* 19, 490–502. doi:10.1038/s41577-019-0162-3

Hoganson, D. M., Owens, G. E., O'Doherty, E. M., Bowley, C. M., Goldman, S. M., Harilal, D. O., et al. (2010). Preserved Extracellular Matrix Components and Retained Biological Activity in Decellularized Porcine Mesothelium. *Biomaterials* 31, 6934–6940. doi:10.1016/j.biomaterials.2010.05.026

Holmes, C., Wrobel, J., Mac Eachern, M. P., and Boles, B. R. (2013). Collagen-based Wound Dressings for the Treatment of Diabetes-Related Foot Ulcers: A Systematic Review. *Dmso* 6, 17–29. doi:10.2147/dmso.s36024

Hortensius, R. A., and Harley, B. A. (2016). Naturally Derived Biomaterials for Addressing Inflammation in Tissue Regeneration. *Exp. Biol. Med. (Maywood)* 241, 1015–1024. doi:10.1177/1535370216648022

Hui, S. P., Sheng, D. Z., Sugimoto, K., Gonzalez-Rajal, A., Nakagawa, S., Hesselson, D., et al. (2017). Zebrafish Regulatory T Cells Mediate Organ-specific Regenerative Programs. *Dev. Cel* 43, 659–672.e5. doi:10.1016/j.devcel.2017.11.010

Hurtgen, B., Ward, C., Garg, K., Pollot, B., Goldman, S., McKinley, T., et al. (2016). Severe Muscle Trauma Triggers Heightened and Prolonged Local Musculoskeletal Inflammation and Impairs Adjacent Tibia Fracture Healing. Available at https://www.ncbi.nlm.nih.gov/pmc/articles/PMC5114355/ (Accessed March 18, 2021).

Hurtgen, B. J., Ward, C. L., Leopold Wager, C. M., Garg, K., Goldman, S. M., Henderson, B. E. P., et al. (2017). Autologous Minced Muscle Grafts Improve Endogenous Fracture Healing and Muscle Strength after Musculoskeletal Trauma. *Physiol. Rep.* 5, e13362. doi:10.14814/phy2.13362

Iismaa, S. E., Kaidonis, X., Nicks, A. M., Bogush, N., Kikuchi, K., Naqvi, N., et al. (2018). Comparative Regenerative Mechanisms across Different Mammalian Tissues. *Npj Regen. Med.* 3, 1–20. doi:10.1038/s41536-018-0044-5

Jacinto, A., Martinez-Arias, A., and Martin, P. (2001). Mechanisms of Epithelial Fusion and Repair. *Nat. Cel Biol.* 3, E117–E123. doi:10.1038/35074643

Jha, A. K., Mathur, A., Svedlund, F. L., Ye, J., Yeghiazarians, Y., and Healy, K. E. (2015). Molecular Weight and Concentration of Heparin in Hyaluronic Acid-Based Matrices Modulates Growth Factor Retention Kinetics and Stem Cell Fate. *J. Control Release* 209, 308–316. doi:10.1016/j.jconrel.2015.04.034

Jin, Y., Shahriari, D., Jeon, E. J., Park, S., Choi, Y. S., Back, J., et al. (2021). Functional Skeletal Muscle Regeneration with Thermally Drawn Porous Fibers and Reprogrammed Muscle Progenitors for Volumetric Muscle Injury. *Adv. Mater.* 33, 2007946. doi:10.1002/adma.202007946

Kelly, R. (2016). "Keratins in Wound Healing," in *Wound Healing Biomaterials* (Elsevier), 353–365. doi:10.1016/B978-1-78242-456-7.00017-9

Kim, J. Y., and Suh, W. (2010). Stem Cell Therapy for Dermal Wound Healing. *Int. J. Stem Cell* 3, 29–31. doi:10.15283/ijsc.2010.3.1.29

Kinsey, G. R., Sharma, R., Huang, L., Li, L., Vergis, A. L., Ye, H., et al. (2009). Regulatory T Cells Suppress Innate Immunity in Kidney Ischemia-Reperfusion Injury. *Jasn* 20, 1744–1753. doi:10.1681/ASN.2008111160

Krzyszczyk, P., Schloss, R., Palmer, A., and Berthiaume, F. (2018). The Role of Macrophages in Acute and Chronic Wound Healing and Interventions to Promote Pro-wound Healing Phenotypes. *Front. Physiol.* 9, 419. doi:10.3389/fphys.2018.00419

Kuo, Y.-R., Chen, C.-C., Goto, S., Lin, P.-Y., Wei, F.-C., and Chen, C.-L. (2012). Mesenchymal Stem Cells as Immunomodulators in a Vascularized Composite Allotransplantation. *Clin. Dev. Immunol.* 2012, 854846. doi:10.1155/2012/854846

Landén, N. X., Li, D., and Ståhle, M. (2016). Transition from Inflammation to Proliferation: A Critical Step During Wound Healing. *Cell. Mol. Life Sci.* 73 (20), 3861–3885. doi:10.1007/s00018-016-2268-0

Lee, H., Ju, Y. M., Kim, I., Elsangeedy, E., Lee, J. H., Yoo, J. J., et al. (2020). A Novel Decellularized Skeletal Muscle-Derived ECM Scaffolding System for *In Situ* Muscle Regeneration. *Methods* 171, 77–85. doi:10.1016/j.ymeth.2019.06.027

Li, J., Zhang, Y.-P., and Kirsner, R. S. (2003). Angiogenesis in Wound Repair: Angiogenic Growth Factors and the Extracellular Matrix. *Microsc. Res. Tech.* 60, 107–114. doi:10.1002/jemt.10249

Lisovsky, A., and Sefton, M. V. (2016). Shh Pathway in Wounds in Non-diabetic Shh-Cre-eGFP/Ptch1-LacZ Mice Treated with MAA Beads. *Biomaterials* 102, 198–208. doi:10.1016/j.biomaterials.2016.06.027

Lisovsky, A., Chamberlain, M. D., Wells, L. A., and Sefton, M. V. (2015). Cell Interactions with Vascular Regenerative MAA-Based Materials in the Context of Wound Healing. *Adv. Healthc. Mater.* 4, 2375–2387. doi:10.1002/adhm.201500192

Liu, Y., Li, Y., Li, N., Teng, W., Wang, M., Zhang, Y., et al. (2016). TGF-β1 Promotes Scar Fibroblasts Proliferation and Transdifferentiation via Up-Regulating MicroRNA-21. *Sci. Rep.* 6, 1–9. doi:10.1038/srep32231

Mann, B. K., Gobin, A. S., Tsai, A. T., Schmedlen, R. H., and West, J. L. (2001). Smooth Muscle Cell Growth in Photopolymerized Hydrogels with Cell Adhesive and Proteolytically Degradable Domains: Synthetic ECM Analogs for Tissue Engineering. *Biomaterials* 22, 3045–3051. doi:10.1016/S0142-9612(01)00051-5

Mann, C. J., Perdiguero, E., Kharraz, Y., Aguilar, S., Pessina, P., Serrano, A. L., et al. (2011). Aberrant Repair and Fibrosis Development in Skeletal Muscle. *Skeletal Muscle* 1, 1–20. doi:10.1186/2044-5040-1-21

Mao, X., Cheng, R., Zhang, H., Bae, J., Cheng, L., Zhang, L., et al. (2019). Self-Healing and Injectable Hydrogel for Matching Skin Flap Regeneration. *Adv. Sci.* 6, 1801555. doi:10.1002/advs.201801555

Mariani, E., Lisignoli, G., Borzì, R. M., and Pulsatelli, L. (2019). Biomaterials: Foreign Bodies or Tuners for the Immune Response? *Ijms* 20, 636. doi:10.3390/ijms20030636

Martin, D. C., Semple, J. L., and Sefton, M. V. (2010). Poly(methacrylic Acid-Co-Methyl Methacrylate) Beads Promote Vascularization and Wound Repair in Diabetic Mice. *J. Biomed. Mater. Res.* 9999A, 429–484. doi:10.1002/jbm.a.32528

Martinez-Sanchez, M. E., Huerta, L., Alvarez-Buylla, E. R., and Villarreal Luján, C. (2018). Role of Cytokine Combinations on CD4+ T Cell Differentiation, Partial Polarization, and Plasticity: Continuous Network Modeling Approach. *Front. Physiol.* 9, 877. doi:10.3389/fphys.2018.00877

Matthias, N., Hunt, S. D., Wu, J., Lo, J., Smith Callahan, L. A., Li, Y., et al. (2018). Volumetric Muscle Loss Injury Repair Using *In Situ* Fibrin Gel Cast Seeded with Muscle-Derived Stem Cells (MDSCs). *Stem Cel Res.* 27, 65–73. doi:10.1016/j.scr.2018.01.008

McKeon-Fischer, K. D., Flagg, D. H., and Freeman, J. W. (2011). Coaxial Electrospun Poly(ε-Caprolactone), Multiwalled Carbon Nanotubes, and Polyacrylic Acid/polyvinyl Alcohol Scaffold for Skeletal Muscle Tissue Engineering. *J. Biomed. Mater. Res.* 99A, 493–499. doi:10.1002/jbm.a.33116

McNally, A. K., and Anderson, J. M. (1995). Interleukin-4 Induces Foreign Body Giant Cells from Human Monocytes/macrophages. Differential Lymphokine Regulation of Macrophage Fusion Leads to Morphological Variants of Multinucleated Giant Cells. *Am. J. Pathol.* 147, 1487–1499. Available at: /pmc/articles/PMC1869534/?report=abstract (Accessed June 23, 2021).

Medzhitov, R. (2008). Origin and Physiological Roles of Inflammation. *Nature* 454, 428–435. doi:10.1038/nature07201

Miguel, S. P., Sequeira, R. S., Moreira, A. F., Cabral, C. S. D., Mendonça, A. G., Ferreira, P., et al. (2019). An Overview of Electrospun Membranes Loaded with Bioactive Molecules for Improving the Wound Healing Process. *Eur. J. Pharm. Biopharm.* 139, 1–22. doi:10.1016/j.ejpb.2019.03.010

Miller, K. M., and Anderson, J. M. (1989). *In Vitro* stimulation of Fibroblast Activity by Factors Generated from Human Monocytes Activated by Biomedical Polymers. *J. Biomed. Mater. Res.* 23, 911–930. doi:10.1002/jbm.820230808

Minutti, C. M., Knipper, J. A., Allen, J. E., and Zaiss, D. M. W. (2017). Tissue-specific Contribution of Macrophages to Wound Healing. *Semin. Cel Dev. Biol.* 61, 3–11. doi:10.1016/j.semcdb.2016.08.006

Mödinger, Y., Teixeira, G., Neidlinger-Wilke, C., and Ignatius, A. (2018). Role of the Complement System in the Response to Orthopedic Biomaterials. *Ijms* 19, 3367. doi:10.3390/ijms19113367

Muire, P. J., Mangum, L. H., and Wenke, J. C. (2020). Time Course of Immune Response and Immunomodulation during Normal and Delayed Healing of Musculoskeletal Wounds. *Front. Immunol.*, 11, 1056. doi:10.3389/fimmu.2020.01056

Nami, N., Feci, L., Napoliello, L., Giordano, A., Lorenzini, S., Galeazzi, M., et al. (2016). Crosstalk between Platelets and PBMC: New Evidence in Wound Healing. *Platelets* 27, 1–6. doi:10.3109/09537104.2015.1048216

Narayanan, N., Jiang, C., Wang, C., Uzunalli, G., Whittern, N., Chen, D., et al. (2020). Harnessing Fiber Diameter-dependent Effects of Myoblasts toward Biomimetic Scaffold-Based Skeletal Muscle Regeneration. *Front. Bioeng. Biotechnol.* 8, 203. doi:10.3389/fbioe.2020.00203

Nissinen, L. M., and Kähäri, V.-M. (2015). Collagen Turnover in Wound Repair--A Macrophage Connection. *J. Invest. Dermatol.* 135, 2350–2352. doi:10.1038/jid.2015.246

Jiang, D., Liang, J., and Noble, P. W. (2011). Hyaluronan as an Immune Regulator in Human Diseases. *Physiol. Rev.* 91, 221–264. doi:10.1152/physrev.00052.2009

Nourian Dehkordi, A., Mirahmadi Babaheydari, F., Chehelgerdi, M., and Raeisi Dehkordi, S. (2019). Skin Tissue Engineering: Wound Healing Based on Stem-Cell-Based Therapeutic Strategies. *Stem Cel Res. Ther.* 10, 1–20. doi:10.1186/s13287-019-1212-2

Nurden, A. T., Nurden, P., Sanchez, M., Andia, I., and Anitua, E. (2008). Platelets and Wound Healing. *Front. Biosci.* 13, 3525–3548. doi:10.2741/2947

Nussbaum, S. R., Carter, M. J., Fife, C. E., DaVanzo, J., Haught, R., Nusgart, M., et al. (2018). An Economic Evaluation of the Impact, Cost, and Medicare Policy Implications of Chronic Nonhealing Wounds. *Value in Health* 21, 27–32. doi:10.1016/j.jval.2017.07.007

Nyström, A., Velati, D., Mittapalli, V. R., Fritsch, A., Kern, J. S., and Bruckner-Tuderman, L. (2013). Collagen VII Plays a Dual Role in Wound Healing. *J. Clin. Invest.* 123, 3498–3509. doi:10.1172/JCI68127

Oishi, Y., and Manabe, I. (2018). Macrophages in Inflammation, Repair and Regeneration. *Int. Immunol.* 30, 511–528. doi:10.1093/intimm/dxy054

Ondeck, M. G., and Engler, A. J. (2016). Mechanical Characterization of a Dynamic and Tunable Methacrylated Hyaluronic Acid Hydrogel. *J. Biomech. Eng.* 138, 1–6. doi:10.1115/1.4032429

Padmore, T., Stark, C., Turkevich, L. A., and Champion, J. A. (2017). Quantitative Analysis of the Role of Fiber Length on Phagocytosis and Inflammatory Response by Alveolar Macrophages. *Biochim. Biophys. Acta (Bba) - Gen. Subj.* 1861, 58–67. doi:10.1016/j.bbagen.2016.09.031

Patapoutian, A., Tate, S., and Woolf, C. J. (2009). Transient Receptor Potential Channels: Targeting Pain at the Source. *Nat. Rev. Drug Discov.* 8, 55–68. doi:10.1038/nrd2757

Politi, S., Carotenuto, F., Rinaldi, A., Di Nardo, P., Manzari, V., Albertini, M. C., et al. (2020). Smart ECM-Based Electrospun Biomaterials for Skeletal Muscle Regeneration. *Nanomaterials* 10, 1–19. doi:10.3390/nano10091781

Pollini, M., and Paladini, F. (2020). Bioinspired Materials for Wound Healing Application: The Potential of Silk Fibroin. *Materials* 13, 3361. doi:10.3390/ma13153361

Pumberger, M., Qazi, T. H., Ehrentraut, M. C., Textor, M., Kueper, J., Stoltenburg-Didinger, G., et al. (2016). Synthetic Niche to Modulate Regenerative Potential of MSCs and Enhance Skeletal Muscle Regeneration. *Biomaterials* 99, 95–108. doi:10.1016/j.biomaterials.2016.05.009

Raphael, I., Nalawade, S., Eagar, T. N., and Forsthuber, T. G. (2015). T Cell Subsets and Their Signature Cytokines in Autoimmune and Inflammatory Diseases. *Cytokine* 74, 5–17. doi:10.1016/j.cyto.2014.09.011

Raziyeva, K., Kim, Y., Zharkinbekov, Z., Kassymbek, K., Jimi, S., and Saparov, A. (2021). Immunology of Acute and Chronic Wound Healing. *Biomolecules* 11, 700. doi:10.3390/biom11050700

Rodero, M. P., Hodgson, S. S., Hollier, B., Combadiere, C., and Khosrotehrani, K. (2013). Reduced Il17a Expression Distinguishes a Ly6c Lo MHCII Hi Macrophage Population Promoting Wound Healing. *J. Invest. Dermatol.* 133, 783–792. doi:10.1038/jid.2012.368

Rognoni, E., and Watt, F. M. (2018). Skin Cell Heterogeneity in Development, Wound Healing, and Cancer. *Trends Cel Biol.* 28, 709–722. doi:10.1016/j.tcb.2018.05.002

Sadtler, K., Estrellas, K., Allen, B. W., Wolf, M. T., Fan, H., Tam, A. J., et al. (2016). Developing a Pro-regenerative Biomaterial Scaffold Microenvironment Requires T Helper 2 Cells. *Science* 352, 366–370. doi:10.1126/science.aad9272

Sahana, T. G., and Rekha, P. D. (2018). Biopolymers: Applications in Wound Healing and Skin Tissue Engineering. *Mol. Biol. Rep.* 45, 2857–2867. doi:10.1007/s11033-018-4296-3

Sahoo, D. R., and Biswal, T. (2021). Alginate and its Application to Tissue Engineering. *SN Appl. Sci.* 3, 1–19. doi:10.1007/s42452-020-04096-w

Sass, F., Fuchs, M., Pumberger, M., Geissler, S., Duda, G., Perka, C., et al. (2018). Immunology Guides Skeletal Muscle Regeneration. *Ijms* 19, 835. doi:10.3390/ijms19030835

Sasaki, M., Abe, R., Fujita, Y., Ando, S., Inokuma, D., and Shimizu, H. (2008). Mesenchymal Stem Cells Are Recruited into Wounded Skin and Contribute to Wound Repair by Transdifferentiation into Multiple Skin Cell Type. *J. Immunol.* 180, 2581–2587. doi:10.4049/jimmunol.180.4.2581

Saxena, A. K., Marler, J., Benvenuto, M., Willital, G. H., and Vacanti, J. P. (1999). Skeletal Muscle Tissue Engineering Using Isolated Myoblasts on Synthetic Biodegradable Polymers: Preliminary Studies. *Tissue Eng.* 5, 525–531. doi:10.1089/ten.1999.5.525

Schmelz, M., and Petersen, L. J. (2001). Neurogenic Inflammation in Human and Rodent Skin. *Physiology* 16, 33–37. doi:10.1152/physiologyonline.2001.16.1.33

Schultz, G. S., and Wysocki, A. (2009). Interactions between Extracellular Matrix and Growth Factors in Wound Healing. *Wound Repair Regen.* 17, 153–162. doi:10.1111/j.1524-475X.2009.00466.x

Schuurmans, C. C. L., Mihajlovic, M., Hiemstra, C., Ito, K., Hennink, W. E., and Vermonden, T. (2021). Hyaluronic Acid and Chondroitin Sulfate (Meth) Acrylate-Based Hydrogels for Tissue Engineering: Synthesis, Characteristics and Pre-Clinical Evaluation. *Biomaterials* 268, 120602. doi:10.1016/j.biomaterials.2020.120602

Sheikh, Z., Brooks, P., Barzilay, O., Fine, N., and Glogauer, M. (2015). Macrophages, Foreign Body Giant Cells and Their Response to Implantable Biomaterials. *Materials* 8, 5671–5701. doi:10.3390/ma8095269

Shook, B. A., Wasko, R. R., Rivera-Gonzalez, G. C., Salazar-Gatzimas, E., López-Giráldez, F., Dash, B. C., et al. (2018). Myofibroblast Proliferation and Heterogeneity Are Supported by Macrophages during Skin Repair. *Science* 362, eaar2971. doi:10.1126/science.aar2971

Sicari, B. M., Dziki, J. L., Siu, B. F., Medberry, C. J., Dearth, C. L., and Badylak, S. F. (2014a). The Promotion of a Constructive Macrophage Phenotype by Solubilized Extracellular Matrix. *Biomaterials* 35, 8605–8612. doi:10.1016/j.biomaterials.2014.06.060

Sicari, B. M., Rubin, J. P., Dearth, C. L., Wolf, M. T., Ambrosio, F., Boninger, M., et al. (2014b). An Acellular Biologic Scaffold Promotes Skeletal Muscle Formation in Mice and Humans with Volumetric Muscle Loss. *Sci. Transl. Med.* 6, 234ra58. doi:10.1126/scitranslmed.3008085

Sill, T. J., and von Recum, H. A. (2008). Electrospinning: Applications in Drug Delivery and Tissue Engineering. *Biomaterials* 29, 1989–2006. doi:10.1016/j.biomaterials.2008.01.011

Silva Garcia, J. M., Panitch, A., and Calve, S. (2019). Functionalization of Hyaluronic Acid Hydrogels with ECM-Derived Peptides to Control Myoblast Behavior. *Acta Biomater.* 84, 169–179. doi:10.1016/j.actbio.2018.11.030

Song, X., Dai, D., He, X., Zhu, S., Yao, Y., Gao, H., et al. (2015). Growth Factor FGF2 Cooperates with Interleukin-17 to Repair Intestinal Epithelial Damage. *Immunity* 43, 488–501. doi:10.1016/j.immuni.2015.06.024

Stanley, E. R., and Chitu, V. (2014). CSF-1 Receptor Signaling in Myeloid Cells. *Cold Spring Harbor Perspect. Biol.* 6, a021857. doi:10.1101/cshperspect.a021857

Strbo, N., Yin, N., and Stojadinovic, O. (2014). Innate and Adaptive Immune Responses in Wound Epithelialization. *Adv. Wound Care* 3, 492–501. doi:10.1089/wound.2012.0435

Sun, J., and Tan, H. (2013). Alginate-based Biomaterials for Regenerative Medicine Applications. *Materials* 6, 1285–1309. doi:10.3390/ma6041285

Sun, L., Li, J., Gao, W., Shi, M., Tang, F., Fu, X., et al. (2021). Coaxial Nanofibrous Scaffolds Mimicking the Extracellular Matrix Transition in the Wound Healing Process Promoting Skin Regeneration through Enhancing Immunomodulation. *J. Mater. Chem. B* 9, 1395–1405. doi:10.1039/d0tb01933j

Takakura, N. (2006). Role of Hematopoietic Lineage Cells as Accessory Components in Blood Vessel Formation. *Cancer Sci.* 97, 568–574. doi:10.1111/j.1349-7006.2006.00223.x

Talior-Volodarsky, I., Mahou, R., Zhang, D., and Sefton, M. (2017). The Role of Insulin Growth Factor-1 on the Vascular Regenerative Effect of MAA Coated Disks and Macrophage-Endothelial Cell Crosstalk. *Biomaterials* 144, 199–210. doi:10.1016/j.biomaterials.2017.08.019

Tamagawa-Mineoka, R. (2015). Important Roles of Platelets as Immune Cells in the Skin. *J. Dermatol. Sci.* 77, 93–101. doi:10.1016/j.jdermsci.2014.10.003

Thurber, A. E., Omenetto, F. G., and Kaplan, D. L. (2015). *In Vivo* bioresponses to Silk Proteins. *Biomaterials* 71, 145–157. doi:10.1016/j.biomaterials.2015.08.039

Tidball, J. G. (2017). Regulation of Muscle Growth and Regeneration by the Immune System. *Nat. Rev. Immunol.* 17, 165–178. doi:10.1038/nri.2016.150

Tonkin, J., Temmerman, L., Sampson, R. D., Gallego-Colon, E., Barberi, L., Bilbao, D., et al. (2015). Monocyte/macrophage-derived IGF-1 Orchestrates Murine Skeletal Muscle Regeneration and Modulates Autocrine Polarization. *Mol. Ther.* 23, 1189–1200. doi:10.1038/mt.2015.66

Uehara, M., Li, X., Sheikhi, A., Zandi, N., Walker, B., Saleh, B., et al. (2019). Anti-IL-6 Eluting Immunomodulatory Biomaterials Prolong Skin Allograft Survival. *Sci. Rep.* 9, 1–13. doi:10.1038/s41598-019-42349-w

Van Luyn, M. J. A., Khouw, I. M. S. L., Van Wachem, P. B., Blaauw, E. H., and Werkmeister, J. A. (1998). Modulation of the Tissue Reaction to Biomaterials. II. The Function of T Cells in the Inflammatory Reaction to Crosslinked Collagen Implanted in T-Cell-Deficient Rats. *J. Biomed. Mater. Res.* 39, 398–406. doi:10.1002/(sici)1097-4636(19980305)39:3<398::aid-jbm8>3.0.co;2-e

Vegas, A. J., Veiseh, O., Doloff, J. C., Ma, M., Tam, H. H., Bratlie, K., et al. (2016). Combinatorial Hydrogel Library Enables Identification of Materials that Mitigate the Foreign Body Response in Primates. *Nat. Biotechnol.* 34, 345–352. doi:10.1038/nbt.3462

Veiseh, O., Doloff, J. C., Ma, M., Vegas, A. J., Tam, H. H., Bader, A. R., et al. (2015). Size- and Shape-dependent Foreign Body Immune Response to Materials Implanted in Rodents and Non-human Primates. *Nat. Mater.* 14, 643–651. doi:10.1038/nmat4290

Voinchet, V. r., Vasseur, P., and Kern, J. r. m. (2006). Efficacy and Safety of Hyaluronic Acid in the Management of Acute Wounds. *Am. J. Clin. Dermatol.* 7, 353–357. doi:10.2165/00128071-200607060-00003

Wang, T., Luu, T. U., Chen, A., Khine, M., and Liu, W. F. (2016). Topographical Modulation of Macrophage Phenotype by Shrink-Film Multi-Scale Wrinkles. *Biomater. Sci.* 4, 948–952. doi:10.1039/c6bm00224b

Wang See, C., Kim, T., and Zhu, D. (2020). Hernia Mesh and Hernia Repair: A Review. *Eng. Regen.* 1, 19–33. doi:10.1016/j.engreg.2020.05.002

Waters, M., VandeVord, P., and Van Dyke, M. (2018). Keratin Biomaterials Augment Anti-inflammatory Macrophage Phenotype *In Vitro*. *Acta Biomater.* 66, 213–223. doi:10.1016/j.actbio.2017.10.042

Weirather, J., Hofmann, U. D. W., Beyersdorf, N., Ramos, G. C., Vogel, B., Frey, A., et al. (2014). Foxp3 + CD4 + T Cells Improve Healing after Myocardial Infarction by Modulating Monocyte/Macrophage Differentiation. *Circ. Res.* 115, 55–67. doi:10.1161/CIRCRESAHA.115.303895

Williams, D. F. (2008). On the Mechanisms of Biocompatibility. *Biomaterials* 29, 2941–2953. doi:10.1016/j.biomaterials.2008.04.023

Witherel, C. E., Abebayehu, D., Barker, T. H., and Spiller, K. L. (2019). Macrophage and Fibroblast Interactions in Biomaterial-Mediated Fibrosis. *Adv. Healthc. Mater.* 8, 1801451. doi:10.1002/adhm.201801451

Wolf, M. T., Dearth, C. L., Ranallo, C. A., LoPresti, S. T., Carey, L. E., Daly, K. A., et al. (2014). Macrophage Polarization in Response to ECM Coated Polypropylene Mesh. *Biomaterials* 35, 6838–6849. doi:10.1016/j.biomaterials.2014.04.115

Wolf, M. T., Dearth, C. L., Sonnenberg, S. B., Loboa, E. G., and Badylak, S. F. (2015). Naturally Derived and Synthetic Scaffolds for Skeletal Muscle Reconstruction. *Adv. Drug Deliv. Rev.* 84, 208–221. doi:10.1016/j.addr.2014.08.011

Wolfram, D., Rabensteiner, E., Grundtman, C., Böck, G., Mayerl, C., Parson, W., et al. (2012). T Regulatory Cells and TH17 Cells in Peri-Silicone Implant Capsular Fibrosis. *Plast. Reconstr. Surg.* 129, 327e–337e. doi:10.1097/PRS.0b013e31823aeacf

Wulff, B. C., and Wilgus, T. A. (2013). Mast Cell Activity in the Healing Wound: More Than Meets the Eye?. *Exp. Dermatol.* 22, 507–510. doi:10.1111/exd.12169

Xue, M., and Jackson, C. J. (2015). Extracellular Matrix Reorganization during Wound Healing and its Impact on Abnormal Scarring. *Adv. Wound Care* 4, 119–136. doi:10.1089/wound.2013.0485

Yamada, K. M. (2000). Fibronectin Peptides in Cell Migration and Wound Repair. *J. Clin. Invest.* 105, 1507–1509. doi:10.1172/JCI10119

Yang, H. S., Ieronimakis, N., Tsui, J. H., Kim, H. N., Suh, K.-Y., Reyes, M., et al. (2014). Nanopatterned Muscle Cell Patches for Enhanced Myogenesis and Dystrophin Expression in a Mouse Model of Muscular Dystrophy. *Biomaterials* 35, 1478–1486. doi:10.1016/j.biomaterials.2013.10.067

Zaiss, D. M., Minutti, C. M., and Knipper, J. A. (2019). Immune- and Non-immune-mediated Roles of Regulatory T-cells during Wound Healing. *Immunology* 157, 190–197. doi:10.1111/imm.13057

Zhang, D., Chen, Q., Shi, C., Chen, M., Ma, K., Wan, J., et al. (2021). Dealing with the Foreign-Body Response to Implanted Biomaterials: Strategies and Applications of New Materials. *Adv. Funct. Mater.* 31, 2007226. doi:10.1002/adfm.202007226

Zhao, Q., Ren, H., and Han, Z. (2016). Mesenchymal Stem Cells: Immunomodulatory Capability and Clinical Potential in Immune Diseases. *J. Cell Immunother.* 2, 3–20. doi:10.1016/j.jocit.2014.12.001

Zhou, T., Wang, N., Xue, Y., Ding, T., Liu, X., Mo, X., et al. (2016). Electrospun tilapia Collagen Nanofibers Accelerating Wound Healing via Inducing Keratinocytes Proliferation and Differentiation. *Colloids Surf. B: Biointerfaces* 143, 415–422. doi:10.1016/j.colsurfb.2016.03.052

Zhu, Y., Ma, Z., Kong, L., He, Y., Chan, H. F., and Li, H. (2020). Modulation of Macrophages by Bioactive Glass/Sodium Alginate Hydrogel Is Crucial in Skin Regeneration Enhancement. *Biomaterials* 256, 120216. doi:10.1016/j.biomaterials.2020.120216

Conflict of Interest: The authors declare that the research was conducted in the absence of any commercial or financial relationships that could be construed as a potential conflict of interest.

Publisher's Note: All claims expressed in this article are solely those of the authors and do not necessarily represent those of their affiliated organizations, or those of the publisher, the editors and the reviewers. Any product that may be evaluated in this article, or claim that may be made by its manufacturer, is not guaranteed or endorsed by the publisher.

frontiers in Bioengineering and Biotechnology

ORIGINAL RESEARCH
published: 28 February 2022
doi: 10.3389/fbioe.2022.749787

Human Growth Factor/ Immunoglobulin Complexes for Treatment of Myocardial Ischemia-Reperfusion Injury

Benjamin Liebman[1,2†], *Claire Schwaegler*[1†], *Andrea T. Foote*[3], *Krithika S. Rao*[1], *Taylor Marquis*[1], *Alexander Aronshtam*[1], *Stephen P. Bell*[1], *Prospero Gogo*[1], *Richard R. LaChapelle*[1] *and Jeffrey L. Spees*[1,3*]

[1]Department of Medicine, Cardiovascular Research Institute, University of Vermont, Colchester, VT, United States, [2]Pharmacology Graduate Program, University of Vermont, Burlington, VT, United States, [3]Cellular and Molecular Biomedical Sciences Program, University of Vermont, Burlington, VT, United States

OPEN ACCESS

Edited by:
Ryang Hwa Lee,
Texas A&M University, United States

Reviewed by:
Carolina Balbi,
University of Zurich, Switzerland
Fei Liu,
Texas A&M University, United States

***Correspondence:**
Jeffrey L. Spees
jspees@uvm.edu

[†]*These authors have contributed equally to this work*

Specialty section:
This article was submitted to Tissue Engineering and Regenerative Medicine, a section of the journal Frontiers in Bioengineering and Biotechnology

Received: *29 July 2021*
Accepted: *26 January 2022*
Published: *28 February 2022*

Citation:
Liebman B, Schwaegler C, Foote AT, Rao KS, Marquis T, Aronshtam A, Bell SP, Gogo P, LaChapelle RR and Spees JL (2022) Human Growth Factor/Immunoglobulin Complexes for Treatment of Myocardial Ischemia-Reperfusion Injury. Front. Bioeng. Biotechnol. 10:749787. doi: 10.3389/fbioe.2022.749787

Hepatocyte Growth Factor (HGF) and Fibroblast Growth Factor 2 (FGF2) are receptor tyrosine kinase agonists that promote cell survival after tissue injury and angiogenesis, cell proliferation and migration during tissue repair and regeneration. Both ligands have potential as systemic treatments for ischemia-reperfusion injury, however clinical use of HGF and FGF2 has been limited by poor pharmacokinetic profiles, i.e., their susceptibility to serum proteases, rapid clearance and short half-lives. Previously, we reported vaso- and cardioprotective protein complexes formed between HGF and polyclonal, non-specific immunoglobulin (IgG) with therapeutic efficacy in a rat model of myocardial ischemia with reperfusion (MI/R). Here, using a pre-clinical porcine MI/R model, we demonstrate human HGF/IgG complexes provide significant myocardial salvage, reduce infarct size, and are detectable in myocardial tissue 24 h after intracoronary injection. Furthermore, we show that multiple daily infusions of HGF/IgG complexes after MI do not lead to production of HGF-specific auto-antibodies, an important concern for administered biologic drugs. In experiments to identify other growth factors that non-covalently interact with IgG, we found that human FGF2 associates with IgG. Similar to human HGF/IgG complexes, FGF2/IgG complexes protected primary human cardiac endothelial cells under simulated ischemia (1% oxygen and nutrient deprivation) for 48–72 h. Molecular modeling studies suggested that FGF2 and HGF both interact with the Fc domain of IgG. Also, we tested whether an Fc-fusion protein would bind FGF2 to form complexes. By native gel electrophoretic assays and biochemical pulldowns, we found that Jagged1, a Notch1 ligand that controls stem cell self-renewal and tissue regeneration, bound FGF2 when presented as a Jagged1- Fc fusion protein. Our results suggest that human growth factor/IgG and FGF2/Fc- fusion complexes have potential to provide a biologics platform to treat myocardial ischemia-reperfusion and other forms of tissue injury.

Keywords: growth factor, protein complex, HGF, FGF2, IgG, reperfusion injury, ischemia

INTRODUCTION

Cardiovascular disease is the leading cause of death worldwide, accounting for 31% of all deaths and the loss of nine million people annually (Virani et al., 2020). Of these deaths, about 50% are attributed to coronary heart disease (Smith et al., 2015). Coronary heart disease (CHD) is the umbrella term for pathologies affecting the ability of the epicardial coronary arteries to provide oxygenated blood and nutrients to the heart (Vogel et al., 2019). Significant and sustained imbalance between coronary oxygen supply and demand results in myocardial ischemia and the progressive death of cardiomyocytes, termed myocardial infarction or MI (Eisen, Giugliano et al., 2016; Anderson and Morrow, 2017). In the United States, the estimated annual incidence of MI is 605,000 new heart attacks and 200,000 recurrent heart attacks; this equates to an American suffering a heart attack every 40 s (Virani et al., 2020).

Rapid and early reperfusion of ischemic myocardium prevents cardiomyocyte death and has been the most effective treatment for preserving jeopardized myocardial tissue and limiting infarct size (Virani et al., 2020). Accordingly, the current standard of care is coronary revascularization, achieved through primary Percutaneous Coronary Intervention (PCI) (O'Gara et al., 2013) or administration of fibrinolytic agents (e.g., Alteplase, Tenecteplase), which enzymatically break down blood clots (Schneider and Sobel, 2008). PCI typically involves catheterization of the femoral or radial artery and catheter insertion into the occluded coronary artery, followed by inflation of an angioplasty balloon with an expandable wire cage (stent), which mechanically opens the vessel. The stent remains in place to stabilize the damaged artery after the balloon is deflated and the catheter is removed. Primary PCI is the most common strategy for revascularization and preferred over fibrinolytic therapy for patients when time-to-treatment delays are relatively short (<120 min), treatment at hospital with a catheterization laboratory is available, and the duration of ischemia is <12 h (O'Gara et al., 2013; Bagai et al., 2014).

Revascularization of the epicardial coronaries is important for patient survival after MI. Paradoxically, however, myocardial reperfusion also causes injury, killing vascular endothelial cells, cardiomyocytes and other vulnerable cells, which greatly reduces the benefits of reperfusion therapy (Yellon and Hausenloy, 2007). Lethal reperfusion injury, or the injury and eventual death of cardiomyocytes that were viable immediately prior to reperfusion, contributes up to 50% of final infarct size (Garcia-Dorado et al., 2009). In addition to PCI and thrombolysis to treat MI, reperfusion injury also occurs during coronary artery bypass (CABG) procedures and heart transplantation (Verma et al., 2002).

Growth factor-based treatments for ischemia-reperfusion and tissue injury have been studied in numerous animal models and proof-of-concept clinical trials that demonstrated positive safety profiles. But most growth factors administered intra-arterially or IV exhibited unfavorable pharmacokinetics (e.g., short half-lives and rapid clearance) and limited efficacy (Appasamy et al., 1993; Lazarous et al., 1997; Simons et al., 2002; Yang et al., 2009). Treatment with factors such as fibroblast growth factor 2 (FGF2)

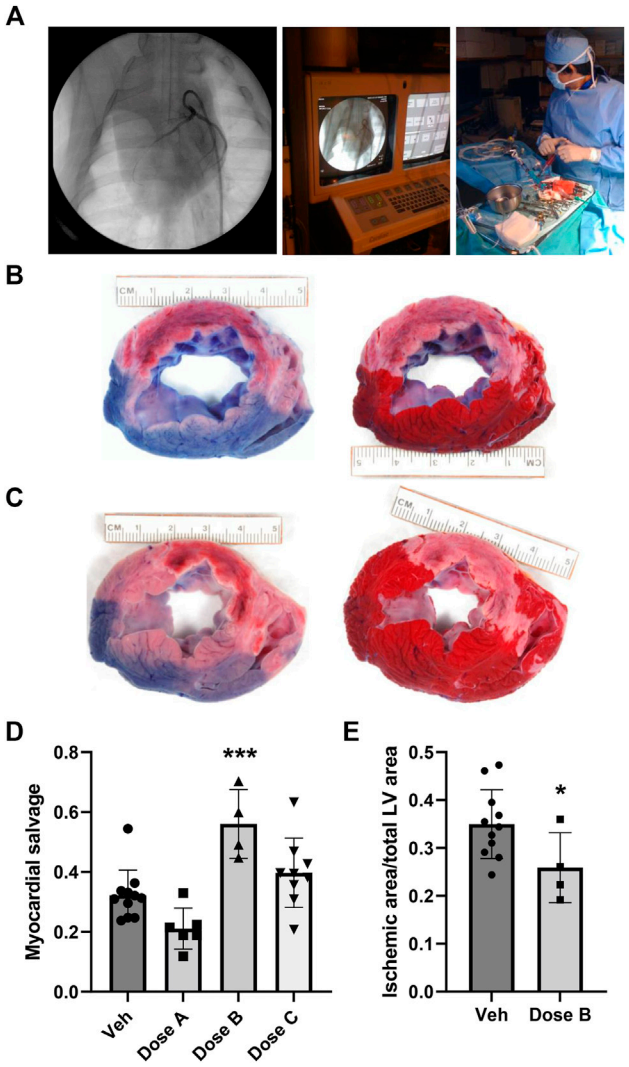

FIGURE 1 | Intracoronary administration of human HGF/IgG complexes from the PCI guide catheter in a pre-clinical porcine model of MI with reperfusion. **(A)** Left, middle: Representative images from fluoroscopic angiography showing guide catheter with contrast dye. Right: Intracoronary infusion of HGF/IgG complexes or vehicle from the indwelling guide catheter at time of reperfusion (60 min post-ischemia). Pigs were treated with 62.5 μg HGF and 105 μg mixed polyclonal IgG, representing a 1: 1: molar ratio. **(B,C)** Left: At 24 h after MI, reperfusion, and treatment, Evan's blue dye stain shows areas with adequate perfusion (blue) and low perfusion (pink; a.k.a. area at risk, AAR) in representative vehicle-treated heart section **(B)** and HGF/IgG-treated heart section **(C)**. Right: TTC stain shows living muscle tissue (red) and necrotic, dying tissue (white; a.k.a. ischemic area, IA). **(D)** Quantification of myocardial salvage following MI/R and treatment with vehicle or three different doses of HGF/IgG complexes (Dose A, 31.25 μg HGF/52.5 μg IgG; Dose B, 62.5 μg HGF/105 μg IgG; Dose C, 125 μg HGF/210 μg IgG. One-way ANOVA with multiple comparisons. ***$p < 0.001$. Myocardial salvage = AAR-IA/AAR. **(E)** Reduction in area of myocardial tissue with infarction, 24 h after MI/R and treatment with Dose B. Data are mean ± SD. n = 4–11 pigs per group. 2-tailed, unpaired T test. *$p = 0.05$.

or hepatocyte growth factor (HGF) is highly attractive due to their potential for synergistic signaling through common protective and pro-survival pathways such as Ras/MAPK and/or PI3K/Akt (Liao et al., 2007; Banquet et al., 2011; Koraishy et al., 2014; Barć et al., 2020). The engagement of these pathways in myocardium with infarction has potential to protect vulnerable cardiomyocytes and endothelial cells from death, reduce vascular leak, and encourage angiogenesis for repair and regeneration.

Previously, our research group identified HGF/immunoglobulin (IgG) complexes in medium that was conditioned by human epicardial-derived cells (Rao et al., 2015). HGF/IgG protein complexes that we formed by ultracentrifugal concentration of recombinant, active human HGF and polyclonal IgG uniquely protected vascular endothelial cells from ischemic injury by signaling through c-Met, the HGF receptor, and by triggering phosphorylation of "related to tyrosine kinase" (RYK), an orphan Wnt co-receptor. Furthermore, in a rat model of myocardial ischemia with reperfusion, we found that intra-arterial treatment with HGF/IgG complexes significantly improved vascular integrity and cardiac function (Rao et al., 2015).

Here we provide additional *in vivo* data for myocardial salvage, infarct size, and distribution and retention of HGF/IgG complexes using a pre-clinical, large animal model with PCI, as well as data showing lack of immunogenicity following multiple administrations after MI with reperfusion. Also, we report the development of two new growth factor protein complexes comprised of low molecular weight (18 kDa) human FGF2 with IgG or Jagged1-Fc fusion protein.

RESULTS

Localization of HGF/IgG Complexes in Myocardial Tissue 24 h Following Infusion From PCI Guide Catheter After MI/R

When administered IV, HGF has a plasma half-life of ~3.8 min and is primarily taken up by the liver (Appasamy et al., 1993). To determine whether intracoronary delivery of human HGF/IgG complexes would improve retention and/or tissue distribution, as opposed to rapid clearance, we performed MI/R surgery in pigs. To mimic a clinical delivery scenario, we used a femoral artery access and PCI guide catheters, wires, angioplasty balloons and stents commonly used for interventional procedures at UVM Medical Center. Under fluoroscopic guidance, we advanced the catheters through the aorta and into the left anterior descending (LAD) (**Figure 1A**). By injecting contrast dye, we estimated the relative degree of dominance for the ventricular blood supply coming from the left circumflex artery and the LAD. Accordingly, the balloon was placed over the guide wire at the first or second diagonal branch of the LAD, inflated, and then left inflated for 60 min to occlude the artery and produce ischemic injury. Immediately upon reperfusion, we infused 12.5 ml of DMEM medium (vehicle) or 12.5 ml DMEM with HGF/IgG complexes into the coronary from the indwelling guide catheter. The total time of infusion was ~2 min.

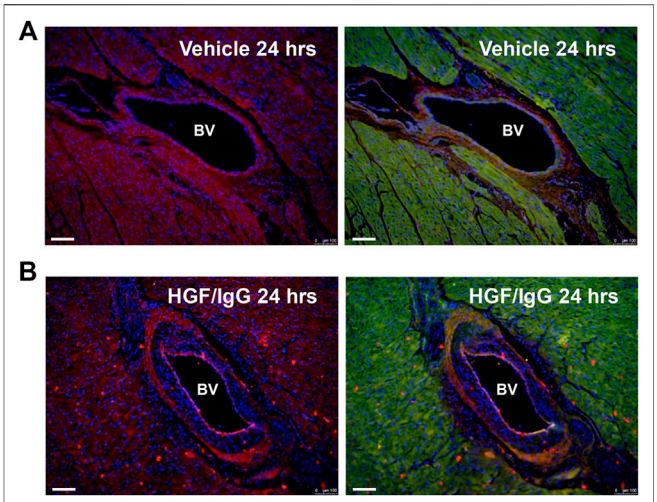

FIGURE 2 | Vascular and myocardial distribution of HGF/IgG complexes 24 h after intracoronary infusion. Note red dots (ALEXA 594-conjugated secondary antibody) on endothelial wall and throughout myocardium in **(B)** that are not present in vehicle-treated heart **(A)**. Prior to staining with secondary antisera and DAPI (blue, nuclei), both **(A)** and **(B)** were stained with polyclonal primary antisera against 6x His-tag to detect recombinant human HGF. Hearts in **(A)** and **(B)** are representative of n = 3 pigs per group that were stained.

After 24 h, pigs were intubated and re-anesthetized. Prior to euthanization, a suture was used to ligate the LAD at the proximal end of the stent and Evan's blue dye was infused to delineate areas of perfusion and risk (**Figures 1B,C**). Hearts were then removed, sliced at 1 cm thickness, and stained with TTC to identify areas of necrosis (**Figures 1B,C**). The sections were digitally-photographed and fixed in formalin for paraffin processing, sectioning and histology. Using Scion Image software, an observer blinded to sample/slide ID determined the area at risk (AAR) and ischemic area (IA), as well as total left ventricle (LV) area. We assayed hearts from pigs treated with three different doses of HGF/IgG, each matched at a 1:1 molar ratio. Compared with vehicle, a single intracoronary dose containing 62.5 μg of human HGF with 105 μg porcine IgG provided a significant degree of myocardial salvage (AAR-IA/AAR) at 24 h after MI/R and intracoronary treatment (**Figure 1D**). The 62.5 μg HGF dose also significantly reduced infarct size, as shown by ischemic area (i.e., necrotic tissue)/total LV area (**Figure 1E**).

We used immunohistochemistry with antisera against the 6x-His tag on our recombinant human HGF to detect the HGF/IgG complexes in tissue sections (**Figures 2A,B**). Staining of left ventricular myocardial tissue bordering zones with infarction demonstrated a wide-spread distribution of HGF/IgG complexes; this pattern was associated with the microvasculature and arterioles as well as within myocardial tissue (n = 3 pigs, **Figure 2B**). As expected, similar staining of vehicle-treated control pigs did not identify any complexes and lacked the

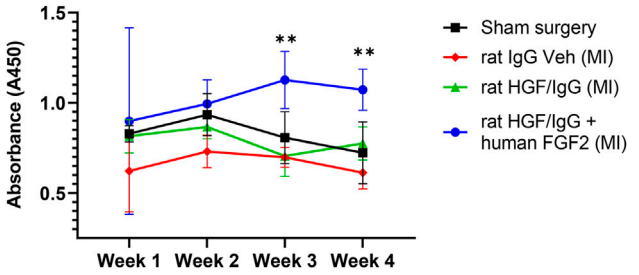

FIGURE 3 | Multiple administrations of HGF/IgG complexes do not induce HGF- specific auto-antibodies in rats subjected to myocardial ischemia-reperfusion. After MI/R surgery or sham surgery, blood plasma was obtained from rats weekly and assessed for circulating antibodies specific to rat HGF. Animals received three separate treatments: one at reperfusion, one on day 3, and one on day 5 post-MI/R with either vehicle (containing IgG), or HGF/IgG. HGF/IgG-treated animals showed no auto-immune reactivity to HGF. However, weekly addition of human FGF2 to HGF/IgG complexes (positive xenogenic control) induced antibodies to rat HGF, as shown by a mild immune response at weeks 3 and 4. Data represent mean ± SD and were analyzed by repeated measures two-way ANOVA. n = 5 animals, $^{**}p < 0.01$.

spotty pattern of complexes throughout the myocardium (n = 3 pigs, **Figure 2A**).

Multiple IV Infusions of HGF/IgG Complexes After MI Do Not Induce Production of Circulating HGF-Specific Auto-Antibodies

Autoimmune reaction is an important concern for clinical application of antibody-based biologics (Her and Kavanaugh, 2016). To examine the potential immunogenicity of HGF/IgG complexes in the context of MI with reperfusion, we performed a set of experiments in Sprague Dawley rats to test for the production of auto-antibodies directed against HGF. Groups of adult rats underwent surgery to temporarily occlude the LAD artery for 2 h, followed by reperfusion. With the use of echocardiography, we confirmed cardiac injury in all rats 1 week after MI, and M-mode images obtained at 2, 3, and 4 weeks after MI demonstrated decreased LV wall thickness, consistent with myocardial damage and necrosis (data not shown).

To form HGF/IgG complexes, we mixed recombinant rat HGF with polyclonal rat IgG and concentrated 40-fold by centrifugation with an ultracentrifugal filter unit. As a positive control for immune reactivity, one group of rats received rat HGF/rat IgG with recombinant human FGF2 added to the complexes. We expected that multiple administrations with a xenogenic protein mixture would facilitate detection of circulating antibodies directed against rat HGF (i.e., auto-antibodies). Immediately after reperfusion, we administered HGF/IgG complexes, HGF/IgG complexes with human FGF2, or IgG alone (vehicle control) to three groups of rats. All treatments were infused directly into the LV lumen through the apex (i.e., intra-arterial). Subsequently, all rats received two additional "booster" injections by tail vein on days 3 and 5 after MI. Blood plasma was obtained at weekly intervals post-surgery for 4 weeks. Using a modified ELISA system, we determined that animals treated with rat HGF/IgG (n = 5) exhibited no autoimmune activity at any of the time points analyzed (**Figure 3**). By contrast, compared with vehicle-treated controls, rats infused with rat HGF/IgG complexes and human FGF2 (n = 5) exhibited a mild immune response at 3 and 4 weeks following MI and treatment (**Figure 3**). These results indicate administered growth factor/IgG complexes may be well-tolerated, particularly with a limited number of infusions and if species-matched for immune compatibility.

Identification of FGF2/IgG Complexes That Protect Human Cardiac Microvascular Endothelial Cells During Simulated Ischemia

Previously, we demonstrated that a mixture of HGF and IgG (1:1 molar ratio) formed protein complexes after 40-fold concentration by centrifugation in Amicon ultracentrifugal filter units (Rao et al., 2015). To investigate whether FGF2 interacted non-covalently (i.e., electrostatically) with IgG, we similarly incubated human FGF2 (LMW isoform, 18 kDa) with IgG in a 1:1 molar ratio and incubated the mixture for 30 min at room temperature. Following 40-fold concentration with Amicon units, the samples were evaluated by native agarose gel electrophoresis as in Rao et al. (2015).

During native gel electrophoresis, protein separation occurs primarily by differences in isoelectric point rather than by size. After electrophoresis of free FGF2, free IgG, and FGF2/IgG protein samples in 1.3% agarose gels (50 mM MES buffer; pH, 7.0–8.5), staining with Coomassie Brilliant Blue dye demonstrated that the higher isoelectric point of FGF2 (pI = 9.58) resulted in a slower migrating species compared with the migration pattern observed for free IgG (pI = 6.6–7.2) (**Figure 4A**). Of special interest, on gel lanes with concentrated FGF2/IgG mixtures, we saw a distinct band shift, whereby FGF2 reduced the migration distance for free IgG in the gel (**Figure 4A**). A series of different gel runs demonstrated that the interaction of FGF2 with IgG occurred across a range of pH (7.0–8.5) (data not shown). Furthermore, by solid phase binding assays, we observed a dose-responsive increase in low molecular weight FGF2 binding to IgG (**Table 1**).

Signaling by FGF2 and HGF increases the survival of many different primary and transformed cell types (Nakamura and Mizuno, 2010; Ornitz and Itoh, 2015). In light of increased endothelial cell survival and vascular integrity conferred by HGF/IgG after MI/R (Rao et al., 2015), we tested FGF2/IgG in cell protection assays with primary human cardiac microvascular endothelial cells under culture conditions that simulated ischemia (nutrient deprivation and 1% oxygen). By MTS assay, a measure of cell metabolism, FGF2/IgG complexes significantly improved endothelial cell viability during 48 h of exposure compared with cells that were incubated in a matched concentration of IgG (**Figure 4B**). In agreement, quantification of cell survival using a nucleic acid dye-binding assay (Cyquant Direct) after 72 h of simulated ischemia demonstrated a significant increase in survival of microvascular endothelial cells incubated in FGF2/IgG complexes (**Figure 4C**). Together, these assays indicated that

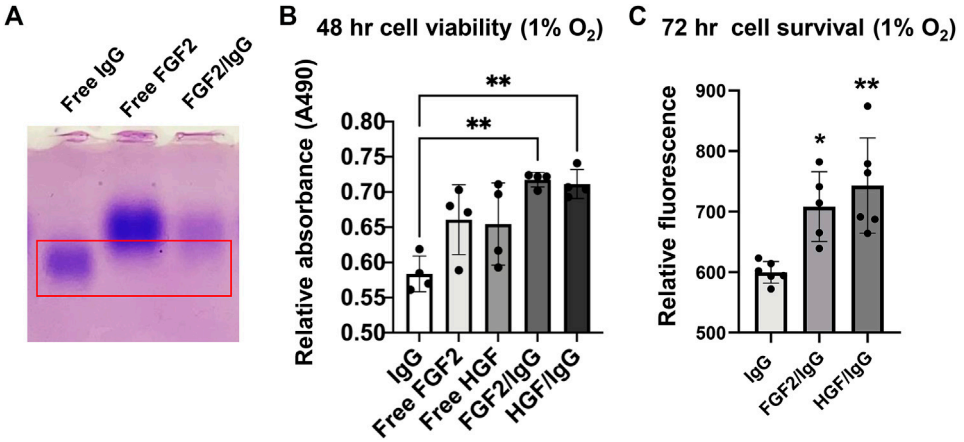

FIGURE 4 | FGF2/IgG complexes protect primary human cardiac microvascular endothelial cells against simulated ischemia for 48–72 h. **(A)** Native isoelectric focusing gel to detect protein complexes. Lanes: 1) free IgG (alone); 2) free FGF2 (alone); 3) FGF2/IgG complexes. Gel was stained for 30 min with Coomassie brilliant blue and de-stained overnight in 10% acetic acid. Red box: note that the protein band expected for free IgG is absent in the right-hand lane with FGF2/IgG complexes. **(B)** MTS assay demonstrated increased cell viability conferred by FGF2/IgG and HGF/IgG complexes relative to IgG alone (matched dose) after 48 h of exposure to 1% oxygen and nutrient deprivation. Data are mean ± SD, n = 4 experimental replicates. *$p < 0.05$, compared with IgG. **(C)** CyQuant assays showed that FGF2/IgG and HGF/IgG complexes protected human cardiac microvascular endothelial cells against simulated ischemia for 72 h. Data are mean ± SD and were analyzed by one-way ANOVA with *post-hoc* comparisons. n = 6 experimental replicates. **$p < 0.01$, compared with IgG.

TABLE 1 | Dose-responsive increase in human FGF2 binding to immobilized IgG. Numbers represent mean absorbance (450 nm) and SD values from human FGF2 ELISA. Assays were run in duplicate.

Input	FGF2	
IgG	4 ng/ml	10 ng/ml
100 ng/ml	0.014 ± 0.011	0.042 ± 0.001
500 ng/ml	0.04 ± 0.003	0.071 ± 0.006
10,000 ng/ml	0.193 ± 0.148	0.46 ± 0.045

FGF2/IgG complexes provided a similar level of microvascular endothelial cell protection as did HGF/IgG complexes, under matched experimental conditions (**Figures 4B,C**).

PatchDock/PyMOL Modeling of Human Growth Factor/IgG Interactions

Binding of FGF2 ligands to their cognate receptor(s) FGFR1, 2, 3 is facilitated by heparan sulphate proteoglycan co-factors (Ornitz and Itoh, 2015). Binding occurs within IgG-like subdomains of the receptor, followed by receptor dimerization; this enables the receptor to bind two FGF2 ligands (Schlessinger et al., 2000). Given the dimeric binding of FGF2 to FGFR, we were curious if the FGF2/IgG complexes mimicked endogenous ligand-receptor binding and whether polyclonal IgG could structurally accommodate two FGF2 molecules. To ascertain the probable conformations of FGF2 and HGF in complex with IgG, we generated 3-dimensional protein docking models based on available crystal structures. We compared our FGF2/IgG model to a published crystal structure of FGF2 with heparin glycan co-factor bound to FGFR1 (FGFR1 PDB ID:1FQ9; **Figure 5A**).

In docking experiments to model the geometry of FGF2/IgG complexes (**Figure 5B**), the IgG1 crystal structure (PDB ID: 1HZH) was prepared in PyMOL, by removing waters and Fab fragments, leaving only the Fc dimer (residues 244–478 of 1HZH). This PDB file was uploaded to the PatchDock server as the "receptor" molecule (Schneidman-Duhovny et al., 2005). Next a single molecule of FGF2 (chain A from PDB ID 1CVS, residues 158–286 of the full-length 288 amino acid isoform 1) was uploaded as the "ligand" molecule. Clustering RMSD and complex type were both set to default before submitting the run. The top 100 solutions, scored based on surface geometric complementarity and area of contact, were retrieved. The first six high-scoring poses were eliminated as they placed the N- and/or C-termini of FGF2 facing into the surface of IgG. In this configuration, the full length FGF2 protein would extend from these residues and clash with IgG. Therefore, the seventh highest ranked pose was selected for use in our model (**Figure 5B**).

A docking experiment to model possible interactions between HGF pan domain and IgG Fc was performed in a manner similar to that of the first docking experiment (**Figure 5C**). First, IgG1 Fc (PDB ID: 1HZH with waters and Fab fragments removed) was uploaded as the "receptor" molecule. Then, the HGF pan domain (chain A from PDB ID: 3HMS, corresponding to residues 36–126 of the full-length 728 amino acid HGF isoform 1, was then uploaded to PatchDock as the "ligand" molecule, and the docking parameters were set as before. The top three poses were eliminated as in the first docking experiment due to clashes that would exist between full-length HGF and IgG. The fourth highest ranking pose was therefore selected for our model (**Figure 5C**).

The majority of docking solutions placed FGF2 or HGF pan at the joint between the first and second Ig domains of the Fc region,

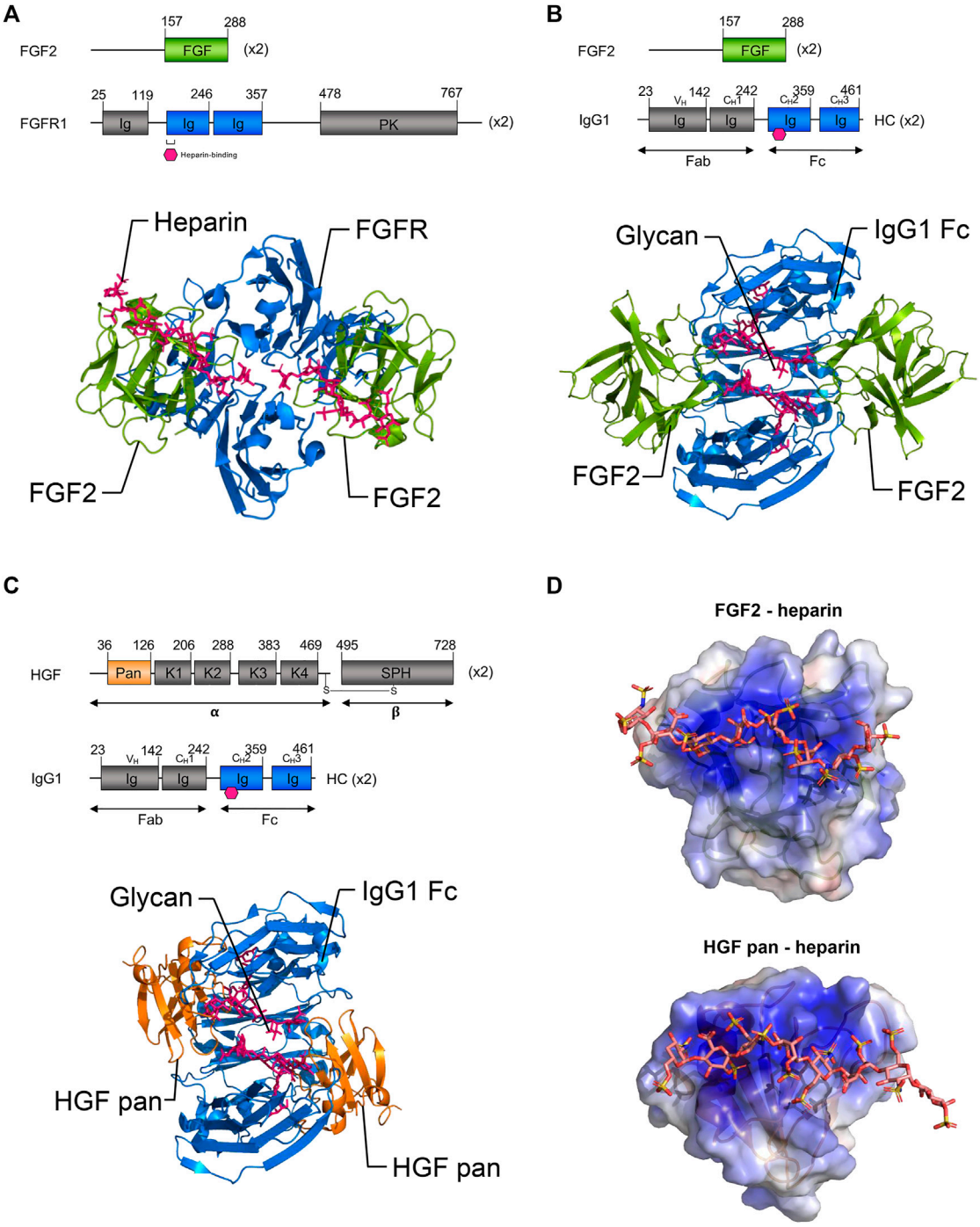

FIGURE 5 | Three-dimensional modeling of proposed growth factor: IgG complexes. **(A)** Top: Schematic representations of full-length FGF2 and FGFR1. Bottom: Ribbon representations of FGF2 (residues 158–286, green) bound to FGFR1 (blue) and heparin (pink) (published crystal structure, PDB ID 1FQ9). Note the binding of FGF2 proteins to FGFR1 occurs within immunoglobulin-like sub-domains. **(B)** Top: Schematic representations of the proposed binding of FGF2 to the IgG1 Fc domain. Bottom: Ribbon model of proposed binding of FGF2 (green) to the Fc domain of IgG1 (blue) within FGF2/IgG complexes. Note that based on similarities to FGF2: FGFR1 binding, it is possible that the Fc domain of IgG may accommodate the binding of two FGF2 ligands. **(C)** Top: Schematic representations of the HGF pan domain and IgG1. Bottom: Ribbon model of proposed binding of HGF pan domain (orange) to the Fc domain of IgG1 (blue) in HGF/IgG complexes. Note that it is also possible that the Fc domain of IgG may accommodate the binding of two HGF ligands. **(B,C)** Pink hexagon (top) and sticks (bottom) = glycosylation. **(D)** Electrostatic surface potential models of FGF2 and HGF pan domain bound to heparin (sticks) (PDB IDs 1FQ9 and 1GMO, respectively). Note growth factors have heparin binding domains that are thought to bind within immunoglobulin-like domains of their respective RTK receptors. Basic patches (blue surface) may be involved in the binding of FGF2 and HGF in the described complexes. PK, protein kinase; HC, heavy chain; K1–K4, Kringle domains; SPH, serine protease homology domain; alpha, HGF alpha chain; beta, HGF beta chain. Gray, domains not shown in ribbon diagrams.

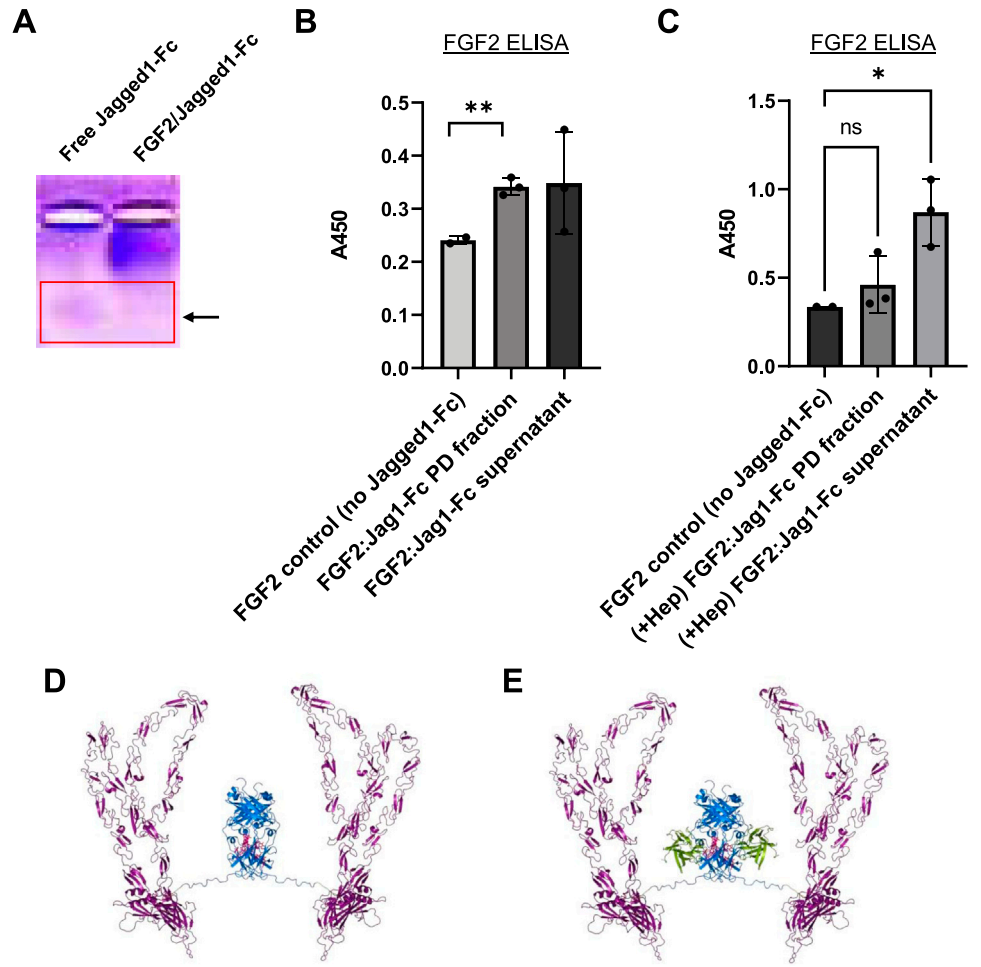

FIGURE 6 | Generation of recombinant human FGF2/Jagged1-Fc complexes. **(A)** Native isoelectric focusing gel to detect protein complexes. Lanes: 1) free Jagged1- Fc fusion protein (alone); 2) FGF2/Jagged1-Fc complex. Red box: note that the protein band expected for free Jagged1-Fc IgG is absent in the right-hand lane with FGF2/Jagged1-Fc complexes. Thus, complexation with FGF2 retards the migration of Jagged1-Fc. **(B)** ELISA data for FGF2 to assay complex formation. FGF2 was incubated either alone or with Jagged1-Fc-His, followed by addition of anti-His-biotin. Streptavidin-agarose was used to pulldown complexes and 0.5% Sodium deoxycholate was used to dissociate protein-protein interactions prior to FGF2 ELISA. Data in **(B,C)** are mean ± SD and were analyzed by one-way ANOVA with *post-hoc* comparisons. n = two to three experimental replicates. $^{**}p < 0.01$. **(C)** Addition of excess heparin (50 μg) during initial incubation of FGF2 with Jagged-Fc-His prevents complex formation. $^{**}p < 0.01$. **(D)** Ribbon representation of modeled Jagged1-Fc fusion protein homodimer. **(E)** Ribbon representation of modeled Jagged1-Fc fusion in complex with FGF2.

with nearly an equal number on either of side of the Fc region of IgG in between the CH3 and CH2 domains. Notably, FGF2 and HGF both have heparin binding domains that are thought to bind within immunoglobulin-like domains of their respective RTK receptors (Spivak-Kroizman et al., 1994). Both FGF2 and HGF pan domain are roughly spherical and are similar in size, suggesting their associations with IgG could be spatially comparable.

The glycosylation sites on the CH3 Ig domain within the Fc portion of IgG are similar in position and size to the heparin-binding sites within the second IgG-like domain of FGFR. Thus, it is plausible that IgG glycosylation may function in a manner analogous with heparin. In agreement with this concept, electrostatic surface potential models generated using the APBS plugin for PyMOL of the growth factor/IgG complexes highlighted the potential for interactions at heparin binding domains (**Figure 5D**).

Complexes Formed Between Human FGF2 and Jagged1-Fc

We next asked whether fusion of the Fc domain from IgG1 to proteins of interest could be utilized to form new protein complexes. Although IgG1 Fc is currently used in many FDA-approved biologics to improve drug half-life and reduce clearance, in this case, we hypothesized here that the Fc domain would allow Jagged1, a Notch1 receptor ligand, to interact in a novel way with FGF2. In concept, growth factors or cytokines that do not naturally bind IgG could potentially expressed as Fc-fusion proteins, and then combined with HGF or

FGF2 to form complexes. In support of this hypothetical system, native gel electrophoresis of concentrated mixtures of FGF2/Jagged1-Fc demonstrated a shift in migration pattern relative to Jagged1-Fc alone (**Figure 6A**).

To confirm complex formation with FGF2 and Jagged1-Fc, we performed a series of biochemical pulldown experiments. Taking advantage of the 6x histidine purification tag on Jagged1-Fc, we combined FGF2 and Jagged1-Fc at an estimated equimolar ratio. Following a 2 h incubation at room temperature and storage overnight at 4°C, we incubated the samples for 2 h with anti-his-biotin. Then, streptavidin-agarose beads and centrifugation were used to pulldown the Jagged1-Fc. Following several washes, 0.5% Sodium Deoxycholate was used to dissociate the putative complexes and FGF2 ELISA was used to detect FGF2 that had complexed with Jagged1-Fc. By FGF2 ELISA, we detected significantly more FGF2 in pulldowns where FGF2 was incubated with Jagged1-Fc relative to control pulldowns, which contained FGF2 but lacked Jagged1-Fc (**Figure 6B**). In support of the hypothesis that the Fc domain of IgG1 interacts with FGF2 in a manner similar to heparin, addition of excess heparin during incubation of FGF2 and Jagged1-Fc prevented complex formation; this resulted in FGF2 remaining in the supernatant rather than being pulled down by streptavidin-agarose (**Figure 6C**).

To visualize a mode of Jagged1-Fc interaction with FGF2 consistent with our FGF2/IgG Fc docking results, we built a model of Jagged1-Fc fusion protein (catalog # 1277-JG, R&D Systems, Minneapolis, MN, United States) using the AlphaFold v2.0 human Jagged-1 model (Ser32-Ser1046) spliced to human IgG1 (residues corresponding to Pro100-Lys330 of Uniprot accession # P01857 of the 1HZH structure), via an Ile-Glu-Gly-Arg-Met-Asp linker using PyMOL (Senior et al., 2020) (**Figures 6D,E**). Our native gel and pulldown results, and models, illustrate how an Fc fusion protein and FGF2 can be combined to form unique protein complexes. Notably, this strategy has exciting potential to provide a customizable platform to create new biologic drugs.

DISCUSSION

Our results in adult pigs demonstrated that intra-arterially administered HGF/IgG complexes distributed throughout the myocardium after PCI and stenting and were retained for at least 24 h after MI/R. Of three intracoronary HGF doses tested, we found that the middle dose with 62.5 μg human HGF and 105 μg porcine IgG was most effective at providing myocardial salvage and reducing infarct size. Furthermore, multiple infusions of species-matched HGF/IgG complexes after MI/R did not induce an immune response against HGF. Thus, as a formulation, HGF/IgG complexes may enhance retention of HGF and the duration of cytoprotective receptor signaling.

HGF is composed of α-subunit and β-subunits that are joined by a disulfide linkage. Functional domains within the subunits include an N-terminal hairpin domain, four kringle domains, and a catalytically inactive serine protease domain (Niemann, 2013). The canonical HGF receptor c-MET is a heterodimeric protein composed of a 50 kD extracellular α-chain and a 145 kD β-chain. In addition to the extracellular region, the β-chain also contains a single-pass transmembrane domain and a cytoplasmic tail which contains the active tyrosine kinase domain (Organ and Tsao, 2011). Analysis of crystal structures of HGF/c-MET showed HGF binding occurs within the β-chain, which contains a heparin sulphate binding domain (Organ and Tsao, 2011). HGF induces dimerization of c-MET, followed by tyrosine kinase activity and autophosphorylation, which triggers the recruitment of downstream adaptor molecules. Signaling through the HGF/c-MET axis results in signal propagation through multiple downstream adaptor pathways including: PI3K/Akt, Ras/Raf/MAPK, JAK/STAT and Wnt/β-Catenin (Organ and Tsao, 2011; Holland et al., 2013; Koraishy et al., 2014; Zhang et al., 2018). HGF signaling regulates tissue growth and morphogenesis during development, as well as cell migration, survival, angiogenesis and fibrosis during repair/remodeling after injury (Bottaro et al., 1991).

In a rat model of MI, Ono et al. reported elevated plasma levels of HGF were present 60 min following reperfusion (Ono et al., 1997). HGF and c-MET mRNA levels increased in the heart 3-fold at 24–48 h following reperfusion, and remained elevated for 120 h. Nakamura et al. reported treatment with recombinant HGF was cardioprotective against ischemia/reperfusion injury in rats (Nakamura et al., 2000), and reduced cardiomyocyte death and infarct size compared with controls. In contrast, administration of neutralizing antisera against endogenous HGF resulted in increased cardiac cell death and infarct expansion (Nakamura et al., 2000).

FGF2 has multiple isoforms ranging from 18 to 34 kDa that enable a wide array of possible quaternary structures that affect protein function (Yu et al., 2007). Several high molecular weight isoforms of FGF2 promote fibrosis after tissue injury. By contrast, low molecular weight FGF2 (18 kDa) and HGF are both reported to reduce fibrosis (Wang et al., 2004; Liao et al., 2007; Koo et al., 2018). Fibroblast Growth Factor Receptors (FGFRs) are tyrosine kinases activated by the binding of FGF ligands and heparan sulphate proteoglycans (HSPGs), which act as co-factors (Yayon et al., 1991). The presence of HSPGs potentiates FGFR activity and also enhances ligand binding via a high affinity binding site (Ornitz and Itoh, 2015). HSPGs exist as cell surface-bound proteoglycans, transmembrane proteoglycans, or, are bound by the extracellular matrix (Matsuo and Kimura-Yoshida, 2013). FGF2-FGFR binding results in signal transduction through multiple pathways including RAS-MAPK, PI3K-AKT, PLCγ and STAT (Eliceiri, 2001; Liao et al., 2007; Ahmad et al., 2012). FGF2 signaling plays fundamental roles in skeletal and neural development and controls the proliferation, differentiation, and survival of numerous adult somatic cell types. Also, it regulates critical processes such as angiogenesis and fibrosis during tissue remodeling/repair (Karajannis et al., 2006; Kardami et al., 2007; Müller et al., 2012).

In a canine model of MI, intracoronary injection of FGF2 was shown to reduce infarct size and improve cardiac function (Yanagisawa-Miwa et al., 1992). Furthermore, the authors reported that FGF2 treatment promoted myocardial angiogenesis, and resulted in increased vessel density in the FGF2-treated group compared with vehicle-treated control animals (Yanagisawa-Miwa et al., 1992). In isolated mouse hearts subjected to 60 min ischemia/reperfusion, specific knockout of low molecular weight FGF2 reduced capacity for

recovery and cardiac performance relative to that of wild type mice (Liao et al., 2007).

Intra-arterially administered FGF2 has been tested in clinical trials for patients with atherosclerotic peripheral arterial disease and intermittent claudication (Lazarous et al., 1997) as well as cardiac atherosclerosis (Simons et al., 2002). Although one or two treatments with FGF2 was well-tolerated, efficacy was limited. For example, in the phase II FGF Initiating RevaScularization Trial (FIRST), a double-blind, randomized, and controlled study, a single intracoronary infusion of FGF2 was given to patients with severe coronary artery disease (Simons et al., 2002). Notably, however, treatment with FGF2 at 0, 0.3, 3, or 30 μg/kg did not improve exercise tolerance, the primary clinical endpoint (Simons et al., 2002). Lack of success in several trials was attributed, in part, to unsatisfactory pharmacokinetic profiles for FGF2 (Bush et al., 2001). Similar to other growth factor proteins, FGF2 is quickly eliminated from the circulation, with a serum half-life of 50 min and poor target tissue distribution (Lazarous et al., 1997). Efforts directed at improving the pharmacokinetic profile of FGF2 may increase its therapeutic potential. For example, treatment with FGF2 encapsulated into sustained-release heparin-alginate coated capsules during coronary bypass graft surgery resulted in improved myocardial perfusion and a near complete cessation of angina related symptoms (Ruel et al., 2002).

In regard to the non-covalent interaction of HGF and FGF2 with polyclonal, non-specific IgG, it is notable that both growth factors bind within IgG-like domains of their respective receptors. Also, ligand-receptor interaction for both growth factors is potentiated by heparin and heparan sulphate proteoglycans embedded within the ECM (Chirgadze et al., 1999; Schlessinger et al., 2000; Basilico et al., 2008). The fusion of the Fc domain of IgG to proteins prolongs serum half-life, reduces clearance, and has been widely adopted for the production of therapeutic biologics. For example, Etanercept, an FDA-approved tumor necrosis factor receptor: Fc fusion protein, is indicated for multiple inflammatory conditions such as rheumatoid arthritis and plaque psoriasis (Scott, 2014). The improved pharmacokinetic profile of Fc fusion proteins is primarily due to Fc domain binding to the neonatal receptor for IgG (FcRn) (Roopenian and Akilesh, 2007; Suzuki et al., 2010; Czajkowsky et al., 2012). Similar to Fc-fusion proteins, the distribution and retention of HGF/IgG and FGF2/IgG complexes in the heart and other target tissues may benefit from interactions with FcRn.

The pro- and anti-inflammatory activities of IgGs are modulated through interaction of the IgG Fc domain with distinct IgG Fc receptors (FcγRs) on cells (Nimmerjahn and Ravetch, 2008). Heavy chain glycosylation of IgG Fc domains determines, in part, whether antibodies can bind FcγRs on immune cells to stimulate antibody-dependent cellular cytotoxicity (Shinkawa et al., 2002). Previous work suggests that IgG Fc core glycosylation, predominantly with sialic acid sugar moieties, may act as an "immunological switch," imparting anti-inflammatory properties to IgGs (Kaneko et al., 2006; Anthony and Ravetch, 2010). In this regard, it is of great interest to determine the anti- or pro-inflammatory properties of FGF2/IgG and HGF/IgG *in vivo* and whether the complexes impact local immune cell responses in myocardial tissue after MI/R injury. Importantly, in the case that IgG Fc core glycosylation state is integral to formation and biological activity of growth factor/IgG and FGF2/Fc-fusion complexes, there may be opportunity to tune the properties of complexes based on the glycosylation state of the Fc domain.

Extensive progress in the areas of biomaterials and bioengineering has improved growth factor delivery to tissues/organs with the purpose of promoting tissue repair and regeneration. Examples include scaffolds composed with biodegradable hydrogels or other substrates and seeded with paracrine-acting, reparative cells or purified growth factors. Diverse permutations and designs are possible, and hydrogels may be further modified with extracellular matrix components, drugs, microparticles or nanoparticles (Bruggeman et al., 2016; Xu et al., 2018; Bruggeman et al., 2019; Dong et al., 2020; Roy et al., 2021). Whereas we used a systemic, intra-arterial route here to administer growth factor/IgG complexes, it seems plausible that therapeutic complexes could be embedded within bioengineered substrates or matrices to control timing and localization of release for different applications. Further study will be required to determine the complement of receptors and signaling pathway(s) engaged by FGF2/IgG and FGF2/Jagged1-Fc fusion protein complexes and whether or not they are cardio- and vasoprotective or improve vascular integrity or angiogenesis after MI/R. In addition to treating MI, growth factor/IgG complexes or FGF2/Fc-fusion complexes may be well suited to improve tissue survival and function after organ transplantation or to treat other forms of injury such as diabetic neuropathy, peripheral artery disease, chronic ulcer, and stroke.

MATERIALS AND METHODS

Purification of Recombinant Human Growth Factors

To facilitate cell adhesion, 150 mm^2 plates (Nunc, Denmark) were pre-coated with human fibronectin (5 μg/ml in PBS). For production of recombinant human HGF, a stable HEK293 HGF-producer cell line (Rao et al., 2015) was grown in DMEM/F12 medium supplemented with 5% FBS (Atlanta Biologicals, Lawrenceville, GA, USA). Medium was changed every 2 days until the cells reached confluence, after which the media was switched to serum-free DMEM/F12. We collected cell-conditioned medium (Cdm) after 24 and 48 h. To remove cell debris, Cdm was filtered (0.2 μm) and stored at −80°C. For purification by SP-Sepharose cation exchange chromatography, the Cdm was adjusted to pH 6.5 to facilitate HGF binding to resin. Cdm was loaded onto a SP-sepharose column that was prepared with an equilibration buffer: 20 mM sodium phosphate (pH 6.5) buffer with 0.02% Tween-80. The column was washed with five volumes of equilibration buffer and then five volumes of equilibration buffer with 0.05 M NaCl. The bound HGF was eluted using a two-step elution: 1) Low salt (equilibration buffer with 0.4 M NaCl), and 2) High salt (equilibration buffer with 0.8 M NaCl). Peak fractions were determined by Bradford protein assay and human HGF ELISA according to the manufacturer's instructions (HGF Duoset Kit, R&D Systems).

Peak fractions eluted off SP-sepharose resin were pooled and diluted 1:1 with equilibration buffer: 20 mM sodium phosphate, 300 mM sodium chloride and 10 mM imidazole, pH 7.4. Fractions were then loaded by gravity onto a column with 2 ml of Ni- NTA resin (ThermoFisher Scientific, Waltham, MA, United States). The column was washed with PBS supplemented with 25 mM imidazole (pH 7.4) and eluted with PBS with 300 mM imidazole.

Recombinant human FGF2 (18 kDa) was purified from a bacterial expression system (*Escherichia coli* strain BL21), as reported previously (Miao et al., 2020). Briefly, bacteria were grown in Luria-Bertani (LB) broth with ampicillin. Cells were lysed by sonication and the cell extract was pelleted (3,600 × *g* for 10 min). The supernatant was loaded onto a 1 ml column with Ni-NTA resin (ThermoFisher Scientific, Waltham, MA, United States). FGF2 was eluted with 400 mM imidazole. Protein concentration was determined by Bradford protein assay and protein composition and purity was assessed by SDS-PAGE. The eluate was desalted and loaded onto a 1 ml heparin-sepharose affinity column (GE Healthcare Bio-Sciences, Pittsburg, PA, USA). Bound FGF2 was eluted from the heparin-sepharose column with PBS supplemented with 1.5 M NaCl.

Human Endothelial Cell Protection Studies Under Simulated Ischemia

Primary human cardiac microvascular endothelial cells (HCMVEC) were from multiple donors and three vendors (Lonza Bioscience, Basel, Switzerland; PromoCell, Heidelberg, Germany; ScienCell, Carlsbad, CA, USA). HCMVEC cells were grown in endothelial cell-specific media with supplements (EGM-2MV SingleQuots, Lonza Bioscience; ECGS, PromoCell; ECGS, ScienCell) containing 5% FCS and PenStrep, at 37°C with 5% CO_2. Cells were seeded in tissue culture plates (Nunc), expanded as needed and frozen down. For cell protection studies, HCMVEC were used between passages 2 and 4. Primary HCMVECs were plated into 48-well plates (Nunc) at 1×10^4 or 2 × 104 cells/well. Cells were grown at 37°C with 5% CO_2 in endothelial cell growth medium with 5% FCS. All cells were plated 48 h prior to the start of the experiment. For simulated ischemia (oxygen and nutrient deprivation), cells were briefly washed with PBS to remove serum and the medium was switched to serum-free DMEM/F12 with or without various treatments. Cells were exposed to hypoxia (1% oxygen) in a dedicated, specialized incubator fed by nitrogen gas. After 48 or 72 h, plates were removed from the incubator, briefly rinsed with PBS, and frozen at −80°C. For MTS assay of cell viability, the CellTiter 96 Aqueous One solution Cell Proliferation Assay Kit (Promega, Madison, WI, United States) was used according to the manufacturer's instructions. For quantification of cell survival, a DNA binding dye was used (CyQuant assay, Molecular Probes Invitrogen, Waltham, MA, United States). To ensure full cell lysis and dye incorporation, cells were subjected to 3× freeze-thaw cycles in lysis buffer. The lysis mixture was loaded into fluoroblock plates (Nunc) and relative fluorescence was determined by plate reader (Synergy HT, Biotek, Winooski, VT, USA).

Preparation of Rat HGF/IgG Complexes

Recombinant rat HGF (Sino Biological US Inc., Wayne, PA, USA) was diluted to a working concentration of 2 μg/ml in sterile PBS. Non-specific, polyclonal IgG from rat serum (Sigma-Aldrich, St. Louis, MO, United States) was diluted to 1.2 μg/ml in sterile PBS. For each injection, a dose of 10 μg of HGF and 6 μg rat IgG was prepared. The HGF was mixed with the IgG in a total volume of 15 ml and concentrated 40-fold (from 15 ml to 375 μl over 45 min) using an Amicon ultracentrifugal filter unit (10 kDa cut-off filter; Millipore Sigma, Bedford, MA, USA).

Myocardial Ischemia-Reperfusion Surgery and Treatment With HGF/IgG Complexes in Rats

All animal work was approved by the University of Vermont College of Medicine's Office of Animal Care in accordance with the American Association for Accreditation of Laboratory Animal Care and National Institutes of Health guidelines. Sprague Dawley rats (8 weeks of age) were anaesthetized with 4% isoflurane (to effect) and endotracheally-intubated. Rats were ventilated (Harvard Apparatus, Holliston, MA, United States) and body temperature was maintained with a heated pad (Gaymar T Pump; Stryker, Kalmazoo, MI, United States). Through a dermal incision, a blunt dissection was performed, and the intercostal muscles were separated. The heart was exposed, the LAD coronary artery was encircled with 10–0 nylon suture, and the LAD was occluded. The occlusion was confirmed by blanching of the anterior wall of the left ventricle. The incision was closed, and the animals were allowed to recover off the ventilator. After 2 h of ischemia, the rats were reintubated under anesthesia, ventilated and the chest wall was reopened. The hearts were exposed, and the suture was released. Reperfusion was confirmed by observing blood flow through the LAD and color returning to the previously blanched area. Immediately after reperfusion, or each rat, 125 μl of PBS containing either rat IgG or rat HGF/IgG complexes was injected through the left ventricle wall and into the LV lumen. After the injection, the chest wall was closed with two to three layers of suture. The rats with MI were returned to the vivarium for recovery and were kept for additional infusions and collection of blood plasma. Subsequently, the animals received tail vein "booster" injections with HGF/IgG or IgG on days 3 and 5 post-operation. For sham-operated animals, the chest wall was opened to visualize the intact pericardium (twice); this approach corresponded to that for the ischemia/reperfusion surgery. In sham-operated animals, the suture was passed under the LAD, but the artery was not ligated. No other surgical manipulations were carried out with the sham-operated animals.

Modified ELISA for Auto-Antibodies Produced Against HGF/IgG Complexes

Following ischemia-reperfusion surgery, blood was drawn at 1, 2, 3 and 4 weeks time points, centrifuged, and the resulting plasma was collected and stored at −80°C. For the detection of auto-antibodies against rat HGF in blood plasma, assays were

performed as previously described (Spees et al., 2004; Gregory et al., 2006). Briefly, 1 μg/ml recombinant rat HGF (Sino Biologics, Beijing, China) suspended in PBS was adsorbed onto high protein-binding plates (Nunc) overnight at 4°C, with shaking. The following day, the plate was blocked in PBS (pH 7.4) with 1% BSA (ThermoFisher Scientific, Waltham, MA, United States) for 2 h at room temperature. Following blocking and additional washes, plasma samples were diluted (50-fold or 100-fold) in blocking buffer (1% BSA in PBS, pH 7.4, 0.2 μm filtered) and incubated overnight at 4°C, with shaking. The next day, the plasma wells were washed and incubated for 2 h with goat anti-rat horseradish peroxidase-conjugated antibodies (1:200, Invitrogen, Waltham, MA, United States). A reference standard curve was created with a polyclonal rabbit anti-HGF antibody (Sigma-Aldrich, St. Louis, MO, United States) and pure rat HGF that was pre-adsorbed to the wells. The reference samples were washed and incubated 2 h with a goat anti-rabbit horseradish peroxidase-conjugated antibody (1:2,000, Sigma-Aldrich, St. Louis, MO, United States). Following PBS washes, the plate was incubated with Ultra TMB substrate solution (ThermoFisher Scientific, Waltham, MA, United States) for 50 min. Following color development, stop solution (2 M sulfuric acid) was added to neutralize the substrate solution and absorbance was determined at 450 nM (Synergy HT; Biotek, Winooski, VT).

Preparation of HGF/IgG Complexes for Porcine Injections

HGF/IgG complexes were prepared 12–16 h prior to injection and stored at 4–6 °C. A dose of 31.25, 62.5, or 125 μg human HGF and 52.5, 105, or 210 μg mixed polyclonal pig IgG was used for each pig, representing a 1:1 molar ratio for each dose tested. Sterile growth factors and IgG were mixed in a total volume of 5 ml and added to an Amicon centrifugal concentration unit. The mixture was then centrifuged at 1,100 × *g* for 30 min at room temperature. In some cases, complexes were centrifuged for an additional 5 min, until a final volume of 300 μl was reached. The complexes were then stored at 4°C overnight. On the day of injection, complexes were reconstituted in sterile DMEM/F12 at a total volume of 12.5 ml.

Myocardial Ischemia-Reperfusion Surgery in Adult Pigs and Treatment With HGF/IgG Complexes

All work with pigs was performed under a UVM Institutional Animal Care and Use Committee-approved protocol and followed USDA guidelines. Commercial swine (Barrows, ~50 kg) were pre-medicated with Meloxicam (0.2 mg/kg, PO) sedated with an injection of ketamine (15–20 mg/kg, IM) and atropine (0.05–0.5 mg/kg, IM), masked with isoflurane (5%), and intubated. Anesthesia was maintained with isoflurane (2.5%, inhaled). Intravenous catheters were placed in each ear for drug and fluid administration. A baseline transthoracic echocardiography (ECHO) was performed. Under sterile conditions, a cut-down was done to access the right femoral artery and a 6F vascular introducer was inserted. A blood sample was taken (20 ml) and heparin administered (300 μl/kg, IV) to prevent clotting during the catheterization procedure. A bolus of amiodarone (50 mg, IV) was given to reduce heart irritability and a bolus of fentanyl (0.05 mg/kg, IV) followed by a fentanyl infusion (0.05 mg/kg/h, IV) was given to reduce the amount of isoflurane required for anesthesia. Under fluoroscopic guidance, a guide catheter was inserted and advanced into the opening of the LAD coronary artery. This was followed by a guide wire that was advanced into the distal LAD. A balloon catheter (with or without a stent) was advanced over the wire and positioned in the LAD. Stents were used to later identify the previous position of the balloon during inflation. An infusion of amiodarone was started (10 mg/kg, IV; over 30 min) to additionally reduce heart irritability. The balloon was inflated to eliminate blood supply to a region of the heart muscle for 60 min. Pigs were monitored by electrocardiogram and pulse-oximetry and provided with fluid and thermal support. In the event that ventricular tachycardia or cardiac arrest occurred during the occlusion, appropriate measures were taken to resuscitate the pig, including intravenous lidocaine, amiodarone, epinephrine, and electrical defibrillation.

The balloon was deflated, and reperfusion was confirmed by injection of a bolus of contrast dye through the guide catheter. DMEM/F12 (vehicle control) or protein complexes in vehicle were infused into the LAD from the indwelling guide catheter. Treatments were administered by manual injection in the LAD artery [a.k.a. intracoronary (12.5 ml)]. Following occlusion, physiological parameters and cardiac arrest events were carefully recorded for all pigs. When present, ventricular fibrillation events were promptly addressed with DC cardioversion. The catheter was removed and the femoral artery blood flow restored. After the access site was repaired, additional pain medication was administered (Meloxicam; 0.02 mg/kg, SC), and the animals were monitored continuously until anesthesia wore off and then were transferred to a housing facility.

At 24 h after MI/R surgery and treatment, animals were re-anesthetized and a median sternatomy was performed to gain access to the heart. Umbilical tape snares (1/8 in wide) were placed around the descending aorta, left subclavian artery, and bracheocephalic artery, but not occluded. A silk suture was placed around the LAD artery at the location of the previous balloon inflation, but not occluded. A 7F catheter was inserted into the right carotid artery and the tip advanced beyond the snare into the ascending aorta above the aortic valve. After ventricular fibrillation was induced by brief contact of the myocardium with a 9 V direct current battery, the LAD and snares were occluded. The isolated coronary circulation was perfused with 1.5% Evans blue via the carotid catheter to identify the area at risk. The heart was then removed, sliced at 1 cm thickness with a sharpened brain knife, and photographed to identify the area at risk. Slices were then incubated with 1.5% triphenyltetrazolium (TTC, 30°C) for 25 min and photographed again to identify areas with infarction (white, necrotic).

Immunohistochemistry

Following Evans Blue/TTC staining of pig hearts, tissue slices were fixed in 10% formalin and paraffin embedding. Ten-micron serial sections were made from blocks of tissue bordering the zone with infarction. Prior to immunohistochemical staining, paraffin was removed by xylenes and alcohol (100%–70%). Tissue sections were washed with PBS and antibody retrieval was performed using 20 μg/ml proteinase K (20 min at RT). Slides were blocked for 1 h in PBS containing 5% normal goat serum and 0.1% Triton X-100, washed with PBS, and incubated at 4°C overnight with primary antibody (anti-6x histidine, 1:1,000, Catalog number MA 1-21315; Invitrogen, Waltham, MA, United States). Following incubation with primary antibody, the slides were washed 3 × 5 min with PBS and incubated with secondary antibody for 1 h at room temperature (1:1,000, rabbit anti-mouse IgG conjugated with ALEXA 594; Invitrogen, Waltham, MA, United States). After 3 × 5 min washes in PBS, slides were mounted with Vectashield containing DAPI (Vector Laboratories, Burlingame, CA, United States). Epifluorescence images were taken using a Leica DM6000B microscope equipped with a CCD camera and Leica imaging software.

Native Gel Electrophoresis for Detection of FGF2/IgG and FGF2/Jagged1-Fc Protein Complexes

Native gel electrophoresis was performed using 50 mM MES sodium buffer with 1.3% agarose (ThermoFisher Scientific, Waltham, MA, United States). Adjustments to pH were made, depending on experimental parameters. All gels were run using ice-cold buffer. Purified FGF2, Jagged1-Fc, or IgG were run individually (i.e., free) or as FGF2/IgG or FGF2/Jagged1- Fc complexes to assess their respective mobilities. Human FGF2 was cloned, expressed, and purified in our laboratory (Rao et al., 2015; Miao et al., 2020). Jagged1- Fc was commercial (R&D Systems). Depending on the molar ratios for different complexes, the total protein load for each lane varied between 3.0 and 4.0 μg. After completion of runs, the gels were stained for 30 min at room temperature with Coomassie Brilliant Blue dye and de-stained overnight in 10% acetic acid in deionized water.

Solid Phase Binding Assays

For solid phase binding assays, polyclonal human IgG was incubated overnight at different concentrations in PBS on ELISA plates (100, 500, or 10,000 ng/ml). Following 3× PBS washes, low molecular weight (18 kDa) human FGF2 was incubated at 4 or 10 ng/ml for 2 h. After additional PBS washes, the amount of bound FGF2 was detected by ELISA (R&D Systems).

Pulldown of FGF2/Jagged 1-Fc Complexes Using Biotinylated Anti-6x Histidine and Streptavidin-Conjugated Agarose

Growth factor complexes were prepared in 25 μl of PBS (pH 7.4) by mixing 0.5 μg human FGF2 with 7.8 μg of rat Jagged1-Fc-His (catalog # 599-JG, R&D Systems). Notably, these amounts represented an estimated 1:1 molar ratio. As a control, we also incubated separate tubes with 25 μl of PBS (pH 7.4) and 0.5 μg human FGF2 alone (i.e., no Jagged1-Fc). The samples were incubated for 2 h at room temperature (with shaking) and the tubes were then placed at 4°C overnight. The following day, 2 μg of a biotinylated anti-6x His antibody (Invitrogen, Waltham, MA, United States) was added to the complexes and incubated for 2 h with shaking at 4°C. The complexes were then incubated with streptavidin-agarose beads (ThermoFisher Scientific, Waltham, MA, United States) for 48 h, with shaking at 4°C. The beads were pelleted by centrifugation for 10 min at 3,000 × *g*. The supernatant was reserved for ELISA and the pelleted beads were washed 4× with PBS prior to incubation with 0.5% Sodium Deoxycholate (SDC) to disrupt protein-protein interactions. The pulldown supernatant and the detergent soluble fractions were diluted and analyzed by ELISA (human FGF2 Duoset Kit, R&D Systems), according to the manufacturer's instructions. In some cases, excess heparin sodium (50 μg) was added to the initial 25 μl incubation. To control for possible effects of SDC on ELISA, we added an equivalent amount of SDC to all samples prior to assay.

Modeling Geometry of Growth Factor/Immunoglobulin Complexes

Docking simulations were made with Patchdock molecular docking server using published crystal structures of IgG, FGF2 and HGF. Separate docking experiments were performed to identify probable associations between: 1) FGF2 and the Fc domain of IgG1, and 2) HGF pan domain and the Fc domain of IgG1. Figures were generated using PyMOL molecular visualization software.

Statistical Analysis

Statistical analysis was performed with GraphPad Prism software (version 6.0e). Values were expressed as means ± SD unless indicated otherwise. Comparisons of data from individual control and treatment groups were made by unpaired Student's t-test. For experiments comparing multiple treatment groups, we performed One-way ANOVA with *post-hoc* testing. For studies comparing multiple treatment groups across multiple time points, a Two-way ANOVA with repeated measures design was used. Values of $p \leq 0.05$ were considered statistically significant.

DATA AVAILABILITY STATEMENT

The original contributions presented in the study are included in the article/supplementary materials, further inquiries can be directed to the corresponding author.

ETHICS STATEMENT

The animal study was reviewed and approved by UVM Institutional Animal Care and Use Committee.

AUTHOR CONTRIBUTIONS

BL, AF, AA, SB, PG, and JS designed the experiments. BL, CS, AF, KR, TM, AA, SB, PG, RL, and JS performed the experiments, assays and data analysis. BL, CS, AF, SB, and JS wrote the paper.

FUNDING

This work was supported, in part, by National Institutes of Health (NIH) grant HL132264 (to JS). Additional support was provided by the Cardiovascular Research Institute of Vermont (CVRI-VT) and the UVM Ventures Program.

REFERENCES

Ahmad, I., Iwata, T., and Leung, H. Y. (2012). Mechanisms of FGFR-Mediated Carcinogenesis. *Biochim. Biophys. Acta (Bba) - Mol. Cel Res.* 1823, 850–860. doi:10.1016/j.bbamcr.2012.01.004

Anderson, J. L., and Morrow, D. A. (2017). Acute Myocardial Infarction. *N. Engl. J. Med.* 376 (21), 2053–2064. doi:10.1056/NEJMra1606915

Anthony, R. M., and Ravetch, J. V. (2010). A Novel Role for the IgG Fc Glycan: The Anti-inflammatory Activity of Sialylated IgG Fcs. *J. Clin. Immunol.* 30, 9–14. doi:10.1007/s10875-010-9405-6

Appasamy, R., Tanabe, M., Murase, N., Zarnegar, R., Venkataramanan, R., Van Thiel, D. H., et al. (1993). Hepatocyte Growth Factor, Blood Clearance, Organ Uptake, and Biliary Excretion in normal and Partially Hepatectomized Rats. *Lab. Invest.* 68 (3), 270–276.

Bagai, A., Dangas, G. D., Stone, G. W., and Granger, C. B. (2014). Reperfusion Strategies in Acute Coronary Syndromes. *Circ. Res.* 114, 1918–1928. doi:10.1161/CIRCRESAHA.114.302744

Banquet, S., Gomez, E., Nicol, L., Edwards-Lévy, F., Henry, J.-P., Cao, R., et al. (2011). Arteriogenic Therapy by Intramyocardial Sustained Delivery of a Novel Growth Factor Combination Prevents Chronic Heart Failure. *Circulation* 124 (9), 1059–1069. doi:10.1161/CIRCULATIONAHA.110.010264

Barć, P., Antkiewicz, M., Śliwa, B., Frączkowska, K., Guziński, M., Dawiskiba, T., et al. (2020). Double VEGF/HGF Gene Therapy in Critical Limb Ischemia Complicated by Diabetes Mellitus. *J. Cardiovasc. Trans. Res.* 14, 409–415. doi:10.1007/s12265-020-10066-9–7

Basilico, C., Arnesano, A., Galluzzo, M., Comoglio, P. M., and Michieli, P. (2008). A High Affinity Hepatocyte Growth Factor-Binding Site in the Immunoglobulin-like Region of Met. *J. Biol. Chem.* 283 (30), 21267–21277. doi:10.1074/jbc.M800727200

Bottaro, D. P., Rubin, J. S., Faletto, D. L., Chan, A. M. L., Kmiecik, T. E., Woude, G. F. V., et al. (1991). Identification of the Hepatocyte Growth Factor Receptor as the C-Met Proto-Oncogene Product. *Science* 251 (4995), 802–804. doi:10.1126/science.1846706

Bruggeman, K. F., Moriarty, N., Dowd, E., Nisbet, D. R., and Parish, C. L. (2019). Harnessing Stem Cells and Biomaterials to Promote Neural Repair. *Br. J. Pharmacol.* 176 (3), 355–368. doi:10.1111/bph.14545Epub 2018 Dec 21. PMID: 30444942; PMCID: PMC6329623

Bruggeman, K. F., Rodriguez, A. L., Parish, C. L., Williams, R. J., and Nisbet, D. R. (2016). Temporally Controlled Release of Multiple Growth Factors from a Self-Assembling Peptide Hydrogel. *Nanotechnology* 27 (38), 385102. doi:10.1088/0957-4484/27/38/385102

Bush, M. A., Samara, E., Whitehouse, M. J., Yoshizawa, C., Novicki, D. L., Pike, M., et al. (2001). Pharmacokinetics and Pharmacodynamics of Recombinant FGF-2 in a Phase I Trial in Coronary Artery Disease. *J. Clin. Pharmacol.* 41 (4), 378–385. doi:10.1177/00912700122010230

Czajkowsky, D. M., Hu, J., Shao, Z., and Pleass, R. J. (2012). Fc-fusion Proteins: New Developments and Future Perspectives. *EMBO Mol. Med.* 4, 1015–1028. doi:10.1002/emmm.201201379

Dong, Y., Cui, M., Qu, J., Wang, X., Kwon, S. H., Barrera, J., et al. (2020). Conformable Hyaluronic Acid Hydrogel Delivers Adipose-Derived Stem Cells and Promotes Regeneration of Burn Injury. *Acta Biomater.* 108, 56–66. doi:10.1016/J.ACTBIO.2020.03.040

Eisen, A., Giugliano, R. P., and Braunwald, E. (2016). Updates on Acute Coronary Syndrome. *JAMA Cardiol.* 1, 718. doi:10.1001/jamacardio.2016.2049

Eliceiri, B. P. (2001). Integrin and Growth Factor Receptor Crosstalk, *Circ. Res.* 89 (12), 1104–1110. doi:10.1161/hh2401.101084

Garcia-Dorado, D., Ruiz-Meana, M., and Piper, H. M. (2009). Lethal Reperfusion Injury in Acute Myocardial Infarction: Facts and Unresolved Issues. *Cardiovasc. Res.* 83, 165–168. doi:10.1093/cvr/cvp185

Gherardi, E., Chirgadze, D. Y., Hepple, J. P., Zhou, H., Byrd, R. A., and Blundell, T. L. (1999). Crystal Structure of the NK1 Fragment of HGF/SF Suggests a Novel Mode for Growth Factor Dimerization and Receptor Binding. *Nat. Struct. Biol.* 6 (1), 72–79. doi:10.1038/4947

Gregory, C. A., Reyes, E., Whitney, M. J., and Spees, J. L. (2006). Enhanced Engraftment of Mesenchymal Stem Cells in a Cutaneous Wound Model by Culture in Allogenic Species-Specific Serum and Administration in Fibrin Constructs. *Stem Cells* 24 (10), 2232–2243. doi:10.1634/stemcells.2005-0612

Her, M., and Kavanaugh, A. (2016). Alterations in Immune Function with Biologic Therapies for Autoimmune Disease. *J. Allergy Clin. Immunol.* 137, 19–27. doi:10.1016/j.jaci.2015.10.023

Holland, J. D., Györffy, B., Vogel, R., Eckert, K., Valenti, G., Fang, L., et al. (2013). Combined Wnt/β-Catenin, Met, and CXCL12/CXCR4 Signals Characterize Basal Breast Cancer and Predict Disease Outcome. *Cel Rep.* 5 (5), 1214–1227. doi:10.1016/j.celrep.2013.11.001

Kaneko, Y., Nimmerjahn, F., and Ravetch, J. V. (2006). Anti-inflammatory Activity of Immunoglobulin G Resulting from Fc Sialylation. *Science* 313 (5787), 670–673. doi:10.1126/science.1129594

Karajannis, M. A., Vincent, L., DiRenzo, R., Shmelkov, S. V., Zhang, F., Feldman, E. J., et al. (2006). Activation of FGFR1β Signaling Pathway Promotes Survival, Migration and Resistance to Chemotherapy in Acute Myeloid Leukemia Cells. *Leukemia* 20 (6), 979–986. doi:10.1038/sj.leu.2404203

Kardami, E., Detillieux, K., Ma, X., Jiang, Z., Santiago, J. J., Jimenez, S. K., et al. (2007). Fibroblast Growth Factor-2 and Cardioprotection. *Heart Fail. Rev.* 12 (3-4), 267–277. doi:10.1007/s10741-007-9027-0

Koo, H. Y., El-Baz, L. M., House, S., Cilvik, S. N., Dorry, S. J., Shoukry, N. M., et al. (2018). Fibroblast Growth Factor 2 Decreases Bleomycin-Induced Pulmonary Fibrosis and Inhibits Fibroblast Collagen Production and Myofibroblast Differentiation. *J. Pathol.* 246 (1), 54–66. doi:10.1002/path.5106

Koraishy, F. M., Silva, C., Mason, S., Wu, D., and Cantley, L. G. (2014). Hepatocyte Growth Factor (Hgf) Stimulates Low Density Lipoprotein Receptor-Related Protein (Lrp) 5/6 Phosphorylation and Promotes Canonical Wnt Signaling. *J. Biol. Chem.* 289 (20), 14341–14350. doi:10.1074/jbc.M114.563213

Lazarous, D. F., Shou, M., Stiber, J. A., Dadhania, D. M., Thirumurti, V., Hodge, E., et al. (1997). Pharmacodynamics of Basic Fibroblast Growth Factor: Route of Administration Determines Myocardial and Systemic Distribution. *Cardiovasc. Res.* 36 (1), 78–85. doi:10.1016/S0008-6363(97)00142-9

Liao, S., Porter, D., Scott, A., Newman, G., Doetschman, T., and Schultz, J. E. J. (2007). The Cardioprotective Effect of the Low Molecular Weight Isoform of Fibroblast Growth Factor-2: The Role of JNK Signaling. *J. Mol. Cell Cardiol.* 42 (1), 106–120. doi:10.1016/j.yjmcc.2006.10.005

Matsuo, I., and Kimura-Yoshida, C. (2013). Extracellular Modulation of Fibroblast Growth Factor Signaling through Heparan Sulfate Proteoglycans in Mammalian Development. *Curr. Opin. Genet. Dev.* 23 (4), 399–407. doi:10.1016/j.gde.2013.02.004

Miao, T., Little, A. C., Aronshtam, A., Marquis, T., Fenn, S. L., Hristova, M., et al. (2020). Internalized FGF-2-Loaded Nanoparticles Increase Nuclear ERK1/2 Content and Result in Lung Cancer Cell Death. *Nanomaterials* 10 (4), 612. doi:10.3390/nano10040612

Müller, A. K., Meyer, M., and Werner, S. (2012). The Roles of Receptor Tyrosine Kinases and Their Ligands in the Wound Repair Process. *Semin. Cell Dev. Biol.* 23 (9), 963–970. doi:10.1016/j.semcdb.2012.09.015

Nakamura, T., Mizuno, S., Matsumoto, K., Sawa, Y., Matsuda, H., and Nakamura, T. (2000). Myocardial protection from Ischemia/reperfusion Injury by Endogenous and Exogenous HGF. *J. Clin. Invest.* 106 (12), 1511–1519. doi:10.1172/JCI10226

Nakamura, T., and Mizuno, S. (2010). The Discovery of Hepatocyte Growth Factor (HGF) and its Significance for Cell Biology, Life Sciences and Clinical Medicine. *Proc. Jpn. Acad. Ser. B: Phys. Biol. Sci.* 86, 588–610. doi:10.2183/pjab.86.588

Niemann, H. H. (2013). Structural Basis of MET Receptor Dimerization by the Bacterial Invasion Protein InlB and the HGF/SF Splice Variant NK1. *Biochim. Biophys. Acta.* 34 (10), 2195–2204. doi:10.1016/j.bbapap.2012.10.012

Nimmerjahn, F., and Ravetch, J. V. (2008). Fcγ Receptors as Regulators of Immune Responses. *Nat. Rev. Immunol.* 8, 34–47. doi:10.1038/nri2206

O'Gara, P. T., Kushner, F. G., Ascheim, D. D., Casey, D. E., Chung, M. K., de Lemos, J. A., et al. (2013). 2013 ACCF/AHA Guideline for the Management of ST-Elevation Myocardial Infarction. *J. Am. Coll. Cardiol.* 61, e78–e140. doi:10.1016/j.jacc.2012.11.019

Ono, K., Matsumori, A., Shioi, T., Furukawa, Y., and Sasayama, S. (1997). Enhanced Expression of Hepatocyte Growth Factor/c-Met by Myocardial Ischemia and Reperfusion in a Rat Model. *Circulation* 95 (11), 2552–2558. doi:10.1161/01.CIR.95.11.2552

Organ, S. L., and Tsao, M. S. (2011). An Overview of the C-MET Signaling Pathway. *Ther. Adv. Med. Oncol.* 3 (1_Suppl. l), S7–S19. doi:10.1177/1758834011422556

Ornitz, D. M., and Itoh, N. (2015). The Fibroblast Growth Factor Signaling Pathway. *Wires Dev. Biol.* 4 (3), 215–266. doi:10.1002/wdev.176

Rao, K. S., Aronshtam, A., McElory-Yaggy, K. L., Bakondi, B., VanBuren, P., Sobel, B. E., et al. (2015). Human Epicardial Cell-Conditioned Medium Contains HGF/IgG Complexes that Phosphorylate RYK and Protect against Vascular Injury. *Cardiovasc. Res.* 107 (2), 277–286. doi:10.1093/cvr/cvv168

Roopenian, D. C., and Akilesh, S. (2007). FcRn: the Neonatal Fc Receptor Comes of Age. *Nat. Rev. Immunol.* 7, 715–725. doi:10.1038/nri2155

Roy, T., James, B. D., and Allen, J. B. (2021). Anti-VEGF-R2 Aptamer and RGD Peptide Synergize in a Bifunctional Hydrogel for Enhanced Angiogenic Potential. *Macromol. Biosci.* 21 (2), 2000337. doi:10.1002/mabi.202000337

Ruel, M., Laham, R. J., Parker, J. A., Post, M. J., Ware, J. A., Simons, M., et al. (2002). Long-term Effects of Surgical Angiogenic Therapy with Fibroblast Growth Factor 2 Protein. *J. Thorac. Cardiovasc. Surg.* 124 (1), 28–34. doi:10.1067/mtc.2002.121974

Schlessinger, J., Plotnikov, A. N., Ibrahimi, O. A., Eliseenkova, A. V., Yeh, B. K., Yayon, A., et al. (2000). Crystal Structure of a Ternary FGF-FGFR-Heparin Complex Reveals a Dual Role for Heparin in FGFR Binding and Dimerization. *Mol. Cel* 6 (3), 743–750. doi:10.1016/S1097-2765(00)00073-3

Schneider, D. J., and Sobel, B. E. (2008). A Novel Role for Tissue-Type Plasminogen Activator: Prevention of Thromboembolic Occlusion. *Circulation* 118 (14): 1408–1409. doi:10.1161/CIRCULATIONAHA.108.807586

Schneidman-Duhovny, D., Inbar, Y., Nussinov, R., and Wolfson, H. J. (2005). PatchDock and SymmDock: Servers for Rigid and Symmetric Docking. *Nucl. Acids Res.* 33, W363–W367. doi:10.1093/nar/gki481

Scott, L. J. (2014). Etanercept: a Review of its Use in Autoimmune Inflammatory Diseases. *Drugs* 74 (12), 1379–1410. doi:10.1007/s40265-014-0258-9

Senior, A. W., Evans, R., Jumper, J., Kirkpatrick, J., Sifre, L., Green, T., et al. (2020). Improved Protein Structure Prediction Using Potentials from Deep Learning. *Nature* 577, 706–710. doi:10.1038/s41586-019-1923-7

Shinkawa, T., Nakamura, K., Yamane, N., Shoji-Hosaka, E., Kanda, Y., Sakurada, M., et al. (2003). The Absence of Fucose but Not the Presence of Galactose or Bisecting N-Acetylglucosamine of Human IgG1 Complex-type Oligosaccharides Shows the Critical Role of Enhancing Antibody-dependent Cellular Cytotoxicity. *J. Biol. Chem.* 278, 3466–3473. doi:10.1074/jbc.M210665200

Simons, M., Annex, B. H., Laham, R. J., Kleiman, N., Henry, T., Dauerman, H., et al. (2002). Pharmacological Treatment of Coronary Artery Disease with Recombinant Fibroblast Growth Factor-2. *Circulation* 105 (7), 788–793. doi:10.1161/hc0802.104407

Smith, J. N., Negrelli, J. M., Manek, M. B., Hawes, E. M., and Viera, A. J. (2015). Efficient Unbound Docking of Rigid Molecules. *Diagnosis and Management of Acute Coronary Syndrome: An Evidence-Based Update* 28 (2), 283–293. doi:10.3122/jabfm.2015.02.140189

Spees, J. L., Gregory, C. A., Singh, H., Tucker, H. A., Peister, A., Lynch, P. J., et al. (2004). Internalized Antigens Must Be Removed to Prepare Hypoimmunogenic Mesenchymal Stem Cells for Cell and Gene Therapy. *Mol. Ther.* 9 (5), 747–756. doi:10.1016/j.ymthe.2004.02.012

Spivak-Kroizman, T., Lemmon, M. A., Dikic, I., Ladbury, J. E., Pinchasi, D., Huang, J., et al. (1994). Heparin-induced Oligomerization of FGF Molecules Is Responsible for FGF Receptor Dimerization, Activation, and Cell Proliferation. *Cell* 79 (6), 1015–1024. doi:10.1016/0092-8674(94)90032-9

Suzuki, T., Ishii-Watabe, A., Tada, M., Kobayashi, T., Kanayasu-Toyoda, T., Kawanishi, T., et al. (2010). Importance of Neonatal FcR in Regulating the Serum Half-Life of Therapeutic Proteins Containing the Fc Domain of Human IgG1: a Comparative Study of the Affinity of Monoclonal Antibodies and Fc-Fusion Proteins to Human Neonatal FcR. *J. Immunol.* 184 (4), 1968–1976. doi:10.4049/jimmunol.0903296

Verma, S., Fedak, P. W. M., Weisel, R. D., Butany, J., Rao, V., Maitland, A., et al. (2002). Fundamentals of Reperfusion Injury for the Clinical Cardiologist. *Circulation* 105 (20), 2332–2336. doi:10.1161/01.CIR.0000016602.96363.36

Virani, S. S., Alonso, A., Benjamin, E. J., Bittencourt, M. S., Callaway, C. W., Carson, A. P., et al. (2020). Heart Disease and Stroke Statistics-2020 Update: A Report from the American Heart Association. *Circulation* 141 (9), e139–e596. doi:10.1161/CIR.0000000000000757

Vogel, B., Claessen, B. E., Arnold, S. V., Chan, D., Cohen, D. J., Giannitsis, E., et al. (2019). ST-segment Elevation Myocardial Infarction. *Nat. Rev. Dis. Primers* 5 (1), 39. doi:10.1038/s41572-019-0090-3

Wang, Y., Ahmad, N., Wani, M., and Ashraf, M. (2004). Hepatocyte Growth Factor Prevents Ventricular Remodeling and Dysfunction in Mice via Akt Pathway and Angiogenesis. *J. Mol. Cell Cardiol.* 37 (5), 1041–1052. doi:10.1016/j.yjmcc.2004.09.004

Xu, Q., Sigen, A., Gao, Y., Guo, L., Creagh-Flynn, J., Zhou, D., et al. (2018). A Hybrid Injectable Hydrogel from Hyperbranched PEG Macromer as a Stem Cell Delivery and Retention Platform for Diabetic Wound Healing. *Acta Biomater.* 75, 63–74. doi:10.1016/j.actbio.2018.05.039

Yanagisawa-Miwa, A., Uchida, Y., Nakamura, F., Tomaru, T., Kido, H., Kamijo, T., et al. (1992). Salvage of Infarcted Myocardium by Angiogenic Action of Basic Fibroblast Growth Factor. *Science* 257 (5075), 1401–1403. doi:10.1126/science.1382313

Yang, Z.-J., Zhang, Y.-R., Chen, B., Zhang, S.-L., Jia, E.-Z., Wang, L.-S., et al. (2009). Phase I Clinical Trial on Intracoronary Administration of Ad-hHGF Treating Severe Coronary Artery Disease. *Mol. Biol. Rep.* 36 (6), 1323–1329. doi:10.1007/s11033-008-9315-3

Yayon, A., Klagsbrun, M., Esko, J. D., Leder, P., and Ornitz, D. M. (1991). Cell Surface, Heparin-like Molecules Are Required for Binding of Basic Fibroblast Growth Factor to its High Affinity Receptor. *Cell* 64 (4), 841–848. doi:10.1016/0092-8674(91)90512-w

Yellon, D. M., and Hausenloy, D. J. (2007). Myocardial Reperfusion Injury. *N. Engl. J. Med.* 357 (11), 1121–1135. doi:10.1056/nejmra071667

Yu, P.-J., Ferrari, G., Galloway, A. C., Mignatti, P., and Pintucci, G. (2007). Basic Fibroblast Growth Factor (FGF-2): The High Molecular Weight Forms Come of Age. *J. Cel. Biochem.* 100 (5), 1100–1108. doi:10.1002/jcb.21116

Zhang, Y., Xia, M., Jin, K., Wu, Y., Lii, X., Zengi, Z., et al. (2018). Function of the C-Met Receptor Tyrosine Kinase in Carcinogenesis and Associated Therapeutic Opportunities. *Mol. Cancer* 17. doi:10.1186/s12943-018-0796-y

Conflict of Interest: JS holds several patents in regard to human epicardial progenitor cells, secreted growth factors, and HGF/IgG and is co-founder and Chief Scientific Officer of Samba BioLogics, Inc.

The remaining authors declare that the research was conducted in the absence of any commercial or financial relationships that could be construed as a potential conflict of interest.

Publisher's Note: All claims expressed in this article are solely those of the authors and do not necessarily represent those of their affiliated organizations, or those of the publisher, the editors and the reviewers. Any product that may be evaluated in this article, or claim that may be made by its manufacturer, is not guaranteed or endorsed by the publisher.

Advantages of publishing in Frontiers

OPEN ACCESS
Articles are free to read for greatest visibility and readership

FAST PUBLICATION
Around 90 days from submission to decision

HIGH QUALITY PEER-REVIEW
Rigorous, collaborative, and constructive peer-review

TRANSPARENT PEER-REVIEW
Editors and reviewers acknowledged by name on published articles

Frontiers
Avenue du Tribunal-Fédéral 34
1005 Lausanne | Switzerland

Visit us: www.frontiersin.org
Contact us: frontiersin.org/about/contact

REPRODUCIBILITY OF RESEARCH
Support open data and methods to enhance research reproducibility

DIGITAL PUBLISHING
Articles designed for optimal readership across devices

FOLLOW US
@frontiersin

IMPACT METRICS
Advanced article metrics track visibility across digital media

EXTENSIVE PROMOTION
Marketing and promotion of impactful research

LOOP RESEARCH NETWORK
Our network increases your article's readership